ACADEMIC YEAR 2010

The Lippmann Session

Centre International des Sciences Mécaniques

International Centre for Mechanical Sciences

CISM

motus est vita

ULTRASOUND STANDING WAVE ACTION ON SUSPENSIONS AND BIOSUSPENSIONS IN MICRO- AND MACRO FLUIDIC DEVICES

Advanced School
coordinated by

Jürg Dual
ETH, Zürich
Switzerland

Jeremy J. Hawkes
University of Manchester
UK

Udine, *June 7 - 11,* 2010

Contents

M8 Applications

- Laurell - Lecture 2: Acoustic valving and mixing in chemical microreactors
- Hill - Surface Acoustic Wave Devices - No Notes
- Laurell - Lecture 3: Free flow acoustophoresis and binary acoustic separation
- Wiklund - Lecture 2: Designing multifrequency force fields in microsystems
- Nilsson - Lecture 2: Ultrasonic trapping, cell culturing and coupling to bioanalysis
- Laurell - Lecture 4: Affinity probing and biospecific extraction in acoustic standing wave chips
- Wiklund - Lecture 6: Bioanalysis: Enhanced immunoassays and agglutination assays
- Dual - Lecture 6: Particle Manipulation Using Acoustic Radiation Forces in Microachined Devices

Posters

- All Posters

Reading List

Lecturers

Henrik Bruus (Technical University of Denmark, Kongens Lyngby, Denmark)
6 lectures on: Theory of ultrasound standing wave action in microfluidics. Governing equations for flow and diffusion. Perturbation theory of ultrasound including acoustophoresis and acoustic streaming. Emphasis will be placed on basic theoretical concepts and their application to experiments.

Juerg Dual (ETH Zentrum, Zuerich, Switzerland)
6 lectures on: Fundamentals of acoustics and vibrations in solids, fluid structure interaction. piezoelectricity, resonant and non resonant modes of excitation, numerical modeling, applications and characterization.

Martyn Hill (University of Southampton, Great Britain)
6 lectures on: Single and multi degree of freedom oscillators and resonance. 2 and 3 port transducer representations & equivalent circuits. 1D matrix models and circuit element models. Fundamentals of cell manipulation including filtration, concentration and biosensing.

Thomas Laurell (Lund University, Sweden)
5 lectures on: Microfabrication of microchip acoustic resonators and transducer characterisation. Acoustic valving, switching, mixing and chip integrated catalytic microreactors. Free flow acoustophoresis and affinity acoustophoresis in acoustic standing wave chips. Ultrasonic trapping, and coupling to biomedical analysis.

Satwindar Singh Sadhal (University of Southern California, Los Angeles, CA 90089-1453, USA)
6 lectures on: “Acoustic streaming with drops, bubbles and particles.” The nonlinear interaction of ultrasound standing waves with interfaces gives rise to a mean dc flow known as streaming. This phenomenon has been analyzed for drops, bubbles and particles by singular perturbation.

Martin Wiklund (KTH - Royal Institute of Technology, Stockholm, Sweden)
7 lectures on: Applications and practical aspects of ultrasonic manipulation, including instrumentation, optical monitoring, handling of bio-samples, safety and biocompatibility.

M1 General Introduction

Introduction
to
Ultrasound Standing Wave Action on Suspensions and Biosuspensions in Micro- and Macro Fluidic Device

Thomas Laurell

Dept. Measurement Tech. & Industrial Electrical Engineering
Div. Nanobiotechnology
Lund Luniversity
Sweden

thomas.laurell@elmat.lth.se
www.elmat.lth.se/english/research

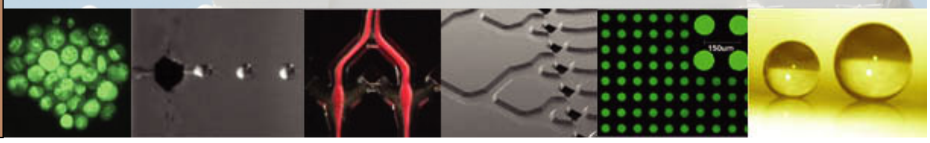

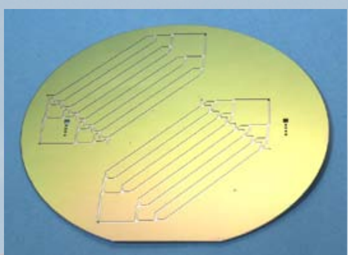

- History
- Acoustic standing wave forces
- Some early players
- $\lambda/2$ resonators
- Microchip integration
- Outline of the week

The Chladni plate

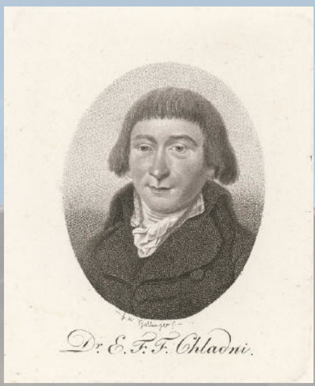

Ernst Chladni (1756-1827) German musician and scientist, sometimes known as 'the father of acoustics,' almost certainly had access to Hooke's work but it is Chladni who history has chosen to acknowledge for his major study of this class of phenomena. He used a sand-strewn brass plate, excited by a violin bow; since brass is a highly resonant material he found that a large number of archetypal geometric patterns could be created, depending on where on the edge of the plate the bow was drawn. These patterns are now known as 'Chladni Figures.'

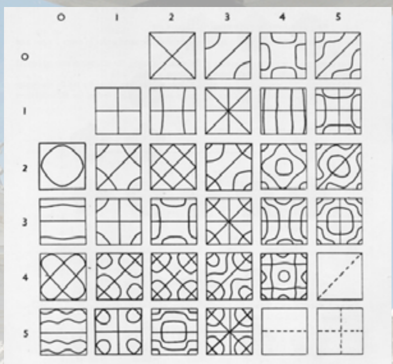

www.cymascope.com

The Chladni plate

Multi nodal excitation

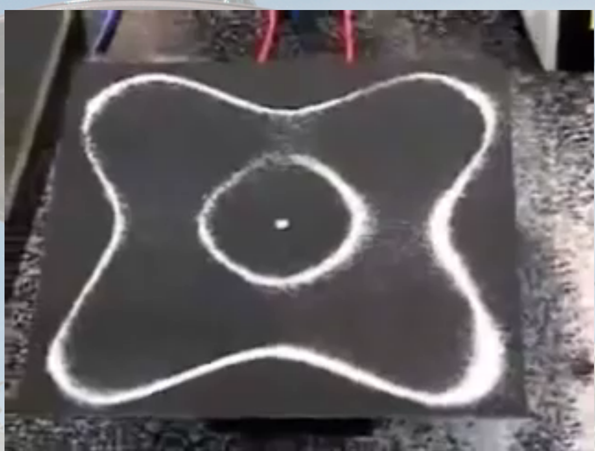

Multi nodal modelling

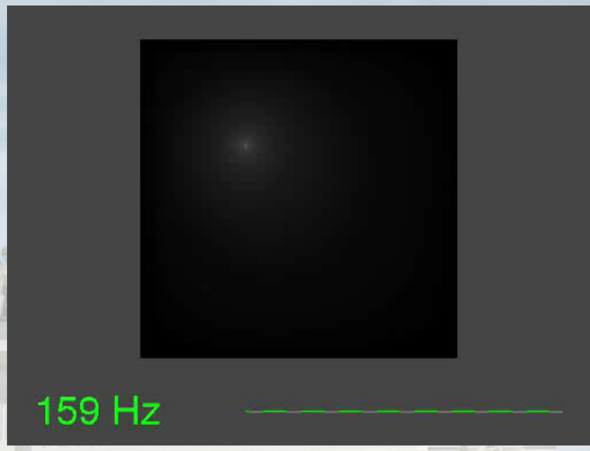

Kundt tube

Drawing from Kundt's original 1866 paper, showing the Kundt's tube apparatus *(fig.6 & 7, top) and the powder patterns created by it (fig.1, 2, 3, 4).*

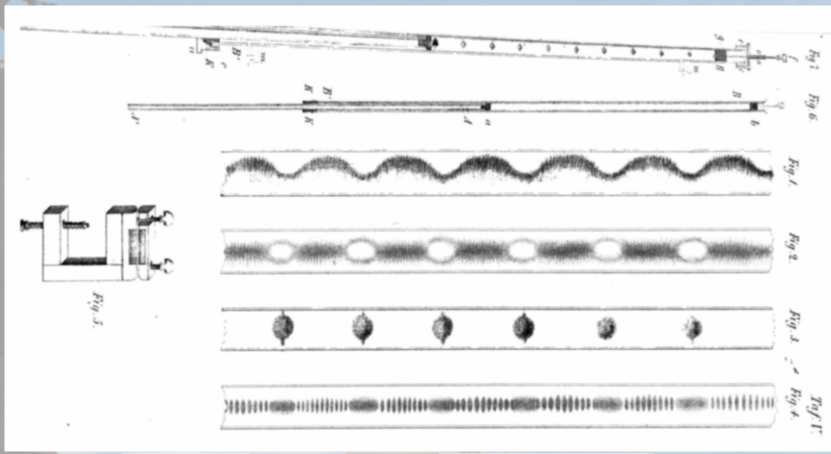

www.wikipedia.com

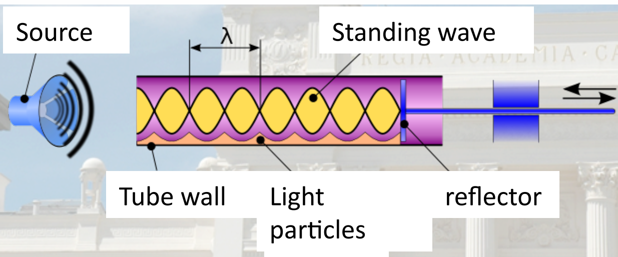

www.wikipedia.com

Kundt tube

www,youtube.com

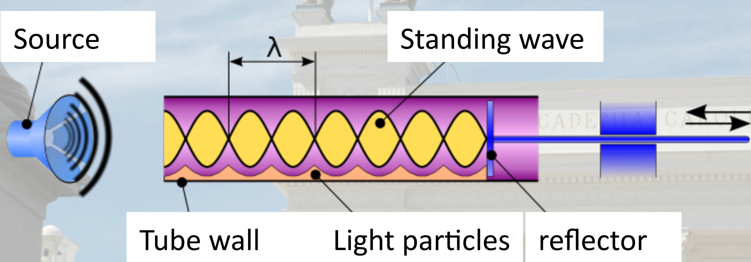

www.wikipedia.com

Particle focusing using ultrasonic standing waves in microscale

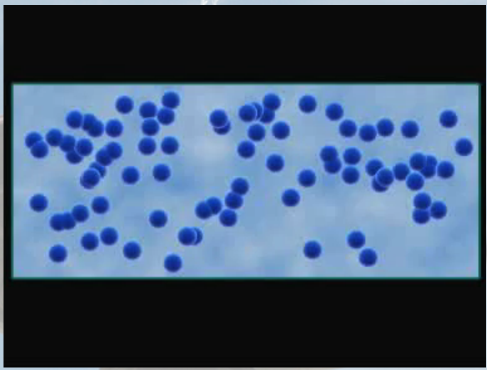

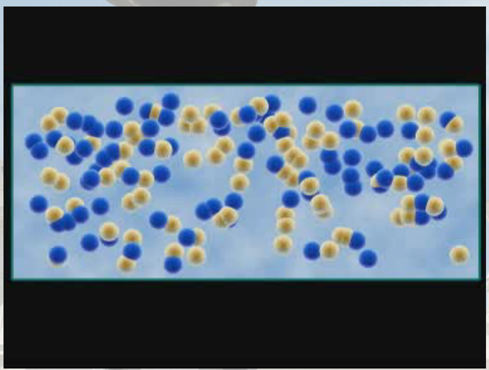

Primary axial acoustic radiation force

$$F_r = -\left(\frac{\pi P_0^2 V_p \beta_m}{2\lambda}\right) \cdot \Phi(\beta, \rho) \cdot \sin\left(\frac{4\pi x}{\lambda}\right)$$

Φ = $(5\rho_c - 2\rho_w)/(2\rho_c + \rho_w) - (\beta_c/\beta_w)$

F_r = acoustic radiation force
P_0 = applied acoustic pressure amplitude
V_c = particle volume
β_w = compressibility of the liquid
β_c = compressibility of the particle
λ = acoustic wave length
z = particle distance to the node
ρ_c = density of the particle
ρ_w = density of the liquid

Acoustic standing wave forces

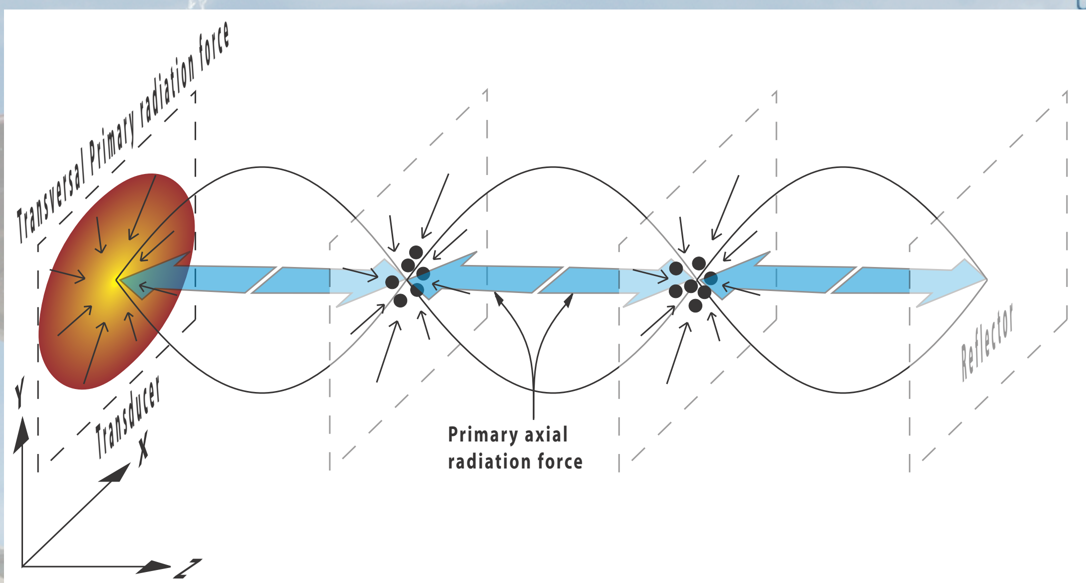

Gorkov, L.P., *On the forces acting on a small particle in an acoustic field inan ideal fluid.* ***Sov. Phys. Doklady***, *1962. 6(9): p. 773-775.*
King, L. V., "On the Acoustic Radiation Pressure on Spheres. ***Proc.R. Soc.***, *a147, 212 (1934).*
Yosioka, K., and Y. Kawasima, "Acoustic Radiation Pressure on a Compressible Sphere. ***Acustica***, *5, 167(1955).*
Woodside, S.M., B.D. Bowen, and J.M. Piret, *Measurement of ultrasonicforces for particle-liquid separations.* ***Aiche J.***, *1997. 43(7): p. 1727-1736*

Transversal acoustic standing wave forces

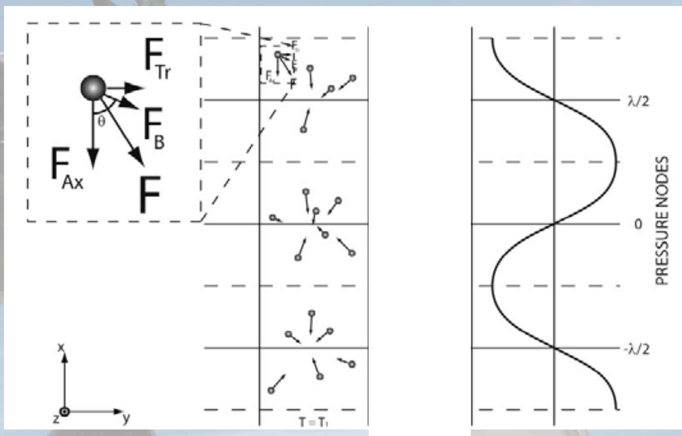

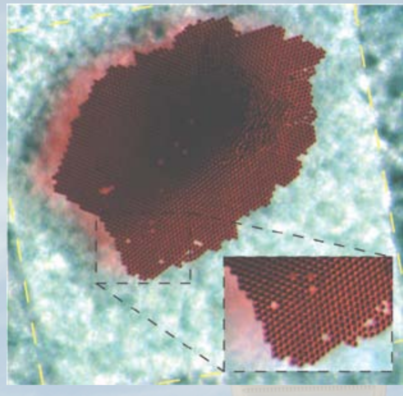

10 LOC Hammarström B. et al accepted

$$F_{Tr} = V_p \nabla \overline{E} \left(\frac{3(\rho_p - \rho_f)}{\rho_f + \rho_p} \cos^2\left(\frac{2\pi x}{\lambda}\right) - \frac{\beta_f - \beta_p}{\beta_f} \sin^2\left(\frac{2\pi x}{\lambda}\right) \right)$$

Primary axial radiation force

$$F_{Ax} = 4\pi \overline{E} R^2 (kR) \sin 2kx \left(\frac{\rho_p + \frac{2}{3}(\rho_p - \rho_f)}{2\rho_p + \rho_f} - \frac{1}{3}\frac{c_f^2 \rho_f}{c_p^2 \rho_p} \right)$$

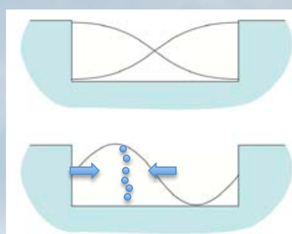

E is the average acoustic energy density
R the radius of the particle
ρ_p is the density of the particle
ρ_f is the density of the surrounding fluid.
c_p and c_f is the speed of sound of the particle and surrounding medium respectively.

$$\overline{E} = \frac{\langle p^2 \rangle}{2\rho_p c_p^2} = \frac{P^2}{4\rho_p c_p^2}$$

$$\beta = \frac{1}{\rho c^2}$$

$$F_{ax} = -\left(\frac{\pi P_0^2 V_p \beta_m}{2\lambda}\right) \cdot \Phi(\beta, \rho) \cdot \sin\left(\frac{4\pi x}{\lambda}\right)$$

$$\Phi = \frac{5\rho_c - 2\rho_w}{2\rho_c + \rho_w} - \frac{\beta_c}{\beta_w}$$

Φ = acoustic contrast factor
F_r = acoustic radiation force
P_0 = applied acoustic pressure amplitude
V_c = particle volume
β_w = compressibility of the liquid
β_c = compressibility of the particle
λ = acoustic wave length
z = particle distance to the node
ρ_c = density of the particle
ρ_w = density of the liquid

Coakley, W.T et al.
Trendsin Biotechnology, 1997. 15(12): p. 506-511.

Secondary radiation force

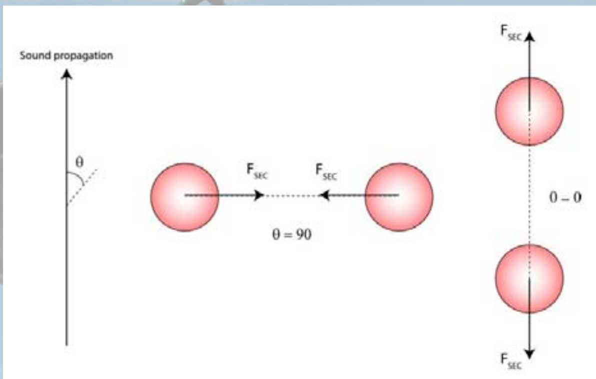

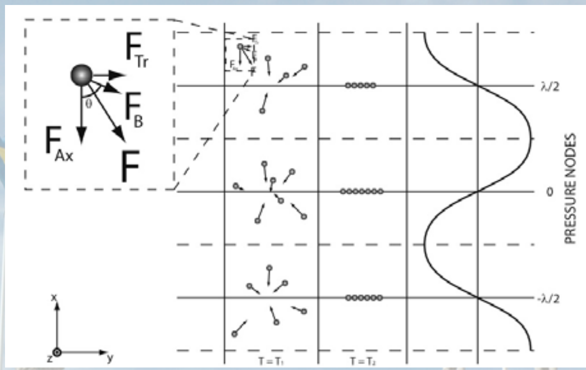

$$F_B(x) = 4\pi R^6 \left[\frac{(\rho_p - \rho_f)^2 (3\cos^2\theta - 1)}{6\rho_f d^4} v^2(x) - \frac{\omega^2 \rho_f (\beta_p - \beta_f)^2}{9d^2} p^2(x) \right]$$

F_B is the secodary acosutic force, also called Bjerknes force, F_B

d is the distance between the particles

Φ is the angle between the center line of the particles and the direction of propagation of the incident acoustic wave

Bjerknes, V.F.K., *Die Kraftfelder. 1909, Vieweg und Sohn: Braunschweig,Germany.*

Acoustic standing wave forces

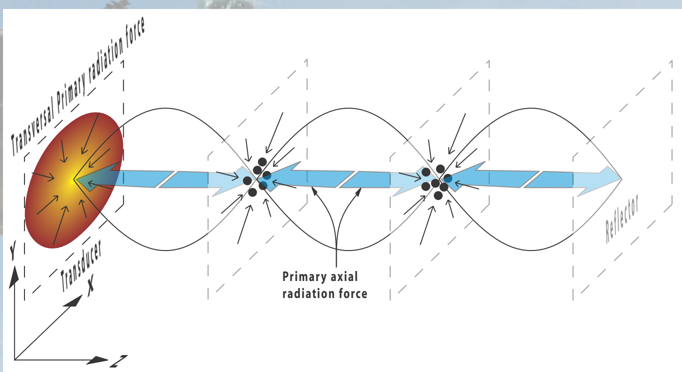

Woodside et al. AIChE, 1997

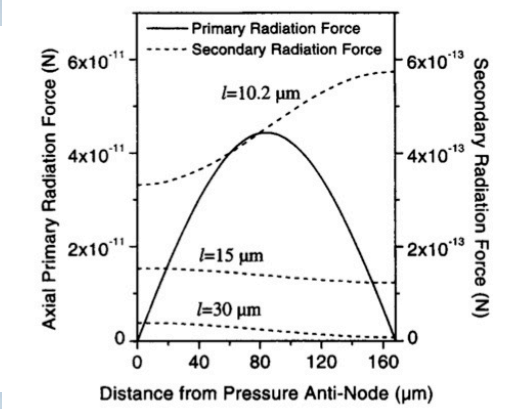

Polystyrene bead; r= 5.1 um

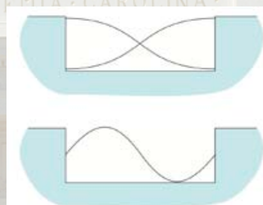

$$F_B(x) = 4\pi R^6 \left[\frac{(\rho_p - \rho_f)^2 (3\cos^2\theta - 1)}{6\rho_f d^4} v^2(x) - \frac{\omega^2 \rho_f (\beta_p - \beta_f)^2}{9d^2} p^2(x) \right]$$

Particels in nodal positions above an ultrasonic transducer plate

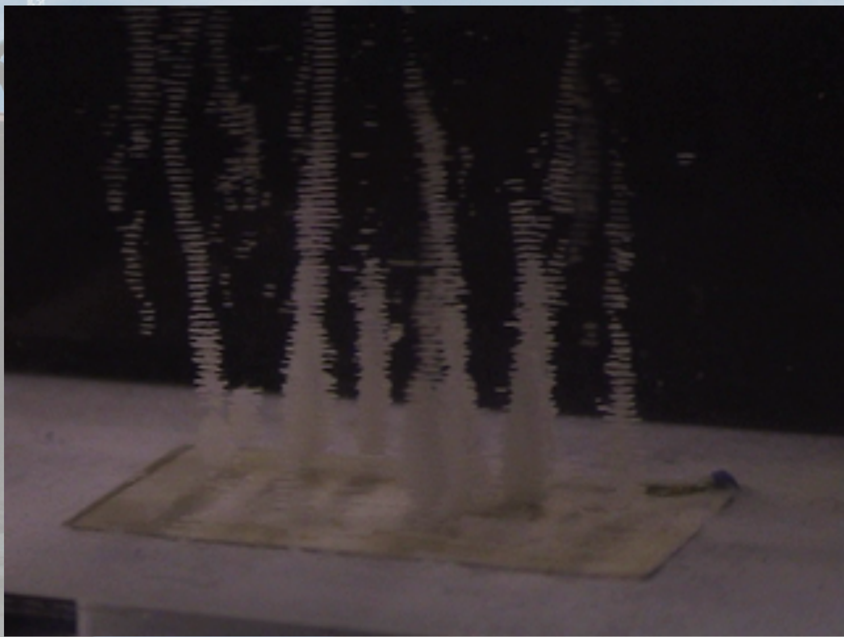

What is happening?

Focused ultrasonic standing wave (USW) resonators

Water immersed acoustic trap

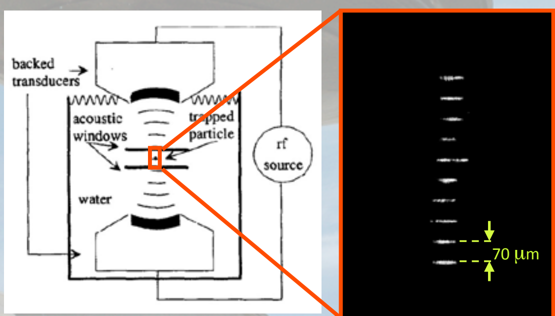

acoustic tweezer
H. M. Hertz *et al*,
J. Appl. Phys., **78**, 4845 (1995)

- Mimic the design of an optical tweezer:

Confinement of the field

- $\Rightarrow$ high gradient both axially and laterally with a **confocal resonator design**
- $\Rightarrow$ 3D manipulation of single microparticles

Courtesy of Martin Wiklund, KTH, Sweden

Capillary system:

Size-selective retention & sample enrichment

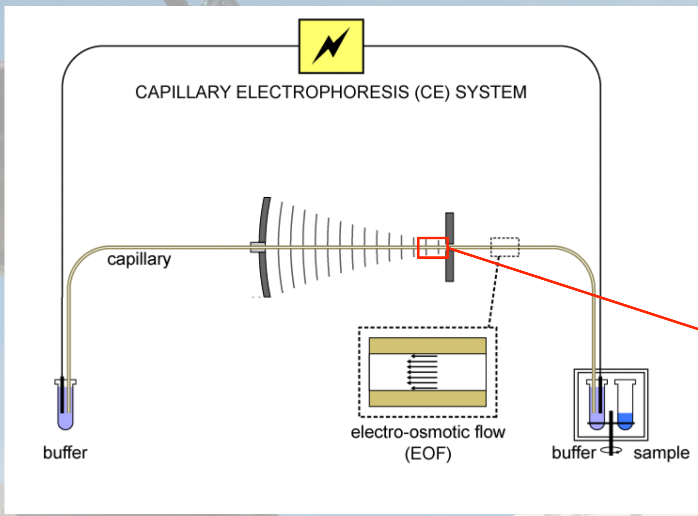

Wiklund *et al.* Ultrasonics 2003

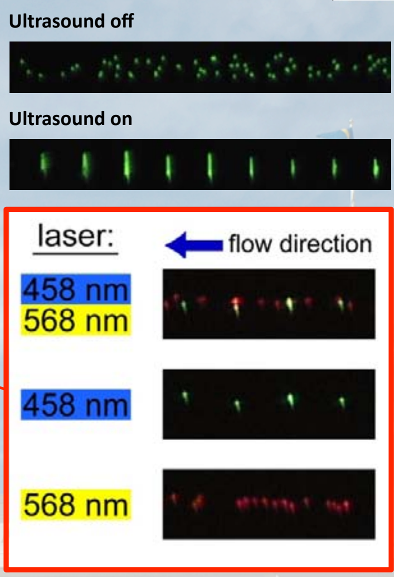

Detection zone

4.5 μm beads (trapped)

3.0 μm beads (non-trapped)

Courtesy of Martin Wiklund, KTH, Sweden

Focused ultrasonic standing wave (USW) resonators

- Controlled picoliter injections in levitated micro fluid volumes
- Sample preparation for capillary electrophoresis injection
- Contact less experiments of single/few cells

Air borne acoustic trap - levitator

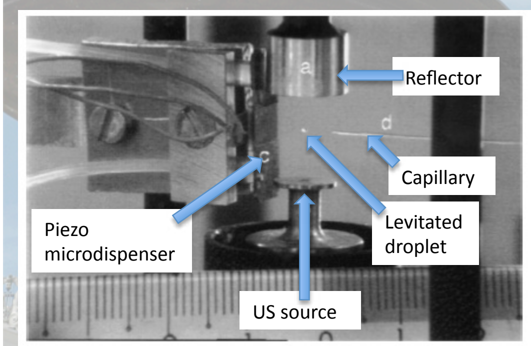

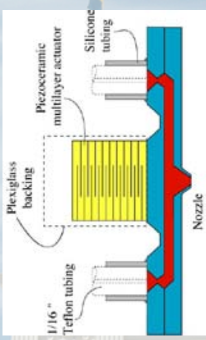

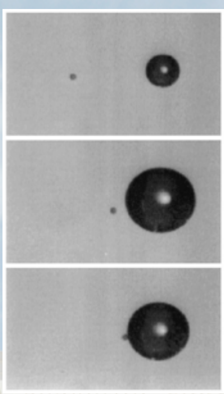

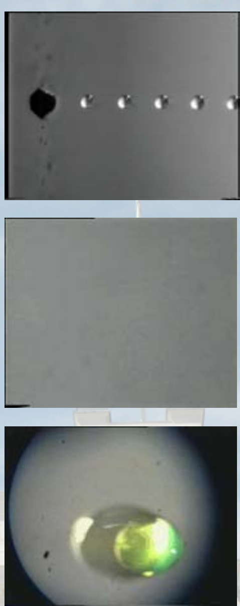

Petersson M, Nilsson S. et al
Journal of Chromatography B,
714 (1998) 39–46

Santesson S & Nilson et al. Cell-cell communication between adipocytes and pancreatic beta-cells in acoustically levitated droplets. Integr Biol. 2009 Oct;1(10):595-601, .

Courtesy of Staffan Nilsson, Lund University, Sweden

Focused ultrasonic standing wave (USW) resonators

A matter of life and death!!!

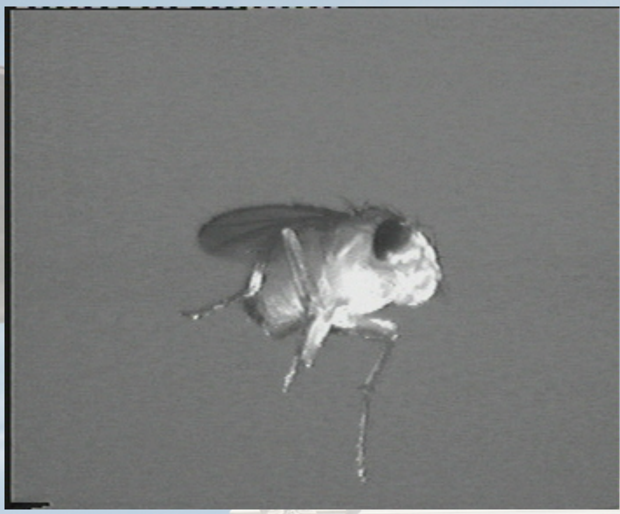

Courtesy of Staffan Nilsson, Lund University

Ultrasonically Enhanced Settling (UES)

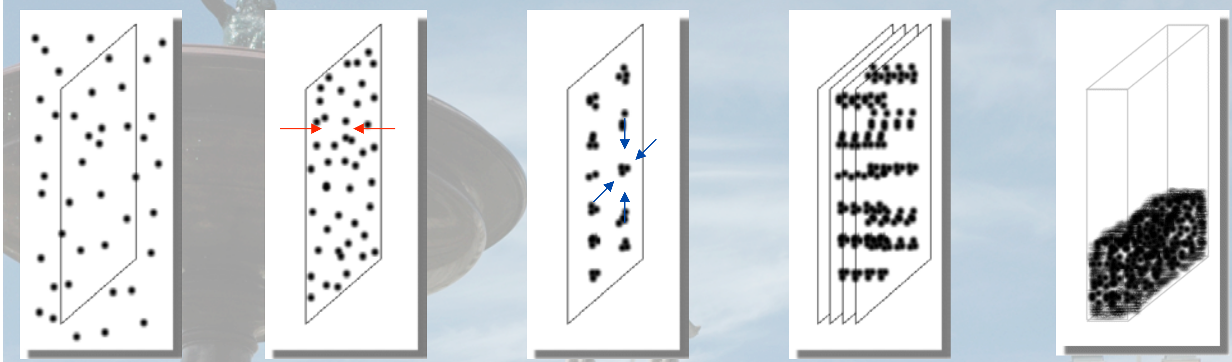

Suspension
randomly distributed particles

Axial primary radiation force
in direction of sound drives particles into nodal plane

Transverse primary radiation force
perpendicular to sound concentration within nodal plane

Inhomogeneous rearrangement
immobilised particles form columns "banding"

Ultrasound switched off
agglomerates settle more rapid than single particles (Stokes)

Courtesy of Stefan Radel, Technical University Vienna

Immobilisation/retention of cells in bioreactors – cell filters

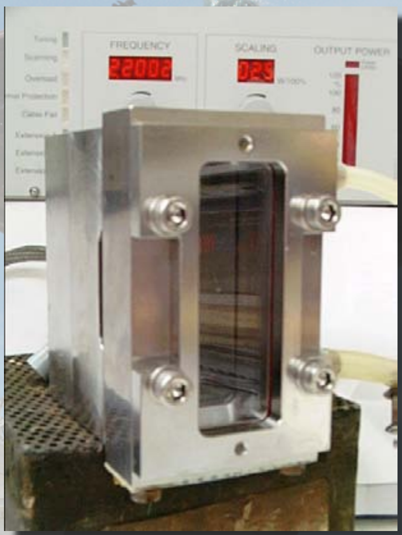

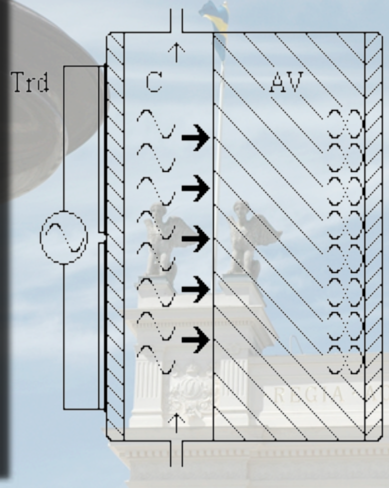

- Two chamber resonator
  - cooling volume (C)
  - active volume (AV) holding the suspension
- Standing wave between
  - PZT-glass-compound transducer (Trd)
  - glass reflector
- Advantages
  - No moving parts
  - No filter cake
  - In-situ sterilisable

Paar USSC-05 und USCS-05
US separation system and control electronics

Courtesy of Stefan Radel, Technical Univerity Vienna

Multinode cell/particle concentration and sedimentation

LUND UNIVERSITY

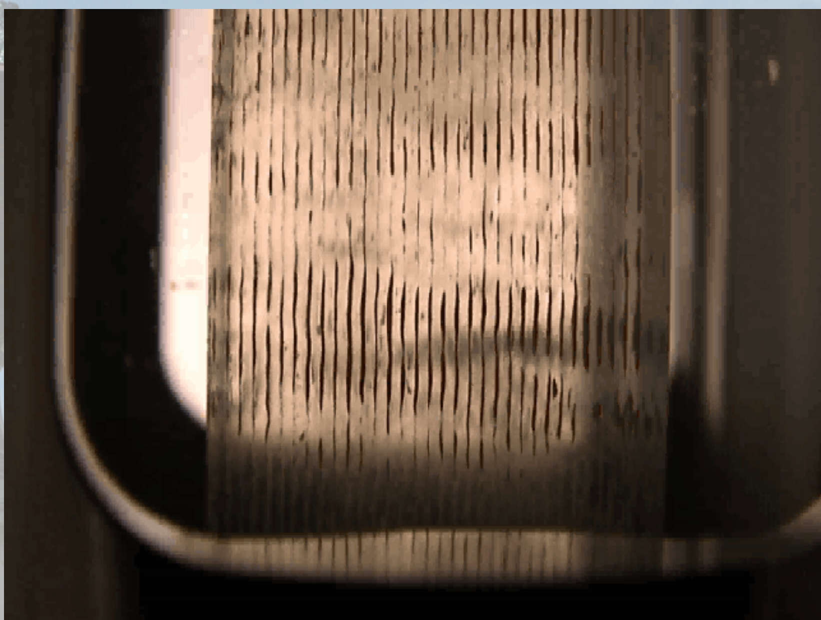

Courtesy of Jeremy Hawkes

Ultrasonically Enhanced Settling (UES)

Biosep 10L (1-10L/d)

Biosep 50L (5-50L/d)

Biosep 250L (25-250L/d)

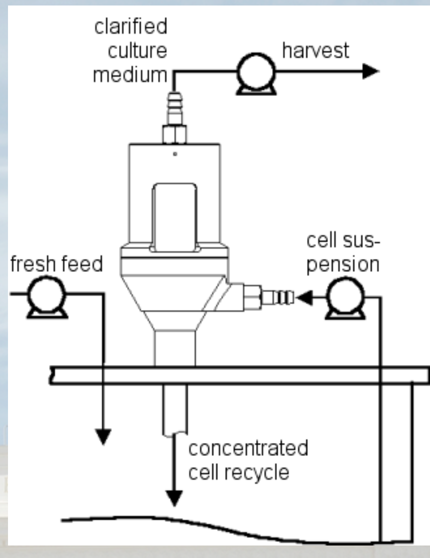

www.applikon-bio.com www.sonosep.com

Courtesy of Stefan Radel, Technical Univerity Vienna

Industrial activities increasing

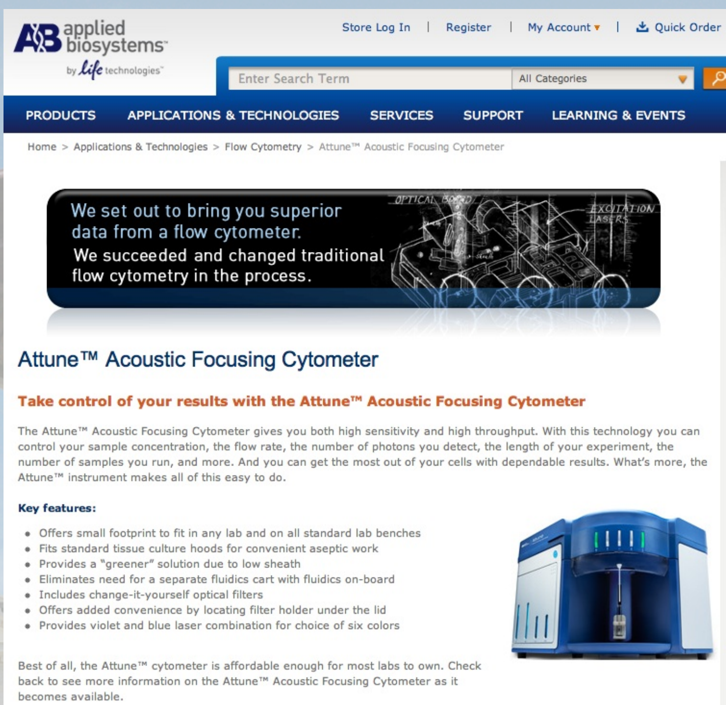

applied biosystems by life technologies

Store Log In | Register | My Account | Quick Order

Enter Search Term All Categories

PRODUCTS APPLICATIONS & TECHNOLOGIES SERVICES SUPPORT LEARNING & EVENTS

Home > Applications & Technologies > Flow Cytometry > Attune™ Acoustic Focusing Cytometer

We set out to bring you superior data from a flow cytometer. We succeeded and changed traditional flow cytometry in the process.

Attune™ Acoustic Focusing Cytometer

Take control of your results with the Attune™ Acoustic Focusing Cytometer

The Attune™ Acoustic Focusing Cytometer gives you both high sensitivity and high throughput. With this technology you can control your sample concentration, the flow rate, the number of photons you detect, the length of your experiment, the number of samples you run, and more. And you can get the most out of your cells with dependable results. What's more, the Attune™ instrument makes all of this easy to do.

Key features:

- Offers small footprint to fit in any lab and on all standard lab benches
- Fits standard tissue culture hoods for convenient aseptic work
- Provides a "greener" solution due to low sheath
- Eliminates need for a separate fluidics cart with fluidics on-board
- Includes change-it-yourself optical filters
- Offers added convenience by locating filter holder under the lid
- Provides violet and blue laser combination for choice of six colors

Best of all, the Attune™ cytometer is affordable enough for most labs to own. Check back to see more information on the Attune™ Acoustic Focusing Cytometer as it becomes available.

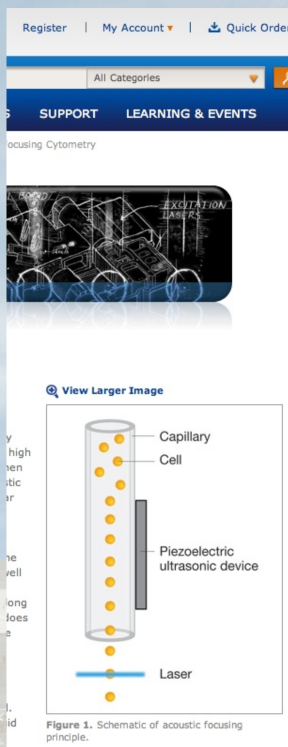

Figure 1. Schematic of acoustic focusing principle.

United States Patent [19]

Benes et al.

[54] METHOD AND APPARATUS FOR SEPARATING PARTICLES

[76] Inventors: **Ewald Benes,** Klosterstrasse 23, A-2362 Biedermannsdorf (NÖ); **Ferdinand Hager,** Berggasse 8/18, A-1090 Wien, both of Austria

PCT Filed 1989
US Approval. 1993

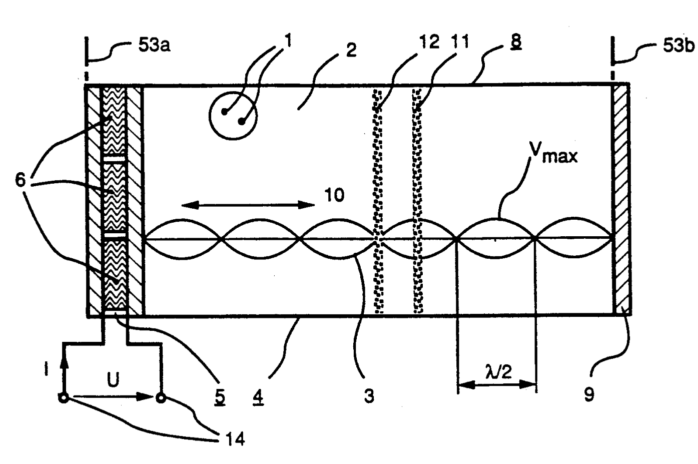

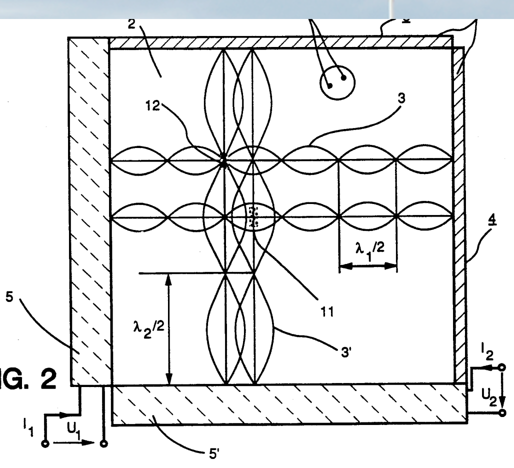

FIG. 2

(12) United States Patent

Yasuda et al.

(54) PARTICLE HANDLING APPARATUS FOR HANDLING PARTICLES IN FLUID BY ACOUSTIC RADIATION PRESSURE

PCT Filed 1996
US Approval. 2001

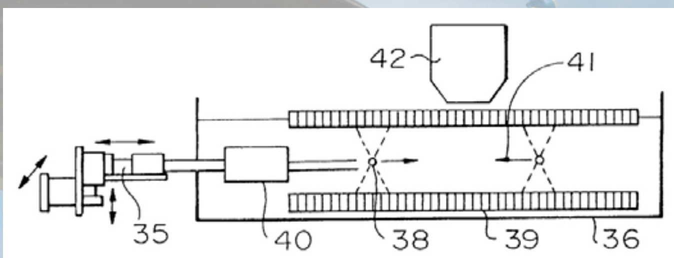

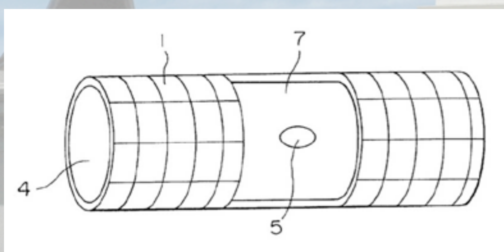

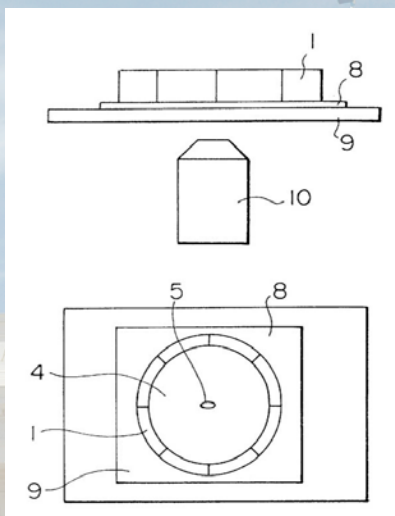

United States Patent [19]

Yasuda et al.

[54] **PARTICLE HANDLING METHOD BY ACOUSTIC RADIATION FORCE AND APPARATUS THEREFORE**

[75] Inventors: **Kenji Yasuda**, Hatoyama-Machi; **Shin-ichiro Umemura**, Hachioji; **Kazuo Takeda**, Tokorozawa; **Mitsuru Tamura**, Kawagoe; **Norio Shimizu**, Sayama, all of Japan

[73] Assignee: **Hitachi, Ltd.**, Tokyo, Japan

Filed 1996

US Approval. 1999

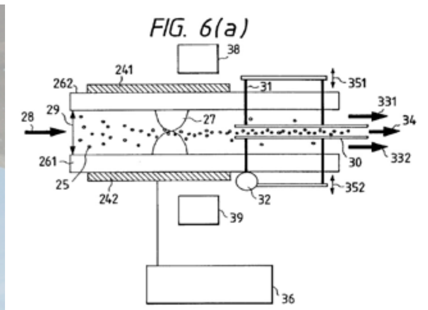

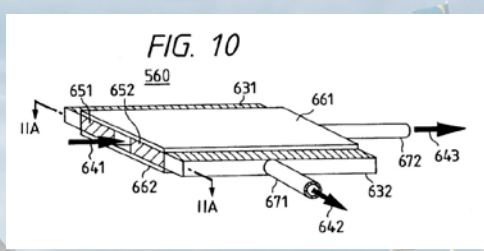

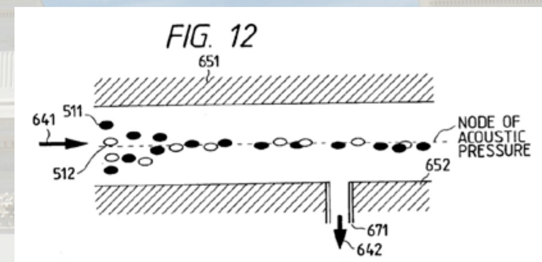

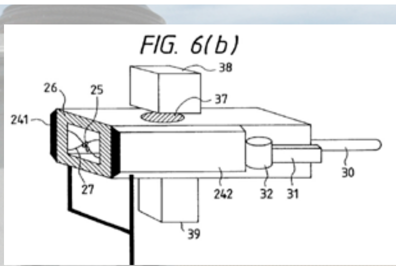

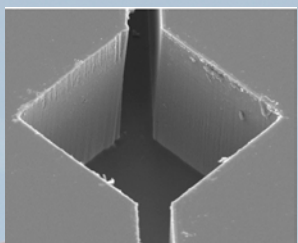

λ/2 resonators

- Requires precision fabrication
  - well defined resonator dimensions
- Resonances matches common dimensions for microfluidic systems
  - ≈10 -500 um => 75 MHz – 1,5 MHz
- Micro fabrication
  - good materials for high q-value resonators
    - Glass
    - silicon
- Particle focus intrinsically defined by the geometries
  - Good microfabrication ➔ good resonators
- Flow through devices
- Trapping devices

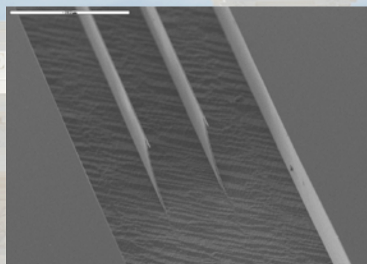

Feke, Separations Technology, 1995

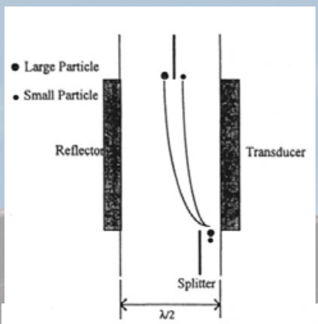

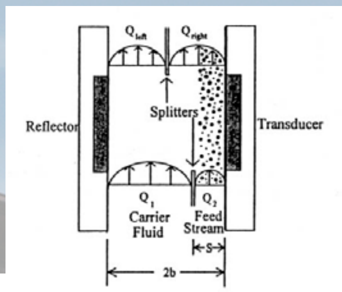

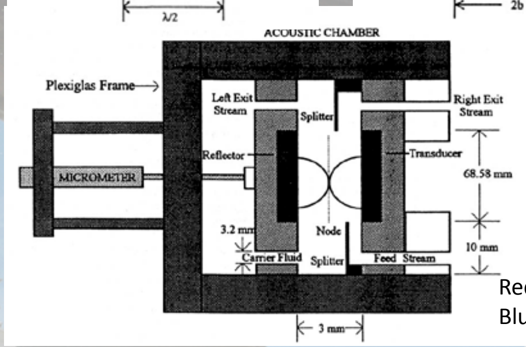

Red particels 170 um
Blue particles 100 um

Q (mm^2/s)	E_{ac} (J/m^3)	N^*_{red} theory	N^*_{red} experiment	N^*_{blue} theory	N^*_{blue} experiment
12.82	0.0162	100%	98.05%	0.00%	3.10%
12.82	0.0162	100%	99.14%	0.00%	0.00%
12.82	0.0149	100%	85.23%	0.00%	8.12%
12.825	0.0149	100%	92.87%	0.00%	9.47%
7.28	0.0142	100%	94.48%	0.00%	1.40%

Kapishnikov,
J. Stat. Mech. 2006

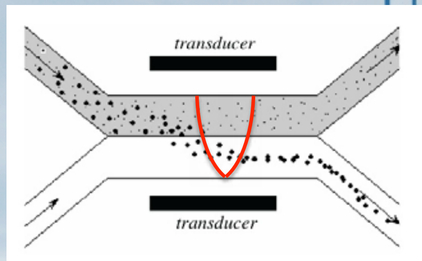

SU-based
λ/4 channel

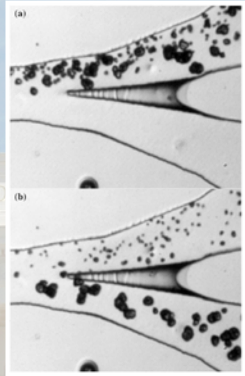

2.5 um
&
10 um
Particles

162 nl/sec

λ/2 resonators

Hill Ultrasonics 2002

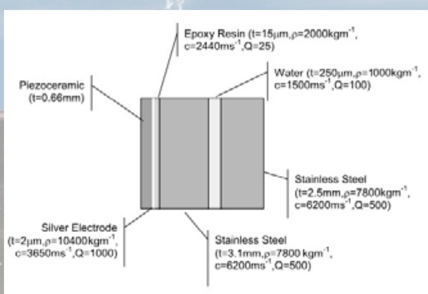

Hawkes et al LOC, 2004

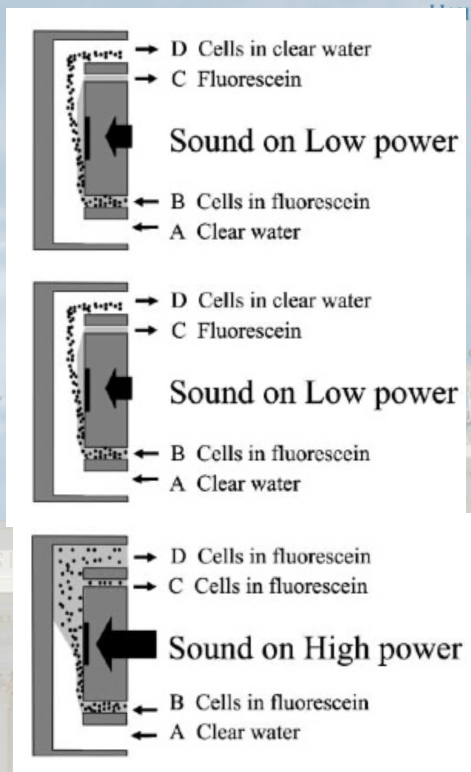

Harris et al, Sensors & Actuators 2003

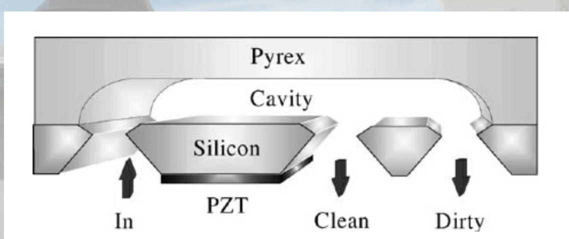

Townsend R. Et al Ultrasonics 2006

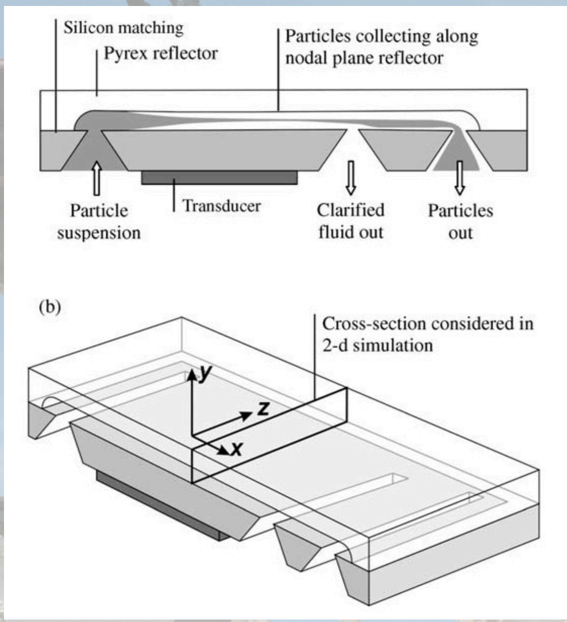

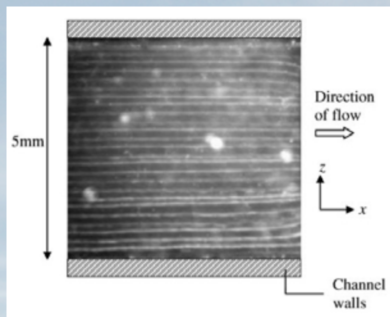

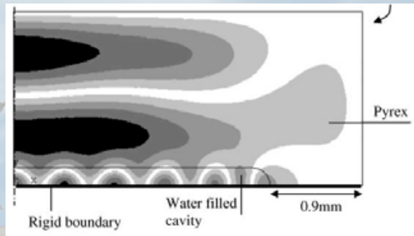

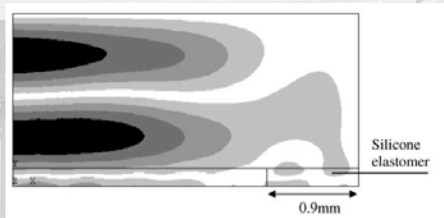

λ/2 resonators

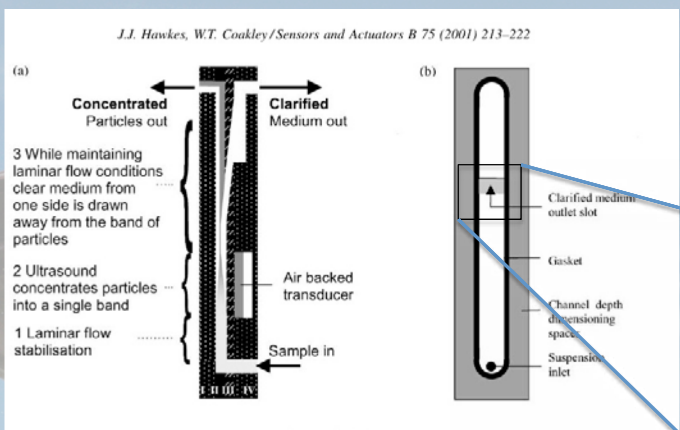

- Transition to micro domain

=> microfabrication techniques
=> microfluidic solutions
=> Lab-on-a-chip implementation

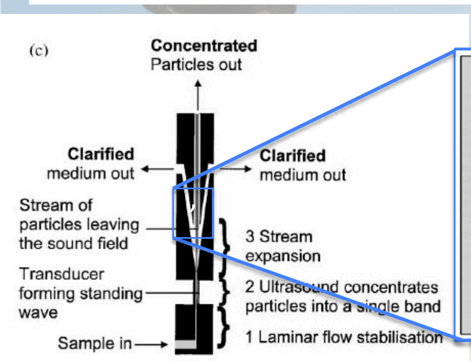

US off

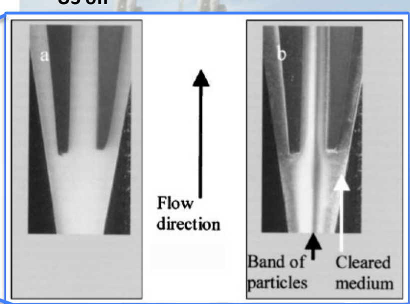

US on => US off

Hawkes & Coaekly, Sensors and Actuators B 75, (2001) 213-222

Courtesy of Jeremy Hawkes,

04 Nilsson A et al. LOC

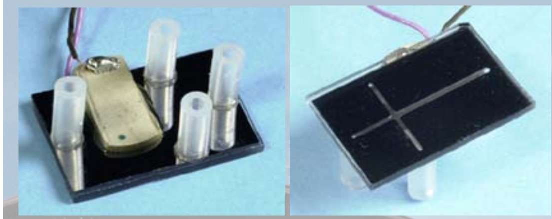

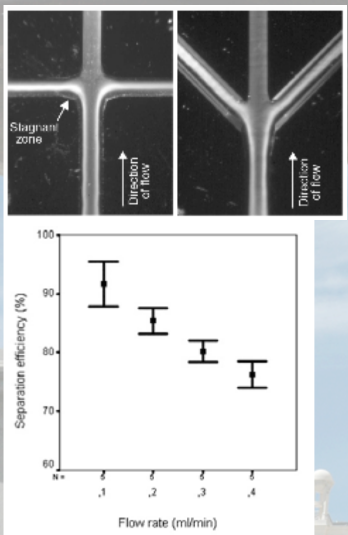

MicroTAS 2002, Nara Japan

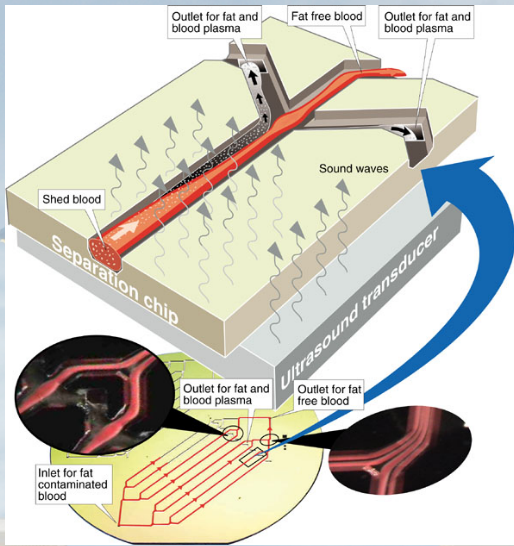

Petersson F., Analyst 2004
Petersson F., LOC, 2005

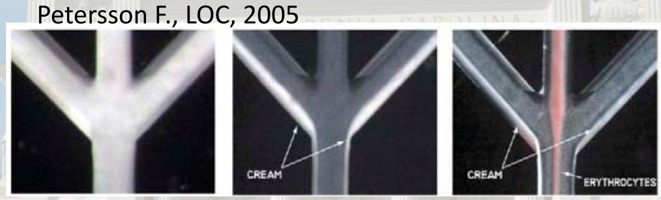

Milk US off | Milk US off | Milk & blood US on

Svennebring J. et al, Biotech Bioeng, 2009

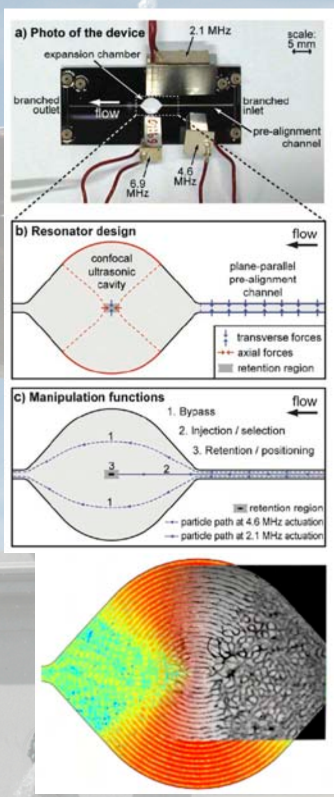

Wiklund M. et al, LOC, 2009

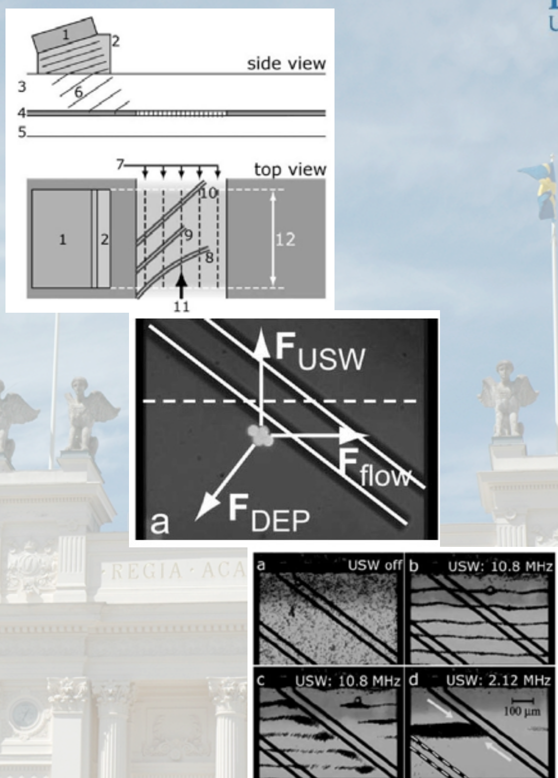

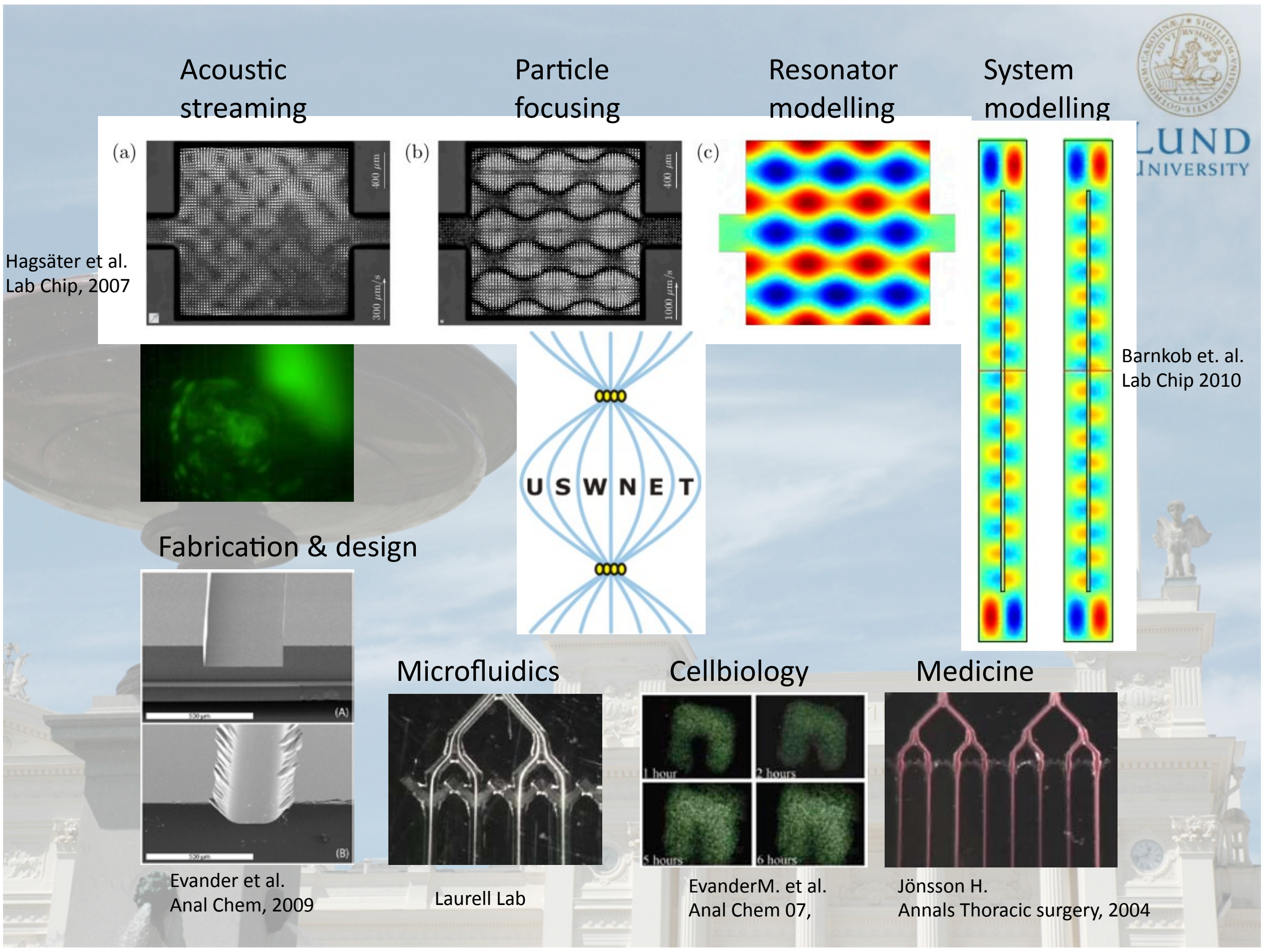
Acoustic streaming
Particle focusing
Resonator modelling
System modelling
LUND UNIVERSITY
(a)
(b)
(c)
Hagsäter et al.
Lab Chip, 2007
Barnkob et. al.
Lab Chip 2010
U S W N E T
Fabrication & design
Microfluidics
Cellbiology
Medicine
1 hour
2 hours
5 hours
6 hours
Evander et al.
Anal Chem, 2009
Laurell Lab
EvanderM. et al.
Anal Chem 07,
Jönsson H.
Annals Thoracic surgery, 2004


LUND UNIVERSITY
U S W N E T
USWNet
Ultrasonic Standing Wave Network
3-7 OCTOBER 2010
µTAS
2010
THE 14TH INTERNATIONAL CONFERENCE ON MINIATURIZED SYSTEMS FOR CHEMISTRY AND LIFE SCIENCES
GRONINGEN
THE NETHERLANDS
USWNet 2010 Conference
2-3 October 2010
www.USWNet.com
A MicroTAS satellite meeting
3 - 7 October 2010
www.microTAS10.org


Questions?
REGIA · ACADEMIA · CAROLINA ·

L1: Applications of nonlinear acoustics in medicine and biology: An overview

Martin Wiklund

Dept. of Applied Physics
Royal Institute of Technology
Stockholm, Sweden

CISM course "*Ultrasound standing wave action on suspensions and biosuspensions in micro- and macro fluidic systems*", June 7-11, 2010

KTH Physics

M. Wiklund

-1-

My background

Started as a PhD student at KTH Stockholm in 1999

My supervisor Hans Hertz was heading a group in X-Ray Physics, but suggested to me to follow up a short work of USW from 1995:

Standing-wave acoustic trap for nonintrusive positioning of microparticles

H. M. Hertz[a]
Department of Physics, Lund Institute of Technology, P.O. Box 118, S-221 00 Lund, Sweden

(Received 17 April 1995; accepted for publication 29 June 1995)

A nonintrusive three-dimensional trap for microscopic particles in a liquid is described. The trap is based on acoustic radiation forces in an ultrasonic confocal standing-wave cavity. Experiments at 11 MHz demonstrate the concept and verify the theoretically calculated forces. Theoretical calculations for higher-frequency systems indicate a significant potential for low-rms-displacement trapping of submicrometer particles, making the trap suitable for nonintrusive scanning near-field optical microscopy. © *1995 American Institute of Physics.*

(H. M. Hertz, J. Appl. Phys. 78, 4875, 1995)

KTH Physics

M. Wiklund

-2-

My background

Since Hans Hertz had limited experience in the USW field, he sent me as a spectator to the Ultrasonics International (UI'99) meeting in Copenhagen 1999.

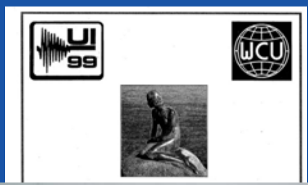

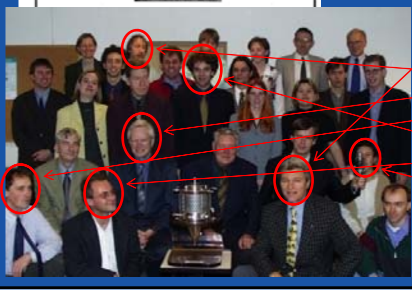

Invited speakers:
Ewald Benes, Vienna
Terry Coakley, Cardiff

90's USW community (EUSS):
Ewald Benes, Vienna
Martin Gröschl, Vienna
Terry Coakley, Cardiff
Jeremy Hawkes, Manchester
Stefan Radel, Vienna
Felix Trampler, SinePhase / SonoSep
Itziar Gonzalez-Gomez, Madrid
...etc

KTH Physics

M. Wiklund

-3-

My background

PhD in 2004

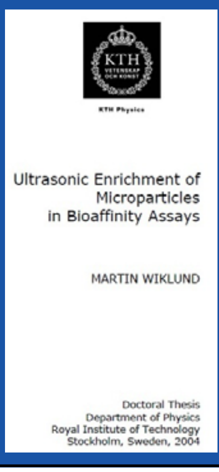
KTH Physics

Ultrasonic Enrichment of Microparticles in Bioaffinity Assays

MARTIN WIKLUND

Doctoral Thesis
Department of Physics
Royal Institute of Technology
Stockholm, Sweden, 2004

Postdoc 2004-2005 at Fraunhofer IBMT (DEP, microfluidics)

Fraunhofer IBMT

Fraunhofer Institute for Biomedical Engineering

Assoc. Prof at KTH in 2009

PhD students:
JessicaSvennebring
Otto Manneberg
Ida Iranmanesh
Athanasia Christakou
Mathias Ohlin

My research profile:

Applied Physics, origin in optics, experimental

Cross-disciplinary (physics-bio)

Applications:
- Bead-based assays
- Immune cell interactions
- Biocompatibility, cell viability

KTH Physics

M. Wiklund

-4-

KTH Physics

M. Wiklund

Outline

1. **Nonlinear acoustics:**
   Introduction and principles
2. **Application I:** **Harmonic imaging (HI)**
   a) Tissue HI
   b) Microbubble HI or Contrast HI
3. **Application II:** **Acoustic streaming**
   In particular in microfluidic systems

15 min

15 min

15 min

-5-

KTH Physics

M. Wiklund

Ultrasound in medical applications?

Medical imaging ("echo")

All three methods use non-linear effects!

Cleaning / cell lysis

Lithotripsy

M. Wiklund

In this lecture:

I Medical imaging (”echo”)

II Ultrasonic streaming in lab-on-a-chip devices

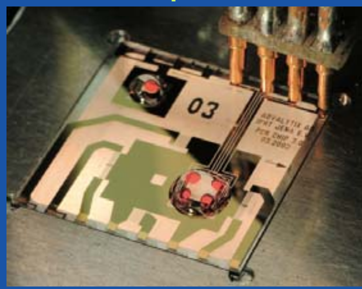

M. Wiklund

Outline

1. **Nonlinear acoustics: Introduction and principles**

2. **Application I: Harmonic imaging (HI)**
   a) Tissue HI
   b) Microbubble HI or Contrast HI

3. **Application II: Radiation pressure and acoustic streaming**
   In particular in microfluidic systems

15 min

15 min

15 min

-8-

M. Wiklund

"It has been argued that every nonlinear problem is really individual, that it requires individual methods, usually very complicated and difficult methods."

(Werner Heisenberg)

Topic of Heisenberg's thesis:

Karman vortices

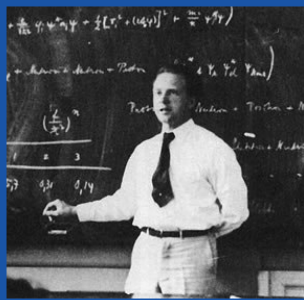

-9-

M. Wiklund

First nonlinear effect:

"Cumulative nonlinear wave propagation"

or

"waveform steepening"

-10-

KTH Physics

M. Wiklund

Wave equation

1D wave equation for the particle displacement, *s*:

$$(1)\quad \frac{\partial^2 s}{\partial t^2} = c_0^2 \frac{\partial^2 s}{\partial x^2}$$ ← Linear acoustics

In fact, above eq. is an approximation. More accurately:

$$(2)\quad \left(1+\frac{\partial s}{\partial x}\right)^{\gamma+1} \frac{\partial^2 s}{\partial t^2} = c_0^2 \frac{\partial^2 s}{\partial x^2}$$ ← Nonlinear acoustics

where $\partial s/\partial x$ is the strain and γ is the ratio of the specific heats (C_P/C_V)

gas	γ @ 20°C
Ar	1.67
O2	1.40
CO_2	1.30

-11-

KTH Physics

M. Wiklund

Wave equation

$$\left(1+\frac{\partial s}{\partial x}\right)^{\gamma+1} \frac{\partial^2 s}{\partial t^2} = c_0^2 \frac{\partial^2 s}{\partial x^2}$$

-12-

Wave equation

Expand the first factor in the (nonlinear) wave equation:

$$\boxed{\left(1+\frac{\partial s}{\partial x}\right)^{\gamma+1}}\frac{\partial^2 s}{\partial t^2}=c_0^2\frac{\partial^2 s}{\partial x^2}$$

$$\left(1+\frac{\partial s}{\partial x}\right)^{\gamma+1}\simeq 1+(\gamma+1)\frac{\partial s}{\partial x}$$

Size of this term?

- Second term generates the second harmonic components in the wave
- The expansion of the equation makes it possible to solve the linear equation and then use perturbation theory

M. Wiklund

-13-

Wave equation

$$\left(1+\frac{\partial s}{\partial x}\right)^{\gamma+1}\simeq 1+(\gamma+1)\frac{\partial s}{\partial x}$$

Size of this term?

$\partial s/\partial x$ is only negligible (compared with unity) if

$(\partial s/\partial x)_{max} << 1$ ⇨ $u_0/c_0 << 1$

u_0/c_0 is called the acoustic Mach number, M

<u>Numerical example</u> (medical imaging, particle manipulation etc.):

$p_0 = 1$ Mpa, $f = 1$ MHz, $c_0 = 1500$ m/s (water or soft tissue)

⇨ $u_0 = 0.7$ m/s ⇨ $M \approx 10^{-3}$

M. Wiklund

-14-

Sound speed (in gases)

Relation between (total) pressure and density (*isothermal* process):

$$\frac{P}{P_0} = \frac{\rho}{\rho_0} \quad \Rightarrow \quad c_0 = \sqrt{\frac{P_0}{\rho_0}} \qquad \text{(Newton, 17th cent.)}$$

(Boyle's law)

Note: Prediction by Newton ~16% lower than measured values!

Relation between (total) pressure and density (*adiabatic* process):

$$\frac{P}{P_0} = \left(\frac{\rho}{\rho_0}\right)^{\gamma} \quad \Rightarrow \quad c_0 = \sqrt{\gamma \frac{P_0}{\rho_0}} \qquad \text{(Laplace, 19th cent.)}$$

Correction factor: $\sqrt{\gamma}$

KTH Physics

M. Wiklund

-15-

The nonlinear parameter B/A

Relation between (total) pressure and density (adiabatic process):

$$\frac{P}{P_0} = \left(\frac{\rho}{\rho_0}\right)^{\gamma} = \left(1 + \frac{\rho - \rho_0}{\rho_0}\right)^{\gamma} = 1 + \gamma\left(\frac{\rho - \rho_0}{\rho_0}\right) + \frac{\gamma}{2!}(\gamma - 1)\left(\frac{\rho - \rho_0}{\rho_0}\right)^2 + \frac{\gamma}{3!}(\gamma - 1)(\gamma - 2)\left(\frac{\rho - \rho_0}{\rho_0}\right)^3 + \ldots$$

condensation — Taylor expansion

Alternatively, in terms of acoustic pressure:

$$p = P - P_0 = A\left(\frac{\rho - \rho_0}{\rho_0}\right) + \frac{B}{2!}\left(\frac{\rho - \rho_0}{\rho_0}\right)^2 + \frac{C}{3!}\left(\frac{\rho - \rho_0}{\rho_0}\right)^3 + \ldots$$

Compare the terms:
⇨ B/A = γ-1

Rewrite, in terms of sound velocity:

$$c^2 = c_0^2\left[1 + \left(\frac{B}{A}\right)\left(\frac{\rho - \rho_0}{\rho_0}\right) + \left(\frac{C}{2A}\right)\left(\frac{\rho - \rho_0}{\rho_0}\right)^2 + \ldots\right] \qquad \text{with} \qquad c_0 = \sqrt{\gamma \frac{P_0}{\rho_0}}$$

Typical values of B/A: 5-10 (water or soft tissue)

KTH Physics

M. Wiklund

-16-

M. Wiklund

-17-

Cumulative nonlinear effects:
Waveform steepening

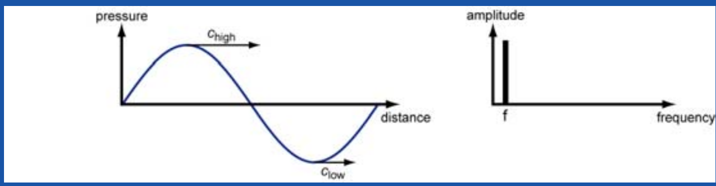

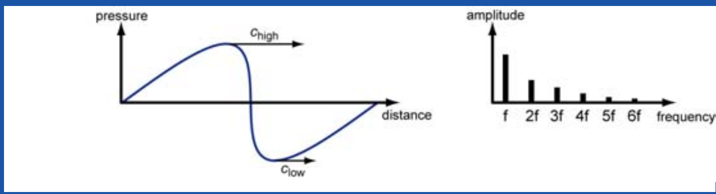

harmonics: 1

$$a(t) = \frac{2}{\pi}\sum_{n=1}^{\infty}\frac{1}{n}\sin(2\pi n f t)$$

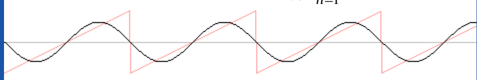

(”sawtooth wave” from Wikipedia)

Waveform steepening:
Pure sine-wave transforms to sawtooth-shaped
⇨ overtones (”harmonics”) are generated

M. Wiklund

-18-

Nonlinear effects

…are more marked for:

-Higher frequencies

-Slower sound speeds (e.g. fluids, soft materials)

-Larger propagation distances

-Larger (initial) amplitudes

-Smaller attenuation coefficients

Outline

1. **Nonlinear acoustics: Introduction and principles**

2. **Application I: Harmonic imaging (HI)**
   a) Tissue HI
   b) Microbubble HI or Contrast HI

3. **Application II: Radiation pressure and acoustic streaming**
   In particular in microfluidic systems

M. Wiklund

-19-

Nonlinear propagation:
Pulsed waves

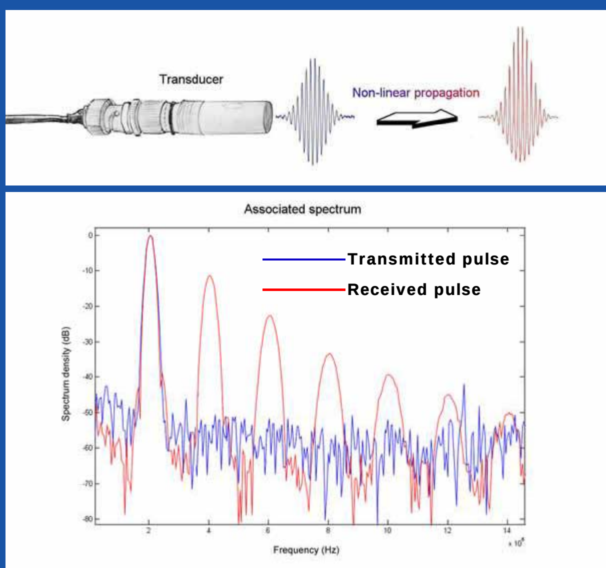

Figures from: http://www2.erasmusmc.nl/ThoraxcenterBME/

M. Wiklund

-20-

Field distribution

Radiated field from the transducer
(Simulation of the fundamental component)

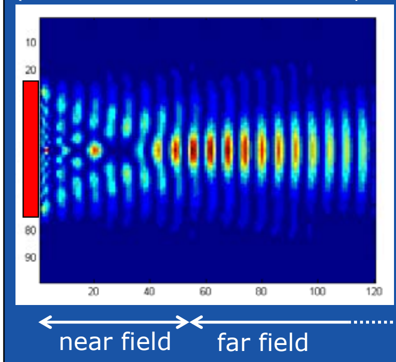

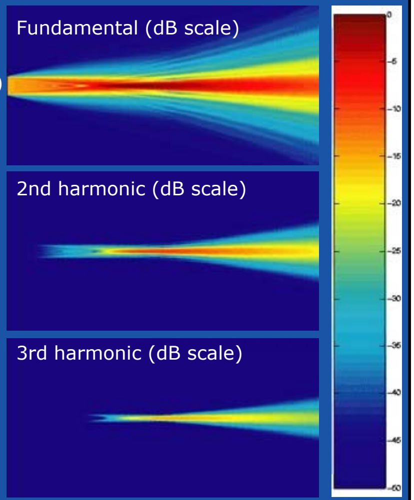

M. Wiklund

-21-

Figures from: http://www2.erasmusmc.nl/ThoraxcenterBME/

Tissue harmonic imaging

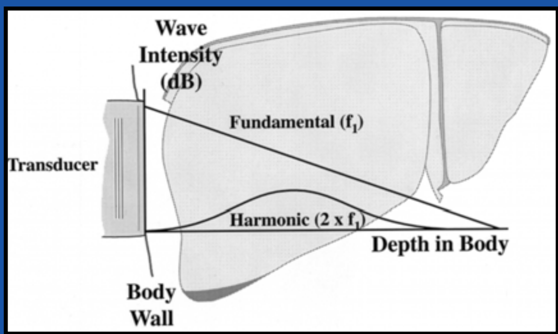

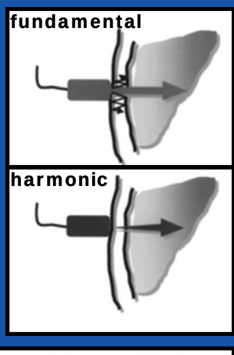

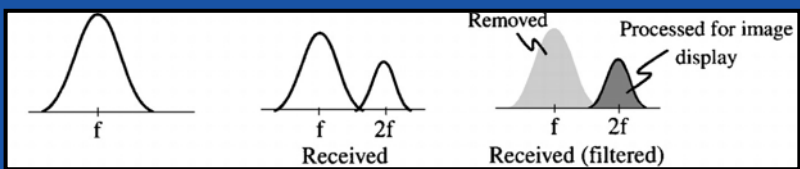

M. Wiklund

-22-

Tissue harmonic imaging

Advantages, harmonic imaging:

-Reduction in near-field artefacts

-Reduction in size of the side lobes

-Narrower beam waist

Compare with optics:
Two-photon excitation microscopy
(and confocal microscopy)

KTH Physics

M. Wiklund

-23-

Tissue harmonic imaging: Clinical example

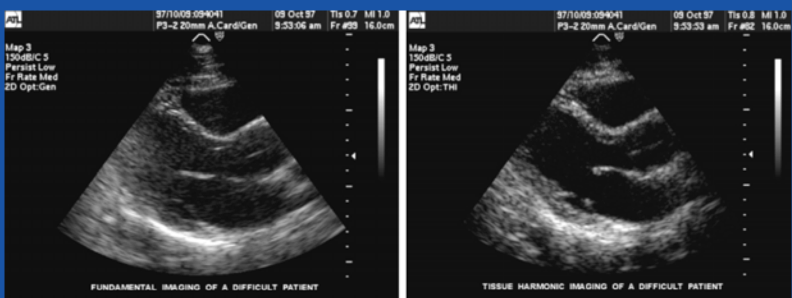

Fundamental imaging | Harmonic imaging

KTH Physics

M. Wiklund

-24-

M. Wiklund

Outline

1. **Nonlinear acoustics: Introduction and principles**

2. **Application I: Harmonic imaging (HI)**
   a) Tissue HI
   b) Microbubble HI or Contrast HI

3. **Application II: Radiation pressure and acoustic streaming**
   In particular in microfluidic systems

-25-

M. Wiklund

Microbubble harmonic imaging

Microbubbles or *contrast agents*:
Stable gas bubbles in fluid suspensions

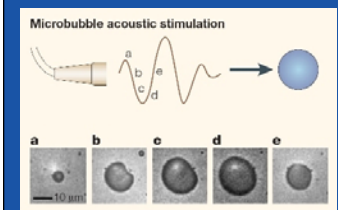

Compression of the bubble retards relative to expansion during an acoustic cycle

⇨ nonlinear oscillation!

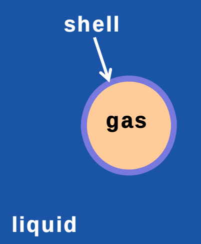

Table 1 | **Examples of microbubble contrast agents**

Name	Manufacturer	Shell	Gas	Mean size (μm)
Albunex	MolecularBiosystems	Albumin	Air	4.3
Optison	Mallinckrodt/Amersham	Albumin	Octafluoropropane	2–4.5
Definity	Bristol-Myers Squibb Medical Imaging	Lipid/surfactant	Octafluoropropane	1.1–3.3
Imagent	Imcor	Lipid/surfactant	N_2/perfluorohexane vapor	6.0
Sonovue	Bracco Diagnostics	Lipid	Sulphur hexafluoride	2–3
Levovist	Schering AG	Lipid/galactose	Air	2–4
Cardiosphere	Point Biomedical	PLGA polymer/ albumin	Nitrogen	
AI-700	Acusphere	PLGA polymer	Perfluorocarbon	
Sonovist	Schering AG	Cyanoacrylate polymer	Air	
Sonazoid	Nycomed/Amersham	Not disclosed	Perfluorocarbon	

PLGA, polylactide co-glycolide.

-26-

Microbubble harmonic imaging

Rayleigh-Plesset equation:
Oscillation of a gas bubble in an incompressible and ∞ fluid medium due to a driving pressure field $p_a(t)$

$$\frac{3}{2}\dot{R}^2 + R\ddot{R} = \frac{1}{\rho_0}(p_L - p_\infty)$$

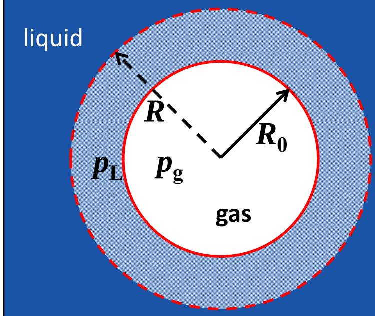

$$p_\infty = p_0 + p_a(t)$$

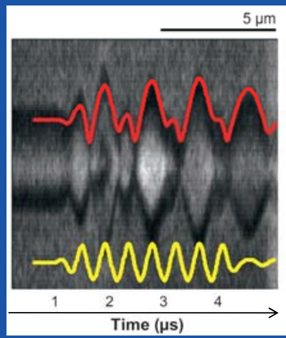

(Ferrara *et al.*, Annu. Rev. Biomed. Eng. **9**, 415, 2007)

bubble oscillation

source oscillation

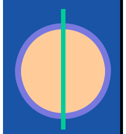

Line-scan images vs. time

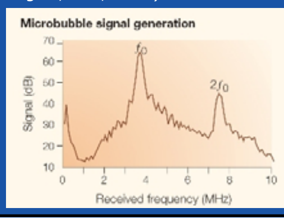

Frequency spectrum

M. Wiklund

-27-

Microbubble harmonic imaging - what is it good for?

Clinical problem:

Blood perfusion in capillaries (d<0.1 mm)

Typical resolution with ”normal” ultrasound:

c=1550 m/s; f=5 MHz ⇨ λ=0.3 mm

Solution:

Microbubbles!

Compare with optics:

Acoustic counterpart to fluorescent probes!

M. Wiklund

-28-

Microbubble harmonic imaging

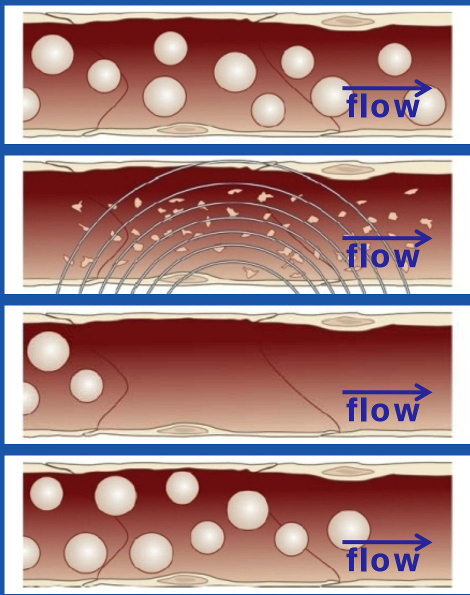

Microbubbles give strong signal

Signal disappears when an intense pulse is applied

Perfusion is quantified by studying the signal recovery

(Ferrara *et al.*, Annu. Rev. Biomed. Eng. **9**, 415, 2007)

KTH Physics

M. Wiklund

-29-

Microbubble harmonic imaging - further developments?

Modes of use:

1. Improved contrast, blood perfusion
2. Targeted imaging
3. Targeted imaging and/or targeted therapy

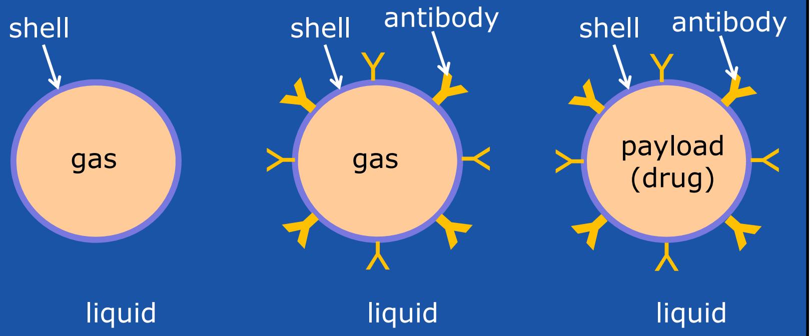

KTH Physics

M. Wiklund

-30-

Outline

1. **Nonlinear acoustics: Introduction and principles**

2. **Application I:** **Harmonic imaging (HI)**
   a) Tissue HI
   b) Microbubble HI or Contrast HI

3. **Application II:** **Radiation pressure and acoustic streaming**
   In particular in microfluidic systems

KTH Physics

M. Wiklund

-31-

Acoustic radiation pressure

"It might be said that radiation pressure is a phenomenon that the observer thinks he understands – for short intervals, and only every now and then."

(Robert T. Beyer, 1978)

KTH Physics

M. Wiklund

-32-

Second nonlinear effect:

”Confusion about coordinates”

KTH Physics

M. Wiklund

-33-

Acoustic radiation pressure

- What is acoustic radiation pressure?
- Note: To get a *static* force, we need a *time-averaged* pressure gradient!
- So, let’s integrate the pressure over a time period

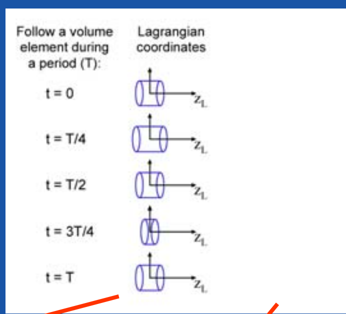

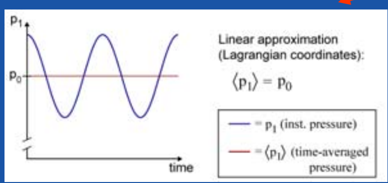

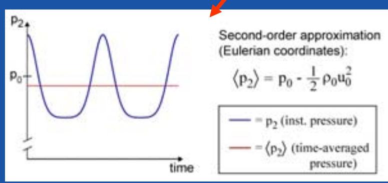

Thus, it is a non-linear effect!

KTH Physics

M. Wiklund

-34-

Acoustic radiation pressure: compare with the Bernoulli principle

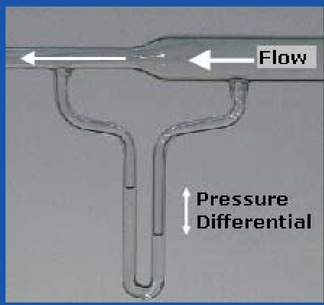

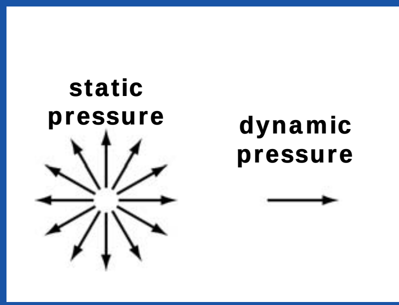

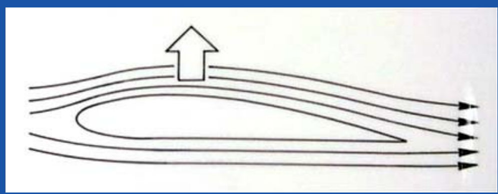

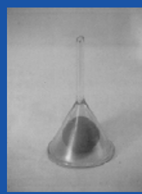

M. Wiklund

-35-

Acoustic radiation pressure: simple model

Radiation pressure!

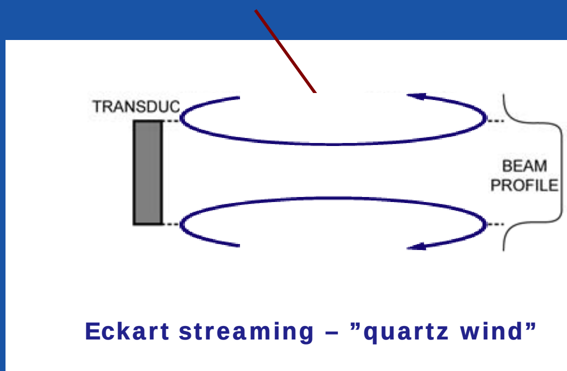

M. Wiklund

-36-

Applications?
Two different effects are used:

1. ~~Manipulation of suspended objects (standing wave fields)~~
   ~~E.g: trapping, separation, concentration…~~

2. Manipulation of the fluid medium (standing or propagating fields)
   E.g: mixing, pumping…

M. Wiklund

First experiment: Kundt's tube

Experimental setup 1866

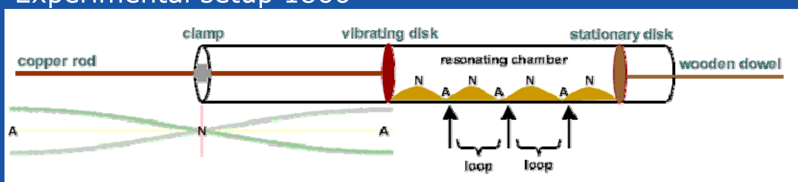

August Kundt

Experimental setup today

M. Wiklund

-38-

KTH Physics

M. Wiklund

First experiment: Kundt's tube

Experimental setup 1866

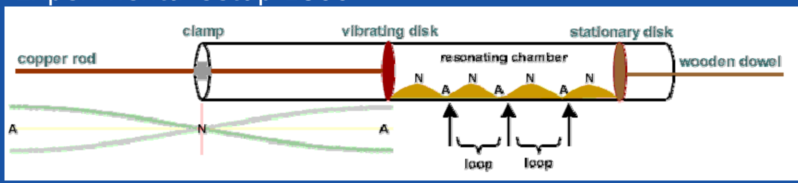

Is the (primary) radiation force really the reason for the pattern?

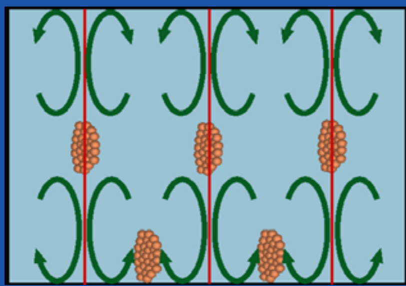

Rayleigh streaming

KTH Physics

M. Wiklund

Acoustic radiation pressure

"The subject of radiation pressure has been one of the most widely studied "small subjects" of acoustics, with virtually every big name applying himself to the subject at some time or another, and with many little names doing likewise."

(Robert T. Beyer, 1978)

Examples of "big names":
Euler, Maxwell, Boltzman, Lord Rayleigh, Brillouin

Gustav Hertz’ ”acoustic fountains”

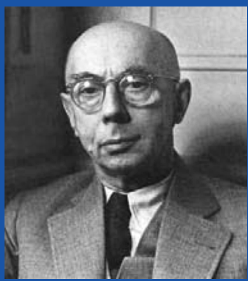

Gustav Hertz:
Radiation pressure on fluid-fluid interfaces

...by the way...
Gustav had a friend...
and a little boy Hellmuth

...who later became the father of echo-cardiography

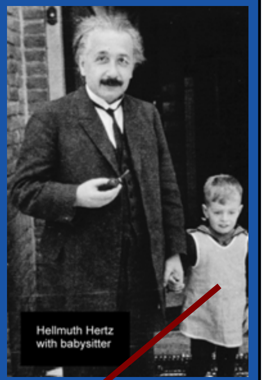

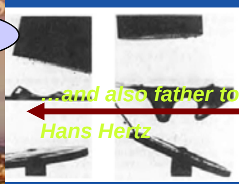

...and also father to Hans Hertz

M. Wiklund

-41-

Outline

1. **Nonlinear acoustics: Introduction and principles**

2. **Application I: Harmonic imaging (HI)**
   a) Tissue HI
   b) Microbubble HI or Contrast HI

3. **Application II: Radiation pressure and acoustic streaming**
   In particular in microfluidic systems

15 min

15 min

15 min

M. Wiklund

-42-

Today: Mixing/pumping/sorting in lab-on-a-chip devices

Method I: Acoustic streaming

Background

Studies by Wesley Nyborg in the 1940s:

Streaming from a gas body in a fluid

(See historical review paper, Ultrasound Med. Biol. 26, 911, 2000)

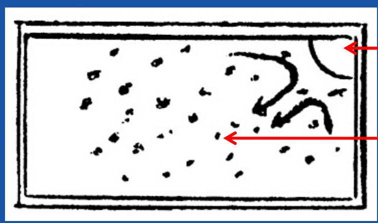

M. Wiklund

-43-

Today: Mixing/pumping/sorting in lab-on-a-chip devices

Method I: Acoustic streaming

Pumping

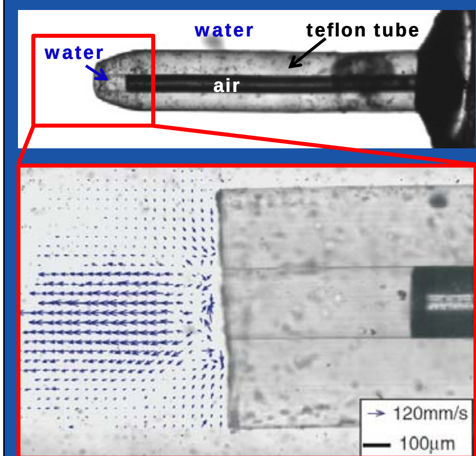

Demo of the application:
"The acoustic windmill"

Averaged fluid velocity field

(Diijkink *et al*., JMM **16**, 1653, 2006)

M. Wiklund

-44-

KTH Physics

M. Wiklund

-45-

Today: Mixing/pumping/sorting in lab-on-a-chip devices

Method I: Acoustic streaming

Application of ”bubble pumping” to a microfluidic chip

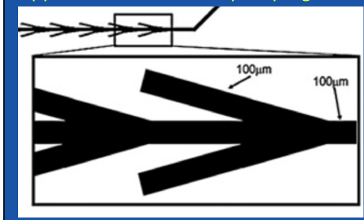

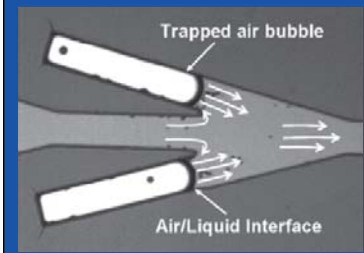

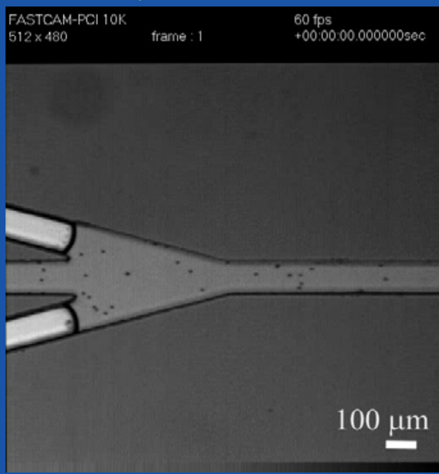

(Lee *et al*., Lab Chip **9**, 41, 2009)

KTH Physics

M. Wiklund

-46-

Today: Mixing/pumping/sorting in lab-on-a-chip devices

Method I: Acoustic streaming

Mixing
(multiple-bubbles acoustic mixing)

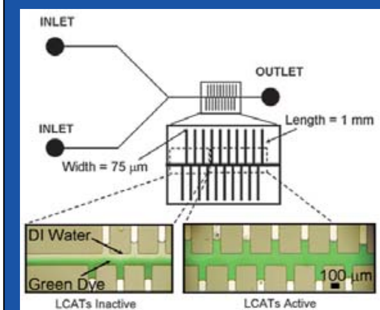

(Lee *et al*., Lab Chip, **9**, 41, 2009)

Mixing
(single-bubble acoustic mixing)

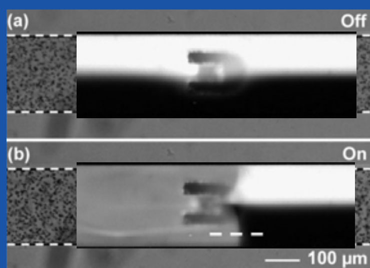

(Jun Huang *et al*., Lab Chip **9**, 2738, 2009)

Today: Mixing/pumping/sorting in lab-on-a-chip devices

Method I: Acoustic streaming

sorting

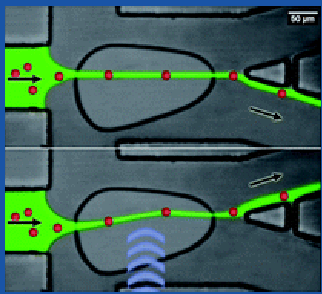

(Franke *et al*., Lab Chip, **10**, 789, 2010)

Method II: Radiation forces at a density interface

(G. Hertz *et al*., Z Phys. **114**, 354, 1939)

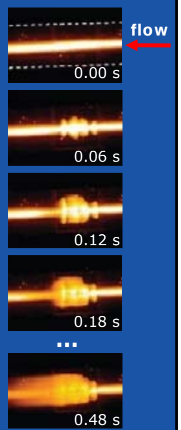

(Johansson *et al*., Lab Chip 9, 297, 2009)

M. Wiklund

Any commercial devices?

Advalytix (Germany):

- Micro-mixing in droplets or microwells by leaky SAWs

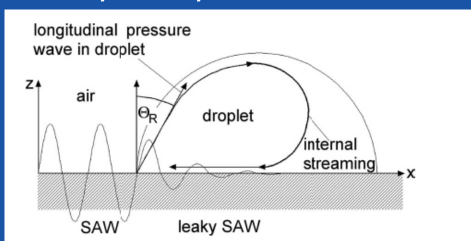

Plate booster96

M. Wiklund

M. Wiklund

-49-

Any commercial devices?

Advalytix (Germany):

- Actuation of droplets by leaky SAWs

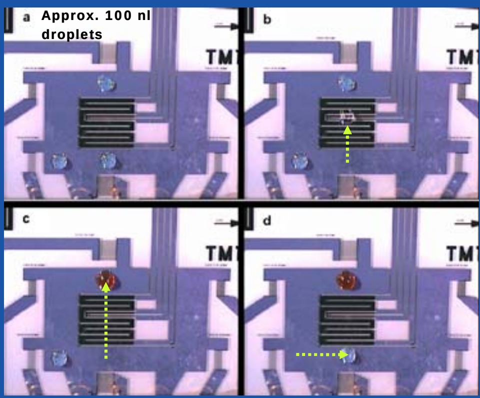

(Wixforth *et al.* Superlatt. Microstruct. **33**, 389, 2003)

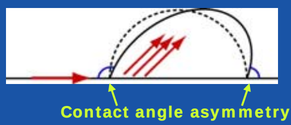

PCR chip

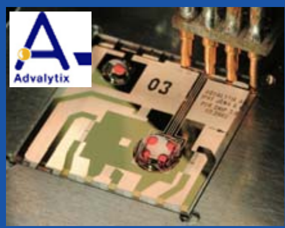

M. Wiklund

-50-

Summary

- Non-linear effects are important in modern ultrasonic technology
- Harmonic imaging and radiation pressure are based on two different non-linear effects
  (a *cumulative* and a *local*)
- The research field is ”blooming” and growing!
  (especially in the lab-on-a-chip community)

M2 Fundamental Acoustics/Vibration

Lecture 1: Linear Acoustics

J. Dual, ETH Zürich, Switzerland

The basic theory of linear acoustics is presented here. It allows to calculate the sound field in a cavity, that is used to do particle manipulation.

1. Basic Equations for Acoustics

In the most simple case, acoustics describes the propagation of disturbances of the pressure field in a fluid, which is compressible, and for situations, where the viscosity may be neglected. For a more extensive explanation the reader is referred to [1].

In the framework of continuum mechanics, we deal with situations, where the wavelength λ >> free path length (which is $6*10^{-8}$m for air at standard conditions and much smaller than this for water in the liquid phase).

Notation: Vector components with respect to a Cartesian coordinate system
We use the indicial notation, i.e. summation convention for repeated indices is used for indices repeated in a term

constant reference pressure	P_0
instantaneous pressure	P
excess pressure or acoustical pressure	p
position vector of a particle	$\underline{x} = x_i \underline{e}_i$
acoustical pressure	$p(\underline{x},t) = P - P_0$
constant equilibrium density	ρ_0
instantaneous density	$\rho(\underline{x},t)$
particle displacement from equilibrium	$\underline{\xi}(\underline{x},t)$
particle velocity	$\underline{u}(\underline{x},t) = \dfrac{\partial \underline{\xi}}{\partial t}$
temperature	$T(\underline{x},t)$
condensation	$s := \dfrac{\rho - \rho_0}{\rho_0}$, $s \ll 1$

In the context of elementary fluid dynamics and thermodynamics, the quantities have to obey the following equations, when the viscosity is neglected.

Continuity equation (conservation of mass)	$\frac{\partial \rho}{\partial t} + (\rho u_i)_{,i} = 0$
Linear momentum equation (Euler)	$\rho \left(\frac{\partial u_i}{\partial t} + u_{i,j}\, u_j\right) + P_{,i} = 0$
Constitutive law	$P = P(\rho, T)$

For linear acoustics these equations are linearized, by assuming a constant reference state with $\underline{u}_0 = \underline{0}$, small disturbances, i.e. $\frac{\partial u_i}{\partial t} >> u_{i,j}\, u_j$). This yields

Continuity equation
$$\frac{\partial s}{\partial t} + u_{i,i} = 0 \qquad (1)$$

Linear momentum equation
$$\rho_0 \frac{\partial u_i}{\partial t} + p_{,i} = 0 \qquad (2)$$

This is the linear inviscid force equation for acoustic processes of small amplitudes. The constitutive law for an adiabatic situation, i.e. when heat flow is neglected, is given by

$$p = B\, s \qquad (3)$$

B is the adiabatic bulk modulus
$$B = \rho_0 \left(\left.\frac{\partial P}{\partial \rho}\right|_{\rho_0}\right)$$

This is also called the equation of state.
After combining equations (1) to (3), we obtain

$$p_{,ii} = \frac{1}{c^2} \frac{\partial^2 p}{\partial t^2} \qquad (4)$$

$$c^2 = \frac{B}{\rho_0} \qquad (5)$$

This is a linear partial differential equation: The classical wave equation in three dimensions, for which many solutions are known in the literature. It allows for dispersion free propagation of waves with the wave speed c.
Eq. 5 allows to rewrite eq. 3 as

$$p = \rho_0\, c^2\, s \qquad (6)$$

Examples:

	ρ_0 [kg/m^3]	B [N/m^2]	c [m/s]	ρ_0 c [Pas/m]
Air at 20˚C	1.21	1.42 10^5	343	415
Mercury Hg	13600.	2.53 10^{10}	1450.	1.97 10^7
Water at 20˚C	998.	2.19 10^9	1481.	1.48 10^6

The characteristic impedance ρ_0 c of the material is the product of density and wave speed. For plane waves it is equal to the quotient of pressure and velocity amplitude.

The particle velocity can also be expressed with the velocity potential Φ

$$u_i = \Phi,_i$$

(7)

The velocity potential also satisfies the wave equation.
When solving eq. 4, an initial value problem must be solved that satisfies the boundary conditions. If all these conditions are properly formulated, a unique solution exists.
For particle manipulation, most often a harmonic solution is sought, as the transducers used to excite the acoustic field are driven for times much longer than the typical response time of the system which is QT, where Q is the quality factor and T the period of the vibration. For a typical system with Q = 100 at 1MHz the response time is a fraction of a ms. We can therefore substitute the time dependence by a harmonic solution of circular frequency ω, i.e. all quantities have $e^{i\omega t}$ or $\cos(\omega t)$ as a factor, which is understood in the following and often omitted.
The complex writing is used whenever damping is involved. In these cases it shall be understood that only the real part of the solution has a physical meaning. From eq. 4 we obtain for the harmonic case

$$p,_{ii} = -\frac{\omega^2}{c^2}\,p = -\,k^2\,p$$

(8)

Here k is the wave number in the fluid and the following quantities are defined:

$f = \omega/2\pi$	frequency	(1/s)
$\lambda = c/f$	wavelength	(m)
$k = \omega/c = 2\pi/\lambda$	wave number	(Radians / m)
$T = 1/f$	period	(s)

k is a number that describes, how many wavelengths will fit into a distance of 2π m.

For harmonic solutions, the initial conditions are not relevant.

Typical boundary conditions are:

Fixed boundary $$u_i n_i = 0 \tag{9}$$

This means, that the particle velocity normal to the boundary surface (characterized by its unit normal n) must disappear. Note that because the fluid is assumed to be inviscid, no condition is imposed on the tangential velocity.
When formulated in terms of the pressure p, eq. 9 together with eq. 2 yields

Fixed boundary $$p_{,i}\, n_i = 0 \tag{10}$$

In reality all fluids have a certain viscosity, which forces the tangential velocity to be zero at the boundary. This happens within a narrow region which is called the Stokes' layer.
The thickness of the Stokes' layer is given by the formula:

$$\delta = \sqrt{\frac{\eta}{\rho\omega}} \tag{11}$$

where η is the dynamic viscosity. For water at 1MHz the thickness δ is about 1 micron and viscosity might become relevant for very small particles or cavities.

Free boundary $$p = 0 \tag{12}$$
when surface tension is neglected.

Fluid/solid boundary:
When an acoustic fluid is in contact with a solid, none of the above boundary conditions is valid in a strict sense. More precisely we have

$$\begin{aligned} u_{iS} n_i &= u_{iF} n_i \\ \sigma_{n_i} &= \sigma_{ij} n_i n_j = -p \end{aligned} \tag{13}$$

The normal displacements at the interface must be equal and the normal stress in the solid must be equal to the negative pressure in the fluid. Here the indices S and F refer to the fluid and solid respectively, and σ_{ij} is the stress tensor in the solid.

The acoustic energy per unit volume is $$e_{tot} = \frac{1}{2}\left(\rho_0 u^2 + \frac{p^2}{\rho_0 c^2} \right) \tag{14}$$

The sound intensity is defined as $$I = \frac{1}{T}\int_0^T pv\,dt \qquad (15)$$

2. Sample Solutions

For general geometries, no analytical solutions exist. For simple geometries, we can find solutions by assuming suitable functional dependencies that allow to satisfy the boundary conditions. This allows us to obtain a feeling for the physics.

2.1 Harmonic Plane Wave Propagating in the Direction of +x

We assume $p = p_0 \sin(k_x x - \omega t)$

and insert it into eq. 8 which yields $k_x = k$

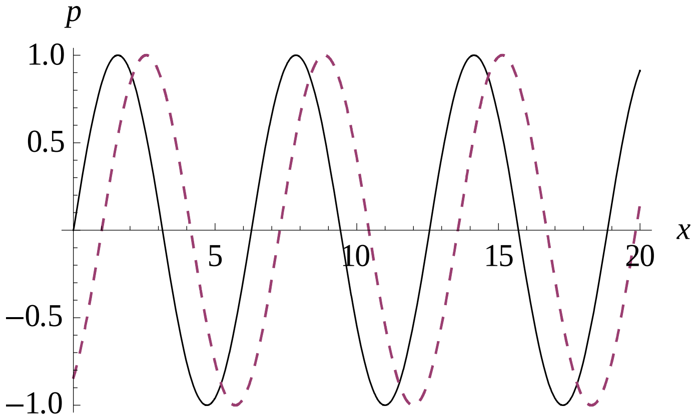

This figure shows the wave patterns of a single wave ($k = 1$, $\omega = 1$) at two times $t_1 = 0$ (solid) and $t_2 = 1$ (dashed). It can be clearly seen that the wave moves to the right. For a traveling wave there are no nodes fixed in space. The nodes move with the wave speed c.

2.2 Superposition of Harmonic Plane Waves Propagating in the Direction of +x and -x

The wave moving in the +x direction might be reflected to yield a wave moving in the –x direction. If these two waves have the same amplitude and are superimposed on each other, the result can be rewritten using simple trigonometry. A typical term then is

$$P = p_0 \sin(k_x x) \cos(\omega t)$$

This is called a standing wave.

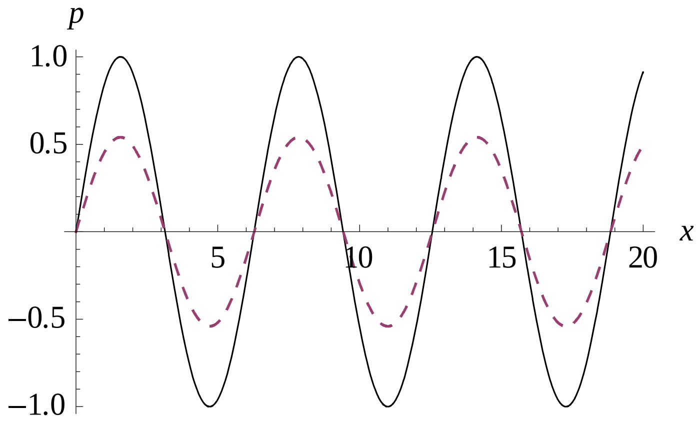

The superposition of the two waves therefore yields a nodal pattern, shown here again for the same parameters as in Chap. 2.1. At certain locations, the pressure is always 0, the maxima remain at the same location.
More generally the solution will look like

$$p = (A\cos(k_x x) + B\sin(k_x x))\cos(\omega t),$$

where A and B need to be determined from the boundary conditions. Standing waves will always occur, if waves are reflected from boundaries.

2.3 General plane wave propagating in the direction n

We assume

$$p = p_0 \sin(k_n n_i x_i - \omega t) = p_0 \sin\{k_n (n_i x_i - ct)\}$$

If the phase (term in brackets) is constant, then it describes the equation of a plane with normal n. If n is a unit vector, then after inserting the assumption into eq. 8, we obtain $k_n = k$.
As can be seen from the second part of the pressure assumption:

$$x_i n_i - ct = \text{constant}$$

the plane moves through space in the direction n with the speed c
This assumption is a special case for the d'Alembert solution to the wave equation: The sin function may be replaced by an arbitrary function, and still satisfies the wave equation (sufficient differentiability is assumed).

2.4 Homogeneous Solution for a One - Dimensional Resonator of Length L with Rigid Walls.

The homogeneous solution has by definition no excitation. Only without damping, a nontrivial homogeneous solution can exist.
The resonator is supposed to be cylindrical and extends from x = 0 to x = L. Because the resonator has a finite length, a wave generated at one end will be reflected at the other end. We therefore assume a standing wave in x direction:

$$p = (A\cos(k_x x) + B\sin(k_x x))\cos(\omega t)$$

In order to satisfy the PDE (eq. 8) $k_x = k$.

Now we have to satisfy all the boundary conditions (rigid walls) for all times t.

$$x = 0:\ p_{,x} = 0 \ \ \text{->}\ B = 0$$
$$x = L:\ p_{,x} = 0 \ \ \text{->}\ A\sin(kL) = 0$$

This means that only certain values of k are admissible, when we search for a non trivial solution!

$$k_m L = m\pi,\ m = 0,1,2,\ldots$$

The corresponding parameters are

$$\omega_m = k_m c \quad , \quad f_m = \frac{\omega_m}{2\pi} = \frac{mc}{2L} \quad , \quad \lambda_m = \frac{c}{f_m} = \frac{2L}{m}$$

$$p = A\cos(k_m x)\cos(\omega t) \tag{16}$$

There are various modes called resonance modes, numbered by m, each having their mode shape, frequency and wavelength.

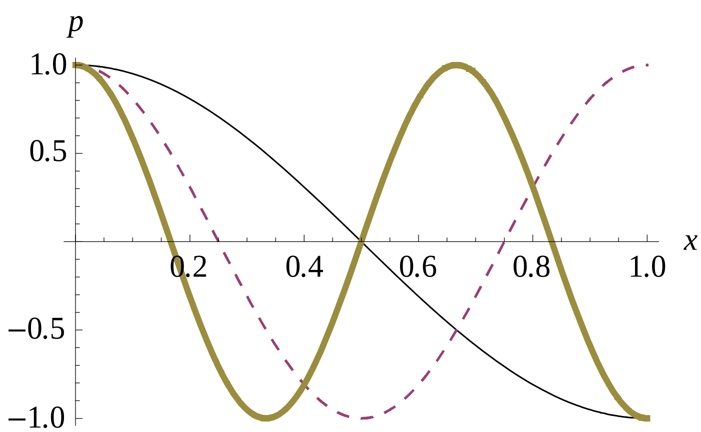

The modes 1 (solid), 2(dashed) and 3 (thick) are shown in the figure for a tube of length 1.
At all other walls, the unit vector normal to the wall is orthogonal to the pressure gradient, i.e. all boundary conditions are satisfied.

2.5 Inhomogeneous Solution for a One - dimensional Resonator of Length L with Rigid Walls, Harmonic Pressure Excitation at x = 0

We assume the same pressure distribution as in Chap. 3.4. However, the boundary condition is now:

$x = 0$: $p = p_0 \cos(\omega t)$ (p_0 is the given excitation amplitude)
$x = L$: $p_{,x} = 0$

The solution is

$$p = p_0 (\cos(kx) + \tan(kL) \sin(kx)) \cos(\omega t)$$

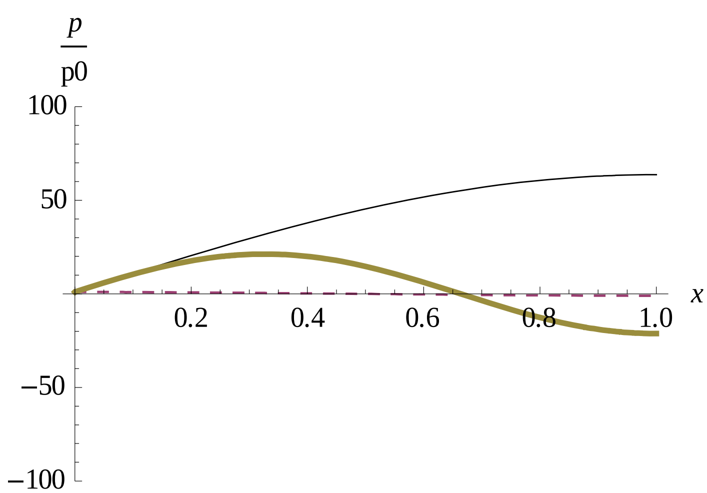

Here the normalized pressure p is plotted vs. x for L = 1 and excitation frequencies and corresponding k close to the first mode ($k=\pi/2$, solid), the second mode ($k = 3\pi/2$, thick) and in between ($k= \pi$).
Please note:
Near the resonance frequencies, there is constructive interference between the outgoing and the reflected waves, leading to an amplification of the pressure amplitudes. In between, there is destructive interference leading to an extinction of the pressure amplitude.

2.6 Homogeneous Solution for a Three - Dimensional Cuboid Resonator of Dimensions L_x, L_y, L_z with Rigid Boundaries

Motivated by eq. 16 we assume a pressure distribution:

$$p = A \cos(k_x x) \cos(k_y y) \cos(k_z z) \cos(\omega t)$$

Using eq. 8 we obtain

$$k_x^2 + k_y^2 + k_z^2 = k^2$$

If we take

$$k_x = p\pi / L_x, \quad p = 0,1,2,..$$
$$k_y = q\pi / L_y, \quad q = 0,1,2,..$$
$$k_z = r\pi / L_z, \quad r = 0,1,2,..$$

all the boundary conditions are satisfied, so we have found an infinite number of solutions. The corresponding frequencies are computed from

$$f_{pqr} = \frac{c}{2}\sqrt{(p/L_x)^2 + (q/L_y)^2 + (r/L_z)^2}$$

by using the definition of k.

For micromanipulation, often the z dimension of the resonators is small, such that $r = k_z = 0$.

The following graphs show a selection of pressure distributions for various values of p, q, r.

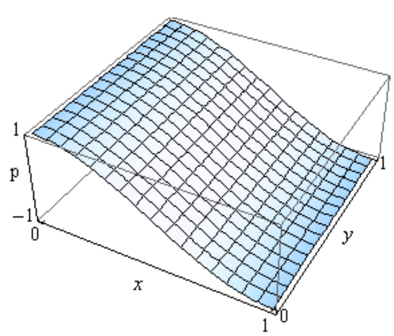

p = 1, q = 0, r = 0

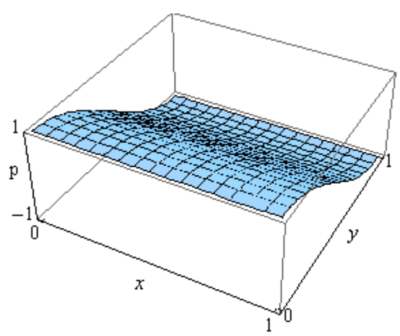

p = 0, q = 1, r = 0

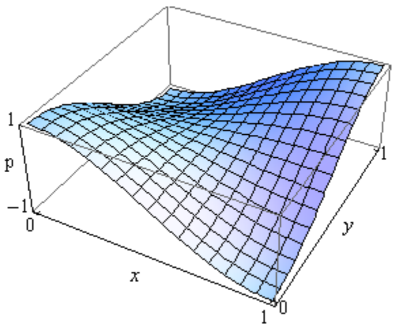

p = 1, q = 1, r = 0

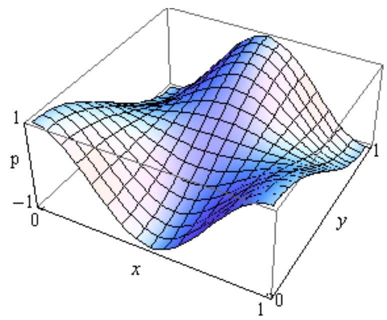

p = 2, q = 1, r = 0

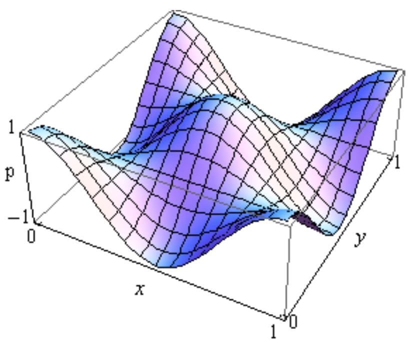

p = 2, q = 2, r = 0

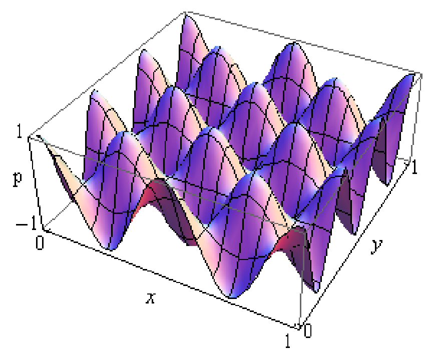

p = 4, q = 6, r = 0

Please note, that any superposition of the above mentioned modes is also a solution. Because there is no rigid boundary, the above ideal solutions have to be modified depending on the impedance of the structure surrounding the cavity.

Exercise: Based on eq. 2, sketch the velocity distributions using arrows in the x-y plane.

3. Literature

1. Kinsler, L.E. et al., **Fundamentals of Acoustics**, Wiley, New York, 1982

Lecture 2: Vibrations in Solids

J. Dual, ETH Zurich, Switzerland

Dynamics of Linear Elastic Solids

The motion of solids is more complicated than the one for fluids, because a solid can support shear stresses. The basic equations in the context of linear elasticity are:

The kinematical relations which connect displacement $\underset{\sim}{\xi}$ with the strain tensor $\underset{\approx}{\gamma}$:

$$\gamma_{ij} = \frac{1}{2}(\xi_i,_j + \xi_j,_i) \qquad (1)$$

i.e. $\gamma_{11} = \xi_{1,1}$ is the longitudinal strain in the x_1 direction,

$\gamma_{12} = \frac{1}{2}(\xi_{1,2} + \xi_2,_1)$ is the shear strain in the 1-2 plane

" $,_j$" means taking the derivative with respect to x_j and the summation convention is used for repeated indices.

e.g. $\gamma_{ii} = \gamma_{11} + \gamma_{22} + \gamma_{33}$ is the volume strain!

With the components of the stress tensor σ_{ij} we can formulate the local linear momentum equation: (σ_{ij} symmetrical !)

In direction x_1: $\sigma_{11},_1 + \sigma_{12},_2 + \sigma_{13},_3 = \rho \ddot{u}_1$

In direction x_2: $\sigma_{12},_1 + \sigma_{22},_2 + \sigma_{23},_3 = \rho \ddot{u}_2$

In direction x_3: $\sigma_{13},_1 + \sigma_{23},_2 + \sigma_{33},_3 = \rho \ddot{u}_3$

Or in indicial notation for

direction x_i: $\sigma_{ij},_j = \rho \ddot{u}_i$ (2)

An **isotropic linearly elastic body** is fully described by two material constants E, G or λ and μ, where E, G are Young's and shear modulus and λ, μ are the Lamé constants.

$$\sigma_{ij} = \lambda \gamma_{kk} \delta_{ij} + 2 \mu \gamma_{ij} \qquad (3)$$

δ_{ij} is the unity tensor.

$$\delta_{ij} = \begin{Bmatrix} 1 \ldots i = j \\ 0 \ldots i \neq j \end{Bmatrix}$$

λ and μ are related to E and G by

$$\mu = G = \frac{E}{2(1+\nu)} \tag{4}$$
$$\lambda = \frac{\nu E}{(1+\nu)(1-2\nu)} = 2\,G\,\frac{\nu}{(1-2\nu)}$$

ν is Poisson's ratio.

Combining eq. 1 to 3 we obtain

$$\sigma_{ij},_j = (\lambda + \mu)\,\xi_k,_{ki} + \mu\,\xi_i,_{kk} = \rho\,\frac{\partial^2 \xi_i}{\partial t^2} \tag{5}$$

These are three coupled differential equations that need to be solved together with

initial conditions $\underline{\xi}(\underline{x}, 0) = \underline{g}\,(\underline{x})$

$$\frac{\partial \xi}{\partial t}(x, 0) = \underline{h}\,(\underline{x})$$

As boundary conditions, either the displacement $\underline{\xi}$ or the stress vector $\underline{t} = \underline{\underline{\sigma}}\ \underline{n}$ must be given on the boundary for all times t. A combination of $\underline{\xi}_t$ together with $\underline{t}_n$ or $\underline{\xi}_n$ with $\underline{t}_t$ is also possible, where the indices n und t denote the normal and tangential components of the vectors, respectively. As an example, for the interface of an inviscid fluid with the solid structure we have

$$\underline{\xi}_{nF} = \underline{\xi}_{nS}, \quad -p\ \underline{n} = \underline{t}_{nS}, \quad \underline{t}_{tS} = \underline{0}$$

There exists a unique solution to these equations, if all the conditions are set up properly.

Eq. 5 are pretty complicated. They can, however, be simplified and it can be shown that two types of waves exist:

P-waves $\quad c_1 := \sqrt{\frac{\lambda+2\mu}{\rho}}$ (6)

S-waves $\quad c_2 := \sqrt{\frac{\mu}{\rho}} < c_1$

Because $c_1 > c_2$ the two types of waves are called **Primary or P - waves** and **Secondary or S – Waves.**

Typical values are c_1 = 6300m/s and c_2 = 3140m/s for aluminium and c_1 = 2650m/s and c_2 = 1080 m/s for PMMA.

For silicon, the situation is more complicated as Si is anisotropic. Therefore the wave speeds are depending on the direction of propagation and the constitutive law must be replaced by

$$\sigma_{ij} = c_{ijkl}\,\gamma_{kl} \quad \text{(summation over k and l!)}$$
$$\gamma_{ij} = s_{ijkl}\,\sigma_{kl} \tag{7}$$

The forth order tensors c_{ijkl} and s_{ijkl} are the stiffness and the compliance tensor of the material, respectively. While the wave propagation in such materials is quite involved, for a numerical vibrational analysis of a structure often only the material properties are changed when compared to an isotropic solution.

Vibrations of Linearly Elastic Solids

The two types of waves interfere and get reflected at boundaries to yield the modes of vibrations. For general geometries as they occur in particle manipulation devices, a numerical solution must be found, which typically is called the Finite Element Method (FEM) solution. The usual steps when applying the FEM are:

- Definition of the geometry
- Definition of material properties
- Choosing suitable elements for the spatial discretization. Important in this decision is whether structural elements (beams, plates, shells) or 3D brick elements are used. Also the approximation of the displacement functions within the element is an important consideration.
- Definition of boundary conditions, interface conditions and loading conditions (possibly depending on the element)
- Choosing the mode of analysis (e.g. harmonic analysis)
- Computation of the results
- Analysis of the results and quality check

If one or two dimensions of a structure are much smaller than the third, there exist a number of models that allow simple interpretation of the vibration:

- Beam (length >> cross-section): Longitudinal, torsional and bending vibration
- Plate (flat, thickness H << other dimensions): Longitudinal and bending vibrations.
- Shell: As plate, except that the middle surface has a curvature.

In view of the applications to micromanipulation we focus here on bending vibrations of thin plates.

Bending Vibrations of Thin Plates

In structures it is customary to refer all quantities to the middle surface. For simplicity we consider here a displacement w of the middle surface in the z direction independent of y.

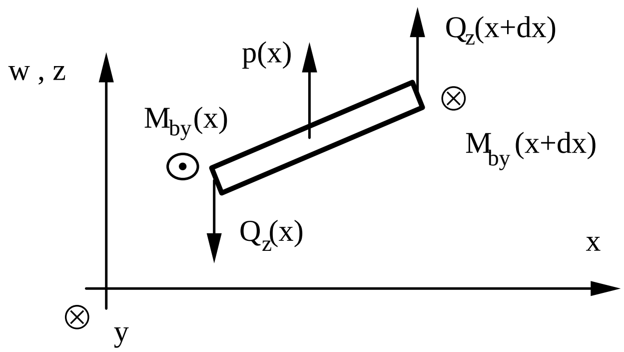

We consider the case of bending vibrations in the context of the Kirchhoff plate theory, which is the equivalent to the Euler-Bernoulli beam theory. For a homogeneous, isotropic, linearly elastic plate of unit width, small strains, small deformation and wavelengths which are large with respect to the thickness h of the plate the following equations are valid:

$$M_{by} = - \frac{E}{1-\nu^2} I_y \, w_{,xx} \qquad \text{onstitutive law and kinematics}$$

$$- Q_z + M_{by,x} = 0 \qquad \text{angular momentum equation} \qquad (8)$$

$$p^* + Q_{z,x} = \rho A \frac{\partial^2 w}{\partial t^2} \qquad \text{inear momentum equation}$$

Here, A is the cross-sectional area, I_y the moment of inertia of the cross-section, M_{by} the bending moment, Q_z the shear force and p^* the load per unit length. Please note that shear deformation has been neglected in the kinematic equation and rotatory inertia has been neglected in the angular momentum equation.

$$\sqrt{\frac{E}{(1-\nu^2)}}$$

is called the longitudinal plate modulus.
Combining eqs. 8 we obtain

$$\frac{E}{1-\nu^2} I_y \, w_{,xxxx} + \rho A \frac{\partial^2 w}{\partial t^2} = p^* \qquad (9)$$

In order to solve eq. 9 we consider harmonic solutions of the type

$$w = w_0 e^{i(\omega t - kx)}, \quad k = \frac{\omega}{c}, \quad \text{c still unknown}$$

If w satisfies eq. 9, for p = 0 we obtain

$$c^2 = \pm \sqrt{\frac{EI_y}{\rho(1-\nu^2)A}}\,\omega = \pm\, c_3\, j_y\, \omega$$

where $c_3 = \sqrt{\dfrac{E}{\rho(1-\nu^2)}}$ longitudinal wave speed in plate

and $j_y = \sqrt{\dfrac{h^2}{12}}$ radius of inertia of the cross-section

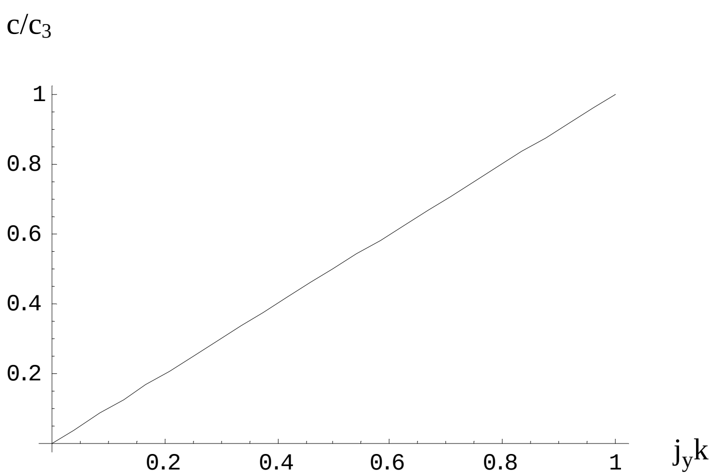

Normalized dispersion curve for bending waves in a plate

The phase speed c is a function of frequency, therefore bending waves are dispersive. Using $\omega = c\,k$ we obtain:

$$\omega = c_3\, j_y\, k^2 \qquad \text{or} \qquad c = c_3\, j_y\, k \tag{10}$$

Note that in general for plate vibrations, the differential equation is

$$D\,(w_{,xxxx} + 2w_{,xxyy} + w_{,yyyy}) + m\,\frac{\partial^2 w}{\partial t^2} = p \tag{11}$$

where

$$D = \frac{Eh^3}{12(1-\nu^2)}, \qquad m = \rho h$$

D is the bending stiffness, m and p are the mass and loading per unit area of the plate.

Example:
Consider vibrations of a plate that are independent of y, with pinned – pinned boundary conditions at x = 0 and x = L.
We assume $w(x,t) = f(x)e^{i\omega t}$
After insertion into eq. (11) we get

$$f_{,xxxx} - k^4 \varphi = 0$$

with the solution

$$f = a_1 \sin(kx) + a_2 \cos(kx) + a_3 \sinh(kx) + a_4 \cosh(kx)$$

a_1 to a_4 are obtained from the application of the boundary conditions

$$f(0) = f(L) = f_{,xx}(0) = f_{,xx}(L) = 0$$

Because the differential equation is of forth order, we need for boundary conditions. This yields a 4x4 homogeneous system of equations for the unknowns a_1 to a_4, the determinant of which must vanish for a non trivial solution to exist, resulting in

$$\sin(kL) = 0$$

and $k_n L = n\pi$

For the corresponding eigenfrequencies one obtains

$$f_n = c_3 j_y \frac{n^2}{2} \frac{\pi}{L^2}$$

For other boundary conditions, the solution is more complicated.
e.g. for clamped – clamped we have [1]

$$k_n L = 4.73, 7.85, 10.99, 14.14, \ldots$$

Note that the resonance frequencies are proportional to $1/L^2$ and increase with n^2.

Damping can easily be incorporated into the equations, if we restrict ourselves to harmonic motion. According to the theory of linear viscoelastic materials [2] and for small damping, the material is described by a complex Young's modulus E^*.

$$E^* = E_0(1 + i\varphi)$$

Here φ is the loss tangent, E_0 the elastic part. For metals φ is about 0.01 – 0.0001 and E^* is nearly independent of frequency. For plastic materials, depending on temperature, a strong frequency dependence might be present.

When solving a specific problem, we have to assume a driving function and proceed with

$$w(x,t) = A(x,y)\, e^{i\omega t}$$

and solve Eq. 11 for the complex amplitude distribution A(x,y).

Literature

1. Graff, K. F. , **Wave Motion in Elastic Solids ,** Ohio State University Press, 1975 (neu aufgelegt)
2. Christensen, R.M., **Theory of Viscoelasticity**, Academic Press, 1971

Lecture 3: Fluid Structure Interaction

J. Dual, ETH Zurich, Switzerland

When a fluid is in contact with a solid, fluid structure interaction takes place. Both the field equations in the solid and in the fluid must be satisfied, as well as the boundary conditions. In addition, at the interface, certain conditions must be satisfied, depending on how the fluid is modeled:

As it has been mentioned, for the interface of an inviscid fluid with the solid structure we have

$$\underline{\xi}_{nF} = \underline{\xi}_{nS}, \qquad -p\,\underline{n} = \underline{t}_{nS},\ \underline{t}_{tS} = \underline{0} \tag{1}$$

At the interface the normal displacements must be equal, the normal stress of the solid must be equal to the negative of the pressure in the fluid, and the shear stress in the solid must vanish, if the fluid's viscosity is neglected. Because of the difficulties in applying all the equations for the complex geometries of specific devices, numerical solutions must be found, which often are based on the Finite Element Method (FEM). Only for some simple problems, analytical solutions exist. Two cases are considered here: A first case, where the fluid motion does not influence the solid motion, and a second case, where there is a strong influence.

Acoustic Radiation from a Surface Vibrating with a Harmonic Amplitude Distribution

In this chapter situations are considered, where the surface of a solid half space ($x < 0$) is vibrating harmonically with a given velocity distribution $u_x(0, y)$. The fluid which occupies the half space $x > 0$ does not influence the motion. We look for the solution in the fluid, which must satisfy

$$p_{,ii} = \frac{1}{c^2}\frac{\partial^2 p}{\partial t^2} = -k^2 p, \qquad k = \frac{\omega}{c}$$
$$\rho_0 \frac{\partial u_i}{\partial t} + p_{,i} = 0 \qquad \text{at } x = 0 \tag{2}$$

a) $u_x(0, y) = u_0 e^{i\omega t}$

we obtain the solution by setting $p = p_0\, e^{i(\omega t - kx)}$ where we have assumed that there is no energy flowing back towards the surface (radiation condition).

$p = \rho_0\, c\, u_0$ i.e. the pressure amplitude is equal to impedance times velocity amplitude as expected. Energy is radiated into the fluid with an intensity

$$I = \frac{1}{2}\rho_0 c u_0^2$$

b) $u_x(0, y) = u_0 \sin(k_y y)e^{i\omega t}$, k_y given
we assume as a possible solution $p = p_0 \sin(k_y y)\, e^{i(\omega t - k_x x)}$ which satisfies eq. 2 if

$$k_x^2 = k^2 - k_y^2$$

We must discriminate between two cases:
1) $k > k_y$ or $\lambda < \lambda_y = \frac{2\pi}{k_y}$

i.e. the wavelength of the surface motion is larger than the wavelength in the fluid for the particular frequency. The frequency is larger than c/λ_y. k_x is a real number and we obtain a wave propagating away from the surface.

2) $k < k_y$ or $\lambda > \lambda_y$

i.e. the wavelength of the surface motion is smaller than the wavelength in the fluid for the particular frequency. The frequency is smaller than c/λ_y, k_x is a purely imaginary number. When inserted into the assumption, we obtain

$$\alpha = \sqrt{k_y^2 - k^2}$$
$$p = p_0 \sin(k_y y)e^{-\alpha x}\cos(\omega t)$$

This is an exponentially decaying pressure field, and no acoustic radiation occurs. The fluid is pumped back and forth between neighbouring valleys and hills according to

$$u_x = \frac{\alpha p_0}{\omega\rho_0} e^{-\alpha x} \sin(k_y y)\sin(\omega t)$$
$$u_y = -\frac{k_y p_0}{\omega\rho_0} e^{-\alpha x} \cos(k_y y)\sin(\omega t)$$

To summarize: For low frequencies, i.e. $f < c/\lambda_y$ no acoustic radiation occurs.

Acoustic Radiation from a Plate Vibrating Harmonically

We now combine the Kirchhoff plate equations in 2D with the acoustic solutions by looking at a situation, where a plate vibrates in contact with a fluid halfspace x > 0 on one side. [1] The plate motion satisfies

$$D\, w,_{yyyy} + m \frac{\partial^2 w}{\partial t^2} = p(x=0) \tag{3}$$

where

$$D = \frac{Eh^3}{12(1-\nu^2)}, \qquad m = \rho h$$

D is the bending stiffness, m and p are the mass and loading per unit area of the plate. The fluid satisfies eq. 2. The boundary condition is:

$$\rho_0 \frac{\partial^2 w}{\partial t^2} = -p,_x \quad \text{at } x = 0 \tag{4}$$

Note, that the top surface of the plate is taken as x = 0. With this boundary we now consider the full interaction between the sound field and the motion of the plate. This will result in a modified wave speed for the wave in the plate. Assuming a wave traveling in the +y-direction we look for solutions of the form (k_y unknown!)

$$p = p_1(x)e^{i(\omega t - k_y y)}$$
$$w = w_0 e^{i(\omega t - k_y y)}$$

which when inserted into the system of equations yields for the fluid:

$$p_{1,xx} + (k^2 - k_y^2)p_1 = 0$$

resulting in

$$p_1 = Ae^{i\gamma x} + Be^{-i\gamma x}$$
$$\gamma^2 = (k^2 - k_y^2) \tag{5}$$

As before we will have to discriminate two cases:

1) $k > k_y$ or $\lambda < \lambda_y$

i.e. the wavelength of the plate motion is larger than the wavelength in the fluid for the particular frequency. The frequency is larger than c/λ_y. We obtain a wave propagating away from the surface.
The radiation condition yields A = 0.
The boundary condition eq. 4 at the plate yields

$$i\gamma B = -\rho_0 \omega^2 w_0$$

We can now introduce the pressure into eq. 3, which yields

$$(Dk_y^4 - \rho h \omega^2) w_0 = \frac{i\rho_0 \omega^2}{\gamma} w_0$$

containing the dispersion relation modified by the fluid:

$$Dk_y^4 - (\rho h + \frac{i\rho_0}{\sqrt{(k^2 - k_y^2)}})\omega^2 = 0$$

The solution k_y must be obtained numerically. It is complex, representing the fact, that the acoustic radiation will introduce an exponential decay of the traveling wave.

2) $k < k_y$ or $\lambda > \lambda_y$

i.e. the wavelength of the plate motion is smaller than the wavelength in the fluid for the particular frequency. The frequency is smaller than c/λ_y.
When inserted into the assumption, we obtain

$$\alpha = \sqrt{k_y^2 - k^2}$$
$$p_1 = Be^{-\alpha x}$$

and the boundary condition yields

$$\alpha B = -\rho_0 \omega^2 w_0$$

Following the same procedure we obtain the dispersion relation for this case

$$Dk_y^4 - (\rho h + \frac{\rho_0}{\sqrt{(k_y{}^2 - k^2)}})\omega^2 = 0$$

In this case, the dispersion relation is only modified in a way, where the mass term is increased by fluid being pumped around.

This is the situation that one would like to have, if one wants to make a density sensor.

A special case of this is when $k << k_y$. We can then neglect k, and also neglect ρ_0 k_y h when compared to ρ (thin plate) and get

$$k_y^5 = \frac{\omega^2 \rho_0}{D} \quad (6)$$

Physically speaking, all the stiffness is provided by the plate and all the mass is provided by the fluid.

In the following some graphs are provided for a Silicon plate (thickness 100microns) and water.

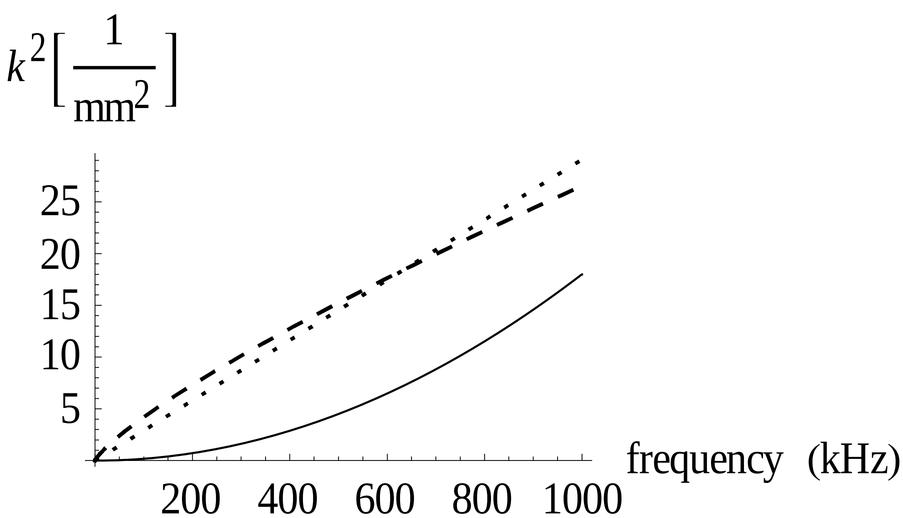

Square of the wave number for waves in water (solid), bending waves in plates (dotted) and interacting bending waves (Eq. 6) (dashed)

Literature:

F. Fahy, Sound and Structural Vibration, Academic Press, 1987

M3 Fundamental Microfluidics

Fundamentals of microfabrication techniques for microchip acoustic resonators

Johan Nilsson

Department of Measurement Technology and Industrial Electrical Engineering
Lund University
Lund, Sweden
johan.nilsson@elmat.lth.se

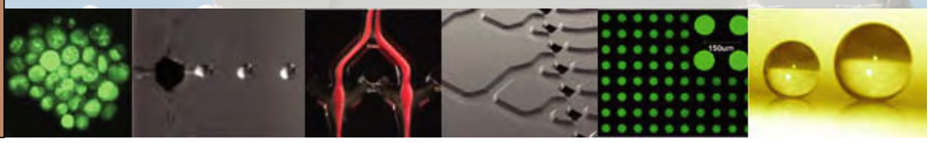

Examples of microchip acoustic resonators

Glass/Glass **Silicon/Glass** **Glass/Silicon/Glass**

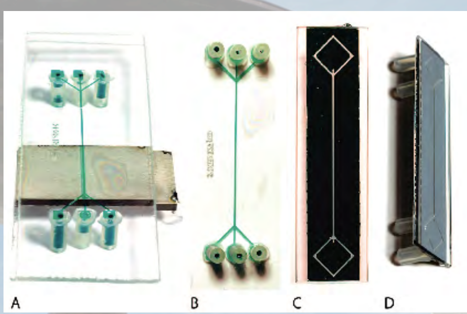

Evander et al. Anal. Chem. 80 (2008) pp 5178

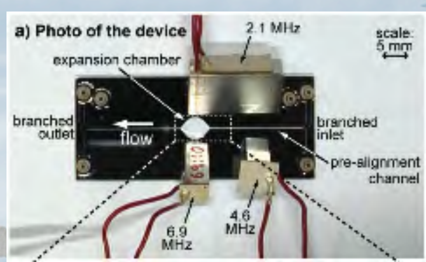

Svennebring et al. Biotech. Bioeng. 103 (2009)

Glass/Transducer/Polymer

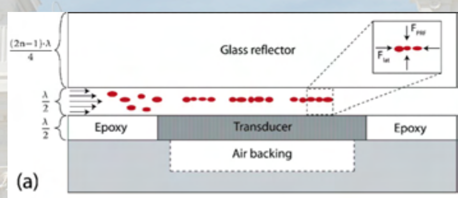

Evander et al. Anal. Chem. 79 (2007) pp 2984

Examples of microchip acoustic resonators - Wall shapes

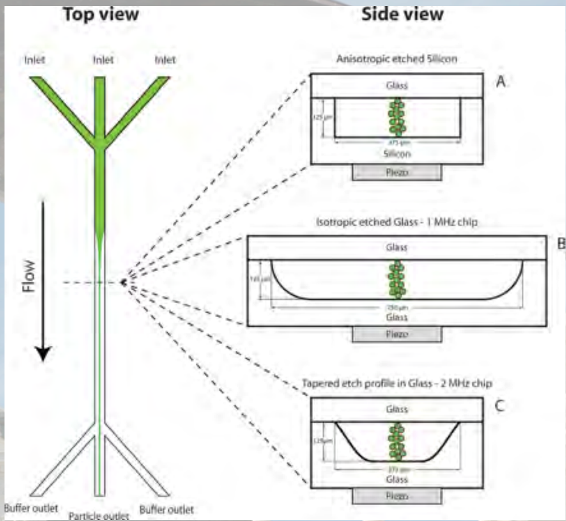

Silicon/Glass

Glass/Glass - Wide

Glass/Glass - Narrow

Evander et al. Anal. Chem. 80 (2008) pp 5178

Microfabrication

High/Low aspect ratio

Bulk/Surface micromachining

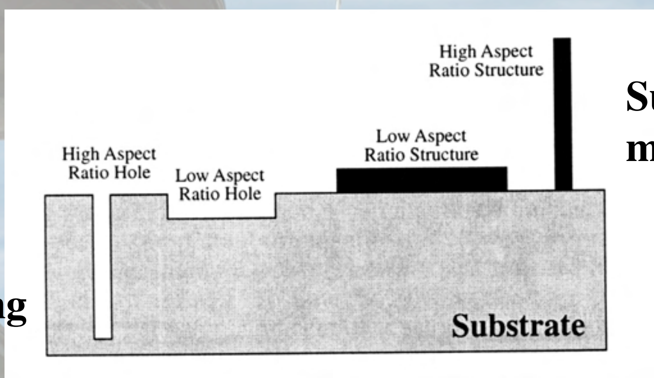

Surface micromachining

Bulk micromachining

(Kovacs, Micromachined Transducers Sourcebook,)

Microfabrication lab

- **Clean room environment**
  - **Typically Class 100 - 1000 (Particles per ft^2)**

Photolithography

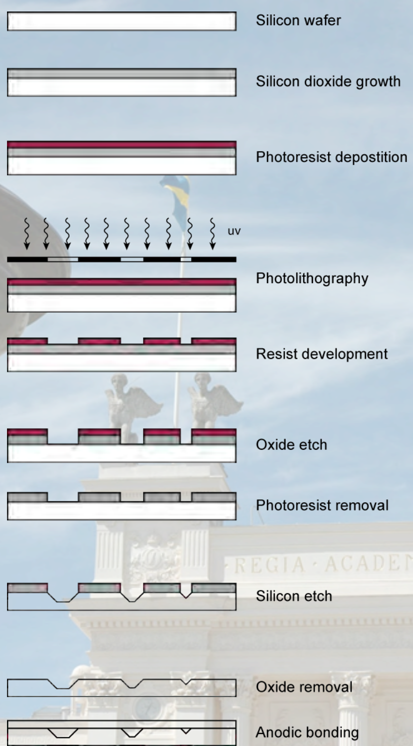

Photolithography

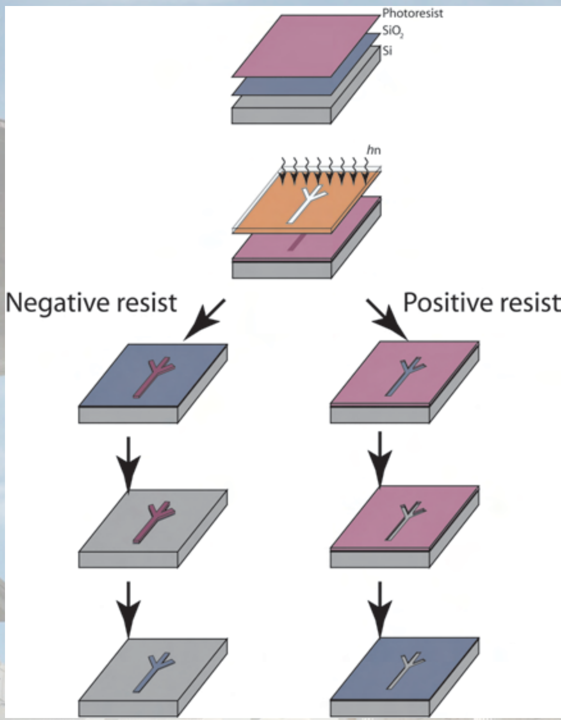

Exposure

Resist development

Etching

Resist removal

Silicon microfabrication

Processing steps

- **Oxidation**
- **Spinning of photoresist**
- **Lithography**
- **Cleaning**
- **Wet etching**
  - **Isotropic**
  - **Anisotropic**
- **Dry etching**
  - **DRIE**
- **Bonding**

Silicon dioxide

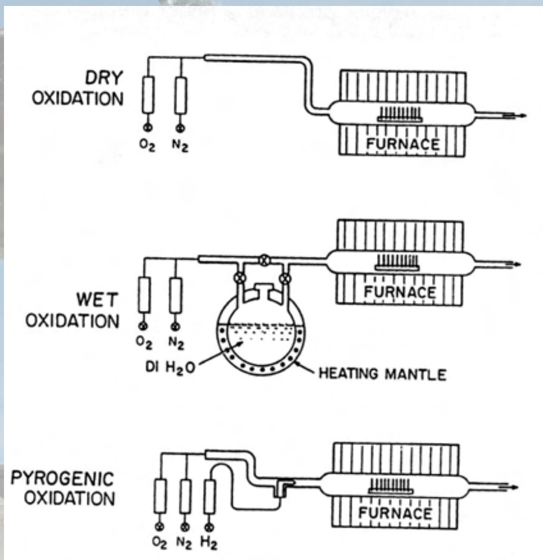

Thermal growth

Oxygen ambient:

Si + 0_2 -> SiO_2

(dry oxidation)

Thin, high quality

Steam ambient:

Si + $2H_2O$ -> SiO_2 + $2H_2$

(wet oxidation)

Thicker

- **N_2 carrier, saturated with steam**
- **H_2 + O_2 combustion**

Spinning of photoresist

- ***Spin coating***
  - **Rotational speeds between 1500 and 8000 rpm**
  - **Resist film uniformity should be ±5 nm from substrate to substrate**
  - **Typical thickness: 0.8 – 3 μm**
  - **Disadvantage: edge bead formation**
- ***Spin speed versus thickness***

$$z = \frac{k \cdot P^2}{\sqrt{\omega}}$$

z: thickness
k: constant
P: percentage of solids
w: rotational speed

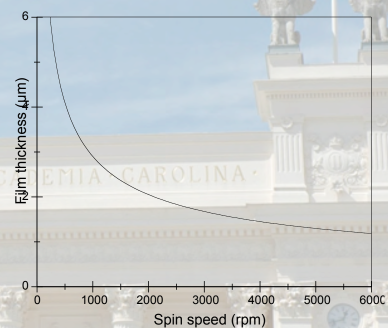

Film thickness vs. spin speed for AZ4620 resist

Microstructuring of silicon

Mono-crystalline Silicon

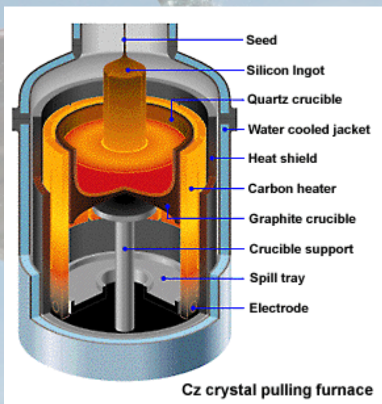

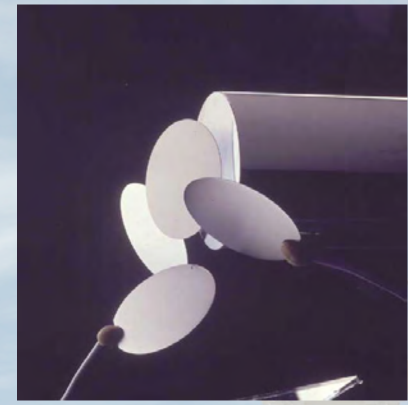

Czochralski technique

Silicon crystal planes

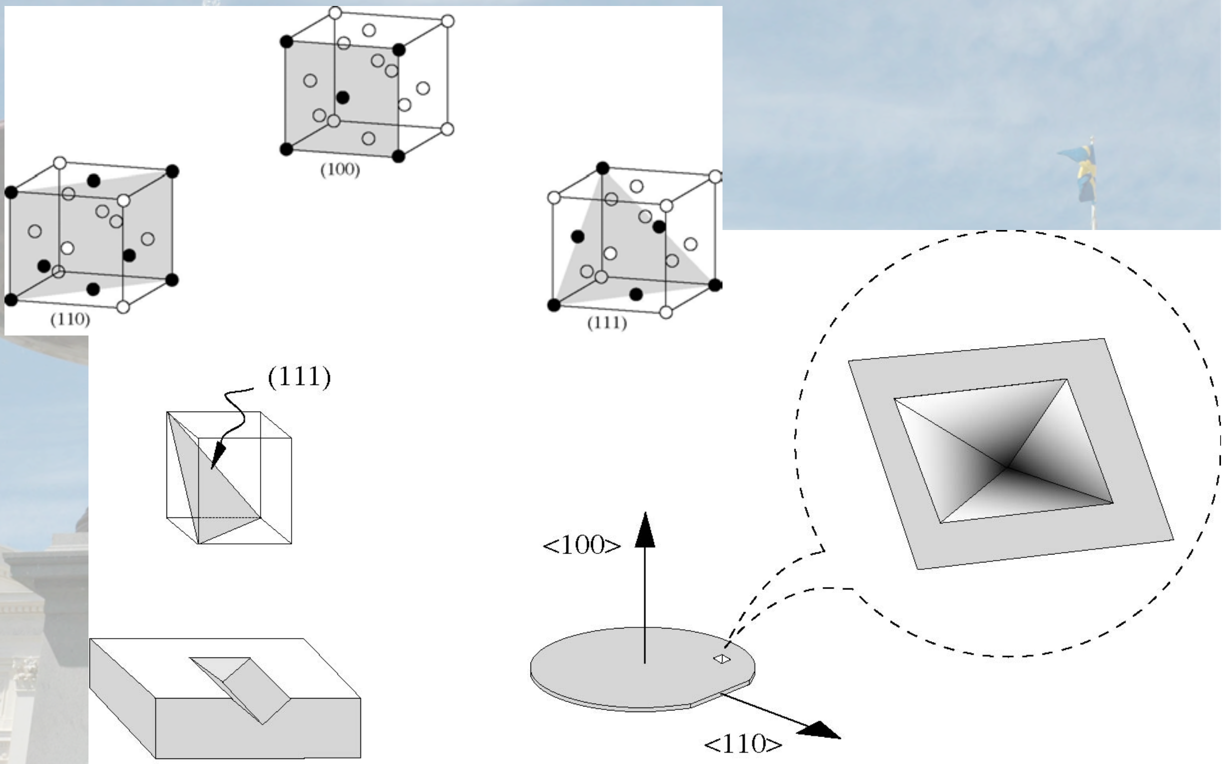

Etching of silicon

Isotropic - Anisotropic

Isotropic
Same etch rate in all directions

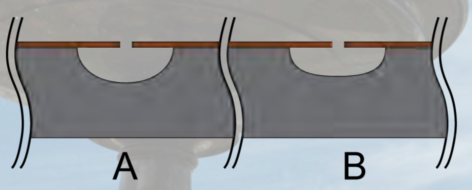

A) Isotropic etching with agitation
B) Isotropic etching without agitation

Common etchant

- HNA – Hydrofluoric acid, Nitric acid, Acetic acid

Anisotropic
Etch rate dependent on crystal planes

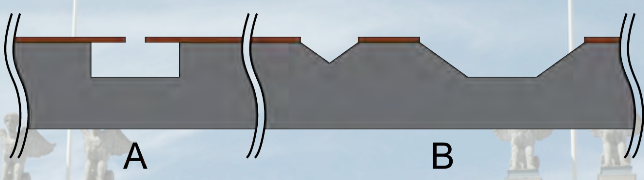

A,B Different orientations of masks on wafer

Common etchants

- KOH – Potassium Hydroxide
- EDP – Ethylenediamene pyrocatecol
- TMAH – Tetramethylammonium hydroxide

Etching of silicon
Isotropic

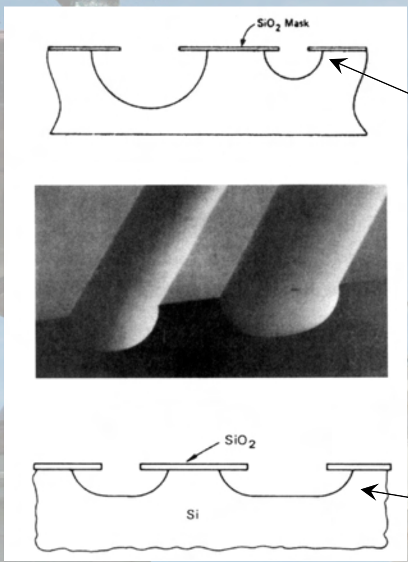

- **Same etch rate in all directions**
- **Underetch!**
- **Agitation important**
  - **Stirring**
  - **Ultrasonic**
- **HF + HNO_3 + CH_3COOH**
- **(Hydrofluoric acid, Nitric acid, Acetic acid)**

- **Without agitation**

(Madou, Fundamentals of microfabrication.)

<100> silicon
Anisotropic etching

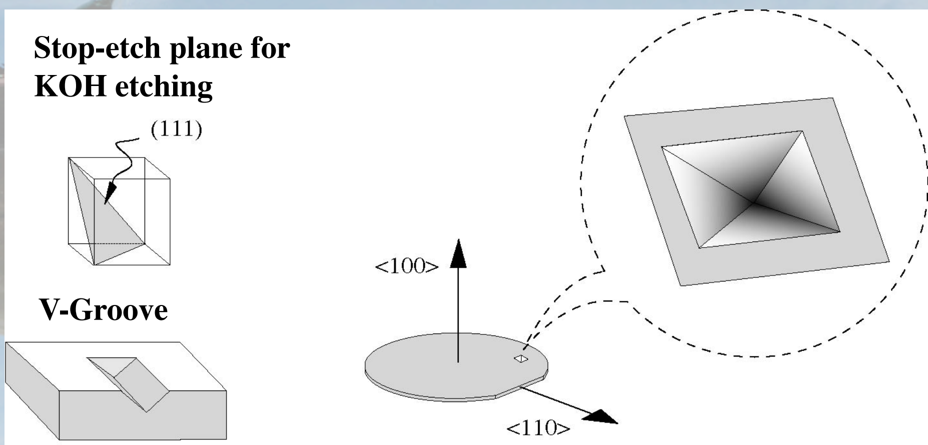

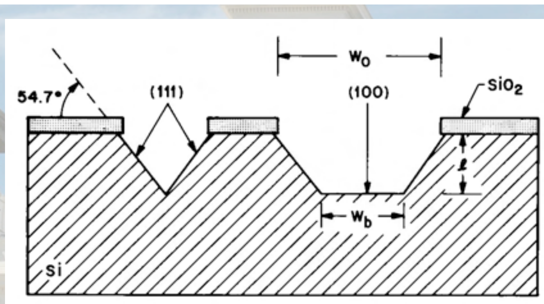

Anisotropic etching

<100> silicon – channel orientation

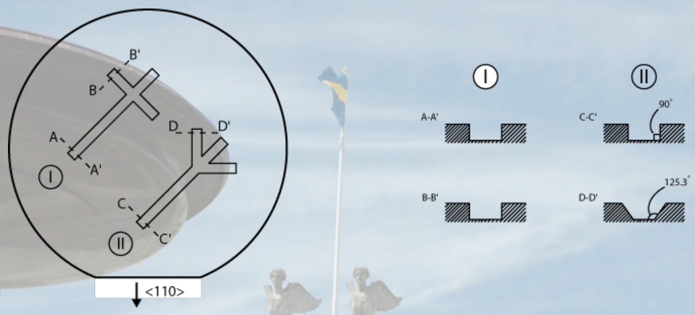

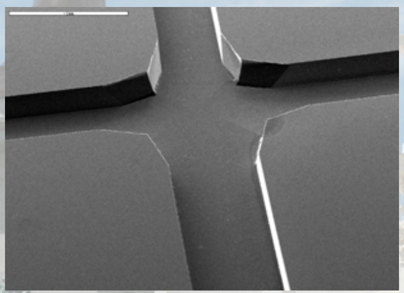

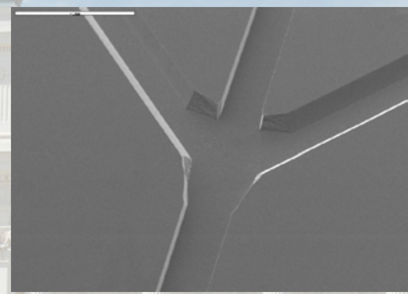

Anisotropic etching

<100> silicon – channel orientation

Vertical walls in <100>-silicon,
but under-etch!
Width > 2 x height

The V-grooves are defined by the mask opening
Due to the <111> stop etch plane in
anisotropic etching

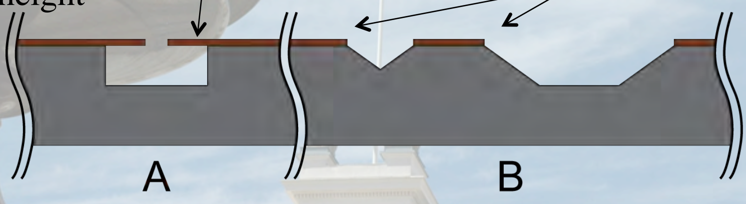

Common etchants

- KOH – Potassium Hydroxide
- EDP – Ethylenediamene pyrocatecol
- TMAH – **Tetramethylammonium hydroxide**

Anisotropic etching
<100> silicon

Y-separator

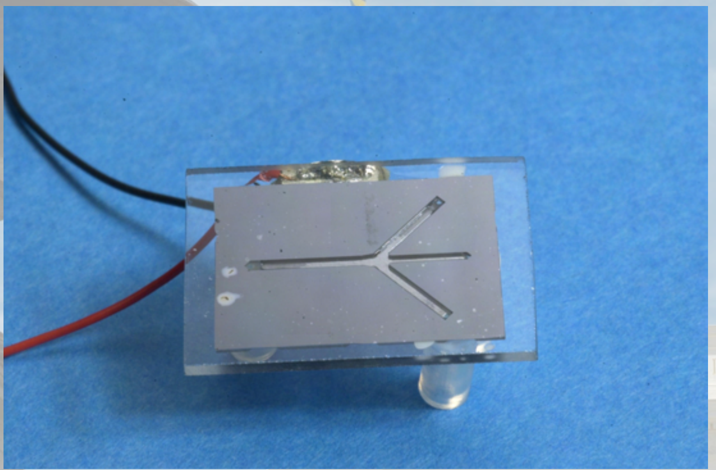

<110> silicon
Anisotropic etching

Again mask alignment/orientation is fundamental for the end result.

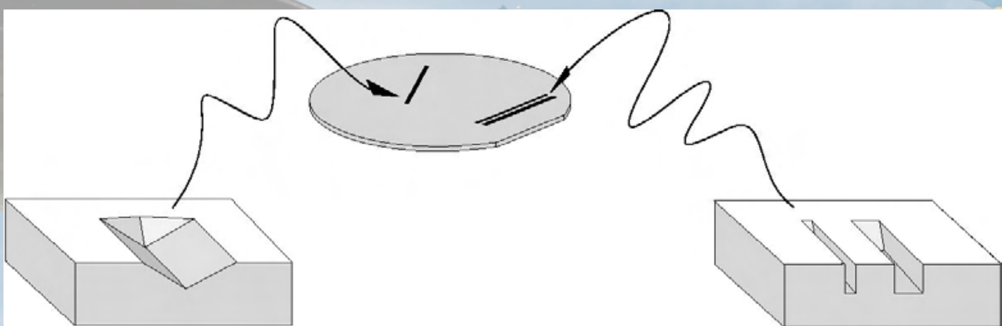

Etch rate ratio:
Vertical/horisontal
~ 500:1

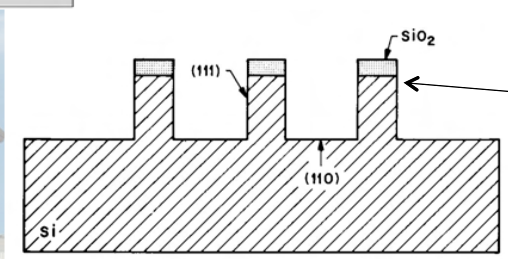

No under etch,
due to the stop-etch plane!
-> Possible to make deep narrow channels.

Anisotropic etching

- KOH/water (isopropyl alcohol)
  - Standard: 40 g KOH + 100 ml H_2O
  - Etch rate 1-2 μm/min
  - Reduced surface roughness at higher concentrations
  - 80 deg C
  - SiO_2 etch mask is etched! Faster in a higher concentration!
  - Sticking of H_2 bubbles reduced by agitation (e.g. ultrasonic)
  - Incompatible with IC (electronics) fabrication

Anisotropic etching

- TMAH - Tetramethyl ammonium hydroxide
  - Expensive compared to KOH
  - Smooth surface finish
  - IC compatible
  - 90 deg C
  - Etch rate ca. 1 μm/min

Dry etching

DRIE - Deep Reactive Ion Etching

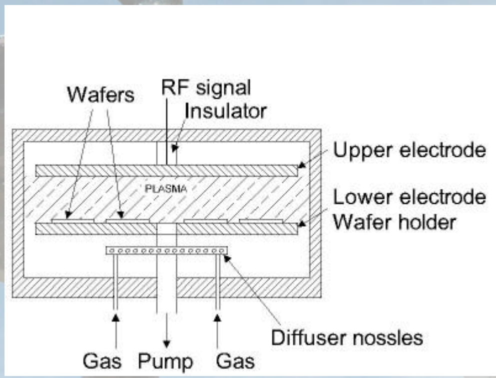

(Sandia National Laboratories)

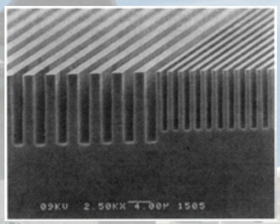

Etch depth dependent on width

- **Very high aspect ratio etching method**
- **Not dependent on crystal planes**

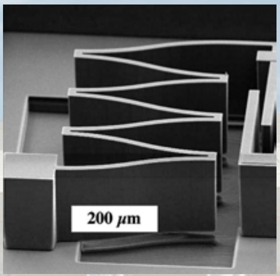

Kovacs et al., Stanford University
http://transducers.stanford.edu/stl/Projects/mems.html

Dry etching

DRIE

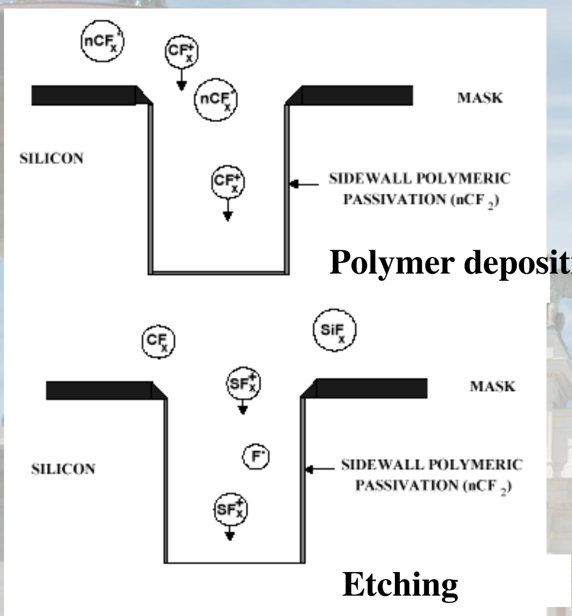

- **plasma used to generate reactive species**
- **process alternates between etching and polymer deposition steps**
- **a fluorocarbon/Ar mix is used for polymer deposition**
- **an SF_6/Ar mix is used for etching; polymer removed from horizontal surface in etch step**

Dry etching

DRIE - Examples

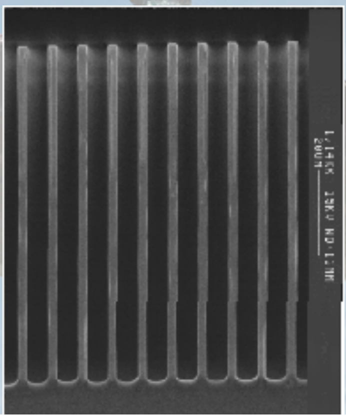

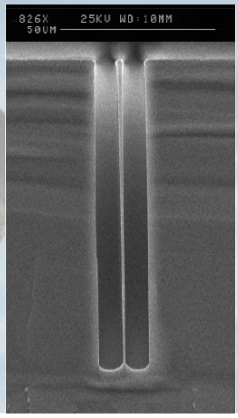

Far left: **Si trenches 80 µm deep x 4.5 µm wide / 2 µm line widths. AR=18:1, etch rate 2.2 µm/min.**

Left: **Si trench: 2.2 µm/min, 100 µm deep, AR=20:1, 90° ± <0.25 ° sidewall angle**

Ref: **J. Bhardwaj et al.*,* (Surface Technology Systems Ltd.)*, Proceedings: Annual Meeting of the Elettrochemical Society, Montreal, May 4-9, 1997.***

Table I Typical results of the STS ASE process

Etch Rate	1.5 to 3.0 µm/min	Selectivity to Resist	50 to 100:1
Selectivity to SiO_2	120 to 200:1	Sidewall Profile	$90^o \pm 2^o$
Uniformity x-wafer	± 2.5 to 5.0%	Feature size	1 to >500 µm
Aspect Ratio	Up to 30	Etch Depth Capability	10 to 800 µm
These results are based on processing of 100 mm and 150 mm wafers.			

Dry etching

DRIE – Undulating walls

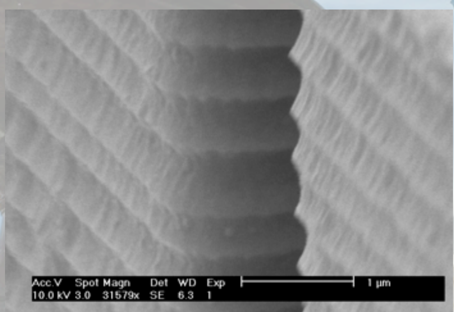

http://en.wikipedia.org/wiki/Deep_reactive-ion_etching

- **Sub micron undulation of wall due to the repeated protect/etch process**

Dry etching

DRIE - Example

Resonance cavity

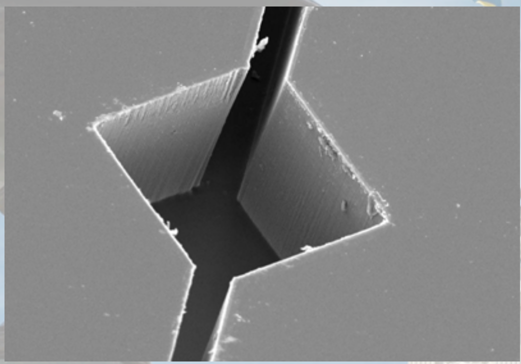

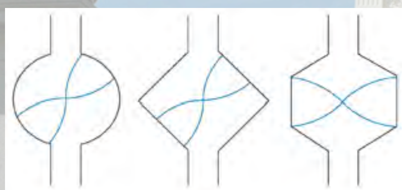

- **2 MHz resonance cavity**
- **Wall – wall distance 375 μm**
- **Depth 200 μm**

Etch-stop techniques

SOI - Silicon-on-Insulator wafers

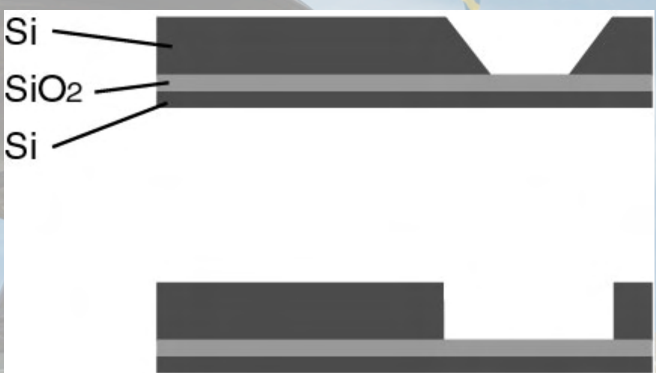

KOH

DRIE

The silicon in etched by KOH or DRIE and the etching stops when the SiO_2 is reached

Microstructuring of glass

Glass microstructuring

- **Glass usually processed by isotropic wet-etching (non-crystalline material)**
- **Dry etching - possible**
- **Laser ablation - possible**
- **Powder blasting - possible**

Glass microstructuring

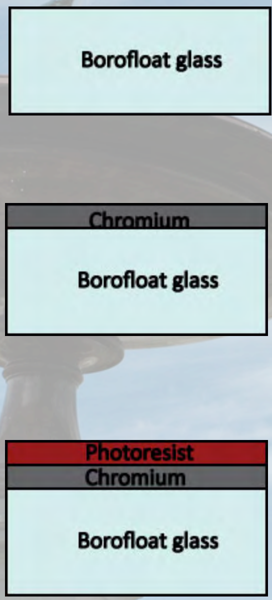

Starting material

Chromium deposition

The chromium improves photoresist adhesion and helps protect the glass

Photoresist spinning and soft bake

4´ wafers can be aquired with deposited chromium and photoresist to save time

Litography

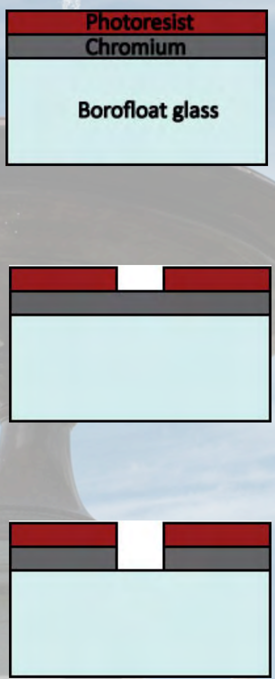

UV or laser exposure

Develop photoresist

Hard bake

Etch chromium

Glass wet etching

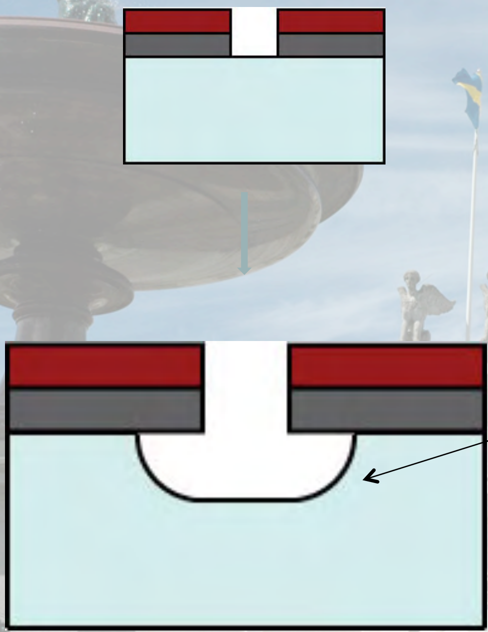

- Glass etchant:
  - Hydrofluoric acid
  - Nitric Acid
  - MilliQ-water

- Glass is amorphous
  - Isotropic etch profile
  - Width = 2x depth + mask opening

Etch Profile

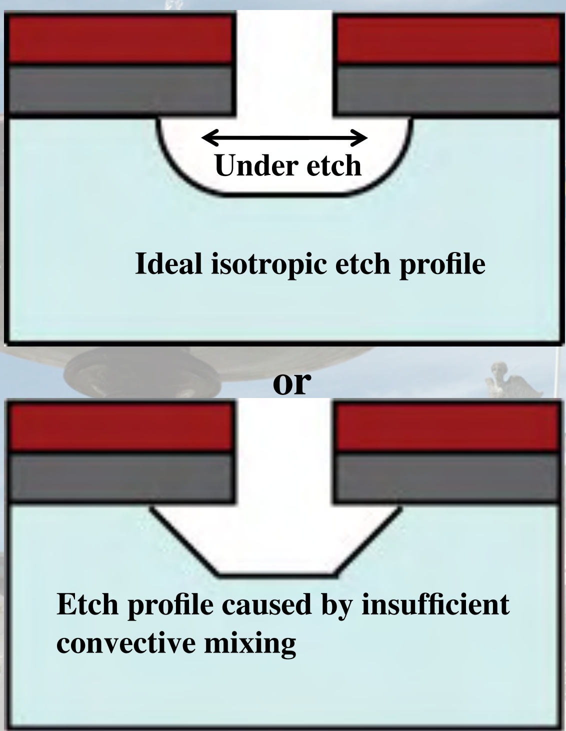

- Ideally the etch profile should be semi-circular

- Factors that can influence shape of side walls are (ref 1-3)
  - Adhesion between masking layer and glass
  - Amount and type of stirring
  - pH and temperature of etch solution

- Wide and large structures usually becomes semi-circular
- Deep and small structures becomes tapered

- 1.Kal, S., Haldar, S., and Lahiri, S. K. *Microelectron. Reliab.* **1990** 30 719 722[CrossRef], [ChemPort]
- 2.Parisi, G. I., Haszko, S. E., and Rozgonyi, G. A. *J. Electrochem. Soc.* **1977** 124 917921[CrossRef], [ChemPort]
- 3.Spierings, G. *J. Mater. Sci.* **1993** 28 6261 6273[CrossRef], [ChemPort]

Etch Profile

Silicon vs Glass

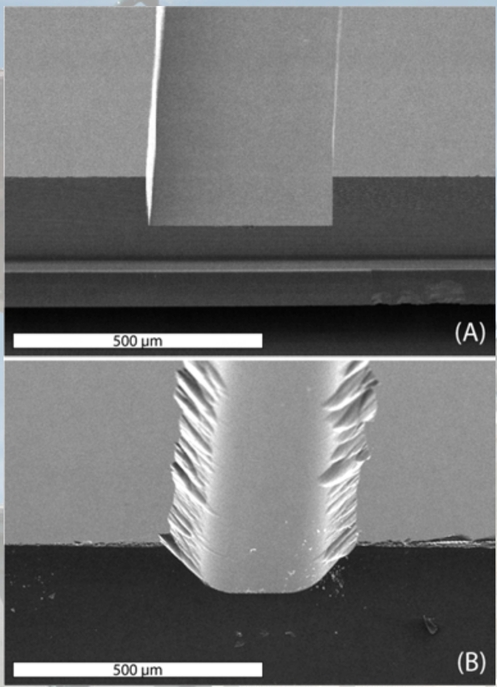

Anisotropic silicon wet etch

Isotropic glass etch
Tapered & jagged walls

Etch profile - Particle focussing

375 µm width

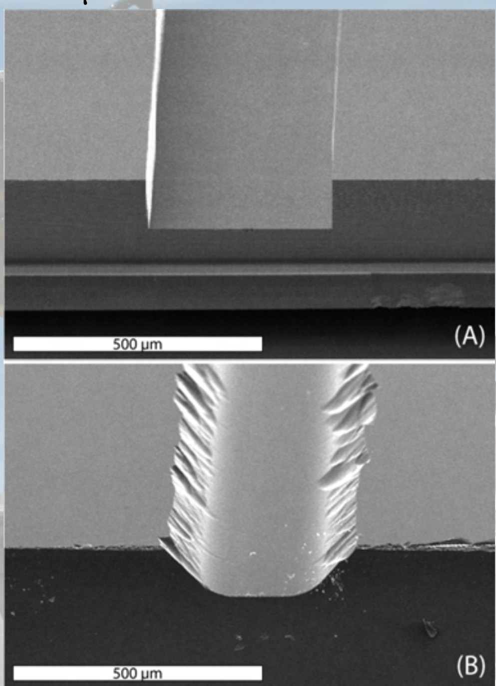

Single node
2 MHz

Double node
4 MHz

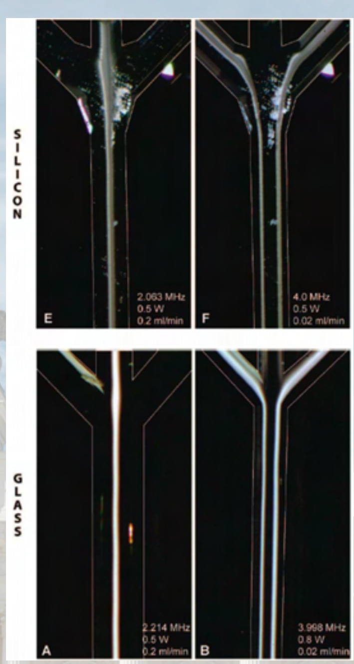

M. Evander,A. Lenshof, T. Laurell, and J. Nilsson; Analytical Chemistry, 2008, 80, 13, 5178-5185

Etch Profile

Insufficient adhesion between glass and chromium gives jagged channel walls

Etch Profile

"Rocking table effect"

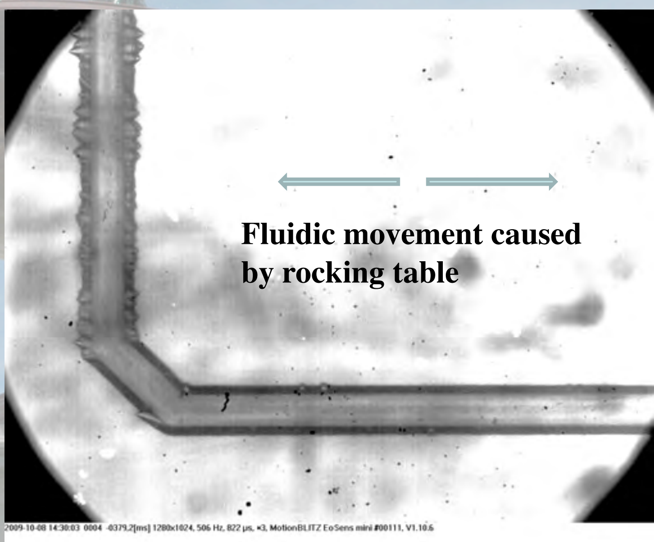

Insufficient adhesion between glass and masking gives jagged channel walls for channels in peripendicular direction to

Glass microstructuring

Resonance cavity trapping of blood cells

Glass microstructuring

Wet etching, Poly-Si mask

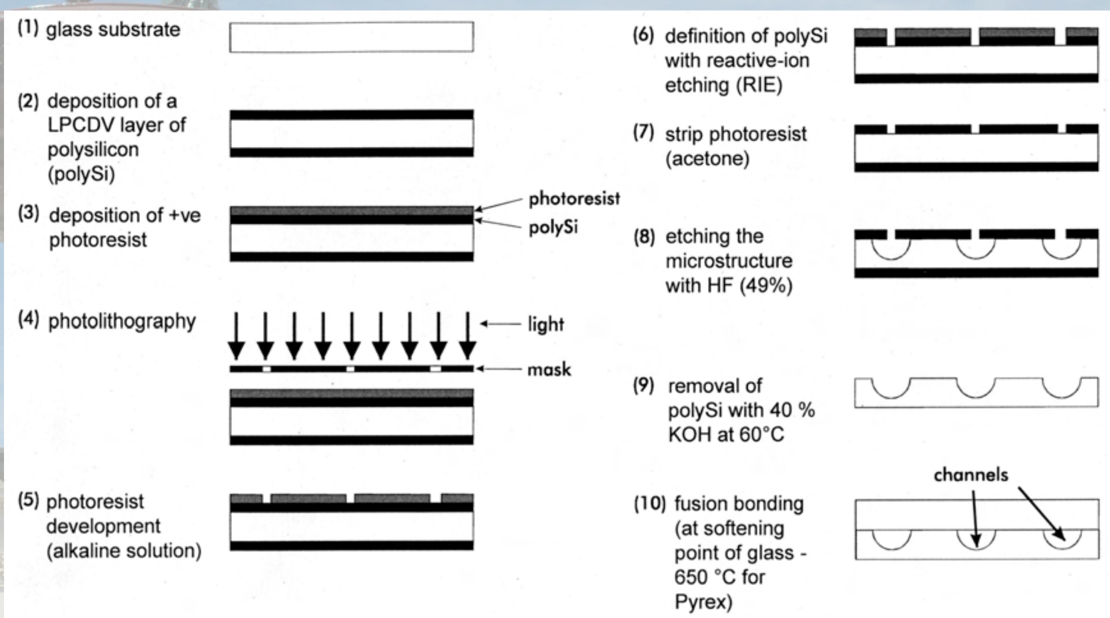

Microstructuring of glass
Intersecting channels, Poly-Si mask

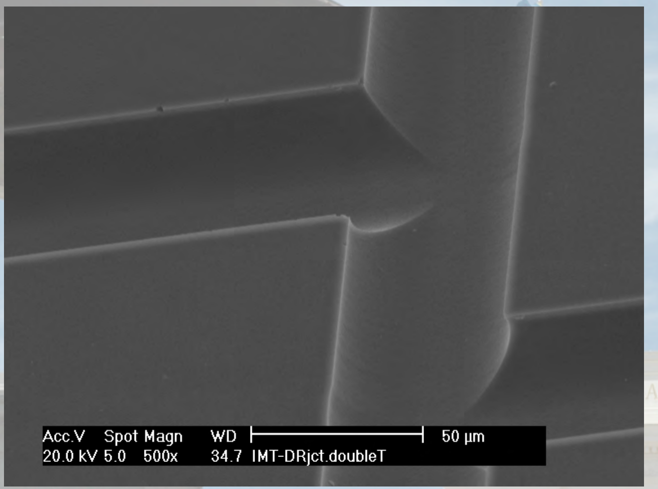

Source: G. Boer et al, SAMLAB, IMT Neuchatel

All geometries possible:
- **every shape on the mask is faithfully reproduced in the photoresist layer**

Etchants used:
- **all contain HF**
- **most use HF:HNO_3 mixed with H_2O (typical ratio 20:14:66)**
- **buffered oxide or conc. HF (49%) also used**
- **surface roughness (nm) dependent on etchant**

Thick film photoresist - SU-8

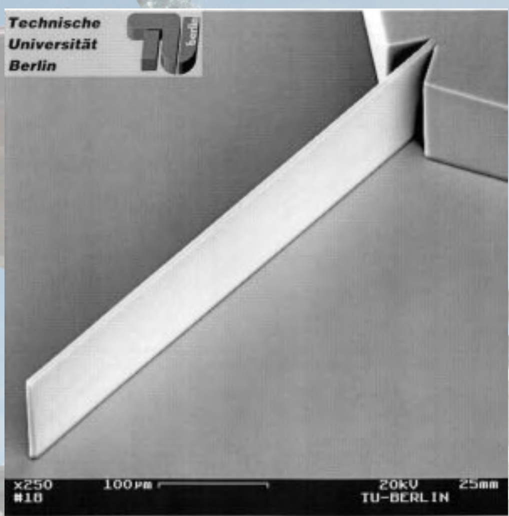

SU-8, Resiststruktur, Dicke > 50 µm

http://www.microresist.de/su-8_en.htm

- **Negative photoresist - becomes insoluble in developing solutions when exposed to optical radiation.**
- **Suitable for high-aspect-ratio structures, AR up to 20:1.**
- **Spin coat layers up to 500 μm thick.**
- **Low absorbance in UV.**
- **Thermally and chemically stable.**
  (Ex. HNO_3, NaOH at 90 deg C)

Ref: J.M. Shaw et al, *IBM Journal of Research and Development*, www.research.ibm.com/journal/rd/411/shaw.html

PDMS

Soft lithography, SU-8 master - Channels in PDMS

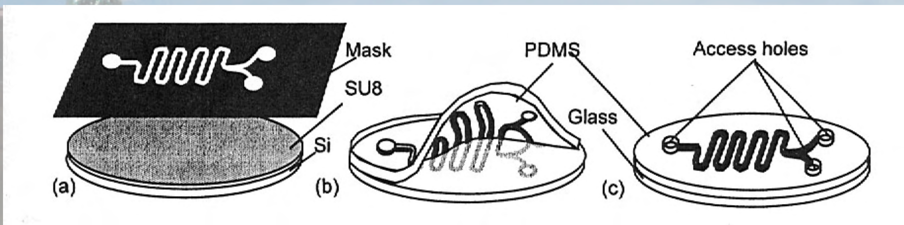

- SU-8 spin coated on silicon wafer
- UV exposure with clear field mask
- Pouring PDMS over the developed SU-8 master
- Oxygen plasma treatment of PDMS surface and bonding to glass

(*from* Nguyen and Wereley, Fundamentals and Application of Microfluidics, Artech House Publishers, 2002)

PDMS

Examples of resonator designs using PDMS

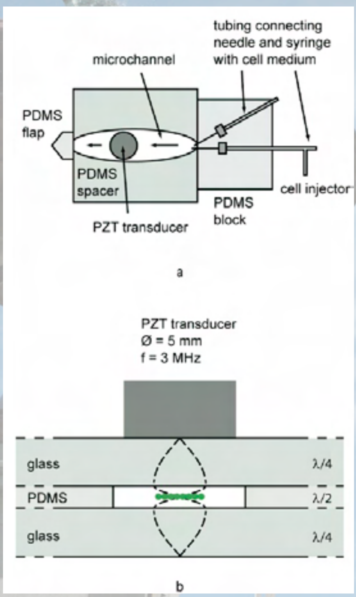

Hultström et al. Ultrasound in Med. & Biol. 33, 2007, 145

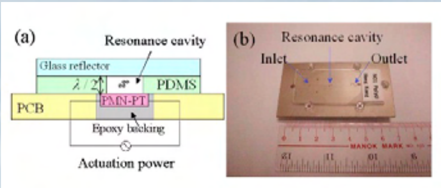

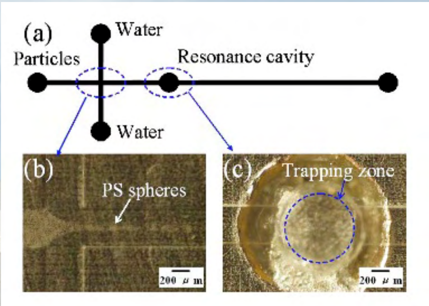

Guo et al. Appl. Phys. Letters. 92, 213901, 2008

Bonding techniques

Joining of components

- **Anodic bonding - Glass/silicon**
- **Silicon fusion bonding - Silicon/silicon**
- **Thermal bonding - Glass/glass**
  - **Local melting of the material**
  - **Low temperature glass bonding**

Anodic bonding

(Field-assisted bonding, electrostatic bonding)

Si-Glass

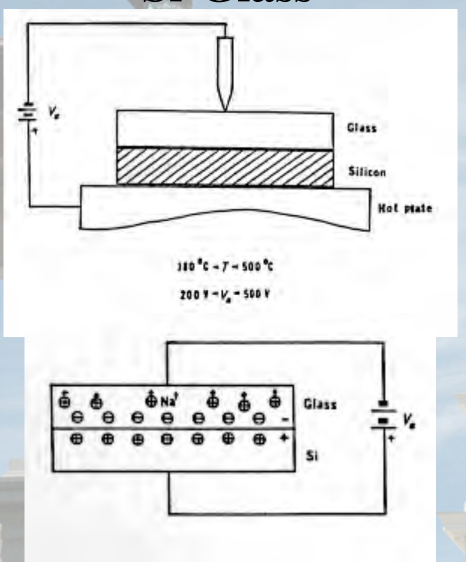

- **Surfaces need to be extremely clean and smooth**
- **Glass: cathode; Si: anode**
- **Applied potential pulls substrates together**
- **Wafers bonded almost immediately**
- **At high T: glass like a solid electrolyte; Na^+ ions in the glass become mobile and move towards cathode**
- **Negative ions in glass left behind, forming a depletion layer**
- **High E in this layer transports oxygen out of the glass to bond with Si surface; seal appears chemical in nature (possibly Si-O bonds)**

Ref: W.H. Ko et al., in *Sensors: A comprehensive survey, Vol. 1*; 1989, VCH Press, Germany

Silicon fusion bonding

(Direct Bonding)

Si-Si

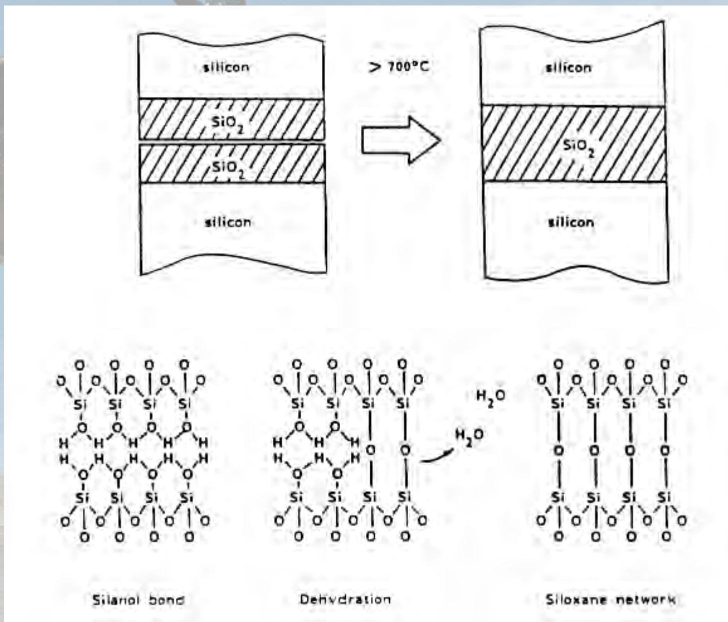

- **surfaces need to be extremely clean and smooth**
- **hydration with e.g. H_2O_2-H_2SO_4 (“piranha”)**
- **dry and put together: this should result in a bond of sorts**
- **then put in oven at T>1000 °C**

Ref: M. Madou, *Fundamentals of Microfabrication*, 1997, CRC Press

Glass bonding

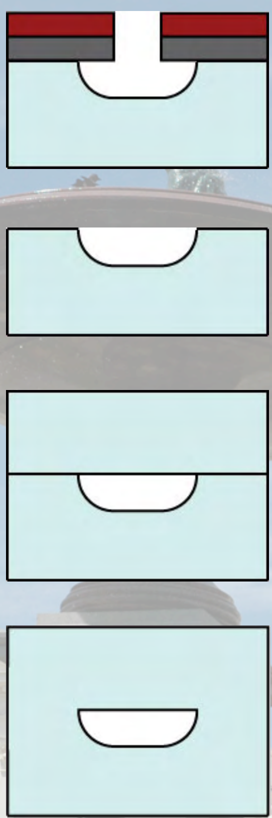

Removal of Photoresist and chromium

Piranha wash or plasma treatment cleans and activates surfaces

Put lid on, sandwich between polished graphite wafers and apply pressure

In furnace 12h@ 500-600°C

”Pray to the glass bonding God” - Student comment

Enable fluidic access e.g. by drilling holes

Low temperature glass-glass bonding

- **HF bonding**
  - **droplet of 1 wt.% HF wicked in between surfaces of 2 cleaned wafers by capillary forces**
  - **about 1 MPa of pressure applied for a number of hours**
  - **temperatures less than 200 °C are used**
  - **bond strengths less than those for direct bonding obtained, but can achieve good sealing**
  - **reported for SiO_2-SiO_2, SiO_2-Si, and Si-Si bonding**

Ref: H. Nakanishi et al., *Transducers'99: Technical Digest, Sendai, Japan, June 7-10, 1999*, pp. 1332-1335.

Microchip resonator microfabrication
Summary

- **Oxidation**
- **Spinning of photoresist**
- **Lithography**
- **Cleaning**
- **Wet etching**
  - **Isotropic**
  - **Anisotropic**
- **Dry etching**
  - **DRIE**
- **Bonding**


Questions?
REGIA · ACADEMIA · CAROLINA ·

Lecture notes for the advanced CISM school

Ultrasound standing wave action on suspensions and biosuspensions in micro- and macrofluidic devices

Udine, Italy, 7 - 11 June 2010

Microfluidics and ultrasound acoustophoresis

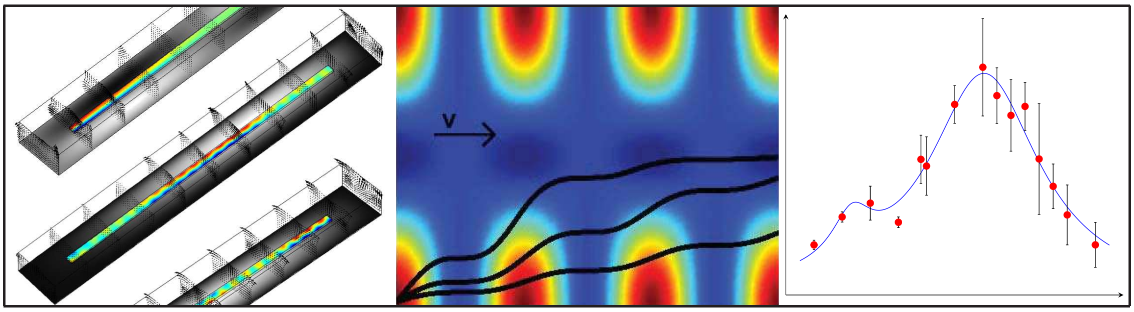

Henrik Bruus

Department of Micro- and Nanotechnology
Technical University of Denmark

DTU

Preface

These lecture notes have been written for the Advanced CISM School, *Ultrasound standing wave action on suspensions and biosuspensions in micro- and macrofluidic devices*, held in Udine, Italy, 7 - 11 June 2010. The notes cover six lectures on basic microfluidics, equivalent circuit models in fluidics, diffusion, ultrasound resonances, acoustic radiation forces, and microchannel acoustophoresis. Much of the material is covered more in-depth in my textbook, *Theoretical Microfluidics* (Oxford University Press, Oxford, 2008), so the reader interested in more details can seek them there.

The past few years my research interests have included ultrasound acoustophoresis in microfluidic lab-on-a-chip systems, and in this context I have enjoyed working together with a number of people. My sincere thanks for interesting and fruitful collaborations go to my talented students at the Technical University of Denmark, Rune Barnkob, Christian Laut Ebbesen, Søren Vedel, Mikkel Settnes, Anders Nysteen, Lasse Mejling Andersen, S. Melker Hagsäter, Peder Skafte-Pedersen, and Thomas Glasdam Jensen, as well as to my colleagues Prof. Thomas Laurell and Per Augustsson of Lund University, Prof. H. Tom Soh and Dr. Jonathan D. Adams of UC Santa Barbara, and Dr. Martin Wiklund and Dr. Otto Manneberg of KTH-Stockholm.

Professor Henrik Bruus
Department of Micro- and Nanotechnology
Technical University of Denmark
June 2010

www.nanotech.dtu.dk/bruus

Chapter 1

Basic concepts in microfluidics

Microfluidics deals flow of fluids and of suspensions in submillimeter-sized systems influenced by external forces. In these lecture notes we focus in particular on acoustic radiation forces from external ultrasound waves on suspended microparticles, an effect known as acoustophoresis. The studies of such forces on particles dates back to the analysis of incompressible particles in acoustic fields [King, 1934] and on compressible particles [Yosioka 1955, Gorkov 1962].

The use of ultrasound standing waves for particle manipulation and separation has received renewed interest in the past decade, especially in the context of the microscale lab-on-a-chip format. As reviewed recently [Laurell 2007, Nilsson 2009], basically two applications have been developed showing great promise for applications within flow cytometry, and much of the current technological development targets cell biology: (i) continuous-flow-based acoustic separation and manipulation of particles and cells based on precision microfabricated flow-through resonators operating in the laminar flow regime; and (ii) acoustic particle trapping in different microchip configurations.

The success of these acoustic microparticle handling methods relies on the laminar nature of the flow in microfluidics of the carrier liquid [Tabeling 2005, Bruus 2008]. Turbulence is absent, resulting in regular and predictable flow patterns and particle motions. In this chapter we study the governing equations of the carrier liquid formulated in terms of the classical continuum description of the velocity field $\mathbf{v}$ and the pressure field p.

1.1 The velocity, pressure and density field

throughout the lecture notes we use the so-called Eulerian picture of the continuum fields, where the spatial coordinates $\mathbf{r}$ are fixed in space, and we then observe how the fields evolve in time at these points. Consequently, the position $\mathbf{r}$ and the time t are independent variables. The Eulerian picture is illustrated by the velocity field in Fig. 1.1(a), and in general the value of any field variable $F(\mathbf{r}, t)$ is defined as the average value of the corresponding molecular quantity $F_{\mathrm{mol}}(\mathbf{r}', t)$ for all the molecules contained in some liquid particle of volume $\Delta\mathcal{V}(\mathbf{r})$ positioned at $\mathbf{r}$ at time t,

$$F(\mathbf{r}, t) = \big\langle F_{\mathrm{mol}}(\mathbf{r}', t) \big\rangle_{\mathbf{r}' \in \Delta\mathcal{V}(\mathbf{r})}. \tag{1.1}$$

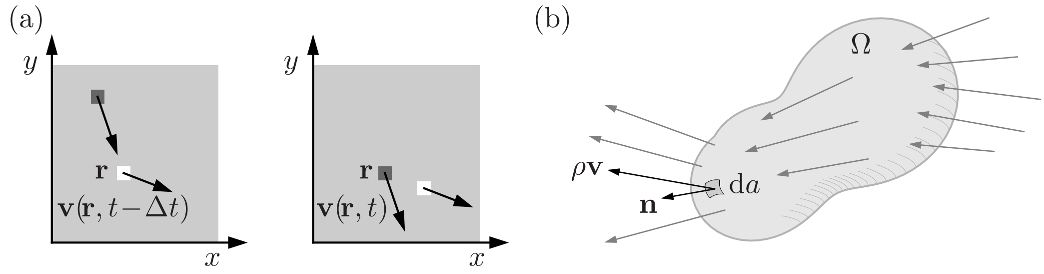

Figure 1.1: (a) The Eulerian picture: the spatial coordinates $\mathbf{r}$ do not follow the flow of the molecules. Instead, the velocity field $\mathbf{v}$ at the fixed point $\mathbf{r}$ is defined by the molecules in the white region at time $t-\Delta t$, and by the those in the dark gray region at time t. (b) A sketch of the mass current density field $\rho\mathbf{v}$ (long arrows) flowing through an arbitrarily shaped region Ω (gray). Any infinitesimal area $\mathrm{d}a$ (dark gray) is associated with an outward-pointing unit vector $\mathbf{n}$ (short arrow) perpendicular to the local surface. The current flowing out through the area $\mathrm{d}a$ is given by $\mathrm{d}a$ times the projection $\rho\mathbf{v}\cdot\mathbf{n}$ of the current density on the surface unit vector.

If we for brevity let m_i and $\mathbf{v}_i$ be the mass and the velocity of molecule i, respectively, and furthermore let $i \in \Delta\mathcal{V}$ stand for all molecules i present inside the volume $\Delta\mathcal{V}(\mathbf{r})$ at time t, then the definition of the density $\rho(\mathbf{r},t)$ and the velocity field $\mathbf{v}(\mathbf{r},t)$ can be written as

$$\rho(\mathbf{r},t) \equiv \frac{1}{\Delta\mathcal{V}} \sum_{i\in\Delta\mathcal{V}} m_i, \tag{1.2a}$$

$$\mathbf{v}(\mathbf{r},t) \equiv \frac{1}{\rho(\mathbf{r},t)\Delta\mathcal{V}} \sum_{i\in\Delta\mathcal{V}} m_i\mathbf{v}_i. \tag{1.2b}$$

Here, we have introduced the "equal-to-by-definition sign" $\equiv$. Notice how the velocity is defined through the more fundamental concept of momentum.

In general, the field variables in microfluidics can be scalars (such as density ρ, viscosity η, pressure p, temperature T, and free energy $\mathcal{F}$), vectors (such as velocity $\mathbf{v}$, current density $\mathbf{J}$, pressure gradient $\boldsymbol{\nabla}p$, force densities $\mathbf{f}$, and electric fields $\mathbf{E}$) and tensors (such as stress tensor σ and velocity gradient $\boldsymbol{\nabla}\mathbf{v}$).

1.2 Mathematical notation

The mathematical treatment of microfluidic problems is complicated due to the presence of several scalar, vector and tensor fields and the non-linear partial differential equations that govern them. To facilitate the treatment some simplifying notation is called for.

First, a suitable co-ordinate system must be chosen. We shall mainly work with Cartesian co-ordinates (x,y,z) with corresponding basis vectors $\mathbf{e}_x$, $\mathbf{e}_y$, and $\mathbf{e}_z$, which have unity length and are mutually orthogonal. The position vector $\mathbf{r} = (r_x, r_y, r_z) = (x, y, z)$ is written as

$$\mathbf{r} = r_x\,\mathbf{e}_x + r_y\,\mathbf{e}_y + r_z\,\mathbf{e}_z = x\,\mathbf{e}_x + y\,\mathbf{e}_y + z\,\mathbf{e}_z. \tag{1.3}$$

In fact, any vector $\mathbf{v}$ can be written in terms of its components v_i (where for Cartesian co-ordinates $i = x, y, z$) as

$$\mathbf{v} = \sum_{i=x,y,z} v_i\,\mathbf{e}_i \equiv v_i\,\mathbf{e}_i. \tag{1.4}$$

In the last equality we have introduced the Einstein summation convention: by definition a repeated index always implies a summation over that index. Other examples of this handy notation, the so-called index notation, is the scalar product,

$$\mathbf{v}\cdot\mathbf{u} = v_i u_i, \tag{1.5}$$

the length v of a vector $\mathbf{v}$,

$$v = |\mathbf{v}| = \sqrt{\mathbf{v}^2} = \sqrt{\mathbf{v}\cdot\mathbf{v}} = \sqrt{v_i v_i}, \tag{1.6}$$

and the ith component of the vector-matrix equation $\mathbf{u} = M\mathbf{v}$,

$$u_i = M_{ij}\,v_j. \tag{1.7}$$

For the partial derivatives of some function $F(\mathbf{r}, t)$ we use the symbols ∂_i, with $i = x, y, z$, and ∂_t,

$$\partial_x F \equiv \frac{\partial F}{\partial x}, \quad \text{and} \quad \partial_t F \equiv \frac{\partial F}{\partial t}, \tag{1.8}$$

while for the total time derivative of a quantity $F\big(\mathbf{r}(t), t\big)$ flowing along with the fluid particles, we use the symbol d_t,

$$\mathrm{d}_t F \equiv \frac{\mathrm{d}F}{\mathrm{d}t} = \partial_t F + \big(\partial_t r_i\big)\partial_i F = \partial_t F + v_i \partial_i F. \tag{1.9}$$

The nabla operator $\boldsymbol{\nabla}$ containing the spatial derivatives plays an important role in differential calculus. It is given by

$$\boldsymbol{\nabla} \equiv \mathbf{e}_x\partial_x + \mathbf{e}_y\partial_y + \mathbf{e}_z\partial_z = \mathbf{e}_i\partial_i. \tag{1.10}$$

The Laplace operator, which appears in numerous partial differential equations in theoretical physics, is just the square of the nabla operator,

$$\boldsymbol{\nabla}^2 \equiv \nabla^2 \equiv \partial_i\partial_i. \tag{1.11}$$

In terms of the nabla operator the total time derivative in Eq. (1.9) can be written as

$$\mathrm{d}_t F\big(\mathbf{r}(t), t\big) = \partial_t F + (\mathbf{v}\cdot\boldsymbol{\nabla})F. \tag{1.12}$$

Since $\boldsymbol{\nabla}$ is a differential operator, the order of the factors does matter in a scalar product containing it. So, whereas $\mathbf{v}\cdot\boldsymbol{\nabla}$ in the previous equation is a differential operator, the product $\boldsymbol{\nabla}\cdot\mathbf{v}$ with the reversed order of the factors is a scalar quantity. It appears so often in mathematical physics that it has acquired its own name, namely the divergence of the vector field,

$$\boldsymbol{\nabla}\cdot\mathbf{v} \equiv \partial_x v_x + \partial_y v_y + \partial_z v_z = \partial_i v_i. \tag{1.13}$$

Concerning integrals, we denote the 3D integral measure by $d\mathbf{r}$, so that in Cartesian co-ordinates we have $d\mathbf{r} = dx\,dy\,dz$. We also consider definite integrals as operators acting on integrands, thus we keep the integral sign and the associated integral measure together to the left of the integrand. As an example, the integral over a spherical body with radius a of the scalar function $S(\mathbf{r})$ is written as

$$\int_{\text{sphere}} S(x,y,z)\,dx\,dy\,dz = \int_{\text{sphere}} d\mathbf{r}\,S(\mathbf{r}) = \int_0^a r^2 dr \int_0^\pi \sin\theta d\theta \int_0^{2\pi} d\phi\,S(r,\theta,\phi). \quad (1.14)$$

When working with vectors and tensors it is advantageous to use the following two special symbols: the Kronecker delta δ_{ij},

$$\delta_{ij} = \begin{cases} 1, & \text{for } i = j, \\ 0, & \text{for } i \neq j, \end{cases} \quad (1.15)$$

and the Levi–Civita symbol ϵ_{ijk},

$$\epsilon_{ijk} = \begin{cases} +1, & \text{if } (ijk) \text{ is an even permutation of (123) or } (xyz), \\ -1, & \text{if } (ijk) \text{ is an odd permutation of (123) or } (xyz), \\ 0, & \text{otherwise.} \end{cases} \quad (1.16)$$

In the index notation, the Levi–Cevita symbol appears directly in the definition of the ith component of the cross-product $\mathbf{u}\times\mathbf{v}$ of two vectors $\mathbf{u}$ and $\mathbf{v}$, and of the rotation $\boldsymbol{\nabla}\times\mathbf{v}$,

$$(\mathbf{u}\times\mathbf{v})_i \equiv \epsilon_{ijk}\,u_j v_k, \quad \text{and} \quad (\boldsymbol{\nabla}\times\mathbf{v})_i \equiv \epsilon_{ijk}\,\partial_j v_k. \quad (1.17)$$

As a last mathematical subject, we mention Gauss's theorem, which we shall employ repeatedly in these notes. For a given vector field $\mathbf{V}(\mathbf{r})$ it relates the volume integral in a given region Ω of the divergence $\boldsymbol{\nabla}\cdot\mathbf{V}$ to the integral over the surface $\partial\Omega$ of the flux $\mathbf{V}\cdot\mathbf{n}\,da$ through an area element da with the surface normal $\mathbf{n}$,

$$\int_\Omega d\mathbf{r}\,\boldsymbol{\nabla}\cdot\mathbf{V} = \int_{\partial\Omega} da\,\mathbf{n}\cdot\mathbf{V} \qquad \text{or} \qquad \int_\Omega d\mathbf{r}\,\partial_j V_j = \int_{\partial\Omega} da\,n_j V_j. \quad (1.18)$$

By definition, the surface normal $\mathbf{n}$ of a closed surface is an outward-pointing unit vector perpendicular to the surface, see Fig. 1.1(b).

1.3 Mass conservation; the continuity equation

The first governing equation of fluid dynamics to be derived is the continuity equation, which expresses the conservation of mass in classical mechanics. We consider a compressible fluid, i.e. a fluid where the density ρ may vary as function of space and time, and an arbitrarily shaped, but fixed, region Ω in the fluid as sketched in Fig. 1.1(b). The total mass $M(\Omega,t)$ inside Ω can be expressed as a volume integral over the density ρ,

$$M(\Omega,t) = \int_\Omega d\mathbf{r}\,\rho(\mathbf{r},t). \quad (1.19)$$

Since mass can neither appear nor disappear spontaneously in non-relativistic mechanics, $M(\Omega, t)$ can only vary due to a mass flux through the surface $\partial\Omega$ of the region Ω. The mass current density $\mathbf{J}$ is defined as the mass density ρ times the convection velocity $\mathbf{v}$, or the mass flow per oriented unit area per unit time (hence the unit $\mathrm{kg\,m^{-2}\,s^{-1}}$),

$$\mathbf{J}(\mathbf{r}, t) = \rho(\mathbf{r}, t)\, \mathbf{v}(\mathbf{r}, t). \tag{1.20}$$

As the region Ω is fixed the time derivative of the mass $M(\Omega, t)$ can be calculated either by differentiating the volume integral Eq. (1.19),

$$\partial_t M(\Omega, t) = \partial_t \int_\Omega \mathrm{d}\mathbf{r}\, \rho(\mathbf{r}, t) = \int_\Omega \mathrm{d}\mathbf{r}\, \partial_t \rho(\mathbf{r}, t), \tag{1.21}$$

or as a surface integral over $\partial\Omega$ of the mass current density using Eq. (1.20) and Fig. 1.1(b),

$$\partial_t M(\Omega, t) = \int_{\partial\Omega} \mathrm{d}a\, (-\mathbf{n})\cdot\mathbf{J} = -\int_{\partial\Omega} \mathrm{d}a\, \mathbf{n}\cdot(\rho\mathbf{v}) = -\int_\Omega \mathrm{d}\mathbf{r}\, \boldsymbol{\nabla}\cdot\big[\rho(\mathbf{r}, t)\mathbf{v}(\mathbf{r}, t)\big]. \tag{1.22}$$

The last expression is obtained by applying Gauss's theorem Eq. (1.18) to the vector field $\mathbf{V} \equiv \rho\mathbf{v}$. We have used $-\mathbf{n}$ because this is the direction of *entering* the region. It follows immediately from Eqs. (1.21) and (1.22) that

$$\int_\Omega \mathrm{d}\mathbf{r}\, \partial_t \rho(\mathbf{r}, t) = -\int_\Omega \mathrm{d}\mathbf{r}\, \boldsymbol{\nabla}\cdot\big[\rho(\mathbf{r}, t)\mathbf{v}(\mathbf{r}, t)\big]. \tag{1.23}$$

This result is true for any choice of region Ω. However, this is only possible if the integrands are identical. Thus we have derived the continuity equation,

$$\partial_t \rho = -\boldsymbol{\nabla}\cdot\big(\rho\mathbf{v}\big) \quad \text{or} \quad \partial_t \rho = -\partial_j(\rho v_j). \tag{1.24}$$

This one of the basic equations in acoustics, but in many other cases, especially in microfluidics, where the flow velocity are much smaller than the velocity of speed of sound (pressure waves) in the fluid, the fluid can be treated as being incompressible. This means that ρ is constant in space and time, and the continuity equation simplifies to,

$$\boldsymbol{\nabla}\cdot\mathbf{v} = 0 \quad \text{or} \quad \partial_i v_i = 0. \tag{1.25}$$

1.4 Momentum Conservation; the Navier–Stokes equation

To derive the second governing equation, the equation of motion for the Eulerian velocity field or the Navier–Stokes equation, we now turn from the mass density ρ of the fluid to its momentum density $\rho\mathbf{v}$ using an approach similar to that which led us to the continuity equation. We consider the ith component $P_i(\Omega, t)$ of the total momentum of the fluid inside an arbitrarily shaped, but fixed, region Ω. In analogy with the mass equation (1.21) the rate of change of the momentum is given by

$$\partial_t P_i(\Omega, t) = \partial_t \int_\Omega \mathrm{d}\mathbf{r}\, \rho(\mathbf{r}, t) v_i(\mathbf{r}, t) = \int_\Omega \mathrm{d}\mathbf{r}\, \Big[(\partial_t\rho) v_i + \rho\partial_t v_i\Big]. \tag{1.26}$$

In contrast to the mass inside Ω, which according to Eq. (1.22) can only change by convection through the surface $\partial\Omega$, the momentum $P_i(\Omega,t)$ can change both by convection and by the action of forces given by Newton's second law. The forces can be divided into body forces that act on the interior of Ω, e.g. gravitational and electrical forces, and contact forces that act on the surface $\partial\Omega$ of Ω, e.g. pressure and viscosity forces. Thus, the rate of change of the ith component of the momentum can be written as

$$\partial_t P_i(\Omega,t) = \partial_t P_i^{\mathrm{body}}(\Omega,t) + \partial_t P_i^{\mathrm{conv}}(\Omega,t) + \partial_t P_i^{\mathrm{pres}}(\Omega,t) + \partial_t P_i^{\mathrm{visc}}(\Omega,t). \tag{1.27}$$

A body force $\mathbf{f}^{\mathrm{body}}$ is an external force that act throughout the entire body of the fluid. The change in the momentum of Ω due to a body force, e.g. gravity in terms of the density ρ and the acceleration of gravity $\mathbf{g}$, is given by

$$\partial_t P_i^{\mathrm{body}}(\Omega,t) = \int_\Omega \mathrm{d}\mathbf{r}\, f_i^{\mathrm{body}} = \int_\Omega \mathrm{d}\mathbf{r}\, (\rho\mathbf{g})_i = \int_\Omega \mathrm{d}\mathbf{r}\, \rho g_i. \tag{1.28}$$

For the convection of momentum $\rho\mathbf{v}$ into Ω, we note that it is described in terms of the tensor $(\rho\mathbf{v})\mathbf{v}$, just as convection of density ρ is described by the vector $(\rho)\mathbf{v}$. Considering the ith momentum component, we see that the flux of momentum into Ω through the infinitesimal area $\mathrm{d}a$ is given by $(\rho v_i)\mathbf{v}\cdot(-\mathbf{n})\mathrm{d}a$, and thus the total change $\partial_t P_i^{\mathrm{conv}}(\Omega,t)$ of momentum in Ω due to convection is given by

$$\partial_t P_i^{\mathrm{conv}}(\Omega,t) = \int_{\partial\Omega} \mathrm{d}a\, (-\mathbf{n})\cdot(\rho v_i\, \mathbf{v}) = -\int_{\partial\Omega} \mathrm{d}a\, n_j\, \rho v_i v_j. \tag{1.29}$$

For the change of momentum due to pressure, we find that at each infinitesimal area $\mathrm{d}a$ on the surface of $\partial\Omega$, the surroundings act with the pressure force $p(-\mathbf{n})\mathrm{d}a$ onto Ω. As a result, the ith component of the momentum will change due to the force $(-p\mathbf{n}\mathrm{d}a)\cdot\mathbf{e}_i = -n_i p\mathrm{d}a$, where $\mathbf{e}_i$ is the unit vector corresponding to the ith component. Hence, we obtain

$$\partial_t P_i^{\mathrm{pres}}(\Omega,t) = -\int_{\partial\Omega} \mathrm{d}a\, \mathbf{n}\cdot(p\mathbf{e}_i) = -\int_{\partial\Omega} \mathrm{d}a\, n_j\, p\delta_{ij}. \tag{1.30}$$

In the last equation we use that $\mathbf{n}\cdot\mathbf{e}_i = n_j\delta_{ij}$, whereby $\mathbf{n}$ can be ascribed the same free index j different from the momentum component index i as in Eq. (1.29).

The momentum in Ω is also changed by viscous friction at the surface $\partial\Omega$ from the surrounding fluid. The frictional force $\mathrm{d}\mathbf{F}$ on a surface element $\mathrm{d}a$ with the normal vector $\mathbf{n}$ must be characterized by a tensor rank of two since two vectors are needed to determine it: the force vector and the surface normal. This tensor is denoted as the viscous stress tensor σ'_{ij}, and it expresses the ith component of the friction force per area acting on a surface element oriented with its surface normal parallel to the jth unit vector $\mathbf{e}_j$. Thus

$$\mathrm{d}F_i = \sigma'_{ij} n_j\, \mathrm{d}a. \tag{1.31}$$

This expression leads immediately to the change in the momentum of Ω due to the viscous forces at the surface $\partial\Omega$,

$$\partial_t P_i^{\mathrm{visc}}(\Omega,t) = \int_{\partial\Omega} \mathrm{d}a\, n_j\, \sigma'_{ij}. \tag{1.32}$$

The internal friction is only non-zero when fluid particles move relative to each other, hence the viscous stress tensor σ' depends only on the spatial derivatives of the velocity. For the small velocity gradients encountered in microfluidics we can safely assume that only first-order derivatives enter the expression for σ', thus σ'_{ij} must depend linearly on the velocity gradients $\partial_i v_j$. Further analysis shows [Bruus 2008] that it must be symmetric. The most general tensor of rank two satisfying these conditions is

$$\sigma'_{ij} = \eta \left(\partial_j v_i + \partial_i v_j\right) + (\beta - 1)\eta \left(\partial_k v_k\right) \delta_{ij}, \tag{1.33}$$

where the first term relates to the dynamic shear viscosity η of an incompressible fluid, while the second term, characterized both by η and by the viscosity ratio β ($\approx 5/3$ for water and other simple fluids), is added when compressibility cannot be neglected. The value of the viscosity η is determined experimentally, and for water we have

$$\eta_{\text{water}}(20\ ^\circ\text{C}) = 1.002 \times 10^{-3}\ \text{Pa s} = 1.002\ \text{mPa s}. \tag{1.34}$$

The viscosity of water has a strong dependence on temperature changing from 1.787 mPa s at 0 ℃ to 0.282 mPa s at 100 ℃.

The general equation of motion for a viscous fluid can now be found from Eq. (1.27) by collecting the results from the previous subsections. In integral form we obtain

$$\int_\Omega \mathrm{d}\mathbf{r}\, \Big[(\partial_t \rho) v_i + \rho \partial_t v_i\Big] = \int_{\partial\Omega} \mathrm{d}a\, n_j \Big[- \rho v_i v_j - p\delta_{ij} + \sigma'_{ij}\Big] + \int_\Omega \mathrm{d}\mathbf{r}\, \rho g_i. \tag{1.35}$$

Utilizing Gauss's theorem the surface integral involving n_j can be rewritten as a volume integral involving ∂_j. Since the resulting volume integral equation is valid for any region Ω the integrands must be identical. After some rewriting we finally arrive at the general equation of motion for the Eulerian velocity field of a viscous fluid,

$$\rho \partial_t v_i + \rho v_j \partial_j v_i = -\partial_i p + \partial_j \sigma'_{ij} + \rho g_i. \tag{1.36}$$

The left-hand side can be interpreted as inertial force densities, density times the sum of the local and the convective acceleration, while the right-hand side is the sum of intrinsic or applied force densities. Normally, for the so-called Newtonian fluids at a given temperature, the viscosity coefficients η and β can be taken as constants, and Eq. (1.36) reduces to the celebrated Navier–Stokes equation,

$$\rho\big[\partial_t v_i + v_j \partial_j v_i\big] = -\partial_i p + \eta\, \partial_j^2 v_i + \beta\eta\, \partial_i(\partial_j v_j) + \rho\, g_i, \tag{1.37a}$$

$$\rho\big[\partial_t \mathbf{v} + (\mathbf{v}\cdot\boldsymbol{\nabla})\mathbf{v}\big] = -\boldsymbol{\nabla} p + \eta\nabla^2\mathbf{v} + \beta\eta\boldsymbol{\nabla}(\boldsymbol{\nabla}\cdot\mathbf{v}) + \rho\,\mathbf{g}. \tag{1.37b}$$

1.5 The Reynolds number and the Stokes equation

Mathematically the richness and beauty of hydrodynamic phenomena is spawned by the non-linear term $\rho(\mathbf{v}\cdot\boldsymbol{\nabla})\mathbf{v}$ in the Navier–Stokes equation. On the other hand, the non-linear term is also responsible for making the mathematical treatment of the equation more complex and difficult; the solutions of the equation have never been fully characterized.

However, as we shall see in the following, in the limit of low flow velocities, a limit highly relevant for microfluidic systems, the non-linear term can be neglected. We enter the regime of the so-called Stokes flow or creeping flow, where analytical solutions to a number of flow problems can be found.

To determine when the non-linear term is negligible, we make the Navier–Stokes equation dimensionless by expressing all physical variables, such as length and velocity, in units of the characteristic scales, e.g. L_0 for length and V_0 for velocity. If the system is characterized by only one length scale L_0 and one velocity scale V_0, the expression of co-ordinates and velocity in terms of dimensionless co-ordinates and velocity is

$$\mathbf{r} = L_0\,\tilde{\mathbf{r}}, \quad \text{and} \quad \mathbf{v} = V_0\,\tilde{\mathbf{v}}, \tag{1.38a}$$

where the tilde on top of a symbol indicates that the symbol is a quantity without physical dimension, i.e. pure numbers. Once the length and velocity scales L_0 and V_0 have been fixed the scales T_0 and P_0 for time and pressure follow,

$$t = \frac{L_0}{V_0}\,\tilde{t} = T_0\,\tilde{t}, \quad \text{and} \quad p = \frac{\eta V_0}{L_0}\,\tilde{p} = P_0\,\tilde{p}. \tag{1.38b}$$

Viscosity is important in microfluidics, so we choose $P_0 = \eta V_0/L_0$ instead of the other possibility $\rho\, {V_0}^2$. By insertion of Eqs. (1.38a) and (1.38b) into the Navier–Stokes equation (1.37b) excluding the body-forces as well as the compressibility term, and using the straightforward scaling of the derivatives, $\partial_t = (1/T_0)\,\tilde{\partial}_t$ and $\boldsymbol{\nabla} = (1/L_0)\,\tilde{\boldsymbol{\nabla}}$, we get

$$\rho\left[\frac{V_0}{T_0}\,\tilde{\partial}_t\tilde{\mathbf{v}} + \frac{{V_0}^2}{L_0}\,\big(\tilde{\mathbf{v}}\cdot\tilde{\boldsymbol{\nabla}}\big)\tilde{\mathbf{v}}\right] = -\frac{P_0}{L_0}\,\tilde{\boldsymbol{\nabla}}\tilde{p} + \frac{\eta V_0}{{L_0}^2}\,\tilde{\boldsymbol{\nabla}}^2\tilde{\mathbf{v}}, \tag{1.39}$$

which after reduction becomes

$$Re\Big[\tilde{\partial}_t\tilde{\mathbf{v}} + \big(\tilde{\mathbf{v}}\cdot\tilde{\boldsymbol{\nabla}}\big)\tilde{\mathbf{v}}\Big] = -\tilde{\boldsymbol{\nabla}}\tilde{p} + \tilde{\boldsymbol{\nabla}}^2\tilde{\mathbf{v}}. \tag{1.40}$$

Here, we have introduced the dimensionless number Re, the so-called Reynolds number,

$$Re \equiv \frac{\rho V_0 L_0}{\eta}. \tag{1.41}$$

For $Re \ll 1$ the viscous term $\tilde{\boldsymbol{\nabla}}^2\tilde{\mathbf{v}}$ in Eq. (1.40) dominates. For water in microfluidics typical values are $\rho/\eta = 10^6$ s/m^2, $L_0 \approx 10^{-4}$m, and $V_0 \approx 10^{-3}$ m/s, so $Re \approx 0.1$.

Returning to physical variables in the limit of low Reynolds number, the non-linear Navier–Stokes equation is reduced to the linear Stokes equation,

$$\mathbf{0} = -\boldsymbol{\nabla} p + \eta\nabla^2\mathbf{v}. \tag{1.42}$$

If the time dependence is controlled by some external time scale different from the intrinsic scale $T_0 = L_0/V_0$, the time derivative is not necessarily negligible, and we must employ the time-dependent, linear Stokes equation,

$$\rho\,\partial_t\mathbf{v} = -\boldsymbol{\nabla} p + \eta\nabla^2\mathbf{v}. \tag{1.43}$$

For zero pressure gradient, and introducing the kinematic viscosity $\nu = \eta/\rho$, this becomes

$$\partial_t\mathbf{v} = \nu\nabla^2\mathbf{v}, \qquad \text{with } \nu = \frac{\eta}{\rho}. \tag{1.44}$$

1.6 Energy conservation; the heat-transfer equation

The third and last governing equation to be established is the heat-transfer equation of the fluid relating the rate of change of the energy density to the energy density flux. When working with thermodynamics of fluids it is natural to work with the thermodynamic quantities per unit mass, which are directly related to the molecules present in the fluid. Thus, we will work with the internal energy ε per unit mass, the entropy s per unit mass, the enthalpy h per unit mass and the volume $1/\rho$ per unit mass instead of the energy E, the entropy S, the enthalpy H and the volume $\mathcal{V}$ of the fluid. The first law of thermodynamics relates internal energy $\mathrm{d}\epsilon$, heat $T\mathrm{d}s$, and pressure work $-p\mathrm{d}(1/\rho)$. When it is expressed per unit mass, it takes the form

$$\mathrm{d}\varepsilon = T\,\mathrm{d}s - p\,\mathrm{d}\Big(\frac{1}{\rho}\Big) = T\,\mathrm{d}s + \frac{p}{\rho^2}\,\mathrm{d}\rho. \tag{1.45}$$

The densities of the quantities involved are obtained by multiplying them by the mass density ρ, e.g. the energy density is written as $\rho\varepsilon$.

In analogy with the study of the mass and momentum densities in the previous sections, we consider the rate of change $\partial_t E(\Omega, t)$ of the energy, i.e. the power conversion, of the fluid inside some fixed region Ω. As the energy density is given by the sum of the kinetic energy density $\frac{1}{2}\rho v^2$ and the internal energy density $\rho\varepsilon$, the rate of change is given by

$$\partial_t E(\Omega, t) = \partial_t \int_\Omega \mathrm{d}\mathbf{r}\,\Big[\tfrac{1}{2}\rho v^2 + \rho\varepsilon\Big] = \int_\Omega \mathrm{d}\mathbf{r}\,\partial_t\Big[\tfrac{1}{2}\rho v^2 + \rho\varepsilon\Big]. \tag{1.46}$$

As for the momentum changes Eq. (1.27), the energy of the fluid inside the region Ω can change by energy convection through the surface $\partial\Omega$, by work done by pressure and friction forces from the surroundings acting on the surface $\partial\Omega$ of Ω, and by heat conduction due to thermal gradients at the surface. For simplicity, we disregard heat sources and sinks that in principle could be present inside Ω. Thus, the rate of change of the energy can be written as

$$\partial_t E(\Omega, t) = \partial_t E^{\mathrm{conv}}(\Omega, t) + \partial_t E^{\mathrm{pres}}(\Omega, t) + \partial_t E^{\mathrm{visc}}(\Omega, t) + \partial_t E^{\mathrm{cond}}(\Omega, t). \tag{1.47}$$

Similar to Eqs. (1.22) and (1.29), the convection of energy into the region is easily expressed in terms of the energy flux density $\mathbf{J}_\varepsilon = (\frac{1}{2}\rho v^2 + \rho\varepsilon)\mathbf{v}$,

$$\partial_t E^{\mathrm{conv}}(\Omega, t) = \int_{\partial\Omega} \mathrm{d}a\,(-\mathbf{n})\cdot\mathbf{J}_\varepsilon = -\int_{\partial\Omega} \mathrm{d}a\, n_j v_j \Big[\tfrac{1}{2}\rho v^2 + \rho\varepsilon\Big]. \tag{1.48}$$

The power transferred into the region Ω through the work done by the stress forces due to pressure and viscosity at the surface is given by the product $\mathbf{v}\cdot(\sigma\mathbf{n}\mathrm{d}a)$ of the velocity of the fluid and the stress force vector,

$$\partial_t E^{\mathrm{pres}}(\Omega, t) + \partial_t E^{\mathrm{visc}}(\Omega, t) = \int_{\partial\Omega} \mathrm{d}a\, v_k \sigma_{kj} n_j = \int_{\partial\Omega} \mathrm{d}a\, n_j \big[-p\delta_{jk} + \sigma'_{jk}\big] v_k. \tag{1.49}$$

Thermal conduction occurs in any medium given a spatially varying temperature field $T(\mathbf{r})$. The heat flux density $\mathbf{J}_{\mathrm{heat}}$, which is the heat-transfer per area per time given in units of $\mathrm{J\,m^{-2}\,s^{-1}}$ or $\mathrm{W\,m^{-2}}$, can therefore be expanded in derivatives of the temperature. For small temperature variations only the first derivative $\boldsymbol{\nabla}T$ are significant, and we arrive at Fourier's law of heat conduction for an isotropic medium,

$$\mathbf{J}_{\mathrm{heat}} = -\kappa\,\boldsymbol{\nabla}T, \tag{1.50}$$

where the coefficient κ, having the unit $\mathrm{W\,m^{-1}\,K^{-1}}$, is called the thermal conductivity of the fluid. For water at 20 ℃ we have $\kappa_{\mathrm{water}}(20\ ℃) = 0.597\ \mathrm{W\,m^{-1}\,K^{-1}}$. The rate of change of energy due to conduction is readily found through the heat flux density and by applying Fourier's law,

$$\partial_t E^{\mathrm{cond}}(\Omega,t) = \int_{\partial\Omega} \mathrm{d}a\,(-\mathbf{n})\cdot\mathbf{J}_{\mathrm{heat}} = \int_{\partial\Omega} \mathrm{d}a\,n_j\,(\kappa\partial_j T). \tag{1.51}$$

The heat-transfer equation now follows from Eq. (1.46) by insertion of the above integrals. As before, we use Gauss's theorem to convert the surface integrals into volume integrals, and then equate the integrands to obtain

$$\partial_t\big[\tfrac{1}{2}\rho v^2 + \rho\varepsilon\big] = -\big(\tfrac{1}{2}v^2+\varepsilon\big)\partial_j(\rho v_j) - \rho v_k\partial_k\big(\tfrac{1}{2}v^2\big) - v_j\partial_j p + v_j\partial_k\sigma'_{jk} + \rho\partial_t\varepsilon, \tag{1.52}$$

where the continuity equation (1.24) and the equation of motion Eq. (1.36) have been used to rewrite $\partial_t\rho$ and $\partial_t v_j$, respectively. The last term $\rho\partial_t\varepsilon$ can be further rewritten by using the first law of thermodynamics (1.45), thereby bringing the entropy s into play as $\rho\partial_t\varepsilon = \rho T\partial_t s + (p/\rho)\,\partial_t\rho = \rho T\partial_t s - (p/\rho)\,\partial_j(\rho v_j)$. Likewise, the third term containing $v_j\partial_j p$ can also be rewritten by use of the first law, and we finally arrive at the heat-transfer equation in the usual form

$$\rho T\big[\partial_t s + v_j\partial_j s\big] = \sigma'_{jk}\partial_k v_j + \partial_j\big[\kappa\partial_j T\big], \tag{1.53a}$$

$$\rho T\big[\partial_t s + (\mathbf{v}\cdot\boldsymbol{\nabla})s\big] = \sigma' : \boldsymbol{\nabla}\mathbf{v} + \boldsymbol{\nabla}\cdot(\kappa\boldsymbol{\nabla}T). \tag{1.53b}$$

The left-hand side is ρT times the total time derivative of the entropy per unit mass, hence it expresses the total gain in heat density per unit time, while the right-hand side represents the sources for heat gain: viscous friction and thermal conduction.

In microfluidics, the fluid velocities are generally much smaller than the speed of sound in the fluid. Consequently, pressure variations are minute, leading to the constant pressure approximation, for which $\mathrm{d}s = c_{\mathrm{p}}\mathrm{d}T$, where c_{p} is the specific heat at constant pressure. In this case the heat-transfer equation reduces to

$$\rho c_{\mathrm{p}}\big[\partial_t T + (\mathbf{v}\cdot\boldsymbol{\nabla})T\big] = \boldsymbol{\nabla}\cdot(\kappa\boldsymbol{\nabla}T) + \sigma' : \boldsymbol{\nabla}\mathbf{v}. \tag{1.54}$$

For a fluid at rest ($\mathbf{v} = \mathbf{0}$) with a constant thermal coductivity κ, this equation becomes the even simpler Fourier equation,

$$\partial_t T = \frac{\kappa}{\rho c_{\mathrm{p}}}\nabla^2 T = D_{\mathrm{th}}\nabla^2 T, \tag{1.55}$$

which introduces the thermal diffusivity D_{th}, which for water at 20 ℃ is $1.43\times10^{-7}\ \mathrm{m^2 s^{-1}}$.

This concludes our short introduction to the basics of theoretical microfluidics, and we move on to study flow solutions and equivalent circuit theory for microfluidic systems.

Chapter 2

Flow solutions and circuit models

The Navier–Stokes equation is notoriously difficult to solve analytically because it is a non-linear partial differential equation. In a few but important cases, analytical solutions for the velocity field $\mathbf{v}$ and pressure field p can be found, and of these we shall treat hydrostatics and the steady-state pressure-driven Poiseuille flow in the following. For many practical applications it suffices to know the flow rate through a given system rather than the detailed flow field. This is treated in the subsequent study of the so-called equivalent circuit models in microfluidics.

2.1 Hydrostatic pressure

A fluid in mechanical equilibrium is at rest relative to the walls of the vessel containing it, and the velocity field is therefore trivially zero everywhere. Thus $\mathbf{v} = \mathbf{0}$, and if we let z-axis point upwards the gravitational acceleration takes the form $\mathbf{g} = -g\mathbf{e}_z$. The Navier–States equation 1.37b then takes the simple form

$$\mathbf{0} = -\boldsymbol{\nabla} p_{\mathrm{hs}} - \rho g \mathbf{e}_z, \tag{2.1}$$

where the subscript "hs" refers to hydrostatic. For an incompressible fluid, say water, the density ρ is constant and p_{hs} is easily found to be

$$p_{\mathrm{hs}}(z) = p^* - \rho g z. \tag{2.2}$$

where p^* is the pressure at the arbitrarily defined zero level $z = 0$. In many microfluidic applications this is the only manifestation of gravity. It is therefore customary to write the total pressure as $p_{\mathrm{tot}} = p + p_{\mathrm{hs}}$, such that in the Navier–Stokes equation the gravitational body force is cancelled by the gradient of hydrostatic pressure. The resulting Navier–Stokes equation thus contains the auxiliary pressure p and no gravitational body force. We shall use this point of view frequently in the book.

The hydrostatic pressure p_{hs} provides an easy way of generating pressure differences in liquids: the pressure at the bottom of a liquid column of height ΔH is higher by $\Delta p = \rho g H$ than the pressure at height H. For water water $\rho g \approx 10^4$ Pa/m, so a vertical water column of height 10 cm creates $\Delta p = 1$ kPa, while it takes a height of 10 m to create 10^5 Pa $= 1$ bar ≈ 1 atm.

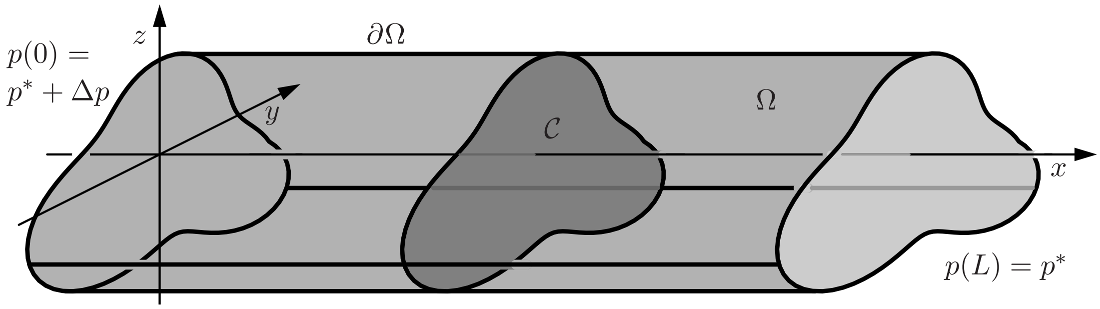

Figure 2.1: Poiseuille flow of liquid through a straight channel Ω (gray), where the flow is subject to the no-slip boundary condition on the surface $\partial\Omega$. The channel is translational invariant in the x direction, and it has an arbitrarily shaped cross-section $\mathcal{C}$ (dark gray) in the yz-plane. The pressure at the left end, $x = 0$, is an amount Δp higher than at the right end, $x = L$.

2.2 Poiseuille flow

Our prime example of a solutions to the Navier–Stokes equation in the dynamic case is the pressure-driven, steady state flows in straight channels, also known as Poiseuille flows or Hagen–Poiseuille flows[1]. This class of flows is of major importance for the basic understanding of liquid handling in lab-on-a-chip systems.

In a Poiseuille flow the fluid is driven through a long, straight, and rigid channel of length L by imposing a pressure difference Δp between the two ends of the channel, see Fig. 2.1. The channel is placed horizontally along the x-axis, so along the vertical z-axis gravity is balanced by the hydrostatic pressure. Furthermore, the cross-section of the channel is constant along the x-axis, so the liquid in the channel is only affected by the force from the pressure drop along the x-axis. The velocity field can therefore be assumed only to have an x-component, and this component depends only on the transverse co-ordinates y and z, such that $\mathbf{v} = v_x(y,z)\,\mathbf{e}_x$[2]. For this special case we note that $(\mathbf{v}\cdot\boldsymbol{\nabla})\mathbf{v} = (v_x\partial_x)v_x(y,z) = 0$ changing the non-linear Navier–Stokes equation into the linear Stokes equation.

For the velocity field we employ the so-called no-slip boundary condition: On all points on the solid surface $\partial\Omega$ the velocity of the fluid equals that of the wall $\mathbf{v}_{\mathrm{wall}}$ (often equal to zero),

$$\mathbf{v}(\mathbf{r}) = \mathbf{v}_{\mathrm{wall}}, \quad \text{for } \mathbf{r} \in \partial\Omega \ \text{(no-slip)}. \tag{2.3}$$

The microscopic origin of this condition is the assumption of complete momentum relax-

[1] Whereas the pronunciation "Har-gen" with a hard "g" of the German name is straightforward for English speakers, the French name Poiseuille is often a minor stumbling block. Its pronunciation lies between "Pwa-soy" and "Pwa-say", but with the second vowel closer to the sound of "i" in the English word "Sir".

[2] Although a valid mathematical solution at any flow speed, the translation-invariant velocity field is only stable at low velocities. The translation-invariance symmetry is spontaneously broken as the flow speed is increased, and eventually an unsteady turbulent flow appears as the physical solution having the smallest possible entropy production rate.

ation between the molecules of the wall and the outermost molecules of the fluid that collide with the wall. The momentum is relaxed on a length scale, which approximately is the molecular mean free path in the fluid, which for liquids and high-density fluids means one intermolecular distance ($\simeq 0.3$ nm).

The final form of the steady-state Navier–Stokes equation for the Poiseuille flow thus becomes

$$\mathbf{v}(\mathbf{r}) = v_x(y,z)\,\mathbf{e}_x, \tag{2.4a}$$

$$\mathbf{0} = \eta\nabla^2\big[v_x(y,z)\,\mathbf{e}_x\big] - \boldsymbol{\nabla} p. \tag{2.4b}$$

Since the y and z components of the velocity field are zero, it follows that both $\partial_y p$ and $\partial_z p$ are zero, and consequently that the pressure field only depends on x, $p(\mathbf{r}) = p(x)$. Using this result, the x component of the Navier–Stokes equation (2.4b) becomes

$$\eta\big[\partial_y^2 + \partial_z^2\big]v_x(y,z) = \partial_x p(x). \tag{2.5}$$

Here, it is seen that the left-hand side is a function of y and z, while the right-hand side is a function of x. The only possible solution is therefore that the two sides of the Navier–Stokes equation equal the same constant. However, a constant pressure gradient $\partial_x p(x)$ implies that the pressure must be a linear function of x, and using the boundary conditions for the pressure we obtain

$$p(\mathbf{r}) = \frac{\Delta p}{L}\,(L-x) + p^*. \tag{2.6}$$

With this we arrive at the second-order partial differential equation that $v_x(y,z)$ must fulfil in the cross-section $\mathcal{C}$ obeying no-slip boundary conditions at the solid walls $\partial\Omega$,

$$\big[\partial_y^2 + \partial_z^2\big]v_x(y,z) = -\,\frac{\Delta p}{\eta L}, \quad \text{for } (y,z)\in\mathcal{C} \tag{2.7a}$$

$$v_x(y,z) = 0, \qquad \text{for } (y,z)\in\partial\Omega. \tag{2.7b}$$

The resulting velocity field can be determined analytically for a limited number of cross-section shapes [Bruus 2008], and here we present two of these solutions: a channel with a circular cross-section of radius a, and a channel formed between two horizontal infinite parallel plates placed at $z=0$ and $z=h$,

$$v_x(y,z) = \frac{\Delta p}{4\eta L}\,\big(a^2 - y^2 - z^2\big), \quad \text{circular channel of radius } a, \tag{2.8a}$$

$$v_x(z) = \frac{\Delta p}{2\eta L}\,\big(h - z\big)z, \qquad \text{parallel-plate channel of height } h. \tag{2.8b}$$

It can easily be verified by inspection that these solutions are correct.

2.3 Flow rate

Once the velocity field is determined, it is possible to calculate the so-called volumetric flow rate Q, which is defined as the fluid volume discharged by the channel per unit time. In the case of the geometry of Fig. 2.1 we have

$$Q = \int_{\mathcal{C}} \mathrm{d}y\, \mathrm{d}z\, v_x(y,z) = \mathcal{A}\, v_{\mathrm{avr}}, \tag{2.9}$$

where $v_{\mathrm{avr}} = (1/\mathcal{A}) \int_{\mathcal{C}} \mathrm{d}y\, \mathrm{d}z\, v_x(y,z)$ is the average velocity and $\mathcal{A}$ is the cross-section area.

The flow rate for three selected Poiseuille flows are

$$Q = \frac{\pi a^4}{8\eta L}\, \Delta p, \qquad \text{circular channel of radius } a, \tag{2.10a}$$

$$Q = \frac{h^3 w}{12\eta L}\, \Delta p, \qquad \text{parallel-plate channel of height } h \ll w, \tag{2.10b}$$

$$Q \approx \left[1 - 0.630\, \frac{h}{w}\right] \frac{h^3 w}{12\eta L}\, \Delta p, \qquad \text{rectangular channel of height } h \leq w. \tag{2.10c}$$

The Poiseuille flow in a rectangular channel of height h and width w cannot be solved analytically in a closed form. However, the error of the approximative result (2.10c) is just 13% for the worst case (a square with $h = w$), while already at an aspect ratio of a half ($h = w/2$) it has decreased to 0.2%.

The SI unit of flow rate is $\mathrm{m^3\, s^{-1}}$, but in microfluidics volume is often measured in $\mathrm{\mu L} = \mathrm{mm^3}$ and time in minutes, so the following conversion factors are useful,

$$1\ \mathrm{\mu L\, s^{-1}} = 10^{-9}\ \mathrm{m^3\, s^{-1}}, \qquad \text{and} \qquad 1\ \mathrm{\mu L\, min^{-1}} = 1.67 \times 10^{-11}\ \mathrm{m^3\, s^{-1}}. \tag{2.11}$$

2.4 Circuit modeling; hydraulic resistance

Above we have found that a constant pressure drop Δp results in a constant flow rate Q. This result can be summarized in the Hagen–Poiseuille law

$$\Delta p = R_{\mathrm{hyd}}\, Q, \qquad \text{or} \qquad R_{\mathrm{hyd}} = \frac{\Delta p}{Q}, \tag{2.12}$$

where we have introduced the proportionality factor R_{hyd} known as the hydraulic resistance; a central concept in characterizing and designing microfluidic channels in lab-on-a-chip systems, see list in Table 2.1. The SI units used in the Hagen–Poiseuille law are

$$[Q] = \frac{\mathrm{m^3}}{\mathrm{s}}, \qquad [\Delta p] = \mathrm{Pa} = \frac{\mathrm{N}}{\mathrm{m^2}} = \frac{\mathrm{kg}}{\mathrm{m\, s^2}}, \qquad [R_{\mathrm{hyd}}] = \frac{\mathrm{Pa\, s}}{\mathrm{m^3}} = \frac{\mathrm{kg}}{\mathrm{m^4\, s}}. \tag{2.13}$$

The Hagen–Poiseuille law is completely analogous to Ohm's law, $\Delta V = R\, I$, relating the electrical current I through a wire with the electrical resistance R of the wire and the electrical potential drop ΔV along the wire. In hydraulic systems volume is moved while in electric systems charge is moved. Q is volume per time as I is charge per time.

Table 2.1: A list of the hydraulic resistance for straight channels with different cross-sectional shapes. The numerical values are calculated using the following parameters: $\eta = 1$ mPa s (water), $L = 1$ mm, $a = 100$ µm, $b = 33$ µm, $h = 100$ µm, and $w = 300$ µm.

shape	length parameters	R_{hyd} expression	R_{hyd} $[10^{11}\ \frac{\mathrm{Pa\,s}}{\mathrm{m}^3}]$	R_{hyd} $[\frac{\mathrm{Pa\,s}}{\mathrm{\mu L}}]$
circle	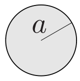	$\frac{8}{\pi}\,\eta L\,\frac{1}{a^4}$	0.25	25
ellipse	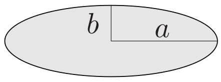	$\frac{4}{\pi}\,\eta L\,\frac{1+(b/a)^2}{(b/a)^3}\,\frac{1}{a^4}$	3.93	393
triangle	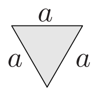	$\frac{320}{\sqrt{3}}\,\eta L\,\frac{1}{a^4}$	18.5	1850
two plates	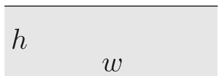	$12\,\eta L\,\frac{1}{h^3 w}$	0.40	40
rectangle	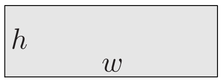	$\frac{12\,\eta L}{1-0.63(h/w)}\,\frac{1}{h^3 w}$	0.51	51
square	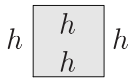	$28.4\,\eta L\,\frac{1}{h^4}$	2.84	284
parabola	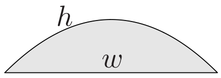	$\frac{105}{4}\,\eta L\,\frac{1}{h^3 w}$	0.88	88
arbitrary	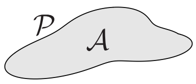	$\approx 2\,\eta L\,\frac{\mathcal{P}^2}{\mathcal{A}^3}$	–	–

Likewise, Δp is energy per volume as ΔV is energy per charge. Hydraulic power is $Q\Delta P$ (vol/time × energy/vol) while electric power is $I\Delta V$ (charge/time × energy/charge).

For low Reynolds numbers fluid flow is described by the linear Stokes equation, and to a good approximation the hydraulic resistances obey the same rules for series and parallel coupling as the electric resistances in linear circuit theory. Thus for two hydraulic resistance R_1 and R_2 we have

$$R_{\mathrm{hyd}}^{\mathrm{series}} = R_1 + R_2, \qquad \text{and} \qquad R_{\mathrm{hyd}}^{\mathrm{parallel}} = \left(\frac{1}{R_1} + \frac{1}{R_2}\right)^{-1} = \frac{R_1\,R_2}{R_1 + R_2}. \tag{2.14}$$

For a general fluidic network or circuit one can apply Kirchhoff's laws,

a) The sum of flow rates entering/leaving any node in the circuit is zero.
b) The sum of all pressure differences in any closed loop of the circuit is zero. (2.15)

2.5 Circuit modeling; hydraulic compliance

The analogy between hydraulic and electric systems can be taken one step further. When the pressure increases by Δp in a liquid inside an elastic channel, the volume available to the liquid increases by $\Delta\mathcal{V}$. This is analogous to the charging of a capacitor where in increase in voltage by ΔV increases the charge on the capacitor by $\Delta q = C\Delta V$. The electric capacitance is given by $C = \partial q/\partial V$, and we are led to introduce hydraulic capacitance C_{hyd}, also known as compliance, given by

$$C_{\mathrm{hyd}} \equiv \frac{\mathrm{d}\mathcal{V}}{\mathrm{d}p}, \qquad \text{with} \qquad [C_{\mathrm{hyd}}] = \mathrm{m}^3\,\mathrm{Pa}^{-1}. \tag{2.16}$$

As an example of compliance we consider a simple model of a soft-walled channel filled with an incompressible liquid as sketched in Fig. 2.2(a). If the pressure increases inside the channel, the latter will expand. The compliance C_{hyd} of the channel is a given constant related to the geometry and the material properties of the channel walls. As a simplification we model the channel as consisting of two subchannels with hydraulic resistances R_1 and R_2, respectively, connected in series. The pressure p_{c} at the point, where the two subchannels connect, determines the expansion of the whole channel. The equivalent model is seen in Fig. 2.2(b). We let the pressure at the inlet be p^* for time $t < 0$ and $p^* + \Delta p$ for time $t > 0$. The flow rate at the inlet and the outlet are given by the Hagen–Poiseuille law $Q_1 = (p^* + \Delta p - p_{\mathrm{c}})/R_1$ and $Q_2 = (p_{\mathrm{c}} - p^*)/R_2$, respectively, while the rate of volume expansion inside the chamber is given by $Q_{\mathrm{c}} = \partial_t\mathcal{V} = C_{\mathrm{hyd}}\partial_t p_{\mathrm{c}}$. Since the liquid is assumed to be incompressible, conservation of mass leads to $Q_1 = Q_2 + Q_{\mathrm{c}}$, and we arrive at the following differential equation for the pressure p_{c} inside the channel:

$$\partial_t p_{\mathrm{c}} = -\Big(\frac{1}{\tau_1} + \frac{1}{\tau_2}\Big)p_{\mathrm{c}} + \Big(\frac{1}{\tau_1} + \frac{1}{\tau_2}\Big)p^* + \frac{1}{\tau_1}\Delta p, \tag{2.17}$$

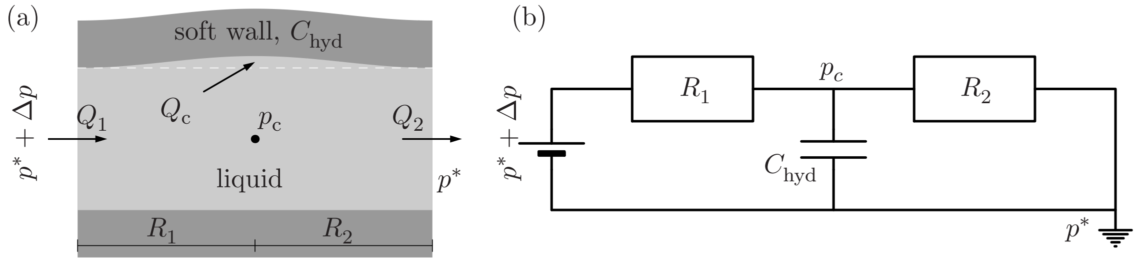

Figure 2.2: (a) Compliance due to a soft-walled channel (dark gray) filled with liquid (light gray). The pressure in the center of the channel is denoted p_{c}, while the hydraulic resistances of the first and second part of the channel are denoted R_1 and R_2, respectively. Mass conservation yields $Q_1 = Q_2 + Q_{\mathrm{c}}$. (b) The equivalent circuit diagram corresponding to the soft-walled channel of panel (a), where R_1 and R_2 are the hydraulic resistances of each part of the channel, while C_{hyd} is the compliance of the soft wall.

where $\tau_1 = R_1 C_{\rm hyd}$ and $\tau_2 = R_2 C_{\rm hyd}$ are the hydraulic RC times. The solution,

$$p_{\rm c}(t) = p^* + \Big(1 - {\rm e}^{-\left[\tau_1^{-1}+\tau_2^{-1}\right]t}\Big)\frac{\tau_2}{\tau_1+\tau_2}\Delta p, \tag{2.18}$$

is analogous to the voltage across a capacitor being charged through a voltage divider.

Often the external tubing may lead to long transient times in the external system due to the RC-time

$$\tau_{RC} = R_{\rm hyd} C_{\rm hyd} \tag{2.19}$$

arising from the hydraulic resistance $R_{\rm hyd}$ and compliance $C_{\rm hyd}$. The thick-wall approximation for the compliance of a tube can be derived from basic theory of elasticity [Landau 1986]. It turns out to be independent of the thickness of the wall,

$$C_{\rm hyd}^{\rm tube} \approx 2\pi(1+\bar{\nu})\frac{a^2 L}{Y}. \tag{2.20}$$

Here a is the inner radius of the relaxed tube, L the length, $\bar{\nu}$ the Poisson ratio, and Y Young's modulus. As an example of transient times consider a tube of with $L = 1$ m and $a = 0.1$ mm leading from a syringe pump to a lab-on-a-chip device. For water in such tubes made of either soft silicone rubber ($Y = 2.1$ MPa and $\bar{\nu} = 0.49$) or hard teflon $Y = 0.5$ GPa and $\bar{\nu} = 0.45$) we get

$$\text{Silicone:}\quad R_{\rm hyd} = 2.5\times 10^{13}\,\frac{\rm Pa\,s}{\rm m^3},\quad C_{\rm hyd} = 4.7\times 10^{-14}\,\frac{\rm m^3}{\rm Pa},\quad \tau_{RC} = 1.2\ {\rm s}, \tag{2.21a}$$

$$\text{Teflon:}\quad R_{\rm hyd} = 2.5\times 10^{13}\,\frac{\rm Pa\,s}{\rm m^3},\quad C_{\rm hyd} = 1.8\times 10^{-16}\,\frac{\rm m^3}{\rm Pa},\quad \tau_{RC} = 4.6\times 10^{-3}\ {\rm s}. \tag{2.21b}$$

2.6 Circuit modeling; hydraulic inductance

The last analogy relates to inductance. The (self-)inductance $L_{\rm el}$, or the electric inertia, is the ability of an electric system to maintain a given current I. A rate of change $\partial_t I$ in the current induces a potential drop $\Delta V = L_{\rm el}\partial_t I$. Hydraulic inductance $L_{\rm hyd}$ therefore relates to maintaining an existing volume current $Q = \mathcal{A} v_{\rm avr}$. Since the rate of change $\partial_t Q = \mathcal{A}\partial_t v_{\rm avr}$ involves acceleration, it follows that $L_{\rm hyd}$ corresponds to inertia.

Consider the flow through a channel of length L and cross-section area $\mathcal{A}$. If the force F driving the flow arises from a pressure drop Δp, we find from Newton's second law that $\Delta p = F/\mathcal{A} = (\rho L \mathcal{A})\partial_t v_{\rm avr}/\mathcal{A}$. This leads to $\Delta p = (\rho L/\mathcal{A})\,\partial_t Q$, from which we can read off the hydraulic inductance $L_{\rm hyd}$ as

$$L_{\rm hyd} = \frac{\rho L}{\mathcal{A}}, \qquad \text{with} \qquad [L_{\rm hyd}] = {\rm Pa\,s^2\,m^{-3}}. \tag{2.22}$$

In analogy with the RC-time there is also a transient RL-time given by $\tau_{RL} = L_{\rm hyd}/R_{\rm hyd}$, which for a tube becomes

$$\tau_{RL}^{\rm tube} = \frac{L_{\rm hyd}}{R_{\rm hyd}} = \frac{\rho a^2}{8\eta} = \frac{a^2}{8\nu}, \tag{2.23}$$

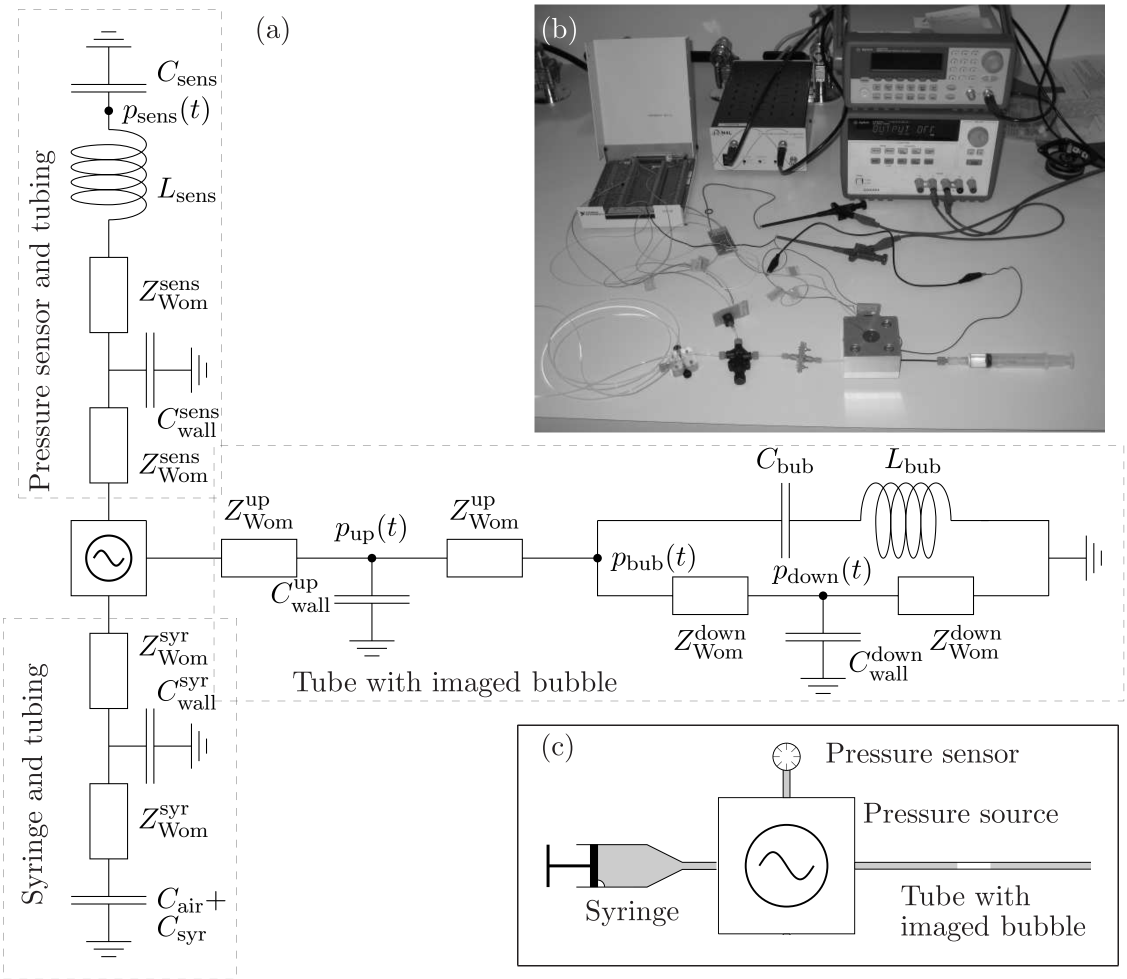

Figure 2.3: An example of an application of circuit modeling: an ac pressure source running up to 1 kHz and driving oscillations in an air bubble placed in an elastic silicone tube. (a) Circuit model of the systems containing the pressure source, a syringe pump, a pressure sensor, and the elastic tube containing the air bubble. (b) Picture of the experimental setup. (c) Sketch of the setup showing the four components. Adapted from the DTU master thesis by Søren Vedel [Vedel 2009].

where in the last equality we have used the kinematic viscosity ν from Eq. (1.44). For the tubes in the previous subsection with $L = 1$ m and $R = 0.1$ mm we find

$$R_{\mathrm{hyd}} = 2.5 \times 10^{13}\ \frac{\mathrm{Pa\,s}}{\mathrm{m}^3}, \quad L_{\mathrm{hyd}} = 3.2 \times 10^{-10}\ \frac{\mathrm{Pa\,s}^2}{\mathrm{m}^3}, \quad \tau_{RC} = 1.2 \times 10^{-3}\ \mathrm{s}. \tag{2.24}$$

2.7 Circuit modeling; an example

We end the chapter by showing an example of the application of circuit modeling on an actual system [Vedel 2010]. The system is built to apply pulsatile microfluidics as an analytical tool for determining the dynamic characteristics of microfluidic systems in general. As a particular case, an air bubble placed in a tube is monitored while exposed to a pulsatile pressure drop.

The system is presented in Fig. 2.3, and it consists of four parts: (*i*) a membrane pump capable of delivering pulsatile pressures up to 1 bar and with frequencies up to 1 kHz, (*ii*) a pressure sensor for monitoring the pressure during operation, (*iii*) a transparent, elastic rubber tube containing an air bubble, and (*iv*) a syringe pump for filling the system with water and adjusting the position of the air bubble. Not shown on the figure is the microscope and CCD camera by which the oscillations of the air bubble inside the tube was observed and recorded.

The system is modeled using the detailed circuit model shown in Fig. 2.3(a). Due to the ac drive the concept of impedance is introduced in analogy with electric ac circuits, e.g. the impedance of a tube with a resistance and an inductance is $Z_{\mathrm{tube}} = R_{\mathrm{hyd}} + i\omega L_{\mathrm{hyd}}$, where ω is the angular frequency.

In Fig. 2.4(a) is shown a raw image of the air bubble in the compliant tube, and in Fig. 2.4(b) the measured motion of the left and right bubble interfaces are compared to the prediction of the circuit model. A good agreement is found thus demonstrating the usefulness of the circuit model approach.

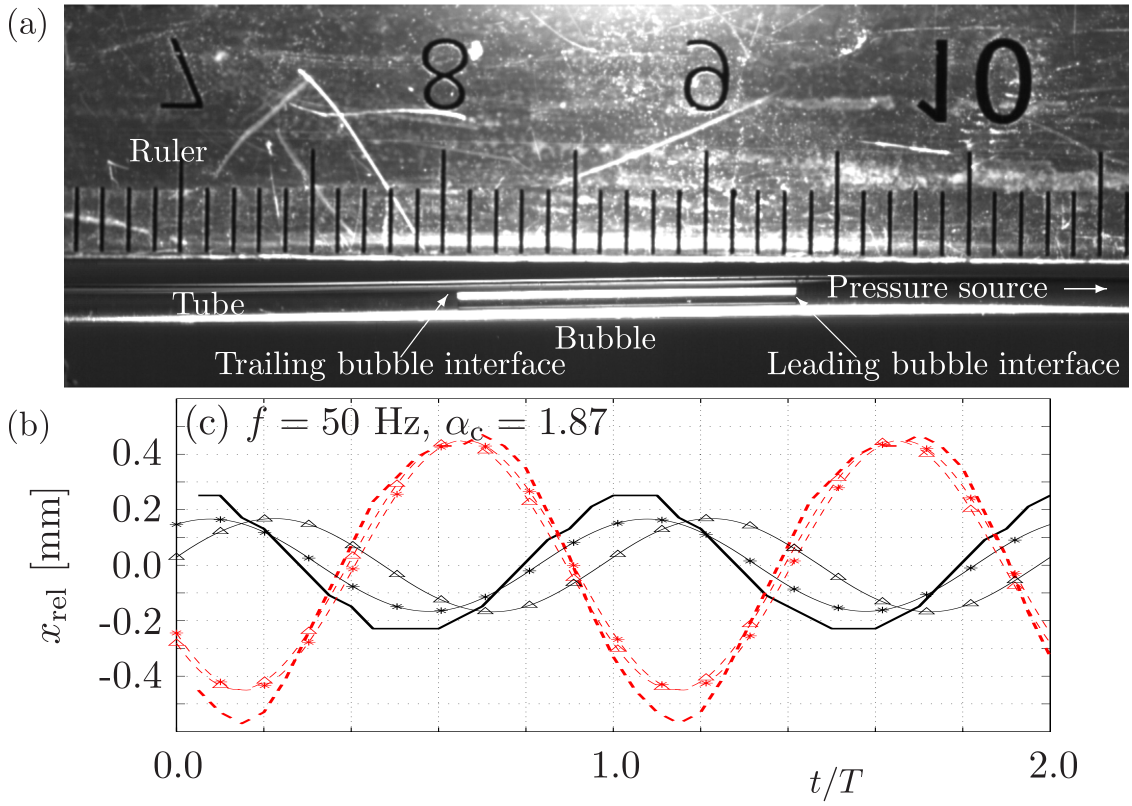

Figure 2.4: (a) A raw bubble image recorded by the CCD camera showing part of the tube exiting the pressure source chamber; the right end of the tube is connected to the pressure source while the left end is left in atmospheric conditions. The bubble is found roughly in the middle of the tube. A mm-scale ruler (inverted and mirrored) is positioned above the tube. (b) Experimental results (thick lines) compared to modeled bubble displacements (balck/red curves correspond to left/right bubble interface) for 50 Hz oscillations (simple model: starred thin lines, extended model: thin lines with triangles). Good agreement is found between the models and the experiments through the entire frequency range, but the simple model predicts displacement amplitudes and phase-lags better. Both models capture the leading interface displacement slightly better than the displacement of the trailing interface. Adapted from the DTU master thesis by Søren Vedel [Vedel 2009].

Chapter 3

Diffusion

The handling of aqueous solutions of microparticles, biological cells, and biomolecules is central to microfluidics and lab-on-a-chip technoloby. The carrier liquid is denoted the solvent and the particle constitute is called the solute. Diffusion is the motion of the solute in the solvent from regions of high to low concentrations of the solute resulting from thermally induced random motion of the particles, such as Brownian motion. Pure diffusion of the solute occurs when the velocity field of the solvent is zero, while in case of non-zero velocity fields the motion of the solute is partly convective, since the dissolved particles are carried along by the solvent.

3.1 A random-walk model of diffusion

To establish some basic features of diffusion, we first study it in terms of the simple constant-step random-walk model. At first we restrict the analysis to motion in one spatial dimension along the x axis. Such a 1D random walk consists of a number of consecutive, uncorrelated steps. Each step i takes the same time τ during which the particle moves the distance $\Delta x_i = \pm\ell$, where ℓ is a constant step length. We assume that there is equal probability for choosing either sign, and that the steps are statistically uncorrelated as is expressed mathematically through the mean value $\langle \Delta x_i \Delta x_j \rangle$ as

$$\langle \Delta x_i \Delta x_j \rangle = \ell^2 \, \delta_{ij}. \tag{3.1}$$

At time $t = 0$ the particle is at $x = x_0 = 0$. At time $t = N\tau$ the particle has performed N steps, and it is at the position x_N given by

$$x_N = \sum_{i=1}^{N} \Delta x_i, \qquad \Delta x_i = \pm\ell, \tag{3.2}$$

with a random distribution of plus and minus signs. In Fig. 3.1(a) is shown the distribution of the final position X_N for $N = 6$. Such a random walk can be analyzed in terms of the binomial distribution, which in the limit of large N approaches the normal distribution.

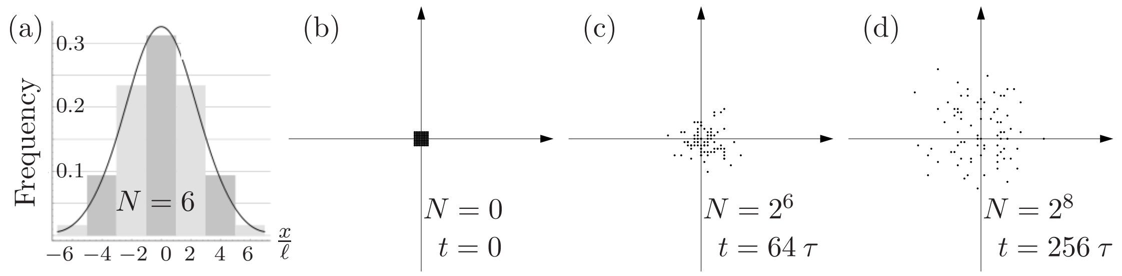

Figure 3.1: (a) Frequency plot of the final position X_N in a constant-step 1D random walk for $N = 6$. For large N the distribution approaches the normal distribution (full line). (b)-(d) Constant-step 2D random walk with step length $\ell = 0.05$ illustrating molecular diffusion. At $N = 0$ 81 particles are place near the origin of the co-ordinate system covering $-4 < x < 4$ and $-4 < y < 4$. The position of the particles are shown after $N = 0$, $N = 2^6$, and $N = 2^8$ random-walk steps corresponding to the times $t = 0$, $64\,\tau$, and $256\,\tau$.

In the following, however, we analyze the random walk directly in terms of the statistics of the step sequence.

Consider M constant-step 1D random walks ending at $x_N^{(j)}$, $j = 1, 2, \ldots, M$. Each of these random walks consists of N random steps $\Delta x_i^{(j)} = \pm\ell$. The mean value $\langle x_N \rangle$ of the final positions is

$$\langle x_N \rangle \equiv \frac{1}{M}\sum_{j=1}^{M} x_N^{(j)} = \frac{1}{M}\sum_{j=1}^{M}\left(\sum_{i=1}^{N}\Delta x_i^{(j)}\right) = \sum_{i=1}^{N}\left(\frac{1}{M}\sum_{j=1}^{M}\Delta x_i^{(j)}\right) = \sum_{i=1}^{N}\langle \Delta x_i \rangle = 0. \quad (3.3)$$

The last equality follows from the assumption of equal probability for stepping either $+\ell$ or $-\ell$. As expected, the mean value is zero, and clearly the quantity $\langle x_N \rangle$ does not reveal the kinematics of diffusion. We therefore continue by calculating $\langle x_N^2 \rangle$ related to the statistical standard deviation in the final position of the particles,

$$\langle x_N^2 \rangle \equiv \frac{1}{M}\sum_{j=1}^{M}\left[x_N^{(j)}\right]^2 = \frac{1}{M}\sum_{j=1}^{M}\left(\sum_{i=1}^{N}\Delta x_i^{(j)}\right)\left(\sum_{k=1}^{N}\Delta x_k^{(j)}\right) = \frac{1}{M}\sum_{j=1}^{M}\sum_{i=1}^{N}\sum_{k=1}^{N}\Delta x_i^{(j)}\Delta x_k^{(j)}, \quad (3.4)$$

where different summation indices i and k are used in the product term. Now follows a trick often used in statistics. In the ik double sum we collect the terms where $k = i$, the so-called diagonal terms, and those where $k \neq i$, the so-called offdiagonal terms. This enables a straightforward evaluation of the average over the ensemble of random walks j,

$$\langle x_N^2 \rangle = \frac{1}{M}\sum_{j=1}^{M}\left(\sum_{i=1}^{N}\left[\Delta x_i^{(j)}\right]^2 + \sum_{i=1}^{N}\sum_{k\neq i}^{N}\Delta x_i^{(j)}\Delta x_k^{(j)}\right) = N\ell^2 + \sum_{i=1}^{N}\sum_{k\neq i}^{N}\langle \Delta x_i^{(j)}\Delta x_k^{(j)} \rangle. \quad (3.5)$$

In the last equality we have used that $\left[\Delta x_i^{(j)}\right]^2 = (\pm\ell)^2 = \ell^2$ regardless of the sign of the random step. Now, since $k \neq i$ in the last term it follows that $\Delta x_i^{(j)}$ and $\Delta x_k^{(j)}$ are statistically independent, so the probability of having the summand equal to $(+\ell)(-\ell) = (-\ell)(+\ell) = -\ell^2$ is the same as that of having $(+\ell)(+\ell) = (-\ell)(-\ell) = +\ell^2$. Thus, the last term vanish upon averaging over random walkers, and we get

$$\langle x_N^2 \rangle = N\ell^2. \tag{3.6}$$

From Eqs. (3.3) and (3.6) we find the root-mean-square displacement by diffusion, the so-called diffusion length $\ell_{\text{diff},N}^{1D}$, of the random walker taking N steps in 1D to be

$$\ell_{\text{diff},N}^{1D} \equiv \sqrt{\langle x_N^2 \rangle - \langle x_N \rangle^2} = \sqrt{N}\,\ell. \tag{3.7}$$

Reintroducing time as $t = N\tau$, where τ is the time it takes to perform one step, leads to

$$\ell_{\text{diff}}^{1D}(t) = \sqrt{\frac{t}{\tau}}\,\ell = \sqrt{\frac{\ell^2}{\tau}\,t} = \sqrt{2Dt}, \tag{3.8}$$

where the so-called diffusion constant D has been introduced,

$$D \equiv \frac{\ell^2}{2\tau}, \tag{3.9}$$

together with a factor of 2 for later convenience. Conversely, the time $t_{\text{diff}}^{1D}(\ell)$ it takes to cover a distance ℓ by diffusion, the so-called diffusion time, is given by

$$t_{\text{diff}}^{1D}(\ell) = \frac{\ell^2}{2D}. \tag{3.10}$$

It is a typical and remarkable feature of diffusion kinematics that the diffusion length depends on the square-root of time, as seen in Eq. (3.8). Ultimately, this dependence makes diffusion an extremely slow process of mixing over macroscopical distances. Even in microfluidic systems diffusion may still be a very slow process, see Eq. (3.22).

The random-walk model of diffusion is easily extended to the 2D xy-plane. Starting at the origin, the particle position $\mathbf{R}_N$ after N steps $\Delta\mathbf{r}_i$ is given by

$$\mathbf{R}_N = \sum_{i=1}^{N} \Delta\mathbf{r}_i, \qquad \Delta\mathbf{r}_i \;=\; (\pm\ell)\,\mathbf{e}_x \;+\; (\pm\ell)\,\mathbf{e}_y, \tag{3.11}$$

where there is an equal probability for any combination of the signs. If we decompose the motion in x and y components, which are statistically independent, we find

$$\langle R_N^2 \rangle = \langle x_N^2 + y_N^2 \rangle = \langle x_N^2 \rangle + \langle y_N^2 \rangle = 2N\ell^2. \tag{3.12}$$

Thus, in 2D (an trivially extended to 3D) the diffusion length becomes

$$\ell_{\text{diff}}^{2D}(t) = \sqrt{2N}\,\ell = \sqrt{4Dt} \quad \text{and} \quad \ell_{\text{diff}}^{3D}(t) = \sqrt{6Dt}. \tag{3.13}$$

A numerical example of such a 2D random walk is shown in Fig. 3.1(b)-(d).

3.2 The convection-diffusion equation for weak solutions

To formulate a differential equation for diffusion we introduce the concentration field $c_\alpha(\mathbf{r},t)$ for the number of particles of species α per volume at the point $\mathbf{r}$ and time t. Neglecting chemical reactions, the number of particles is conserved, and we can use the same method involving fluxes and Gauss's theorem as in Section 1.3 for conservation of mass.

Considering the arbitrary volume Ω, we note that the number of particles α can change in time in two ways; by a convection current $c_\alpha\,\mathbf{v}$ and by a diffusion current $\mathbf{J}^{\text{diff}}$, yet to be determined. In analogy with Eqs. (1.21) and (1.22) we obtain

$$\int_\Omega \mathrm{d}\mathbf{r}\,\partial_t c_\alpha = \int_{\partial\Omega} \mathrm{d}a\,(-\mathbf{n})\cdot\big(c_\alpha\mathbf{v}+\mathbf{J}^{\text{diff}}\big) = -\int_\Omega \mathrm{d}\mathbf{r}\,\boldsymbol{\nabla}\cdot\big(c_\alpha\mathbf{v}+\mathbf{J}^{\text{diff}}\big). \tag{3.14}$$

This equation can only be true for arbitrary Ω if the integrands are identical, and further using that for an incompressible fluid we have $\boldsymbol{\nabla}\cdot\mathbf{v}=0$, we arrive at

$$\partial_t c_\alpha + \mathbf{v}\cdot\boldsymbol{\nabla} c_\alpha = -\boldsymbol{\nabla}\cdot\mathbf{J}^{\text{diff}}. \tag{3.15}$$

The diffusion current density $\mathbf{J}^{\text{diff}}$ is non-zero only when gradients in the density of the solute are present. For weak solutions we expect only the lowest-order gradients to play a role, which is expressed by Fick's law,

$$\mathbf{J}^{\text{diff}}_\alpha = -D_\alpha\,\boldsymbol{\nabla} c_\alpha. \tag{3.16}$$

Inserting Fick's law into Eq. (3.15) leads to the convection-diffusion equation for the concentration c_α of solutes in weak solutions having a velocity field $\mathbf{v}$,

$$\partial_t c_\alpha + \mathbf{v}\cdot\boldsymbol{\nabla} c_\alpha = D_\alpha\,\nabla^2 c_\alpha. \tag{3.17}$$

The constant D_α is in analogy with Eq. (3.9) known as the diffusion constant or the diffusivity of solute α in the solvent,

$$D_\alpha \text{ with } [D_\alpha] = \mathrm{m}^2\,\mathrm{s}^{-1}\text{: Diffusivity of solute } \alpha \text{ in the solvent.} \tag{3.18}$$

3.3 The diffusion equation for mass, momentum, and heat

In the following we consider the diffusion of a single solute and therefore suppress the index α. If the velocity field $\mathbf{v}$ of the solvent is zero, convection is absent and Eq. (3.17) becomes the diffusion equation,

$$\partial_t c = D\,\nabla^2 c. \tag{3.19}$$

Simple dimensional analysis of this equation can already reveal some important physics. It is clear that if T_0 and L_0 denotes the characteristic time and length scale over which the concentration $c(\mathbf{r},t)$ varies, then

$$L_0 = \sqrt{DT_0} \qquad \text{or} \qquad T_0 = \frac{L_0^2}{D}, \tag{3.20}$$

which resembles Eq. (3.8). The diffusion constant D thus determines how fast a concentration diffuses a certain distance. Typical values of D are

$$D \approx 2 \times 10^{-9}\ \ \mathrm{m^2/s},\quad \text{small ions in water,} \tag{3.21a}$$
$$D \approx 5 \times 10^{-10}\ \mathrm{m^2/s},\quad \text{sugar molecules in water,} \tag{3.21b}$$
$$D \approx 4 \times 10^{-11}\ \mathrm{m^2/s},\quad \text{30-base-pair DNA molecules in water,} \tag{3.21c}$$
$$D \approx 1 \times 10^{-12}\ \mathrm{m^2/s},\quad \text{5000-base-pair DNA molecules in water,} \tag{3.21d}$$

which for diffusion across the typical microfluidic distance $L_0 = 100$ µm give the times

$$T_0(100\ \mu\mathrm{m}) \approx 5\ \mathrm{s},\quad \text{small ions in water,} \tag{3.22a}$$
$$T_0(100\ \mu\mathrm{m}) \approx 20\ \mathrm{s},\quad \text{sugar molecules in water,} \tag{3.22b}$$
$$T_0(100\ \mu\mathrm{m}) \approx 250\ \mathrm{s} \approx 4\ \mathrm{min},\quad \text{30-base-pair DNA molecules in water,} \tag{3.22c}$$
$$T_0(100\ \mu\mathrm{m}) \approx 10^4\ \mathrm{s} \approx 3\ \mathrm{h},\quad \text{5000-base-pair DNA molecules in water.} \tag{3.22d}$$

It is not only mass that can diffuse as described above. In fact, we have already encountered the diffusion equation in Eqs. (1.44) and (1.55) in context of momentum and heat. Taken as a whole, we have established that both mass, momentum and energy can diffuse, and that that this diffusion in all three cases is described by the diffusion equation,

$$\partial_t v_x = \nu\, \nabla^2 v_x,\quad \text{momentum diffusion with}\quad \nu \approx 10^{-6}\ \mathrm{m^2/s}, \tag{3.23a}$$
$$\partial_t T = D_\mathrm{th} \nabla^2 T,\quad \text{heat diffusion with}\quad D_\mathrm{th} \approx 10^{-7}\ \mathrm{m^2/s}, \tag{3.23b}$$
$$\partial_t c = D\, \nabla^2 c,\quad \text{mass diffusion with}\quad D \approx 10^{-9}\ \mathrm{m^2/s}. \tag{3.23c}$$

Using Eq. (3.20) we can estimate the following diffusion times in a microfluidic channel with radius a for momentum, heat and mass:

$$T_0^\mathrm{mom.} = \frac{a^2}{\nu} \approx 0.01\ \mathrm{s},\qquad T_0^\mathrm{heat} = \frac{a^2}{D_\mathrm{th}} \approx 0.1\ \mathrm{s},\qquad T_0^\mathrm{mass} = \frac{a^2}{D} \approx 10\ \mathrm{s}. \tag{3.24}$$

Thus momentum diffuses faster than heat, which diffuses faster than mass.

3.4 Analytical solutions to the diffusion equation

As already hinted at in Fig. 3.1, diffusion can be described by the normal distribution. We denote this distribution $P(s)$, where s is a normalized dimensionless variable with mean value $\langle s\rangle$ and variance $\langle s^2\rangle$, the width of the distribution. Its basic properties are

$$P(s) \equiv \frac{1}{\sqrt{2\pi}}\, \mathrm{e}^{-\frac{1}{2}s^2},\qquad \langle s\rangle = \int_{-\infty}^{\infty} \mathrm{d}s\, s\, P(s) = 0,\qquad \langle s^2\rangle = \int_{-\infty}^{\infty} \mathrm{d}s\, s^2\, P(s) = 1. \tag{3.25}$$

These results will be useful in the following analysis of diffusion.

Limited point-source diffusion. Consider a fixed number N_0 of molecules is injected at position $x = 0$ at time $t = 0$ in the middle of a infinitely thin and infinitely long water-filled tube aligned along the x axis. The initial point-like concentration acts as the source of the diffusion, and it can be written as a Dirac delta function[1]

$$c(x, t = 0) = N_0\, \delta(x). \tag{3.26}$$

The ink molecules immediately begins to diffuse out into the water, and by inspection it can be shown that the solution to the diffusion equation (3.19), which in 1D reduces to $\partial_t c = D\partial_x^2 c$, given the initial condition Eq. (3.26) is

$$c(x, t) = N_0\, (4\pi Dt)^{-\frac{1}{2}}\, \exp\Big[-\frac{x^2}{4Dt}\Big] = N_0\, P(s_x), \tag{3.27}$$

where we have introduced the normal distribution $P(s_x)$ of the dimensionless variable

$$s_x \equiv \frac{x^2}{2Dt}. \tag{3.28}$$

It is natural to define the square $\ell^2_{\mathrm{diff,1D}}$ of the 1D diffusion length $\ell_{\mathrm{diff,1D}}$ as the width of the distribution. So from Eqs. (3.25), (3.27) and (3.28) we get

$$\ell^2_{\mathrm{diff,1D}} \equiv \langle x^2\rangle = 2Dt\, \langle s_x^2\rangle = 2Dt. \tag{3.29}$$

Generalization of this result to 2D and 3D with the initial conditions $c(x, y, t = 0) = N_0\, \delta(x)\, \delta(y)$ and $c(x, y, z, t{=}0) = N_0\, \delta(x)\, \delta(y)\, \delta(z)$, respectively, gives

$$c(x, y, t) = N_0\, (4\pi Dt)^{-1}\, \exp\Big[-\frac{x^2 + y^2}{4Dt}\Big] = N_0\, P(s_x)\, P(s_y), \tag{3.30}$$

and

$$c(x, y, z, t) = N_0\, (4\pi Dt)^{-\frac{3}{2}}\, \exp\Big[-\frac{x^2 + y^2 + z^2}{4Dt}\Big] = N_0\, P(s_x)\, P(s_y)\, P(s_z), \tag{3.31}$$

where we have introduced the two dimensionless variables $s_y = y^2/(2Dt)$ and $s_z = z^2/(2Dt)$. The 3D result Eq. (3.31) for $c(x, y, z, t)$ is presented in Fig. 3.2(a). In 2D and 3D ℓ^2_{diff} becomes

$$\ell^2_{\mathrm{diff,2D}} \equiv \langle r^2\rangle_{\mathrm{2D}} = \langle x^2 + y^2\rangle = 2Dt\, \langle s_x^2 + s_y^2\rangle = 4\, Dt, \tag{3.32a}$$

$$\ell^2_{\mathrm{diff,3D}} \equiv \langle r^2\rangle_{\mathrm{3D}} = \langle x^2 + y^2 + z^2\rangle = 2Dt\, \langle s_x^2 + s_y^2 + s_z^2\rangle = 6\, Dt, \tag{3.32b}$$

and we see that the diffusion lengths (not their squares) are $\sqrt{2}$ and $\sqrt{3}$ times larger in 2D and 3D, respectively, than that in 1D.

Limited planar-source diffusion. Another limited diffusion process is limited planar-source diffusion. Let the semi-infinite half-space $x > 0$ be filled with some liquid. Consider then an infinitely thin slab covering the yz-plane at $x = 0$ containing n_0

[1]The Dirac delta function $\delta(x)$ is defined by: $\delta(x) = 0$ for $x \neq 0$ and $\int_{-\infty}^{\infty} \mathrm{d}x\, \delta(x) = 1$.

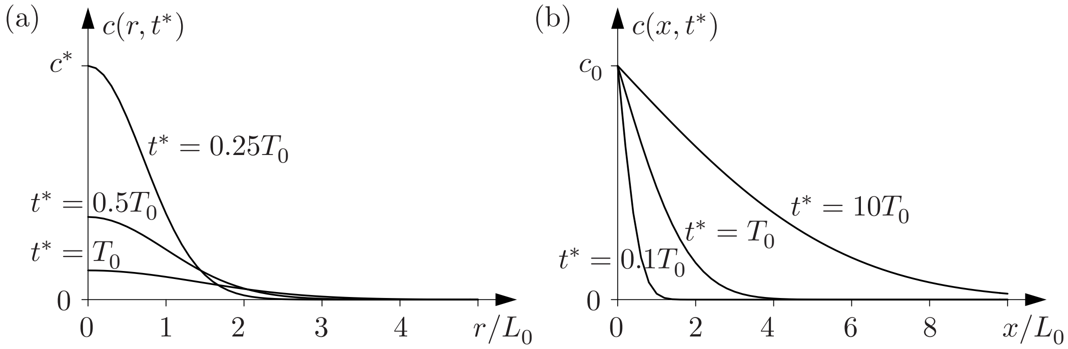

Figure 3.2: Concentration profiles $c(\mathbf{r}, t > 0)$ choosing the length scale to be L_0, which fixes the time scale to be $T_0 = L_0^2/D$. (a) Limited point-source diffusion $c(r, t^*)$ Eq. (3.31) for three given times $t^* = 0.25T_0$, $0.5T_0$, and T_0. (b) Constant planar-source diffusion $c(x, t^*)$ Eq. (3.34b) for three given times $t^* = 0.1T_0$, T_0, and $10T_0$.

molecules per area that at time $t = 0$ begin to diffuse out into the liquid. With a factor 2 inserted to normalize the half-space integration, the initial condition and solution is

$$c(\mathbf{r}, t = 0) = n_0\, 2\delta(x), \tag{3.33a}$$

$$c(\mathbf{r}, t > 0) = \frac{n_0}{(\pi D t)^{\frac{1}{2}}}\, \exp\Big(-\frac{x^2}{4Dt}\Big). \tag{3.33b}$$

Constant planar-source diffusion. We end by an example of diffusion with a constant source, i.e. an influx of solute is maintained at one of the boundary surfaces. Consider the same geometry as in the previous example, but change the boundary condition as follows. At time $t = 0$ a source filling the half-space $x < 0$ suddenly begins to provide an influx of molecules to the boundary plane $x = 0$ such that the density there remains constant c_0 at all later times. The initial condition and solution is, see Fig. 3.2(b),

$$c(x = 0, y, z, t > 0) = c_0, \tag{3.34a}$$

$$c(x, y, z, t > 0) = c_0 \operatorname{erfc}\bigg(\frac{x}{\sqrt{4Dt}}\bigg), \tag{3.34b}$$

where we have introduced the complementary error function $\operatorname{erfc}(s) \equiv \frac{2}{\sqrt{\pi}} \int_s^\infty \mathrm{e}^{-u^2}\, \mathrm{d}u$.

3.5 Taylor dispersion; a convection-diffusion phenomenon

We now step up in complexity and allow the solvent to have a nonzero velocity field $\mathbf{v}$, thus moving from pure diffusion to convection-diffusion. Let us first follow the Reynolds number analysis of Section 1.5, and determine the dimensionless number characterizing the convection-diffusion equation (3.17). Using the same dimensionless co-ordinates and velocity as in Eq. (1.38a), we find in analogy with Eq. (1.40) that Eq. (3.17) becomes

$$P\acute{e}\Big[\tilde{\partial}_t \tilde{c} + \big(\tilde{\mathbf{v}}\cdot\tilde{\boldsymbol{\nabla}}\big)\tilde{c}\Big] = \tilde{\boldsymbol{\nabla}}^2 \tilde{c}, \tag{3.35}$$

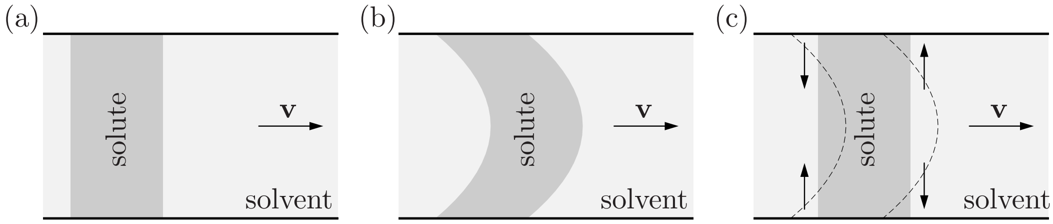

Figure 3.3: A sketch of the Taylor dispersion problem in a cylindrical microchannel of radius a with a steady Poiseuille flow (horizontal arrow $\mathbf{v}$). (a) The initial flat concentration (dark gray) of the solute. (b) Neglecting diffusion the solute gets stretched out into a paraboloid-shaped plug. (c) Including diffusion, indicated by the vertical arrows, the deformed concentration profile gets evened out.

where the so-called Péclet number $P\acute{e}$ appears. It is given by

$$P\acute{e} = \frac{V_0 L_0}{D} = \frac{\text{convection speed}}{\text{diffusion speed}}. \tag{3.36}$$

The convection speed is the chosen velocity scale V_0, while the diffusion speed is defined as diffusion length divided by diffusion time, or $v_\text{diff} = \sqrt{DT_0}/T_0 = L_0/(L_0^2/D) = D/L_0$.

For high Péclet numbers, where $V_0 \gg v_\text{diff}$ and convection thus happens much faster than diffusion, the terms on the left-hand side of the convection-diffusion equation dominate, and we are in the convection-dominated regime. Conversely, for low Péclet numbers, where $V_0 \ll v_\text{diff}$ and diffusion happens much faster than convection, the terms on the right-hand side dominate, and we are in the diffusion dominated regime.

In the Taylor dispersion problem, sketched in Fig. 3.3 we consider a homogeneous band of solute placed in the microchannel at $t = 0$ and study how this concentration profile disperses due to convection from the Poiseuille flow and due to diffusion from the concentration gradients. If diffusion did not play any role the band of solute would become stretched into an increasingly longer paraboloid-shaped band due to the Poiseuille flow. However, diffusion is present and it counteracts the stretching: in the front end of the concentration profile diffusion brings solute particles from the high concentration near the center out towards the low concentration sides, whereas in the back end it brings solute particles from the high-concentration sides towards the low concentration near the center. As we shall see, the result is a quite evenly shaped plug moving downstream with a speed equal to the average Poiseuille flow velocity V_0.

We can get a good insight into the nature of Taylor dispersion by the following heuristic argument. We are interested in estimating the effective diffusion constant D_eff for diffusion along the x axis of a long, narrow cylinder of radius a. For a given time interval t there is the ever present Brownian diffusion, which yields a contribution Dt to the square of the diffusion length along the x axis. However, due to the convection flow there is one more contribution.

For simplicity imagine the liquid of the cylinder parted into three concentric cylinder shells each of thickness $a/3$, the middle of which moves with the average flow velocity

V_0. Let us now fix the time interval t so that it correspond to the time it takes to diffusive radially the distance $a/3$, i.e. $t \equiv a^2/(9D)$. We note that this radial diffusion is transformed into an axial motion by the flow, because a random jump form one liquid shell to its neighbor will result in an axial displacement of $\pm(V_0/2)\,t$ as the liquid shells move relative to each other approximately with the speed $V_0/2$.

The square of the axial diffusion length can therefore be written as the sum of the two above-mentioned contributions,

$$\ell_\text{diff}^2 \approx \left[\sqrt{Dt}\right]^2 + \left[\frac{V_0 t}{2}\right]^2 = \left[D + \frac{V_0^2\,t}{4}\right]t = \left[D + \frac{V_0^2\,a^2}{36D}\right]t. \tag{3.37}$$

Using the standard diffusion relation $\ell^2 = Dt$, Eq. (3.37) leads to the prediction of an effective axial diffusion constant D_eff. In more an accurate calculation [Aris 1954] the number 36 is replaced by 48, and the final result for the effective diffusion constant or Taylor diffusivity is

$$D_\text{eff} \approx D + \frac{V_0^2\,a^2}{48D} = \left[1 + \frac{P\acute{e}^{\,2}}{48}\right]D. \tag{3.38}$$

3.6 The Einstein diffusivity of particles

There exist a remarkably simple expression for the diffusivity D of a spherical particle. To derive this so-called Einstein diffusivity we consider a sphere of radius a moving with velocity $\mathbf{v}$ through a liquid of viscosity η experiences the Stokes drag force $\mathbf{F}_\text{drag}$ given by

$$\mathbf{F}_\text{drag} = -6\pi\eta a\mathbf{u}. \tag{3.39}$$

Consider a position-dependent solution of density $c(\mathbf{r})$ of spherical molecules. Due to gradients in the density these molecules will diffuse with a velocity $\mathbf{u}$ according to Fick's law, $\mathbf{J} = c\mathbf{u} = -D\,\boldsymbol{\nabla} c$. Since the chemical potential μ by definition is the free energy of the last added molecule, the force $\mathbf{F}_\text{diff}$ driving the diffusion is given by minus the gradient of μ,

$$\mathbf{F}_\text{diff} = -\boldsymbol{\nabla}\mu = -\frac{k_\text{B}T}{c}\,\boldsymbol{\nabla} c, \tag{3.40}$$

where we have used the ideal-gas expression $\mu(T,\rho) = \mu_0 + k_\text{B}T\ln(c/c_0)$ valid for low concentrations. The concentration-dependent term is due to entropy.

In steady state the forces from diffusion and drag balance each other, $\mathbf{F}_\text{diff} = \mathbf{F}_\text{drag}$. Writing the latter force as

$$\mathbf{F}_\text{drag} = 6\pi\eta a\,\mathbf{u} = \frac{6\pi\eta a}{c}\,\mathbf{J} = -\frac{6\pi\eta a}{c}\,D\boldsymbol{\nabla} c, \tag{3.41}$$

the Einstein diffusivity follows from Eqs. (3.40) and (3.41),

$$D = \frac{k_\text{B}T}{6\pi\eta a}. \tag{3.42}$$

Here, k_B is Boltzmann's constant, and it is useful to note that at room temperature $k_\mathrm{B}T = 4.14 \times 10^{-21}$ J. For a microbead with $a = 0.5$ µm frequently used in microfluidics and for an ion-sized bead with $a = 0.1$ nm diffusing in water at 300 K, we find from Eq. (3.42)

$$D_\mathrm{bead}(0.5\ \mu\mathrm{m}, 300\ \mathrm{K}) = 4.4 \times 10^{-13}\ \mathrm{m}^2\,\mathrm{s}^{-1}, \tag{3.43a}$$

$$D_\mathrm{bead}(0.1\ \mathrm{nm}, 300\ \mathrm{K}) = 2.2 \times 10^{-9}\ \mathrm{m}^2\,\mathrm{s}^{-1}. \tag{3.43b}$$

Note the good agreement between the prediction Eq. (3.43b) and the table value Eq. (3.21a).

As in the force balance argument above, we often utilize that the inertia of a microparticle moving in a viscous liquid is negligible. To verify this assumption we end this chapter by calculating the transient time for a sphere of radius a and mass $(4\pi/3)a^3\rho_\mathrm{sph}$ moving under the influence of an external force. Initially, both the sphere and the fluid are at complete rest. Suddenly, at time $t = 0$ a constant external force $F_\mathrm{ext}\,\mathbf{e}_x$ begins to act on the sphere. As the force is constant all motion in the following takes place along the direction given by $\mathbf{e}_x$, and the resulting velocity of the sphere is denoted $\mathbf{u}(t) = u(t)\,\mathbf{e}_x$. The equation of motion for the sphere becomes

$$\tfrac{4}{3}\pi a^3 \rho_\mathrm{sph} \partial_t u = -6\pi\eta a\, u + F_\mathrm{ext}. \tag{3.44}$$

The solution to this standard differential equation is

$$u(t) = \frac{F_\mathrm{ext}}{6\pi\eta a} - u_0\, \exp\Big(-\frac{9\eta}{2\rho_\mathrm{sph}a^2}\, t\Big), \tag{3.45}$$

where u_0 is an integration constant to be specified by the boundary conditions. If the sphere is at rest for $t = 0$ then

$$u(t) = \frac{F_\mathrm{ext}}{6\pi\eta a}\left[1 - \exp\Big(-\frac{9\eta}{2\rho_\mathrm{sph}a^2}\, t\Big)\right]. \tag{3.46}$$

The characteristic time scale τ_acc appearing in the exponential is very small for a microspheres. For a cell with $a \approx 5$ µm and a density nearly equal to that of water, we find

$$\tau_\mathrm{acc} = \frac{2\rho_\mathrm{sph}a^2}{9\eta} \approx 5\ \mu\mathrm{s}. \tag{3.47}$$

Thus, in a viscous environment inertial forces are indeed negligible, and for the case of the microsphere it is reasonable to assume that it is always moving in local steady state.

References

Adams, J. D., Thévoz, P., Bruus, H., and Soh, H. T. (2009). Integrated acoustic and magnetic separation in microfluidic channels. *Appl. Phys. Lett.* **95** 254101 1-3.

Andersen, M. J., Nysteen, A, Settnes, M. (2009).
Forces acting on microparticles in acoustofluidic systems.
DTU bachelor thesis, http://www.nanotech.ctu.dk/microfluidics

Aris, R. (1956). On the dispersion of a solute in a fluid flowing through a tube.
Roy. Soc. **A235**, 67–77.

Barnkob, R. (2009). Acoustofluidics in microsystems: investigation of resonances.
DTU master thesis, http://www.nanotech.ctu.dk/microfluidics

Barnkob B. and Bruus H. (2009b), Acoustofluidics: theory and simulation of radiation forces at ultrasound resonances in microfluidic devices. *Procs. Meetings on Acoustics* **6**, 020001. 157th Meeting Acoust. Soc. Am. 2009, (doi:10.1121/1.3186746).

Barnkob, R. Augustsson P. Laurell T., and Bruus H. (2010). Measuring the local pressure amplitude in microchannel acoustophoresis. *Lab Chip* **10**, 563–570.

Brown D. (2009). Tracker 2.60, Free video analysis and modeling tool for physics education. *Online open source*: http://www.cabrillo.edu/dbrown/tracker/

Batchelor, G. K. (2000). *An introduction to fluid dynamics.*
Cambridge University Press, Cambridge.

Berthier, J. and Silberzan, P. (2006). *Microfluidics for biotechnology.*
Artech House, Boston.

Bruus, H. (2008). *Theoretical microfluidics*
Oxford University Press, Oxford.

Gorkov, L. P. (1962). On the forces acting on a small particle in an acoustic field in an ideal fluid. *Sov. Phys. Doklady*, **6**, 773–776.

Grenvall, C., Augustsson, P., Folkenberg, J. R., and Laurell, T. (2009).
Harmonic Microchip acoustophoresis: a route to online raw milk sample precondition in protein and lipid content quality control. *Anal. Chem.* **81**, 6195.

Hagsäter, S. M., Glasdam Jensen, T., Bruus, H. and Kutter, J. P. (2007).
Acoustic resonancesin microfluidic chips: full-image micro-PIV experiments and numerical simulations. *Lab Chip*, **7**, 1336–1344.

Hagsäter, S. M. (2008). Development of micro-PIV techniques for applications in microfluidic systems. DTU PhD thesis, http://www.nanotech.ctu.dk/microfluidics

Hultström, J., Manneberg, O., Dopf, K., Hertz H. M., Brismar, H., and Wiklund, M. (2007). Proliferation and viability of adherent cells manipulated by standing-

wave ultrasound in a microfluidic chip. *Ultrasound Med. & Biol.*, **33**, 145–151.
King, L. V. (1934). On the acoustic radiation pressure on spheres. *Proc. R. Soc. (London)* **A147**, 212–240.
Landau, L. D. and Lifshitz, E. M. (1982). *Statistical physics part 1, 3rd edn.* Course of theoretical physics vol. 5. Pergamon Press, Oxford.
Landau, L. D. and Lifshitz, E. M. (1986). *Theory of elasticity, 3rd edn.* Course of theoretical physics vol. 7. Pergamon Press, Oxford.
Landau, L. D. and Lifshitz, E. M. (1993). *Fluid mechanics, 2nd edn.* Course of theoretical physics vol. 6. Pergamon Press, Oxford.
Laurell, T., Petersson, F., and Nilsson A. (2007). Chip integrated strategies for acoustic separation and manipulation of cells and particles. *Chem. Soc. Rev.* **36**, 492–506.
Lenshof, A., Ahmad-Tajudin, A., Järås, K., Swärd-Nilsson, A.-M., Åberg, L., Marko-Varga, G., Malm, J., Lilja, H., and Laurell, T. (2009). Acoustic whole blood plasmapheresis chip for prostate specific antigen microarray diagnostics. *Anal.Chem.***81**,6030.
Lighthill, J. (2003). *Waves in fluids.* Cambridge University Press, Cambridge.
Manneberg, O., Vanherberghen, B., Önfeltab, B., and Wiklund, M. Flow-free transport of cells in microchannels by frequency-modulated ultrasound. *Lab Chip* **9**, 833.
Nilsson, J., Evander, M., Hammarström, B., and Laurell, T. (2009). Cell and particle trapping in microfluidic systems. *Anal. Chim. Acta* **649**, 141–157.
Norris, J. V., Evander, M., Horsman-Hall, K. M., Nilsson, J., Laurell, T., and Landers, J. P. (2009). Acoustic differential extraction for forensic analysis of sexual assault Evidence. *Anal. Chem.* **81**, 6089.
Petersson, F., Nilsson, A., Holm, C., Jönsson, H. and Laurell, T. (2005). Continuous separation of lipid particles from erythrocytes by means of laminar flow and acoustic standing wave forces. *Lab Chip* **5**, 20–22.
Tabeling, P. (2005). *Introduction to microfluidics.* Oxford University Press, Oxford.
Svennebring, J., Manneberg, O., Skafte-Pedersen, P., Bruus, H., and Wiklund, M. (2009). Selective bioparticle retention and characterization in a chip-integrated confocal ultrasonic cavity.*Biotech Bioeng* **103**, 323–328.
Thévoz, P., Adams, J. D., Shea, H., Bruus, H., and Soh, H. T. (2010). Acoustophoretic Synchronization of Mammalian Cells in Microchannels. *Anal. Chem.* **82**, 3094.
Vedel, S. (2009). Millisecond dynamics in microfluidics: Equivalent circuit theory and experiment. DTU master thesis, http://www.nanotech.ctu.dk/microfluidics
Vedel, S., Olesen, L. H., and Bruus, H. (2010). Pulsatile microfluidics as an analytical tool for determining the dynamic characteristics of microfluidic systems *J. Micromech. Microeng.*, **20**, 035026 1–11.
Wiklund, M., Spégel, P., Nilsson, S., and Hertz, H. M. (2003). Ultrasonic-trap-enhanced selectivity in capillary electrophoresis. *Ultrasonics*, **41**, 329–333.
Yosioka, K. and Kawasima, Y. (1955). Acoustic radiation pressure on a compressible sphere. *Acoustica* **5**, 167–173.

M4 Fundamental Electroacoustics

Electromechanical Systems & Transducers.

Martyn Hill. Tuesday 0945.

More detailed treatments of the principles of electroacoustics can be found in Hunt [1], Hueter and Bolt [2], Stansfield [3], and Kinsler and Frey [4] chapter 14.

Network representations of transducers and impedance

Electromechanical transducers have, by definition, both electrical and mechanical components. Their behaviour has traditionally been described by models that use electromechanical analogies (typically that apportion equivalent electrical characteristics to the mechanical component).

We shall consider the behaviour of thickness-mode piezoelectric transducers using a simple lumped element equivalent circuit, a two-port circuit model and a three port model. The detailed behaviour of the piezoelectric material itself will be covered in the following lecture.

Equivalent circuit model

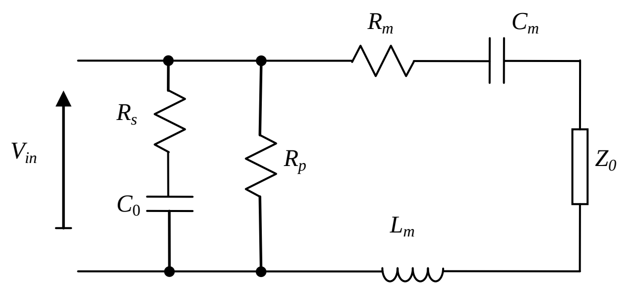

Figure 1. Equivalent circuit model for a thickness-mode piezoelectric transducer

Figure 1 shows an equivalent circuit model for a thickness mode piezoceramic transducer operating near its first thickness resonant frequency. The transducer is driven by voltage V_{in} and at low frequencies the response is dominated by its clamped capacitance C_0, the capacitance of the disk when its dimensions are not modified by electromechanical coupling. The other purely electrical parameters are R_s and R_p. These represent electrical losses within the transducer: R_p due to leakage current and R_s due to higher frequency dielectric resistive losses. Parameters C_m, L_m, and R_m denote the electro-mechanical equivalences of capacitance, inductance and resistance respectively, and C_m and L_m can be determined through calculating the mechanical parameters of the transducer using the method described by Stansfield [3] and Hueter and Bolt [2]. The mechanical resistance R_m, along with other damping values within the system, are often estimated experimentally. The impedance Z_0 denotes the electro-mechanical equivalent impedance that the transducer is driving. If the transducer is operating in a vacuum, or a very low acoustic impedance this will appear as an electrical short circuit.

It is important to note that in such a model:

- does not take account of dynamic behaviour in the out-of-thickness directions. For a plate or disk in which the thickness is much less than the lateral dimensions a series of resonances at frequencies much lower than the mode of interest will exist in reality but will not be predicted by the model
- is only applicable at frequencies up to and a little above the first thickness mode. This is due to the need to make simplifying assumptions about the motion of the piezoceramic in order to reduce its dynamic response to straightforward electrical equivalences

In the most common electro-mechanical analogy the mechanical capacitance, C_m, represents the compliance (inverse of stiffness) of the piezoceramic and the mechanical inductance, L_m, represents the mass of the transducer.

An important use of equivalent circuit models is to estimate its electrical input characteristics. Electrical impedance and admittance are amongst the easiest parameters to measure either of an isolated transducer of a transducer that is coupled to a device of interest.

Electrical impedance

The impedance of an electrical circuit is defined as the ratio of the complex voltage to the complex current:

$$Z = \frac{V}{I} = R + jX \tag{1}$$

where the real part of the impedance, R , is the resistance and the imaginary part, X , is the reactance. The reactive elements of the equivalent circuit shown in Figure 1 are the inductor and the capacitors (plus any reactive component of the load impedance, Z_0) and it is from these reactive elements that the frequency dependence of the impedance comes, with the impedance of a capacitor being:

$$Z = \frac{1}{j\omega C} \tag{2}$$

and that of an inductor being

$$Z = j\omega L \tag{3}$$

It is clear that the input impedance into the circuit of Figure 1 will change as Z_0 changes, just as the measured impedance of a transducer will change depending on the loading of the transducer. Hence two special input impedance conditions are typically defined for an acoustic transducer:

- the blocked impedance, when the transducer is constrained from moving – equivalent to $Z_0 = \infty$, an open circuit, in Figure 1
- the free impedance, when the transducer is free to move without constraint - equivalent to $Z_0 = 0$, an open circuit, in Figure 1

Figure 2 shows a plot of the impedance of the circuit driving into air (approximating the free impedance) using parameter values that are representative of a 1 MHz transducer.

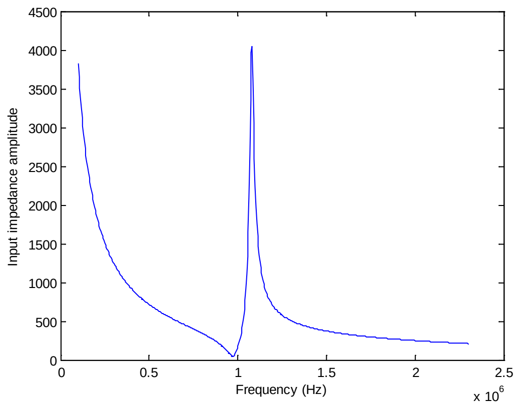

Figure 2. Magnitude of the free impedance of the circuit in Figure 1

Away from the resonance the behaviour is dominated by the electrical terms C_0, R_s and R_p. However near the resonance the mechanical parameters become dominant. An impedance minimum can be seen just below 1 MHz and an impedance maximum at about 1.1 MHz. These features can be seen more clearly on the logarithmic plot of Figure 3 which also shows the phase of the impedance.

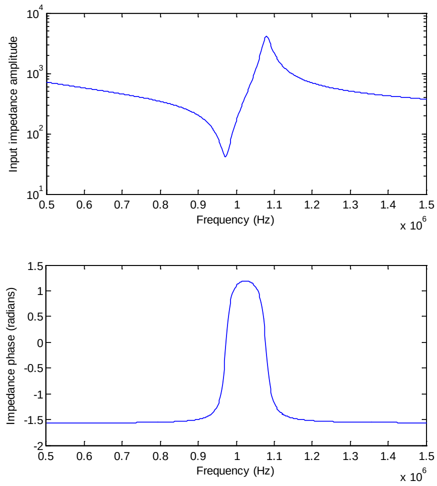

Figure 3. Phase and magnitude of circuit within vicinity of resonance.

The impedance minimum lies very close to the frequency at which the phase rises through zero (and the reactance passes through zero). This is known as the series resonance of the transducer, or simply the resonance frequency. The impedance maximum lies close to the frequency at which the phase falls back through zero (and the reactance again passes through zero). This is known as the parallel resonance frequency (or in some texts the anti-resonance). Transducers typically output their maximum between these two frequencies (when the impedance is predominantly inductive).

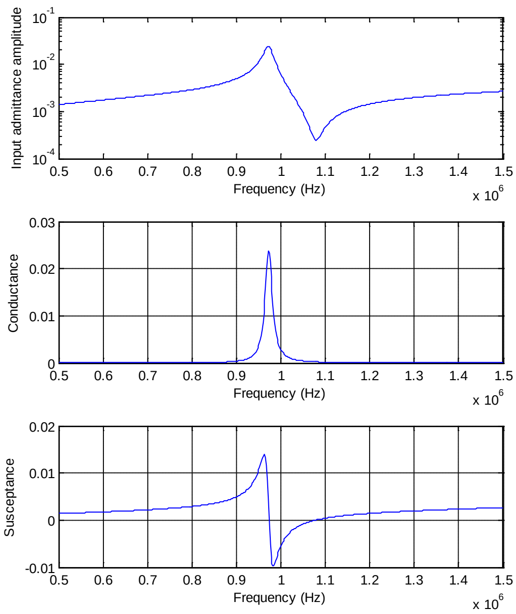

Figure 4. The magnitude of the admittance, along with the susceptance and conductance of the transducer.

Transducer designers often work with the inverse of impedance, the electrical admittance (Y):

$$Y = \frac{1}{Z} = G + jB \tag{4}$$

where G is known as the conductance and B as the susceptance. These are related to the resistance and reactance as follows:

$$
\begin{aligned}
G &= \frac{R}{R^2 + X^2} \\
B &= -\frac{X}{R^2 + X^2}
\end{aligned}
\tag{5}
$$

Figure 4 shows the magnitude of the admittance along with the conductance and susceptance for the transducer under consideration. It will be noted that the series resonance coincides with an admittance maximum and the parallel resonance with an admittance minimum.

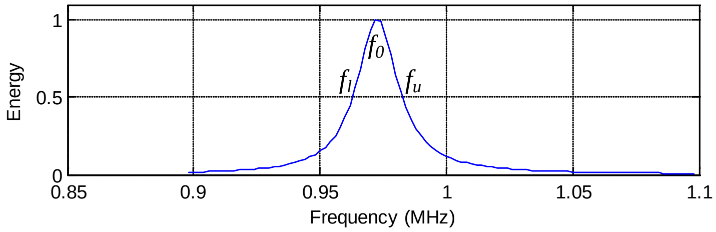

Figure 5. Change in normalised energy within a resonator through a resonance.

The Q-factor, or quality factor, is used as a measure of the sharpness of a resonant system. It is a measure of the ratio of the energy stored in a resonator to the energy dissipated each cycle. In the example system of Figure 5 the frequency corresponding to maximum energy is f_0, and frequencies f_l and f_u are the lower and upper frequencies respectively at which the energy curve passes through half of its maximum energy. The difference between these half power frequencies $(f_u - f_l)$ is defined as the bandwidth of the system and the Q factor can be calculated from:

$$
Q = \frac{f_0}{f_u - f_l} \tag{6}
$$

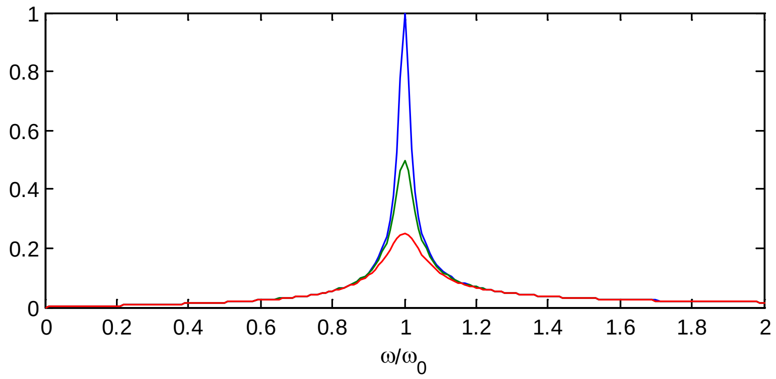

Figure 6. Typical shapes of resonant responses for Q factors of 10 (lowest peak), 20 and 40.

The mechanical Q factor of a transducer can similarly be calculated from the conductance plot around resonance. Figure 6 shows typical resonant responses for Q factors of 10, 20 and 40, where 40 is the higher, sharper peak. It can be seen that as the Q factor increases the peak becomes higher but the bandwidth reduces. Alternatively the Q factor can be estimated by plotting the admittance against the conductance and extracting the values as shown in Figure 7.

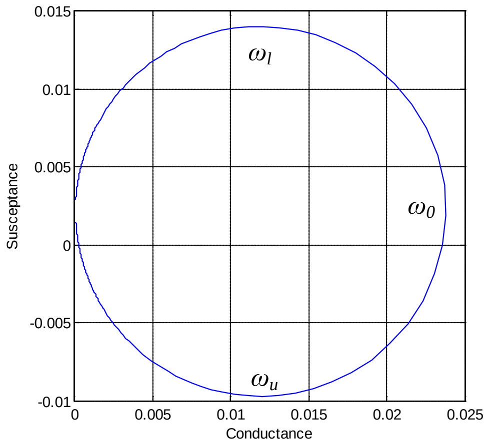

Figure 7. Susceptance vs conductance for circuit simulated in Figure 2

Two port and three port transducer representations

The equivalent circuit of Figure 1 takes the mechanical properties of the transducer and treats them as equivalent electrical components through which a current flows due to an applied voltage. This can be represented in a slightly different way by separating the mechanical and electrical circuits using a two-port representation. In this approach the electrical elements of the system are represented by a current and voltage input which is transformed into force and velocity for a mechanical output.

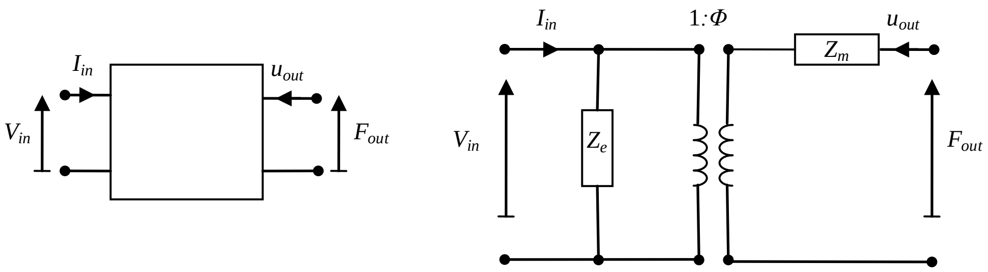

Figure 8. Two port model for a transducer

This approach is represented diagrammatically in Figure 8. In the two port circuit diagram on the right the impedance Z_e represents the blocked electrical input impedance and the impedance Z_m is the mechanical impedance of the transducer. The transformation of electrical parameters into mechanical parameters is via a transformer with turns ratio Φ. The turns ratio of this transformer, unlike a real transformer, has dimensions.

The two-port modelling approach requires assumptions to be made about the transducer backing (e.g. air backing, or symmetrical loading on each face) as it assumes an electrical input and a single mechanical output. However a piezoelectric transducer has two faces and will typically be driving different mechanical impedances on each, so is more correctly considered to be a three port device with one electrical port and two mechanical ports.

The Mason model shown in Figure 9 has two mechanical ports so that different impedances can be included on each face of the transducer. Further, the lumped element model of the ceramic itself has been replaced with impedances which are the products of the mechanical impedance of the ceramic (Z_c) and trigonometric functions of the wavenumber and thickness of the ceramic (k_c and t_c respectively). This allows the model to represent thickness modes other than the fundamental.

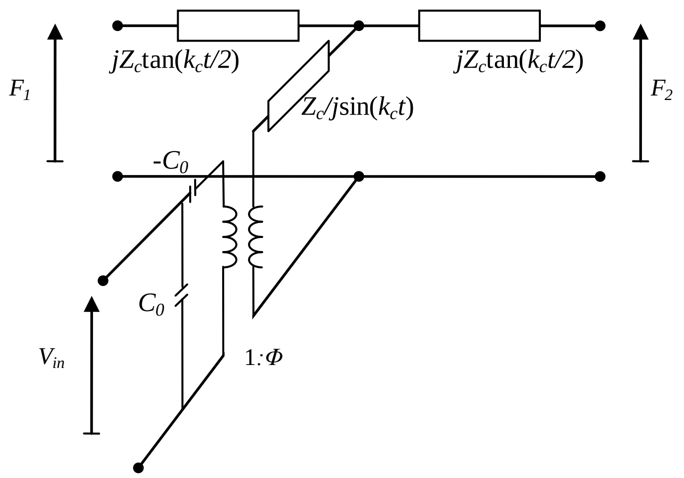

Figure 9. Mason three port model for a transducer

The Mason model includes a physically unrealistic negative capacitance, and this is one reason why a number of alternative models have been proposed, including the KLM representation [5, 6].

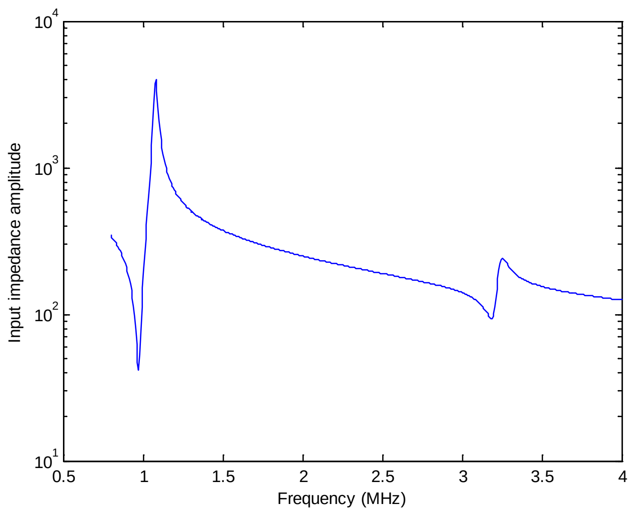

Figure 10. KLM model of the transducer modelled in Figure 2 showing the mode at about 3 MHz

A KLM representation has been used to model the impedance plot of Figure 2 but extended to 4 MHz. A second thickness resonance can be seen at a frequency a little above 3 MHz. A resonance is visible when the thickness equals a half wavelength and three half wavelengths, but no resonance is visible when the frequency is equal to a wavelength. This is typical of the behaviour of piezoelectric transducers in thickness mode. A solid plate excited by an external source will exhibit mechanical resonances at both odd and even multiples of a half wavelength. However the piezoelectric excitation mechanism relies on bulk expansion and contraction of the plate. This can couple into the mechanical resonance when opposite faces are moving out of phase, as in odd half wavelength modes. In even half wavelength modes the opposite faces move in phase and the piezoelectrically induced expansion is not able to couple into this motion.

[1] F. V. Hunt, *et al.*, *Electroacoustics : the analysis of transduction, and its historical background*, 2nd ed. Woodbury, N.Y.: American Institute of Physics for the Acoustical Society of America, 1982.

[2] T. Hueter and R. Bolt, *Sonics techniques for the use of sound and ultrasound in engineering and science*. New York: Wiley, 1955.
[3] Stansfield, *Underwater electroacoustic transducers a handbook for users and designers*. Bath: Bath University, 1990.
[4] L. E. Kinsler*, et al.*, *Fundamentals of acoustics*, 4th ed. New York: Wiley, 2000.
[5] R. Krimholtz*, et al.*, "Erratum: New equivalent circuits for elementary piezoelectric transducers," *Electronics Letters,* vol. 6, p. 560, 1970.
[6] R. Krimholz*, et al.*, "New Equivalent Circuit for Elementary piezoelectric transducers," *Electronics Letters,* vol. 6, pp. 398-399, 1970.

Piezoelectricity and Application to the Excitation of Acoustic Fields for Ultrasonic Particle Manipulation

J. Dual, ETHZ Switzerland

1. Introduction

Exciting and detecting motion in solids by means of piezoelectric materials, in which an electric signal is converted into a mechanical motion and vice versa, has several **advantages**:

- With the availability of programmable signal generators, *waves of arbitrary shape* and *frequency content* can be produced with a high degree of repeatability. Therefore, compared to excitation by mechanical impact, a *large number* of *identical* transient experiments can be performed in a *short period of time*, opening up the possibility of averaging and other signal processing techniques.

- By appropriate tailoring of the transducer set-up, different modes of waves and vibrations can be excited and measured very selectively.

- The low coupling of the electrical circuit with the mechanical motion at frequencies far below the resonance frequencies of the piezoelectric transducer allows very precise phase measurements and stabilization of resonance frequencies.

However, a necessary condition to make use of the above - mentioned advantages, is the availability of materials with sufficiently high piezoelectric constants. This is the case in piezoelectric ceramics. While quartz has a piezoelectric charge constant of about 10^{-12} C/N, the same constant for PXE 41, which is a modified lead zirconate titanate manufactured by Philips, amounts to 10^{-10} C/N. The interaction between the piezoelectric transducer and the attached material will be described in the following. Basics regarding this field can be found e.g. in [1].

A typical transducer as used in ultrasonics is shown below. It is brought in contact with the structure to be excited using a coupling agent or glue. Ultrasonic transducers work in a resonant mode, i.e. they have a precisely defined frequency, where they work best. Other transducers are used far below their resonance frequency.

Piezoelectric materials have an intrinsic polarization. Depending on the direction of the applied field, which is controlled by the electrodes, extension/contraction occurs (for E parallel to P) or shear (for E orthogonal to P)

When used in a continuous mode, one has to be careful not to heat up the transducer too much. This is particularly true for ceramic transducers, as they loose polarization when heated above their Curie temperature.

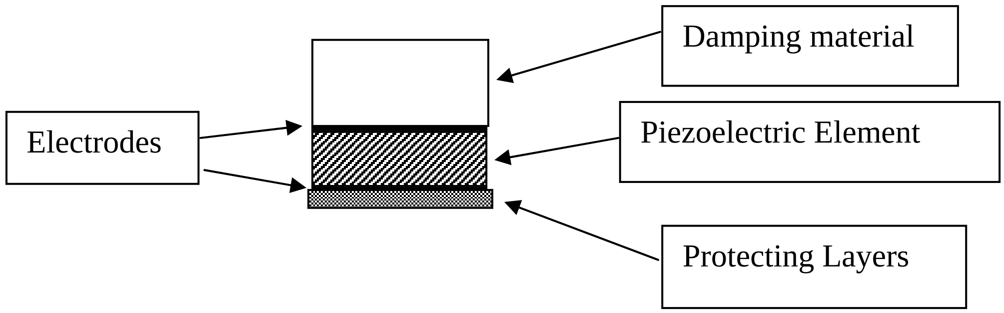

2. Basic Equations

Constitutive relations for piezoelectric materials relate the four quantities (given together with their SI units)

E_i	electric field	1st order tensor	(N / C)
D_i	electric displacement	1st order tensor	(C / m^2)
γ_{ij}	strains	2nd order tensor	(-)
σ_{ij}	mechanical stress	2nd order tensor	(N / m^2)

by the material properties

s_{Eijkl}	mechanical compliance for constant electric field	4th order tensor	(m^2 / N)
d_{ijk}	piezoelectric charge constant	3rd order tensor	(C / N) od. (m / V)
$\varepsilon_{ij} = \varepsilon_{ij\sigma}$	permittivity at constant mechanical stress	2nd order tensor	(C^2 / m^2N)

The *electric displacement* is defined as

$$D_i = \varepsilon_0 E_i + P_i$$

where P is the polarization vector, expressing the fact, that the electron cloud shifts with respect to the nucleus under the influence of an external electric field or an applied stress. Constitutive equations for a piezoelectric material can then be given in the form

$$\gamma_\lambda = s_{E\lambda\mu}\sigma_\mu + d_{k\lambda}E_k$$
$$D_i = d_{i\mu}\sigma_\mu + \varepsilon_{ik}E_k \qquad (1)$$

where the components are referred to an orthogonal system of coordinates and Einstein_s summation convention for repeated indices is invoked. Latin and Greek indices take values from 1 .. 3 and 1 .. 6 , respectively, and the correspondence between Greek matrix indices and Latin tensor indices is given by

ij	11	22	33	23 , 32	13 , 31	12 , 21
λ	1	2	3	4	5	6

For simplicity a uniaxial state will be assumed for both electrical and mechanical quantities in the following. All coupling effects with other components of stress, strain, electric displacement and electric field will be neglected and also indices will be dropped for simplicity of writing. For more complicated situations, a finite element analysis has to be made.

Eqs. 1 can be rewritten with σ and D as independent quantities:

$$\gamma = s_D\,\sigma + g\,D$$
$$E = -\,g\,\sigma + \frac{D}{\varepsilon} \qquad (2)$$

where

$g = \dfrac{d}{\varepsilon}$ piezoelectric voltage constant

$s_D = s_E - \dfrac{d^2}{\varepsilon}$ mechanical compliance for constant electric displacement

It should be noted, that piezoelectric ceramics have an axis of symmetry, which is parallel to the direction of poling. The material is transversely isotropic. It is customary to take the 3 - direction as the axis of symmetry.

The permittivity tensor is diagonal with $\varepsilon_{11} = \varepsilon_{22}$. The tensor containing the charge constants is zero except for the elements d_{33} , $d_{31} = d_{32}$ and $d_{15} = d_{24}$.

Typical values for the material constants in extension and shear for PXE 41 are summarized in the following table.

In addition the equation of mechanical equilibrium (for the case of harmonic loading)

$$\sigma_{ij,j} + \rho\,\omega^2\,\xi_i = 0 \qquad (3)$$

Table : Material Constants for PXE 41 Piezoelectric Ceramic Material

Property	Units	Extension in the Poling Direction	Shear in Plane Ortho - gonal to Poling Direction
Mech. Compliance s_E	(10^{-12} m^2/N)	s_{E33}= 14.6	s_{E55}= 32.0
Mech. Compliance s_D	(10^{-12} m^2/N)	s_{D33}= 7.85	s_{D55}= 20.8
Charge Constant d	(10^{-12} C/N)	d_{33}= 268.	$d_{15} = d_{24}$ = 335.
Permittivity ε	(10^{-8} C^2/m^2N)	ε33= 1.06	ε22= ε11= 1.00
Voltage Constant g	(10^{-3} m^2/C)	g_{33} = 25.2	$g_{15} = g_{24}$ = 33.5
Density ρ	(10^3 kg/m^3)	ρ = 7.9	

The mechanical strain is defined as

$$\gamma_{ij} = 1/2 (\xi_{i,j} + \xi_{j,i})$$

$$2 \gamma_{ij} = (1 + \delta_{ij}) \gamma_\lambda$$

and Maxwell_s first equation for dielectric materials

$$D_{i,i} = 0 \tag{4}$$

The right hand side is zero, because there are no free charges in a dielectric. In the uniaxial case one obtains for all cases considered

$$D = D_0 \qquad D_0 = \text{constant} \tag{5}$$

3. Free - Free Vibration of a Piezoelectric Element

First, the motion of a transducer with stress - free boundaries will be considered. Using the definition of mechanical strain , Eq. 2, 3 and 5 one obtains the differential equation and boundary conditions

$$\begin{aligned} &\xi_{,11} + k_D^2 \xi = 0 \\ &k_D^2 = s_D \rho \omega^2 \\ &\xi_{,1}(0) = g D_0 \\ &\xi_{,1}(L) = g D_0 \end{aligned} \tag{6}$$

which yield

$$\xi = \frac{gD_0}{k_D}(\sin k_D x + \frac{\cos k_D L - 1}{\sin k_D L}\cos k_D x) \qquad (7)$$

From Eqs. 2 and 5 the corresponding σ and E are computed

$$\sigma = \frac{gD_0}{s_D}(\cos k_D x - 1 - \frac{\cos k_D L - 1}{\sin k_D L} \sin k_D x)$$

$$E = -\frac{g^2 D_0}{s_D}(\cos k_D x - \frac{\cos k_D L - 1}{\sin k_D L} \sin k_D x) + D_0 \frac{s_E}{s_D \varepsilon}$$

The electric potential is defined as

$$V = -\int_0^L E dx = D_0 \left[\frac{2g^2}{k_D s_D}(\frac{1-\cos k_D L}{\sin k_D L}) - L\frac{s_E}{\varepsilon s_D} \right]$$

For a given applied voltage V_0 , the displacement is then

$$\xi(0) = V_0 \frac{s_D}{g} \frac{\cos k_D L - 1}{2(1-\cos k_D L) - (k_D L \sin k_D L)\frac{1}{k^2}} \qquad (8)$$

$$k^2 = \frac{gd}{s_E} \quad \text{coupling coefficient}$$

For $k_D L << 1$ Eqs. 7 to 8 can be simplified to yield for the quasistatic or " long wave-length " case:

$$D_0 = -\frac{\varepsilon V}{L} [1 + O((k_D L)^2)]$$

$$\xi = d V (\frac{1}{2} - \frac{x}{L}) [1 + O((k_D L)^2)]$$

$$\sigma = 0 + O((k_D L)^2) \qquad (9)$$

$$E = -\frac{V}{L} [1 + O((k_D L)^2)]$$

Piezoelectric Transducers Used to Excite Mechanical Vibrations

In the next step, a situation will be considered, in which a circular piezoelectric disk excites longitudinal motion in a circular rod.

The transfer function between excitation voltage and the resulting motion will be determined for the long wavelength case, i.e. the wavelength both in the transducer and in the rod is assumed to be much larger than the diameter of the rod and transducer. Again a uniaxial state will be assumed for all elements involved. If the excitation voltage has the form $V = \mathrm{Re}\,(V_0\, e^{i\omega\tau})$, also all other quantities will have the same time - dependence. To develop the equations the same procedure will be used as before. The only difference are the boundary conditions, which now are

$$\begin{aligned} \xi_{,1}(0) &= g\, D_0 \\ \xi_{,1}(L) &= s_D\, \sigma_0 + g\, D_0 \end{aligned} \qquad (10)$$

σ_0 is the stress between transducer and rod and can be expressed in terms of $\xi_0 = \xi\,(L)$ and the impedance Z_R of the rod.

$$\sigma_0 = i\,\omega\, Z_R\, \xi_0 \qquad (11)$$

Dependent on the type of motion, the impedance is

a) for a **wave propagation** problem in an infinite rod

$$\xi = \xi_0 \exp(i(\omega t - k_R x_R)) \qquad k_R = \frac{\omega}{c_R} \qquad c_R = \sqrt{\frac{E_R}{\rho_R}}$$

$$\sigma_0 = - i\, E_R\, k_R\, \xi_0 \qquad 2.34$$

$$Z_R = - \sqrt{E_R \rho_R} \qquad (12)$$

b) for a **vibration problem** in a rod of length L_R and stress - free boundary at $x_R = L_R$

$$\xi = \xi_0 \left(\cos k_R x_R + \tan k_R L_R \sin k_R x_R \right)$$

$$\sigma_0 = E k_R \xi_0 \tan k_R L_R$$

$$Z_R = -i \sqrt{E_R \rho_R} \tan k_R L_R \qquad (13)$$

One should note at this point that the impedance gets very small for the case of resonance, dependent on the amount of damping.
For a weakly viscoelastic material in sinusoidal loading

$$E_R = E_0\left(1+i\varphi\right) \qquad , \ \varphi \ll 1$$

$$k_R = k_0\left(1-i\,\varphi/2\right) \qquad , \ k_0 = \frac{\omega}{c_0} \qquad , \ c_0 = \sqrt{\frac{E_0}{\rho}}$$

In the case of resonance, where $\mathrm{Im}\left\{Z_R\right\} = 0$, and assuming $k_0 L_R \varphi \ll 1$

$$Z_R = -\sqrt{E_0 \rho_R}\ k_0 L_R\, \varphi/2 \tag{14}$$

From Eqs. 10, 11 and 2 and setting

$$V_0 = -\int_0^L E \cdot dx$$

one obtains

$$D_0 = \frac{V_0 k_D s_D}{g^2 \beta}$$

$$\beta = \sin k_D L + \alpha(\cos k_D L - 1) - k_D L\left(1 + \frac{s_D}{dg}\right)$$

$$\alpha = \frac{\cos k_D L - 1 - i\,\dfrac{Z_R}{Z}\sin k_D L}{\sin k_D L + i\,\dfrac{Z_R}{Z}\cos k_D L} \tag{15}$$

$$Z = \sqrt{\frac{\rho}{s_D}}$$

and

$$\xi = \frac{V_0 s_D}{g\beta}\left(\sin k_D x + \alpha \cos k_D x\right)$$

$$\sigma = \frac{V_0 k_D}{g\beta}\left(\cos k_D x - 1 - \alpha \sin k_D x\right)$$

$$E=-\frac{V_0 k_D}{\beta}\left\{\cos k_D x-\alpha\sin k_D x-\left(1+\frac{s_D}{dg}\right)\right\}$$

In the limit $k_D L \ll 1$, the above equations reduce to

$$D_0=-\frac{V_0\varepsilon}{L\psi}$$

$$\xi=-\frac{V_0 d}{\psi}\left(\frac{x}{L}-\gamma\right)$$

$$\sigma=\frac{V_0 d}{\psi}\rho\omega^2 L\left(\frac{x^2}{2L^2}-\gamma\frac{x}{L}\right) \tag{16}$$

$$E=-\frac{V_0}{\psi L}\left(1-\gamma\frac{dg}{s_D}k_D^2 Lx\right)$$

where $\gamma=\dfrac{\dfrac{k_D L}{2}+i\dfrac{Z_R}{Z}}{k_D L+i\dfrac{Z_R}{Z}}$

and $\psi=1-\gamma\dfrac{dg}{s_D}\dfrac{\left(k_D L\right)^2}{2}$

If the transducer is used to excite **waves**, Z_R and Z have the same order of magnitude. Eq. 16 can be simplified and the transfer function $G(\omega)$ can be calculated.

$$\psi=1$$

$$\gamma=1+\frac{i}{2}\frac{Z}{Z_R}k_D L-\frac{1}{2}\left(\frac{Z}{Z_R}k_D L\right)^2$$

and

$$G(\omega):=\frac{\xi(L)}{V_0}=\frac{d}{2}\frac{\omega\rho L}{\sqrt{E_R\rho_R}}\left(i+\frac{\omega\rho L}{\sqrt{E_R\rho_R}}\right) \tag{17}$$

This expression for the transfer function can also be obtained directly by considering a rigid mass (transducer), the center of which is displaced by an amount $\Delta L/2 = d\,V_0/2$ with respect to the interface with the rod. One obtains

$$G(\omega) = \frac{d}{2} \frac{\omega}{\omega + i\,\dfrac{Z_R}{\rho L}} \tag{18}$$

and with Eq. 12

$$G(\omega) = \frac{d}{2} \frac{\omega}{\omega + i\omega_C}$$

where $\omega_C = \dfrac{\sqrt{E_R \rho_R}}{\rho L}$

This result is equivalent to Eq. 17 for $\omega \ll \omega_C$ and represents a high-pass behaviour with ω_C as cut-off frequency.

Magnitude and phase of the transferfunction for a typical configuration of transducer and rod are given in Fig. 1 for the exact solution according to Eqs. 15 and the rigid mass approximation of Eq. 18. The magnitude is normalized to yield 1 in the high frequency limit of equation 18.
Up to a value of twice the cut-off frequency of 12.7 kHz Eq. 18 is an excellent approximation. For higher frequencies the effect of transducer resonance is noticeable as an increase of the displacement amplitude.

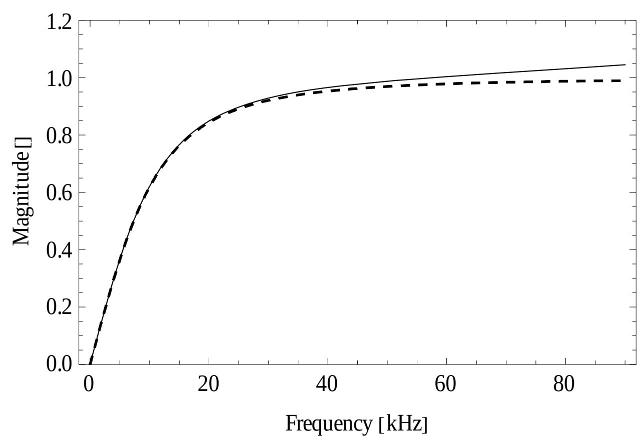

Figure 1: Normalized magnitude of the transfer function for the excitation of waves according to Eqs. 15(——) and 18(-----) for the low frequency range.
Transducer: PXE 41, L = 0.004 m
Rod: Lucite with $E_R = 5.29 \cdot 10^9\ \mathrm{N \cdot m^{-2}}$, $\rho_R = 1.2 \cdot 10^3\ \mathrm{kg \cdot m^{-3}}$

A frequency range up to the first transducer resonance frequency is shown in Fig. 2. Additional phase jumps occur and the amplitude gets very large for the resonance frequency of the crystal. These effects adversely effect wave propagation experiments, where it is desirable to have excitation which is constant over a wide frequency range. Digital filtering can be used to overcome the problem.

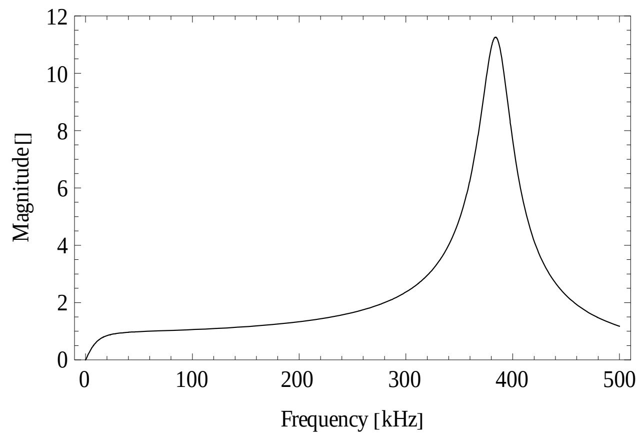

Figure 2: Normalized magnitude of the transfer function for the excitation of waves according to Eq. 15 up to the first transducer resonance.

Transducer: PXE 41, $L = 0.004$ m

Rod: Lucite with $E_R = 5.29 \cdot 10^9 \ \mathrm{N \cdot m^{-2}}$, $\rho_R = 1.2 \cdot 10^3 \ \mathrm{kg \cdot m^{-3}}$

The situation is different, if the transducer is used to excite **resonance vibrations**. In Eq. 14 it was shown that the impedance of the rod Z_R in the vicinity of resonance is proportional to the loss angle φ and can be quite small. If we impose the condition for resonance

$$\mathrm{Re}\left\{ \frac{\xi(L)}{V_0} \right\} = 0$$

assume that $\varphi \ll 1$ and use the expression from Eq. 13 for the impedance of the rod, a modified characteristic equation for resonance is obtained

$$\varepsilon k_0 L_R + \tan(k_0 L_R) = 0 \qquad (19)$$

with $\varepsilon = \dfrac{\text{mass of the transducer}}{\text{mass of the rod}}$

This corresponds to the characteristic equation for the resonance of a rod with an attached rigid mass. Using Eq. 16 and 19, it can be shown that

$$\gamma = 1 - i\frac{\rho L}{\rho_R L_R \varphi} = 1 - i\frac{\varepsilon}{\varphi}$$

at resonance. For low damping φ, γ becomes very large and mechanical quantities in the transducer are completely dominated by a rigid mass type behaviour: ξ is constant and the stress is linearly distributed.

Eqs. 16 can only be simplified further for sufficiently high damping. Because dg/s_D is of the order 1, one is allowed to set

$$\psi = 1 \quad \text{for} \quad \varphi \gg \varepsilon \left(k_D L\right)^2$$

For this case the mechanical motion does not influence the electrical circuit, i.e. the coupling is low. Again the rigid mass approximation of Eq. 18 yields the same result. On the other hand, if the damping is too small, very little energy pumped into the system will produce extremely large displacements, which in turn change the electric displacement. Then, no simplification of Eq. 16 is possible.
The transfer function for a transducer which excites resonant vibrations is shown in Fig. 3. It is completely dominated by the resonances in the rod and the amount of damping present.

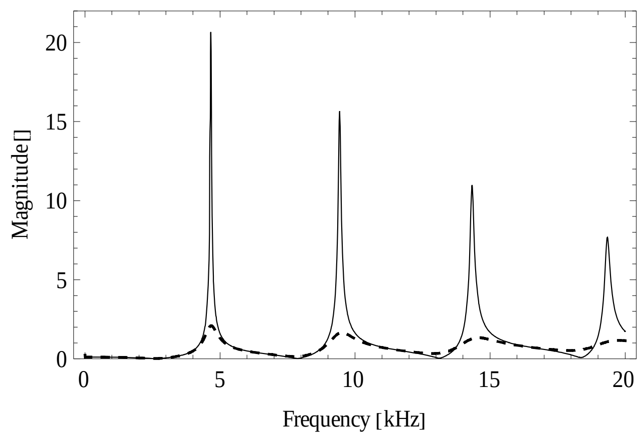

Figure 3: Normalized magnitude of the transfer function according to Eq. 15 for excitation of a resonant rod at low frequencies and various values of the damping φ: $\varphi = 0.01$ (——) and $\varphi = 0.1$ (-----)
Transducer: PXE 41, $L = 0.004$ m
Rod: Lucite with $E_R = 5.29 \cdot 10^9\ \mathrm{N \cdot m^{-2}}$, $\rho_R = 1.2 \cdot 10^3\ \mathrm{kg \cdot m^{-3}}$, $L_R = 0.2$ m

If we extend the frequency range and take a smaller rod length we obtain Fig. 4. At the low frequencies, the peaks of the rod are visible, then they diminish in magnitude because of damping and increase again because of the transducer resonance.

When characterizing devices for micromanipulation, very often impedance plots or admittance plots are determined for the transducer as shown in Fig. 5 and 6. It is seen, that the low frequency peaks almost disappear because of the low electromechanical coupling far away from the transducer resonance.

If we increase the damping ten times, all the system resonance peaks disappear and only the transducer resonance remains as seen in Fig. 7.

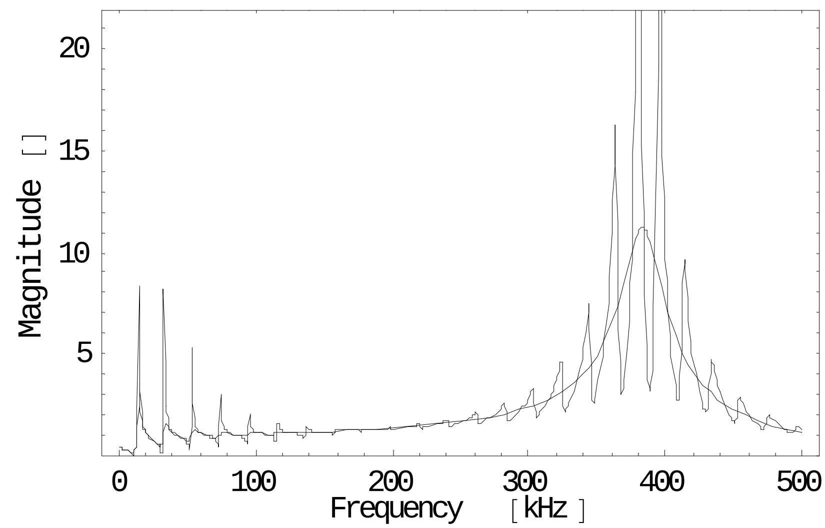

Figure 4: Normalized magnitude of the transfer function according to Eq. 15 for excitation of a resonant rod at higher frequencies and various values of the damping φ : $\varphi = 0.01$ (—–) and $\varphi = 0.1$ (-----)

Transducer: PXE 41, $L = 0.004$ m

Rod: Lucite with $E_R = 5.29 \cdot 10^9\ \mathrm{N \cdot m^{-2}}$, $\rho_R = 1.2 \cdot 10^3\ \mathrm{kg \cdot m^{-3}}$, $L_R = 0.05$ m

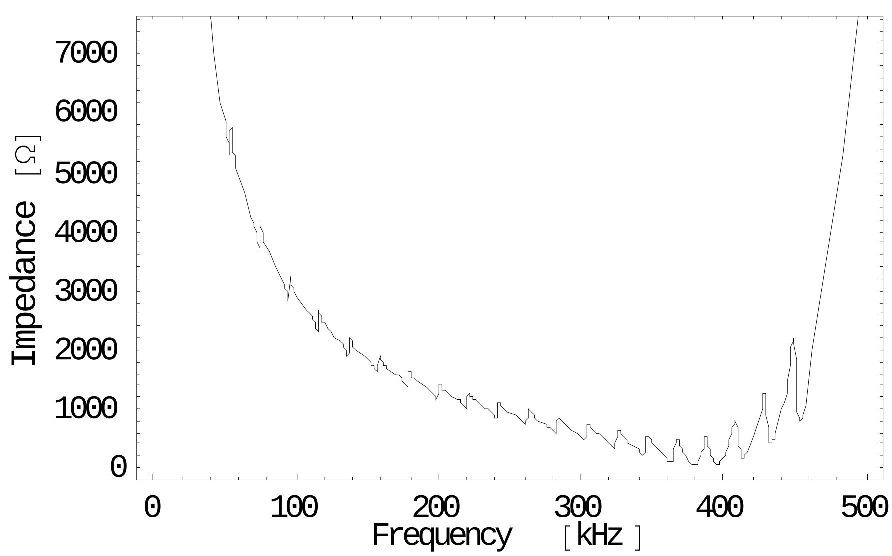

Figure 5: Impedance magnitude plot of the transducer according to Eq. 15 for excitation of a resonant rod at higher frequencies and damping $\varphi = 0.01$ (—–)

Transducer: PXE 41, $L = 0.004$ m

Rod: Lucite with $E_R = 5.29 \cdot 10^9\ \mathrm{N \cdot m^{-2}}$, $\rho_R = 1.2 \cdot 10^3\ \mathrm{kg \cdot m^{-3}}$, $L_R = 0.05$ m

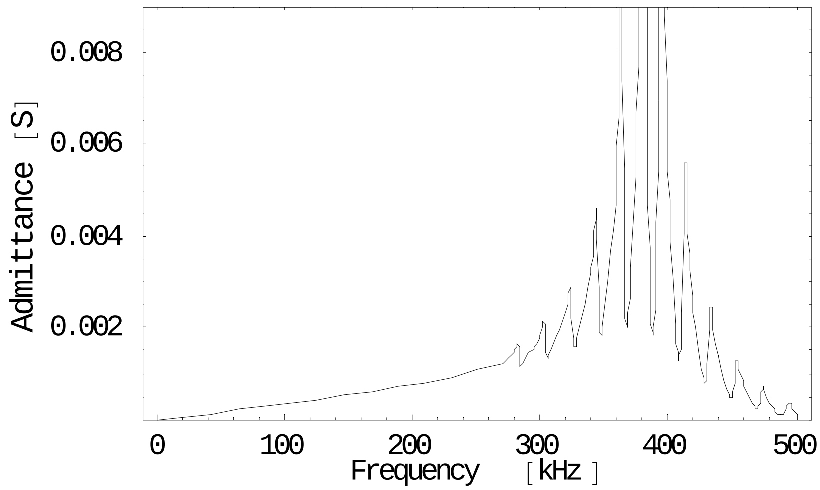

Figure 6: Admittance magnitude plot of the transducer according to Eq. 15 for excitation of a resonant rod at higher frequencies and damping $\varphi = 0.01$ (—)

Transducer: PXE 41, $L = 0.004$ m

Rod: Lucite with $E_R = 5.29 \cdot 10^9 \text{ N} \cdot \text{m}^{-2}$, $\rho_R = 1.2 \cdot 10^3 \text{ kg} \cdot \text{m}^{-3}$, $L_R = 0.05$ m

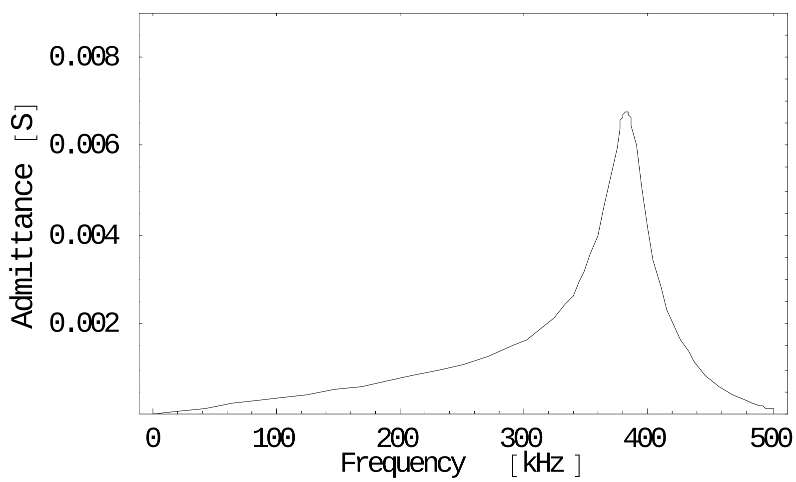

Figure 7: Admittance magnitude plot of the transducer according to Eq. 15 for excitation of a resonant rod at higher frequencies and damping $\varphi = 0.1$ (—)

Transducer: PXE 41, $L = 0.004$ m

Rod: Lucite with $E_R = 5.29 \cdot 10^9 \text{ N} \cdot \text{m}^{-2}$, $\rho_R = 1.2 \cdot 10^3 \text{ kg} \cdot \text{m}^{-3}$, $L_R = 0.05$ m

Literature:

1. Ristic, V.M,"Principles of Acoustic Devices", Wiley, New York, 1983

M5 Device Design, Modelling and Experimental Techniques

One dimensional models and planar resonator design.

Martyn Hill. Tuesday 1145 and 1430.

As will be clear from previous lectures, modes in microfluidic resonators generally comprise a complex three dimensional pattern of acoustic pressure and velocity (and hence radiation force potential) that can not be fully modelled by a simple one dimensional approach [1-3]. Nonetheless a one dimensional model represents an important starting point for many designs, and a helpful way of interpreting resonator behaviour [4-9].

Transfer impedance one dimensional modelling

There are many different ways of generating the acoustic excitation required to carry out ultrasonic particle manipulation. Sound can be coupled into cavities using surface acoustic waves [10, 11], interface waves [12], plate waves [13, 14], wedges [15, 16], orthogonal excitation [17, 18], cylindrical modes of a tube [19] or transducer pairs [20-22].

However the planar excitation of a rectangular cavity with a single transducer is probably the simplest approach and is certainly the approach most amenable to simple modelling. While manipulation can be brought about by progressive waves and by interference fields at frequencies away from resonance, the most efficient way of ordering particles is through resonant operation and this is the approach will be considered here.

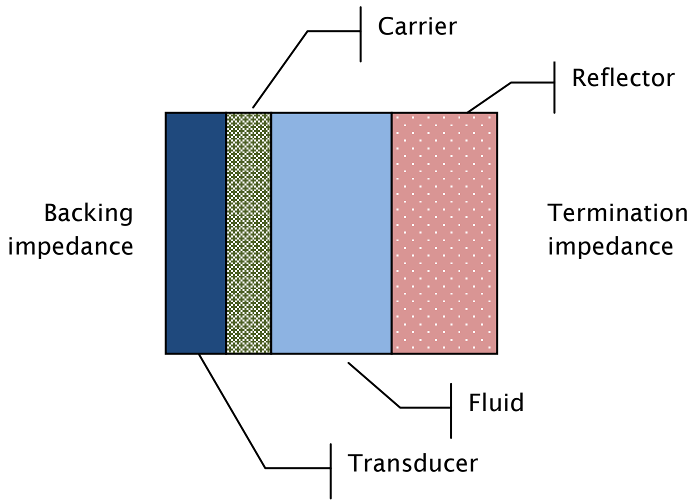

Figure 1. Typical structure of a planar layered resonator.

A planar resonator will typically consist of a transducer, a fluid layer within which the manipulation takes place, and a reflector layer (Figure 1). Often a carrier layer is included (sometimes called a *coupling layer* or a *matching layer*) to provide structural rigidity and/or to isolate the transducer from the fluid

A number of 1D models have been developed. One of the first to be used in the design of resonators for ultrasonic manipulation was that of Nowotny, Benes *et al.* [23, 24] which was used in the work of Gröschl [5, 25]. Other workers (including Cegla and Hawkes) have applied models based on guided wave formulations [26].

The model used in Southampton [7, 27] is less general but more straightforward than these. The concepts underlying the approach and the outcomes (within limits of applicability) are the same so it is this approach that is explained here

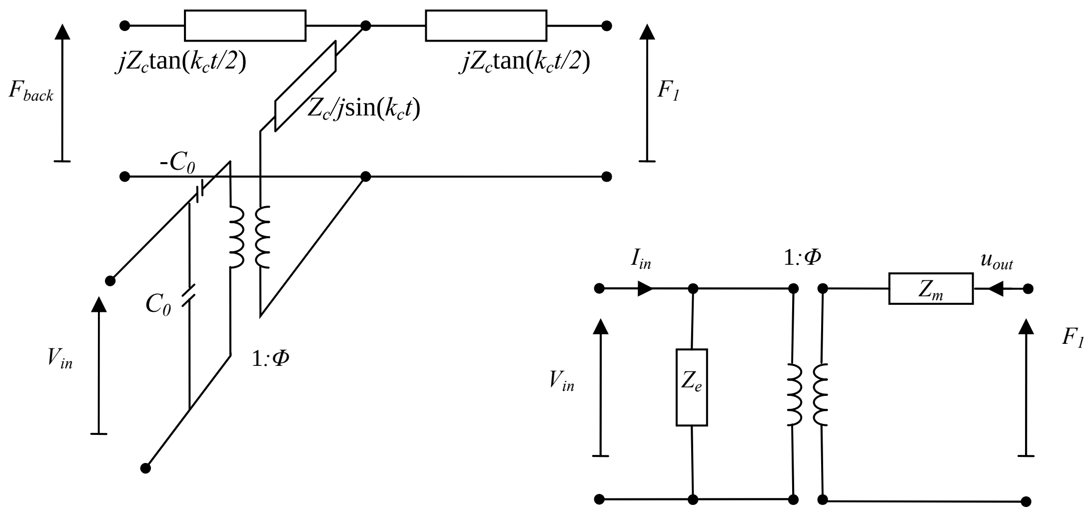

Figure 2. Two and three port models for a transducer

The aim of the modelling process is to predict the acoustic velocity and pressure amplitudes and patterns associated with particular modes. The generation of acoustic forces begins in the transducer, but in either the two port or three port models shown in Figure 2, the force and velocity exerted by the transducer face needs to be known, and this in turn can not be calculated without knowing what impedance the transducer is driving into. This has to be calculated from the impedances of the layers that make up the device.

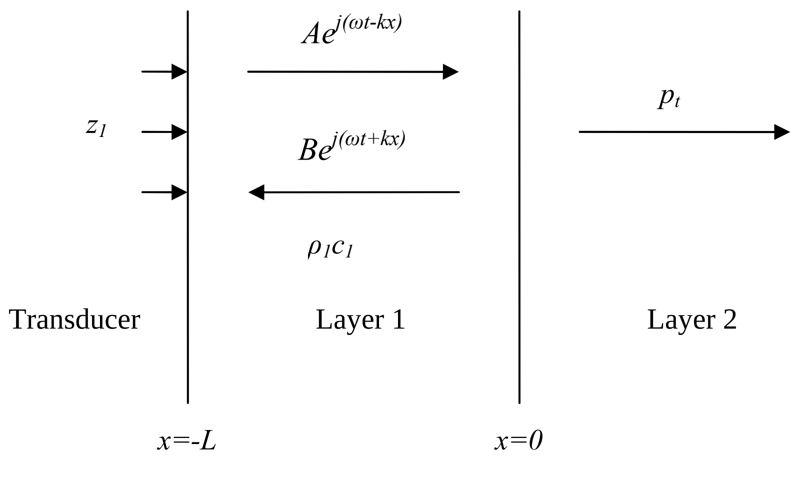

Figure 3 Incident, transmitted and reflected waves at a surface.

Consider a simple system (Figure 3) in which a transducer drives a layer at $x=-L$ (see [28] chapter 10). This layer has a characteristic acoustic impedance $\rho_1 c_1$ and is terminated by a boundary at $x=0$ with a second layer with a different acoustic impedance.

The pressure in layer in Layer 1 is the sum of the positive and negative going waves

$$p = Ae^{j(\omega t-kx)} + Be^{j\omega t+kx} \quad (1)$$

Using an analysis identical to that used to look at transmission through a boundary (see equation 6 in the notes on Fundamentals of Acoustics II), the acoustic impedance at $x = 0$ (i.e. the summed pressures divided by the summed velocities of the two waves) is

$$z_{x=0} = \rho_1 c_1 \frac{A+B}{A-B} \tag{2}$$

Similarly at the transducer boundary $x = -L$

$$z_1 = \rho_1 c_1 \frac{Ae^{jk_1L} + Be^{-jk_1L}}{Ae^{jk_1L} - Be^{-jk_1L}} \tag{3}$$

Combining these to eliminate A & B gives

$$z_1 = \rho_1 c_1 \frac{z_{x=0} + j\rho_1 c_1 \tan k_1 L}{\rho_1 c_1 + jz_{x=0} \tan k_1 L} \tag{4}$$

where k_1 is the wavenumber in layer 1. Hence the acoustic impedance looking into the layer is a function of the characteristic acoustic impedance of the layer, the thickness of the layer and the impedance that terminates the layer ($z_{x=0}$ in this example). Looking back to the layered structure of Figure 1, the only impedances that are known a-priori are the backing impedance on the left, which is incorporated into the transducer model, and the termination impedance on the right. Hence the transmission line approach uses equation (4) and the knowledge of the termination impedance to calculate the impedance at the boundary between the fluid and the reflector, then use that to calculate the impedance between the fluid and the carrier, and finally use that to model the impedance at the face of the transducer. The acoustic impedance at the transducer face (relating pressure and velocity) can then be multiplied by the surface area to generate a mechanical impedance (relating force and velocity) which can be included directly in the two or three port transducer model of Figure 2.

Modelling of acoustic parameters within the layers

The approach outlined above provides an estimate of the electrical impedance characteristics of the resonator. In order to model the performance of the resonator in more detail, it is also necessary to model the acoustic behaviour within the layers, and in particular within the fluid layer.

If we base our analysis on an air-backed transducer and incorporate that into the two port model of Figure 2, the force acting on the layer immediately adjacent to the transducer (F_1) is simply the transformed voltage split through a potential divider:

$$F_1 = \Phi V_{in} \frac{Z_1}{Z_m + Z_1} \tag{5}$$

where Z_1 is the mechanical impedance looking into the first layer. This is derived from the area and the acoustic impedance looking into layer 1. The acoustic field in layer 1 generates a force on the boundary with layer 2 and so on, such that successive force inputs at the boundary of layer *n*+1 based on properties and inputs to layer *n* are:

$$F_{n+1} = \frac{F_n Z_{n+1}}{Z_{n+1} \cos k_n t_n + jr_n S \sin k_n t_n} \tag{6}$$

where r denotes characteristic acoustic impedance, t is layer thickness, k wavenumber and S is the cross sectional area.

For layer n of thickness t_n, we let $x = 0$ at the start of the layer, and the spatial variation of the acoustic pressure, $p_n(x)$, through the layer may be expressed as:

$$p_n(x) = \frac{F_n}{S} \cdot \frac{Z_{n+1} \cos k_n (t_n - x) + j r_n S \sin k_n (t_n - x)}{Z_{n+1} \cos k_n t_n + j r_n S \sin k_n t_n} \tag{7}$$

The corresponding relationship for acoustic velocity variation through the layer is:

$$u_n(x) = \frac{F_n}{r_n S} \cdot \frac{r_n S \cos k_n (t_n - x) + j Z_{n+1} \sin k_n (t_n - x)}{Z_{n+1} \cos k_n t_n + j r_n S \sin k_n t_n} \tag{8}$$

Acoustic Energy Measures

The pressure and velocity measurements in each layer can then be used to calculate the instantaneous energy density, ε_n, at a point within layer *n*:

$$\varepsilon_n(x) = \frac{1}{2} \rho \left(u_n(x)^2 + \frac{p_n(x)^2}{r_f^{\,2}} \right) \tag{9}$$

The time average of the instantaneous energy density $\langle \varepsilon_n(x) \rangle_t$ can be calculated using the real parts of pressure and velocity above. This can then be integrated numerically to calculate the total time averaged, energy stored in the layer:

$$E_n = S \int_0^{t_n} \langle \varepsilon_n(x) \rangle_t \, dx \tag{10}$$

Designing planar resonators

The remainder of the two lectures that comprise *One dimensional models and planar resonator design* are split into three sections which are mentioned here in outline only but will be expanded upon during the presentations

Applications of one dimensional models

This will take selected examples from an existing paper [29] (a preprint of which is included in the course notes) as an appendix to this document.

It will also discuss approaches (illustrated in Figure 4) that allow the use of a 1D model as a way of estimating component parameters

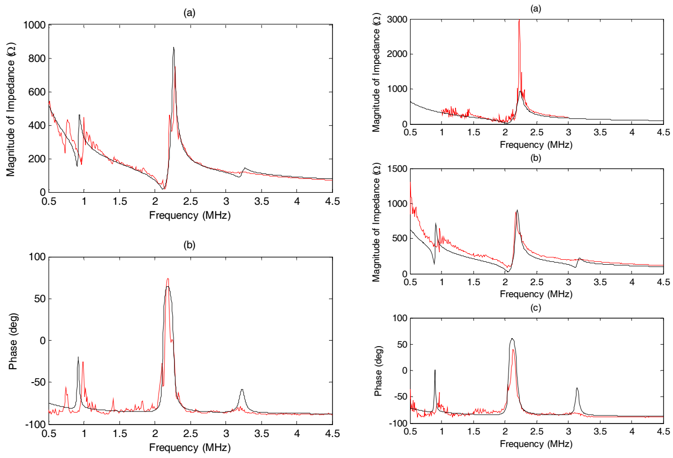

Figure 4 Modelled (black) and measured (red) plots for estimating component acoustic parameters.

Two and three dimensional modelling

While one dimensional models can be very useful for the preliminary design and understanding of devices, investigators have been making increasing use of two and three dimensional models [1-3, 14, 30, 31]. Several examples of pressure plots and radiation force potential contours for designing devices and understanding their behaviour are included (Figure 5)

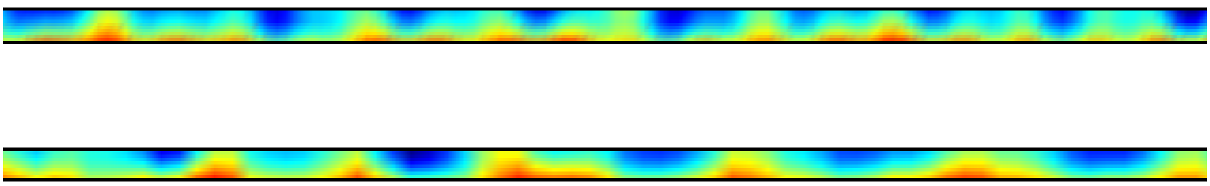

Figure 5 COMSOL pressure amplitude simulations for planar channel with different edge boundary conditions.

Examples of recent applications of planar resonators

The presentation ends with a discussion of:

- multi-modal resonators
- mode switching to overcome some of the constraints of fixed resonant patterns [32]
- thin “reflector” designs [33]
- dual force design incorporating magnetic and acoustic forces

[1] K. A. Fisher and R. Miles, "Modeling the acoustic radiation force in microfluidic chambers (L)," *Journal of the Acoustical Society of America,* vol. 123, pp. 1862-1865, Apr 2008.

[2] S. M. Hagsater*, et al.*, "Acoustic resonances in straight micro channels: Beyond the 1D-approximation," *Lab on a Chip,* vol. 8, pp. 1178-1184, 2008.

[3] R. J. Townsend*, et al.*, "Investigation of two-dimensional acoustic resonant modes in a particle separator " *Ultrasonics,* vol. 44, pp. e467-e471, 2006.

[4] L. Gherardini*, et al.*, "A new immobilisation method to arrange particles in a gel matrix by ultrasound standing waves," *Ultrasound In Medicine And Biology,* vol. 31, pp. 261-272, Feb 2005.

[5] M. Gröschl, "Ultrasonic separation of suspended particles - Part I: Fundamentals," *Acustica,* vol. 84, pp. 432-447, May-June 1998.

[6] N. R. Harris*, et al.*, "A dual frequency, ultrasonic, microengineered particle manipulator," *Ultrasonics,* vol. 42, pp. 139-44, 2004.

[7] M. Hill*, et al.*, "Modelling of layered resonators for ultrasonic separation," *Ultrasonics,* vol. 40, pp. 385-92, 2002.

[8] S. P. Martin*, et al.*, "Spore and micro-particle capture on an immunosensor surface in an ultrasound standing wave system," *Bio-sensors and Bioelectronics,* vol. 21, pp. 758-767, 2005.

[9] S. M. Woodside*, et al.*, "Acoustic force distribution in resonators for ultrasonic particle separation," *Aiche Journal,* vol. 44, pp. 1976-1984, Sep 1998.

[10] J. Shi*, et al.*, "Focusing microparticles in a microfluidic channel with standing surface acoustic waves (SSAW)," *Lab on a Chip,* vol. 8, pp. 221 - 223, 2008.

[11] C. D. Wood*, et al.*, "Formation and manipulation of two-dimensional arrays of micron-scale particles in microfluidic systems by surface acoustic waves," *Applied Physics Letters,* vol. 94, Feb 2009.

[12] V. Yantchev*, et al.*, "A micromachined Stoneley acoustic wave system for continuous flow particle manipulation in microfluidic channels," *Journal Of Micromechanics And Microengineering,* vol. 20, p. 035031, 2010.

[13] A. Neild*, et al.*, "A micro-particle positioning technique combining an ultrasonic manipulator and a microgripper," *Journal Of Micromechanics And Microengineering,* vol. 16, pp. 1562-1570, Aug 2006.

[14] S. Oberti*, et al.*, "Manipulation of micrometer sized particles within a micromachined fluidic device to form two-dimensional patterns using ultrasound.," *Journal of the Acoustical Society of America,* vol. 121, pp. 778-785, 2007.

[15] O. Manneberg*, et al.*, "Spatial confinement of ultrasonic force fields in microfluidic channels," *Ultrasonics,* vol. 49, pp. 112-119, 2009.

[16] O. Manneberg*, et al.*, "Wedge transducer design for two-dimensional ultrasonic manipulation in a microfluidic chip," *Journal Of Micromechanics And Microengineering,* vol. 18, Sep 2008.

[17] T. Laurell*, et al.*, "Chip integrated strategies for acoustic separation and manipulation of cells and particles," *Chemical Society Reviews,* vol. 36, pp. 492-506, 2007.

[18] F. Petersson*, et al.*, "Separation of lipids from blood utilizing ultrasonic standing waves in microfluidic channels," *Analyst,* vol. 129, pp. 938-943, 2004.

[19] G. Goddard and G. Kaduchak, "Ultrasonic particle concentration in a line-driven cylindrical tube," *Journal of the Acoustical Society of America,* vol. 117, pp. 3440-3447, Jun 2005.

[20] Y. Abe*, et al.*, "Study on the bubble motion control by ultrasonic wave," *Experimental Thermal and Fluid Science,* vol. 26, pp. 817-826, Aug 2002.

[21] B. Lipkens*, et al.*, "The effect of frequency sweeping and fluid flow on particle trajectories in ultrasonic standing waves," *Ieee Sensors Journal,* vol. 8, pp. 667-677, May-Jun 2008.

[22] G. Whitworth*, et al.*, "Transport And Harvesting Of Suspended Particles Using Modulated Ultrasound," *Ultrasonics,* vol. 29, pp. 439-444, Nov 1991.

[23] H. Nowotny and E. Benes, "General One-Dimensional Treatment of the Layered Piezoelectric Resonator with 2 Electrodes," *Journal of the Acoustical Society of America,* vol. 82, pp. 513-521, Aug 1987.

[24] H. Nowotny*, et al.*, "Layered Piezoelectric Resonators with an Arbitrary Number of Electrodes (General One-Dimensional Treatment)," *Journal of the Acoustical Society of America,* vol. 90, pp. 1238-1245, Sep 1991.

[25] M. Gröschl, "Ultrasonic separation of suspended particles - Part II: Design and operation of separation devices," *Acustica,* vol. 84, pp. 632-642, Jul-aug 1998.

[26] M. J. S. Lowe, "MATRIX TECHNIQUES FOR MODELING ULTRASONIC-WAVES IN MULTILAYERED MEDIA," *IEEE Transactions on Ultrasonics Ferroelectrics and Frequency Control,* vol. 42, pp. 525-542, Jul 1995.

[27] M. Hill and R. J. K. Wood, "Modelling in the design of a flow-through ultrasonic separator," *Ultrasonics,* vol. 38, pp. 662-665, Mar 2000.

[28] L. E. Kinsler*, et al.*, *Fundamentals of acoustics*, 4th ed. New York: Wiley, 2000.

[29] M. Hill*, et al.*, "Modelling for the robust design of layered resonators for ultrasonic particle manipulation," *Ultrasonics,* vol. 48, pp. 521-528, Apr 09-12 2008.

[30] A. Neild, *et al.*, "Finite element modeling of a microparticle manipulator," *Ultrasonics*, vol. 44, pp. e455-e460, 2006.
[31] R. Barnkob, *et al.*, "Measuring the local pressure amplitude in microchannel acoustophoresis," *Lab on a Chip*, vol. 10, pp. 563-570, 2010.
[32] P. Glynne-Jones, *et al.*, "Mode-switching: A new technique for electronically varying the agglomeration position in an acoustic particle manipulator," *Ultrasonics*, vol. 50, pp. 68-75, 2010.
[33] P. Glynne-Jones, *et al.*, "Robust acoustic particle manipulation: A thin-reflector design for moving particles to a surface," *The Journal of the Acoustical Society of America*, vol. 126, pp. EL75-EL79, 2009.

Modelling for the robust design of layered resonators for ultrasonic particle manipulation

Martyn Hill, Rosemary J. Townsend, Nicholas R. Harris[1]
School of Engineering Sciences, University of Southampton, SO17 1BJ, UK
[1]School of Electronics and Computer Science, University of Southampton, SO17 1BJ, UK

Pre-print from "Modelling for the robust design of layered resonators for ultrasonic particle manipulation." Ultrasonics 48: 521-528 (2008).

Abstract: Several approaches have been described for the manipulation of particles within an ultrasonic field. Of those based on standing waves, devices in which the critical dimension of the resonant chamber is less than a wavelength are particularly well suited to microfluidic, or "lab on a chip" applications. These might include pre-processing or fractionation of samples prior to analysis, formation of monolayers for cell interaction studies, or the enhancement of biosensor detection capability.

The small size of microfluidic resonators typically places tight tolerances on the positioning of the acoustic node, and such systems are required to have high transduction efficiencies, for reasons of power availability and temperature stability. Further, the expense of many microfabrication methods precludes an iterative experimental approach to their development. Hence, the ability to design sub-wavelength resonators that are efficient, robust and have the appropriate acoustic energy distribution is extremely important.

This paper discusses one-dimensional modelling used in the design of ultrasonic resonators for particle manipulation and gives example of their uses to predict and explain resonator behaviour. Particular difficulties in designing quarter wave systems are highlighted, and modelling is used to explain observed trends and predict performance of such resonators, including their performance with different coupling layer materials.

Keywords: acoustic radiation force, layered resonators, robust design, particle manipulation

Introduction

Ultrasonic standing waves (USWs) can be used to trap and manipulate particles, and are particularly well suited for the manipulation of micron-scale biological particles in devices of a microfluidic scale [1]. Several different approaches have been employed for the manipulation of particles using ultrasonic fields. For example, focussed ultrasound [2,3] or near-field effects [4] can be used to trap particles prior to analysis, particles can be moved by using two or more opposing transducers to modulate the standing wave field [5,6], or particles can be held and moved within USWs excited by plate waves coupled into the containing fluid [7,8]. However, the use of a simple planar layered resonator with a single transducer [9-11] offers the simplest approach to establishing a USW suitable for particle movement.

Planar USW systems may employ resonators that are larger than a wavelength and contain multiple pressure nodal planes [12,13], but for microfluidic scale devices, a resonant cavity with an axial dimension that is lower than the operating wavelength may be employed [14-16]. Such sub-wavelength resonators typically rely for their operation on precise positioning of the pressure node, to which particles will migrate. In these systems the ability to design a resonator that will operate with a good efficiency and have the required acoustic mode shapes is critical.

A variety of approaches to modelling resonators have been described (see for example [9,17,18]). This paper uses one dimensional models implementing impedance transfer relationships [11,19,20].

Layered resonators for particle manipulation

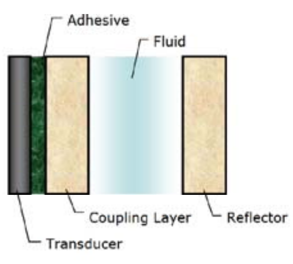

Fig. 1. Typical structure of a planar layered resonator

The structure of a typical planar resonator is shown in Fig. 1 and consists of a transducer which is, in general, bonded to a coupling layer (also known as a carrier layer or matching layer) that serves to isolate the adjacent fluid layer from the transducer. A standing wave is established in the fluid layer by a solid reflector layer.

Particles within the standing wave experience a force, which in most cases of interest acts towards a pressure node of the standing wave. The force on a particle of radius a at position x within the standing wave can be expressed as a function of the spatial gradients of the time averaged kinetic ($E_{kin}(x)$) and potential ($E_{pot}(x)$) energies [21]

$$F(x)=\frac{\partial}{\partial x}\left(\frac{4\pi a^3}{3}\left(\frac{3(\rho_p-\rho_f)}{(2\rho_p+\rho_f)}E_{kin}(x)-\left(1-\frac{\beta_p}{\beta_f}\right)E_{pot}(x)\right)\right) \quad (1)$$

where β and ρ are the compressibility and the mass density of the fluid and the particle, indicated by subscripts f and p respectively. The wave number, k is equal to $2\pi/\lambda$ where λ is the wavelength of the standing wave.

The problem of modelling particle behaviour in the standing wave then becomes one of describing the variation of acoustic parameters through the acoustic field such that the energy parameters $E_{kin}(x)$ and $E_{pot}(x)$ can be calculated. The rest of the paper discusses the characterisation of the field itself in order to provide the behaviour required for the correct operation of the device (chiefly nodal position and energy density).

Simple two-layer model

Background theory

An approach to the characterisation of the underlying properties of resonators is to begin by looking at the modal solutions of a two layer system consisting of a fluid layer with a rigid boundary coupled with a reflector layer with a pressure-release boundary [20]. Such a model is not, in itself, sufficient to understand the behaviour of a resonator such as that shown in Fig. 1. However it can act as a starting point, suggesting layer properties able to provide the required nodal behaviour. Additional layers can then be added and their parameters adjusted in a fuller model to maintain, or fine-tune resonator response. The two-layer approach simplifies to solving

$$k_f t_f=\tan^{-1}\left(\frac{r_f\left(r_r^{\,2}+r_0^{\,2}\tan^2(k_r t_r)\right)}{r_r\tan(k_r t_r)\left(r_r^{\,2}-r_0^{\,2}\right)}\right) \quad (2)$$

where t_r and t_f are the thicknesses of the reflector and fluid layers respectively, k is the wave number and r_f and r_0 are the acoustic impedances of the fluid and reflector layers respectively. A given ratio of the thicknesses of the two layers (i.e a fixed design) is represented by a straight line passing through 0,0 on the graph in Fig. 2, which shows the first 4 solutions of equation (2), plotted as the ratio of thickness to wavelength of the fluid layer to the ratio of thickness to wavelength of the reflector layer.

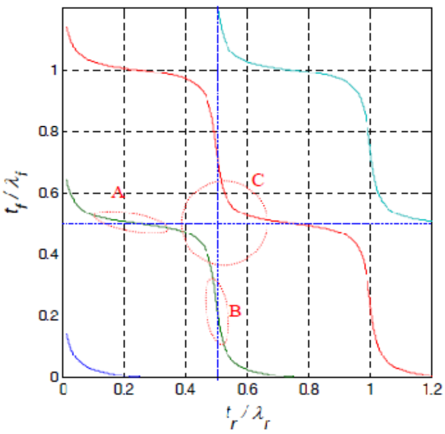

Fig. 2. The first four solutions of equation (2), based on [20].Parameters *tr* and *tf* are the thicknesses of the reflector and fluid layers respectively and *λr* and *λf* are ultrasonic wavelengths in those layers

A fluid layer having two perfectly rigid boundaries would have modal solutions corresponding to horizontal lines at t_f/λ_f =0.5, 1, etc. where λ_f is the ultrasonic wavelength in the fluid layer. Similarly, a reflector bounded by two pressure release surfaces would show half wave resonances as vertical lines corresponding to t_r/λ_r=0.5, 1, etc. There is, however, no modal solution at (0.5, 0.5) on the graph, but region *C* shows how the modes of the coupled system split when adjacent layers would have coincident resonances if isolated. The parameter in Fig. 2 that indicates the position of the pressure node within the fluid layer is t_f/λ_f. In order to place a node centrally, in this two layer model, a reflector thickness of a quarter wavelength is required, i.e. t_r/λ_r=0.25, as shown in area *A* of Fig. 2. It can also be seen from area *A* that the solid line representing the solution to equation (2) is relatively flat in that region, indicating that the position of the node should be stable with regards to the reflector layer thickness. Even with the combination of a half wavelength fluid layer and a quarter wavelength reflector layer, the influences of the coupling layer and transducer need to be considered, and Fig. 3a shows how the frequency of maximum energy density in the fluid layer, and hence the position of the node within the fluid layer, varies as a function of coupling layer thickness. With the parameters used in this system (taken from [11]) the variation in frequency is relatively small, and selection of a quarter wavelength coupling gives the most stable frequency, but a relatively low value of peak energy. The material used for the coupling layer is investigated in more detail later.

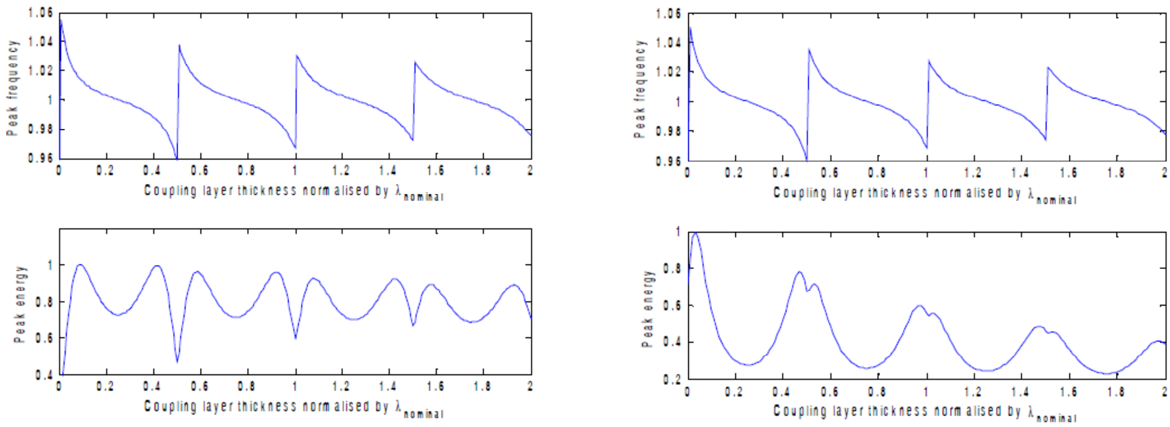

(a) (b)

Fig. 3. Variation of the frequency and energy density of the most energetic resonance as coupling thickness layer varies. (a) Parameters based on simulations in [11], and normalised against the nominal resonance frequency. (b) With lower Q factors in coupling and fluid layers.

The highest values of energy density occur either side of the points at which the coupling layer equals half wavelength multiples, but with a significant dip for the half wavelength coupling layer itself. This dip, however, becomes less pronounced at lower Q factors. If the Q factors are reduced from 200 and 500 for the coupling and fluid layers respectively (Fig 3a) to 50 for both (Fig 3b), the frequency variation of the peak remains similar, but the peak energy density characteristics change significantly. These Q factors seem low, but their values represent observed losses throughout the resonant device and will in general be much lower than material Q factors [9]. A similar observation is made later for quarter-wavelength fluid layer systems where coupling layer materials have been investigated.

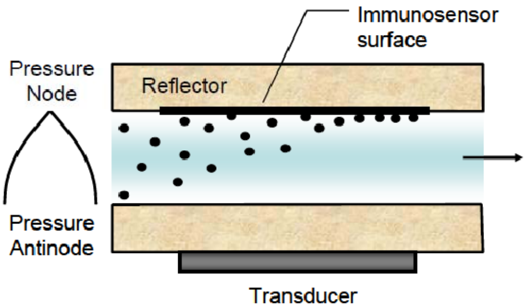

Fig. 4. Schematic representation of a quarter wavelength resonator forcing particles up against a solid surface with an immunosensor coating.

Modelling of quarter wavelength devices

The need for robust design of resonators becomes particularly important when dealing with quarter wavelength devices. A quarter wavelength resonance is observed when the fluid layer is at a quarter wavelength and the reflector layer is a half wavelength thick, in the region marked *B* in Fig. 2. Such a system may be used to force particles against, or close to, a solid surface as shown in Fig. 4 which is designed to enhance particle capture on an immunosensor surface.

A simple simulation suggests that for fixed values of coupling layer and reflector thickness, simply varying the fluid layer thickness should enable the pressure node to be positioned at, or close to, the reflector layer. This can be seen from the simulations of a silicon/Pyrex resonator shown in Fig. 5, which use the parameters shown in Table 1.

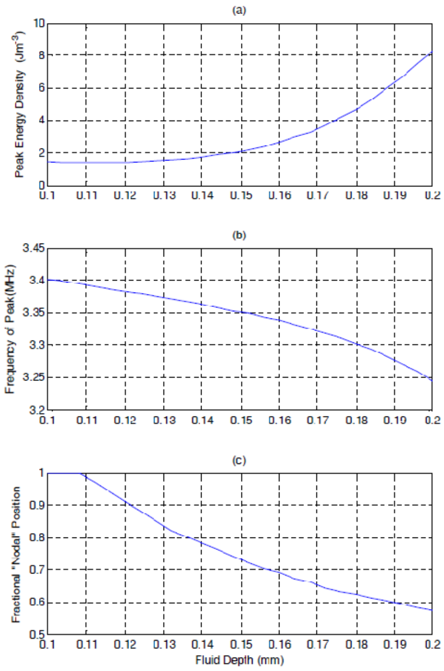

Fig. 5. Simulated values of peak energy density, peak frequency and nodal position for silicon microfabricated quarter wavelength resonator

Table 1. Quarter wave simulation parameters

	Coupling	*Fluid*	*Reflector*
Thickness (m)	5.25e-4	Varying	1.60e-3
Density (kg m^{-3})	2.34e+3	1.00e+3	2.20e+3
Speed of Sound (m s^{-1})	8.43e+3	1.50e+3	5.43e+3

However the gradient of the solution line in region *B* of Fig. 2 suggests that the nodal position is likely to be extremely sensitive to reflector layer thickness

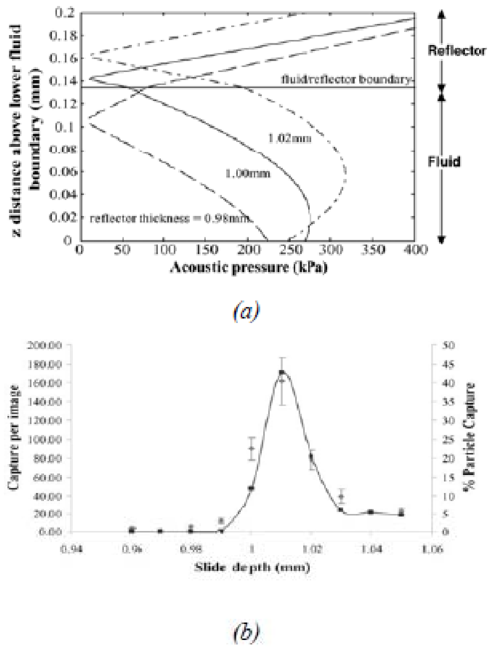

Fig. 6. Acoustic simulation of the pressure profile across the chamber used by Martin et al. [22] for different reflector thicknesses (a), and simulations of particle capture (line) compared with experimental data (b). Reproduced from [22] with permission from Elsevier.

Martin *et al.* [22] investigated the acoustics of such a system with the aim of forcing spores onto an antibody coated surface using a 3 MHz USW. The device was tested in batch and flow-through modes and it was found that the efficacy of capture was critically dependent on the reflector layer thickness. When a 980 µm thick reflector was used, there was almost no capture of the BG spores. Capture increased with a 1000 µm reflector, peaked with a thickness of about 1100 µm and fell away significantly with a reflector thickness of 1300 µm. This was explained by 1D simulations of the acoustic pressure for different reflector thicknesses, as shown in Fig. 6(a). With a reflector thickness of 980 µm, the pressure node is in the fluid, away from the reflector boundary, so particles are forced away from the antigen surface. With a 1000 µm reflector, the node is just in the reflector, so particles will be forced to the surface. A 1200 µm reflector places the node well into the reflector, but also brings a pressure antinode into the fluid, causing many particles to be forced to the opposite boundary. Hence there is an optimum positioning of the node that is dependent on the reflector thickness and a significant decrease in capture efficiency on each side of this thickness. When flow and particle tracking were added to the acoustic model [23] it was possible to predict the nature of the dependence of particle capture on reflector depth, as shown in Fig. 6(b).

Selecting operating points from 2D plots

There are other applications in which it is required to place a pressure node close to, but not on, a boundary with a solid layer. Such a "near quarter-wave" resonator has been designed for concentrating particles prior to analysis [24] and is shown schematically in Fig. 7.

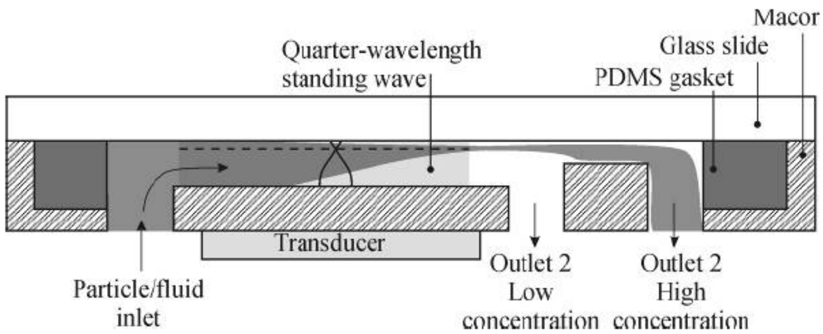

Fig. 7. Schematic representation of a "near quarter-wave" concentrator.

In this case the aim was to move particles to within 20 µm of the reflector layer in a 180 µm cavity. In order to achieve this, multiple simulations were completed to predict the sensitivity of the energy density and nodal position to relevant geometric parameters. An example is shown in Fig. 8 in which these parameters are plotted against reflector and coupling layer thickness. For each geometric design, the acoustic energy within the fluid layer is determined over a small range of frequencies in order to isolate the fluid quarter wavelength mode. Acoustic energy density and corresponding position of the pressure minimum are recorded for the frequency where energy density is seen to peak.

The parameters used in the simulations are shown in the Table 2, with the values of Q-factor inferred by matching modelled and experimentally derived electrical input impedance spectra for:

1. the isolated transducer,
2. the transducer, glue and coupling layers,
3. the full system.

Table 2. Concentrator simulation parameters

Layer	Thickness (µm)	Density (kg/m^3)	Sonic velocity (m/s)	Q-factor
Glue	10	1080	2640	2
Macor coupling	800-1800	2540	5510	100
Fluid	180	1000	1480	50
Reflector	1200-1550	2470	5600	100

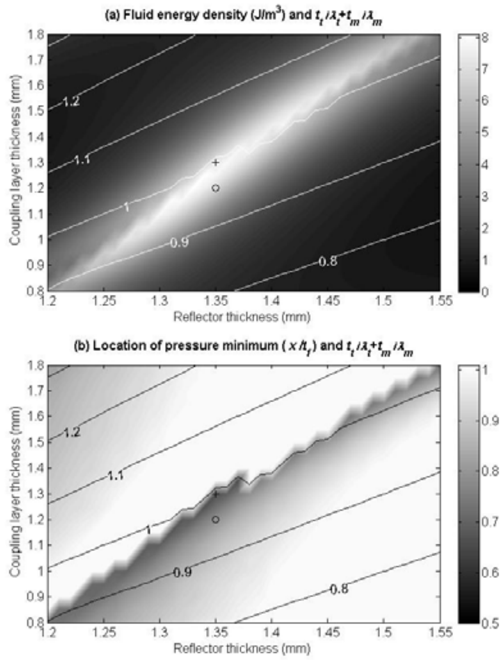

Fig. 8. Acoustic energy density in the fluid layer (upper) and fractional position of pressure minimum (lower) with contours representing the coupled transducer and coupling layer thickness in wavelengths.

In Fig. 8 the white diagonal bar across plot (a) suggests that both reflector and coupling layer thicknesses are important parameters to consider when designing to maximise acoustic energy density and therefore radiation force. Similarly, plot (b) indicates how the design influences the position of the pressure minimum within the fluid layer and how the thicknesses chosen can result in the pressure node moving from within the fluid layer a small distance from the reflector layer (grey) and into the reflector such that particles are pushed up to the reflector surface (white). The irregularity of the contour representing a single wavelength is due to a coincidence of the coupled transducer/matching layer resonance and the half wavelength resonance of the reflector. Pressure amplitude plots for the two points (‘o’ t_r = 1350 µm and t_c = 1200 µm, and ‘+’ t_r = 1350 µm and t_c = 1300 µm) marked in Fig. 8 are shown in Fig. 9.

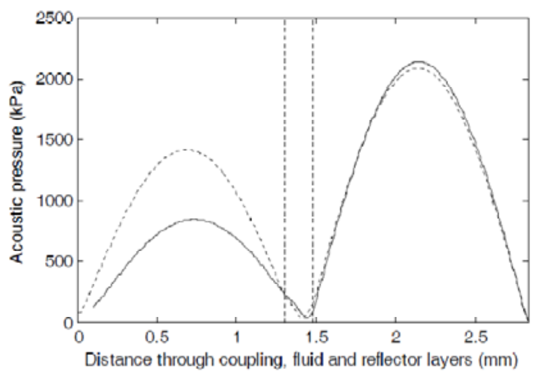

Fig. 9. Acoustic pressure profile for the two potential design points marked in Fig. 8 – ‘o’ (solid) and ‘+’ (dotted).

It can be seen that point ‘+’ corresponds to a higher energy in the coupling layer, although the pressure profile in the fluid layer is similar. However from Fig. 8 point ‘o’ is far more robust in terms of nodal position, despite having a lower energy.

Just as the damping in the system alters the characteristics between Fig. 3a and Fig. 3b, this system is also sensitive to changes in Q factors. Fig. 10 is a repeat of the simulation shown in Fig. 8 but with a significantly higher reflector Q factor. The nodal position (lower figure in each case) as a function of layer thicknesses remains robust to layer thicknesses and is similar in both figures. Not surprisingly the magnitude of the energy density in the fluid layer (upper figure) changes significantly between the simulations. Further, the form of the energy density surface has changed. In the more highly damped system of Fig. 8, the maximum energy density lies close to the irregular single wavelength contour, while for the higher Q Fig. 10, the maximum energy lies either side of this contour in a manner similar to the coupled resonances described in [11]. Hence the position of the node in these systems appears to be relatively robust to the damping factors.

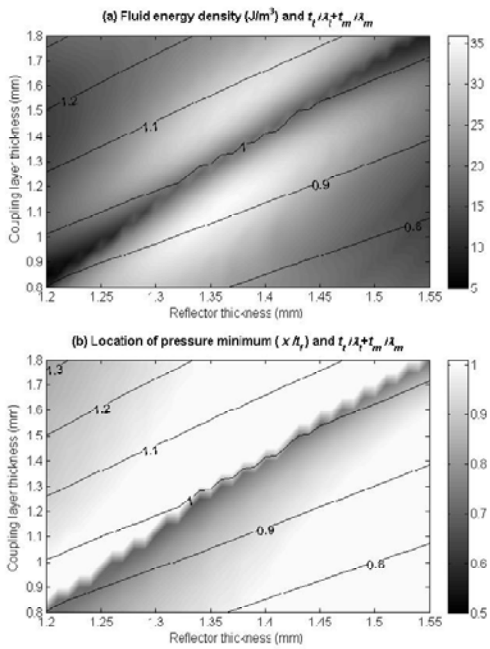

Fig. 10. Acoustic energy density in the fluid layer (upper) and fractional position of pressure minimum (lower) with contours representing the coupled transducer and coupling layer thickness in wavelengths but with higher Q factors in the layers than used in Fig. 8

Fig. 11 shows a prototype quarter wave concentrator in which t_r = 1440 µm and t_c = 1040 µm. This device provided a factor of 4 concentration with one micron diameter particles and the nodal position was as predicted by modelling using high Q factors, although the damping and hence energy density characteristics proved to be closer to those shown in Fig. 8 on experimental evaluation.

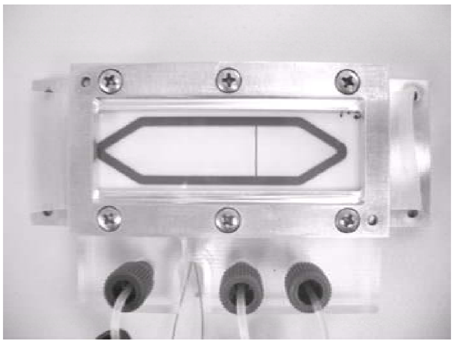

Fig. 11. Prototype quarter-wavelength concentrator

Effect of Varying the Coupling Layer Material

As discussed previously, the coupling layer material can have an effect on the nodal positions, and the amount of energy stored within the fluid layer. Practical considerations are also important in designing particle manipulators, such as bio-compatibility, ease of manufacture, and cost, so it is useful to know what range of materials can be used and how they affect the performance. The device shown in Fig. 11 has a coupling layer manufactured from Macor, a machinable ceramic, similar to glass. Devices with coupling layers made from other materials were also constructed. The materials investigated were aluminium and brass. It is known that the coupling layer material influences the acoustic energy density and the maximum radiation force experienced by a particle. This is highly relevant to quarter-wavelength systems as the success of a resonator typically relies on maximising the acoustic energy density. In the case of a quarter wave device, the quarter wave mode is a lot less energetic than a typical half wave device and maximizing the efficiency to avoid heating effects in the other layers requires careful design. Quarter wave devices are much less efficient than half wave devices because of the reliance on a reflector layer resonance where much of the acoustic energy is dissipated.

Initial simulations were used to design near quarter-wavelength resonators operating around 2MHz for each coupling layer material. The acoustic pressure profiles within these devices are similar to that shown in Fig.9

where a half-wavelength resonance is seen in the reflector layer above the fluid chamber. This resonance imposes a node at the fluid/reflector boundary and for certain fluid depths will result in a quarter-wavelength “resonance” in the fluid layer. This mode forces suspended particles up to this surface.

For the experimental devices a transducer with a resonance close to the operating frequency of the assembled chamber was used (Ferroperm PZ26, 1mm thick). To give comparable acoustic pressure profiles in the fluid layer, the model was used to select coupling layer and fluid layer thickness dimensions. In each case the fluid layer thickness was chosen to be 0.18mm and coupling layer thicknesses of 1.0, 1.4, and 1.2 were selected for brass, aluminium and Macor, respectively. Table 3 contains the measured thickness dimensions and acoustic properties used in the initial modelling.

Although the modelling suggests good results for the pressure profile, the model requires calibrating with experimental data to provide absolute values for the acoustic parameters. This is done by taking acoustic energy density measurements for the different chambers and then adjusting the model parameters such as material Q factors, to get the best match. Acoustic energy density measurements are taken between 1.96 and 2.1 MHz at 10 kHz intervals. These measurements are made by levitating a polystyrene particle and recording the threshold voltage where the particles begin to sediment, similar to the method described by Martin *et al.* [22]. For the particles, fluid (water) and frequency used, this threshold voltage corresponds to a pressure amplitude of 33kPa. During experiments, the position of the node is difficult to measure accurately but is reasonably consistent with predictions of the pressure profile such as that shown in Fig. 9. As the acoustic pressure amplitude is proportional to the transducer voltage, the pressure amplitude P_0 resulting from a 10 V_{pkpk} voltage is recorded and converted to an energy density measurement using (3):

$$\langle \bar{\varepsilon} \rangle = \tfrac{1}{4} P_0^{\,2} \beta_w , \qquad (3)$$

where $\langle \bar{\varepsilon} \rangle$ is the acoustic energy density and β_w is the bulk modulus of water, with the results presented in Fig. 12.

Table 3. Dimensions of experimental samples. Properties of materials taken from [25].

Coupling layer material	Coupling layer thickness (mm)		Fluid layer thickness (mm)		Density (kg/m^3)	Sonic velocity (m/s)	Acoustic impedance (MRayl)
	Design	Measured	Design	Measured			
Brass	1.00	1.08	0.18	0.17	8640	4700	40.6
Aluminium	1.40	1.42	0.18	0.175	2700	6420	17.3
Macor	1.20	1.17	0.18	0.19	2540	5510	14.0

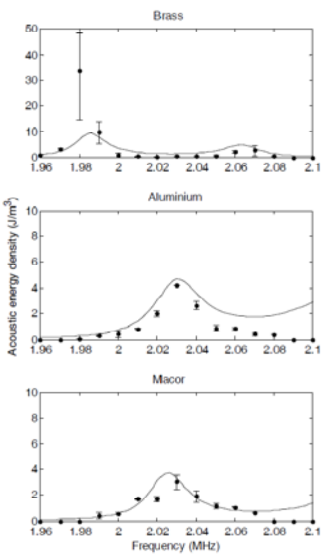

Fig. 12. Comparison between measured (pointes with error bars) and modelled (solid lines) acoustic energy density.

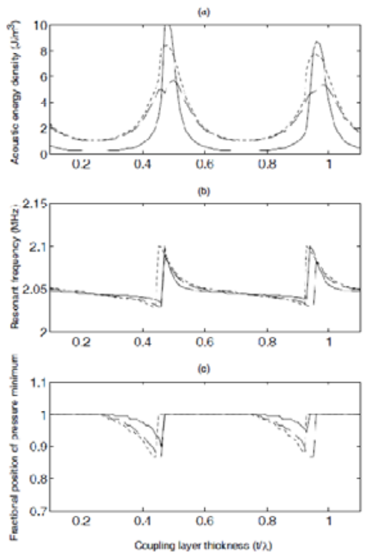

Fig. 13. Predicted peak acoustic energy density in the fluid layer for a range of coupling layer thicknesses for brass (solid), aluminium (dashed) and Macor (dotted). Showing (a) acoustic energy density, (b) the quarter wavelength excitation frequency and (c) the fractional position of the pressure minimum within the fluid chamber..

The plots of fig. 12 show that the acoustic energy density peaks at frequencies where resonant modes are encountered. Predicted energy density is also shown, where the input parameters to the model have been modified to improve the match with both impedance and energy density measurements. Notably the Q factors have been adjusted to 300, 100 and 100 for brass, aluminium and Macor, respectively. Similarly, the Q factors in the fluid and reflector are low at ~30 and ~100, respectively. In the case of brass, two peaks can be seen although the model suggests that the peak around 1.98MHz is a combined transducer and coupling layer resonance. This mode appears to be particularly energetic and may be reinforced, for example, by structural modes.

To compare each material more directly, the model was used to simulate the effect of varying coupling layer thickness whilst applying identical reflector and fluid layer properties. Fig. 13 shows the predicted peak energy density for a range of coupling layer thicknesses as a fraction of wavelength (t_m/λ) and where the transducer voltage is a constant 10 Vpkpk. Note that Fig. 13 is generated by locating the frequency at which the quarter-wavelength mode (reflector resonance) occurs and omits any other resonant modes close to this frequency. It therefore does not include the high energy resonance seen at 1.98MHz in the experimental results for the brass coupling material.

In general, the energy density is comparable for the materials considered, although the material does have a limited impact in the maximum energy density achievable. Peaks suggest that for all the materials tested a coupling layer thickness of just under $n.t_m/2\lambda$ (n = 1, 2 only shown) results in a higher acoustic energy. The trade-off in this case is that the acoustic node moves away from the surface and further into the fluid layer at these dimensions as shown in Fig. 13c. As the transducer is operating close to a half-wavelength, the peaks also coincide with a wavelength resonance in the transducer and coupling layer combined where if this structure were isolated from the fluid and reflector would have a pressure node located on the coupling layer surface. The close proximity of this coupled resonance to the quarter-wavelength mode may therefore be responsible for the change in energy density and movement of the node towards the coupling layer surface. Also, for an increase in n the energy density decreases, probably due to greater losses within a progressively thicker coupling layer.

The observations made in Fig. 13 are similar to those in Fig. 3b for a half-wavelength system. This suggests that the design of the coupling layer and transducer can be decoupled from the fluid and reflector layer to some extent. For example, the position of the nodal plane(s) within a fluid chamber depends on the controlled design of the fluid and reflector design and aided by Fig. 2. Although the coupling layer and transducer will influence the node position and energy density, they have a small effect relative to fluid/reflector design and considering the wide range of coupling layer/transducer designs which could feasibly drive the system.

Conclusions

One-dimensional acoustic modelling has helped identify specific parameters which influence the robust design of resonators for particle manipulation. The nodal position and energy density are typically important factors in resonator performance, and the choice of layer dimensions and material properties influence these factors significantly. For example, the careful selection of Q factors for the various materials and layers used to construct these resonators may be used to help relax dimensional tolerances. It appears that the influence of the coupling layer on the performance of both half and quarter-wavelength resonances is related, with the proximity of the coupling layer/transducer mode impacting upon the characteristics of fluid/reflector modes.

It has also been shown that the behaviour of quarter-wavelength modes can be more fully understood based on a comparison of modelled and experimental data. Using experimental data to refine the simulation input parameters it is possible to predict the acoustic energy density to well within the correct order of magnitude. This is important, for example, for bio-sensing applications where the location of the pressure node and strength of the field influences significantly the feasibility of such devices. The choice of material used to couple between the transducer and fluid manipulation chamber determines to a limited extent the maximum energy density achievable, although coupling layer thickness appears to have a greater impact. Therefore a range of materials can be used for the construction of the coupling layer.

While 1D models are able to provide very useful, and in the case of nodal position accurate, predictions of device behaviour, the influences of lateral field variations are also of significance [26]. These variations are the main limitation on the performance of the concentrator described here [24]

Acknowledgements

The authors gratefully acknowledge the support and funding from the Defence Science and Technology Laboratory (DSTL), Porton Down, UK.

References

[1] T. Laurell, F. Petersson, A. Nilsson, Chip integrated strategies for acoustic separation and manipulation of cells and particles, Chemical Society Reviews 36 (2007) 492-506.

[2] M. Wiklund, J. Toivonen, M. Tirri, P. Hanninen, H.M. Hertz, Ultrasonic enrichment of microspheres for ultrasensitive biomedical analysis in confocal laser-scanning fluorescence detection, Journal Of Applied Physics 96 (2004) 1242-1248.

[3] H.M. Hertz, Standing-Wave Acoustic Trap For Nonintrusive Positioning Of Microparticles, Journal Of Applied Physics 78 (1995) 4845-4849.

[4] T. Lilliehorn, U. Simu, M. Nilsson, M. Almqvist, T. Stepinski, T. Laurell, J. Nilsson, S. Johansson, Trapping of microparticles in the near field of an ultrasonic transducer, Ultrasonics 43 (2005) 293-303.

[5] G. Whitworth, M.A. Grundy, W.T. Coakley, Transport And Harvesting Of Suspended Particles Using Modulated Ultrasound, Ultrasonics 29 (1991) 439-444.

[6] Y. Abe, M. Kawaji, T. Watanabe, Study on the bubble motion control by ultrasonic wave, Experimental Thermal and Fluid Science 26 (2002) 817-826.

[7] A. Haake, A. Neild, G. Radziwill, J. Dual, Positioning, displacement, and localization of cells using ultrasonic forces, Biotechnology And Bioengineering 92 (2005) 8-14.

[8] A. Neild, S. Oberti, F. Beyeler, J. Dual, B.J. Nelson, A micro-particle positioning technique combining an ultrasonic manipulator and a microgripper, Journal Of Micromechanics And Microengineering 16 (2006) 1562-1570.

[9] M. Gröschl, Ultrasonic separation of suspended particles - Part I: Fundamentals, Acustica 84 (1998) 432-447.

[10] J.J. Hawkes, W.T. Coakley, Force field particle filter, combining ultrasound standing waves and laminar flow, Sensors and Actuators B-Chemical 75 (2001) 213-222.

[11] M. Hill, Y. Shen, J.J. Hawkes, Modelling of layered resonators for ultrasonic separation., Ultrasonics 40 (2002) 385-392.

[12] O. Doblhoffdier, T. Gaida, H. Katinger, W. Burger, M. Groschl, E. Benes, A Novel Ultrasonic Resonance Field Device for the Retention of Animal-Cells, Biotechnology Progress 10 (1994) 428-432.

[13] H. Bohm, L.G. Briarty, K.C. Lowe, J.B. Power, E. Benes, M.R. Davey, Quantification of a novel h-shaped ultrasonic resonator for separation of biomaterials under terrestrial gravity and microgravity conditions, Biotechnology And Bioengineering 82 (2003) 74-85.

[14] N.R. Harris, M. Hill, S.P. Beeby, Y. Shen, N.M. White, J.J. Hawkes, W.T. Coakley, A Silicon Microfluidic Ultrasonic Separator, Sensors and Actuators B 95 (2003) 425-434.

[15] J.J. Hawkes, M. Gröschl, H. Nowotny, S. Armstrong, P. Tasker, W.T. Coakley, E. Benes, Single half wavelength ultrasonic particle filter: Predictions of the transfer matrix multi-layer resonator model and experimental filtration results., Journal of the Acoustical Society of America 111 (2002) 1259-1266.

[16] F. Petersson, A. Nilsson, C. Holm, H. Jonsson, T. Laurell, Continuous separation of lipid particles from erythrocytes by means of laminar flow and acoustic standing wave forces, Lab On A Chip 5 (2005) 20-22.

[17] A. Neild, S. Oberti, J. Dual, Design, modeling and characterization of microfluidic devices for ultrasonic manipulation Sensors and Actuators B: Chemical 121 (2007) 452-461.

[18] H. Nowotny, E. Benes, General One-Dimensional Treatment of the Layered Piezoelectric Resonator with 2 Electrodes, Journal of the Acoustical Society of America 82 (1987) 513-521.

[19] M. Hill, R.J.K. Wood, Modelling in the design of a flow-through ultrasonic separator, Ultrasonics 38 (2000) 662-665.

[20] M. Hill, The selection of layer thicknesses to control acoustic radiation force profiles in layered resonators, JASA 114 (2003) 2654-2661.

[21] L.P. Gor'kov, On the forces acting on a small particle in an acoustical field in an ideal fluid, Sov. Phys. Dokl. 6 (1962) 773-775.

[22] S.P. Martin, R.J. Townsend, L.A. Kuznetsova, K.A.J. Borthwick, M. Hill, M.B. McDonnell, W.T. Coakley, Spore and micro-particle capture on an immunosensor surface in an ultrasound standing wave system, Biosensors and Bioelectronics 21 (2005) 758-767.

[23] R.J. Townsend, M. Hill, N.R. Harris, N.M. White, Modelling of particle paths passing through an ultrasonic standing wave, Ultrasonics 42 (2004) 319-324.

[24] R.J. Townsend, M. Hill, N. Harris, M.B. McDonnell, Performance of quarter-wavelength particle concentrators, in: International Congress on Ultrasonics (Vienna, 2007).

[25] Onda Corporation, Tables of Acoustic Properties of Materials, http://www.ondacorp.com/tecref_acoustictable.html, Accessed March 2007

[26] R.J. Townsend, M. Hill, N.R. Harris, N.M. White, Investigation of two-dimensional acoustic resonant modes in a particle separator Ultrasonics 44 (2006) e467-e471.

L4:
Visualization and microscopy

Martin Wiklund

Dept. of Applied Physics
Royal Institute of Technology
Stockholm, Sweden

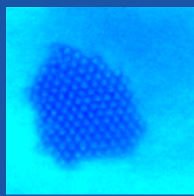

CISM course ”*Ultrasound standing wave action on suspensions and biosuspensions in micro- and macro fluidic systems*”, June 7-11, 2010

M. Wiklund

-1-

Outline

1. **Practical principles of optical microscopy**
2. **Microscopy for lab-on-a-chip devices**
3. **Contrast, fluorescence and confocal techniques**
4. **Particle image velocimetry**

M. Wiklund

-2-

What is the size of biological objects?

Molecule Example: Biotin 1 nm Antibody 15 nm	0.5 – 50 nm	sizes fitting well into lab-on-a-chip systems:
Virus	10 – 100 nm	sizes covered by optical microscopy:
Cluster of molecules	up to 5 μm	
Bacteria (prokaryotic)	0.5 – 5 μm (length)	
Cell (eukaryotic) Example: Red blood cell 2×7 μm White blood cell 15 μm	5 – 50 μm	

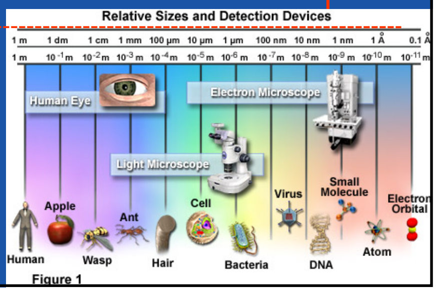

M. Wiklund

Basic modes/terms of microscopy

1. **Wide-field microscopy**
   Entire sample (or field of view) is uniformly illuminated
2. **Confocal microscopy**
   Small focused spot is illunimating one sample point, and then scanned over the sample (or field of view)
3. **Bright-field microscopy**
   The sample is illuminated with white light
4. **Fluorescence microscopy**
   The sample is illuminated with color-specific light and then observed in another color band (i.e., the excitation light is filtered out from the image)
5. **Trans-illumination microscopy**
   Illuminate from one side, look from the other side, often combined with condenser optics (e.g., for contrast techniques)
6. **Epi-illumination microscopy**
   Illuminate and look from the same side, used for surface imaging and fluorescence imaging

M. Wiklund

Wide-field microscopy

Two lenses (lens systems):
The objective and the eyepiece (or ocular)

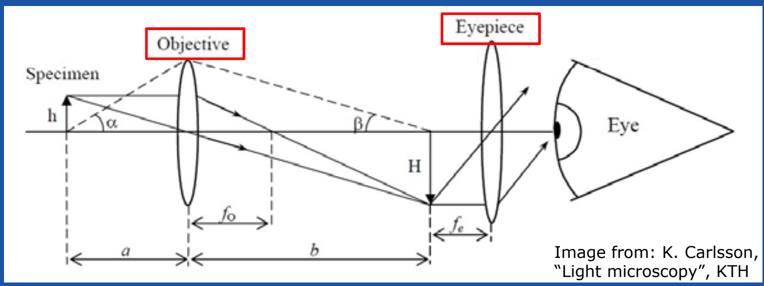

Image from: K. Carlsson, "Light microscopy", KTH

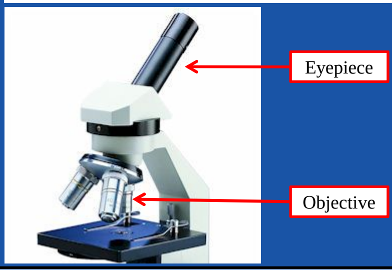

Magnification:

$$M_{objective} = H/h = b/a$$

$$M_{eyepiece} = 250\,(mm)/f_e\,(mm)$$

$$M_{tot} = M_{objective} \cdot M_{eyepiece}$$

KTH Physics

M. Wiklund

-5-

Wide-field microscopy

Two lenses (lens systems):
The objective and the eyepiece (or ocular)

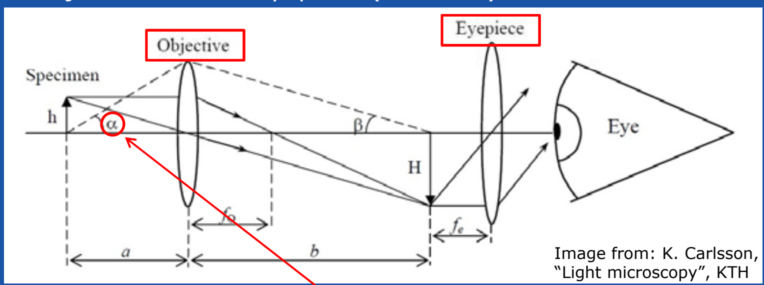

Image from: K. Carlsson, "Light microscopy", KTH

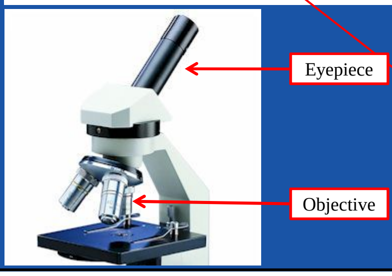

Numerical aperture:

$$N.A. = n \cdot \sin\alpha$$

KTH Physics

M. Wiklund

-6-

Wide-field microscopy

Köhler illumination:
The standard alignment of the condenser illumination light
Principle: Separation of the illumination and imaging ray path
(When one is focused, the other one is defocued)

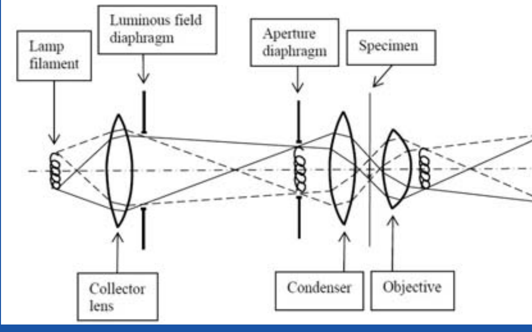

Image from: K. Carlsson, "Light microscopy", KTH

Motive:
-Uniform illumination of the sample
-High light throughput
-Adjustable light intensity and illuminated area

M. Wiklund

-7-

Wide-field microscopy

Epi-illumination:
The objective is also the condenser
(illuminate and look from the same side)

Very useful in fluorescence microscopy

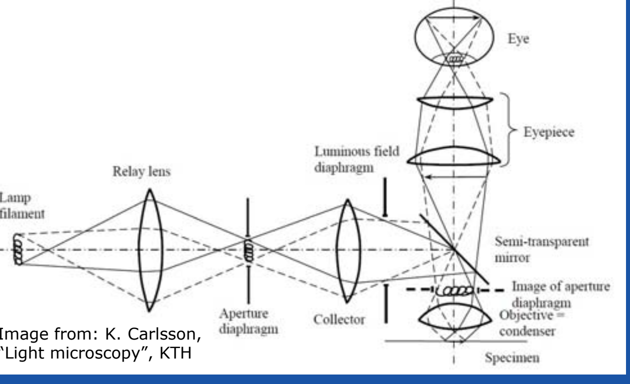

Image from: K. Carlsson, "Light microscopy", KTH

M. Wiklund

-8-

Wide-field microscopy

Epi-fluorescence microscopy:

The beam splitter is a filter cube consisting of an excitation filter, a dichroic beam splitter and a barrier filter

Simpler condenser optics (it does not matter from where we illuminate)

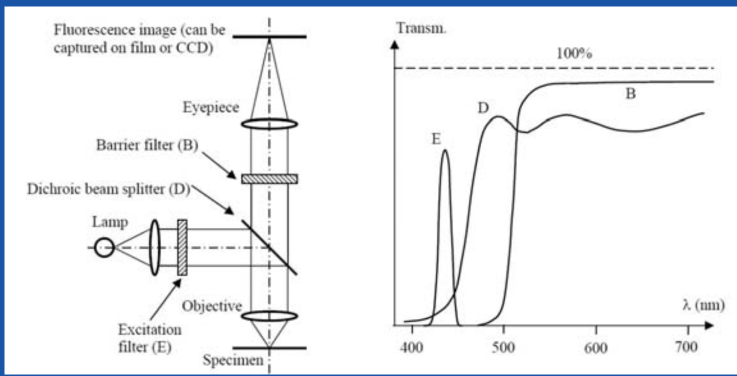

Image from: K. Carlsson, "Light microscopy", KTH

M. Wiklund

Basic microscopy properties

Numerical aperture (more):

$N.A. = n \cdot \sin\alpha$

Coding of the objectives:

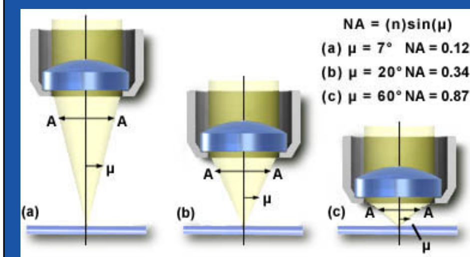

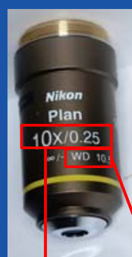

High *N. A.* means high resolution, but also small depth of field, and small working distance

Magn. / N.A.

Working distance

M. Wiklund

Basic microscopy properties

More advanced objectives:

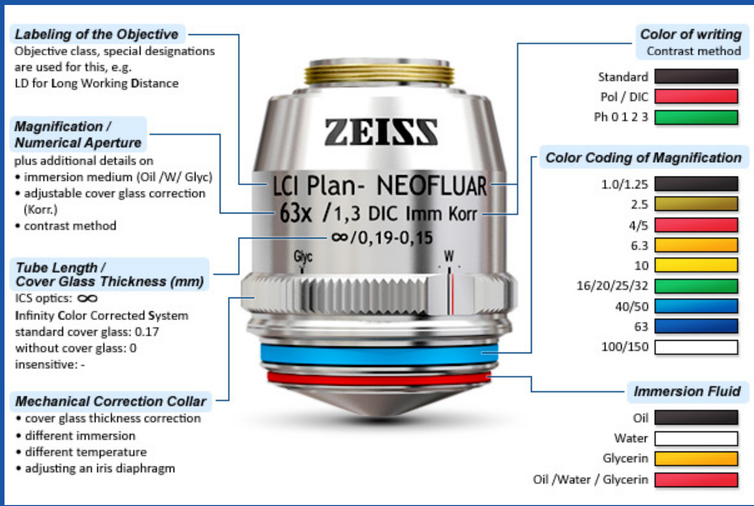

From: http://zeiss-campus.magnet.fsu.edu/tutorials/

M. Wiklund

Basic microscopy properties

Resolution:

The imaged pattern of a point source (the point spread function)

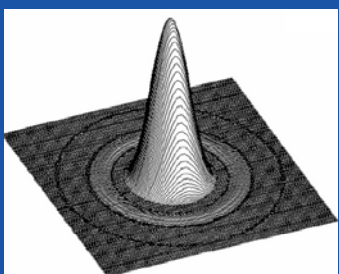

Smallest resolvable distance between two point spread functions?

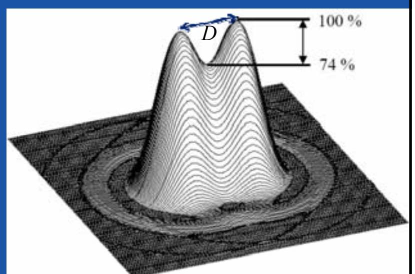

$$D = \frac{0.61 \cdot \lambda}{N.A.}$$

Object:

Image:

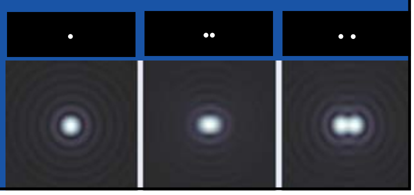

Example: $N.A.$ = 1.4 (oil imm.)
λ = 458 nm (blue) ⇨ $\boldsymbol{D}$ **= 200 nm**

M. Wiklund

Basic microscopy properties

Aberrations:

The fundamental resolution limit is diffraction-limited

Thus, the 200 nm resolution is close to the fundamental limit for standard (visual) light microscopy

In reality, aberrations are often the bottle-neck for the resolution

Aberration-correction is made by combining several lenses:

An objective with very high performance (and cost), high *N.A.* and low levels of aberrations

From: http://www.microscopyu.com/

M. Wiklund

-13-

Basic microscopy properties

Aberrations:

Most important aberrations to correct:

Chromatic aberration

Field curvature

Principle:

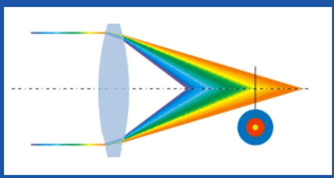

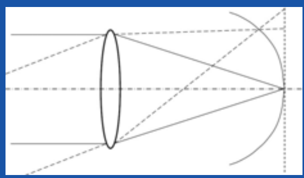

Examples:

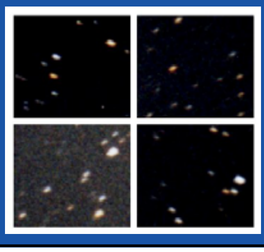

M. Wiklund

-14-

Basic microscopy properties

Aberrations:

Classes of aberration-corrected objectives:

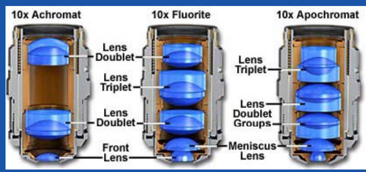

From: http://www.microscopyu.com/

NAME	PERFORMANCE	COST
Achromat	Color-corrected, narrow band	$
Plan Achromat	Including field curvature correction	$$
Fluorites	Color-corrected, intermediate band	$$$
Plan Fluorites	Including field curvature correction	$$$$
Apochromat	Color-corrected, wide band	$$$$$
Plan Apochromat	Including field curvature correction	$$$$$$

(The price range is typically 100-10.000 Euros)

M. Wiklund

-15-

Microscopy for lab-on-a-chip devices

What objective should I choose?

Let's take the chip in the Wiklund group as an example!

5 × λ/4-reflector
= 1 mm top glass

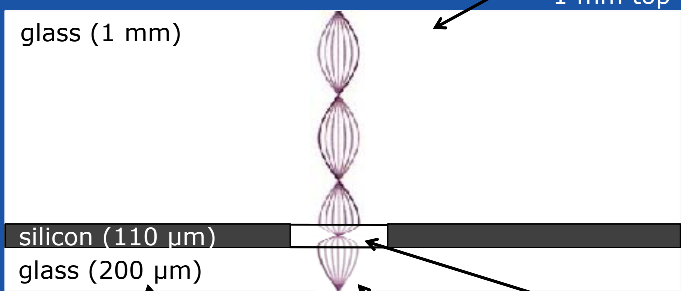

High resolution
⇨ coverslip-thickness
of bottom glass

λ/4-reflector
⇨ 6.9 MHz
in Pyrex

λ/2-chamber
⇨ 110 µm
in water

M. Wiklund

-16-

Microscopy for lab-on-a-chip devices

What objective should I choose?

Best objective for imaging a "levitated" cell?

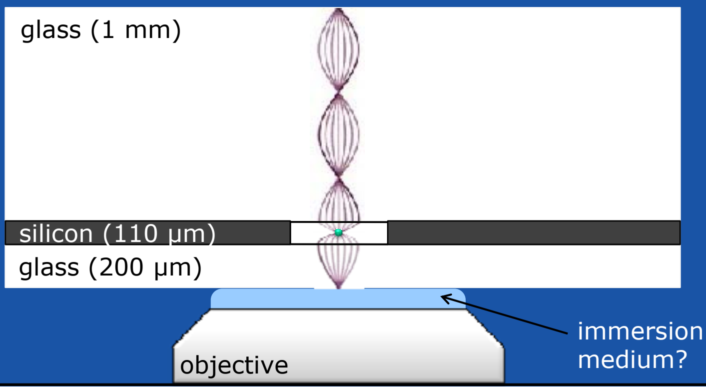

M. Wiklund

Microscopy for lab-on-a-chip devices

What objective should I choose?

Immersion medium:

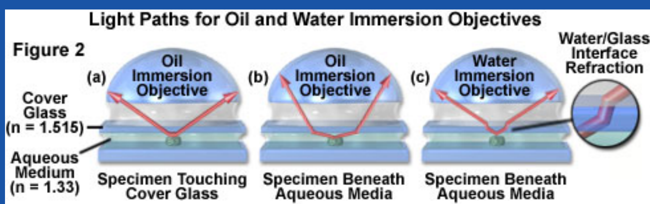

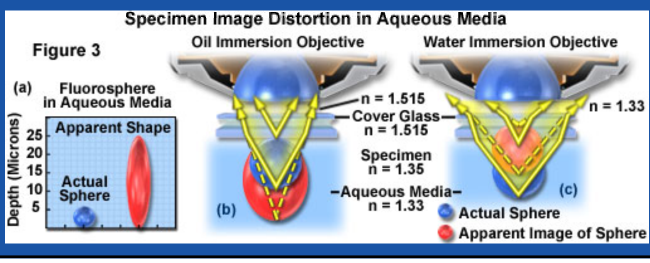

M. Wiklund

Microscopy for lab-on-a-chip devices

What objective should I choose?

Low-N.A., no immersion medium (just air):
Good for imaging sharp *in the whole channel*
(depth-of-focus matching the channel height)

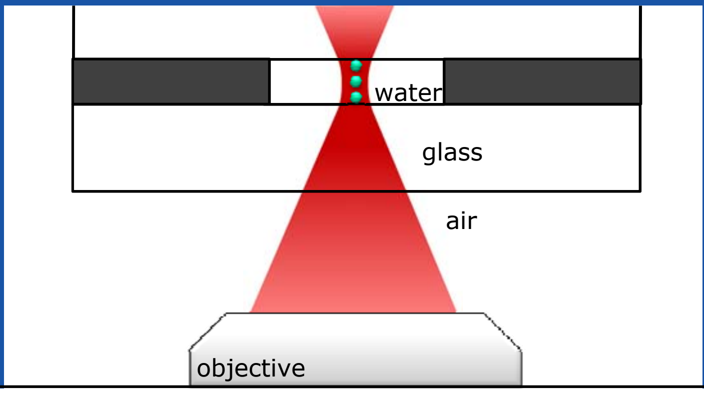

M. Wiklund

-19-

Microscopy for lab-on-a-chip devices

What objective should I choose?

High-N.A., oil immersion medium:
Good for high-resolution imaging *on the bottom* of the channel (smaller working distance, smaller depth-of-focus)

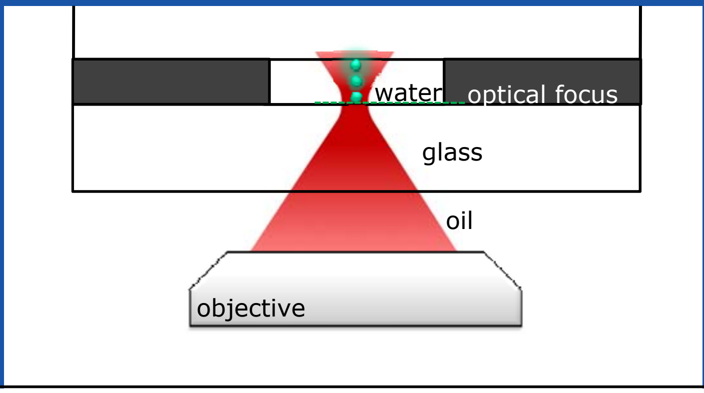

M. Wiklund

-20-

Microscopy for lab-on-a-chip devices

What objective should I choose?

<u>High-N.A., water immersion medium:</u>
Good for high-resolution imaging <u>*in the middle*</u> of the channel (smaller working distance, smaller depth-of-focus)

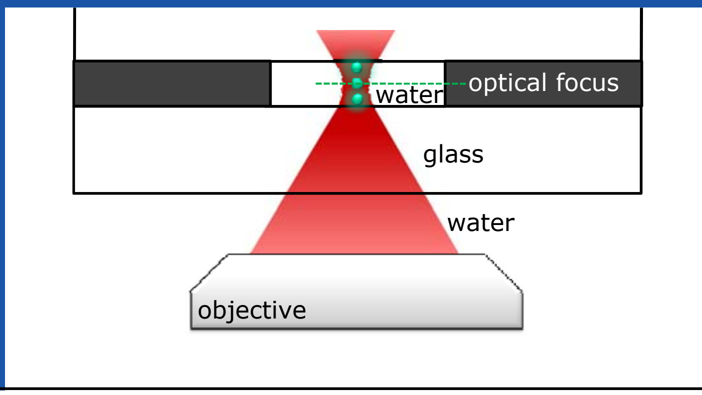

M. Wiklund

-21-

Microscopy for lab-on-a-chip devices

What objective should I choose?

<u>Summary</u>

Do you need:

- Large or small depth-of-focus
- Large or small field-of view
- Low or high magnification
- Low or high resolution

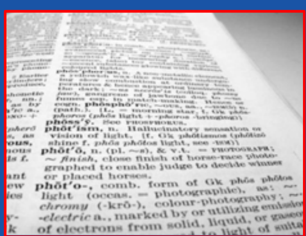

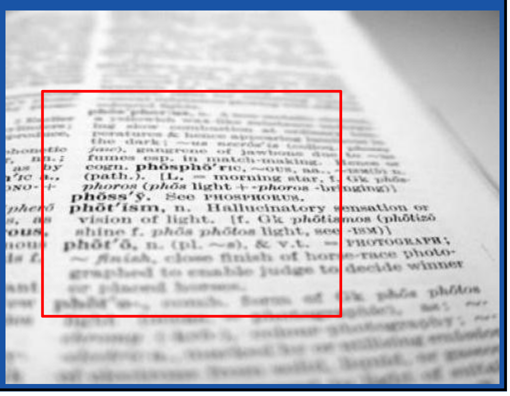

M. Wiklund

-22-

Microscopy for lab-on-a-chip devices

How to design a chip compatible with (any kind of) high-resolution optical microscopy?

You need a transparent chip with thin glass (from one side)!

Cross-section side-view

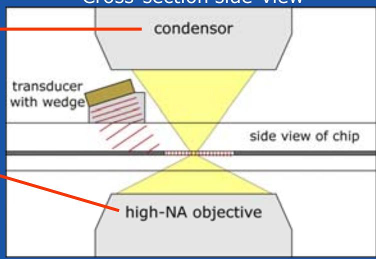

Top-view

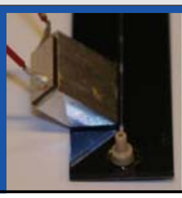

M. Wiklund

-23-

Microscopy for lab-on-a-chip devices

How to design a chip compatible with (any kind of) high-resolution optical microscopy?

You need a transparent chip with thin glass (from one side)!

But, do we really need transmission? Why not use reflection microscopy?

Reflection microscopy is primarily designed for surface investigations (such as printed circuit boards)

But, it works fine for non-transparent, or semi-transparent objects (such as polystyrene beads, metals)

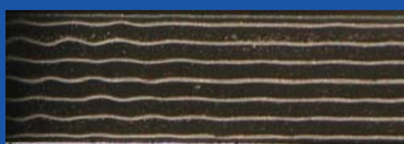

2 µm beads, non-transparent chip

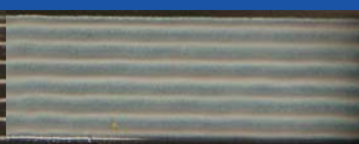

400 nm beads, non-transparent chip

M. Wiklund

-24-

Microscopy for lab-on-a-chip devices

How to design a chip compatible with (any kind of) high-resolution optical microscopy?

You need a transparent chip with thin glass (from one side)!

But, do we really need transmission? Why not use reflection microscopy?

Cells, however, are very transparent!

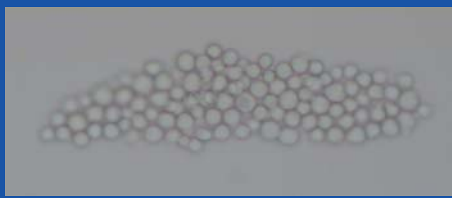

Trapped COS-7 cells imaged with trans-Illumination microscopy

KTH Physics

M. Wiklund

-25-

Constrast modes

Even if you have good resolution, your image is useless without good contrast

Tricky imaging task: Cells in a water-based medium (cells are very transparent and contains mostly of water)

Solution: Add constrast by either a constrast agent (fluorescent probe) or a constrast imaging technique

high contrast

low contrast

KTH Physics

M. Wiklund

-26-

Contrast techniques

Examples of contrast techniques
(for bright-field microscopy)

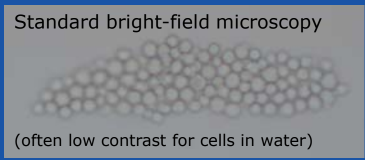

...and the winner is...

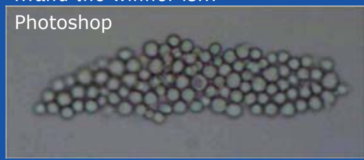

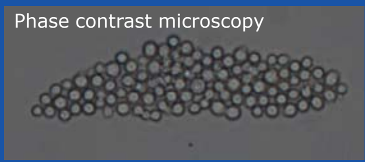

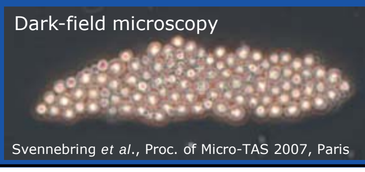

Differential interference contrast (DIC) microscopy

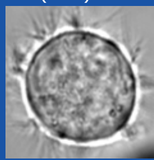

Manneberg *et al.*,
Appl. Phys. Lett. 2008

M. Wiklund

-27-

Contrast techniques

Phase contrast: Principles

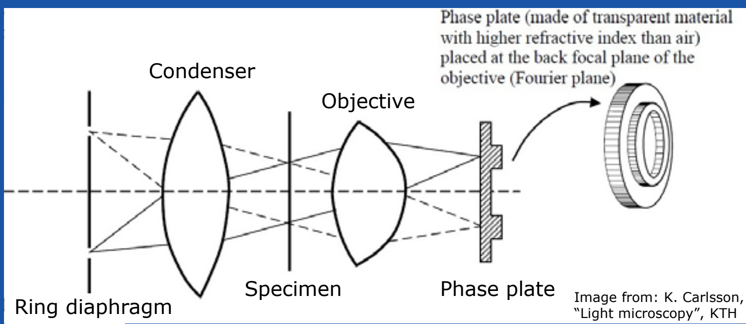

Best for thin and highly transparent materials

M. Wiklund

-28-

Contrast techniques

Dark field: Principles

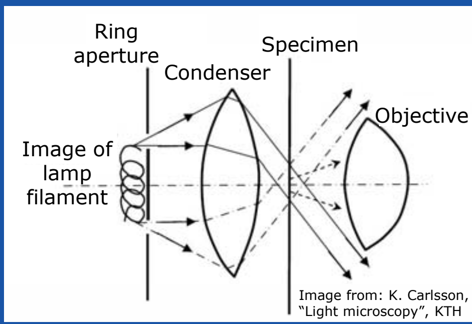

Image from: K. Carlsson, "Light microscopy", KTH

Dark field microscopy

Only scattered light can enter the objective

Need higher N.A. of the condensor than of the objective

M. Wiklund

Contrast techniques

Differential interference contrast (DIC): Principles

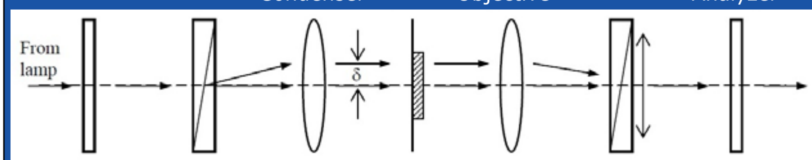

Image from: K. Carlsson, "Light microscopy", KTH

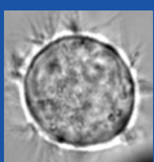

DIC microscopy

Produces "relief landscape" images with "3D impression"

However, no topology information!

Can be used on thicker samples

M. Wiklund

Contrast techniques

Contrast in epi-reflection mode (bright-field), cells in suspensions?

In general, this should not be a very successful idea

However, a nice example from the Cardiff device (Prof. Coakley group, now Despina Bazou):

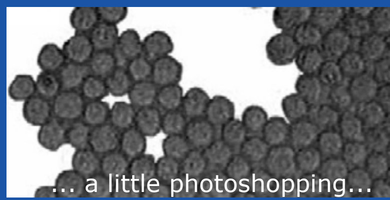

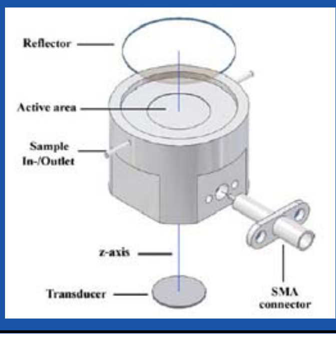

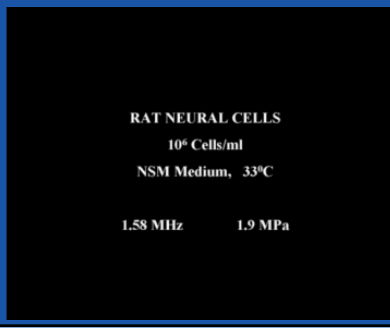

M. Wiklund

-31-

Contrast agents – fluorescent probes

Fluorescence: Basic principles

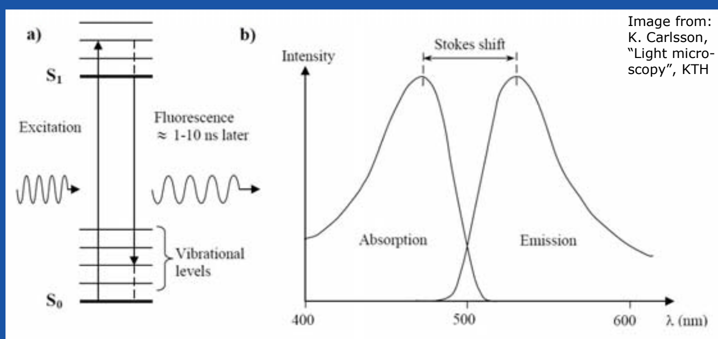

Energy level diagram with the electronic states S_0 and S_1, and the vibrational levels

Absorption and emission spectra of a typical fluorophore

M. Wiklund

-32-

Combining trans- and epi-illumination

Bright field: Trans-illumination (from above)
Fluorescence: Epi-illumination (from below)
Yellow background due to the fluorescence filter cube (blocking the blue wavelength band)

Full bright-field + fluorescence

Low bright-field + fluorescence

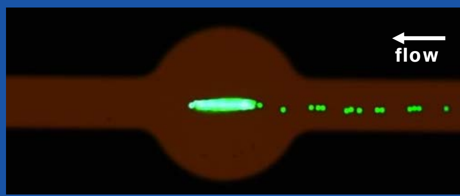

M. Wiklund

Combining trans- and epi-illumination

Bright field: Trans-illumination (from above)
Fluorescence: Epi-illumination (from below)

White light sources:

Mercury lamps often used in fluorescence microscopy
(can not be intensity-tuned, gray filters must be used)
Halogen lamps better suited for white light illumination
(can be intensity-tuned)

From: http://zeiss-campus.magnet.fsu.edu/

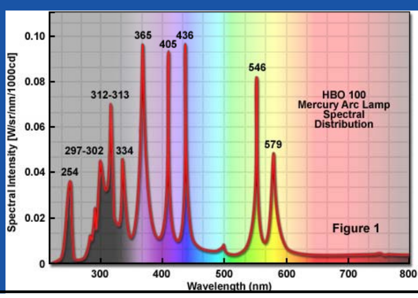

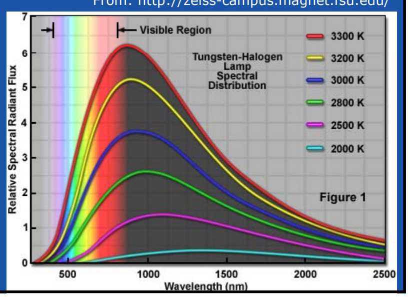

M. Wiklund

Contrast agents – fluorescent probes

Immuno-fluorescence: Contrast + specific imaging!
(Attach a fluorophore to an antibody)

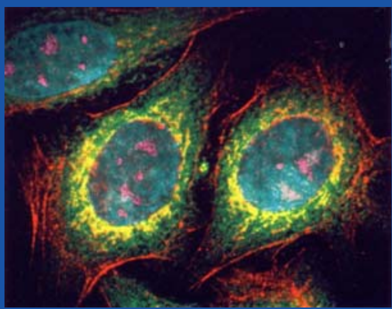

Image from: http://www.probes.com/

Example image:

Cyan:	Nuclei
Magneta:	Ki-67 (growth fraction marker)
Orange:	Mitochondria
Green:	Microtubules
Red:	Actin filaments

KTH Physics

M. Wiklund

-35-

Confocal microscopy

Basic principles

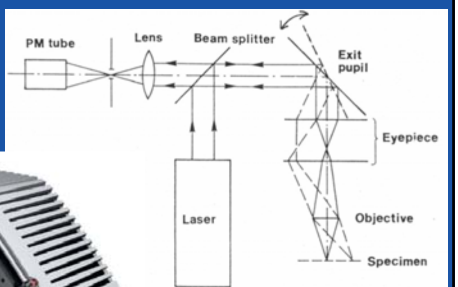

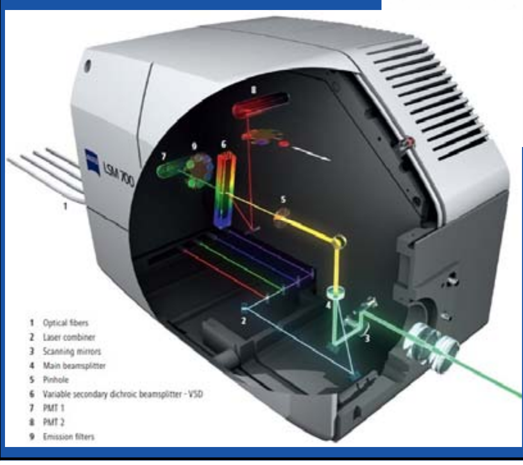

Images from:
http://www.zeiss.com/

KTH Physics

M. Wiklund

-36-

Summary of microscopy techniques

Left: DIC bright field　　Right: confocal fluorescence

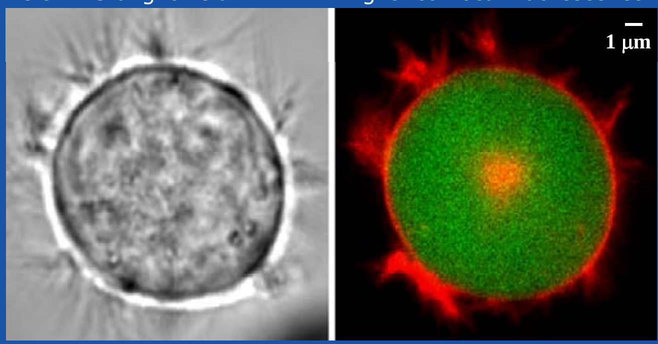

100x-objective imaging of a B cell (human immune cell)

Red label: membrane probe (DiD)

Green label: viability probe (calcein-AM)

Manneberg *et al.*, Appl. Phys. Lett., 2008

M. Wiklund

-37-

Confocal microscopy: 2D projections from 3D stacks

Rotating 3D view

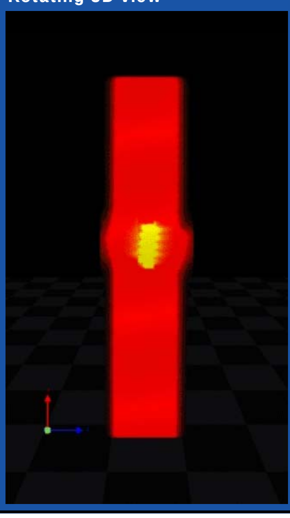

A stack of 2D scans through the depth

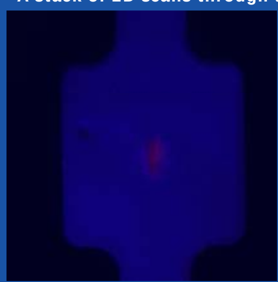

Fluorescent beads in a rhodamine solution

side view　top view　side view　top view

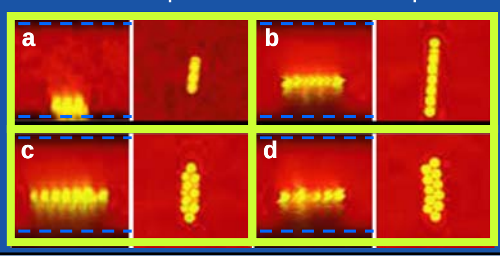

M. Wiklund

Positioning performance with B cells

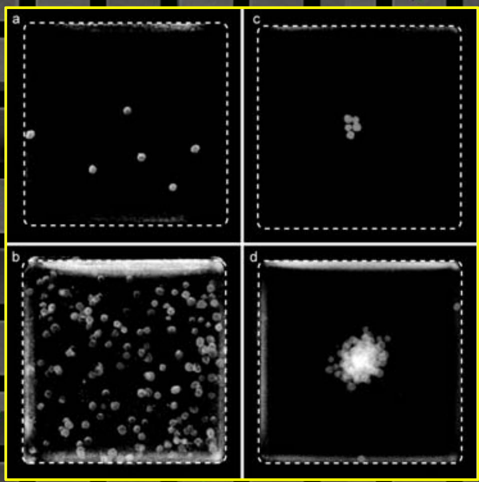

Vanherberghen *et al*, submitted manuscript

KTH Physics

M. Wiklund

Video demo

Vanherberghen *et al*, submitted manuscript

KTH Physics

M. Wiklund

Imaging the immune synapse in cells trapped with ultrasound

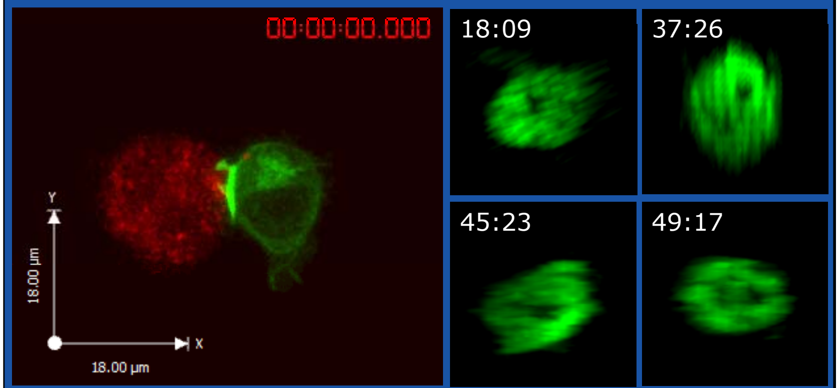

M. Wiklund

Particle image velocimetry

5 µm bead

1 µm bead

Acoustic *streaming* characterization
with particle image velocimetry (PIV)

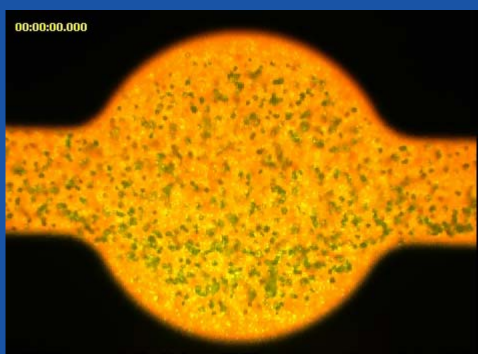

M. Wiklund

Particle image velocimetry

5 µm bead

1 µm bead

Acoustic *streaming* characterization
with particle image velocimetry (PIV)

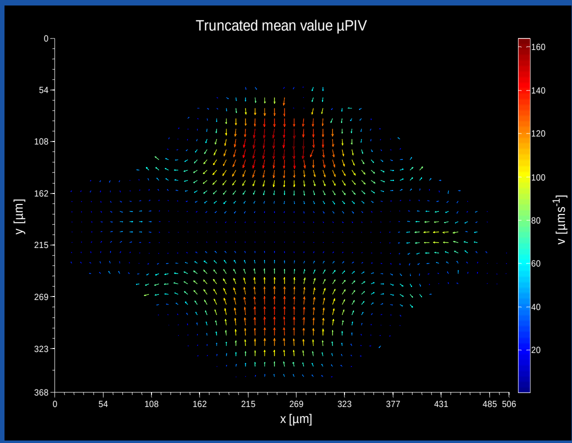

M. Wiklund

Particle image velocimetry

5 µm bead

Acoustic *radiation force* characterization
with particle image velocimetry (PIV)

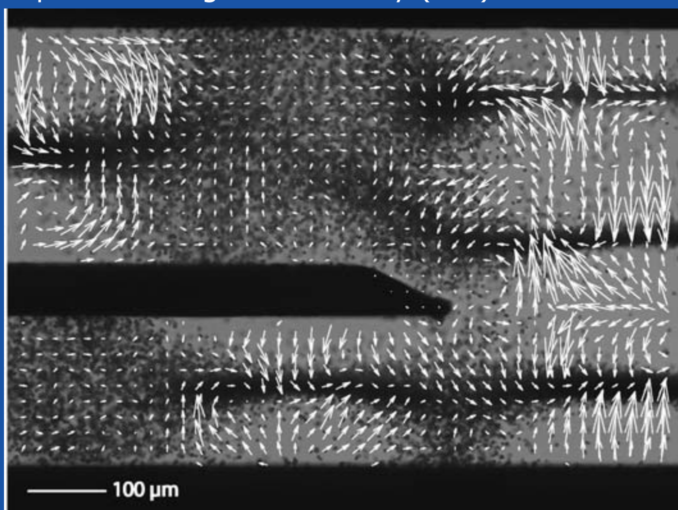

Overlay of the PIV vector field when turning on the transducer, with the image of trapped beads when a near-static bead distribution is obtained

M. Wiklund

Particle image velocimetry (PIV)

Basic principle:
-Pair-wise image correlation for particle tracking

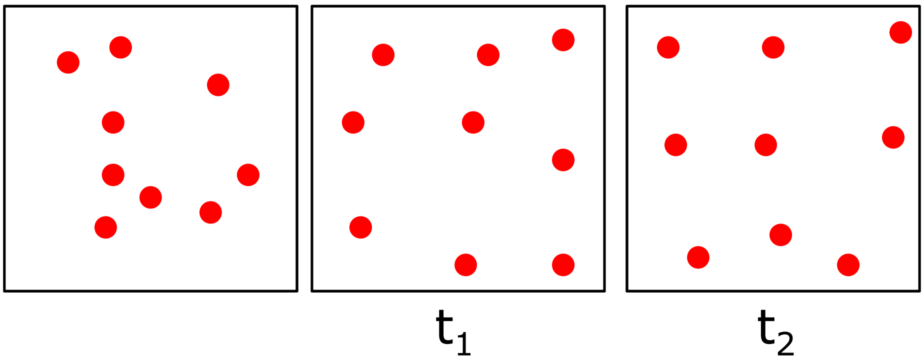

Mathias Ohlin, Diploma Thesis, KTH, 2010

Particle image velocimetry (PIV)

Basic principle:
-Pair-wise image correlation for particle tracking

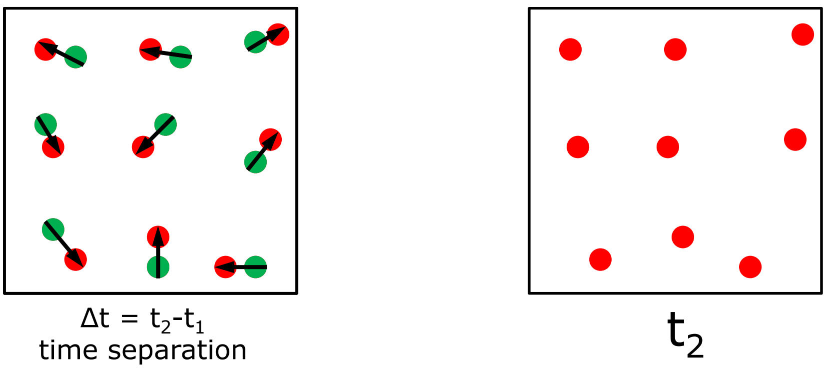

Mathias Ohlin, Diploma Thesis, KTH, 2010

Particle image velocimetry (PIV)

Implementation:
-Defining interrogation windows

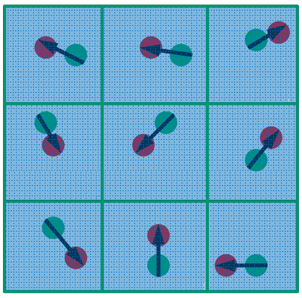

Mathias Ohlin, Diploma Thesis, KTH, 2010

Particle image velocimetry (PIV)

Implementation:
-Defining interrogation windows, correlation example

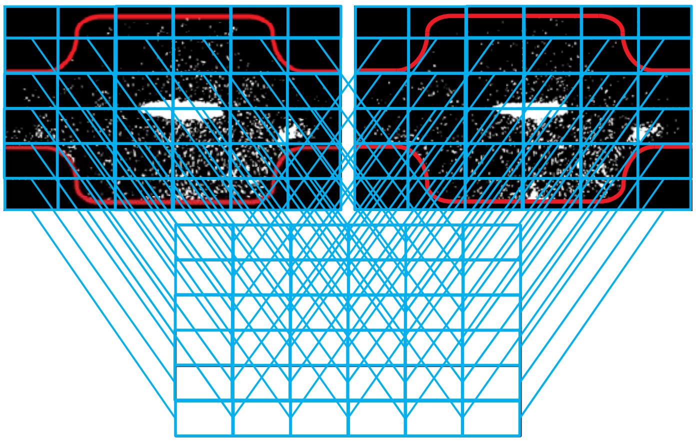

Mathias Ohlin, Diploma Thesis, KTH, 2010

Particle image velocimetry (PIV)

<u>What do you need?</u>

1. A microscope and a camera
2. Open source PIV algorithms
   (*http://www.oceanwave.jp/softwares/mpiv/*)
3. Optional: Graphical user interface (GUI)
   (in-house developed, Mathias Ohlin, KTH, 2009)

sis, KTH, 2010

Particle image velocimetry (PIV)

Eckart streaming in a 96-well microplate

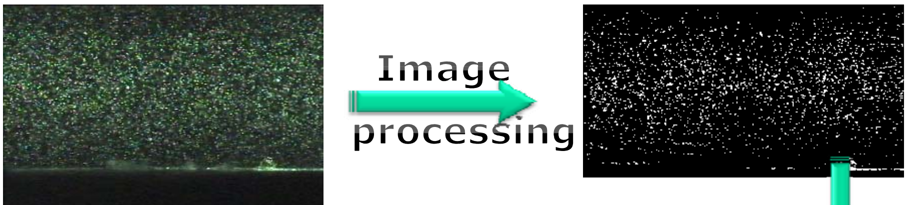

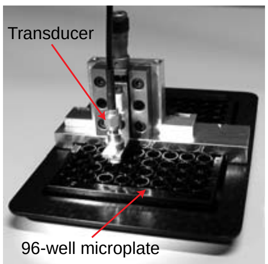

Wiklund et al., J. Appl. Phys., 2004

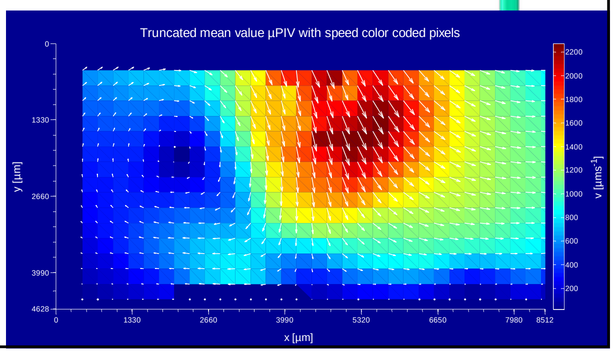

Electrical considerations and Bubble behaviour in ultrasonic particle manipulation.

Peter Glynne-Jones

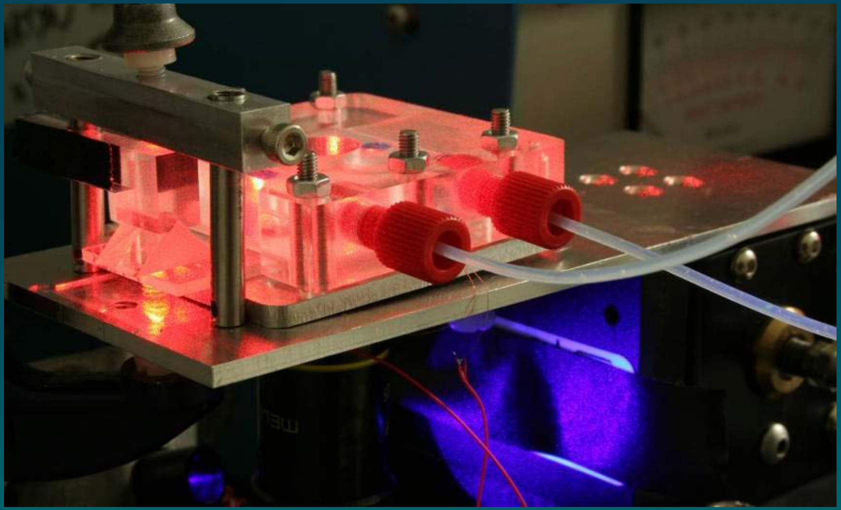

In this talk:

- Electrical considerations
  - How do we drive our devices, and choose the correct operating frequency?
  - Electrical matching and cable effects
- Cavitation and behaviour of bubbles

Back to the impedance spectrum…

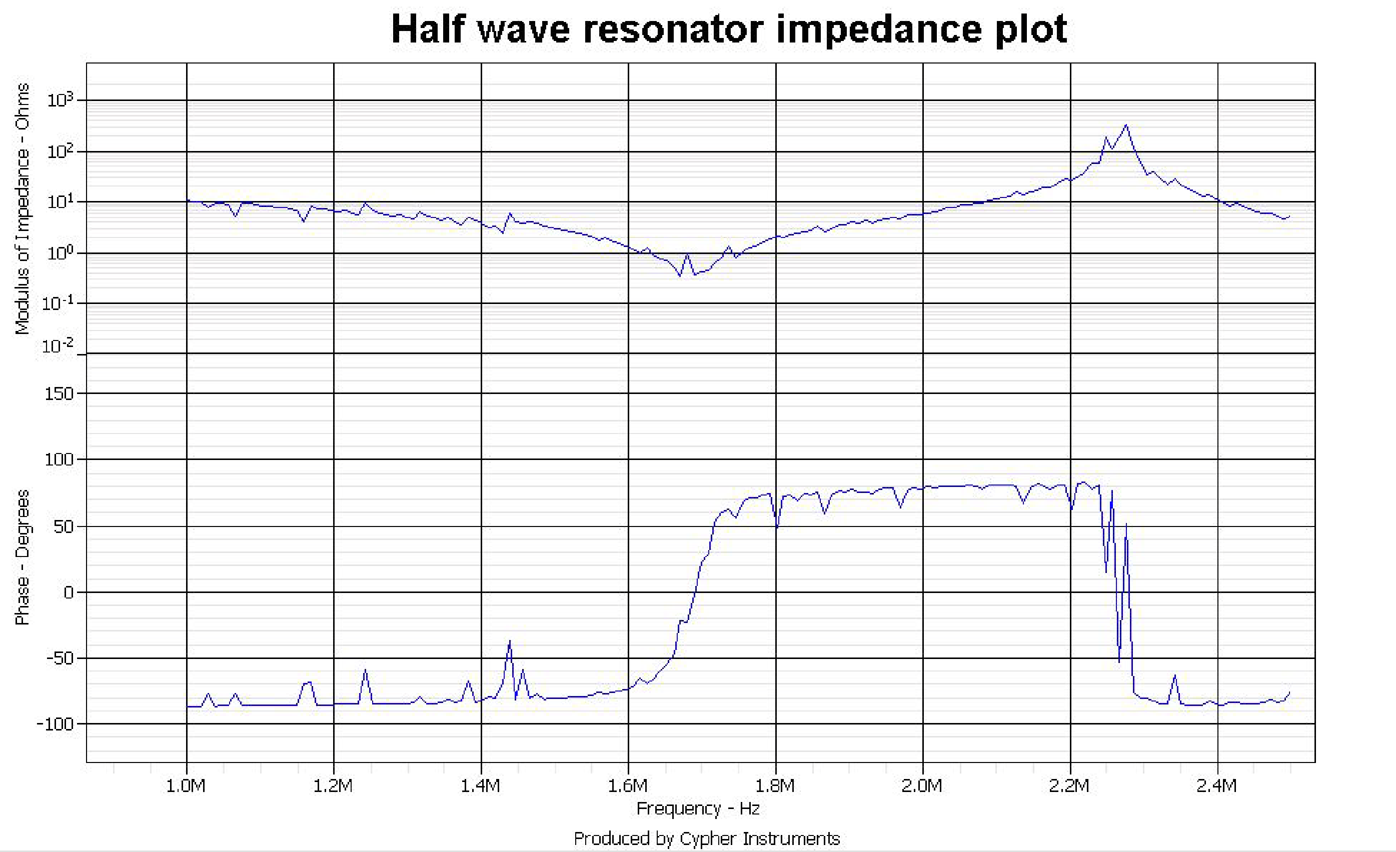

The origins of the Impedance spectrum

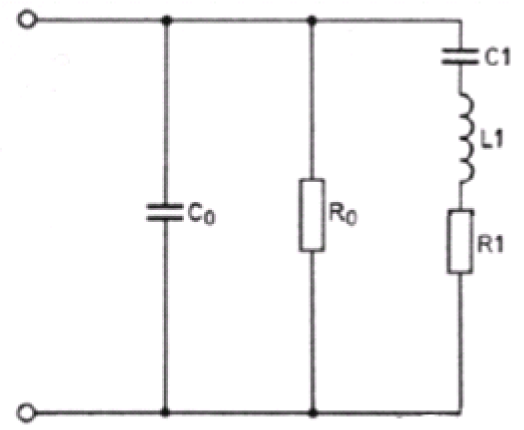

Simple model of a transducer near resonance

C0, R0 represent the electrical domain

C1, L1, R1 the mechanical domain

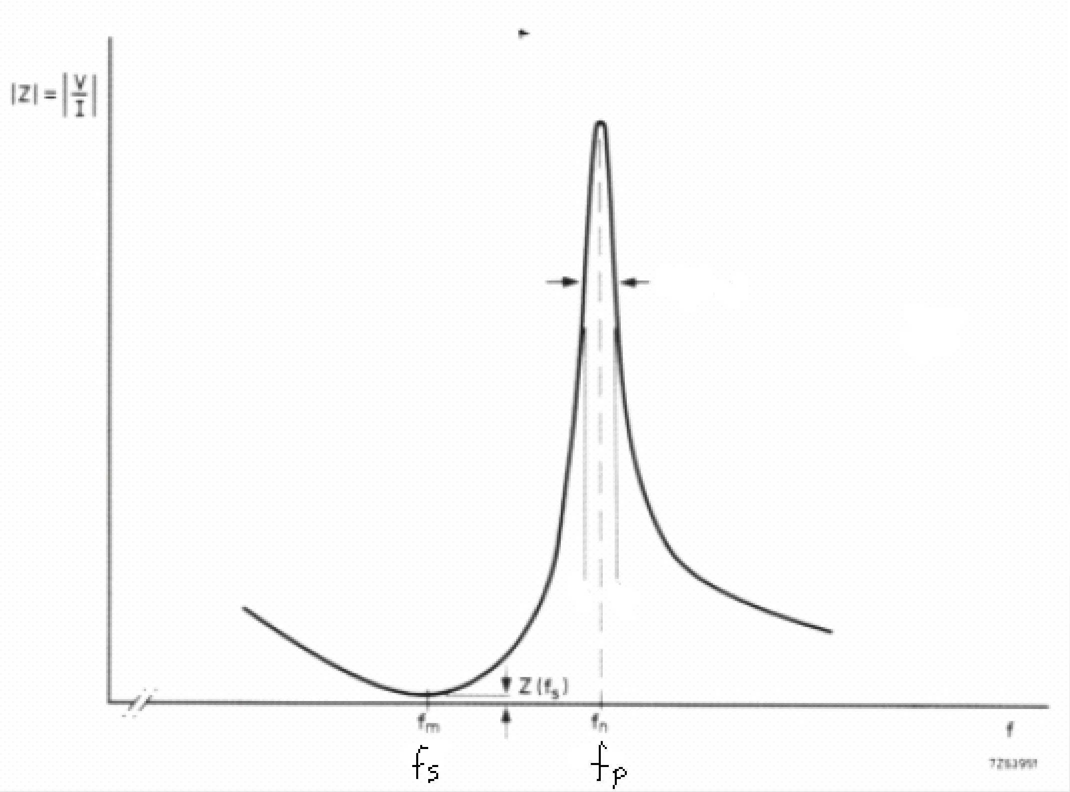

Series resonance includes C1,L1, R1 only. Parallel resonance includes all components

Images from “Guide to piezoelectric and dielectric ceramics”, Morgan Electroceramics.

http://www.morganelectroceramics.com/resources/guide-to-piezoelectric-dielectric-ceramic/

How do we choose our operating frequency?

Impedance of a quarter wave layered resonator

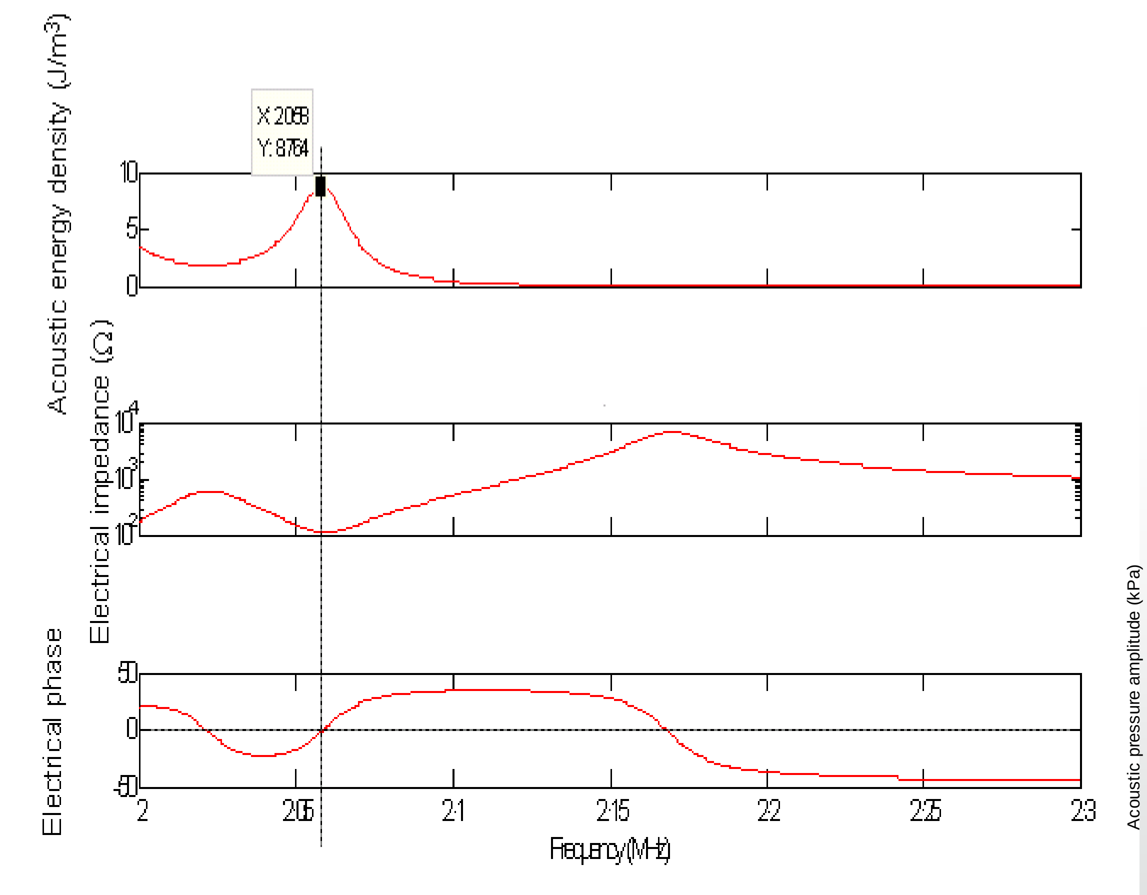

Transducer (PZT26): 1mm thick

Matching Layer (ceramic): 1.42mm

Fluid Layer: 0.17mm

Reflector (glass): 1.45mm

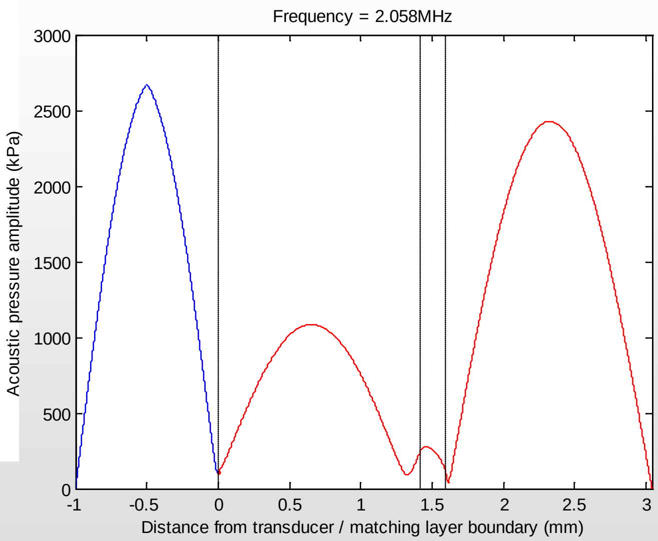

A case with weaker transducer/fluid coupling:

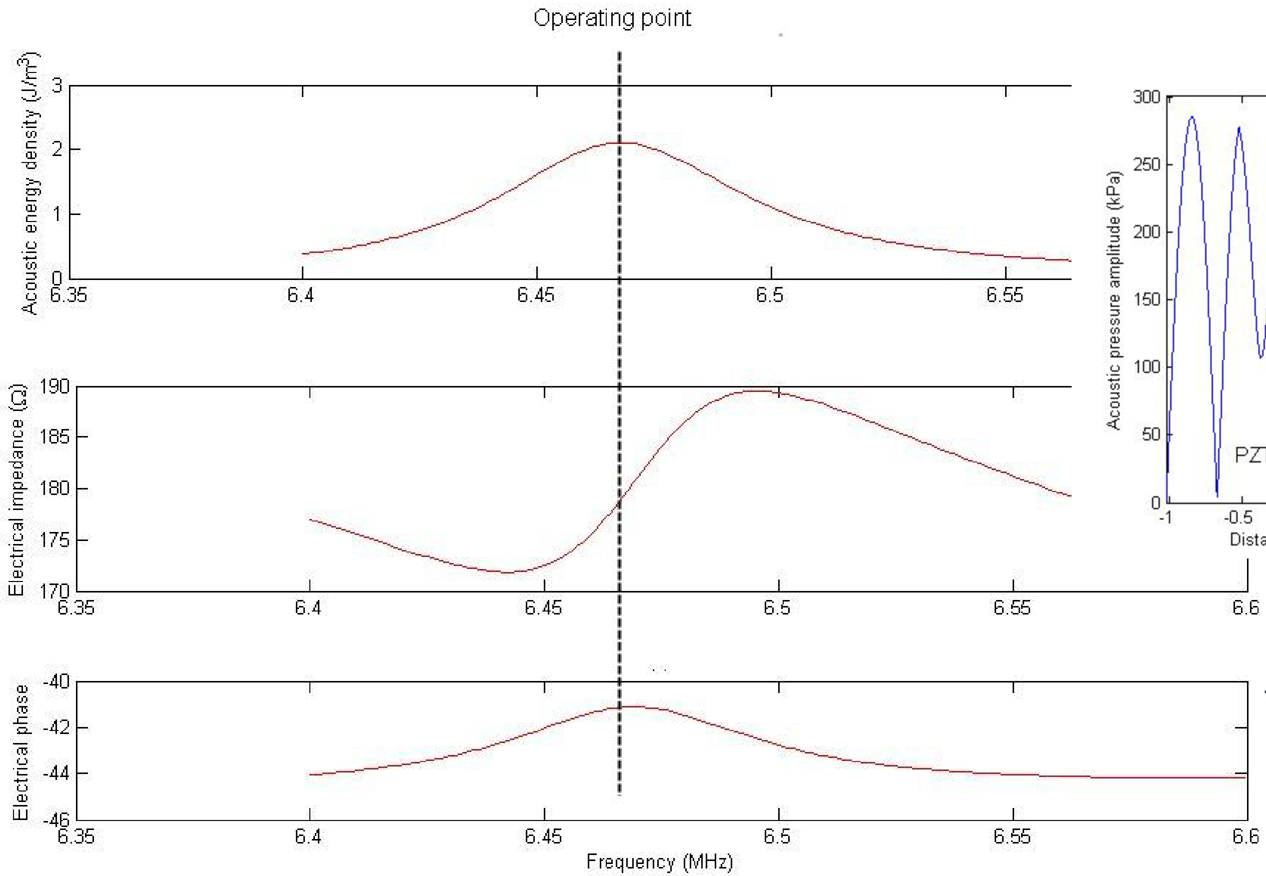

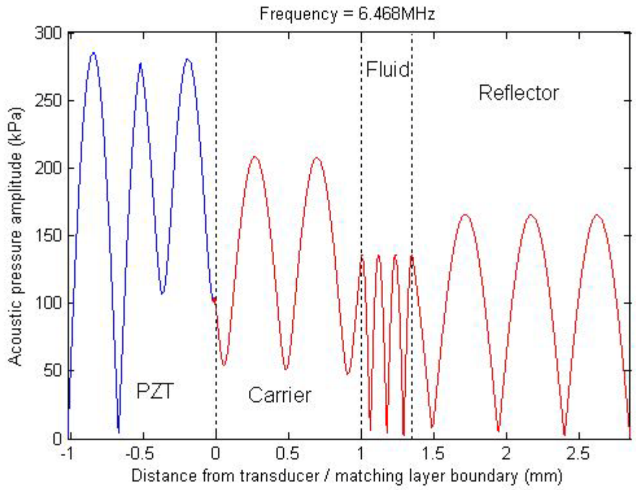

Transducer (PZT26): 1mm thick

Matching Layer (ceramic): 1mm

Fluid Layer: 0.35mm

Reflector (glass): 1.5mm

The resonance no longer occurs at the impedance minimum!

Electrical Phase and Impedance at resonance

- The acoustic energy density in the fluid layer is often used in models to identify the desired operating point.
- If the transducer is strongly coupled to the device resonance, the phase will often be zero with an associated impedance minimum at this resonance.
- If the transducer is weakly coupled, the resonance does not occur at a well defined point on the impedance curve.

Automatic resonance tracking

- In those cases where the electrical impedance is at a minimum, and the phase zero at resonance, tracking is straightforward.

- If the transducer is only weakly coupled to the resonance what can be done?
  - Frequency sweeping (at expense of efficiency)
  - Feedback from a detector hydrophone

Driving electronics

- Signal generators
  - Can drive small transducers directly
- RF power amplifiers
  - Expensive, power hungry, and large
- Custom electronics:
  - Consider the BUF634T driver opamp: 250mA drive current at up to 180MHz, 36Vpp maximum.
  - Or: LT1210: 1.1A drive at up to 35MHz, 30Vpp.

These can be operated in pairs to double the output swing

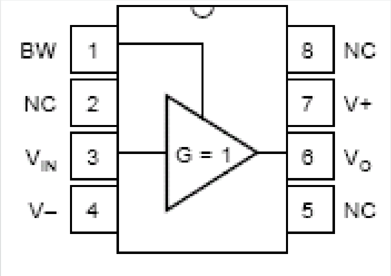

Southampton UNIVERSITY OF

Matching

- In traditional transducer design inductive elements are often added to increase drive efficiency by forming a resonant circuit with the electrical capacitance, C_0. This tuning can be difficult (Due to drift: thermal, mechanical)
- In layered standing wave ultrasonic devices this is not helpful as the transducer impedance is usually real at resonance.
- A transformer can be used to match this real impedance to the impedance of the driving amplifier and provide voltage gain. Typically 1-10 turns on a ferrite core up to 20mm in diameter.
- Transmission line transformers can also be used. These can be smaller and more efficient

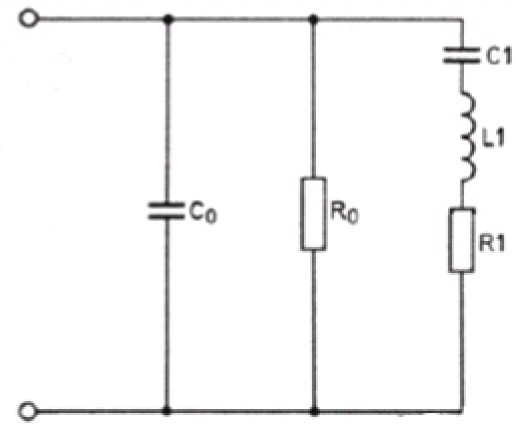

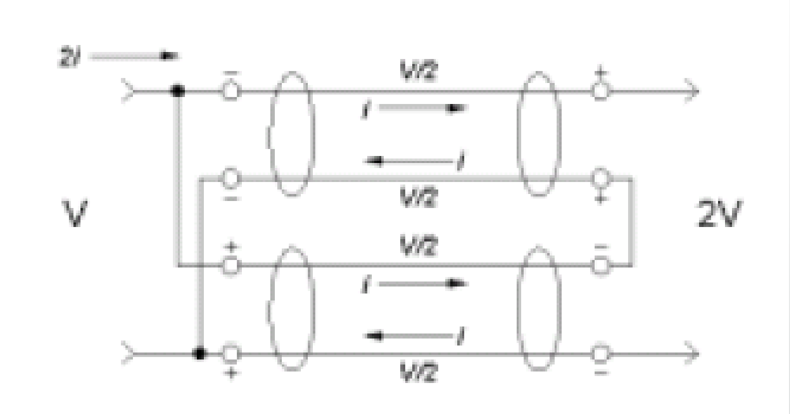

The Guenalla 1:4 transmission line transformer. After Trask, “A Tutorial on Transmission Line Transformers”

Cable effects

- Resonance shift in a transducer (50mmx 25mm) with changing lengths of coax cable (up to ~1.5m).

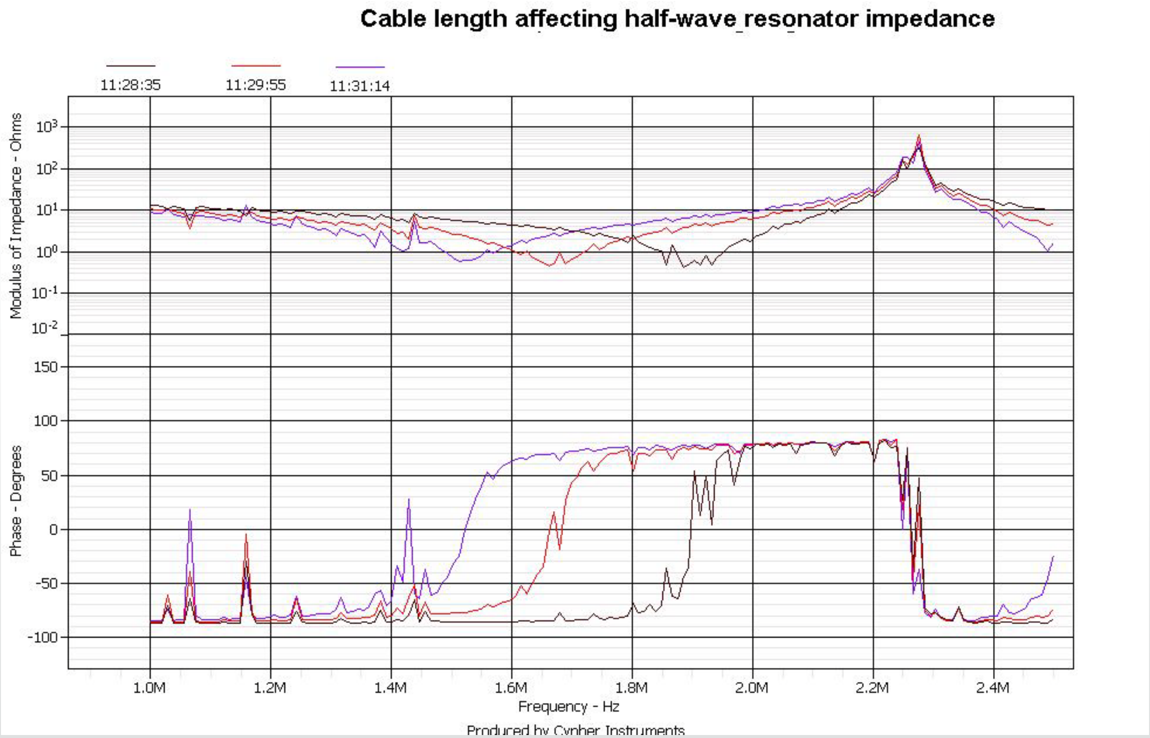

Cable effects

- BNC cables are often used to hook-up devices. What effect do they have on the system resonance?
  - At 10MHz transmission line wavelength is ~20m so transmission line effects can usually be ignored.
  - However, cables posses distributed capacitance and inductance, that can be of same order of magnitude as transducer parameters, causing a shift in the resonant frequency. This must be modelled.

Other wire types also have an effect

Modelled cable effects

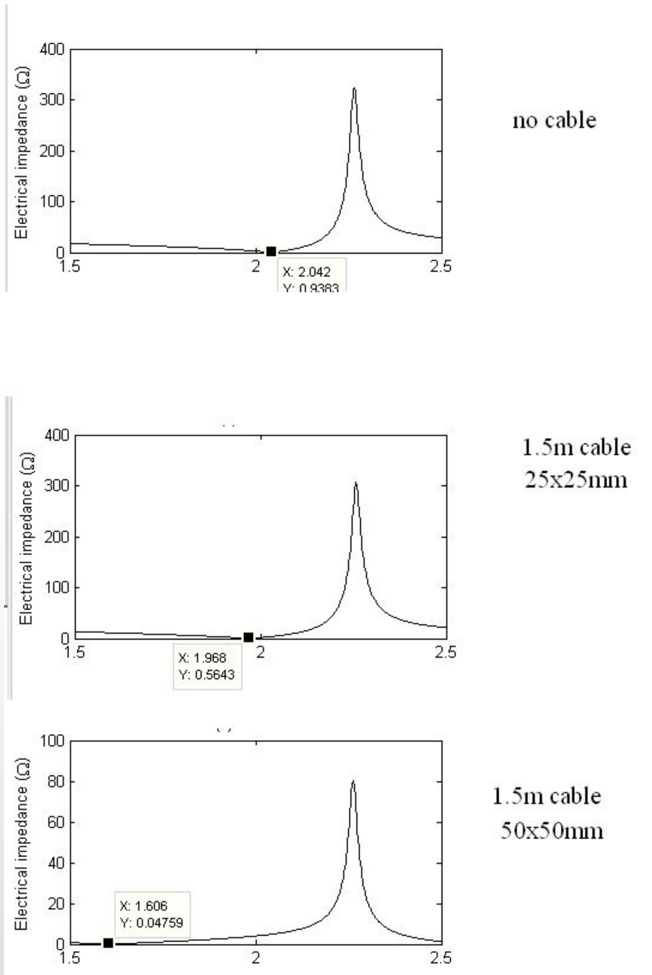

Larger transducers

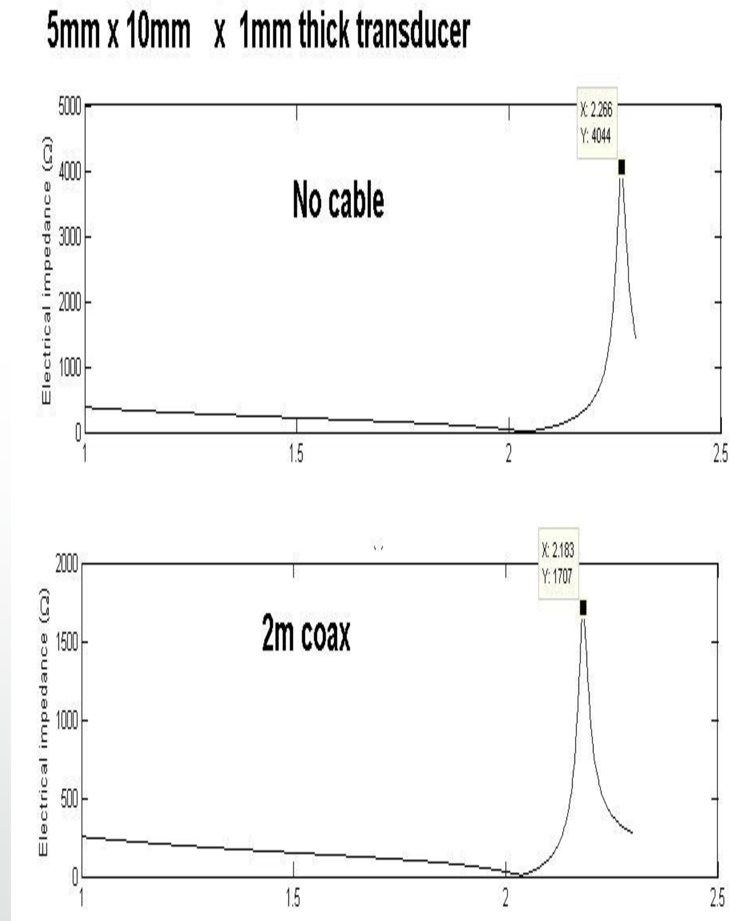

Smaller transducer

Cable matching

- With 50Ω co-ax cable, larger transducers tend to have a shifted mechanical (series) resonance, while smaller ones have more of an electrical (parallel) resonance shift.

- Even with smaller transducers, higher inductance cables (eg. thin twisted pair wires), can cause a significant shift in the mechanical resonance.

- This may be useful for actively shifting resonances and node positions.

Cavitation

- Types of cavitation
  - Transient / Unstable
  - Stable

  And also:
  - Cavitation microstreaming
  - Rectified diffusion

Effects of transient cavitation:

Surface damage
Cell lysis

Photo Prof. LA Crum. Previously published: Prosperetti, A., "Bubble phenomena in sound fields: Part Two," Ultrasonics 22, 115-124, 1984

Types of transient cavitation

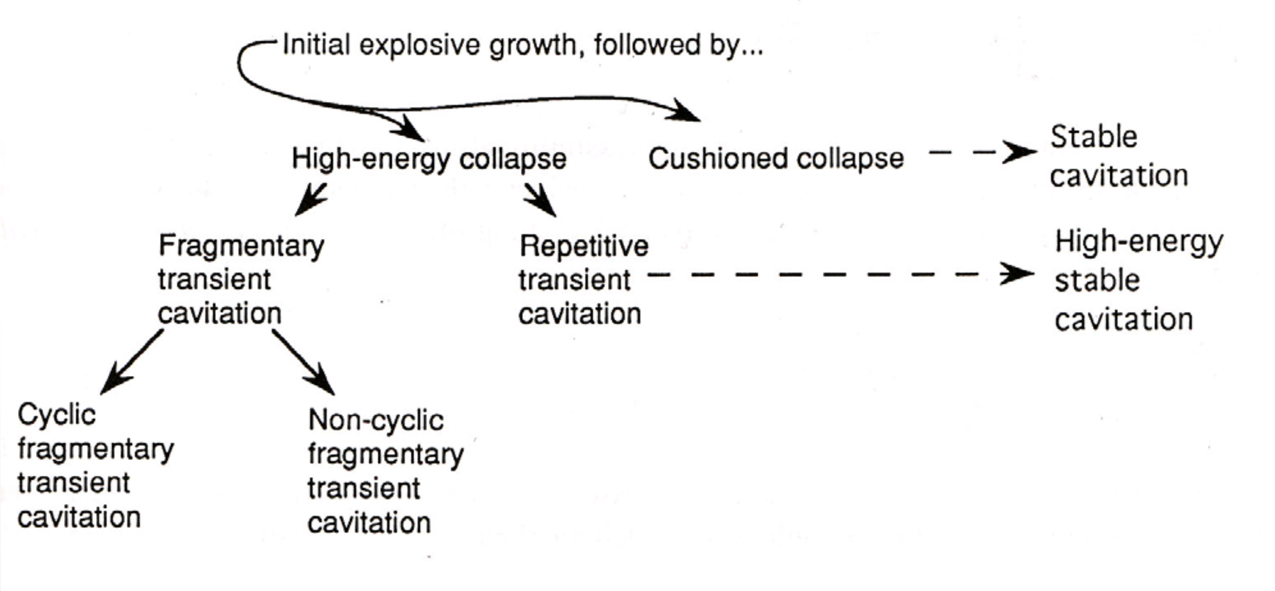

From Tim Leighton 'The Acoustic Bubble'

Transient cavitation thresholds

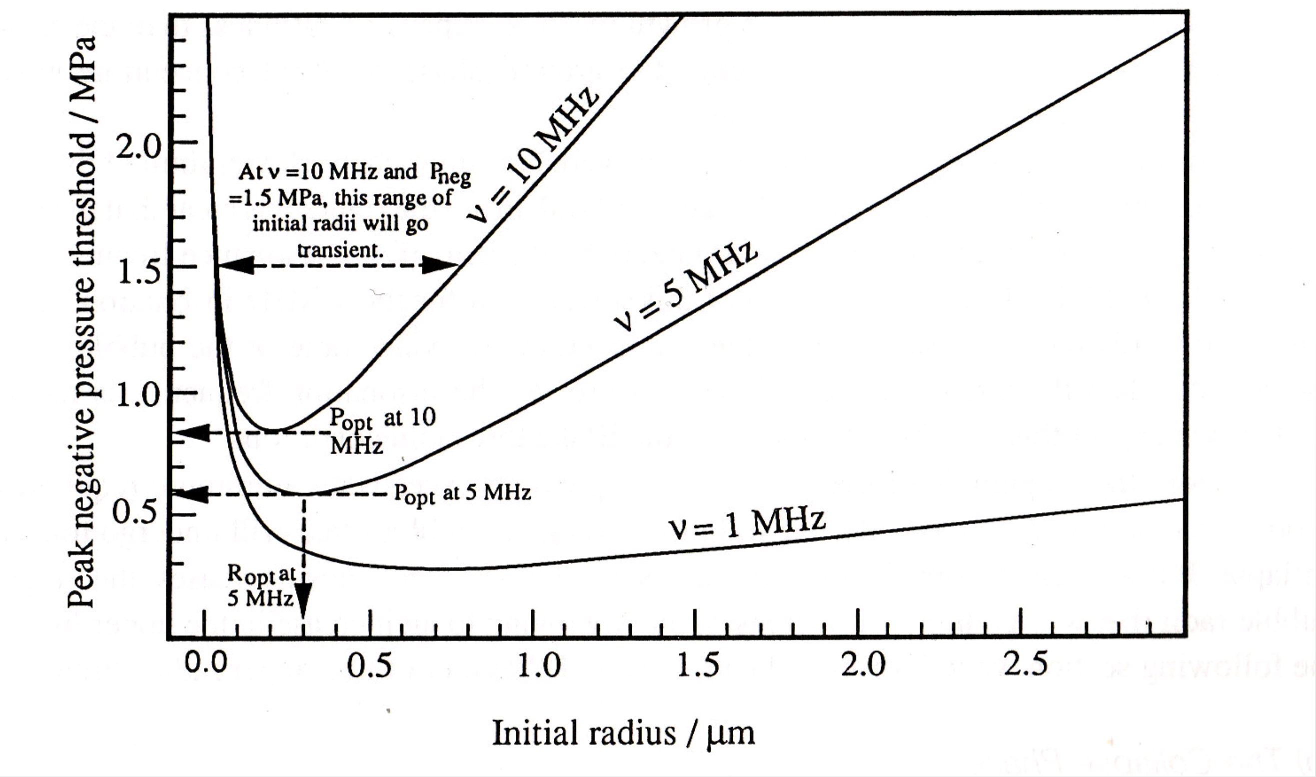

After Apfel and Holland

Ultrasound in Medicine and Biology, vol. 18, pp. 267–281;

Detection of cavitation

- Broadband noise
- Sonoluminescence

When bubbles are present there are increased sub- and super- harmonic acoustic emissions (f/2, 2f, …) due to non-linear behaviour.

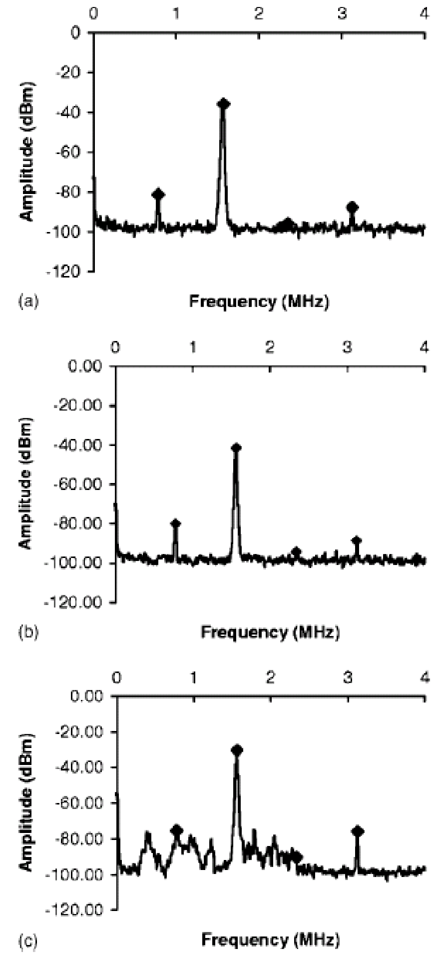

FIG. 9. Measured acoustic spectrum of microparticles and CA: (a) 0.98 MPa; (b) 1.47 MPa; (c) 1.96 MPa.

Kuznetsova et al, 2004

Other Bubble behaviours

- Radiation forces:
  - Amplitude dependent
- Streaming (sometimes called cavitation microstreaming)
- Rectified diffusion
- Growth with temperature change
- Rotational phenomena (Miller 1977 / Coakley)

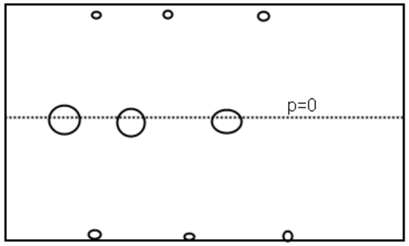

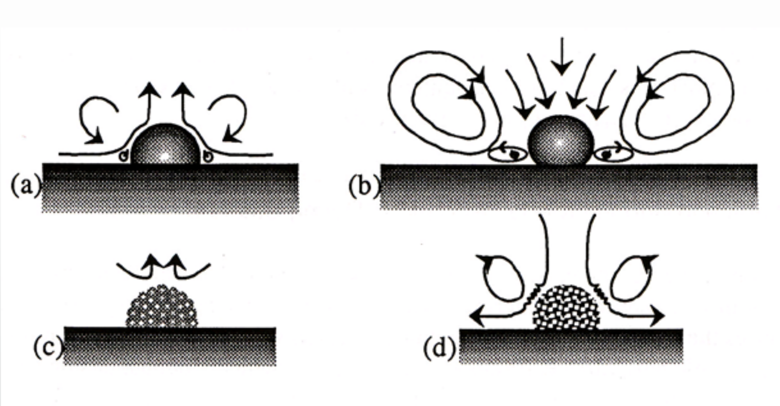

A.E. Elder , Cavitation microstreaming. *J Acoust Soc Am* **31** (1959), pp. 54–64.

L5: Alternative contactless manipulation methods: Dielectrophoresis and optical tweezers

Martin Wiklund

Dept. of Applied Physics
Royal Institute of Technology
Stockholm, Sweden

CISM course "*Ultrasound standing wave action on suspensions and biosuspensions in micro- and macro fluidic systems*", June 7-11, 2010

KTH Physics

M. Wiklund

-1-

Outline

1. **Motivation**
2. **Background: Micro-manipulation of cells**
3. **Optical manipulation**
4. **Electrical (dielectrophoretic) manipulation**
5. **Combined approaches:**
   - Optical-electrical
   - Electrical-acoustical

KTH Physics

M. Wiklund

-2-

Motivation

Micro-manipulation:

- Manipulation of **micrometer-sized** bio-objects by external force fields

Target bio-objects:

- Cells, functionalized micro-beads – approx. 1-30 µm
- Bacteria – approx. 1 µm

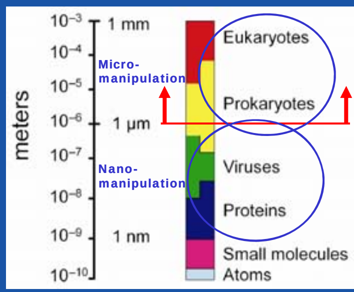

Future: Nano-manipulation?

M. Wiklund

Manipulation methods – an overview

Available techniques for manipulation of differently sized objects

Scale	Techniques (examples)
Macro-manipulation (>mm-range)	Manual, tweezers etc.
"mini"-manipulation (sub-mm or mm-range)	Fine tweezers, still manual, microscope-aided
Micro-manipulation (µm-range)	Micro-pipettes, patch clamp approaches Contactless: Optical tweezers **Ultrasound** Dielectrophoresis (DEP)
Nano-manipulation (sub µm-range)	Atomic force microscopy (AFM)* DEP* Optical tweezers* **Ultrasound?** **⇨ not yet, really!**

Applications (examples)

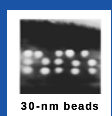

* Under certain fulfilled circumstances (e.g. particle type)

M. Wiklund

M. Wiklund

-5-

Background: Micro-manipulation of cells

- State of technology for one century:
  Grasp a cell with suction through a glass micropipette tip
  [M. A. Barber, J. Kansas Med.Sot. **4**, 489 (1904)]

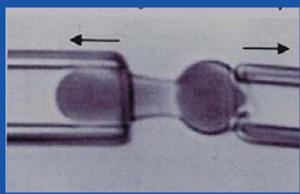

Handling can be stressful

=> Alternative: Contactless manipulation

M. Wiklund

-6-

Contactless methods:

- Optical tweezers (OT)
- Dielectrophoresis (DEP)

- Opto-electronic tweezers (OET)

- Ultrasonic Standing Waves (USWs)

- ~~Magnetic manipulation~~

M. Wiklund

-7-

Method 1:
Optical tweezers (OT)

M. Wiklund

-8-

Optical tweezers

- Developed in the 70s (Arthur Ashkin, Bell Labs)
- Found applications in the late 80s and 90s

Basic principle: Conservation of momentum (mass x velocity) generates a force

You need a laser and a high-NA lens (microscope objective)

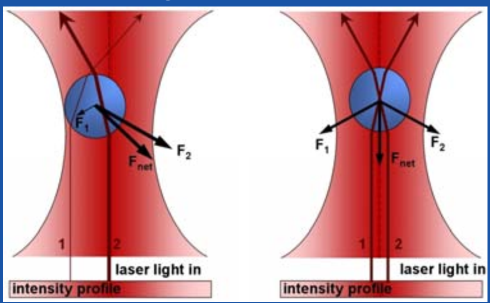

M. Wiklund

-9-

Optical tweezers

- **First demonstration in the 70s (Arthur Ashkin, Bell Labs):**

  Two counter-directed laser beams

- **First single-beam trap in the 80s (Arthur Ashkin, Steven Chu, Bell Labs):**

  Vertical highly focused laser beam

M. Wiklund

-10-

Optical tweezers - Principles

Why is the trapping point not in the focus?

Force: Transfer of momentum from incident photons to a dielectric particle, due to reflection, absorption, refraction

<u>Two components:</u>

1) **Scattering force**
   (in the direction of light propagation)
2) **Gradient force**
   (in the direction of spatial light gradient)

Gradient force only significant in highly focused laser beams!

M. Wiklund

-11-

Optical tweezers - Principles

Scattering force:
Due to reflection and absorption

Gradient force:
Due to refraction

($n_{particle}$ > n_{medium}
⇨ Force towards field maximum)

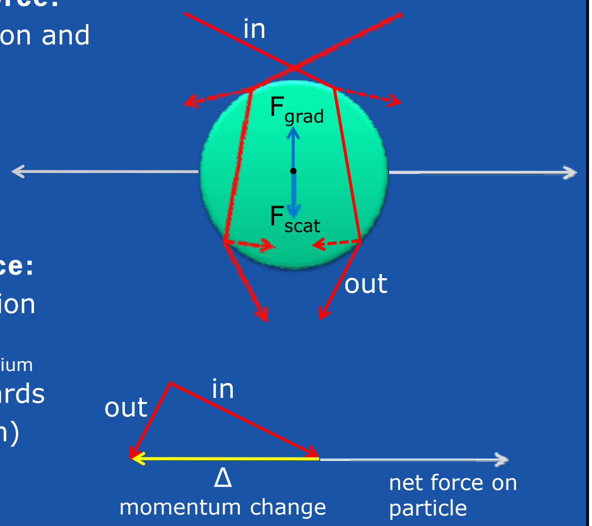

M. Wiklund

-12-

Optical tweezers - Principles

Note:
If the particle is transparent, F_{grad} dominates ➡ trapping close to the laser focus

If the particle is opaque, F_{scat} dominates ➡ particle is pushed away from the focus

If the particle is semi-transparent ➡ particle is trapped slightly away from the laser focus

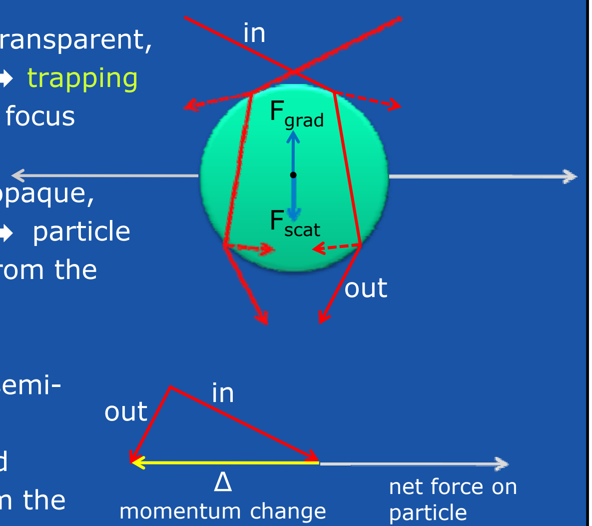

Laser tweezers – using F_{grad}

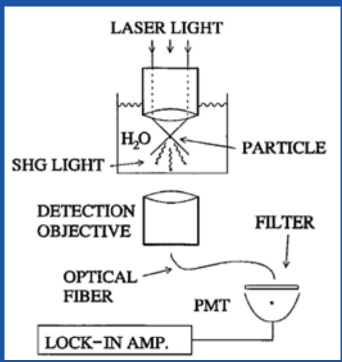

H. M. Hertz *et al*, Ultramicroscopy, **57**, 309 (1995)

3-D positioning for single-cell imaging

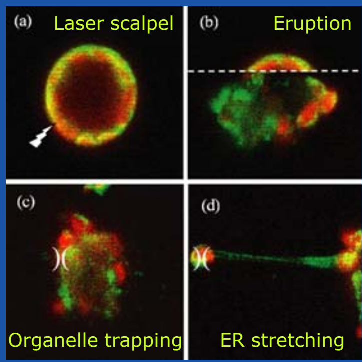

Intracellular manipulation:

Protoplast from *Arabidopsis thaliana*, chloroplast trapping and stretching of endoplasmic reticulum (f>400 pN)

Eriksson *et al.*, J. Opt. A: Pure. Appl. Opt. 9, S113 (2007)

M. Wiklund

-13-

Laser tweezers – using F_{scat}

Lifting cells from wells:

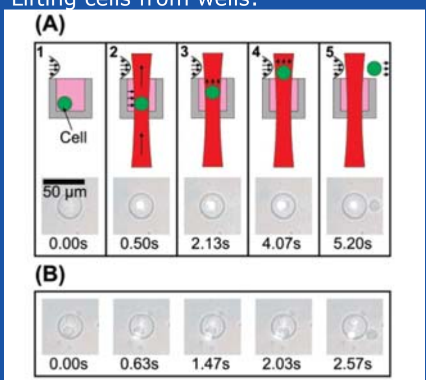

Figure 3. Cell release. (A) Sequence of images showing levitation and removal of a target cell. Illustrations qualitatively show the cell state in each frame. 1—Cell at rest, 100 ms before the laser is turned on. 2—Lateral optical gradient force moves the cell to the lateral center of the beam. 3—Optical scattering force begins to levitate the cell. 4—Scattering force levitates the cell into flow field. 5—Fluid drag force overwhelms the optical gradient force, releasing the cell. (B) Tight localization of the optical force. We demonstrate the ability to remove a single targeted cell residing in a doubly loaded well.

J. R. Kovac and J. Voldman, Anal. Chem. **79**, 9321, 2007

In bead-based immunoassays:

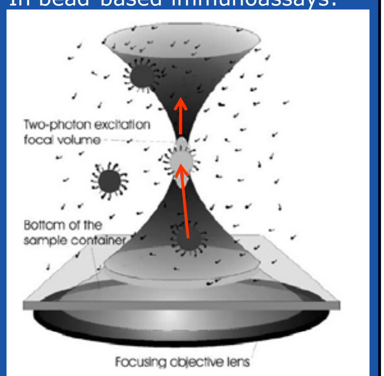

"Throw away" the bead you just have analyzed

J. T. Soini *et al.*, J. Pharm. Biomed. Anal. **34**, 753, 2004

M. Wiklund

-14-

Complex light patterns

- **Multiple laser foci with diffractive elements or spatial light modulation**

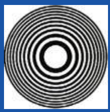

- **Opto-electronic tweezers (use optical images on a photo-conductive layer to produce ”virtual electrodes”) => dielectrophoresis**

Prof. Ming Wu, UC Berkeley
Nature, July 21, 2005

M. Wiklund

-15-

Complex light patterns

Opto-electronic tweezers (OETs)

Video example: Parallel transport of 4.5 µm beads

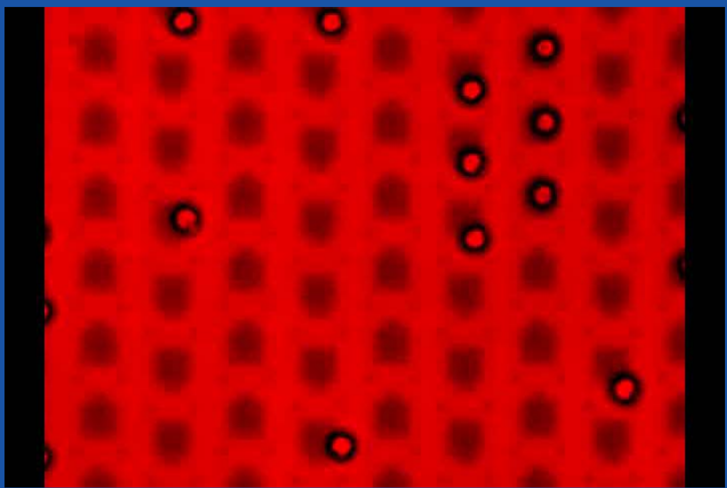

Prof. Ming Wu, UC Berkeley in Nature, July 21, 2005

M. Wiklund

-16-

Complex light patterns

Opto-electronic tweezers (OETs)

Video example: Concentration of live human B cells

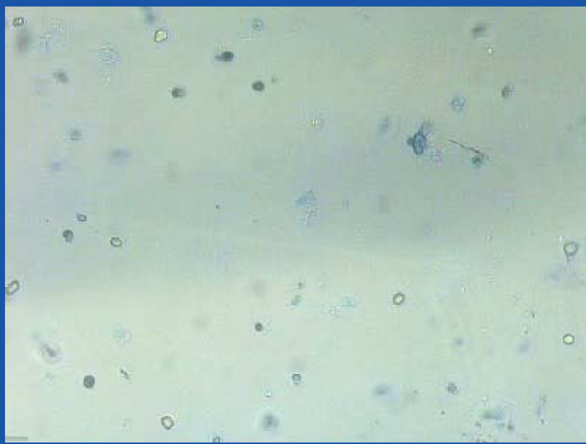

Prof. Ming Wu, UC Berkeley in Nature, July 21, 2005

M. Wiklund

-17-

Complex light patterns

Opto-electronic tweezers (OETs)

Video example: Optical conveyor belt for >10 μm beads

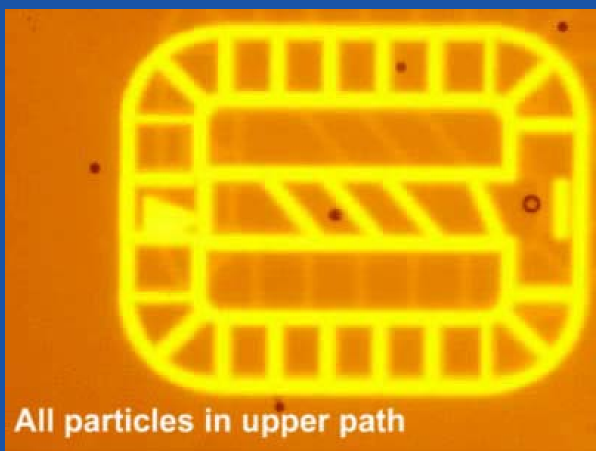

Prof. Ming Wu, UC Berkeley in Nature, July 21, 2005

M. Wiklund

-18-

M. Wiklund

-19-

Method 2: Dielectrophoretic (DEP) manipulation

M. Wiklund

-20-

Dielectrophoresis: Basics

- Manipulation in high-frequency electromagnetic fields
- Contrast of the electric polarisability (particle rel. medium)
- Size and direction of induced dipole moment:
Depend on the dielectric constant ε (conductivity and permittivity)
=> *Frequency-dependent*
- If $\varepsilon_{par} > \varepsilon_{med}$
  => negative dielectrophoresis (nDEP)
  else
  => positive dielectrophoresis (pDEP)

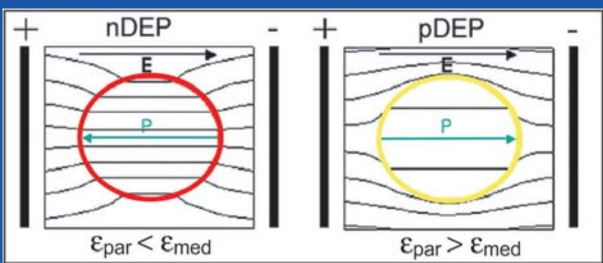

Dielectrophoresis: Basics

- How do we get a force?
  => Inhomogeneous a.c. electric field
- nDEP: Particles are driven away from the electrodes
  pDEP: Particle are attracted by the electrodes
- Most often used:
  nDEP (multielectrode geometries drive the particles to the field minima)
- Length scale of the field inhomogeneities ~ 10 μm

⇒ **for μm-sized particles, electrodes must have corresponding dimensions!**

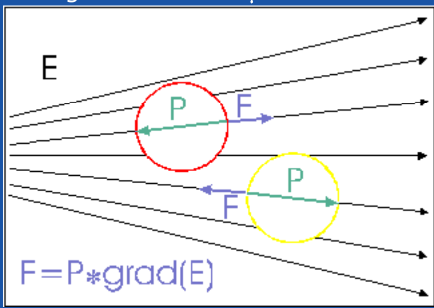

M. Wiklund

-21-

DEP manipulation: Principles

- Microelectrode design:

  Most simple:
  - Pair of face-to-face mounted linear electrodes

  More sophisticated:
  - ”Shaped” electrode pairs (zig-zag, curved, etc.)
  - Octopole cages (many electrodes)
  - 2D arrays

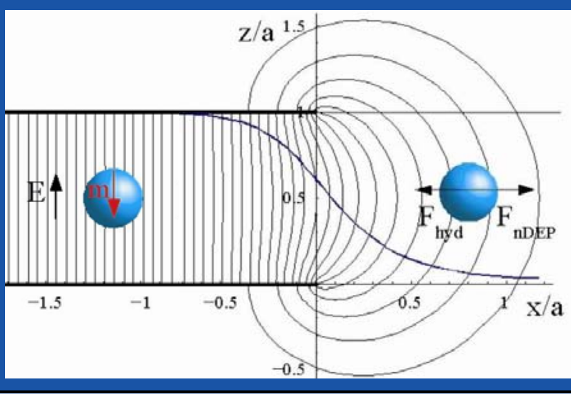

M. Wiklund

-22-

M. Wiklund

-23-

Instrumentation:
DEP chip (GeSim/Evotec)

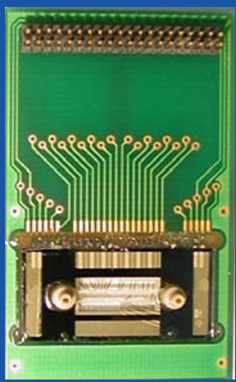

- Chip: overview and fluid channel

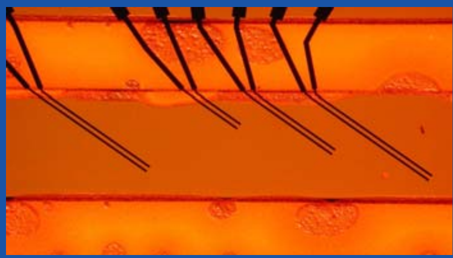

M. Wiklund

-24-

Three-layer chip design

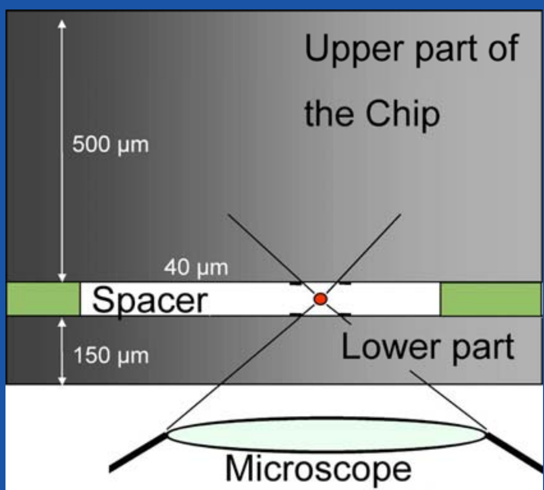

M. Wiklund

-25-

Typical DEP chip architecture

the Cytocon™-chip "SORTER" (Evotec Technologies)

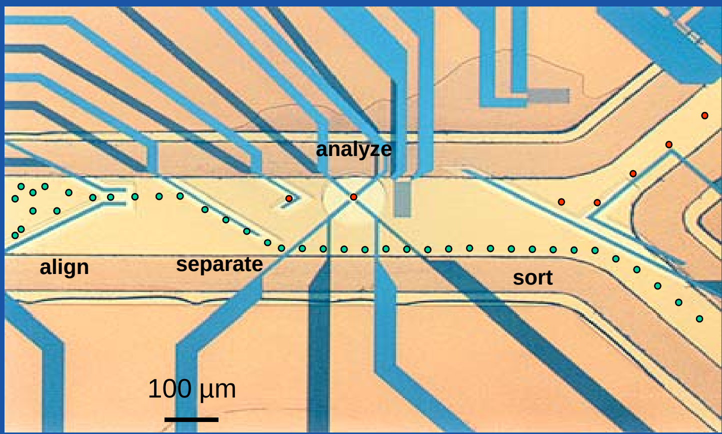

Thus: spatially separated manipulation functions (conveyor belt principle)

M. Wiklund

-26-

Deflector elements

- Sized-based separation (erythrocytes from leukocytes)

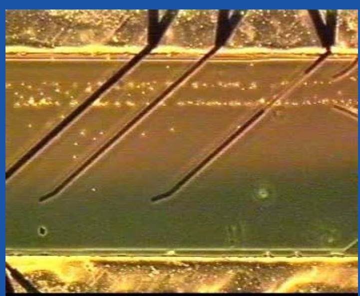

Linear deflector elements

Curved deflector elements

Videos: Courtesy of Dr. Magnus Jäger, Fraunhofer Intitute of Biomedical Engineering

Combine two deflector elements

- Fast incubation by carrier medium exchange (particle ”dipping”)

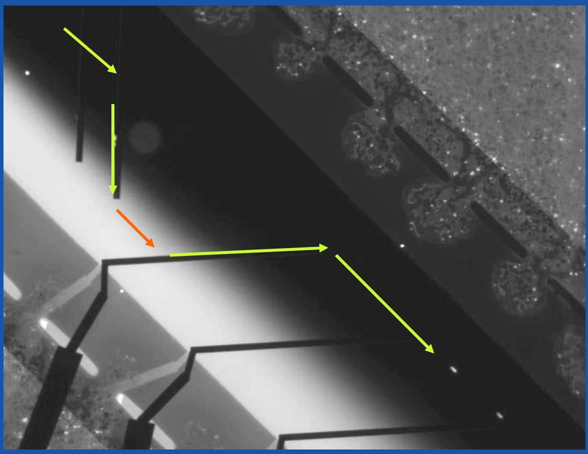

M. Wiklund

-27-

Combine two deflector elements

- Fast incubation by carrier medium exchange (particle ”dipping”)

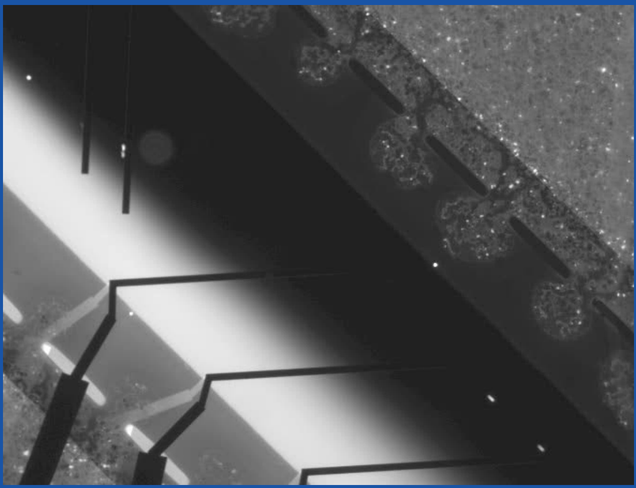

Videos: Courtesy of Dr. Magnus Jäger, Fraunhofer Intitute of Biomedical Engineering

M. Wiklund

-28-

Array of deflector elements

- Electric (flow-free) transport of particles

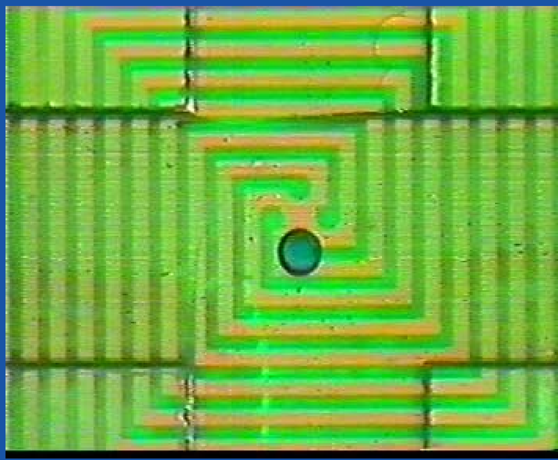

Videos: Courtesy of Dr. Magnus Jäger, Fraunhofer Intitute of Biomedical Engineering

KTH Physics

M. Wiklund

-29-

Array of cages

- Electric (flow-free) transport of particles

  320×320 array of indepentent electrodes using CMOS technology

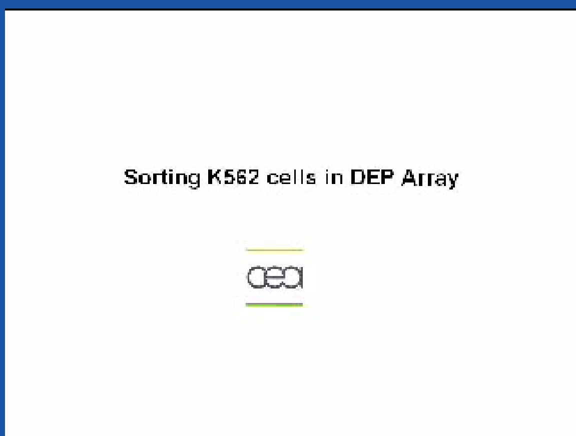

Fuchs *et al.*, Lab Chip, **6**, 121, 2006

KTH Physics

M. Wiklund

-30-

Field cage: nDEP with octode geometry

- 3D electrode arrangement,
  8 electrodes with individually controlled amplitude and phase

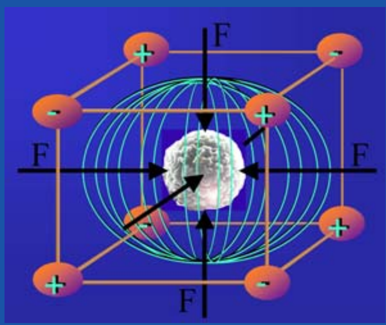

M. Wiklund

-31-

Electro-rotation of a cell in a field cage

Videos: Courtesy of Dr. Magnus Jäger,
Fraunhofer Intitute of Biomedical Engineering

M. Wiklund

-32-

Individual cell handling with a field cage: Cell screening

- Controlled parking time for each cell
- “Waiting room” outside the cage
- Optical characterization, separation etc.

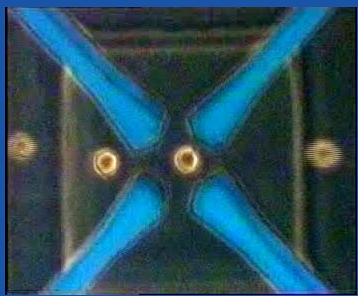

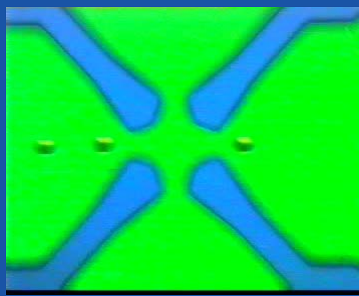

Videos: Courtesy of Dr. Magnus Jäger,
Fraunhofer Intitute of Biomedical Engineering

M. Wiklund

Time-dependent fluorescence analysis of individual cells

- Calcein-AMTM image of a trapped lymphoma cell (Jurkat) in a field cage
- Washing without centrifugation

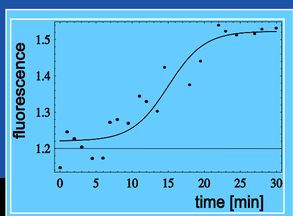

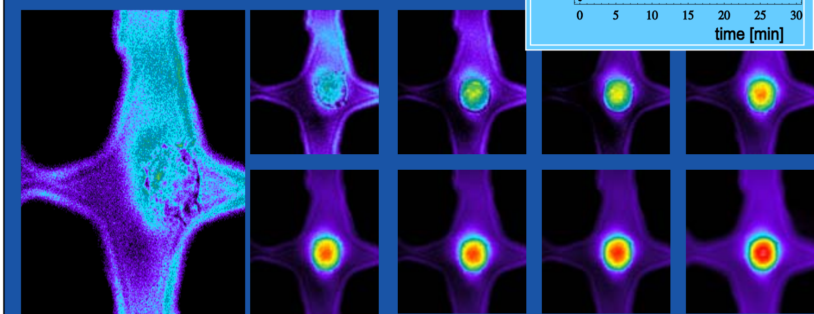

M. Wiklund

Programmable particle movement

Modulation of the field amplitude

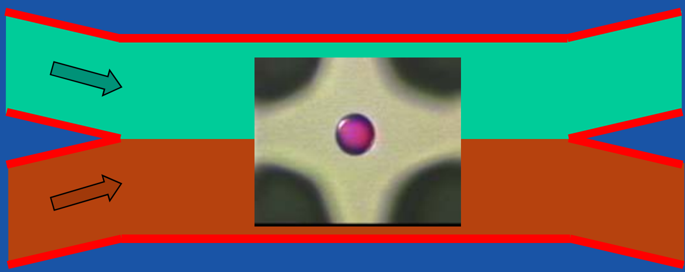

Application: Fluid mixing

M. Wiklund

Videos: Courtesy of Dr. Magnus Jäger,
Fraunhofer Intitute of Biomedical Engineering

-35-

Driving modes and field geometry of a cell cage

Geometry, phase angles of electric driving and force potential of octode field cages

Phase shift:
0° 90° 180° 270°

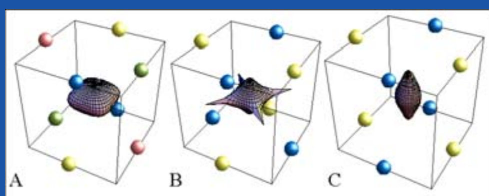

Surface of constant mean square of E

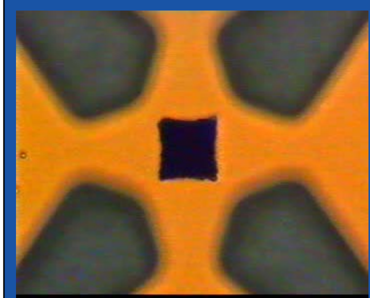

E visualised by
1 µm beads

Application:
Microcasting?

M. Wiklund

Videos: Courtesy of Dr. Magnus Jäger,
Fraunhofer Intitute of Biomedical Engineering

-36-

Controlled positioning

- Amplitude modulation

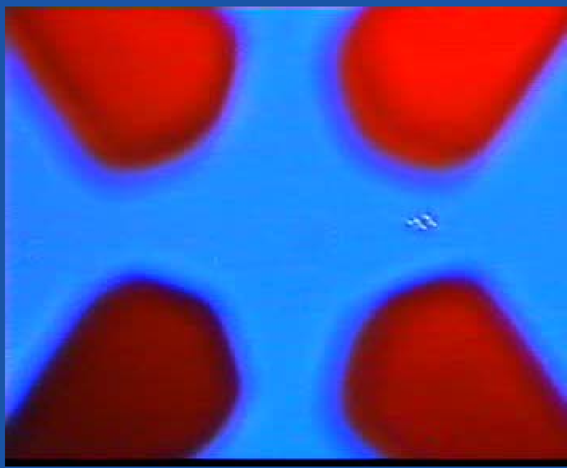

Videos: Courtesy of Dr. Magnus Jäger,
Fraunhofer Intitute of Biomedical Engineering

KTH Physics

M. Wiklund

-37-

Cell proliferation experiment

- Yeast cell cultivation in field cage

Videos: Courtesy of Dr. Magnus Jäger,
Fraunhofer Intitute of Biomedical Engineering

KTH Physics

M. Wiklund

-38-

Single-molecule trapping with DEP

Electrodes:

60 nm curvature of tip,
500 nm tip-to-tip distance

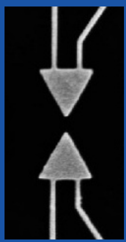

Trapping of *R*-phycoerythrin (RPE) from red algae
(240 kDa protein, 11×6 nm)

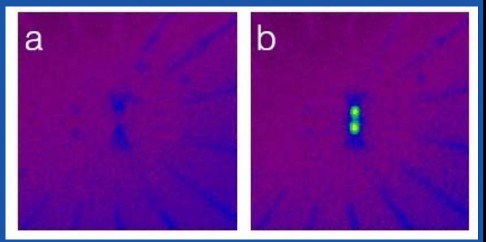

Hölzel *et al.*, Phys. Rev. Lett. **95**, 128102, 2005

M. Wiklund

-39-

Combine methods:
DEP + OT
DEP + USW

M. Wiklund

-40-

DEP + OT

Two similar tools, but no mutual interference!

• Force measurements of ligand – receptor interactions

Cell: DEP manipulation

Bead (functionalized): OT manipulation

Binding forces: 2 pN - 200 pN

KTH Physics

M. Wiklund

-41-

DEP + USW

- Parallel alignment of particles in one or several bands
- Combine with DEP elements
- Three independent forces:

  - USW (long-range)
  - DEP (short range)
  - flow

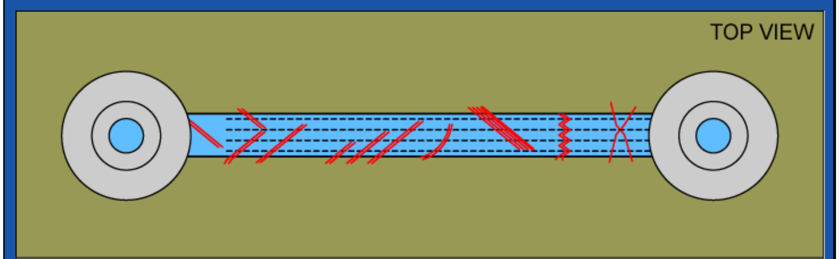

KTH Physics

M. Wiklund

-42-

DEP + USW

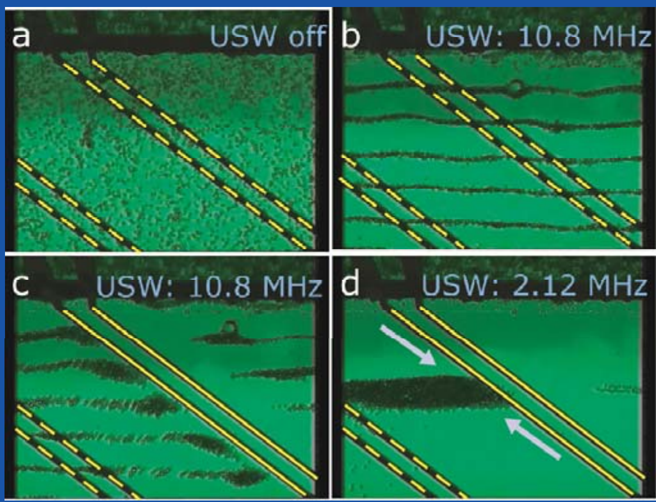

5 μm beads, switch between 10 and 2 MHz

M. Wiklund

DEP + USW

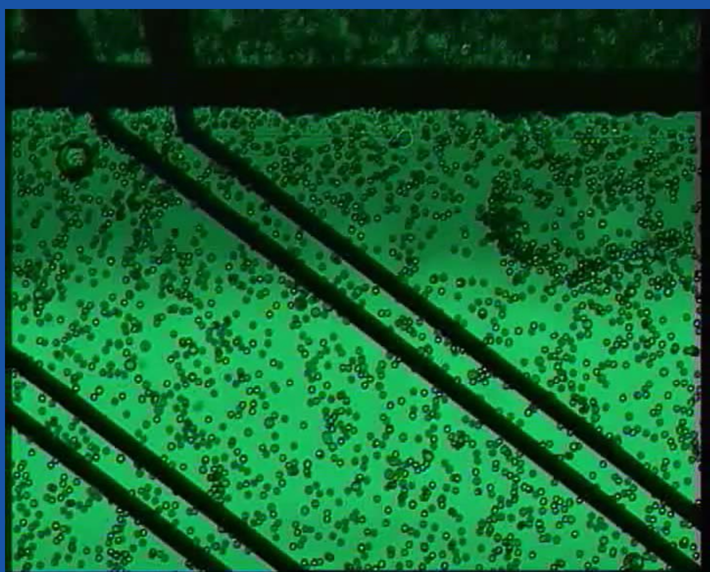

5 μm beads, switch between 10 and 2 MHz

Videos: Courtesy of Martin Wiklund, KTH and Fraunhofer Intitute of Biomedical Engineering

M. Wiklund

DEP + USW

- High flexibility and precision with three independent forces

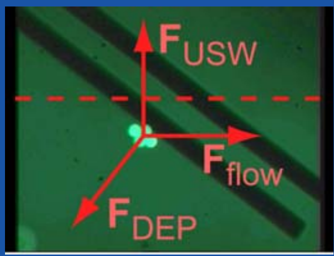

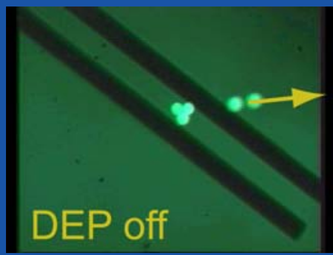

DEP + USW

- Alignment, parking and enrichment of particles at exact positions (μm-precision)

USW on, DEP on (hold)

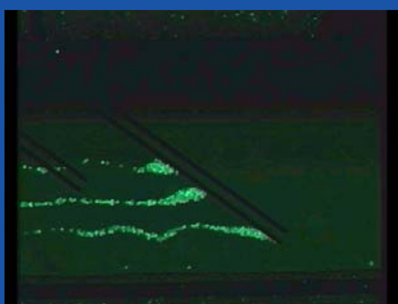

USW on, DEP off (release)

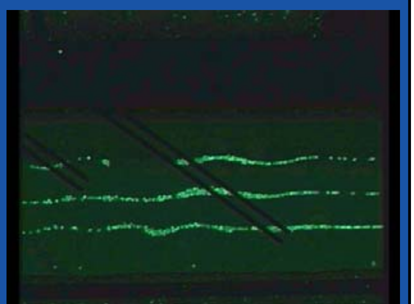

DEP + USW

- The different force field scales allow for handling of high particle concentrations

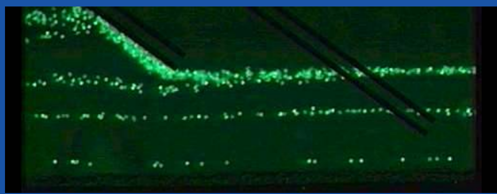

Low USW field,
DEP deflector on

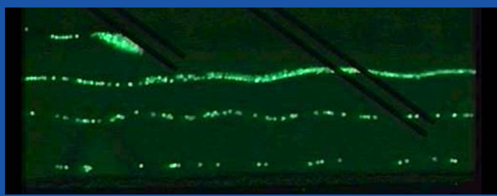

High USW field,
DEP deflector on

KTH Physics

M. Wiklund

4 June, 2010
-47-

DEP + USW

- Curved electrodes
- Step-wise merging and aggregation of particles

KTH Physics

M. Wiklund

4 June, 2010
-48-

Final question:
Can we manipulate nano-particles with USW?

Micro-manipulation:
Only radiation forces

2 µm beads

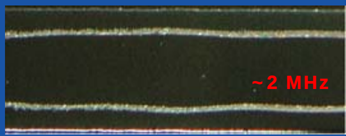

Nano-manipulation:
Radiation forces + acoustic streaming

400 nm beads

Or, just high bead concentrations
(radiation forces are enough!)

KTH Physics

M. Wiklund

-49-

Conclusion

- Optical and electric (dielectrophoretic) manipulation of cells in microfluidic chips are sophisticated tools with high spatial accuracy (3D and single-particle compatibility)
- Acoustic manipulation is traditionally more suitable for long-range bulk manipulation, but is today also compatible with 3D and near-single-particle precision
- The different methods can be combined for inproved performance and flexibility
- Optical and electrical manipulation can, under certain circumstances, be used for single nano-particle (<1 µm) manipulation
- This is not yet demonstrated with acoustic manipulation

KTH Physics

M. Wiklund

-50-

L3:
Ultrasonic cell handling: Safety, biocompatibility and cell-cell interaction

Martin Wiklund

Dept. of Applied Physics
Royal Institute of Technology
Stockholm, Sweden

CISM course "*Ultrasound standing wave action on suspensions and biosuspensions in micro- and macro fluidic systems*", June 7-11, 2010

M. Wiklund

-1-

What is "cell manipulation"?

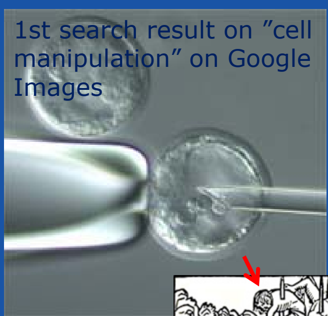

State of technology for one century:
"*Grasp a cell with suction through a glass micropipette tip*"
[M. A. Barber, J. Kansas Med. Sot. **4**, 489 (1904)]

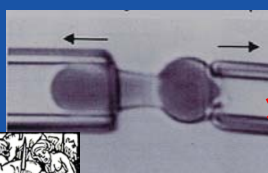

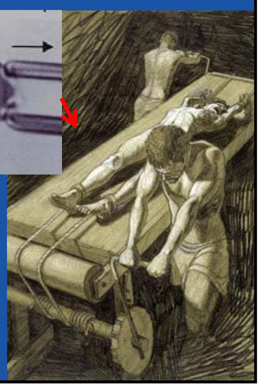

Contactless alternative: Ultrasound!

Stressful handling?

M. Wiklund

-2-

M. Wiklund

Is ultrasound harmful?

YES!

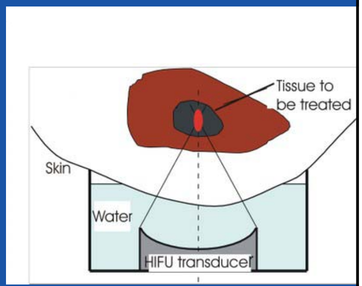

HIFU lesions in tissue

-3-

M. Wiklund

Is ultrasound harmful?

YES!

High-speed movie of acoustic cavitation

Movie from Dr. Claus-Dieter Ohl, Nanyang Tech. University, Singapore

-4-

Is ultrasound harmful?

NO!

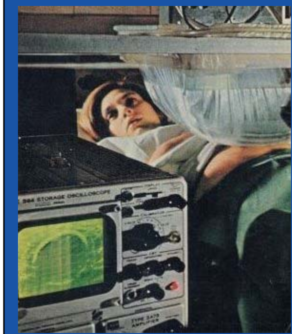

Diagnostic ultrasound 1965 (Marvin Ziskin lab)

Diagnostic ultrasound today (45 years later)

KTH Physics

M. Wiklund

-5-

Is ultrasound harmful?

Balanced answer:

Depends on system design, amplitudes, frequencies, application/device design, cell/tissue type ...etc, etc.

What do we need to control?

Primarily: Temperature and occurance of cavitation and/or microjets/flow

KTH Physics

M. Wiklund

-6-

Compare with diagnostic ultrasound

We keep track of the thermal index (TI) and the mechanical index (MI):

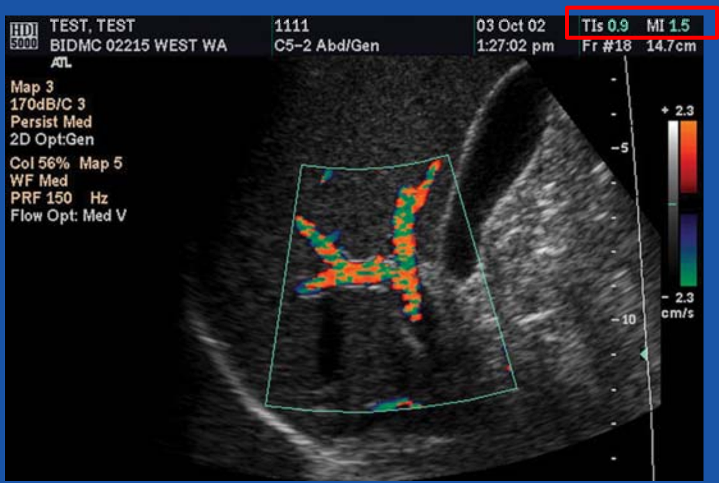

M. Wiklund

-7-

Thermal and mechnical index

Definitions:

Thermal index (TI):

$$TI = \frac{P_{transducer}}{P_{1^\circ C}}$$

$P_{transducer}$ ⟵ Power produced by the transducer

$P_{1^\circ C}$ ⟵ Power needed to raise the temperature 1°C

Mechanical index (MI):

$$MI = \frac{p_{np}}{\sqrt{f_c}}$$

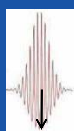

p_{np} ⟵ Negative peak pressure (absolute value) [in MPa]

f_c ⟵ Center frequency [in MHz]

Safe side: Both TI and MI should be less than 1!

M. Wiklund

-8-

Biocompatibility of Ultrasonic Standing Wave (USW) manipulation systems

M. Wiklund

What about standing waves?

"Because cavitation tends to be greatest at maxima of the pressure amplitude, the radiation force provides a protective effect on cells in test tubes"
(Wesley Nyborg, Ultrasound Med. Biol. **27**, 301, 2001)

"Standing wave ultrasound appears to be less damaging than propagating ultrasound"
(Yusuf Chisti, Trend. Biotechnol. **21**, 89, 2003)

"As a concequence of the trapping of cells in the anti-nodes planes of the standing wave, propagating wave fields reduced cellular viability compared with standing wave fields at equal energy density."
(Hannes Böhm, Ultrasonics **38**, 629, 2000)

-9-

Biocompatibility of Ultrasonic Standing Wave (USW) manipulation systems

M. Wiklund

What about radiation pressure?

No evidence of any direct damaging effect on cells (in vitro)

Exceptions: In vivo measurements on nerve cells

Tactile sensations in humans
(Dalecki et al., J. Acoust. Soc. Am. 97, 3165, 1995)

Altering of bioelectric activity in frog sciatic nerve
(Mihran et al., Ultrasound Med. Biol. 16, 297, 1990)

However 1: The effect in above examples does not need to be harmful! (Cf: Physiotherapeutic ultrasound)

However 2: Radiation pressure is least at the pressure nodes of a standing wave

-10-

Biocompatibility of Ultrasonic Standing Wave (USW) manipulation systems

What about acoustic streaming?

Streaming is known to cause shear stress damage on cells, potentially leading to cell lysis
(W. Nyborg, Ultrasound Med. Biol. **27**, 301, 2001)

However, significant streaming velocities are needed to create damage, such as from acoustic microstreaming/jets generated by stable cavitation bubbles
(S. B. Barnett, Ultrasound Med. Biol. 20, 205, 1994)

Smaller streaming velocities may be beneficial!
E.g. for fluid stirring, exchange of nutrients, enhanced metabolic productivity of cells, proliferation rates, etc.
(Y. Chisti, Trend. Biotechnol. **21**, 89, 2003)

KTH Physics

M. Wiklund

-11-

Any effects by unknown causes?

Vacuole membrane damage in yeast (USW field)

S. Radel *et al*, Ultrasonics, 38, 633, 2000 (left images)

S. Radel *et al*, Bioseparation 9, 369, 2001 (right images)

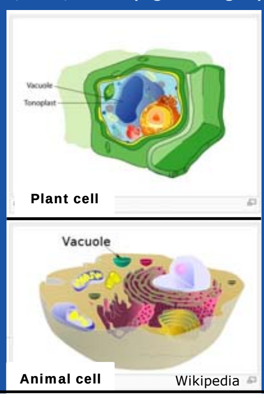

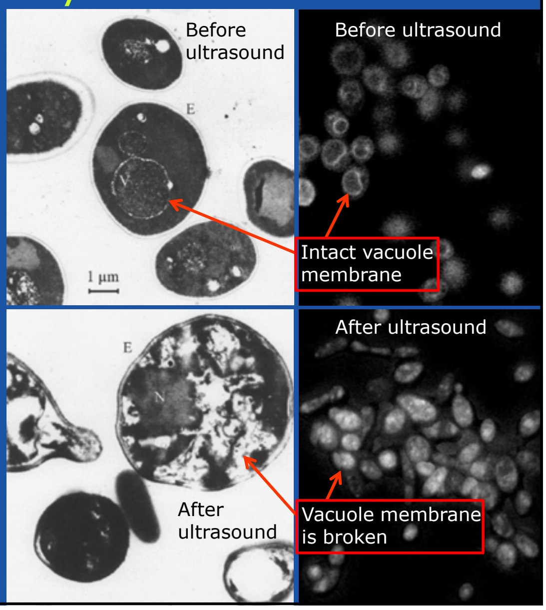

KTH Physics

M. Wiklund

-12-

Any effects by unknown causes?

A recent study with pregnant mice (Ang *et al*, PNAS, 103, 12903, 2006):

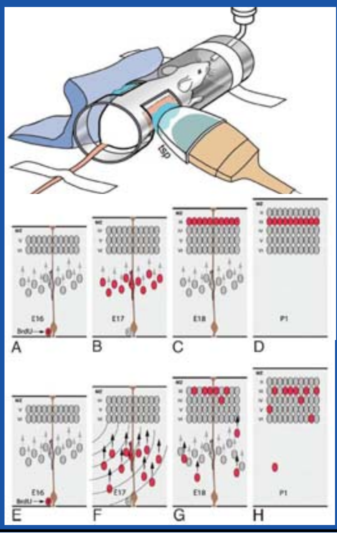

Brain damage due to heterotopia (disturbance in the migration of neurons to the cortex in the brain)

"The dosimetry data and output parameters suggest that the mechanism may be a nonthermal, noncavitational, mechanically mediated effect, perhaps involving radiation force or microstreaming, or shear effects on cellular walls" (Ang *et al*)

Applicable to humans?

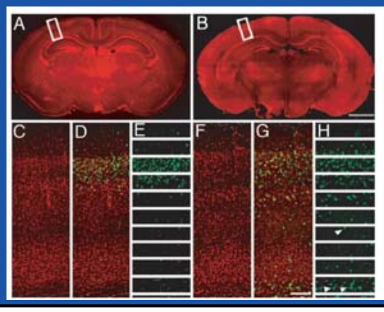

KTH Physics

M. Wiklund

-13-

Biocompatibility of Ultrasonic Standing Wave (USW) manipulation systems

Conclusion:

You must investigate the biocompatibility of you own device in your own application!

KTH Physics

M. Wiklund

-14-

Biocompatibility of Ultrasonic Standing Wave (USW) manipulation systems

Best example of a biocompatible USW device:

Acoustic cell filters/bioreactors

Up to 700 h (≈1 month) of continuous acoustic exposure did not alter the viability or antibody secretion rates of hybridoma cells
(Felix Trampler et al., Bio/Technology **12**, 281, 1994; review article: Shirgaonkar et al., Biotech. Adv. **22**, 433, 2004)

Later (1997): SonoSep™ and BioSep™

Claimed performance: Cultivation >60 days
Typical power: 0.1-1 W/ml
Perfusion rate: ~1 l/h
Note: Cells not always in the acoustic chamber!

KTH Physics

M. Wiklund

-15-

Biocompatibility of Ultrasonic Standing Wave (USW) manipulation systems

Corresponding pressure levels?

0.1-1 Mpa (acoustic pressure amplitude)

Compare: Cavitation threshold was 2 MPa in a study by Bazou/Coakley
(D. Bazou et al., Ultrasound Med. Biol. **31**, 423, 2005)

Claimed performance: Cultivation >60 days
Typical power: 0.1-1 W/ml
Perfusion rate: ~1 l/h
Note: Cells not always in the acoustic chamber!

KTH Physics

M. Wiklund

-16-

Measuring viability of trapped cells in USW manipulation devices

How do we know if a cell is alive or dead?

Most commonly used: Dye/fluorescence exclusion methods (integrity of the cell membane)

Ex: Trypan Blue (blue dye goes into dead cells)
Propodium Iodide, PI (can not penetrate the cell membrane, its red fluorescence is enhanced 20-30-fold when it binds to DNA ⇨ dead cell turns red)
Calcein AM (penetrates the cell membrane, its green fluorescence is activated by an enzymatic process in live cells ⇨ dead cells loose their green color)

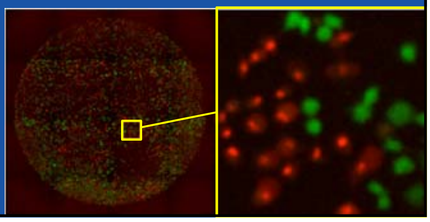

Double-labeled cells (calcein AM + PI) in one well of a 384-well plate (Green=live; red=dead)

M. Wiklund

-17-

Measuring viability of trapped cells in USW manipulation devices

How do we know if a cell is alive or dead?

Other more refined methods: Cell morphology

Ex: ”Cell blebbing” during the initiation of apoptosis

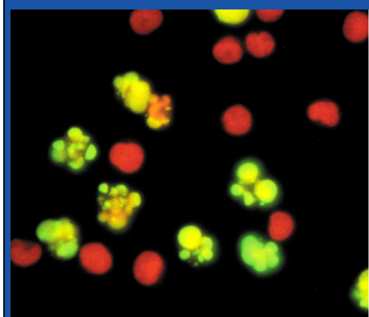

Images from: http://www.xinkexue.com/

M. Wiklund

-18-

Measuring viability of trapped cells in USW manipulation devices

How do we know if a cell is alive or dead?

Other more refined methods: Cell morphology

Ex: ”Cell blebbing” during the initiation of apoptosis

Killing of human embryonic kidney (HEK) cells by natural killer (NK) cells

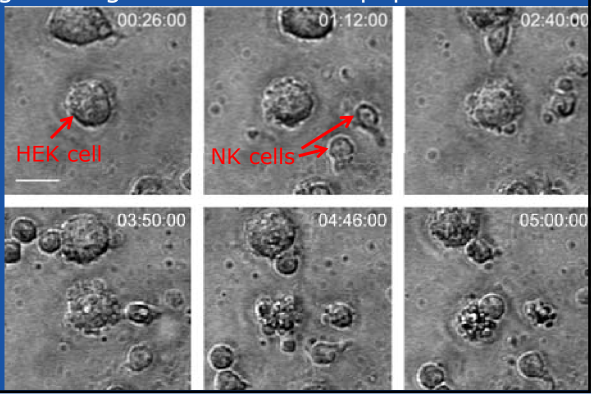

Images from
Bruno Vanherberghen
KTH

M. Wiklund

-19-

Measuring viability of trapped cells in USW manipulation devices

By the use of high-resolution optical (confocal) fluorescence microscopy: Both morphology and fluorescent probe classification can be used

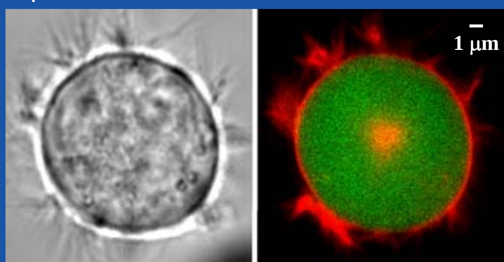

100x-objective imaging of a B cell (human immune cell)
Red label: membrane probe (DiD)
Green label: viability probe (calcein-AM)

Manneberg *et al.*, Appl. Phys. Lett., 2008

M. Wiklund

-20-

M. Wiklund

-21-

Biocompatibility of Ultrasonic Standing Wave (USW) **miniaturized** manipulation systems

My own investigations (Wiklund group)

Initial study 2006-2007:

- Cells trapped and retained in a glass-PDMS chip
- Proliferation measurements after ultrasound exposure

⇨ 75 min exposure to 0.85 Mpa and 3 MHz is OK!

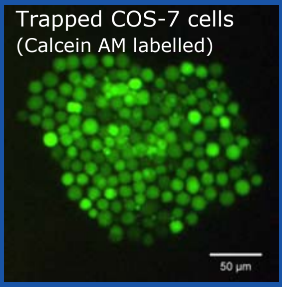

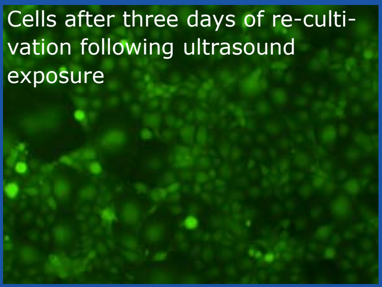

J. Hultström et al, Ultrasound Med. Biol., 33, 145 (2007)

M. Wiklund

-22-

Biocompatibility of Ultrasonic Standing Wave (USW) **miniaturized** manipulation systems

- No deviations from expected proliferation rates
- Cell-cell contact beneficial for proliferation? (compare control cells – USW exposed cells)

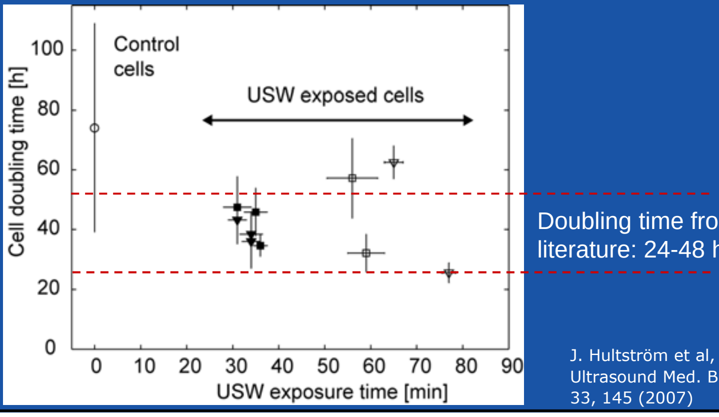

J. Hultström et al, Ultrasound Med. Biol., 33, 145 (2007)

M. Wiklund

-23-

Biocompatibility of Ultrasonic Standing Wave (USW) **miniaturized** manipulation systems

Temperature control

- Calibration of the temperatre increase vs. transducer voltage
- Can be used for heat regulation together by pre-setting of the external temperature

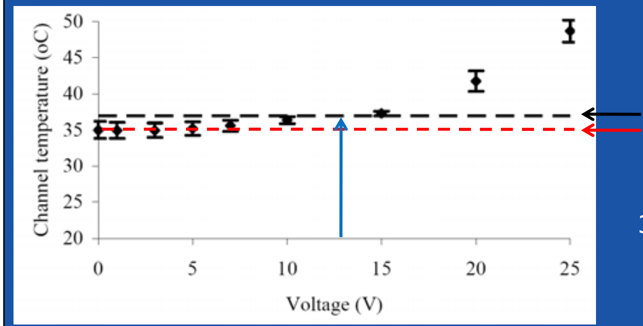

37°C @ 13 V

Svennebring *et. al.*, J. Micromech. Microeng., 17, 2469, 2007

M. Wiklund

Biocompatibility of Ultrasonic Standing Wave (USW) **miniaturized** manipulation systems

Temperature control: Demo

a) Temp. versus time, varying the actuation frequency

b) Temp. versus time, varying the actuation voltage

c) Temp. versus actuation voltage

d) Demo of temp. control

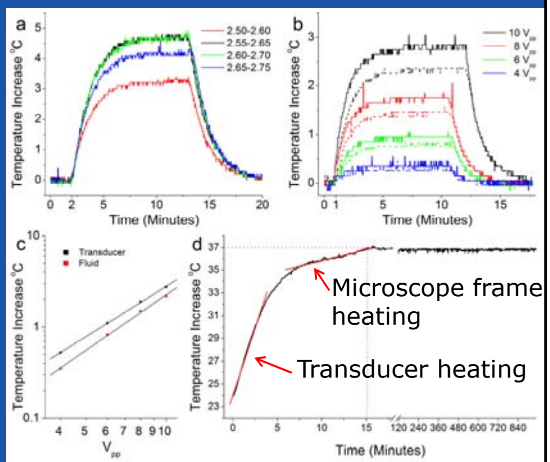

Vanherberghen *et al*, submitted manuscript (2010)

Biocompatibility of Ultrasonic Standing Wave (USW) **miniaturized** manipulation systems

Proliferation of B cells over 3 days
during continuous ultrasound exposure

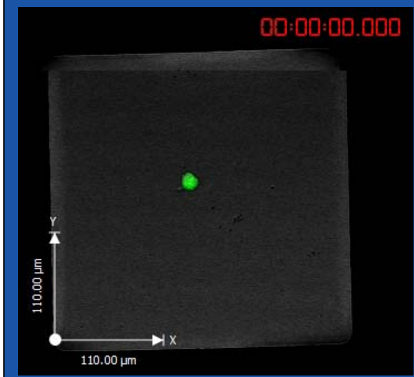

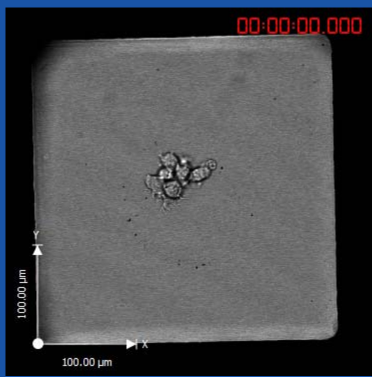

M. Wiklund

Vanherberghen *et al*, submitted manuscript (2010)

Biocompatibility of Ultrasonic Standing Wave (USW) **miniaturized** manipulation systems

Viability data

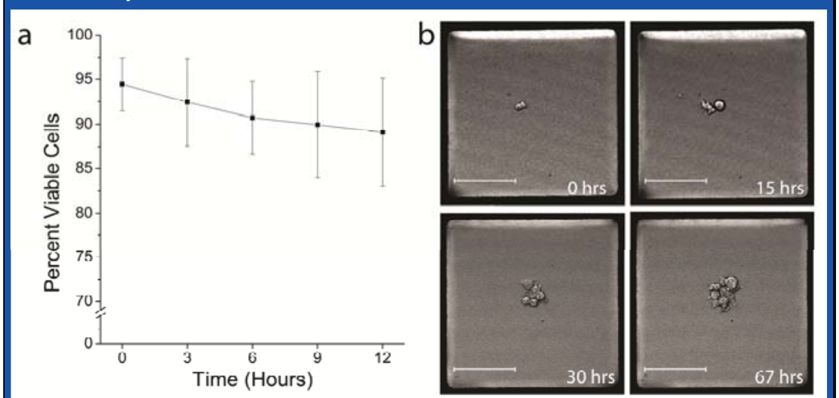

M. Wiklund

Vanherberghen *et al*, submitted manuscript (2010)

M. Wiklund

Some application examples: Cell-cell interaction studies

M. Wiklund

Imaging protein clustering and membrane spreading in nerve cells trapped with ultrasound

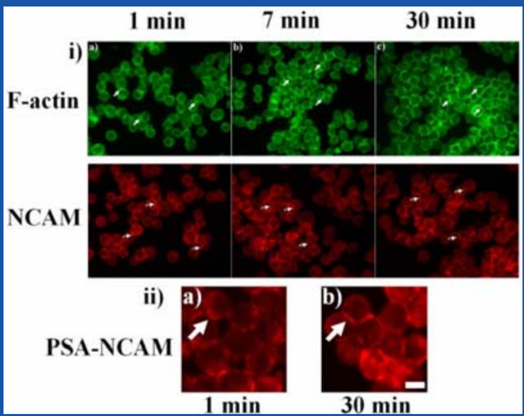

spot-like protein cluster

spread protein cluster

D. Bazou et al., Mol. Membr. Biol. **25**, 102, 2008

3D aggregates produced by ultrasound, stabilized with lectin crosslinking

Different resonators for cell aggregate formation, based on plane-parallel and/or tubular geometries

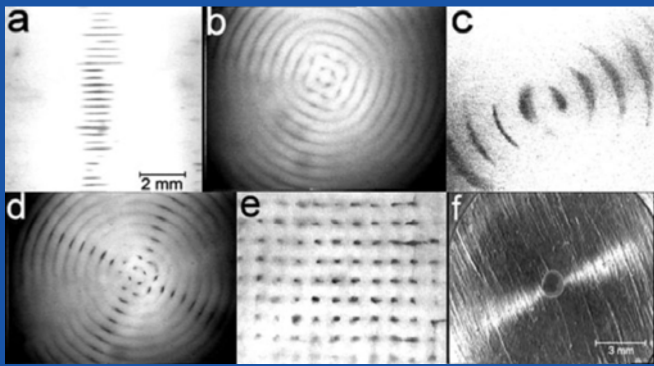

M. Wiklund

L. A. Kuznetsova et al., AIChE, **25**, 834, 2009

3D aggregates produced by ultrasound, stabilized with lectin crosslinking

Electron microscope image of RBC aggregates

Electron microscope image of HepG2 cell aggregates

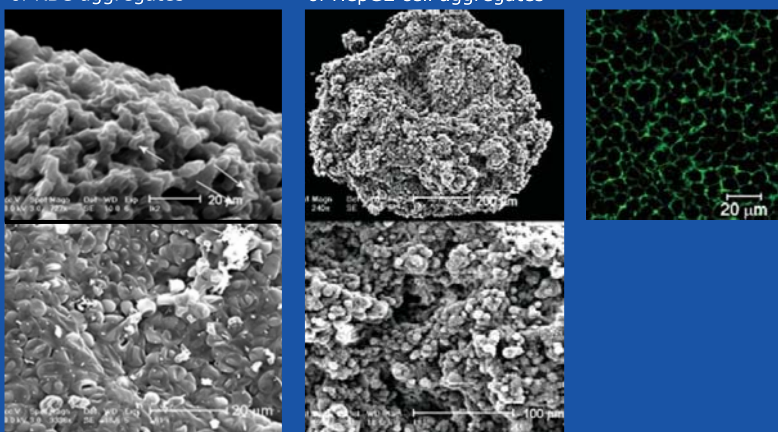

M. Wiklund

L. A. Kuznetsova et al., AIChE, **25**, 834, 2009

3D aggregates produced by ultrasound, followed by gel encapsulation

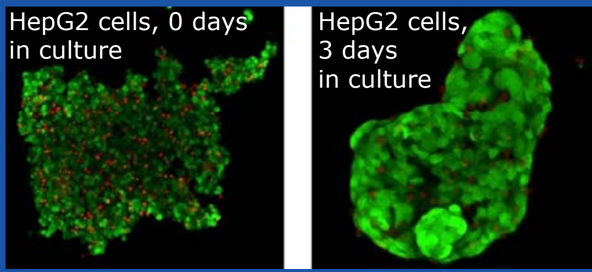

Conclusion:
Higher viability for thinner aggregates (~10 cell layers), otherwise hypoxia!

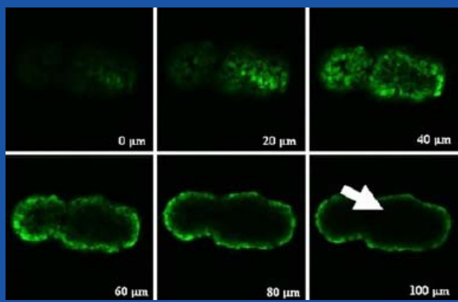

Confocal slices at different depths (Calcein AM), 10 days in culture

D. Bazou et al., Toxicol. In Vitro, **22**, 1321, 2008;
D. Bazou et al., Cell Biol. Toxicol. **26**, 127, 2010

M. Wiklund

Imaging the immune synapse in cell pairs trapped with ultrasound

Background, Natural killer (NK) cells:

- Third largest population of white blood cells
- NK cells are part of the innate immunity and can act fast, e.g. during initial stages of infections
- NK cells recognize and kill tumour cells or virus infected cells
- Killing is mediated through recognition of cell surface ligands during formation of an "immune synapse"

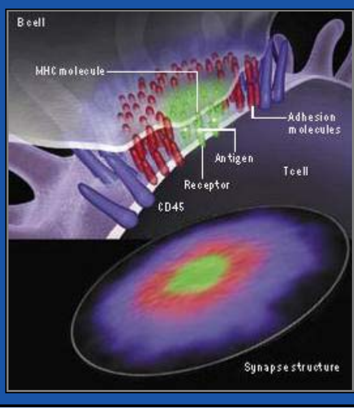

M. Wiklund

Imaging the immune synapse in cell pairs trapped with ultrasound

Activating or inhibitory interaction:

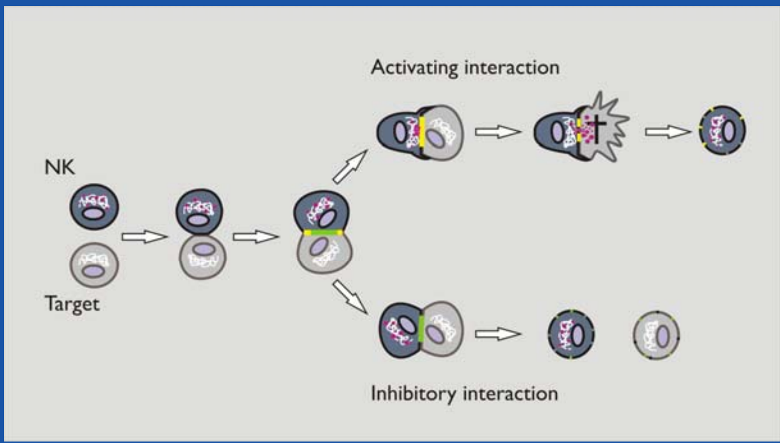

M. Wiklund

Imaging the immune synapse in cell pairs trapped with ultrasound

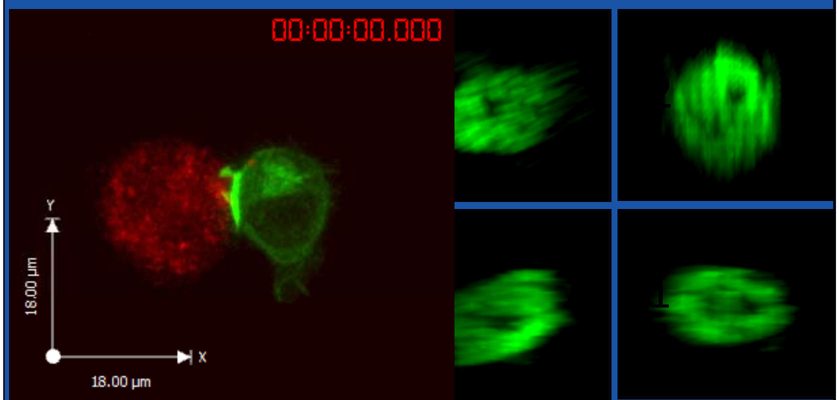

M. Wiklund

B. Vanherberghen et al., unpublished

Summary

- Biocompatibility of USW devices depend on many factors: Amplitude, frequency, device design, cell type, application, ...etc.
- Some investigations suggest that ultrasound can damage cells or cell functions
- Other investigations suggest that ultrasound may be beneficial for the cells or cell functions

KTH Physics

M. Wiklund

-35-

Lecture 5: Experimental Characterization

J. Dual, ETH Zurich, Switzerland

When characterizing devices used for ultrasound manipulation, a number of techniques are valuable, among others:

- microscopy (see lect. By M. Wiklund)
- admittance curves for the transducer (see lecture on piezoelectricity by M.Hill and J. Dual)
- laser interferometry
- modal analysis

In this lecture the focus is put on laser interferometry, modal analysis and a specific example, described in [1].

Laser Interferometry

Laser interferometry is a very useful technique, when displacements or velocities on surfaces need to be measured, because it is a contactless measurement technique. Therefore, the measurement does not disturb the motion to be measured.
The propagation of light is described by Maxwell's equations. Linearly polarized harmonic light (e.g. from a laser with sufficiently long coherence length) propagates with the wave speed c = 2.998 10^8 m/s in vacuum. It is described by

$$\underline{E} = E_y\, \underline{e}_y = A\, \mathrm{Cos}(\omega t - kz)\, \underline{e}_y ,$$

where $\underline{E}$ is the electrical field, ω is the circular frequency and $k = \omega/c$. The typical wavelength is around 600 nm.
The frequency of the visible light (10^{15} Hz) is too high to be detected directly, therefore detectors are used that measure the time averaged energy flux, the intensity I, which is proportional to

$$I = \; b \,\{\, \underline{E}^2 \,\}$$

b is an arbitrary constant,which is dropped in the following. If two light waves are superimposed on each other, the resulting intensity is

$$I = \{\, \underline{E}_1{}^2 \,\} + \{\, \underline{E}_2{}^2 \,\} + 2\, \{\, \underline{E}_1 \cdot \underline{E}_2 \,\}$$

If they have the same polarization direction and are described by

$E_1 = A_1 \text{Cos}(\omega t - \underline{k}_1 \cdot \underline{r})$ und $E_2 = A_2 \text{Cos}(\omega t - \underline{k}_2 \cdot \underline{r} + \phi)$

One obtains

$$I = I_1 + I_2 + 2\sqrt{I_1 I_2} \cos\delta \qquad (1)$$

where $\delta = \underline{k}_2 \cdot \underline{r} - \underline{k}_1 \cdot \underline{r} - \phi = \frac{2\pi}{\lambda}\Delta s - \phi$.

Δs is the difference in path length. Therefore the intensity varies between a minimum ($\delta = (2N-1)\pi$) and a maximum ($\delta = 2N\pi$) , depending on the phase difference δ between the two waves.

Michelson Interferometer

In a Michelson interferometer configuration the two waves are generated with a beam splitter (that preferably is polarization sensitive). The object beam is reflected from the object, the reference beam from a fixed reference mirror.

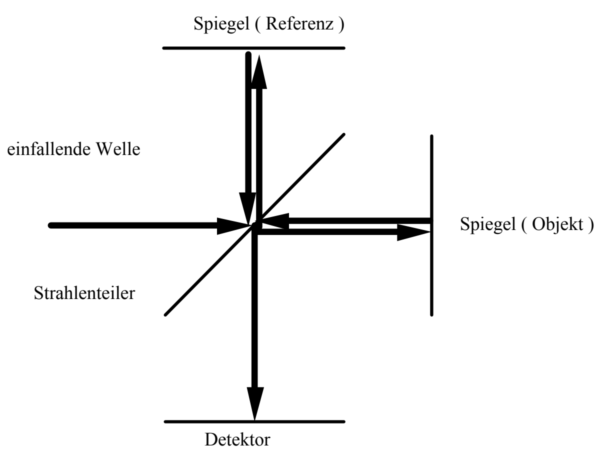

If the object moves, the intensity acc. to eq. 1 will vary, as the path length difference is a function of time. The interferometer therefore measures the displacement of the object point in the direction of the laser beam.
This intensity variation is detected with a photodiode and demodulated using:

- fringe counting or phase demodulation to yield displacement
- frequency demodulation to yield velocity

In order to eliminate low frequency motions (caused by thermal drift, shocks, etc.) the reference mirror can be mounted on a piezoelectric element (for low frequency path length stabilization) or its influence on the signal is eliminated in the demodulation process.

In order to discriminate between motion towards and motion away from the laser, often a process called heterodyning is used, where at least one of the beams is shifted in frequency e.g. using an acoustooptic modulator. Upon interference the voltage signal then has a carrier frequency equal to the difference frequency of the two beams.

More specifically: Let us assume the two beams have a path difference given by

$$\Delta s(t) = s_0 + 2\,\xi(t) \qquad (2)$$

s_0 is the static difference, which needs to be smaller than the coherence length of the laser. The two beams are described by

$$a_1 = a_{10} \sin(\, 2\,\pi\,(\,\nu + f_1)\,t + k\,x\,)$$
$$a_2 = a_{20} \sin(\, 2\,\pi\,(\,\nu + f_2)\,t + k\,x\,)$$

where a_{i0} are the respective amplitudes and f_i are the frequency shifts. This results in an intensity at the detector

$$I(t) = a_{10}^2 \sin^2[\, 2\,\pi\,(\,\nu + f_1)\,t\,] + a_{20}^2 \sin^2[\, 2\,\pi\,(\,\nu + f_2)\,t + k\,\Delta s\,] +$$
$$a_{10}\,a_{20}\,\{\cos[\, 2\,\pi\,(\,f_1 - f_2)\,t - k\Delta s\,] - \cos[\, 2\,\pi\,(\,2\nu + f_1 + f_2)\,t + k\Delta s\,]\}$$

Because of the low pass behavior of the photodetector, all the terms containing ν are averaged to yield a DC voltage V_0.

$$V(t) = V_0 + K\,a_{10}\,a_{20} \cos[\, 2\,\pi\,(\,f_1 - f_2)\,t - \frac{2\pi}{\lambda}(s_0 + 2\xi(t)\,] \qquad (3)$$

where K is a constant. Eq. 3 describes a phase modulated signal with carrier frequency $f_C = f_1 - f_2$.

Alternatively, this can be interpreted as a frequency modulated signal

$$\phi(t) = 2\pi \int f^*(t)\,dt \qquad \text{or} \qquad \frac{d\phi}{dt} = 2\pi\,f^*$$

where ϕ und f^* are phase and frequency of the signal.

Combined with eq. 3 one obtains

$$\frac{d\phi}{dt} = 2\pi\, f_c - \frac{4\pi}{\lambda}\frac{d\xi}{dt} = 2\pi\,(f_c - f_D)$$

$$f_D = \frac{2}{\lambda}\frac{d\xi}{dt} \qquad (4)$$

is the Doppler frequency. The frequency modulated signal is then

$$V(t) = V_0 + K\, a_{10}\, a_{20} \cos[\, 2\,\pi\, (\, f_c - f_D)\, t\,] \qquad (5)$$

When the structure to be investigated is very small, the object beam needs to be precisely focused. This is best done with a fiber optic interferometer, where a spot size of < 5µm can be obtained. When both arms of such an interferometer are reflected at different points on the object, the difference of the displacements is measured.
In plane displacements can also be measured, e.g. in the following configuration:

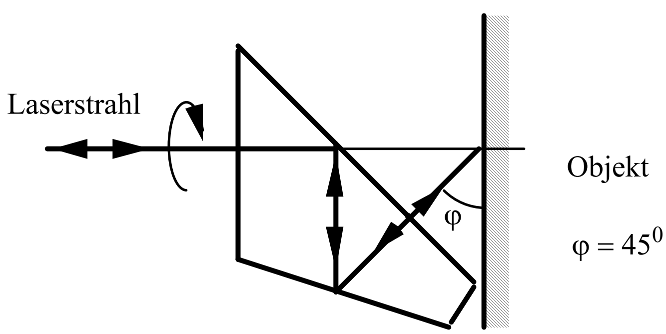

Because here the light needs to be retroreflected, a special tape is used for this purpose. However, this might not be feasible if the structures are very small, because of the additional mass loading.

There are various other methods available, e.g. a **Fabry Perot Interferometer**, where a frequency dependent multiple reflection is used as the basic principle.

Obtainable resolution in interferometry

When comparing different interferometer systems, the SNR (signal to noise ratio) and the frequency range are crucial. The theoretical maximum resolution is limited by shot noise at the detector.
As a measure for the resolution one can take the displacement for SNR = 1. In general it is given by

$$\delta_{min} = k\sqrt{\frac{\Delta f}{P_0 \eta}}$$

where	η	Detector efficiency e.g. 10%)
	P_0	Laser power (e.g. 1 mWatt)
	Δf	bandwidth
	k	a constant

For all interferometers in the text, a typical value is

$$\delta_{min} \cong 1\ 10^{-14}\ m/\sqrt{Hz}$$

For a bandwidth of 1 MHz one can therefore expect a maximum resolution of 10^{-11}m. By averaging this value can be further improved.

Modal Analysis

Modal analysis is a widely used method to characterize a structure dynamically in terms of its resonance frequencies, damping and modes of vibrations. For every device an infinite number of resonances exist. In many cases the lowest resonances are most important. For every mode, in principle the whole structure is involved.

For ultrasonic manipulation devices, typically piezoelectric elements are used to excite the structure and as well to measure the response. (Admittance curves) Alternatively, a laser interferometer can be used.

If only the resonance frequencies and their damping are needed, in principle it is sufficient to measure the transfer function between excitation at position $\underline{r}_1$ and response at position $\underline{r}_2$. If neither of the two positions is a node of one of the resonance modes, all the frequencies and damping values can be found.
If the mode shapes are also important, then the structure can be scanned, which might be a challenge, if the structure is small, however gives much more information about the particular mode shapes.

If the resonance modes are separated enough (depending on damping) one can decouple the resonances and consider them as single degree of freedom oscillators. This corresponds to the modal decomposition in a FEM analysis.

$$m\, x_{,tt} + \delta\, x_{,t} + cx = F$$

with the transfer function G for harmonic excitation

$$G = \frac{x}{F} = \frac{1}{m} \; \frac{1}{\omega_0^2 - \omega^2 + i\, \omega\, \delta/m} \tag{6}$$

Also the quality factor Q can be defined for the respective mode

$$Q = \frac{m\omega_0}{\delta} = \frac{\omega_0}{\omega_2 - \omega_1} = \frac{\omega_0}{\Delta\omega}$$

ω_2 and ω_1 are the circular frequencies, which correspond to phase values of the resonance phase +/- $\pi/4$. For Q >10 these are also the frequencies, for which the amplitude is $\sqrt{2}/2$ of the maximum amplitude. Q is therefore given by the resonance frequency divided by the bandwidth.
The total transfer function can then be composed of the sum

$$G = G_1 + G_2 + \ldots$$

where each mode will have different parameters. Using partial fractions one obtains

$$G = \frac{1}{2\, i\, \omega_0\, m} \left(\frac{1}{i\omega + \lambda} - \frac{1}{i\omega + \lambda^*} \right) \tag{7}$$

where $\lambda = \frac{\delta}{2\,m} - i\omega_0$

and $\lambda^* = \frac{\delta}{2\,m} + i\omega_0$

For positive ω and damping which is not too large, the first term in eq. 7 dominates in the vicinity of ω_0. If one plots Re(G) = x and Im(G) = y in the complex plane, we obtain the equation of a circle, which can be used to fit the damping.

$$x^2 + \left(y + \frac{1}{2\, \omega_0\, \delta} \right)^2 = \left(\frac{1}{2\, \omega_0\, \delta} \right)^2$$

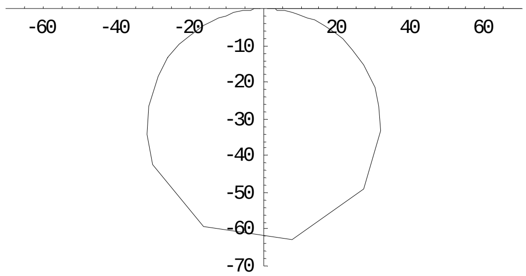

Complex representation of the transfer function in the complex plane. Please note the insufficient frequency resolution that might result from the application of the discrete Fourier transform, when the damping is low.

Literature

1. Neild A, Oberti S, Dual J, Design, modeling and characterization of microfluidic devices for ultrasonic manipulation, SENSORS AND ACTUATORS B-CHEMICAL **121**, 2, pp. 452-461 Published: FEB 20 2007
2. Wagner, J.W., Optical Detection of Ultrasound, **Physical Acoustics XIX**, Academic Press, 1990, p. 201 - 266

Available online at www.sciencedirect.com
ScienceDirect
Sensors and Actuators B 121 (2007) 452–461
SENSORS AND ACTUATORS B CHEMICAL
www.elsevier.com/locate/snb

Design, modeling and characterization of microfluidic devices for ultrasonic manipulation

Adrian Neild *, Stefano Oberti, Jürg Dual

Center of Mechanics, ETH Zurich, 8092 Zurich, Switzerland

Received 21 December 2005; received in revised form 27 March 2006; accepted 6 April 2006
Available online 16 May 2006

Abstract

An ultrasonic micropositioning system which is capable of separating particles into distinct and observable lines has been modeled using a finite element approach. The use of such a contactless manipulation method is believed to have many applications in the fields of microtechnology, life-sciences and lab-on-a-chip devices, one example would be in cell assays. The device consists of an etched silicon wafer which is bonded to a piece of glass the etched area can thus be filled with a fluid containing suspended particles. When the system is excited to vibration by the macro-piezoelectric plate attached on the underside of the silicon wafer, a pressure field is established throughout the fluid volume. When an inhomogeneity in a fluid is exposed to an ultrasonic field the acoustic radiation force results, this is found by integrating the pressure, retaining second order terms, over the surface of the field and taking the time average. Consequently, due to the presence of a pressure field in the fluid in which the particles are suspended, a force field is created. The finite element model is shown to be able to predict the frequencies at which resonance occurs, and the resulting modal shapes.

Keywords: Particle; Resonance; Positioning; Non-linear; Finite element

1. Introduction

The manipulation of suspended particles, a term used here to refer to inhomogeneities within a fluid which may consist of micro-sized solid particles, biological cells or droplets of an immiscible fluid, within microfluidic systems has many applications. One method of doing this is to use acoustic radiation forces generated by an ultrasonic pressure field. When a suspended particle interacts with an ultrasonic wave, when the pressure is integrated over the surface of the sphere whilst retaining second order terms, and time averaged the result is the acoustic radiation force. Other methods for the contactless manipulation of particles include laser traps, suction pipettes and dielectrophoresis (DEP). These will be briefly described, so that the advantages of ultrasonic methods can be established. Laser traps or optical tweezers are capable of exerting forces on particles of a refractive index different to that of the surrounding medium. With this method it is possible to manipulate single particles. However, a particle can only be manipulated after its position was identified. A well-established method for the manipulation of single cells is the suction pipette, again a single particle can be handled after it has been located. DEP refers to the force exerted on the induced dipole moment on an uncharged dielectric and/or conductive particle by a non-uniform electric field. Thus it is necessary to expose the particles to electrical fields, a point which may not be desirable in the handling of cells; in addition the induced force field only extends a short distance from the electrodes.

The limitation of optical tweezers to the manipulation of single micron-sized particles is due to the optical wavelength being similar in size to the particle diameter, whilst in an ultrasonic system these would typically differ by two or more orders of magnitude; hence the periodicity of the standing wave field can be used to simultaneously position many particles. In addition, as the ultrasonic field is present throughout the fluidic volume, it is not necessary to first identify the location of particles prior to handling, and exposure to large electrical fields does not occur. A major area in which the handling of particles is of importance is that of life-sciences. Much work has recently been focused on micro-total analysis systems (μTAS) and lab-on-a-chip devices

* Corresponding author at: Institute of Mechanical Systems, CLA G21.1, ETH Zentrum, 8092 Zürich, Switzerland. Tel.: +41 1 632 77 57; fax: +41 1 632 11 45.
E-mail address: adrian.neild@imes.mavt.ethz.ch (A. Neild).

0925-4005/$ – see front matter © 2006 Elsevier B.V. All rights reserved.
doi:10.1016/j.snb.2006.04.065

[1,2], in which many steps are taken in the analysis of a substance in a single microfluidic device. Whilst the handling of very small structures such as DNA and proteins would require a step change in the ultrasonic frequencies currently being used in ultrasonic manipulation devices, the handling of cells is a proven possibility. Thus possible applications in life-sciences include flow cytometry, cell fusion, and applications where cells need to be divided into clumps to be treated differently whilst being kept under observation such as cell assays.

Filtration is an area in which a substantial quantity of work has been done using acoustic forces. Acoustic filters have been shown to be capable of partially separating two phases, provided that at least one is liquid or gaseous [3–5]. These devices are multilayered resonators and as such are treated as 1D systems [6,7]; the layers include a fluid and piezoelectric plate. The system is actuated by the piezoelectric layer, which causes a pressure field to be established in the fluid, the nodal planes of which are parallel to the piezo. When operated as a filter, the particles are collected at the nodal planes and the clarified fluid can then be removed separately, leaving a concentrated solution of particles.

By extending the concept of capturing particles in planes using a sound field varying in one dimension, it is possible to trap particles in lines or points by using more complicated two- or three-dimensional sound fields. Various suggestions and efforts have been made in this direction. One principle uses two focused ultrasound beams that propagate in opposite direction, analogous to optical tweezers. Particles are collected between the focal points of these two beams [8]. Other approaches use a plurality of transducers that are driven independently. Often these transducers are created by one piezoelectric plate or shell with the electrode being cut into many areas. These approaches include the use of line-focused transducer with multiple electrodes, as described by Kozuka et al. [9], resulting in the possibility of transporting particles two-dimensionally. Numerous ultrasound transducers functioning independently of each other is also an approach taken by Mitome et al. [10] and Umemura et al. [11]. The resulting sound field is a superposition of the sound field from each of the transducers. Barmatz and Allen [12] have described an apparatus for levitating an object acoustically. Particles and cells have also been positioned in both clumps and lines by the pressure field coupled into a fluid volume by the movement of a glass plate excited to vibration by shear piezoelectric elements which are attached between the outer edge of the plate and a clamping mechanism [13–15].

In addition an increasing number of microfabricated devices have been described in the literature. These include acoustic filters, using a 1D acoustic field excited by a macro-piezoelectric [16,17]. A further essentially 1D device is described by Lilliehorn et al. [18], in which particles are trapped at certain locations, by multiple piezoelectric elements, within a microfluidic system. Devices for micropostioning have been also devised, which collect particles in planes perpendicular to the plane of the piezoelectric plate used to activate them. As this dimension is usually kept small it means that particles throughout the nodal planes can be observed. Hence particles can be positioned for purposes such as flow cytometry [19] or automated gripping by external bodies [20]. The pressure fields of these devices are typically 1D, however the behavior of the system to generate such a field is considerable more complicated that in the case of an acoustic filter. Dougherty and Pisano [19] presented a system which uses two coplanar transducers which are driven out of phase to each other. Whilst Petersson et al. [21] dispensed with the need for two out of phase drive signals by activating a piezoelectric plate in phase at frequencies in which such a resonance in the fluid perpendicular to the plate occurs. Furthermore, Wiklund et al. [22] have presented a device in which the actuation is a piezoelectric element coupled through a wedge into the system. The device used here and first described in [23] is a micropositioner, it is activated by a strip of electrode defined at the edge of the piezoelectric plate. Advantages of this method include the removal of the requirement for a phase shifted signal, a larger number of modes can be excited and that it is believed that by arrangement of two orthogonal electrodes a system can be developed in the future which is capable of positioning particles in lines or points in a manner akin to that used by the authors previously [13,14]. This system has been modeled using a finite element approach, and the emphasis of this work is assessment of the accuracy of such a model, the cause of inaccuracies detected, and the demonstration of the necessity of modeling such systems for design purposes.

2. Device and model description

The ultrasonic micropositioning system presented here is depicted in Fig. 1. It consists of three layers adhered together. The 2D is shown in Fig. 1b, it extends a distance of 25 mm in the z-direction. The upper layer is glass (shown as white in the cross-sectional view), and so allows visual access to the particles suspended in the fluid cavity beneath, it is fabricated by cutting of a standard glass slide with a wafer saw, and has a width of 12 mm and thickness of 1 mm. The center layer is made of silicon (black), it has a 5 mm wide and 200 μm deep DRIE etched recess, when this layer is adhered to the glass the recess forms the fluid cavity (light gray). For a device of this size it is sufficient to glue these layers together, for smaller devices anodic bonding may be required. For the purpose of experimentation the cavity

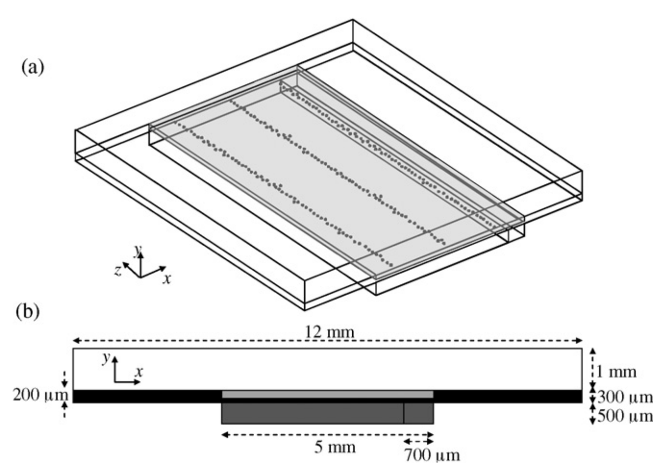

Fig. 1. 3D (a) and 2D cross-sectional (b) schematics of the micropositioning device.

is loaded by applying a droplet into a well at either end of the device (not shown in Fig. 1), these wells are also etched into the silicon layer (200 μm deep, half circles of 5 mm diameter), but are not covered by the piece of glass. The cavity is then filled by capillary forces. The third layer is the piezoelectric plate (dark gray). This is 5 mm in width and 0.5 mm in depth, it is glued to the underside of the silicon, and is aligned with the fluid cavity. The upper electrode of the piezoelectric plate is grounded. The lower electrode has been cut to a depth of 30 μm, in order to break the electrical contact; this cut is a distance of 700 μm from the edge and travels the full length (25 mm) of the piezoelectric plate. The resulting strip electrode is activated with the required electrical signal, the remaining area of the lower electrode is grounded. The reason for such a method is that it allows a wave to be excited which travels along the piezoelectric and 100 μm thick silicon composite plate, this vibrating plate couples to the adjacent fluid volume. The result is a large number of resonant modes, more than if the full surface is activated, which is beneficial for this work as a larger set of results can be compared with simulation. In addition, research into this arrangement will allow future possibilities of using orthogonally orientated electrodes to set up pressure fields capable of positioning particles into clumps [13], as well as the lines possible in this device. The device is held at each end, by attaching the underside of the silicon part to a support at the location where the wells are etched.

A finite element approach has been used to model the system in the two dimensions shown in Fig. 1b. This has been done using the commercially available program Femlab, a partial differential equation solver with combined meshing abilities. The electrical boundary conditions used were a sinusoidal signal applied to the strip electrode on the lower surface of the piezoelectric plate, and ground on the upper and remaining part of the lower electrode. For the structural boundary conditions free displacement was defined at all external edges of the 2D model. In addition it was necessary to define a fluid structure interaction, between the fluid and adjacent bodies. The program is modular based, the modules used being piezoplane strain, plane strain for the glass and silicon parts, and acoustic for the fluid. The governing variables being displacements in the x- and y-directions (u, v) for the first two modules, and pressure (p) for the third, in addition voltage (V) for the piezoelectric module is required. Consequently in defining the fluid structure interaction, the force balance becomes an area load (F_n/A) applied on the solid elements:

$$F_n = -A\rho_f \left.\frac{\partial\phi}{\partial t}\right|_s \Rightarrow \frac{F_n}{A} = -n_s p \tag{1}$$

with n_s being the vector normal to the interface surface, ϕ the velocity potential (in the fluid) and ρ is the fluid density. In addition the equating of the velocities becomes a normal acceleration (a_n) applied to the fluid:

$$v_n = -\nabla\phi|_s n_s \Rightarrow (-\omega^2\bar{u})n_s = a_n = -\frac{\nabla p}{\rho_f} n_s \tag{2}$$

with $\bar{u}$ being the displacement vector and ω is the angular frequency. A mesh of 6000 triangular elements was found to be sufficient.

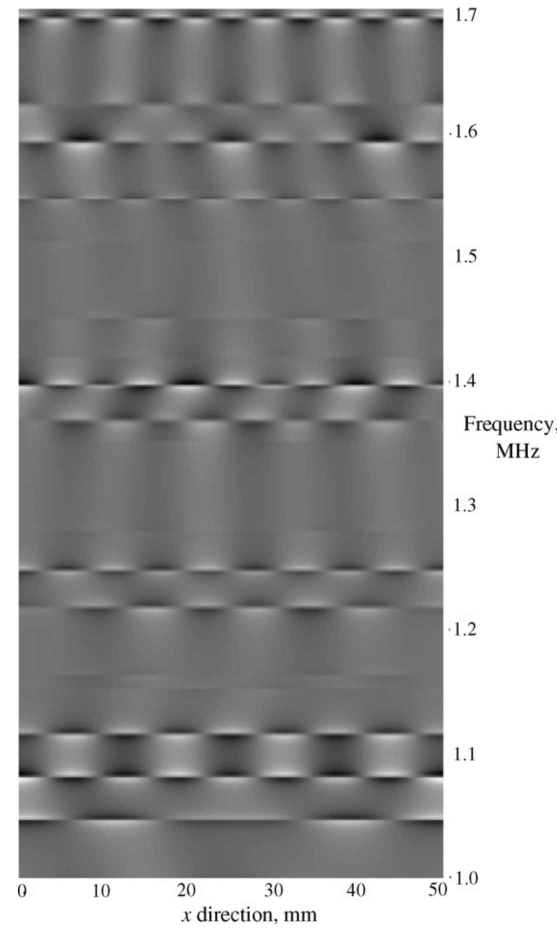

Fig. 2. A plot of the pressure (grayscale) along the lower surface of the fluid chamber as a function of distance across this surface (x-axis) and frequency (y-axis).

Damping was applied in the model by the use of complex stiffness parameters for the solid parts, and a complex speed of sound for the fluid, the values used are from [3]. The piezoelectric parameters used are from the supplier.

The model has been used to find the frequencies at which resonance occurs between 1 and 1.7 MHz. The result can be seen in Fig. 2, where the pressure along the lower surface of the channel is plotted against the distance across the channel (x-axis) and frequency (y-axis). The plot is a grayscale with black being minimum and white maximum. One such resonant frequency is 1.25 MHz, for this frequency the absolute value of the pressure field and displacement of the solid parts of the system (the deformation is scaled by a factor of 15 000) are shown in Fig. 3a and b respectively. It can be seen that the pressure field is predominantly 1D in the x-direction.

In addition to providing the resonant frequencies, the data generated by the model can also be used to predict the number of lines of particles that can be expected, and their locations. Such knowledge is useful for design of these systems, for example so that outlets and inlets can be positioned in the correctly, this is especially true for systems of more complicated geometry than the channel used here, i.e. the next generation of ultrasonic micromanipulation devices.

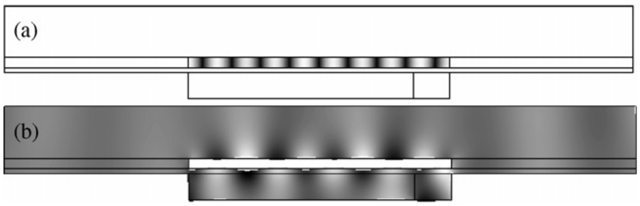

Fig. 3. (a) The simulated pressure field plotted using the absolute values, and (b) the vertical displacement of the device when operated at 1.25 MHz.

Yosioka and Kawasima [24] give an expression for the force acting on a compressible particle in a planar standing wave, hence in a 1D pressure field. Gor'kov [25] has considered the force arising from an arbitrary pressure field. It should be noted that in both cases the assumption is made that the particle is not near a wall, hence reflection of the scattered field is not considered. This assumption can not be applied to a microfluidic system, however it seems reasonable to make the further assumption that any discrepancy between the existing theory and the microfluidic case is a difference in amplitude of the forces rather than a major change in the shape of the force field, hence the lines which are formed will be at locations predictable by the equations presented by Gor'kov. Even though most resonances of the device being examined result in a 1D force field, the equation of Gor'kov has been used as it applies in all cases. Gor'kov states that the time-averaged (indicated throughout by $\langle\cdot\rangle$) force is given by

$$\langle \vec{F} \rangle = -\nabla \langle U \rangle, \tag{3}$$

where $\langle U \rangle$ is the force potential, which was found to be

$$\langle U \rangle = 2\pi \rho_f r^3 \left(\frac{1}{3} \frac{\langle p^2 \rangle}{\rho_f^2 c_f^2} f_1 - \frac{1}{2} \langle q^2 \rangle f_2 \right). \tag{4}$$

The terms $\langle p^2 \rangle$ and $\langle q^2 \rangle$ are the mean-square-fluctuations of the pressure and (fluid) particle velocity in the incident wave at the point where the particle is located, $f_1 = 1 - \rho_f c_f^2/(\rho_s c_s^2)$ and $f_2 = 2(\rho_s - \rho_f)/(2\rho_s + \rho_f)$. The terms ρ_s and ρ_f refer to the density and c_s and c_f to the speed of sound in the objects and fluid, respectively, and r refers to the object radius. For the calculation of $\langle p^2 \rangle$ and $\langle q^2 \rangle$, the linear equation of the sound field can be used; therefore, $p = \rho_f \partial\phi/\partial t$ and $q^2 = v_x^2 + v_y^2 + v_z^2$, with $v_x = -\partial\phi/\partial x$, etc. The particles collect at areas of minima in the force potential. In the case of copolymer spheres (ρ_s is $1050\,\mathrm{kg\,m^{-3}}$, c_s is $3000\,\mathrm{m\,s^{-1}}$) suspended in water, the $\langle p^2 \rangle$ term dominates; consequently the particles are arranged at the pressure nodes, and within these nodes at the locations of maximum $\langle q^2 \rangle$. Similarly in acoustic filters the term "lateral forces" is often applied, meaning those forces which act in the nodal plane and collect the particles in clumps of areas of the maximum pressure gradient.

In Fig. 3a the absolute value of the pressure is given in order that the expected location of the particles is clearly identifiable as black. It can be seen that in these two dimensions nine vertical lines of particles are formed, which become vertical planes when the third dimension is considered. As the upper layer is glass the system can be viewed from above (i.e. negative y-direction), what can be seen are clearly separated lines of particles. This allows application in which differently handled particles, or perhaps more interestingly cells, can be held at distinct locations and simultaneously viewed. It should be noted that the acoustic radiation force is not the only force generated by the presence of an ultrasonic pressure field; there are also secondary forces which occur between particles, and drag forces due to acoustic streaming. In the experiments performed with this system however, the resultant orientation of the particles appears to be dictated by the acoustic radiation force.

3. Design considerations

One of the major differences between the ultrasonic micropositioners described in the literature is the method of actuation. Various options have been described, including actuation across the full channel width [21], out of phase actuation applied to two electrodes [19], and coupling of a piezoelectric element through a wedge designed such that a planar waves passes across the width of the channel [22], in addition actuation along the edge of the channel is used here. With the development of a model of the device described here a comparison of some of these actuation methods becomes possible. Fig. 4 shows the absolute pressure at the lower left corner (the point of minimum x and y which lies in the chamber) of the fluid chamber as a function of frequency for four different actuation modes. This point is chosen as a pressure maximum occurs there at resonance (see Fig. 2). In each of the four examples the same voltage electrical signal is applied to the active electrode. In Fig. 4a the response for edge actuation is shown, it can be seen that the most modes result. In Fig. 4b the electrode is extended across half the width of the channel, this increases the pressure amplitude in some cases. In Fig. 4c the electrode stretches across the full width of the channel, again those modes which still occur have a larger pressure amplitude, however as the system is now symmetrical, those modes which are asymmetric (1.22, 1.25 and 1.54 MHz) have disappeared. In Fig. 4d, two out of phase signals are applied, this has the effect of applying a signal over the whole area whilst breaking the symmetry of the system, however the only frequency at which a larger pressure is obtained than in the edge actuation case is 1.54 MHz. This is different in aim to the method Dougherty et al. used, in that they wished to create just one mode which would result in a single line along the center of the channel [19]. It should be noted that for each of the four cases the voltage used was the same, however in the case of a device filled with a non-flowing fluid the operational limit is more likely to be the heat generated due to the input of electrical power rather than the maximum voltage which can be applied to the piezoelectric. It can be seen firstly that different actuation methods give the maximum pressure for different resonant frequencies, furthermore each of these methods give a range of resonances which arise in 1D pressure field (in almost all cases), hence more complicated methods of actuation are not required to achieve this aim.

The majority of the resonances which occur between 1.0 and 1.7 MHz in this device are essentially 1D varying in the x-direction. An alteration to the geometry of the device will now be briefly described to demonstrate that this is not always the case.

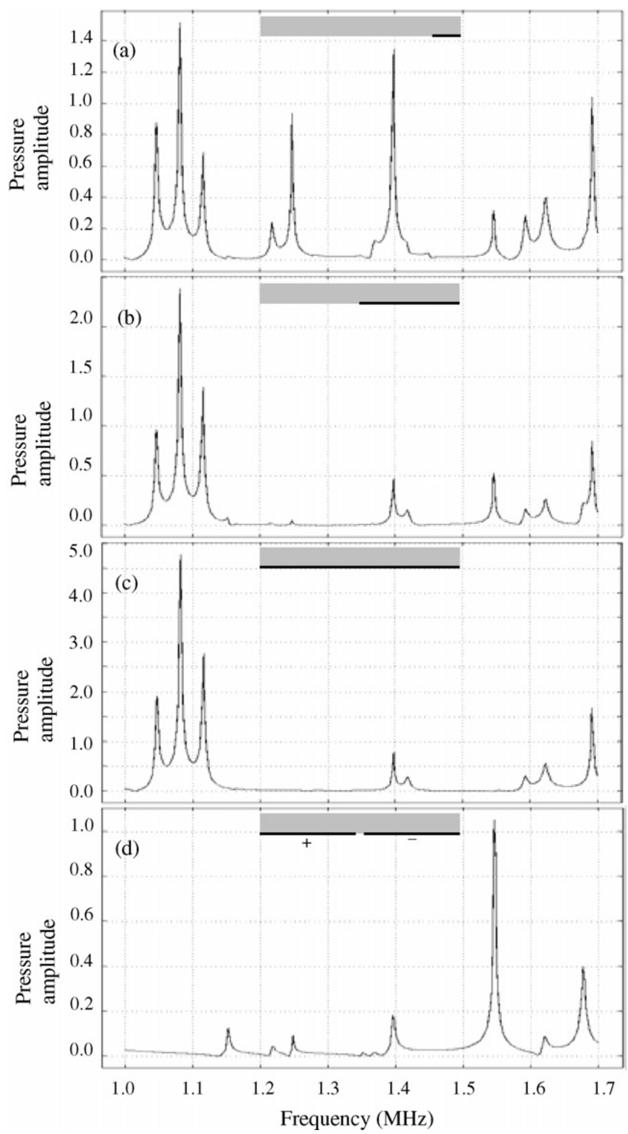

Fig. 4. The absolute value of the pressure which occurs at the point at one end (lowest x) of the lower surface of the fluid chamber plotted against frequency for different actuation methods. The actuation methods, as depicted, are (a) 700 μm strip electrode, (b) half width electrode, (c) full width electrode, and (d) two half width electrodes driven out of phase.

In making this system consideration was given to what the source of glass ought to be for the upper glass layer, the device presented here uses glass cut from a standard slide, the readily available alternative was a glass coverslip (approximately 100 μm thickness). In modeling a device identical to that depicted in Fig. 1 except for the use of a 100 μm glass plate, it became clear that in the range of investigated frequencies (1.0–1.7 MHz), no resonance exists in which a 1D field exists. An example of a resonance which occurs, at 1.21 MHz, is shown in Fig. 5a and b in which the absolute pressure and vertical displacement (deformation scaling factor is 1000) are shown, respectively. The maximum vertical displacement which occurs is 88 nm (at 10 V excitation), resulting in a predicted pressure maximum of 2.1 MPa. This can be compared with Fig. 3, where the maximum displacement is 3.1 nm and the pressure is 0.93 MPa. If

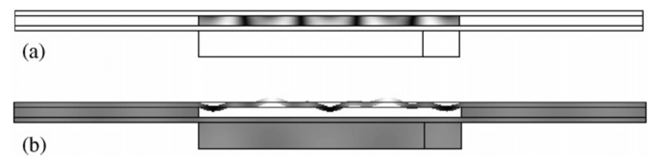

Fig. 5. (a) The simulated pressure field plotted using the absolute values, and (b) the vertical displacement of a device with a 100 μm glass layer when operated at 1.21 MHz.

the coupling condition from the solid to the fluid, as given in Eq. (2) is considered, then it can be seen that the vertical displacement is coupled to the fluid as an acceleration. This acceleration causes a variation in the amplitude in the pressure field in the vertical direction at (and near) the surface, as can be seen by the ∇p term. In the case of a pure 1D field the pressure variation in the vertical direction is zero, hence reference has been made to what are essentially 1D fields. This means that when the device with a 1 mm glass layer is considered a small variation can be expected, whilst for the case of the 100 μm glass layer device the displacements are so large that the result is that the field is no longer 1D as can be seen in Fig. 5a. The aim of such micropositioners has been stated as being the separation of particles into distinct areas all of which are simultaneously viewable, with the $\langle p^2 \rangle$ term being dominant in Eq. (4), the optimum field for such a system is a 1D field varying in the x-direction, as between each observable location a pressure maximum occurs. In fact the system utilizing a thin glass layer is closer in nature to an evanescent field device [26] used to move particles lying on or being very close to a thin membrane.

What this demonstrates is that a simplified model, such as considering just the fluid vibration, firstly does not accurately predict the frequencies [23] but secondly does not offer a clear understanding of the modal response of the system, for this a finite element model is required.

4. Modeling and experimental results

An experiment has been performed with the micropositioning system shown in Fig. 1 in order to determine the frequencies at which resonance occurs. This was done by observation of the orientation of particles suspended within the fluid volume, if the particles were observed to move to distinct locations then a resonance was deemed to have been identified. For this experiment the chamber was loaded with 26 μm diameter copolymer spheres in DI water, in order to achieve this a droplet of the fluid was placed in the well at one end, through capillary forces the channel fills, afterwards by applying or removing fluid in the wells a fluid flow can be created. Whilst the frequency was slowly increased from 1.0 to 1.7 MHz in steps of 0.01 MHz, resonant frequencies were sought whilst fluid flow was present. The presence of fluid flow has two advantages, firstly the location of the resonances is clearer as for each new frequency the particles are randomly orientated so it is a matter of looking for particle positioning rather than movement of lines created by the previous resonant point. Furthermore, it is believed that a lower amplitude force field is required as the affect of the flow is that the forces in the x-direction are effectively averaged over

Table 1
Summary of resonant frequencies which occur between 1 and 1.7 MHz and the corresponding number of lines of particles

Frequency		No. of lines	
Simulation	Experiment	Simulation	Experiment
1.05	–	4	–
1.08	1.08	8	8
1.12	1.12	8	8
1.22	1.20	7	9
1.25	1.24	9	9
1.37	–	9	–
1.40	1.42	10	10
1.54	1.52	11	11
1.58	–	10	–
1.62	–	10	–
1.69	1.69	12	12

z, hence lines are more clearly observed. Table 1 shows the simulated and experimentally obtained resonant frequencies and the number of lines formed at these frequencies. Once a resonant frequency was observed an attempt was made to form lines with no fluid flow, this was successful in three cases, those of 1.20, 1.24 and 1.52 MHz. It should be noted that this experiment was performed without reference to the model results, and hence it was a matter of looking for resonant frequencies without using the knowledge, obtained from the model, of where they should be.

The simulated frequencies listed in Table 1 come from the results shown in Figs. 2 and 4a. When compared with the results of the experimental work it can be seen that four resonances have been missed those at 1.05, 1.37, 1.58 and 1.62 MHz, these frequencies correspond to the four cases in which the predicted pressure is not 1D. This can be seen by examination of Fig. 6 which shows the absolute value of the pressure field for each of the resonant frequencies. A further difference, which is less easily explained, is the number of lines found at 1.22 MHz, this differs from that predicted. In the other cases the agreement is good, both in terms of the number of lines and in the accuracy to which the resonant frequency is predicted, which has a maximum error of 0.02 MHz. Fig. 7 shows particles aligned at the resonant frequencies, these images are views from above, and hence are in the xz plane, in these cases a flow is present in the chamber. Larger images, in the same plane, of the three cases in which lines were clearly formed in a static fluid volume are shown in Fig. 8.

A further examination of the accuracy of the model was undertaken by measuring the vertical displacement of the

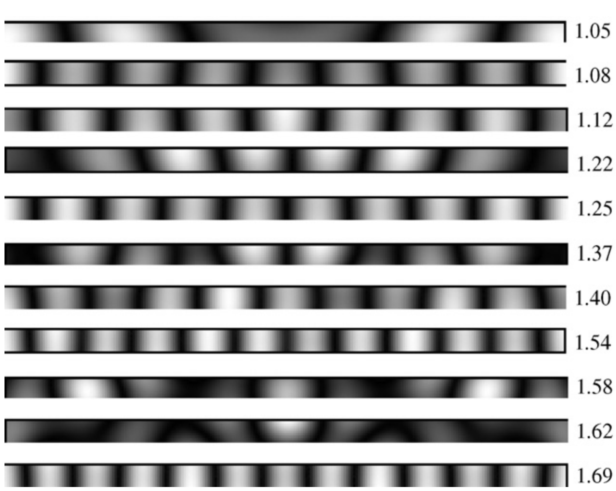

Fig. 6. The simulated absolute pressure value across the cross-section of the fluid chamber at each pf the identified resonance frequencies.

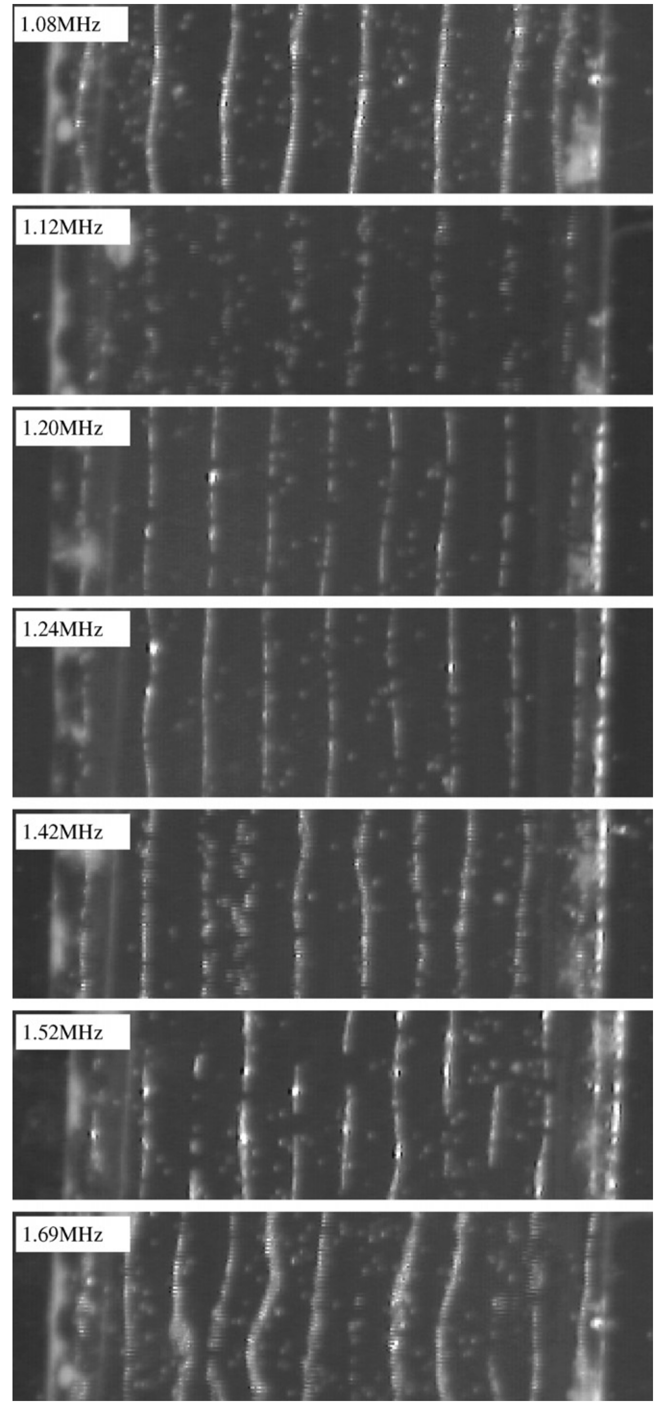

Fig. 7. Lines of 26 μm diameter copolymer formed in a flowing fluid at each of the frequencies which were identified through experimental work, the images show the xz plane.

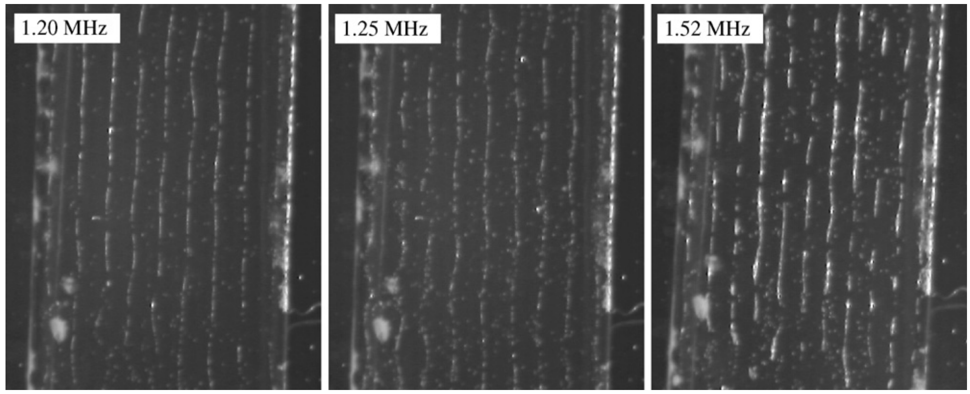

Fig. 8. Lines of particles formed in a non-flowing fluid volume at the three frequencies at which this proved possible.

underside of the piezoelectric plate. This was done by applying a 400 μs long linearly frequency swept signal to the strip electrode. The signal swept from 0.7 to 2.0 MHz, and was enveloped by a Hanning window, this allowed measurements to be detected from 1.0 to 1.7 MHz. The measurement was performed using a Polytec interferometer, the laser head being displaced over 5 mm in 0.1 mm steps using a positioning stage. Fig. 9 shows the (a) simulated and (b) experimental results, as a plot of distance across the plate against frequency, a grayscale is used, with the maximum amplitude being 8.3 and 9.4 nm in the simulation and experimental data, respectively, based on an 18 V input signal, which is that used for the particle experiments. The experimental results were analyzed by using a Fourier transform on each measured signal, and for each frequency plotting the value in phase with the input voltage. It can be seen that the frequencies show good agreement. The number of peaks and troughs agree at most frequencies, an exception is at 1.22 MHz in the simulation were 4 wavelengths can be seen, whilst in the experiment 4.5 wavelengths are seen. This is the same frequency at which the number of lines predicted differed to the number observed experimentally. A hypothesis was thus made that the piezoelectric material parameters are not sufficiently accurately known. This could be expected to lead to a certain degree of inaccuracy, especially in modes in which large displacements in the piezoelectric plate occurs, such as the mode in which the erroneous result occurs.

It is important to notice that the peaks shown in these data, do not necessarily represent the best operational frequencies, many of the frequencies at which resonances are observed in the pressure field analysis show little displacement on the underside of the piezoplate, for example at 1.25 MHz as shown in Fig. 3.

An efficient method of establishing the resonant frequencies of an acoustic filter is the examination of the electrical admittance of the system [3]. This method has been applied to the micropositioning device and compared to that predicted by the finite element model. For the simulated results Femlab allows the calculation of the current across the strip electrode for a given voltage, hence the admittance can be found, this is shown in Fig. 10a. A current probe (Le Croy AP015) was used in conjunction with a Le Croy 9344 CM oscilloscope (Chestnut Ridge, NY) to find the current applied to the active electrode. The experiment was performed using a linearly frequency swept excitation signal. The frequency range was 0.5–3.5 MHz in a time of 400 μs, and the signal was enveloped by a Hanning window, this allowed the calculation of the admittance across a frequency range from 1.0 to 3.0 MHz. The calculation was performed by taking the Fourier transform of the current and voltage signal, and then

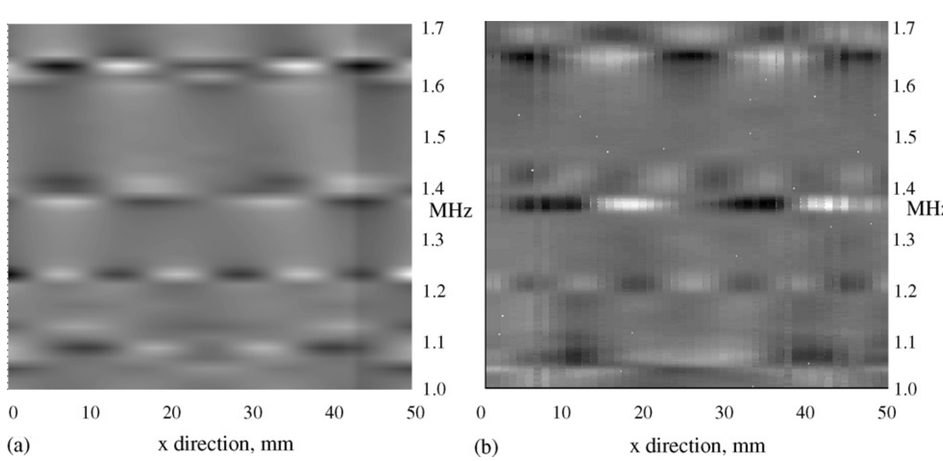

Fig. 9. The vertical displacement (grayscale) of the underside of the piezoelectric element, plotted against distance (x-direction) and frequency, obtained through (a) modeling and (b) experimental work.

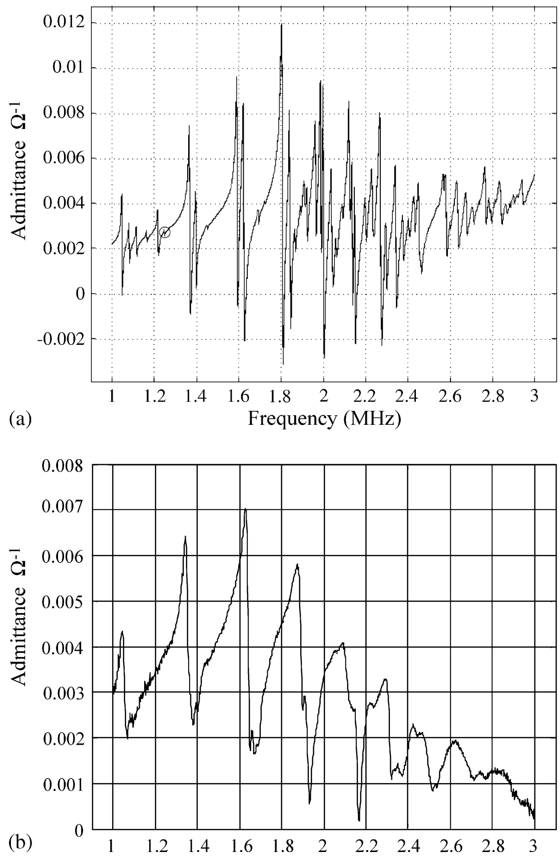

Fig. 10. The electrical admittance of the system over a range of 1.0–3.0 MHz, obtained using (a) simulation and (b) experimentation.

dividing the first by the latter for each frequency of interest. Fig. 10b shows the real value of the admittance, resulting in the phase being the same as that for the simulated data. A comparison of the two sets of data shows the presence of eight major peaks in the admittance, the agreement of the location of these peaks worsens considerably with increasing frequency. It was believed that this is a demonstration of poorly defined piezoelectric parameters, and this will be confirmed below. Within the frequency range of 1.0–1.7 MHz, it can be seen that the location of the major peaks is accurate. What are missing in the experimental work are the smaller peaks shown in the simulation data. However these smaller peaks correspond to resonances in which large pressure fields are predicted, an as illustration the peak which occurs at 1.25 MHz is circled in the simulation data. In the case of an acoustic filter, devices in which the nodal pressure planes are parallel to the actuating piezoelectric plate, the system can be treated as 1D. If a large pressure field occurs then large displacements in the piezoelectric plate can be expected and hence admittance values change. However, in the case of a device such as described in this work the interrelationship is not as clear. Large amplitude pressure fields can occur at frequencies at which relatively low displacements, or thickness changes in the piezoelectric plate occurs, 1.25 MHz is an example of this (also see Fig. 9), it is these frequencies which have a very small influence on the admittance. It can therefore be seen that a finite element model provides a useful tool in the location of resonant frequencies, as well as aiding the understanding of the resultant modes.

The hypothesis was put forward in relation to the results of modeling and measuring the displacement of the underside of the piezoelectric plate that the inaccuracies which occur could be caused due to the piezoelectric parameters used. This point was again raised in relation to the electrical properties of the device, the measured values of which can be seen to clearly diverge from theory with increasing frequency. In order to investigate the accuracy of the piezoelectric parameters dispersion curves were measured, this seemed suitable as the device couples a bending plate to the fluid, albeit causing an asymmetric load on the plate itself. A piezoelectric plate measuring 48 mm × 10 mm, with a thickness of 0.5 mm, was cut. A strip electrode measuring 0.7 mm was cut using a wafer saw at one end (across the 10 mm width). The resultant plate was operated in air by an excitation signal applied to this strip electrode. A linearly swept driving signal was used, sweeping from 0.3 to 8 MHz (although only data from 1 to 3 MHz is used here), over a period of 400 μs, the displacement of the surface of the piezoelectric plate was measured using a Polytec interferometer at 1251 points, separated by 40 μm, the digitized signal of 25 000 points separated by 40 ns was recorded by an oscilloscope and logged by computer. A 2D FFT was performed on the data, firstly in the temporal domain then the spatial domain, such that data about the wave number against frequency was found, this data was re-sampled such that the phase velocity against frequency could be plotted as shown in Fig. 11b. This re-sampling requires the high temporal and spatial resolution used in the measurement. At lower frequencies this re-sampling has the affect of smearing the fairly noisy data in the velocity direction, hence the vertical lines in the plot. This can be compared with a 2D model made of the plate (in the cross-section measuring 50 mm × 0.5 mm), a mesh of 4040 elements was used, such that 1000 elements were along the upper surface, an analysis was made at frequencies from 1 to 3 MHz in steps of 0.1 MHz. For each frequency the wave number was calculate using a Fourier transform. The data is plotted in Fig. 11a. As a relatively low number of frequencies are used, when the resultant data is plotted it appears smeared in the frequency direction. What can be seen is that the curves disagree fairly strongly at higher frequencies, meaning that certain, if not all, values in the stiffness matrix are inaccurately defined. This is believed to be an important limitation to the accuracy of the manipulator model. In the case of this more complicated system in which the piezoelectric plate is coupled to a silicon layer and in turn a fluid, it is not surprising that a mode involving large displacements in the piezoelectric, even at a relatively low frequency (for example 1.22 MHz), is inaccurately modeled.

The resonant mode within the fluid is influenced by the displacement of the solid bodies surrounding it, as shown in the case of the cover glass device, and also in a comparison of a simple fluid resonant model and the actual model results obtained here. Hence as the displacement data for the piezoelectric plate appears to be limited by the accuracy of the parameters for this material, this would also explain why the resonant frequencies at which the maximum pressures occur are not necessarily the frequencies at which the device works best. Another factor is

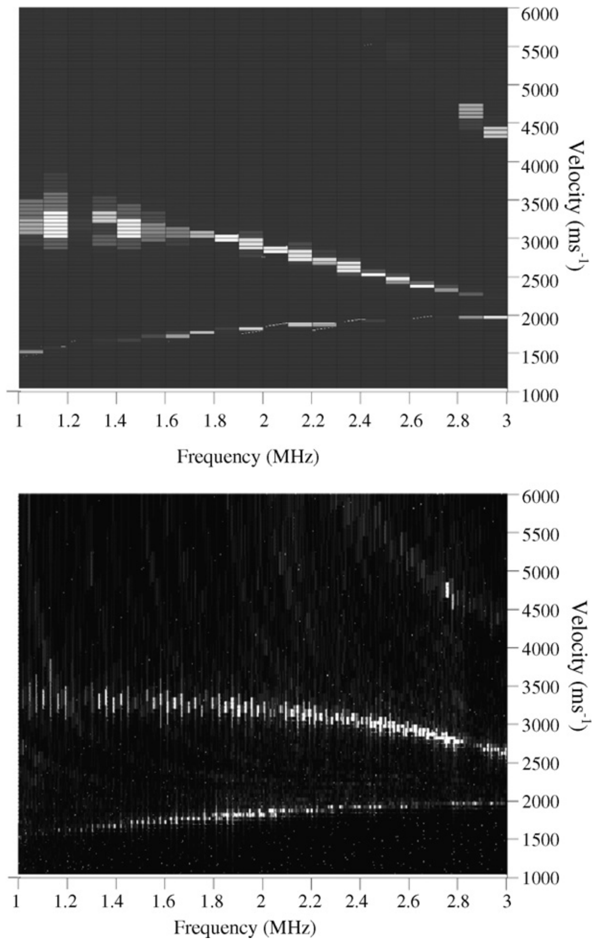

Fig. 11. The dispersion curve for a 0.5 mm thick piezoelectric plate as obtained (a) theoretically using the manufactures parameters and (b) experimentally.

the damping in the fluid (containing suspended particles) layer, the value used is that found empirically for an acoustic filter by Gröschl [3]. The model is thus limited in its' ability to predict the best resonant condition and one error has been observed in the predicted mode shapes, both of which are believed to be due to poorly defined input parameters. The models' usefulness is in the understanding of the influence of device geometry and demonstrating the importance of considering the fluid–structure interaction, investigating different actuation methods, the prediction of most resonant modes and frequencies, and for assessing the usefulness of approaches such as electrical and displacement measurements for finding resonant conditions.

5. Conclusions

The micropositioning system presented here has been modeled using a finite element approach, this has been seen to give an accurate prediction of the location of the resonances, and by first identifying which of the resultant modes are essentially 1D a comparison with experimental results is good in six out of the seven cases. The absolute importance of such a model has been demonstrated by trying to establish the resonant frequencies by examination of the displacement of the piezoelectric and secondly the electrical properties, neither of which give all the frequencies. Furthermore the actuation method has been examined, and the model shows which type of actuation is required for best generation of each mode, and the interaction between the plate and fluid has been briefly examined by changing one of the geometrical parameters. The amplitude of the pressure field it not so well predicted, with the best operating frequency, 1.25 MHz, having the forth largest amplitude. It was suspected that the inaccuracy stems from the piezoelectric parameters, and a comparison between the modeled dispersion curves using those parameters and experimental data support that assertion.

Acknowledgements

This work was supported by KTI/CTI, Switzerland, through a Top Nano 21 grant, project nos. 6643.1 and 6989.1.

References

[1] S.J. Lee, S.Y. Lee, Micro-total analysis systems (μ-TAS) in biotechnology, Appl. Microbiol. Biotechnol. 64 (2004) 289–299.
[2] T. Vilkner, D. Janasek, A. Manz, Micro-total analysis systems, Recent Develop. Anal. Chem. 76 (2004) 3373–3386.
[3] M. Gröschl, Ultrasonic separation of suspended particles. Part I. Fundamentals, Acustica 84 (1998) 432–447.
[4] M. Gröschl, W. Burger, B. Handl, Ultrasonic separation of suspended particles. Part III. Application in biotechnology, Acustica 84 (1998) 815–822.
[5] J.J. Hawkes, W.T. Coakley, A continuous flow ultrasonic cell-filtration method, Enzyme Microb. Technol. 19 (1996) 57–62.
[6] M. Hill, Y. Shen, J.J. Hawkes, Modeling of layered resonators for ultrasonic separation, Ultrasonics 40 (2002) 385–392.
[7] H. Nowotny, E. Benes, General one-dimensional treatment of the layered piezoelectric resonator with two electrodes, J. Acoust. Soc. Am. 82 (1987) 513–521.
[8] J.R. Wu, Acoustical tweezers, J. Acoust. Soc. Am. 89 (1991) 2140–2143.
[9] T. Kozuka, T. Tuziuti, H. Mitome, T. Fukuda, Micromanipulation using a focused ultrasonic standing wave field, electronics and communications in Japan, part Iii, Fund. Electr. Sci. 83 (2000) 53–60.
[10] H. Mitome, T. Kozuka, T. Tuziuti, Non-contact micromanipulation method and apparatus, US Patent 6,055,859 (May 2, 2000).
[11] S.I. Umemura, M. Kamahori, K Sasaki, Particle handling apparatus for handling particles in fluid by acoustic radiation pressure, US Patent 6,216,538 (April 17, 2001).
[12] M.B. Barmatz, J.L. Allen, Single mode levitation and translation, US Patent 4,736,815 (April 18, 1988).
[13] A. Haake, J. Dual, Contactless micromanipulation of small particles by an ultrasound field excited by a vibrating body, J. Acoust. Soc. Am. 117 (2005) 2752–2760.
[14] A. Haake, A. Neild, G. Radziwill, J. Dual, Positioning, displacement, and localization of cells using ultrasonic forces, Biotechnol. Bioeng. 92 (2005) 8–14.
[15] A. Haake, A. Neild, D.-H. Kim, J.-E. Ihm, Y. Sun, J. Dual, B.-K. Ju, Manipulation of cells using an ultrasonic pressure field, Ultrasound Med. Biol. 31 (2005) 857–864.
[16] N.R. Harris, M. Hill, S. Beeby, Y. Shen, N.M. White, J.J. Hawkes, W.T. Coakley, A silicon microfluidic ultrasonic separator, Sens. Actuators B: Chem. 95 (2003) 425–434.
[17] N. Harris, M. Hill, Y. Shen, R.J. Townsend, S. Beeby, N.M. White, A dual frequency, ultrasonic, microengineered particle manipulator, Ultrasonics 42 (2004) 139–144.
[18] T. Lilliehorn, M. Nilsson, U. Simu, S. Johansson, M. Almqvist, J. Nilsson, T. Laurell, Dynamic arraying of microbeads for bioassays in microfluidic channels, Sens. Actuators B: Chem. 106 (2005) 851–858.
[19] G.M. Dougherty, A.P. Pisano, Ultrasonic particle manipulation in microchannels using phased co-planar transducers, in: Proceedings of

the 12th International Conference on Solid State Sensors, Actuators and Microsystems, vol. 670, Boston, 2003, p. 373.
[20] A. Neild, S. Oberti, F. Beyeler, J. Dual, B. Nelson, A micro-particle handling system combining an ultrasonic manipulator and microgripper, J. Micromech. Microeng., submitted for publication.
[21] F. Petersson, A. Nilsson, C. Holm, H. Jönsson, T. Laurell, Continuous separation of lipid particles from erythrocytes by means of laminar flow and acoustic standing wave forces, Lab-on-a-Chip 5 (2005) 20–22.
[22] M. Wiklund, C. Günther, R. Lemor, M. Jäger, G. Fuhr, H.M. Hertz, Ultrasonic features integrated into DEP chips, in: Proceedings of NanoTech 2005, Montreux, 2005.
[23] A. Neild, S. Oberti, A. Haake, J. Dual, Finite element modeling of a micro-particle manipulator, Ultrasonics, in press.
[24] K. Yosioka, Y. Kawasima, Acoustic radiation pressure on a compressible sphere, Acustica 5 (1955) 167–173.
[25] L.P. Gor'kov, Forces acting on a small particle in an acoustic field within an ideal fluid, Doklady Akademii Nauk Sssr 140 (1961) 88–92.
[26] P. Luginbuhl, S.D. Collins, G.-A. Racine, M.-A. Grétillat, N.F. de Rooij, K.G. Brooks, N. Setter, Microfabricated lamb wave device based on PZT sol–gel thin film for mechanical transport of solid particles and liquids, J. Microelectromech. Syst. 6 (1997) 337–346.

Biographies

Adrian Neild received a PhD in engineering from the University of Warwick, in 2003. He has since become a postdoctoral researcher at the Institute for Mechanical Systems at ETH Zürich (Swiss Federal Institute of Technology Zurich). His research interests lie in the fields of non-contact ultrasound, micromachined transducers, nondestructive evaluation and the use of acoustic radiation force to manipulate small particles in micro-fluidic systems.

Stefano Oberti graduated in 2004 from the Swiss Federal Institute of Technology (ETH Zurich) with a degree in mechanical engineering with focus on micro- and nanofabrication and control systems. During his diploma project he worked on the development of a microsqueeze force sensor useful as contact-free profilometer and viscometer at the IBM Research Laboratory in Rüschlikon (Switzerland). He is currently a PhD student and his main research area is ultrasonic manipulation within microfluidic devices.

Jürg Dual studied mechanical engineering at the ETH Zurich, Switzerland. He then spent 2 years on a Fulbright grant at the University of California in Berkeley, where he graduated with a MS and a MEng degree in mechanical engineering. For his dissertation again at ETH Zurich he was awarded the Latsis Prize of the ETH Zurich in 1989. After 1 year as visiting assistant professor at Cornell University, Ithaca, NY, he returned to the ETH Zurich as assistant professor. Since 1998 he has been full professor of mechanics and experimental dynamics in the Center of Mechanics of the Institute of Mechanical Systems at the ETH in Zurich. He is a Fellow of the ASME and Honorary Member of the German Association for Materials Research and Testing.His research focuses on wave propagation and vibrations in solids as well as micro- and nanosystem technology. In particular he is interested in both basic research and applications in the area of sensors (viscometry), nondestructive testing, mechanical characterization of microstructures and gravitational interaction of vibrating systems.

M6 Radiation Force Theory

Lecture notes for the advanced CISM school

Ultrasound standing wave action on suspensions and biosuspensions in micro- and macrofluidic devices

Udine, Italy, 7 - 11 June 2010

Microfluidics and ultrasound acoustophoresis

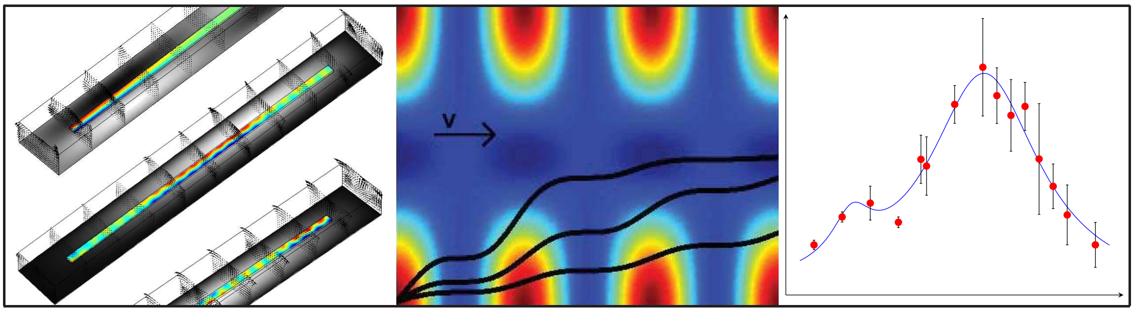

Henrik Bruus

Department of Micro- and Nanotechnology
Technical University of Denmark

Chapter 4

Ultrasound acoustofluidics

Acoustofluidics refers to the application of acoustic pressure fields in microfluidic systems. As the speed of sound in water at room temperature is $c_\mathrm{a} \approx 1.5 \times 10^3$ m/s, the application of ultrasound frequencies $f \gtrsim 1.5$ MHz will lead to wavelengths $\lambda \lesssim 1$ mm, which will fit into the submillimeter-sized channels and cavities in microfluidic systems. The ultrasound is typically generated by on-chip, ac-biased piezo-ceramic transducer.

When the acoustic waves are propagating in liquids, the associated fast-moving and rapidly oscillating density, pressure and velocity fields can impart a slow non-oscillating velocity component to the liquid or to small particles suspended in the liquid. In microfluidic systems these normally quite minute effects can be of significance. Interestingly, the origin of these effects can be traced back to two hydrodynamic properties largely ignored in the preceding chapters, namely the non-linearity of the Navier–Stokes equation and the small but non-zero compressibility of ordinary liquids.

The linear wave equation for acoustics is only an approximate equation derived by combining the thermodynamic equation of state expressing pressure in terms of density, the kinematic continuity equation (1.24), and the dynamic Navier–Stokes equation (1.37b). Discarding all external fields such as gravitation and electromagnetism, as well as considering only the isothermal case, these three equations form the starting point for the theory of acoustics or sound,

$$p = p(\rho), \tag{4.1a}$$

$$\partial_t \rho = -\boldsymbol{\nabla}\cdot\big(\rho\mathbf{v}\big), \tag{4.1b}$$

$$\rho\partial_t \mathbf{v} = -\boldsymbol{\nabla} p - \rho(\mathbf{v}\cdot\boldsymbol{\nabla})\mathbf{v} + \eta\nabla^2\mathbf{v} + \beta\eta\,\boldsymbol{\nabla}(\boldsymbol{\nabla}\cdot\mathbf{v}). \tag{4.1c}$$

This set of coupled non-linear, partial differential equations is notoriously difficult to solve numerically. However, approximate solutions can be found by perturbation theory.

4.1 The first-order acoustic wave equation

Consider a quiescent liquid, which before the presence of an acoustic wave has constant density ρ_0 and pressure p_0. Then let an acoustic wave be the origin to tiny perturbations in the density, the density and the velocity field,

$$\rho = \rho_0 + \rho_1, \qquad p = p_0 + c_{\mathrm{a}}^2 \rho_1, \qquad \text{and} \quad \mathbf{v} = \mathbf{v}_1. \tag{4.2}$$

Here, in the (isentropic) expansion of the equation of state $p(\rho) = \rho_0 + (\partial p/\partial \rho)_s \rho_1$, the derivative has the dimension of a velocity squared, which has been written as c_{a}^2. Below we shall see that c_{a} can be identified with the (isentropic) speed of sound in the liquid. Insertion of these expansions into Eqs. (4.1b) and (4.1c), and neglecting products of first-order terms, lead to the first-order continuity and Navier–Stokes equation,

$$\partial_t \rho_1 = -\rho_0 \boldsymbol{\nabla}\cdot \mathbf{v}_1, \tag{4.3a}$$

$$\rho_0 \partial_t \mathbf{v}_1 = -c_{\mathrm{a}}^2 \boldsymbol{\nabla} \rho_1 + \eta \nabla^2 \mathbf{v}_1 + \beta\eta\, \boldsymbol{\nabla}(\boldsymbol{\nabla}\cdot \mathbf{v}_1). \tag{4.3b}$$

A single equation for ρ_1 is obtained by taking the time derivative of Eq. (4.3a) and insertion of Eq. (4.3b) in the resulting expression,

$$\partial_t^2 \rho_1 = -\boldsymbol{\nabla}\cdot(\rho_0 \partial_t \mathbf{v}) = c_{\mathrm{a}}^2 \nabla^2 \rho_1 - (1+\beta)\eta \nabla^2 \big(\boldsymbol{\nabla}\cdot \mathbf{v}_1\big) = c_{\mathrm{a}}^2 \left[1 + \frac{\eta}{\rho_0 c_{\mathrm{a}}^2} \partial_t\right] \nabla^2 \rho_1. \tag{4.4}$$

To make further analytical progress, we assume harmonic time dependence of all fields,

$$\rho_1(\mathbf{r},t) = \rho_1(\mathbf{r})\, e^{-\mathrm{i}\omega t}, \qquad p_1(\mathbf{r},t) = c_{\mathrm{a}}^2 \rho_1(\mathbf{r})\, e^{-\mathrm{i}\omega t}, \qquad \text{and} \quad \mathbf{v}_1(\mathbf{r},t) = \mathbf{v}_1(\mathbf{r})\, e^{-\mathrm{i}\omega t}, \tag{4.5}$$

where $\omega = 2\pi\, f$ is the angular frequency and f the frequency of the acoustic field. The harmonic time dependence is expressed by the complex phase $e^{-\mathrm{i}\omega t}$ to ease the mathematical treatment. The physical fields are obtained simply by taking the real part. With this, each time derivative ∂_t in Eq. (4.4) gives a factor $-\mathrm{i}\omega$, and the equation becomes

$$\nabla^2 p_1 = -k^2\, p_1, \tag{4.6a}$$

$$k = (1+\mathrm{i}\gamma) k_0 = (1+\mathrm{i}\gamma) \frac{\omega}{c_{\mathrm{a}}}, \tag{4.6b}$$

$$\gamma = \frac{\eta\omega}{2\rho_0 c_{\mathrm{a}}^2} \approx 10^{-6}, \tag{4.6c}$$

where we have used $p_1 = c_{\mathrm{a}}^2 \rho_1$ as well as introduced the wavenumber k_0, the damped wavenumber k, and the viscous damping factor $\gamma \approx 10^{-6}$ (for water at $f = 1$ MHz). Eq. (4.6a) is a damped Helmholtz equation for a wave with damped wavenumber k and angular frequency ω. As $\gamma \ll 1$ we can neglect the viscosity in the bulk part of the acoustic wave, and going back to the explicitly time-dependent Eq. (4.4) we get

$$\nabla^2 p_1 = \frac{1}{c_{\mathrm{a}}^2}\, \partial_t^2 p_1, \quad \text{for } \eta = 0. \tag{4.7}$$

The solutions in 1D to this standard wave equation have the form $p_1(x,t) = p_1(x \pm c_{\mathrm{a}} t)$ showing that c_{a} indeed is the speed of sound. In the inviscid limit it furthermore follows by inserting Eq. (4.2) into Eq. (4.3b) that $\mathbf{v}_1 = \mathbf{v}(\mathbf{r})\, \mathrm{e}^{-\mathrm{i}\omega t}$ is a gradient of a potential ϕ_1,

$$\mathbf{v}_1 = -\mathrm{i}\, \frac{1}{\rho_0 \omega}\, \boldsymbol{\nabla} p_1 = \boldsymbol{\nabla}\phi_1, \quad \text{for } \eta = 0, \tag{4.8a}$$

$$\phi_1 = \frac{-\mathrm{i}}{\rho_0 \omega}\, p_1, \qquad \text{for } \eta = 0. \tag{4.8b}$$

Table 4.1: Acoustic parameters for modeling of inviscid liquids and elastic solids.

material	Speed of sound		density		Young's modulus		Poisson's ratio	
water	c_{wa}	1483 m/s	ρ_{wa}	998 kg/m^3	–		–	
silicon	c_{si}	8490 m/s	ρ_{si}	2331 kg/m^3	E_{si}	164 GPa	$\bar{\nu}_{\mathrm{si}}$	0.10
pyrex	c_{py}	5647 m/s	ρ_{py}	2230 kg/m^3	E_{py}	64 GPa	$\bar{\nu}_{\mathrm{py}}$	0.20
polystyrene	c_{ps}	1700 m/s	ρ_{ps}	1050 kg/m^3	–		–	

Thus both the density ρ_1 and velocity $\mathbf{v}_1$ can be calculated from the pressure p_1, which itself is found by the Helmholtz equation.

4.2 Acoustic resonances, basic concepts for viscous liquids

When operating an acoustofluidic device, it is often advantageous to run it at acoustic resonances for two reasons: the resonance patterns are usually both stable and reproducible, and at resonance a maximum of power is delivered from the transducer to where it is needed in the system.

To illustrate the fundamental properties of acoustic resonances, we study the simple 1D setup sketched in Fig. 4.1(a). Two planar walls are placed parallel to the yz-plane at $x = -L$ and $x = L$, respectively, and the gap is filled with water. The walls are forced to oscillate in anti-phase at a frequency $f \approx 1$ MHz and with an amplitude $\ell \approx 1$ nm. As a simplification we neglect the actual tiny displacement of the walls and instead model the oscillation by the velocity boundary condition sketched in Fig. 4.1(a),

$$v_1(-L,t) = -\omega\ell\,\mathrm{e}^{-\mathrm{i}\omega t}, \qquad v_1(+L,t) = +\omega\ell\,\mathrm{e}^{-\mathrm{i}\omega t}. \tag{4.9}$$

Starting from rest the resonance builds up until the incoming power equals the heat dissipation due to viscosity. The standing 1D wave $\mathbf{v}_1 = f(x)\mathrm{e}^{-\mathrm{i}\omega t}\,\mathbf{e}_x$ has $\boldsymbol{\nabla}\times\mathbf{v}_1 = \mathbf{0}$, so $\mathbf{v}_1 = \boldsymbol{\nabla}\phi_1$ and $\partial_j v_i = \partial_i v_j$. To find the viscid velocity potential ϕ_1, we note that $\partial_j\partial_j v_i = \partial_j\partial_i v_j = \partial_i\partial_j v_j$, i.e. $\nabla^2\mathbf{v}_1 = \boldsymbol{\nabla}(\boldsymbol{\nabla}\cdot\mathbf{v}_1)$, and from Eq. (4.3a) we have $\boldsymbol{\nabla}\cdot\mathbf{v}_1 = \mathrm{i}\omega p_1/(\rho_0 c_{\mathrm{a}}^2)$. Inserting these two expressions together with $\mathbf{v}_1 = \boldsymbol{\nabla}\phi$ into Eq. (4.3b), we find,

$$\phi_1(\mathbf{r},t) = \frac{-\mathrm{i}}{\omega\rho_0(1+\mathrm{i}\gamma)^2}\,p_1(\mathbf{r},t), \quad \text{for } \boldsymbol{\nabla}\times\mathbf{v}_1 = \mathbf{0}. \tag{4.10}$$

Because $\phi_1 \propto p_1$ the wave equation (4.6a) also holds for ϕ_1, and we can therefore write the solution for ϕ_1 as a superposition of a pair of counter-propagating plane waves with a complex wave number $k = k_0(1+\mathrm{i}\gamma)$ and unknown coefficients ϕ_+ and ϕ_- to be determined,

$$\phi_1(x,t) = \Big[\phi_+\mathrm{e}^{\mathrm{i}kx} + \phi_-\mathrm{e}^{-\mathrm{i}kx}\Big]\,\mathrm{e}^{-\mathrm{i}\omega t}. \tag{4.11}$$

The corresponding first-order velocity is

$$v_1(x,t) = \partial_x\phi_1(x,t) = \mathrm{i}k\Big[\phi_+\mathrm{e}^{\mathrm{i}kx} - \phi_+\mathrm{e}^{-\mathrm{i}kx}\Big]\,\mathrm{e}^{-\mathrm{i}\omega t}. \tag{4.12}$$

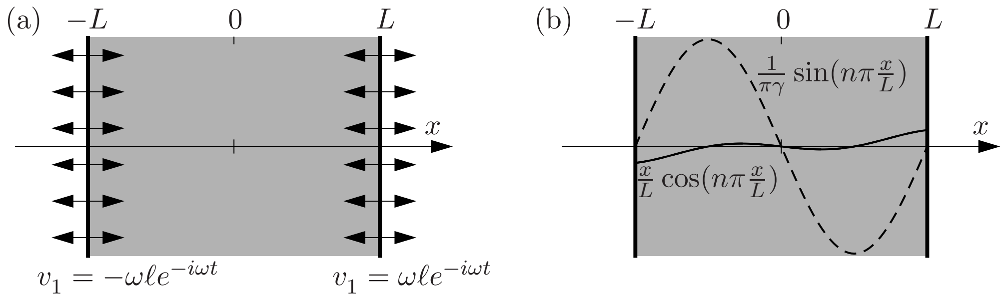

Figure 4.1: (a) A liquid slab (dark gray) between two parallel planar walls (thick lines) that oscillates harmonically in counter-phase (double arrows). As the amplitude is minute, $\ell \ll L$, the wall positions are considered fixed, while the first-order velocity $v_1(t)$ at the walls is changing harmonically, $v_1(t) = \pm\omega\ell\, \mathrm{e}^{-\mathrm{i}\omega t}$. (b) Sketch of the two terms in the resonant velocity field v_1 Eq. (4.14a). The small component (full line) proportional to $(x/L)\cos(\pi x/L)$ obeys the oscillatory boundary condition with amplitude $\pm\omega\ell$. The large resonant component (dashed line) proportional to $(1/\pi\gamma)\sin(\pi x/L)$ is an eigenmode obeying the hard-wall condition with amplitude zero.

The antisymmetric boundary condition on v_1 in Eq. (4.9) combined with Eq. (4.12) leads to $\phi_+ = \phi_-$, as well as an expression for the coefficients,

$$\phi_+ = \phi_- = \frac{-\omega\ell}{2k\sin(kL)}. \tag{4.13}$$

Consequently, we can obtain the following expression for v_1,

$$v_1(x,t) = \omega\ell\,\frac{\sin(kx)}{\sin(kL)}\,\mathrm{e}^{-\mathrm{i}\omega t} \approx \omega\ell\,\frac{\sin(k_0x) + \mathrm{i}\gamma k_0 x\cos(k_0x)}{\sin(k_0L) + \mathrm{i}\gamma k_0 L\cos(k_0L)}\,\mathrm{e}^{-\mathrm{i}\omega t}, \tag{4.14a}$$

where we have used $\gamma k_0 L \ll 1$ to make Taylor expansions in kL around k_0L. We note that when k_0L differs sufficiently from integer multiples of π, i.e. $\gamma \ll |k_0L - n\pi|$, then the imaginary parts of the denominators can be neglected. This corresponds to off-resonance characterized by a small magnitude of the velocity,

$$|v_1(x,t)| \approx \omega\ell \approx 10^{-6}c_\mathrm{a}, \quad \text{(off resonance)}, \tag{4.15a}$$

where the value is calculated by assuming $\omega \approx 10^7$ rad/s, $\ell \approx 0.1$ nm and $c_\mathrm{a} \approx 10^3$ m/s.

More interesting perhaps is the acoustic resonances, where the acoustic field acquires particularly large amplitudes and thus stores a large amount of energy, see Fig. 4.1(b). Theoretically, the resonances are identified by the minima in the denominators of the fields in Eq. (4.14), i.e. for $\sin(k_0L) = 0$ or $k_0L = n\pi$, $n = 1, 2, 3, \ldots$,

$$k_0 = k_n \equiv n\,\frac{\pi}{L}, \quad n = 1, 2, 3, \ldots \quad \text{(resonance condition)}. \tag{4.16}$$

In practice, the resonance is achieved by tuning the frequency ω to ω_n given by

$$\omega = \omega_n \equiv c_\mathrm{a}k_n = n\,\frac{\pi c_\mathrm{a}}{L}, \quad n = 1, 2, 3, \ldots \quad \text{(resonance frequency)}. \tag{4.17}$$

At the nth resonance $\sin(k_nL) = 0$ and $\cos(k_nL) = \mathrm{e}^{\mathrm{i}n\pi}$, so the acoustic fields become

$$\phi_1(x,t) \approx c_\mathrm{a}\ell \left[\frac{\mathrm{i}}{n\pi\gamma}\cos\left(n\pi\frac{x}{L}\right) + \frac{x}{L}\sin\left(n\pi\frac{x}{L}\right)\right]\mathrm{e}^{-\mathrm{i}(\omega_n t - n\pi)}, \tag{4.18a}$$

$$v_1(x,t) \approx \omega\ell \left[\frac{-\mathrm{i}}{n\pi\gamma}\sin\left(n\pi\frac{x}{L}\right) + \frac{x}{L}\cos\left(n\pi\frac{x}{L}\right)\right]\mathrm{e}^{-\mathrm{i}(\omega_n t - n\pi)}. \tag{4.18b}$$

From these expressions it follows that each of the fields acquires a resonant component with an amplitude that is a factor of $1/(n\pi\gamma) \approx (3/n)\times 10^4$ larger than the non-resonant component, e.g.

$$|v_1(x,t)| \approx \frac{1}{n\pi\gamma}\,\frac{\omega_n\ell}{c_\mathrm{a}}\,c_\mathrm{a} \approx \frac{1}{n}\,10^{-2}\,c_\mathrm{a}, \quad \text{(at the } n\text{th resonance)}. \tag{4.19}$$

In spite of the huge multiplication factor, $1/(\pi\gamma) \approx 10^4$, the velocity remains small enough, $v_1 \ll c_\mathrm{a}$ to ensure the validity of the perturbation approach.

From (4.18b) we see that the term actually obeying the velocity boundary condition $v_1(\pm L) = \pm\omega\ell$ is 10^4 times smaller than the other term, which obeys the hard-wall condition $v_1(\pm L, t) = 0$ and thus in fact is an eigenmode of the system. Thus, when coupling into a system with a frequency near an eigenmode frequency, the corresponding eigenmode gets excited with huge amplitude approximately a factor $1/\gamma$ larger than the coupling amplitude, independent of the actual boundary condition, see Fig. 4.1(b).

Finally, as the total energy E_ac for an harmonically oscillating system is twice the kinetic energy, Eq. (4.14a) implies $E_\mathrm{ac} = \frac{1}{2L}\int_{-L}^{L}\mathrm{d}x\,\frac{1}{2}\rho_0|v_1(x)|^2 = \frac{1}{4}\rho_0\omega^2\ell^2/|\sin(kL)|^2$. By Taylor expansion in $kL = \frac{L}{c_\mathrm{a}}\omega$ around the nth resonance at $n\pi$ we find a Lorentzian peak,

$$E_\mathrm{ac}(\omega) = \frac{\frac{1}{4}\rho_0\omega^2\ell^2}{\left|\frac{L}{c_\mathrm{a}}(\omega-\omega_n) - \mathrm{i}\gamma n\pi\right|^2} = \frac{\rho_0\omega^2\ell^2}{4n^2\pi^2}\,\frac{\omega_n^2}{(\omega-\omega_n)^2+\gamma^2\omega_n^2}, \quad \text{for } \omega\approx\omega_n. \tag{4.20}$$

4.3 Eigenmodes, inviscid liquids and shear-free solids

The above result indicates that we can gain insight in the nature of acoustic resonances in a driven systems by analyzing the eigenmodes $p_n = p_n(\mathbf{r})\,e^{-\mathrm{i}\omega_n t}$ of the equivalent isolated inviscid system. We simplify our treatment further by assuming that the solids that surrounds our water-filled microchannels are shear-free and thus characterized only by a pressure field governed by the Helmholtz equation (4.6a) with $\eta = 0$. We use three boundary conditions in the following, (i) the hard-wall condition, where the normal velocity is zero and thus by Eq. (4.8a) also the normal gradient of the pressure is zero, (ii) the soft-wall condition, where the pressure is zero, and (ii) the continuity condition for both pressure and velocity at the interface between two materials (a) and (b). We thus have

$$p_1 = 0, \qquad \text{soft-wall boundary condition,} \tag{4.21a}$$

$$\mathbf{n}\cdot\boldsymbol{\nabla}p_1 = 0, \qquad \text{hard-wall boundary condition,} \tag{4.21b}$$

$$\frac{1}{\rho_1^{(a)}}\mathbf{n}\cdot\boldsymbol{\nabla}p_1^{(a)} = \frac{1}{\rho_1^{(b)}}\mathbf{n}\cdot\boldsymbol{\nabla}p_1^{(b)}, \text{ and } p_1^{(a)} = p_1^{(b)}, \qquad \text{continuity boundary condition.} \tag{4.21c}$$

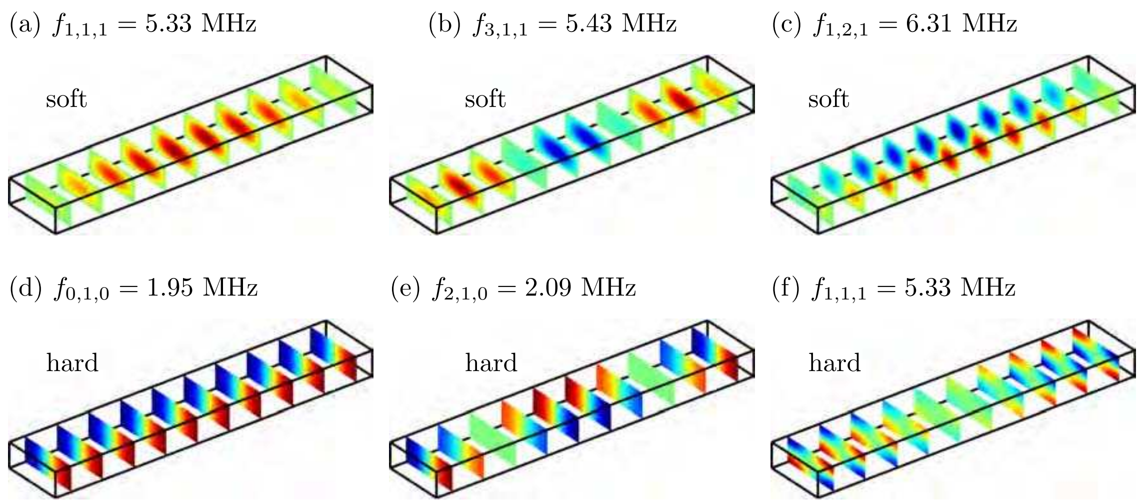

Figure 4.2: Color slice plots (red positive, green zero, blue negative) in the inviscid limit of some eigenmodes of the pressure field p_1 in a rectangular, single, water-filled microchannel of length $\ell = 2$ mm, width $w = 0.38$ mm, and height $h = 0.15$ mm. (a) - (c) Soft-wall boundary conditions $p_1 = 0$ at the surface, i.e. a zero-density wall surrounds the channel. (d) - (f) Hard-wall boundary condition $\mathbf{n}\cdot\boldsymbol{\nabla} p_1 = 0$, i.e. the surrounding wall is of infinite density. Reproduced from the DTU master thesis by Rune Barnkob [Barnkob 2009].

For a rectangular water-filled channel placed along the coordinate axes with its opposite corners at $(0,0,0)$ and (ℓ, w, h) surrounded by an ideal shear-free solid having $\rho = \infty$ or $\rho = 0$, the following eigenmodes are found as can easily be verified by direct substitution,

$$p_1(x,y,z) = p_\mathrm{a} \sin(k_x x)\sin(k_y y)\sin(k_z z), \text{ with } k_j = n_j \frac{\pi}{L_j}, \text{ (soft wall)}, \tag{4.22a}$$

$$p_1(x,y,z) = p_\mathrm{a} \cos(k_x x)\cos(k_y y)\cos(k_z z), \text{ with } k_j = n_j \frac{\pi}{L_j}, \text{ (hard wall)}, \tag{4.22b}$$

where p_a is the pressure amplitude, where $(L_x, L_y, L_z) = (\ell, w, h)$, and where $n_j = (0,)1,2,3,\dots$ is the number of half wavelengths ($n_j > 0$ for the sine-waves). The corresponding three-index resonance frequencies $f_{n_x,n_y,n_z} = \omega_{n_x,n_y,n_z}/(2\pi)$ are

$$f_{n_x,n_y,n_z} = \frac{c_\mathrm{wa}}{2}\sqrt{\frac{n_x^2}{\ell^2} + \frac{n_y^2}{w^2} + \frac{n_z^2}{h^2}}, \quad \text{with} \quad n_x, n_y, n_z = (0,)1,2,3,4,\dots. \tag{4.23}$$

Examples of these analytically determined eigenmodes are shown in Fig. 4.2. Note the low frequency of (d) and (e) having $n_z = 0$ along the smallest dimension in contrast to $n_z = 1$ of the other four eigenmodes. In (f) one half-length is squeezed in along the z-direction ($n_z = 1$) and the frequency increases significantly. In fact, as (a) and (f) have the same indices they also have the same frequency, namely $f_{1,1,1}$ despite their different boundary conditions. It turns out that the anti-symmetric resonance (d) having a perfect nodal plane in the vertical center plane is the ideal configuration for acoustophoretic separation.

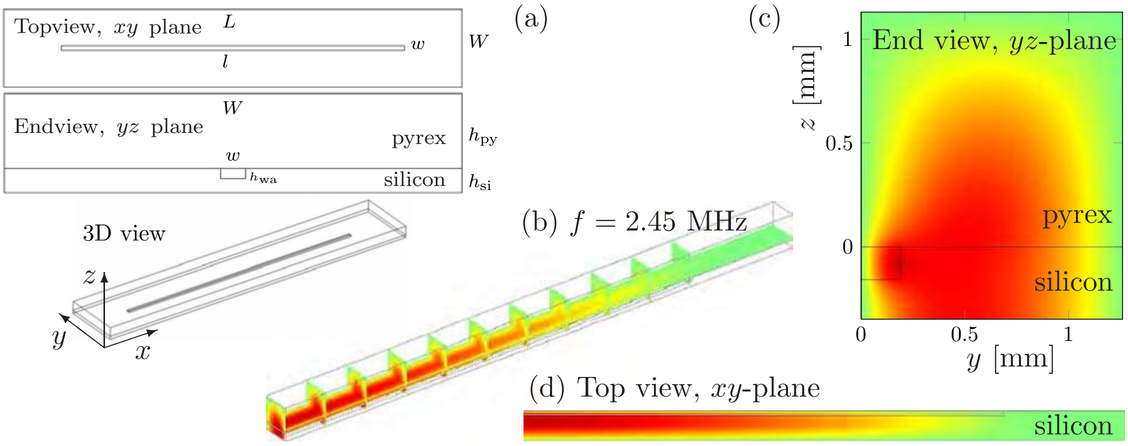

Figure 4.3: COMSOL simulation of the lowest antisymmetric eigenmode for the $L \times W \times (h_{\mathrm{si}}+h_{\mathrm{py}})$ rectangular pyrex/Si chip denoted α=1 in Fig. 6.1, with a narrow $\ell \times w \times h_{\mathrm{wa}}$ rectangular water-filled microchannel. (a) The chip geometry. (b) Color slice plot of the pressure (red positive, green zero) in a 3D $L/2\times W/2\times(h_{\mathrm{si}}+h_{\mathrm{py}})$ view. (c) End view of half the chip $W/2 \times (h_{\mathrm{si}}+h_{\mathrm{py}})$ in the yz-plane. Left edge is the antisymmetry plane. (d) Top view of one quarter of the chip $L/2 \times W/2$ in the xy-plane. Top edge is the antisymmetry plane. Adapted from the DTU master thesis by Rune Barnkob [Barnkob 2009].

To make the description of the acoustic eigenmodes more realistic, we can include the finite density and compressibility (speed of sound) of the surrounding shear-free wall, see Table 4.1 for a list of some relevant acoustic material parameters. Only a few highly symmetric geometries, like the above one, can be solved analytically, and one must therefore solve the given problem numerically. As an example we show in Fig. 4.3 some results from a COMSOL simulation of the pressure field in the piezo-activated pyrex/silicon chip presented in Fig. 6.1, which containing a water-filled microchannel.

In the model we solve the Helmholtz equation $\nabla^2 p_i = -(\omega^2/c_{\mathrm{a}}^2)\, p_i$ for the silicon, pyrex and water domain i = si, py, and wa, respectively. The boundary condition for the internal water/silicon, water/pyrex and pyrex/silicon interfaces are all the continuity condition (4.21c). We use the soft-wall condition (4.21a) for all five outer pyrex surfaces and the four vertical outer silicon surfaces that faces the air, while the bottom silicon surface facing the piezo transducer is modeled using the hard-wall condition (4.21b).

The eigenmode solution shown in Fig. 4.3 is the one that resembles the ideal nodal plane configuration Fig. 4.2(d) the most. The eigenmode does have a vertical nodal plane along the x direction, as can seen by the green color along the respective antisymmetry planes in Fig. 4.3(b)-(d). But we also note deviations from the ideal configuration: there are pressure gradients both vertically along the z axis, see panel (c), and horizontally along the x axis, see panel (d). Such gradients may lead to less than optimal operation of the acoustophoretic devices. More seriously, however, is the fact that the eigenfrequency comes out to be 2.45 MHz, which is about 20% larger than the experimentally observed resonance frequencies around 2 MHz, see Fig. 6.3(b). While the former deviations is something that must be taken into account when designing acoustofluidic devices, the latter deviation calls for an improvement of the theoretical model.

4.4 Acoustic resonances, elastic walls

The next step up in the theoretical modeling of ultrasound waves in lab-on-a-chip systems is to take into account the shear-stresses in the elastic walls surrounding the water-filled microchannels. This can be handled by employing the classical theory of elastic solids [Landau 1986]. The basic entity in this theory is the displacement $\mathbf{u}(\mathbf{r},t)$ of a solid element away from its equilibrium position $\mathbf{r}$ to its new temporary position $\hat{\mathbf{r}}(\mathbf{r},t) = \mathbf{r} + \mathbf{u}(\mathbf{r},t)$. As in the previous part of the lecture notes, we assume a steady harmonic oscillation of the form $\mathbf{u}(\mathbf{r},t) = \mathbf{u}(\mathbf{r})\ \exp(-\mathrm{i}\omega t)$. The wave equation for elastic waves is derived in a similar way as the equation of motion (1.36) for liquids through. It is Newton's second law expressed as a balance between the divergence of the stress tensor σ_{ik} and the inertia due to the density and acceleration of the solid, $\rho\partial_t^2\mathbf{u} = -\rho\omega^2\mathbf{u}$, and it takes the forms

$$\rho\partial_t^2 u_i = \partial_k\sigma_{ik}, \quad \text{general time dependence,} \tag{4.24a}$$

$$\partial_k\sigma_{ik} + \rho\omega^2 u_i = 0, \quad \text{steady harmonic time dependence.} \tag{4.24b}$$

For small-amplitude oscillations, the stress tensor is related linearly to the strain tensor $u_{lm} = \frac{1}{2}\big(\partial_l u_m + \partial_m u_l\big)$ through the elastic tensor λ_{iklm} of rank four by Hooke's law,

$$\sigma_{ik} = \frac{1}{2}\lambda_{iklm}\big(\partial_l u_m + \partial_m u_l\big). \tag{4.25}$$

For an isotropic solid the elastic tensor is fully characterized by two parameters, Young's modulus E and Poisson's ratio $\bar{\nu}$ and the explicit form of the stress tensor becomes

$$\sigma_{ik} = \bigg[\frac{1}{2}\big(\partial_i u_k + \partial_k u_i\big) + \frac{\bar{\nu}}{1-2\bar{\nu}}\big(\partial_j u_j\big)\,\delta_{ik}\bigg]\frac{E}{1+\bar{\nu}}, \quad \text{isotropic solid.} \tag{4.26}$$

In an infinite solid it is easy to identify two types of elastic waves: the longitudinal pressure waves and the transverse shear waves found be taking the divergence and the rotation of Eq. (4.24a), respectively. However, in a finite solid these two types of elastic waves mix due to scattering at the boundaries. This mixing of the purely longitudinal and purely transverse waves complicates the theory of elastic waves in solids.

The boundary conditions resemble those of inviscid fluids, Eq. (4.21). For a free surface and for one subject to an external force $\mathbf{f}$ per area, e.g. from a piezo transducer, we have

$$n_k\sigma_{ik} = 0, \quad \text{free surface,} \tag{4.27a}$$

$$n_k\sigma_{ik} = f_i, \quad \text{forced surface,} \tag{4.27b}$$

$$u_i = \frac{a_i}{\omega^2}, \quad \text{accelerated surface.} \tag{4.27c}$$

For the interface between a solid and an inviscid fluid, with the normal $\mathbf{n}$ and tangent $\mathbf{t}$, three conditions must be fulfilled: (i) the normal stress component of the solid must equal the acoustic pressure in the fluid, (*ii*) the tangential stress component of the solid must be zero as an inviscid fluid cannot sustain a shear stress, and (*iii*) the normal component of the accelerations of the solid and of the fluid must be identical. Therefore

$$n_i n_k \sigma_{ik} = p, \qquad \text{inviscid fluid/solid interface (normal stress)}, \tag{4.28a}$$

$$t_i n_k \sigma_{ik} = 0, \qquad \text{inviscid fluid/solid interface (tangential stress)}, \tag{4.28b}$$

$$\omega^2 n_i u_i = \frac{1}{\rho_{\mathrm{wa}}}\, n_i \partial_i p \qquad \text{inviscid fluid/solid interface (normal acceleration)}. \tag{4.28c}$$

Here ρ_{wa} and p is the density and the pressure of the inviscid fluid, respectively.

We present no analytical solutions of the coupled fluid/elastic solid equations. Instead we outline how to formulate the equations in the so-called weak form suitable for implementation in the finite element method (FEM) used by COMSOL. In FEM analysis the governing equation is not satisfied in each and every point of the computational domain Ω_1. To discretize the solution of the elastic wave equation (4.24b), a number of vector and scalar test functions $\tilde{u}_i$ and $\tilde{p}$ are introduced, each being different from zero only in a tiny part of domain, but together covering it all. A so-called weak solution of the problem only satisfy that the following integrals are zero for all test functions,

$$\int_{\Omega_1} \mathrm{d}\mathbf{r}\; \tilde{u}_i \Big[\partial_k \sigma_{ik} + \rho\omega^2 u_i\Big] = 0, \tag{4.29}$$

which upon partial integration becomes

$$\int_{\partial\Omega_1} \mathrm{d}a\; \tilde{u}_i n_k \sigma_{ik} + \int_{\Omega_1} \mathrm{d}\mathbf{r}\; \Big[\partial_k \tilde{u}_i(-\sigma_{ik}) + \tilde{u}_i(\rho\omega^2 u_i)\Big] = 0, \tag{4.30}$$

where $\mathbf{n}$ is the outward-pointing surface normal of $\partial\Omega$. Likewise, the inviscid Helmholtz equation (4.6a) with $k = \omega/c_{\mathrm{wa}}$ for the acoustic pressure p in the water-filled domain Ω_2 is written in weak form after introducing the test functions $\tilde{p}$,

$$\int_{\partial\Omega_2} \mathrm{d}a\; \tilde{p} n_k \partial_k p + \int_{\Omega_2} \mathrm{d}\mathbf{r}\; \Big[\partial_k \tilde{p}(-\partial_k p) + \tilde{p}\frac{\omega^2}{c_{\mathrm{wa}}^2} p\Big] = 0. \tag{4.31}$$

To implement the boundary conditions in weak form we insert Eqs. (4.28a) and (4.28b) into the boundary part of Eq. (4.30) using $\tilde{u}_i = (n_j \tilde{u}_j) n_i + (t_j \tilde{u}_j) t_i$, and Eq. (4.28c) into the boundary part of Eq. (4.31). We choose the normal vector $\mathbf{n}$ at the solid/liquid interface to point from the solid to the liquid, thus it appears as $-\mathbf{n}$ in the $\tilde{p}$-equation. The resulting governing equations in weak form become

$$\int_{\partial\Omega_1} \mathrm{d}a\; \tilde{u}_j n_j p + \int_{\Omega_2} \mathrm{d}\mathbf{r}\; \Big[\partial_k \tilde{u}_i(-\sigma_{ik}) + \tilde{u}_i(\rho\omega^2 u_i)\Big] = 0, \tag{4.32a}$$

$$\int_{\partial\Omega_1} \mathrm{d}a\; \tilde{p}\rho_{\mathrm{wa}}\omega^2(-n_k u_k) + \int_{\Omega_2} \mathrm{d}\mathbf{r}\; \Big[\partial_k \tilde{p}(-\partial_k p) + \tilde{p}\frac{\omega^2}{c_{\mathrm{wa}}^2} p\Big] = 0. \tag{4.32b}$$

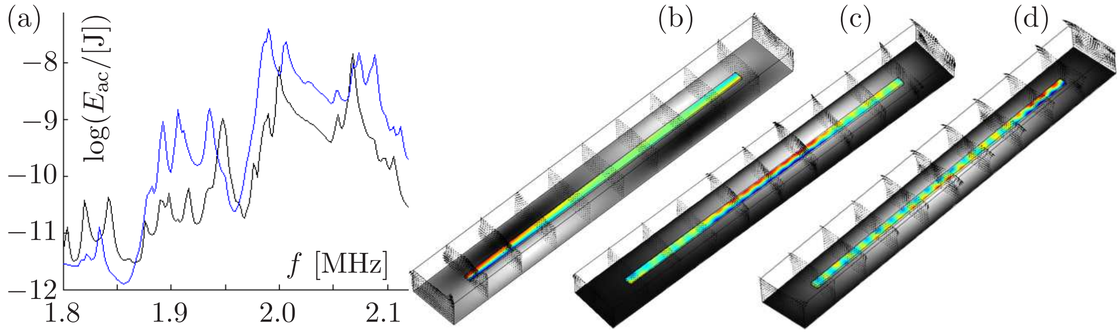

Figure 4.4: COMSOL simulation of the glass/silicon chip of Fig. 4.3 using the inviscid liquid/elastic wall model. (a) A log-linear plot of the acoustic energy E_{ac} as a function of frequency f for odd-odd symmetric (upper) and asymmetric (lower) actuation. (b) Color plot of the pressure p in the center plane of the water-filled microchannel, 11 arrow slice plots of the displacement field $\mathbf{u}$, and gray scale plot of the actuation at the bottom plane of the silicon chip here with odd-odd symmetry. (c) as panel (b) but with asymmetric actuation symmetry. (d) as panel (b) but with even-even actuation symmetry.

Simulations were performed in COMSOL using different piezo actuation modes, each with the same frequency ω but with different spatial symmetry, implemented using the accelerated surface condition (4.27c) with the following functions,

$$u_z^{(b)}(x,y,0) \propto \frac{1}{\omega^2}\sin(2\pi\tfrac{x}{L})\,\sin(2\pi\tfrac{y}{W}), \qquad \text{even-even symmetric,} \tag{4.33a}$$

$$u_z^{(c)}(x,y,0) \propto \frac{1}{\omega^2}(\tfrac{x}{L})^2(\tfrac{y}{W})^2\,(1-\tfrac{x}{L})(1-\tfrac{y}{W}), \quad \text{asymmetric,} \tag{4.33b}$$

$$u_z^{(d)}(x,y,0) \propto \frac{1}{\omega^2}\sin(\pi\tfrac{x}{L})\,\sin(\pi\tfrac{y}{W}), \qquad \text{even-even symmetric.} \tag{4.33c}$$

To allow for dissipation of the energy pumped into the system by the acceleration condition, an artificial bulk dissipation is included by introducing a small imaginary part in the frequency given by the viscous damping factor, $\omega \to (1+\mathrm{i}\gamma)\omega$. The geometry of the system is chosen to be that of the silicon/glass $\alpha = 1$ chip of Figs. 4.3 and 6.1, except that due to computer memory restrictions L was changed from 50 mm to 20 mm.

With the elastic solid model, we are now able to predict the existence of anti-symmetric resonances around 2 MHz in agreement with experimental observations. This is a clear improvement of the results obtained by the shear-free model in Fig. 4.3. Furthermore, we find Lorentzian peaks in agreement with Eq. (4.20) with spacings between the peaks of the order of 10-20 kHz. Finally, the elastic solid model does predict the existence of vertical nodal planes, but we see that the resulting pressure patterns deviate from the ideal straight pattern seen in Fig. 4.2(d).

Chapter 5

Acoustic radiation force

If an ultrasound field is imposed on a liquid (subscript "a" or "0") containing a suspension of particles (subscript "p"), the latter will be affected by the so-called acoustic radiation force arising from the scattering of the acoustic waves on the particle. The force depends on the density ratio ρ_p/ρ_0 and on the speed of sound ratio $c_\mathrm{p}/c_\mathrm{a}$. The motion of the particle resulting from the acoustic radiation force is called acoustophoresis.

The studies of acoustic radiation forces on suspended particles have a long history. The analysis of incompressible particles in acoustic fields dates back to the work in 1934 by King [King 1934], while the forces on compressible particles in plane acoustic waves was calculated in 1955 by Yosioka and Kawasima [Yosioka 1955]. Their work was admirably summarized and generalized in 1962 in a short paper by Gorkov [Gorkov 1962], and in this chapter we shall follow this paper in deriving the acoustic radiation force.

5.1 Time-averaged second-order pressure field and force

The observed acoustophoretic motion is not resolved on the µs time scale of the imposed MHz ultrasound wave, but is the result of the radiation force averaged over a full oscillation cycle. This in turn implies that to account for acoustophoresis, we must go beyond the time-harmonic first-order equations established in Section 4.1, since the time average of these fields are all zero. Therefore we consider the second-order expansion

$$\rho = \rho_0 + \rho_1 + \rho_2, \qquad p = p_0 + c_\mathrm{a}^2\rho_1 + p_2, \qquad \text{and} \quad \mathbf{v} = \mathbf{v}_1 + \mathbf{v}_2, \tag{5.1}$$

and study time averages $\langle X \rangle$ over a full oscillation period τ of quantities $X(t)$,

$$\langle X \rangle \equiv \frac{1}{\tau}\int_0^\tau \mathrm{d}t\, X(t). \tag{5.2}$$

Assuming the inviscid limit $\eta = 0$, as in Eq. (4.8a), we find the time-averaged second-order pressure $\langle p_2 \rangle$ by inserting the expansion (5.1) into the Navier–Stokes equation (4.1c),

$$\boldsymbol{\nabla}\langle p_2 \rangle = -\langle \rho_1 \partial_t \mathbf{v}_1 \rangle - \rho_0 \langle (\mathbf{v}_1 \cdot \boldsymbol{\nabla})\mathbf{v}_1 \rangle, \tag{5.3}$$

where we note that $\rho_0\langle\partial_t \mathbf{v}_2\rangle = 0$, since the time derivative eliminates the time-independent component in $\mathbf{v}_2$ leaving only periodic terms, which time averages to zero. Next we use $\partial_t\mathbf{v}_1 = -(1/\rho_0)\boldsymbol{\nabla}p_1$ from Eq. (4.8a) as well as $\rho_1 = p_1/c_\mathrm{a}^2$ to obtain $\langle\rho_1\partial_t\mathbf{v}_1\rangle = \langle p_1\boldsymbol{\nabla}p_1\rangle/(\rho_0 c_\mathrm{a}^2)$. Finally, since $\langle p_1\boldsymbol{\nabla}p_1\rangle = (1/2)\boldsymbol{\nabla}\langle p_1^2\rangle$ and $\langle(\mathbf{v}_1\cdot\boldsymbol{\nabla})\mathbf{v}_1\rangle = (1/2)\boldsymbol{\nabla}\langle v_1^2\rangle$ (given that $\mathbf{v}_1$ is a gradient field and thus has no rotation), we find a sum of pressure fluctuations and the negative Bernouilli effect,

$$\langle p_2\rangle = \frac{1}{2\rho_0 c_\mathrm{a}^2}\langle p_1^2\rangle - \frac{1}{2}\rho_0\langle v_1^2\rangle. \tag{5.4}$$

In analogy with Eqs. (1.29) and (1.30), the time-averaged second-order acoustic radiation force $\mathbf{F}^\mathrm{rad}$ now follows from a surface integral over any fixed surface $\partial\Omega$ encompassing the oscillating particle of the time-averaged second-order pressure $\langle p_2\rangle$ and momentum flux $\rho_0\langle\mathbf{v}_1\mathbf{v}_1\rangle$

$$\mathbf{F}^\mathrm{rad} = -\int_{\partial\Omega}\mathrm{d}a\left\{\left[\frac{1}{2\rho_0 c_\mathrm{a}^2}\langle p_1^2\rangle - \frac{1}{2}\rho_0\langle v_1^2\rangle\right]\mathbf{n} + \rho_0\langle(\mathbf{n}\cdot\mathbf{v}_1)\mathbf{v}_1\rangle\right\}. \tag{5.5}$$

5.2 The velocity potential in the long-wave limit

We are going to treat the acoustic radiation force on an elastic micrometer-sized particle of radius a in an ultrasound field of wavelength λ, thus $a \ll \lambda$, and from the point of view of wave scattering, the particle is approximately a point particle. It is customary to analyze the associate scattering problem in terms of the velocity potential ϕ_1. Using Eq. (4.8a) we can express $\mathbf{v}_1$ and p_1 in terms of ϕ_1 as

$$\mathbf{v}_1 = \boldsymbol{\nabla}\phi_1, \tag{5.6a}$$

$$p_1 = \mathrm{i}\rho_0\omega\phi_1. \tag{5.6b}$$

Consequently, ϕ_1 must fulfill the same wave equation (4.6a) as p_1, which after changing $-\mathrm{i}\omega$ back to ∂_t reads

$$\nabla^2\phi_1 = \frac{1}{c_\mathrm{a}^2}\,\partial_t^2\phi_1. \tag{5.7}$$

The main point in the calculation of the radiation force is to consider the total first-order velocity potential ϕ_1 as a sum of the incoming acoustic field ϕ_in and of the scattered acoustic field ϕ_sc arising due the presence of the elastic particle,

$$\phi_1 = \phi_\mathrm{in} + \phi_\mathrm{sc}. \tag{5.8}$$

Generally, the scattering potential from a point-like particle placed in the center of the co-ordinate system can be expanded in a multipole expansion, where the coefficients are functions of the so-called time-retarded argument $t - r/c_\mathrm{a}$, where t is the time and r is the radial distance. The strategy in this treatment is to evaluate the radiation force integral Eq. (5.5) in the so-called far-field limit $r \gg \lambda$, but to determine the coefficients of the velocity potential in the so-called near-field limit $r \ll \lambda$ at the surface of the particle. In this way we obtain the most general derivation of the radiation force using the special properties of the velocity potential in each of these two limits.

To evaluate the velocity potential ϕ_1 in the near-field limit at the surface at the particle we use that $r/c_{\mathrm{a}} \approx a/c_{\mathrm{a}} \ll \lambda/c_{\mathrm{a}} = 1/f \approx t$, so the general time-retarded argument of ϕ can be replaced by the instant argument t, and in the spatial co-ordinates ϕ_{sc} is a solution to the Laplace equation $\nabla^2\phi_{\mathrm{sc}} = 0$. Consequently, we can represent the scattering potential by a multipole expansion. In this expansion we only need the first two terms: (i) The monopole term due to the presence of a point-like massive particle, and (ii) the dipole term due to the introduction of the direction set by the instant velocity $\mathbf{v}_{\mathrm{p}} - \mathbf{v}_{\mathrm{in}}$ of the particle relative to the incoming liquid. Suppressing the explicit time dependence of α, β, and $\mathbf{v}_{\mathrm{p}} - \mathbf{v}_{\mathrm{in}}$ we obtain

$$\phi_{\mathrm{sc}} = \frac{\alpha}{r} + \frac{\beta(\mathbf{v}_{\mathrm{p}} - \mathbf{v}_{\mathrm{in}})\cdot\mathbf{e}_r}{r^2}, \quad r \ll \lambda. \tag{5.9}$$

In the following we determine the coefficient α by use of mass conservation and β by the continuity of pressure and velocity at the surface of the particle.

5.3 The monopole term in the velocity potential

The presence of the particle implies that a mass rate $\partial_t m$ carried by the incoming acoustic wave through ρ_{in}, that would have entered the region now occupied by the particle, is being ejected by the oscillating particle surface independent of the particle velocity $\mathbf{v}_{\mathrm{p}}$. This oscillatory part of the surface velocity is given by $\mathbf{v}_{\mathrm{sc}}^{(\alpha)} = \alpha\boldsymbol{\nabla}(r^{-1}) = -\alpha\mathbf{e}_r/r^2$. Thus, since the particle is a sphere with $\mathbf{e}_r = \mathbf{n}$, we get

$$\partial_t m = \int_{\partial\Omega} \mathrm{d}a\, \mathbf{e}_r\cdot\big(\rho_0\mathbf{v}_{\mathrm{sc}}^{(\alpha)}\big) = -\alpha\rho_0 \int_{\partial\Omega} \mathrm{d}a\, \frac{1}{r^2} = -4\pi\alpha\rho_0. \tag{5.10}$$

On the other hand the rate of ejected mass can also be written in terms of rate of change of incoming density $\rho_0 + \rho_{\mathrm{in}}$ as well as volume V_{p} and compressibility K_{p},

$$K_{\mathrm{p}} = -\frac{1}{V_{\mathrm{p}}}\frac{\partial V_{\mathrm{p}}}{\partial p} = \frac{1}{\rho_{\mathrm{P}}}\frac{\partial \rho_{\mathrm{P}}}{\partial p} = \frac{1}{\rho_{\mathrm{P}} c_{\mathrm{p}}^2}, \tag{5.11}$$

of the particle as follows,

$$\begin{aligned}\partial_t m &= \partial_t\big[(\rho_0 + \rho_{\mathrm{in}})V_{\mathrm{p}}\big] = V_{\mathrm{p}}\partial_t\rho_{\mathrm{in}} + \rho_0\partial_t V_{\mathrm{p}} = V_{\mathrm{p}}\partial_t\rho_{\mathrm{in}} + \rho_0\frac{\partial V_{\mathrm{p}}}{\partial p}\,\partial_t p_{\mathrm{in}}\\ &= V_{\mathrm{p}}\partial_t\rho_{\mathrm{in}} - \rho_0\frac{V_{\mathrm{p}}}{\rho_{\mathrm{P}} c_{\mathrm{p}}^2}\, c_{\mathrm{a}}^2\partial_t\rho_{\mathrm{in}} = \left[1 - \frac{\rho_0 c_{\mathrm{a}}^2}{\rho_{\mathrm{P}} c_{\mathrm{p}}^2}\right] V_{\mathrm{p}}\partial_t\rho_{\mathrm{in}}.\end{aligned} \tag{5.12}$$

From this using $V_{\mathrm{p}} = (4/3)\pi a^3$ we find the monopole coefficient α, and thus the potential

$$\phi_{\mathrm{sc}}^{(\alpha)} = -\frac{a^3}{3\rho_0}\left[1 - \frac{\rho_0 c_{\mathrm{a}}^2}{\rho_{\mathrm{P}} c_{\mathrm{p}}^2}\right]\partial_t\rho_{\mathrm{in}}\,\frac{1}{r}. \tag{5.13}$$

5.4 The dipole term in the velocity potential

We proceed in a different way to determine the dipole coefficient β. Let the a spherical coordinate system be located at the center of the particle with the polar axis pointing along the instantaneous incoming acoustic field velocity $\mathbf{v}_{\mathrm{in}}$ such that

$$\phi_{\mathrm{in}} = v_{\mathrm{in}} r \cos\theta. \tag{5.14}$$

For an inviscid liquid only the normal velocity components at a given boundary needs to be continuous. At the boundary of the particle we have according to Eq. (5.8) that $\mathbf{v}_{\mathrm{p}} = \mathbf{v}_{\mathrm{in}} + \mathbf{v}_{\mathrm{sc}}^{(\beta)}$ independent of the mass monopole term, so we find from the velocity dipole term in Eq. (5.9) that

$$(\mathbf{v}_{\mathrm{p}} - \mathbf{v}_{\mathrm{in}})\cdot\mathbf{e}_r = \partial_r \phi_{\mathrm{sc}}^{(\beta)} = -\frac{2\beta}{r^3}\bigg|_{r=a} (\mathbf{v}_{\mathrm{p}} - \mathbf{v}_{\mathrm{in}})\cdot\mathbf{e}_r = -\frac{2\beta}{a^3}\,(\mathbf{v}_{\mathrm{p}} - \mathbf{v}_{\mathrm{in}})\cdot\mathbf{e}_r. \tag{5.15}$$

so that $\beta = -a^3/2$ and the scattering potential becomes

$$\phi_{\mathrm{sc}}^{(\beta)} = -\frac{a^3}{2r^2}\,(\mathbf{v}_{\mathrm{p}} - \mathbf{v}_{\mathrm{in}})\cdot\mathbf{e}_r. \tag{5.16}$$

To determine $\mathbf{v}_{\mathrm{p}}$ or equivalently ϕ_{p} we need to solve the Laplace equation $\nabla^2\phi = 0$ inside the moving particle ϕ_{p} and outside in the liquid ϕ_1. At infinity the scattered wave vanished and $\phi_1 \to \phi_{\mathrm{in}} = v_{\mathrm{in}} r\cos\theta$. At the boundary the radial velocity is continuous, $\partial_r v_1 = \partial_r v_{\mathrm{p}}$ Eq. (5.6a), and the pressure is continuous, $\rho_0\phi_1 = \rho_{\mathrm{P}}\phi_{\mathrm{p}}$ Eq. (5.6b). These boundary condition are satisfied for the angular dependence, if we seek solutions proportional to $\cos\theta$. Only two such solutions exist for the Laplace equation, $r\cos\theta$ and $r^{-2}\cos\theta$. It is easily checked that the proper solution is

$$\phi_1(r,\theta) = v_{\mathrm{in}}\left[r + \frac{\rho_{\mathrm{P}} - \rho_0}{2\rho_{\mathrm{P}} + \rho_0}\,\frac{a^3}{r^2}\right]\cos\theta, \tag{5.17a}$$

$$\phi_{\mathrm{p}}(r,\theta) = v_{\mathrm{in}}\frac{3\rho_0}{2\rho_{\mathrm{P}} + \rho_0}\, r\cos\theta. \tag{5.17b}$$

From the last equation we find $\mathbf{v}_{\mathrm{p}}\cdot\mathbf{e}_r = \partial_r\phi_{\mathrm{p}} = 3\rho_0/(2\rho_{\mathrm{P}} + \rho_0) v_i n\cos\theta$, and $\phi_{\mathrm{sc}}^{(\beta)}$ becomes

$$\phi_{\mathrm{sc}}^{(\beta)} = \frac{\rho_{\mathrm{P}} - \rho_0}{2\rho_{\mathrm{P}} + \rho_0}\,\frac{a^3 v_{\mathrm{in}}\cos\theta}{r^2}. \tag{5.18}$$

5.5 The radiation force, general expression

Combining Eqs. (5.13) and (5.18) we obtain the full near-field scattering potential,

$$\phi_{\mathrm{sc}} = -f_1\,\frac{a^3\partial_t\rho_{\mathrm{in}}}{3\rho_0 r} + f_2\,\frac{a^3 v_{\mathrm{in}}\cos\theta}{2r^2}, \quad r \ll \lambda \tag{5.19}$$

where the material-dependent coefficients f_1 and f_2 are given by

$$f_1 = 1 - \frac{\rho_0 c_\mathrm{a}^2}{\rho_\mathrm{P} c_\mathrm{P}^2}, \qquad \text{and} \qquad f_2 = \frac{2(\rho_\mathrm{P} - \rho_0)}{2\rho_\mathrm{P} + \rho_0}. \tag{5.20}$$

Given the near-field potential, the full far-field scattering potential follows from general wave theory

$$\phi_\mathrm{sc}(\mathbf{r}, t) = -f_1 \, \frac{a^3}{3\rho_0} \, \frac{\partial_t \rho_\mathrm{in}(t - r/c_\mathrm{a})}{r} - f_2 \, \frac{a^3}{2} \, \boldsymbol{\nabla}\cdot\left(\frac{\mathbf{v}_\mathrm{in}(t - r/c_\mathrm{a})}{r}\right), \quad r \gg \lambda. \tag{5.21}$$

With this final expression for ϕ_sc at hand we are in position to calculate the radiation force Eq. (5.5), consisting of a sum of terms all proportional to squares of $\phi_1 = \phi_\mathrm{in} + \phi_\mathrm{sc}$. This results in three types of contributions, (i) squares of ϕ_in containing no information about the scattering and therefore yielding zero, (ii) squares of ϕ_sc proportional to the square of the particle volume a^6 and therefore negligible compared to (iii) the mixed products $\phi_\mathrm{in}\phi_\mathrm{sc}$ proportional to particle volume a^3, and therefore the most dominant contribution to the radiation force.

Keeping only these mixed terms, which physically can be interpreted as interference between the incoming and the scattered wave, the ith component of Eq. (5.5) becomes

$$F_i^\mathrm{rad} = -\int_{\partial\Omega} \mathrm{d}a \, n_j \left\{ \left[\frac{c_\mathrm{a}^2}{\rho_0} \langle \rho_\mathrm{in} \rho_\mathrm{sc} \rangle - \rho_0 \langle v_k^\mathrm{in} v_k^\mathrm{sc} \rangle \right] \delta_{ij} + \rho_0 \langle v_i^\mathrm{in} v_j^\mathrm{sc} \rangle + \rho_0 \langle v_i^\mathrm{sc} v_j^\mathrm{in} \rangle \right\} \tag{5.22a}$$

$$= -\int_{\Omega} \mathrm{d}\mathbf{r} \, \partial_j \left\{ \left[\frac{c_\mathrm{a}^2}{\rho_0} \langle \rho_\mathrm{in} \rho_\mathrm{sc} \rangle - \rho_0 \langle v_k^\mathrm{in} v_k^\mathrm{sc} \rangle \right] \delta_{ij} + \rho_0 \langle v_i^\mathrm{in} v_j^\mathrm{sc} \rangle + \rho_0 \langle v_i^\mathrm{sc} v_j^\mathrm{in} \rangle \right\} \tag{5.22b}$$

$$= -\int_{\Omega} \mathrm{d}\mathbf{r} \left\{ \frac{c_\mathrm{a}^2}{\rho_0} \Big[\langle \rho_\mathrm{in} \partial_i \rho_\mathrm{sc} \rangle + \langle \rho_\mathrm{sc} \partial_i \rho_\mathrm{in} \rangle \Big] + \rho_0 \Big[\langle v_i^\mathrm{in} \partial_j v_j^\mathrm{sc} \rangle + \langle v_i^\mathrm{sc} \partial_j v_j^\mathrm{in} \rangle \Big] \right\} \tag{5.22c}$$

$$= -\int_{\Omega} \mathrm{d}\mathbf{r} \left\{ - \langle \rho_\mathrm{in} \partial_t v_i^\mathrm{sc} \rangle - \langle \rho_\mathrm{sc} \partial_t v_i^\mathrm{in} \rangle + \rho_0 \langle v_i^\mathrm{in} \partial_j v_j^\mathrm{sc} \rangle - \langle v_i^\mathrm{sc} \partial_t \rho_\mathrm{in} \rangle \right\} \tag{5.22d}$$

$$= -\int_{\Omega} \mathrm{d}\mathbf{r} \left\{ \langle v_i^\mathrm{in} \partial_t \rho_\mathrm{sc} \rangle + \rho_0 \langle v_i^\mathrm{in} \partial_j v_j^\mathrm{sc} \rangle \right\} \tag{5.22e}$$

$$= -\rho_0 \int_{\Omega} \mathrm{d}\mathbf{r} \left\langle v_i^\mathrm{in} \Big(\partial_j^2 \phi_\mathrm{sc} - \frac{1}{c_\mathrm{a}^2} \partial_t^2 \phi_\mathrm{sc} \Big) \right\rangle. \tag{5.22f}$$

Here, we have used $p_1 = c_\mathrm{a}^2 \rho_1$ in Eq. (5.22a), Gauss's theorem in Eq. (5.22b), exchange of indices $\partial_i v_k = \partial_i \partial_k \phi = \partial_i \partial_k \phi = \partial_i v_k$ to cancel terms in Eq. (5.22c), introduction of time derivatives by the continuity equation $\partial_t \rho_1 = -\rho_0 \partial_j v_{1,j}$ and Navier–Stokes equation $\rho_0 \partial_t v_{1,i} = -\partial_i p_1 = -c_\mathrm{a}^2 \partial_i \rho_1$ in Eq. (5.22d), vanishing of time-averages of total time derivatives $\langle \partial_t (\rho v) \rangle = 0$ or $\langle \rho \partial_t v \rangle = -\langle v \partial_t \rho \rangle$ for cancelation and rearrangement in Eq. (5.22e), and finally reintroduction of the vector potential ϕ_sc in Eq. (5.22e).

We notice that the d'Alembert wave operator $\nabla^2 - (1/c_\mathrm{a}^2)\partial_t^2$ acting on ϕ_sc appears in the above integrand. That is good news, since we know that ϕ_sc is a sum of simple monopole and dipole terms. Just as the Laplace operator acting on the monopole potential $\phi = q/(4\pi\epsilon_0 r)$ yields the delta function point-charge distribution, $\nabla^2\phi = -(q/\epsilon_0)\delta(\mathbf{r})$, the d'Alembert operator acting on the retarded-time monopole and dipole expressions (5.21) also yields delta function distributions,

$$\nabla^2\phi_{\mathrm{sc}} - \frac{1}{c_{\mathrm{a}}^2}\partial_t^2\phi_{\mathrm{sc}} = f_1\,\frac{4\pi a^3}{3\rho_0}\,\partial_t\rho_{\mathrm{in}}\,\delta(\mathbf{r}) + f_2\,2\pi a^3\,\boldsymbol{\nabla}\cdot\Big[\mathbf{v}_{\mathrm{in}}\,\delta(\mathbf{r})\Big], \quad r \gg \lambda. \tag{5.23}$$

Now we see the great advantage of working in the far-field limit. The first term is easily integrated, but for the second term we need to get rid of the divergence operator acting on the delta function before we can evaluate the integral. This we manage by Gauss's theorem. First we note that $\boldsymbol{\nabla}\cdot\big[g(\mathbf{r})\mathbf{u}(r)\big] = g\boldsymbol{\nabla}\cdot\mathbf{u} + \mathbf{u}\cdot\boldsymbol{\nabla}g$ for any function g and vector function $\mathbf{u}$. Therefore $\int_{\partial\Omega} \mathrm{d}a\,\mathbf{n}\cdot(g\mathbf{u}) = \int_\Omega \mathrm{d}\mathbf{r}\,\boldsymbol{\nabla}(g\mathbf{u}) = \int_\Omega \mathrm{d}\mathbf{r}\,(g\boldsymbol{\nabla}\cdot\mathbf{u} + \mathbf{u}\cdot\boldsymbol{\nabla}g)$, and we have derived the expression $\int_\Omega \mathrm{d}\mathbf{r}\,g\boldsymbol{\nabla}\cdot\mathbf{u} = -\int_\Omega \mathrm{d}\mathbf{r}\,\mathbf{u}\cdot\boldsymbol{\nabla}g + \int_{\partial\Omega}\mathrm{d}a\,\mathbf{n}\cdot(g\mathbf{u})$. Now, since $\mathbf{u} \propto \mathbf{v}\delta(\mathbf{r})$ we obtain a volume integral encompassing the delta function thus yielding a contribution and a surface integral not encompassing the delta function thus yielding zero. So we get

$$\begin{aligned}
\mathbf{F}^{\mathrm{rad}} &= -f_1\,\frac{4\pi}{3}a^3\,\big\langle\mathbf{v}_{\mathrm{in}}\partial_t\rho_{\mathrm{in}}\big\rangle + f_2\,2\pi a^3\rho_0\,\big\langle(\mathbf{v}_{\mathrm{in}}\cdot\boldsymbol{\nabla})\mathbf{v}_{\mathrm{in}}\big\rangle && \text{(5.24a)}\\
&= f_1\,\frac{4\pi}{3}a^3\,\big\langle\rho_{\mathrm{in}}\partial_t\mathbf{v}_{\mathrm{in}}\big\rangle + f_2\,2\pi a^3\rho_0\,\big\langle(\mathbf{v}_{\mathrm{in}}\cdot\boldsymbol{\nabla})\mathbf{v}_{\mathrm{in}}\big\rangle && \text{(5.24b)}\\
&= -f_1\,\frac{4\pi}{3\rho_0 c_{\mathrm{a}}^2}a^3\,\big\langle p_{\mathrm{in}}\boldsymbol{\nabla}p_{\mathrm{in}}\big\rangle + f_2\,2\pi a^3\,\rho_0\big\langle(\mathbf{v}_{\mathrm{in}}\cdot\boldsymbol{\nabla})\mathbf{v}_{\mathrm{in}}\big\rangle && \text{(5.24c)}\\
&= -f_1\,\frac{2\pi}{3\rho_0 c_{\mathrm{a}}^2}a^3\,\boldsymbol{\nabla}\big\langle p_{\mathrm{in}}^2\big\rangle + f_2\,\pi a^3\rho_0\,\boldsymbol{\nabla}\big\langle v_{\mathrm{in}}^2\big\rangle. && \text{(5.24d)}
\end{aligned}$$

where we have integrated over the delta function in Eq. (5.24a), applied the previously used rule $\big\langle\rho_{\mathrm{in}}\partial_t\mathbf{v}_{\mathrm{in}}\big\rangle = -\big\langle\mathbf{v}_{\mathrm{in}}\partial_t\rho_{\mathrm{in}}\big\rangle$ in Eq. (5.24b), inserted $\rho_{\mathrm{in}} = p_{\mathrm{in}}/c_{\mathrm{a}}^2$ and $\partial_t\mathbf{v}_{\mathrm{in}} = -p_{\mathrm{in}}/\rho_0$ in Eq. (5.24c), and finally pulled the nabla operator outside the time averages in Eq. (5.24d). We see that the radiation force is a gradient force. It is therefore customary to introduce a radiation potential U^{rad}, and write the final expression for the radiation force acting on a small particle ($a \ll \lambda$) placed in an arbitrary acoustic field as follows,

$$\begin{aligned}
\mathbf{F}^{\mathrm{rad}} &= -\boldsymbol{\nabla}U^{\mathrm{rad}}, && \text{(5.25a)}\\
U^{\mathrm{rad}} &= \frac{4\pi}{3}\,a^3\bigg[f_1\,\frac{1}{2\rho_0 c_{\mathrm{a}}^2}\,\langle p_{\mathrm{in}}^2\rangle - f_2\,\frac{3}{4}\rho_0\,\langle v_{\mathrm{in}}^2\rangle\bigg], && \text{(5.25b)}\\
f_1 &= 1 - \frac{\rho_0 c_{\mathrm{a}}^2}{\rho_{\mathrm{P}} c_{\mathrm{P}}^2} = 1 - \frac{K_{\mathrm{p}}}{K_0}, && \text{(5.25c)}\\
f_2 &= \frac{2(\rho_{\mathrm{P}} - \rho_0)}{2\rho_{\mathrm{P}} + \rho_0}. && \text{(5.25d)}
\end{aligned}$$

The radiation potential U^{rad} is proportional to the volume of the particle, and it contains a positive contribution from the acoustic pressure fluctuations and a negative contribution originating from the Bernouilli effect of the acoustic flow speed. As mentioned in the beginning of the chapter, we also see in the f_1 and f_2 coefficient how the potential depends on the density ratio ρ_{P}/ρ_0 and on the speed of sound ratio $c_{\mathrm{p}}/c_{\mathrm{a}}$, or alternatively on the compressibility ratio K_{p}/K_0.

5.6 The radiation force, standing plane wave

Our prime example of the acoustic radiation force is the case of a 1D planar standing wave. This condition has been realized in numerous applications of the acoustic radiation force in acoustophoresis, as we shall see in the following chapter. Here we simply state the mathematical form of the first-order acoustic field, and then based on Eq. (5.25) write down the expression for the radiation force

The first-order incoming acoustic fields are given by

$$\phi_{\mathrm{in}}(y,t) = \qquad \frac{1}{k}\,u_0\,\cos(ky)\,\cos(\omega t), \tag{5.26a}$$

$$\mathbf{v}_{\mathrm{in}}(y,t) = \boldsymbol{\nabla}\phi_{\mathrm{in}} = -u_0\,\sin(ky)\,\cos(\omega t)\,\mathbf{e}_x, \tag{5.26b}$$

$$p_{\mathrm{in}}(y,t) = -\rho_0\partial_t\phi_{\mathrm{in}} = \rho_0 c_{\mathrm{a}}\,u_0\,\cos(ky)\,\sin(\omega t), \tag{5.26c}$$

$$\rho_{\mathrm{in}}(y,t) = -\frac{\rho_0}{c_{\mathrm{a}}^2}\,\partial_t\phi_{\mathrm{in}} = \rho_0\frac{u_0}{c_{\mathrm{a}}}\,\cos(ky)\,\sin(\omega t), \tag{5.26d}$$

where we have used the usual real-time representation and introduced the wavenumber $k = 2\pi/\lambda$, which also fulfils $\omega = kc_{\mathrm{a}}$. The time averages needed in Eq. (5.25) are simply $\big\langle\cos^2(\omega t)\big\rangle = \big\langle\sin^(\omega t)\big\rangle = \frac{1}{2}$, and we arrive at the following expression for the radiation potential

$$U^{\mathrm{rad}} = \pi\,a^3\rho_0 u_0^2\left[f_1\,\frac{1}{3}\,\cos^2(ky) - f_2\,\frac{1}{2}\,\sin^2(ky)\right]. \tag{5.27}$$

The corresponding radiation force is easily found by differentiation,

$$F_y^{\mathrm{rad}} = -\partial_y U^{\mathrm{rad}} = 2\pi k a^3\rho_0 u_0^2\left[f_1\,\frac{1}{3}\,\cos(ky)\sin(ky) + f_2\,\frac{1}{2}\,\sin(ky)\cos(ky)\right] \tag{5.28a}$$

$$= \pi k a^3\rho_0 u_0^2\left[\frac{1}{3}f_1 + \frac{1}{2}f_2\right]\,\sin(2ky) \tag{5.28b}$$

$$= 4\pi k a^3\Big(\frac{1}{4}\rho_0 u_0^2\Big)\left[\frac{\rho_{\mathrm{P}} + \frac{2}{3}(\rho_{\mathrm{P}}-\rho_0)}{2\rho_{\mathrm{P}}+\rho_0} - \frac{1}{3}\frac{\rho_0 c_{\mathrm{a}}^2}{\rho_{\mathrm{P}}c_{\mathrm{P}}^2}\right]\,\sin(2ky), \tag{5.28c}$$

which is usually written as

$$F_y^{\mathrm{rad}} = 4\pi a^2(ka)\,E_{\mathrm{ac}}\Phi\,\sin(2ky), \tag{5.29a}$$

$$\Phi = \frac{\rho_{\mathrm{P}} + \frac{2}{3}(\rho_{\mathrm{P}}-\rho_0)}{2\rho_{\mathrm{P}}+\rho_0} - \frac{1}{3}\frac{\rho_0 c_{\mathrm{a}}^2}{\rho_{\mathrm{P}}c_{\mathrm{P}}^2}, \tag{5.29b}$$

$$E_{\mathrm{ac}} = \frac{1}{4}\rho_0 u_0^2 = \frac{p_{\mathrm{a}}^2}{4\rho_0 c_{\mathrm{a}}^2}, \tag{5.29c}$$

where $4\pi a^2$ is the surface area of the sphere, $ka = 2\pi a/\lambda$ is the size-to-wavelength ratio, E_{ac} is the acoustic energy density in the standing wave, Φ is the acoustophoretic contrast factor, and $p_{\mathrm{a}} = \rho_0 c_{\mathrm{a}} u_0$ is the pressure amplitude. A sketch of the acoustic radiation force is given in Fig. 5.1.

Most of the parameters can easily be estimated from table values of materials and from the geometry of the given acoustofluidic device. However, the energy density is not so easy

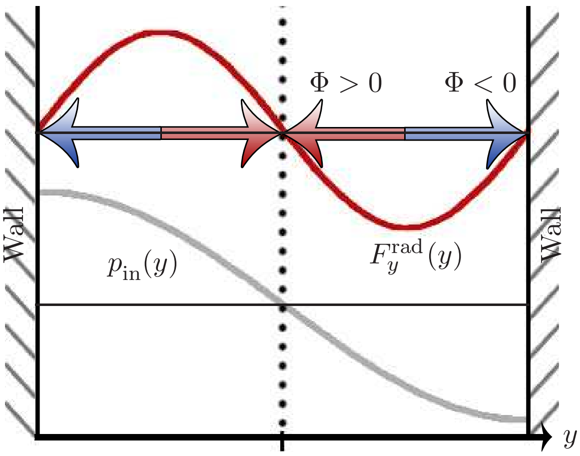

Figure 5.1: End view of a straight water filled channel (hatched walls) with a transverse standing ultrasound resonant half-wavelength pressure wave (gray, half cosine wave). The radiation force F_y^{rad} is period doubled and phase shifted (red, full sine wave) relative to the pressure wave. Red (blue) arrows correspond to the acoustophoretic force for a particle with a positive (negative) acoustophoretic contrastfactor Φ. Particles with a positive Φ moves towards the central nodal line (dotted line), while those with a negative Φ moves in the opposite direction towards the anti-nodes at the wall. Figure adapted from the DTU Nanotech bachelor thesis by Andersen, Nysteen and Settnes [Andersen 2009].

to estimate, since the coupling of acoustic energy from the piezo transducer into the fluidic system is hard to predict. A typical value [Barnkob 2010] for low-voltage ($\lesssim 10$ V) piezo transducers running at a few MHz is

$$E_{\mathrm{ac}} \approx 10 - 100\ \mathrm{J\,m^{-3}}. \tag{5.30}$$

In the following chapter we look into the experimental realizations of the acoustic radiation force.

Chapter 6

Microchannel acoustophoresis

In this chapter we study some of the practical aspect of particle handling in microchannel acoustophoresis. The major part of the material has been developed in a collaboration between Prof. Thomas Laurell and his PhD student Per Augustsson at Lund University and Prof. Henrik Bruus and his PhD student Rune Barnkob of DTU. In Section 6.5 is mentioned some recent examples in the literature of various applications of the acoustic radiation force in acoustofluidic microsystems.

6.1 Particle handling in acoustophoresis

Basic physical properties of acoustophoresis, such as energy density, local pressure amplitudes, resonance line shapes, and resonance Q factors, are most easily studied in simple rectangular channels embedded in silicon/glass chips [Barnkob 2010]. An example of such chips is shown in Fig. 6.1(a), where each chip consists of a straight channel with one inlet and one outlet fabricated using standard silicon microfabrication techniques. The channel was sealed by an anodically bonded pyrex glass lid, and short pieces of silicone tubing were glued to their respective 1-mm-diameter holes in the glass lid. The width W of the chip can be characterized by the ratio α of the number of acoustic wavelengths in silicon and that of water. With the parameters of Table 4.1 we find $\lambda_{\mathrm{si}} = 5.7\lambda_{\mathrm{wa}}$ and $\alpha = (W - w)/(5.7w)$.

An actual experimental setup for carrying out basic acoustophoretic measurements is shown In Fig. 6.1(b). The acoustofluidic chip is mounted on a piezoelectric PZT transducer (piezo), and sufficient acoustic coupling is provided by a thin glycerol layer. To isolate the system acoustically at least to some degree, the two elements are fixed in a PMMA holder, such that the chip is only in contact with the holder through its inlet/outlet silicone tubing and via the piezo, which in turn was mounted so that all contact with the PMMA holder is restricted to its edges. The piezo is actuated by applying a harmonically oscillating voltage drop generated from a tone generator in series with an amplifier, and the applied peak-to-peak voltage across the piezo transducer is measured by an oscilloscope. The channel was monitored through an microscope with an attached CCD camera.

When carrying out the experiments a liquid suspension of 5 µm polystyrene microbeads

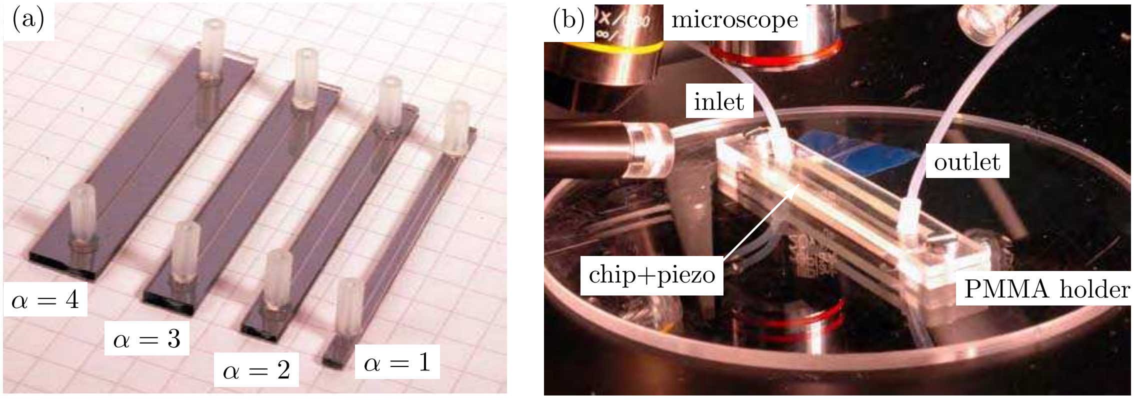

Figure 6.1: (a) Microfluidic silicon/glass chips fabricated by Per Augustsson at the Laurell Group, Lund University. The chips contain straight channels of length $l = 40$ mm, width $w = 377$ µm, and height $h = 157$ µm. The channels are etched down into the silicon chip of thickness $h_{\mathrm{si}} = 350$ µm, and they are covered by a pyrex lid of thickness $h_{\mathrm{py}} = 1.13$ mm. The lengths of the chips are $L = 50$ mm and the widths are $W = 2.52$ mm ($\alpha = 1$) and $W = 4.67$ mm ($\alpha = 2$), respectively. (b) A photograph of the experimental setup at Lund University with the chip including inlet/outlet tubes and the PZT piezo crystal mounted under the microscope and the CCD camera. The piezo has the dimension 50.0 mm $\times$ 12.0 mm $\times$ 1.0 mm, and thus the entire chip rests on it. Pictures adapted from the DTU master thesis by Rune Barnkob [Barnkob 2009].

was injected into the microchannel. The microbead concentrations were in the range from 0.1 g/L to 0.5 g/L. The sample liquid is contained in a 1 mL plastic syringe, in which a small magnet resides. By stirring with an external magnet, a homogeneous microbead distribution is ensured and significant sedimentation is avoided. A syringe pump was used to purge the microchannel with the sample liquid prior to each run. During all measurements the flow was temporarily stopped.

6.2 Particle paths in acoustophoresis

The path of a microbead moving by acoustophoresis is traced out by the time-dependent co-ordinates $\big(x(t), y(t)\big)$. A particularly simple analytical expression for the transverse part $y(t)$ of such a path can be obtained from the acoustic radiation force Eq. (5.29a) valid in the case of a standing 1D transverse ultrasound wave. As in Section 3.6 we can neglect inertial effects and determine the transverse path $y(t)$ by balancing the acoustophoretic force F_y^{rad} with the viscous Stokes drag force F_y^{drag} from the quiescent liquid. The force balance results in the following differential equation,

$$6\pi\eta a \frac{\mathrm{d}y}{\mathrm{d}t} = 4\pi a^2 (ka)\, E_{\mathrm{ac}} \Phi\, \sin(2k_y y), \tag{6.1}$$

Separating the variables y and t, and using the integral $2\int \mathrm{d}s/\sin(2s) = \log\big|\tan(s)\big|$ lead to an analytical expression for the transverse path,

$$y(t) = \frac{1}{k_y}\arctan\left\{\tan\big[k_y y(0)\big]\exp\left[\frac{4\Phi}{9}(k_y a)^2\frac{E_\mathrm{ac}}{\eta}\,t\right]\right\}, \tag{6.2}$$

where $y(0)$ is the transverse position at time $t = 0$. Inverting the expression, we can also calculate the time t it takes a particle to move from any initial position $y(0)$ to any final position $y(t)$,

$$t = \frac{9\eta}{4\Phi(ka^2)E_\mathrm{ac}}\ln\left[\frac{\tan\big[k_y y(t)\big]}{\tan\big[k_y y(0)\big]}\right] = \frac{9}{4\Phi}\frac{c_\mathrm{a}^2}{\omega^2 a^2}\frac{\eta}{E_\mathrm{ac}}\ln\left[\frac{\tan\big[k_y y(t)\big]}{\tan\big[k_y y(0)\big]}\right]. \tag{6.3}$$

This expression is important for designing acoustofluidic devices to separate particles having the same sign of their acoustophoretic contrast factor Φ. In this case separation must be based on variations in the time $t(w)$ it takes a particle to be focused transversely given the width w of the microfluidic channel. If the axial convection speed of the carrier liquid is v_0, then the distance $\Delta\ell(v_0, w)$ a given particle has to flow along the channel before it has been traversed the transverse focus distance w can be written as

$$\Delta\ell(v_0, w) = v_0 t(w) \propto V^{-\frac{2}{3}}\Phi^{-1}\, v_0\,\omega^{-2}E_\mathrm{ac}^{-1}, \tag{6.4}$$

where $V \propto a^3$ is the volume of the particle. The larger a particle, the shorter it has to be convected before it has been focused.

The acoustic parameters was measured *in situ* by observing the transient acoustophoretic focusing of the microbeads. First, the driving frequency is tuned until observing a strong, resonant, acoustic focusing of the polystyrene microbeads towards the center of the channel. Then the ultrasound field is turned off, and a fresh solution of microbeads from the syringe pump is injected into the channel. When a homogeneous microbead distribution is observed, the flow is stopped, Fig. 6.2(a). Finally, the ultrasound is turned back on, and the transient focusing of the microbeads towards the channel center is recorded by the CCD camera, Fig. 6.2(b). From the frames of the resulting movie we can then determine the transverse paths $y(t)$ of the microbeads, an example of which is shown in Fig. 6.2(c).

The transverse path $y(t)$ is extracted from the video recordings by employing the free video analysis tool *Tracker 2.6* [Brown 2009]. This software enables tracking of a polystyrene microbead by simple manual mouse-clicking on the microbead position y on each movie frame, for which the time t is known. The length scale in the y-direction is calibrated by the distance between the visible channel walls as shown in Fig. 6.2(a). The resulting list of (t, y)-coordinates can be extracted for any tracked microbead path, see Fig. 6.2(b), and plotted as shown in Fig. 6.2(c) for a driving frequency of $f = 1.9940$ MHz and a driving voltage $U_\mathrm{pp} = 1.52$ V.

The axial motion $x(t)$ seen in the last part of the paths shown in Fig. 6.2(b) is due to hydraulic compliance of the system leading to difficulties in keeping the liquid at complete rest.

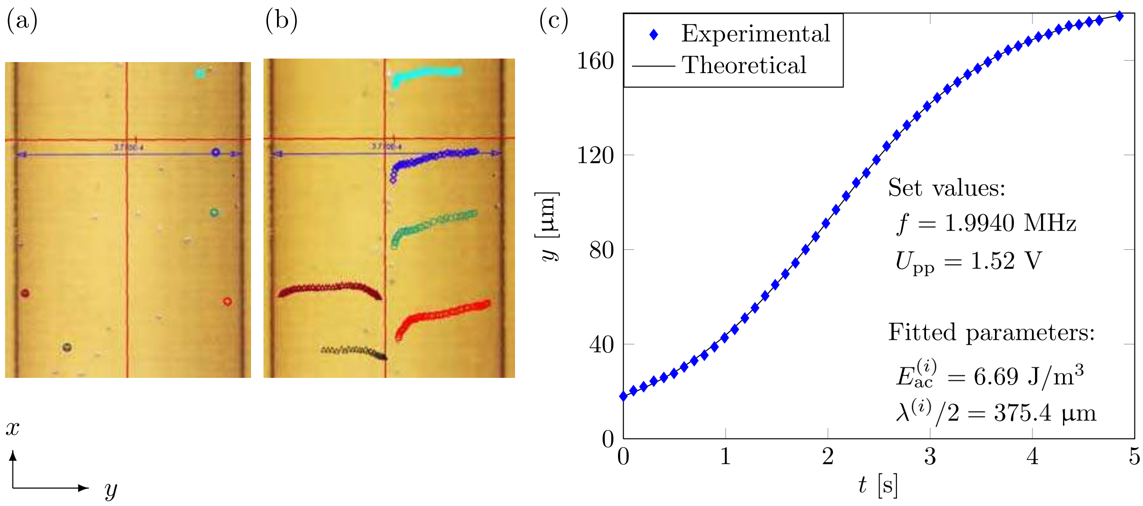

Figure 6.2: (a) Starting position (circles) of six microbeads in the channel of the chip with $\alpha = 2$. The channel walls are the two thick vertical lines separated by $w = 377$ µm. (b) Tracking of the paths of the six microbeads. (c) Measurement (circles) for one of the microbeads of its transverse position y from the left wall as a function of time t. The fitted curve (full line) is given by Eq. (6.2) with only two fitting parameters: the acoustic energy density E_{ac} and the half wavelength $\lambda/2$ of the transverse standing pressure wave. Reproduced from the DTU master thesis by Rune Barnkob [Barnkob 2009].

6.3 Energy density as function of voltage and frequency

Using the energy density E_{ac} and the half-wavelength $\lambda/2$ as the only fitting parameters, a curve of the form $y(t)$ given by Eq. (6.2) is fitted to the data points by the least-squares method. As shown by the full curve in Fig. 6.2(c), this fitting procedure yields good results: the observed path has the theoretically predicted shape, and we can extract reliable values for the acoustic energy density E_{ac}. In the given case we found $E_{\mathrm{ac}} = 6.69$ J/m^3, and we also note that the fitted value for $\lambda/2$ is 375 µm, very close to the expected value, namely the width of the channel $w = 377$ µm.

From Eq. (5.29c) we find the pressure amplitude in the chip with $\alpha = 2$ to be

$$p_{\mathrm{a}} = 2\sqrt{\rho_{\mathrm{wa}} c_{\mathrm{wa}}^2 \, E_{\mathrm{ac}}} \approx 0.242 \text{ MPa}, \tag{6.5}$$

which is 10^{-4} times the cohesive energy density 2.6 GPa of water. Equivalently, the density fluctuations are 10^{-4} times ρ_{wa}, and thus the acoustic perturbation theory holds even at resonance. In our low-voltage experiments we have measured energy densities in the range 0.65 – 50 J/m^3 corresponding to pressure amplitudes in the range 0.08 – 0.66 MPa. The upper range of these results are consistent with previously reported estimates in the literature for microbead acoustophoresis in microsystems. Using external electric forces, Wiklund *et al.* [Wiklund 2003] measured energy densities in the range 65 – 650 J/m^3 corresponding to pressure amplitudes in the range 0.76 – 2.4 MPa, while Hultström *et*

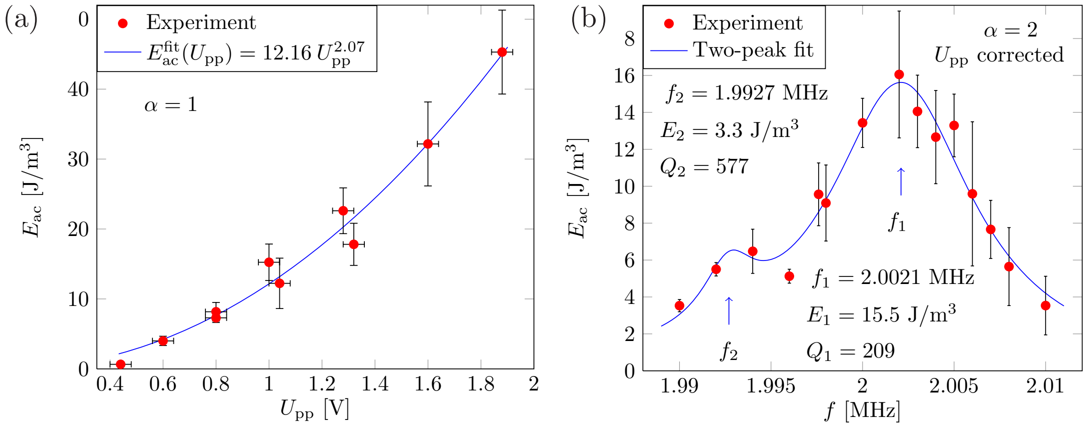

Figure 6.3: (a) Measured acoustic energy density E_{ac} versus applied peak-to-peak voltage U_{pp} on the piezo transducer (points) for $\alpha = 1$. A power law fit (full line) to the data is close to the expected square law, $E_{ac} \propto (U_{pp})^2$. (b) Measured acoustic energy density E_{ac} versus applied frequency f on the piezo transducer (circles) for the $\alpha = 2$ chip for $U_{pp} = 1.48$ V. The data points are fitted by a sum (full line) of two Lorentzian peaks (dashed lines). The values of the fitting parameters are listed on the figure. The peak spacing is $\Delta f_{12} = 9.4$ kHz, while the line widths are $\delta f_1 = 9.6$ kHz and $\delta f_2 = 3.5$ kHz. Reproduced from the DTU master thesis by Rune Barnkob [Barnkob 2009].

al. [Hultström 2007] used force balance between gravity and acoustophoretic forces to measure energy densities in the range 37 – 82 J/m^3 corresponding to pressure amplitudes in the range 0.57 – 0.85 MPa,

We now use the above procedure to extract the acoustic energy density E_{ac} and half the wavelength $\lambda/2$ for 5 – 15 (typically 8) individual microbeads properly chosen in the field of view for any given setting of the external parameters. When plotting the resulting data as a function of the parameters, each data point is a statistical average of these individual measurements, and the error bars are the associated standard deviations. First, at the driving frequency $f = 1.9976$ MHz, we study the energy density and the half wavelength as a function of the peak-to-peak value U_{pp} of the driving voltage on the piezo transducer in the range from 0.5 V to 1.9 V. In Fig. 6.3(a) we see that the resulting ten data points are well fitted to a power law of the form $E_{ac} \propto (U_{pp})^{2.07}$. This is close to a power of 2, which is expected since the acoustic pressure delivered by the piezo transducer is proportional to the applied voltage, and the acoustic energy density is proportional to the square of the pressure, see Eq. (6.5). We also note that the statistically determined error bars increase with increasing driving voltage and thus with increasing microbead velocity. This is as result of the decreased temporal resolution of the paths given the fixed rate of 16 CCD frames per second and the increased microbead velocity.

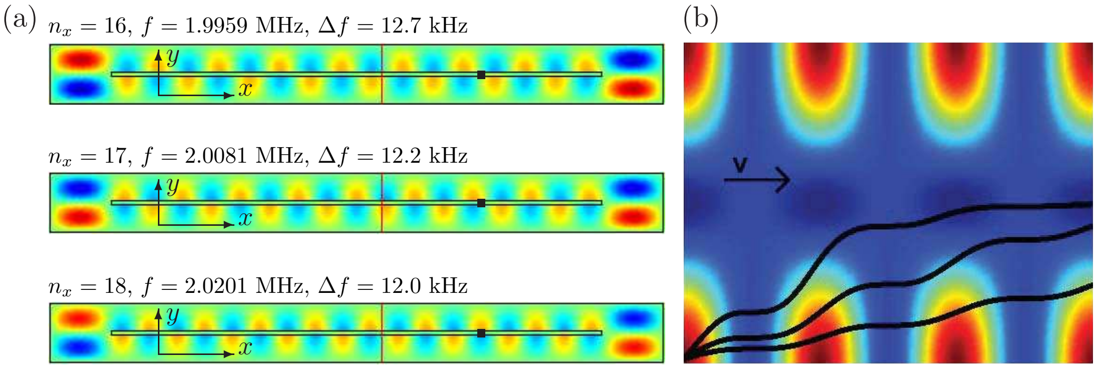

Figure 6.4: A top view color plot (blue negative, red positive) of the pressure field of three ultrasound resonances calculated in the shear-free 2D model. For each resonance is shown the number of n_x of half wavelengths in the axial direction, the resonance frequency f, and the distance Δf in frequency space to the neighboring resonance. The small black rectangles mark the microscope field of view. (b) Zoom-in on calculated particle paths in the given pressure field. The color plot is the potential U^{rad} calculated from Eq. (5.25b) (red high, blue low). Reproduced from the DTU bachelor thesis by Andersen, Nysteen, and Settnes [Andersen 2009].

6.4 Resonance frequencies and Q factors

By measuring the acoustic energy density E_{ac} as a function of the applied piezo transducer frequency f we can characterize the acoustic resonances in more detail. The following results were obtained on the chip $\alpha = 2$ of width $W = 4.67$ mm, see Fig. 6.1(a). The driving frequency f was varied from 1.9900 MHz to 2.0100 MHz, while the tone generator and the amplifier were set to fixed values. However, due to the piezo-electric coupling of the transducer, the actual peak-to-peak voltage U_{pp} varied between 1.44 V and 1.60 V as a function of frequency. We used the quadratic dependency of E_{ac} on U_{pp}, as derived in Fig. 6.3(a), to correct all measured values of E_{ac} to correspond to the same average voltage 1.48 V.

The measured acoustic energy spectrum $E_{\mathrm{ac}}(f)$ is shown in Fig. 6.3(b). A clear maximum is seen at $f_1 = 2.0021$ MHz while a smaller, less pronounced peak is seen at $f_2 = 1.9927$ MHz. According to Eq. (4.20), a simple acoustic resonance can be described by a Lorentzian line shape, and we therefore fit the measured spectrum by the sum of two Lorentzian line shapes. In this case we thus end up with six fitting parameters, three per peak, the energy density maxima $E_{\mathrm{ac},1}$ and $E_{\mathrm{ac},2}$, the resonance frequencies f_1 and f_2, and the Q factors Q_1 and Q_2. The values of these parameters are listed in the caption of Fig. 6.3, and from the energy densities we extract as in Eq. (6.5) the pressure amplitudes $p_{1,1} = 0.37$ MPa and $p_{1,2} = 0.16$ MPa for peak 1 and 2 respectively.

The two resonance peaks in Fig. 6.3 are separated by a spacing $\Delta f_{12} = f_2 - f_1 = 9.4$ kHz, while the line width of the two peaks are of the same order of magnitude, namely $\delta f_2 = 9.6$ kHz and $\delta f_2 = 3.5$ kHz. These values emphasize, as is also seen directly on the graph, that the individual acoustic resonances are barely resolved.

The origin of the observed two-peak structure is explained qualitatively by the 2D pressure eigenmode simulations shown in Fig. 6.4. It is seen how axial modes appear and gives rise to close-lying resonances. While our non-shear-wave model does not allow for accurate determination of these resonance frequencies, it nevertheless provide a reliable order-of-magnitude estimate for the spacing between them, $\Delta f \approx 12$ kHz, close to the observed $\Delta f_{12} = 9.4$ kHz. Furthermore, we speculate that the difference in amplitude between the two peaks shown in Fig. 6.3 is mainly due to the shift in wave pattern going from one value n_x to the neighboring peak at $n_x + 1$ as illustrated by black rectangles in 6.4, representing the microscope field of view. For $n_x = 17$ the pressure amplitude in the field of view is much smaller than that for $n_x = 18$. For more details on axial modes see Ref. [Barnkob 2009b].

In 6.4(b) is shown how individual particle paths looks like for three different flow speeds v for a fixed acoustic field. The color plot is the potential U^{rad} calculated from Eq. (5.25b), and it is seen how the potential landscape induces bumps in the particle trajectories, bumps that get more pronounced the lower the flow rate is in the microchannel.

6.5 Examples of acoustophoretic devices

To give the reader an impression where the research on acoustophoresis stands right now, I have selected the few papers from 2009 and 2010 and present an ultra short abstract for each of them.

Acoustic whole blood plasmapheresis chip for prostate specific antigen microarray diagnostics by A. Lenshof, A. Ahmad-Tajudin, K. Järås, A.-M. Swärd-Nilsson, L. Åberg, G. Marko-Varga, J. Malm, H. Lilja, and Thomas Laurell. *Anal. Chem.* ***81****, 6030 (2009).* Acoustophoresis has been employed to generate high quality plasma from whole blood, whcih is of major interest for many biomedical analyses and clinical diagnostic methods. The red blood cells were focused in the center of thechannel, from where they were removed by outlets placed in the bottom of the channel.

Flow-free transport of cells in microchannels by frequency-modulated ultrasound by O. Manneberg, B. Vanherberghen, B. Önfeltab and M. Wiklund. *Lab Chip* ***9****, 833 (2009).* A flow-free transport of cells and particles is demonstrated by the use of frequency-modulated ultrasonic actuation of a microfluidic chip. The method is used for controlling the motion and position of cells monitored with high-resolution optical microscopy,

Acoustic differential extraction for forensic analysis of sexual assault Evidence by J. V. Norris, M. Evander, K. M. Horsman-Hall, J. Nilsson, T. Laurell, and J. P. Landers. *Anal. Chem.* ***81****, 6089 (2009).* An acoustic differential extraction method has been developed, which relies on acoustic trapping of sperm cells in the presence of epithelial cell lysate (which is unretained), and laminar flow valving to direct the male and female fractions to separate outlets. The method has led to a significant speed-up compared to the conventional separation method used by crime laboratories.

Selective bioparticle retention and characterization in a chip-integrated con-

focal ultrasonic cavity by J. Svennebring, O. Manneberg, P. Skafte-Pedersen, H. Bruus, and M. Wiklund. *Biotech Bioeng **103**, 323-328 (2009).* Selective retention and positioning of cells or other bioparticles ultrasonic manipulation in a microfluidic expansion chamber during microfluidic perfusion. By triple-frequency ultrasonic actuation during continuous microfluidic sample feeding, a set of several manipulation functions performed in series is demonstrated: sample bypass, injection, aggregation, and retention-positioning.

Integrated acoustic and magnetic separation in microfluidic channels by J. D. Adams, P. Thévoz, H. Bruus, and H. T. Soh. *Appl. Phys. Lett. **95** 254101 1-3 (2009).* A monolithic device for multiparameter particle separation based on integrated acoustic and magnetic bioparticle separation is presented. The device is capable of high-purity separation of a multicomponent particle mixture at a throughput of up to 10^8 particles/h.

Harmonic Microchip Acoustophoresis: A Route to Online Raw Milk Sample Precondition in Protein and Lipid Content Quality Control by C. Grenvall, P. Augustsson, J. R. Folkenberg, and T. Laurell. *Anal. Chem. **81**, 6195 (2009).* A microfluidic acoustophoresis approach for raw milk sample preconditioning prior to protein and lipid content analysis in the context of raw milk quality control has been developed. Two higher harmonic acoustophoresis modes, $2\lambda/2$ and $3\lambda/2$, are explored offering lipid content enrichment or depletion, respectively. Lipid content depletion above 90% was accomplished bypassing the problem of lipid aggregation and subsequent clogging inherent in the usual $\lambda/2$ acoustophoresis systems.

Acoustophoretic Synchronization of Mammalian Cells in Microchannels by P. Thévoz, J. D. Adams, H. Shea, H. Bruus, and H. T. Soh. *Anal. Chem. **82**, 3094 (2010).* In a microfluidic system acoustophoresis is used to achieve cell cycle phase synchronization in an asynchronous mixture of mammalian cells in a high-throughput and reagent-free manner based on cell cycle-dependent fluctuations in cell size. The system allows for gentle, scalable, and label-free synchronization with high G1 phase synchrony ($\simeq$84%) and throughput (3×10^6 cells/h per microchannel).

6.6 Acoustic radiation versus acoustic streaming

We finish this brief introduction to the radiation force $\mathbf{F}^{\mathrm{rad}}$ in acoustophoresis by a short discussion of one of its limitations. We have seen that $\mathbf{F}^{\mathrm{rad}}$ scales with the particle volume $(4\pi/3)a^3$, but we also know that given a particle has the velocity $\mathbf{v}$ relative to the surrounding liquid, the Stokes drag force is $\mathbf{F}_{\mathrm{drag}} = -6\pi\eta a\mathbf{v}$, which scales with the radius a. It is therefore expected that the radiation force will be insignificant for small particles.

It so happens that acoustic waves in a liquid imparts momentum to the liquid. To second order a rectification is introduced by the convective acceleration $\rho_0(\mathbf{v}_1\cdot\boldsymbol{\nabla})\mathbf{v}_1$, and as a result a time-averaged second-order velocity field $\mathbf{v}_{\mathrm{str}}$ appears. The motion is generated in the so-called viscous boundary layer near liquid/solid interfaces, within which the magnitude of the first-order velocity is forced to decrease from its bulk value to zero [Landau 1993]. The thickness δ of this layer can be estimated by momentum diffusion Eqs. (3.20) and (3.23a) as $\delta \approx \sqrt{2\nu/\omega} \approx 1$ µm. Here we have exploited that $1/\omega$ sets the time scale of the problem. Viscosity is responsible for the appearance of $\mathbf{v}_{\mathrm{str}}$, however, it

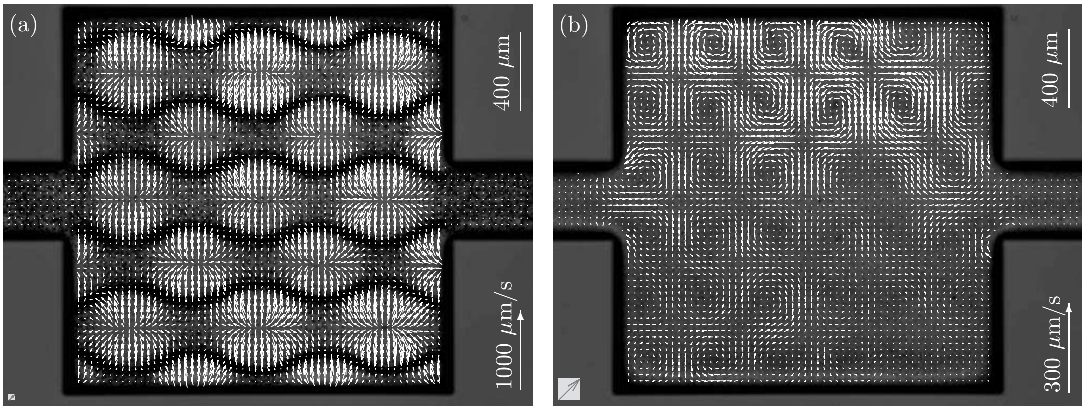

Figure 6.5: Experimental comparison of acoustic radiation and streaming forces on microbeads in a square water-filled chamber of side length 2 mm and depth 0.2 mm in a silicon/glass chip. Initial condition: homogeneous mix in a quiescent carrier liquid (water). An ultrasound field at $f = 2.17$ MHz is then turned on. Transient PIV measurements after 1 ms (white velocity arrows) and microscope picture after 1 s when steady state has been reached. (a) 5 µm polyamide tracer beads under transient motion (white arrows) and focesd by radiation forces in steady state (black bands). (b) 1 µm polystyrene microbeads in vortex motion due to acoustic streaming after 1 ms, and no accumulation observed after 1 s. Reproduced from the DTU PhD thesis by S. Melker Hagsäter [Hagsäter 2008].

only sets the length scale of the boundary layer and not the magnitude v_{str} of the acoustic streaming. To estimate v_{str} we argue that the only meaningful way to generate a velocity to second order in the acoustic velocity v_1 is

$$v_{\mathrm{str}} = \Psi\,\frac{v_1^2}{c_{\mathrm{a}}}, \quad \text{where } \Psi \approx 1. \tag{6.6}$$

Here Ψ is a geometry dependent factor of order unity, e.g. $\Psi = 3/8$ for a standing wave parallel to a planar wall. A particle kept fixed in an acoustic streaming field is subject to an acoustic streaming force of magnitude

$$F_{\mathrm{str}} = 6\pi\eta a\, v_{\mathrm{str}} = 6\pi\eta a\, \Psi\,\frac{v_1^2}{c_{\mathrm{a}}}. \tag{6.7}$$

We can now obtain an estimate for the critical particle radius a_c below which the radiation force no longer dominates. We just assume that it is F_{drag} that keeps the particle fixed in the acoustic streaming. Combining the demand $F^{\mathrm{rad}} = F_{\mathrm{str}}$ with the expressions (5.29a) and (6.7) for the forces, we get

$$\pi a_c^3 k\, \rho_0 v_1^2 \Phi = 6\pi\eta a_c\, \Psi\,\frac{v_1^2}{c_{\mathrm{a}}}, \tag{6.8}$$

from which we obtain the critical particle radius a_c or diameter d_c,

$$a_c = \sqrt{\frac{3\Psi}{\Phi}\,\frac{2\nu}{\omega}} = \sqrt{\frac{3\Psi}{\Phi}}\,\nu \approx 1\ \text{µm} \quad \text{or} \quad d_c \approx 2\ \text{µm}. \tag{6.9}$$

In Fig. 6.5 is shown an experimental example of the cross-over from radiation dominated to streaming dominated acoustophoresis [Hagsäter 2007]. An acoustophoretic experiment was first carried out with the 5-µm-diameter microbeads, see panel (a), then the sample was replaced with a suspension of 1-µm-diameter microbeads, and the experiment was repeated keeping the values of all other parameters fixed, see panel (b). In a single experiment a well mixed solution was led into the square chamber (side width 2 mm and depth 0.2 mm), the external flow was stopped, and a 2.17 MHz ultrasound field was set up via a piezo-transducer underneath the chamber. About 1 ms later the transient velocity was determined by particle image velocimetry (white arrows on the figure). Finally, after about 1 s a photo was taken of the device. The large particles collect in bands coinciding with the pressure nodal planes. The small particles never collected but continued to flow in the vortices clearly visible in panel (b).

This result emphasizes the difficulties we currently face trying to apply acoustophoresis to sub-micrometer particles such as proteins, enzymes, and other biomolecules. The acoustic streaming is not so easy to control as the radiation force, so more studies are needed in this particular area of acoustofluidics.

References

Adams, J. D., Thévoz, P., Bruus, H., and Soh, H. T. (2009). Integrated acoustic and magnetic separation in microfluidic channels. *Appl. Phys. Lett.* **95** 254101 1-3.

Andersen, M. J., Nysteen, A, Settnes, M. (2009).
Forces acting on microparticles in acoustofluidic systems.
DTU bachelor thesis, http://www.nanotech.ctu.dk/microfluidics

Aris, R. (1956). On the dispersion of a solute in a fluid flowing through a tube. *Roy. Soc.* **A235**, 67–77.

Barnkob, R. (2009). Acoustofluidics in microsystems: investigation of resonances.
DTU master thesis, http://www.nanotech.ctu.dk/microfluidics

Barnkob B. and Bruus H. (2009b), Acoustofluidics: theory and simulation of radiation forces at ultrasound resonances in microfluidic devices. *Procs. Meetings on Acoustics* **6**, 020001. 157th Meeting Acoust. Soc. Am. 2009, (doi:10.1121/1.3186746).

Barnkob, R. Augustsson P. Laurell T., and Bruus H. (2010). Measuring the local pressure amplitude in microchannel acoustophoresis. *Lab Chip* **10**, 563–570.

Brown D. (2009). Tracker 2.60, Free video analysis and modeling tool for physics education. *Online open source*: http://www.cabrillo.edu/dbrown/tracker/

Batchelor, G. K. (2000). *An introduction to fluid dynamics.*
Cambridge University Press, Cambridge.

Berthier, J. and Silberzan, P. (2006). *Microfluidics for biotechnology.*
Artech House, Boston.

Bruus, H. (2008). *Theoretical microfluidics*
Oxford University Press, Oxford.

Gorkov, L. P. (1962). On the forces acting on a small particle in an acoustic field in an ideal fluid. *Sov. Phys. Doklady*, **6**, 773–776.

Grenvall, C., Augustsson, P., Folkenberg, J. R., and Laurell, T. (2009).
Harmonic Microchip acoustophoresis: a route to online raw milk sample precondition in protein and lipid content quality control. *Anal. Chem.* **81**, 6195.

Hagsäter, S. M., Glasdam Jensen, T., Bruus, H. and Kutter, J. P. (2007).
Acoustic resonancesin microfluidic chips: full-image micro-PIV experiments and numerical simulations. *Lab Chip*, **7**, 1336–1344.

Hagsäter, S. M. (2008). Development of micro-PIV techniques for applications in microfluidic systems. DTU PhD thesis, http://www.nanotech.ctu.dk/microfluidics

Hultström, J., Manneberg, O., Dopf, K., Hertz H. M., Brismar, H., and Wiklund, M. (2007). Proliferation and viability of adherent cells manipulated by standing-wave ultrasound in a microfluidic chip. *Ultrasound Med. & Biol.*, **33**, 145–151.

King, L. V. (1934). On the acoustic radiation pressure on spheres. *Proc. R. Soc. (London)* **A147**, 212–240.

Landau, L. D. and Lifshitz, E. M. (1982). *Statistical physics part 1, 3rd edn.* Course of theoretical physics vol. 5. Pergamon Press, Oxford.

Landau, L. D. and Lifshitz, E. M. (1986). *Theory of elasticity, 3rd edn.* Course of theoretical physics vol. 7. Pergamon Press, Oxford.

Landau, L. D. and Lifshitz, E. M. (1993). *Fluid mechanics, 2nd edn.* Course of theoretical physics vol. 6. Pergamon Press, Oxford.

Laurell, T., Petersson, F., and Nilsson A. (2007). Chip integrated strategies for acoustic separation and manipulation of cells and particles. *Chem. Soc. Rev.* **36**, 492–506.

Lenshof, A., Ahmad-Tajudin, A., Järås, K., Swärd-Nilsson, A.-M., Åberg, L., Marko-Varga, G., Malm, J., Lilja, H., and Laurell, T. (2009). Acoustic whole blood plasmapheresis chip for prostate specific antigen microarray diagnostics. *Anal.Chem.***81**,6030.

Lighthill, J. (2003). *Waves in fluids.* Cambridge University Press, Cambridge.

Manneberg, O., Vanherberghen, B., Önfeltab, B., and Wiklund, M. Flow-free transport of cells in microchannels by frequency-modulated ultrasound. *Lab Chip* **9**, 833.

Nilsson, J., Evander, M., Hammarström, B., and Laurell, T. (2009). Cell and particle trapping in microfluidic systems. *Anal. Chim. Acta* **649**, 141–157.

Norris, J. V., Evander, M., Horsman-Hall, K. M., Nilsson, J., Laurell, T., and Landers, J. P. (2009). Acoustic differential extraction for forensic analysis of sexual assault Evidence. *Anal. Chem.* **81**, 6089.

Petersson, F., Nilsson, A., Holm, C., Jönsson, H. and Laurell, T. (2005). Continuous separation of lipid particles from erythrocytes by means of laminar flow and acoustic standing wave forces. *Lab Chip* **5**, 20–22.

Tabeling, P. (2005). *Introduction to microfluidics.* Oxford University Press, Oxford.

Svennebring, J., Manneberg, O., Skafte-Pedersen, P., Bruus, H., and Wiklund, M. (2009). Selective bioparticle retention and characterization in a chip-integrated confocal ultrasonic cavity.*Biotech Bioeng* **103**, 323–328.

Thévoz, P., Adams, J. D., Shea, H., Bruus, H., and Soh, H. T. (2010). Acoustophoretic Synchronization of Mammalian Cells in Microchannels. *Anal. Chem.* **82**, 3094.

Vedel, S. (2009). Millisecond dynamics in microfluidics: Equivalent circuit theory and experiment. DTU master thesis, http://www.nanotech.ctu.dk/microfluidics

Vedel, S., Olesen, L. H., and Bruus, H. (2010). Pulsatile microfluidics as an analytical tool for determining the dynamic characteristics of microfluidic systems *J. Micromech. Microeng.*, **20**, 035026 1–11.

Wiklund, M., Spégel, P., Nilsson, S., and Hertz, H. M. (2003). Ultrasonic-trap-enhanced selectivity in capillary electrophoresis. *Ultrasonics*, **41**, 329–333.

Yosioka, K. and Kawasima, Y. (1955). Acoustic radiation pressure on a compressible sphere. *Acoustica* **5**, 167–173.

M7 Streaming Theory

Acoustic Streaming with Drops, Bubbles and Particles

CISM Course on Ultrasound standing wave action on suspensions and biosuspensions in micro- and macro fluidic devices

S.S. Sadhal
Department of Aerospace & Mechanical Engineering
University of Southern California
Los Angeles, CA 90089-1453
USA

Updated June 3, 2010

Contents

Chapter 1

Fundamentals of Nonlinear Acoustics and Streaming

Acoustic streaming can be classified as two common types. One happens because of the spatial attenuation of a wave in free space, e.g., an attenuating beam of plane traveling wave. This type of streaming is usually associated with a high Reynolds number flow. The second mechanism arises from the friction between the fluid medium and a solid wall when the former is vibrating in contact with the latter, e.g., a wave traveling down a wave-guide, a standing wave in a resonant chamber, or a wave scattering off a solid object. Unlike the spatial attenuation mentioned earlier, this effect is largely confined to a thin viscous boundary layer of thickness $\delta = (2\nu/\omega)^{1/2}$ on the surface, where ν is the kinematic viscosity of the medium and ω is the angular frequency of the wave. It is also a significant dissipation mechanism, and provides a strong force in driving acoustic streaming. While the medium outside the layer vibrates irrotationally as in a sound field, the one inside the layer is forced to vibrate rotationally (i.e., with vorticity) because its motion has to conform to the no slip condition on wall. Most of the discussion in this lecture series will be on the second mechanism of streaming.

If a body of typical dimension a oscillates with velocity $U_\infty \cos(\omega t)$ in a viscous fluid and $\varepsilon = U_\infty/\omega a \ll 1$, then, although the leading order solution is oscillatory, higher order terms include not only higher harmonics but steady contributions to the velocity. Mathematically, this can be explained by existence of the nonlinear terms which may have steady nonzero component. For example, $\cos\omega t \cos\omega t = \cos^2\omega t = \frac{1}{2}(1+\cos 2\omega t)$ has $\frac{1}{2}$ as a steady component. Physically, the condition $\varepsilon \ll 1$ implies that the amplitude of the oscillation is small compared with a. The existence of this steady streaming was first pointed out by Rayleigh [18] in his work on Kundt's dust tube and was later studied in a boundary layer context by Schlichting [23] who considered flows with the additional constraint $|M|^2 = \omega a^2/\nu \gg 1$, where ν denotes the kinematic viscosity of the fluid. For such a flow it is now well established that the first order fluctuation vorticity is confined to a shear-wave region of thickness $O(\nu/\omega)^{1/2}$ beyond which steady velocities $O(\varepsilon U_\infty)$ persist. Riley [20] has considered the case of an oscillating sphere for both $|M| \gg 1$ and $0 < |M| < 1$. He calculated the streaming around the sphere which is at the velocity antinode of the wave that vibrates vertically. Lee & Wang [11] considered an oscillating sphere slightly displaced from the antinode of a standing wave for $|M| \gg 1$. Their analysis relied on the tangential velocity (slip) calculation based on an analytical algorithm.

1.1 Oscillatory Flows

For sound waves, the basic equations of fluid mechanics are applicable. While our focus is nonlinear acoustics, we shall start with the development of the linear theory. In the general tensor form for an compressible fluid, we have (see, e.g. Landau & Lifshitz [10]):
continuity:

$$\frac{\partial \rho}{\partial t} + \frac{\partial}{\partial x_i}(\rho u_i) = 0 \qquad \text{or} \qquad \frac{\partial \rho}{\partial t} + \boldsymbol{\nabla} \cdot (\rho \boldsymbol{u}) = 0 \tag{1.1}$$

momentum:

$$\rho\left(\frac{\partial u_i}{\partial t} + u_i\frac{\partial u_i}{\partial x_k}\right) = -\frac{\partial p}{\partial x_i} + \frac{\partial}{\partial x_i}\left[\mu\left(\frac{\partial u_i}{\partial x_k} + \frac{\partial u_k}{\partial x_i} - \tfrac{2}{3}\delta_{ik}\frac{\partial u_m}{\partial x_m}\right)\right] + \frac{\partial}{\partial x_i}\left(\beta\frac{\partial u_m}{\partial x_m}\right), \tag{1.2}$$

For most practical situations, the viscosities, μ and β, may be treated as constant, resulting in the following vector form of the momentum equation,

$$\rho\left(\frac{\partial \boldsymbol{u}}{\partial t} + \boldsymbol{u}\cdot\boldsymbol{\nabla}\boldsymbol{u}\right) = -\boldsymbol{\nabla}p + +\mu\nabla^2\boldsymbol{u} + \left(\beta + \tfrac{1}{3}\mu\right)\boldsymbol{\nabla}\left(\boldsymbol{\nabla}\cdot\boldsymbol{u}\right). \tag{1.3}$$

Sound waves consist compression and rarefaction of a compressible fluid which can be characterized by oscillatory motion of small amplitude. We begin with the linearized form of the above equations by considering small acoustic disturbances to the pressure and density, i.e.,

$$p = p_0 + p' \qquad \text{and} \qquad \rho = \rho_0 + \rho', \qquad \text{with} \qquad \rho' \ll \rho_0 \qquad \text{and} \qquad p' \ll p_0. \tag{1.4}$$

Similarly, the velocity is taken to be of the form

$$\boldsymbol{u} = \boldsymbol{u}_0 + \boldsymbol{u}' \tag{1.5}$$

but since the undisturbed state here is a quiescent fluid, $\boldsymbol{u}_0 = \boldsymbol{0}$, and the disturbed atate velocity $\boldsymbol{u}'$ is the only one that needs to be considered. In addition, $\boldsymbol{u}'$ is considered to be small whereby the inertial effects (the term $\boldsymbol{u}\cdot\boldsymbol{\nabla}\boldsymbol{u}$) can be neglected. This linearization is of course not valid near regions of large changes in the velocity (such as a solid boundary) and under those circumstances, we will need to include this nonlinear term in the analysis. In addition, ignoring any viscous effects, equations (1.1) and (1.3) takes the form,

$$\frac{\partial \rho'}{\partial t} + \rho_0\boldsymbol{\nabla}\cdot\boldsymbol{u} = 0, \tag{1.6}$$

and

$$\rho_0 \frac{\partial \boldsymbol{u}}{\partial t} = -\boldsymbol{\nabla} p'. \tag{1.7}$$

Now, assuming adiabatic compression and rarefactions, and a linear relationship between pressure and density,

$$p' = \left(\frac{\partial p}{\partial \rho_0}\right)_s \rho' \tag{1.8}$$

and considering the flow to be irrotational, i.e., allowing the velocity to be described by a potential,

$$\boldsymbol{u} = -\boldsymbol{\nabla}\phi, \tag{1.9}$$

equation (1.7) becomes

$$\boldsymbol{\nabla}\left(p' + \rho\frac{\partial \phi}{\partial t}\right) = \boldsymbol{0}, \tag{1.10}$$

which may be integrated to give

$$p' = -\rho\frac{\partial \phi}{\partial t}. \tag{1.11}$$

Next, using this in the continuity equation (5.17), we obtain the wave equation

$$\frac{1}{c^2}\frac{\partial^2 \phi}{\partial t^2} = \nabla^2\phi. \tag{1.12}$$

This is of course the linearized version which is applicable in many practical circumstances. Here c is the speed of sound given by

$$c = \sqrt{\frac{\partial p}{\partial \rho}} = \sqrt{\frac{\gamma R T}{m}}, \tag{1.13}$$

where $\gamma = c_p/c_v$ is the ratio of the specific heats, and m is the molecular weight of the medium.

One familiar solution to the wave equation is the plane wave (one-dimensional)

$$\phi(x,t) = Ae^{i(kx-\omega t} \tag{1.14}$$

where $k = \omega/c$ is known as the wavenumber, and ω is the wave frequency. This expression represents a traveling wave, i.e., a wave traveling with a specific velocity. Admitting other possible forms of solutions and superimposing several solutions with various frequencies, we may write

$$\phi(x,t) = \sum_{n=0}^{\infty} a_n e^{i\omega_n(x/c-t)} + b_n e^{-i\omega_n(x/c-t)} + c_n e^{i\omega_n(x/c+t)} + d_n e^{-i\omega_n(x/c+t)}, \tag{1.15}$$

or in real variables, we have

$$\phi(x,t) = \sum_{n=0}^{\infty} \left[A_n^* \sin(\omega_n x/c) + B_n^* \cos(\omega_n x/c)\right]\left[C_n^* \sin(\omega_n t) + D_n^* \cos(\omega_n t)\right] \tag{1.16}$$

By introducing parameters α_n and β_n, it is not difficult to see that

$$\phi(x,t) = \sum_{n=0}^{\infty} A_n \cos(\omega_n x/c + \alpha_n)\cos(\omega_n t + \beta_n) \tag{1.17}$$

Each term in the summation represents a standing wave of the given frequency,

$$\phi(x,t) = A\cos(\omega x/c + \alpha)\cos(\omega t + \beta),$$

where we have dropped the index n. Here we refer to A as the amplitude of the wave. For a single-frequency wave, the phase-differences α and β can be dropped by just choosing appropriate coordinate reference frames so that

$$\phi(x,t) = A\cos(\omega x/c)\cos(\omega t).$$

The velocity now is

$$u(x,t) = -\frac{\partial\phi(x,t)}{\partial x} = \frac{A\omega}{c}\sin(\omega x/c)\cos(\omega t),$$

and the pressure is

$$p'(x,t) = -\rho\frac{\partial\phi(x,t)}{\partial t} = A\omega\cos(\omega x/c)\sin(\omega t).$$

The velocity takes on zero values at positions $\omega x/c = n\pi$, or $x = n\pi c/\omega$. These points are called the velocity nodes. The velocity has maximum magnitude at $x = \left(n + \frac{1}{2}\right)\pi c/\omega$. At these points known as the antinodes, the pressure is zero. These nodes and antinodes are shown in Figure 1.1

This is an example of a simple standing wave in which the flow field is both inviscid and irrotational. However, as mentioned earlier, there are two types of situations in which nonlinearities can set in. One is due to the presence of solid boundaries which can change this (inviscid and irrotational) characteristic by causing sufficiently large velocity gradients so that viscous forces are significant, and at the same time vorticity $\boldsymbol{\zeta} = \boldsymbol{\nabla}\times\boldsymbol{u}$ is generated at the surface. Mathematically, the term $\boldsymbol{u}\cdot\boldsymbol{\nabla}\boldsymbol{u}$ in equation (1.3) becomes relevant. Among the simplest examples to illustrate this concept is Rayleigh streaming which is mentioned later. Another type of nonlinearity comes about without any boundaries when an ultra-high-frequency beam penetrates the half-space $x > 0$. The leads to what is known as the quartz wind which is discussed next.

As a visual example of the solid-boundary effect can be seen in Figure 1.2 of the flow around an oscillating cylinder. Here, one can see recirculating zones near the cylinder walls where the flow is not irrotational.

One of the earliest examples of this type of streaming is Rayleigh's problem [18] in which standing sound waves between two walls a distance $2a$ apart were considered. Away from the walls, the velocity field is described by the inviscid, irrotational flow

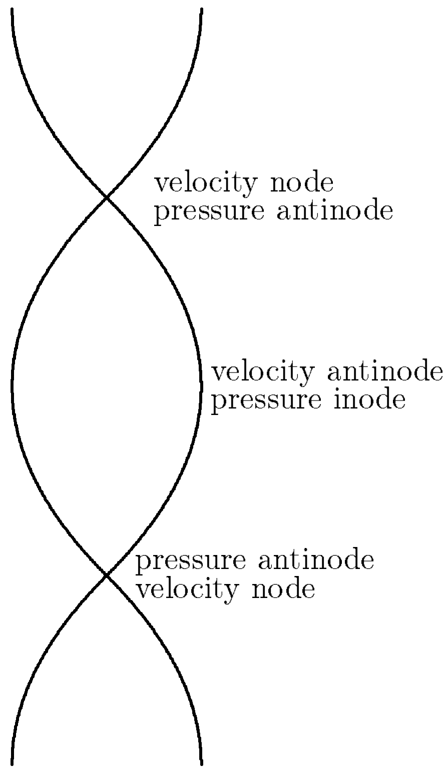

Figure 1.1: Node and antinode identification

wave equation (1.12). Assuming only an x-component of velocity for the inviscid field, the solution in non-dimensional form is

$$\boldsymbol{u} = (\sin(akx)\cos t, 0), \tag{1.18}$$

which, of course, has zero time-average velocity. For this case, there is a streaming velocity at the edge of the stokes layer given by

$$u_e = -\tfrac{3}{8}ak\sin 2akx,$$

As discussed later on page 15, detailed calculation yield a higher-order steady streaming velocity field with both x and y components in the form

$$\boldsymbol{u}_1^{(s)} = \left\{\tfrac{3}{16}ak(1-3y^2)\sin 2akx, -\tfrac{3}{8}a^2k^2(y-y^3)\cos 2akx,\right\} \tag{1.19}$$

or equivalently, as a stream function,

$$\psi_1^{(s)}(x,y) = \tfrac{3}{16}(y-y^3)\sin 2akx, \tag{1.20}$$

where the superscript (s) refers to the steady streaming, i.e., a mean dc component. For proper scaling, these higher-order expressions (1.20) and (1.19) should be multiplied by the small parameter $\varepsilon = U_0/\omega a$. The streamlines are exhibited (schematically) in Figure 1.3 for half the vertical region, below the plane of symmetry. The coordinate y is scaled with half the vertical dimension.

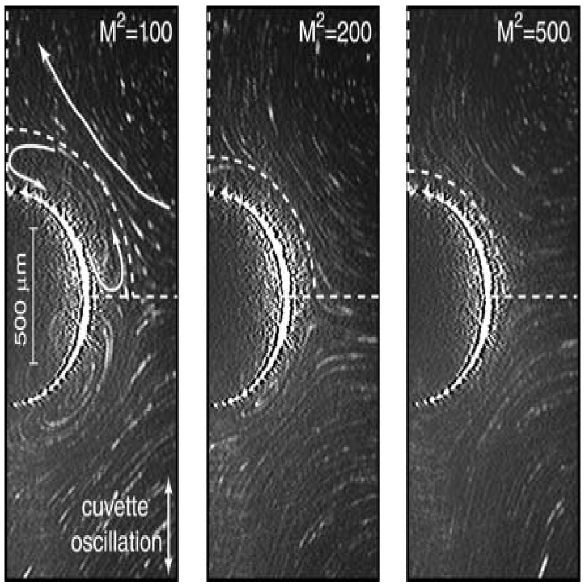

Figure 1.2: Images of steady acoustic streaming near a cylindrical electrode for vertical oscillations. Three different dimensionless acoustic oscillation frequencies are shown (M = 100, 200, and 500). [15]

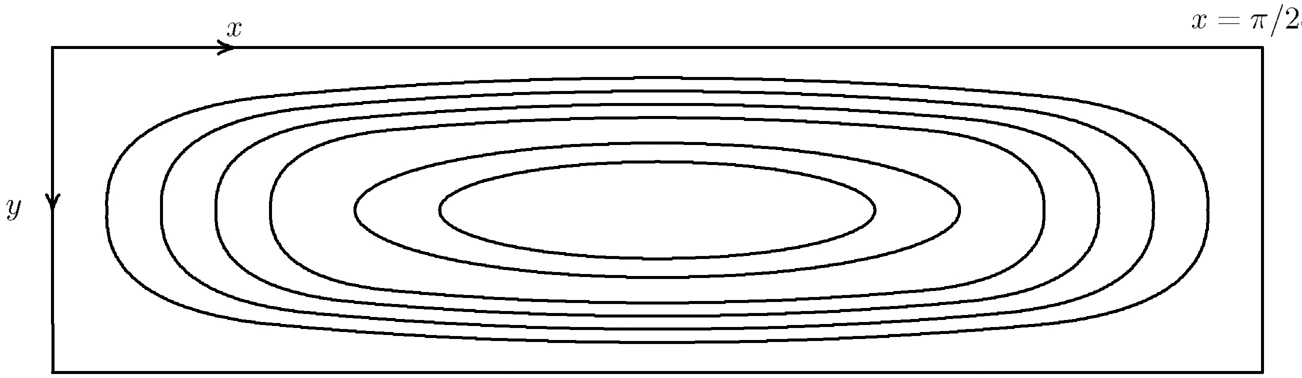

Figure 1.3: A schematic of the flow streamlines in Rayleigh's problem [18]

Chapter 2

Singular Perturbation Analysis of Nonlinear Acoustics

2.1 The Quartz Wind

In the half-space $x > 0$ consider a one-dimensional beam of frequency ω. Taking $1/\omega$ as a time scale, c/ω as a length scale, U_0 the velocity amplitude as a velocity scale, and $\rho_0 c^2$ for pressure, we obtain from equations (1.3) and (1.1)

$$\frac{\partial u}{\partial t} + \varepsilon u \frac{\partial u}{\partial x} = -\frac{1}{\varepsilon}\frac{\partial p}{\partial x} + \tfrac{4}{3}\delta \frac{\partial u}{\partial x}, \qquad \frac{\partial \rho}{\partial t} + \varepsilon \frac{\partial u}{\partial x} = 0, \tag{2.1}$$

where $\varepsilon = U_0/c \ll 1$, $\delta = \omega\mu/\rho_0 c^2 \ll 1$. Using the adiabatic linear relationship between pressure and density (1.8), and combining the set of equations (2.1), we obtain

$$\frac{\partial^2 u}{\partial t^2} - \frac{\partial^2 u}{\partial x^2} - \tfrac{4}{3}\delta \frac{\partial^3 u}{\partial x^2 \partial t} = -\varepsilon \frac{\partial}{\partial t}\left(u \frac{\partial u}{\partial x}\right) \tag{2.2}$$

Now, if we expand $u(x,t)$ in powers of ε,

$$u(x,t) = u_0(x,t) + \varepsilon u_1(x,t) + \varepsilon^2 u_2(x,t) \cdots,$$

then the leading-order form of equation (2.2) is

$$\frac{\partial^2 u_0}{\partial t^2} - \frac{\partial^2 u_0}{\partial x^2} - \tfrac{4}{3}\delta \frac{\partial^3 u_0}{\partial x^2 \partial t} = 0. \tag{2.3}$$

This has the solution

$$u_0(x,t) = e^{-2\delta x/3}\cos(x - t), \tag{2.4}$$

for a beam originating at $x = 0$. Not considering the nonlinear term in equation (2.2) as a Renolds stress, then we may consider its time-average as the net force,

$$-\left\langle \varepsilon u_0 \frac{\partial u_0}{\partial x} \right\rangle = \tfrac{1}{3}\varepsilon\delta e^{-4\delta x/3}, \tag{2.5}$$

where $\langle \cos^2(x - t)\rangle = \frac{1}{2}$ has played in.

2.2 Rayleigh Streaming

This development is based on the reviews by Riley [21, 22], following which, we write equation (1.3) for an incompressible fluid in the form

$$\frac{\partial \boldsymbol{u}'}{\partial t} - \boldsymbol{u}' \times \boldsymbol{\zeta}' = -\frac{1}{\rho} \boldsymbol{\nabla} \left(p + \tfrac{1}{2} \boldsymbol{u}' \cdot \boldsymbol{u}' \right) + \boldsymbol{F}' + \nu \nabla^2 \boldsymbol{u}', \tag{2.6}$$

where the primes are introduced to denote dimensioned quantities. In addition, we are using the kinematic viscosity $\nu = \mu/\rho$, and we have introduced $\boldsymbol{F}'$ as a body force per unit mass. With a as a length scale, F_0 as a typical body force, and $U_0 = F_0/\omega$ as velocity, we nondimensionalize as follows:

$$\boldsymbol{F} = \boldsymbol{F}'/F_0, \quad \boldsymbol{x} = \boldsymbol{x}'/a, \quad t = \omega t', \quad \boldsymbol{u} = \boldsymbol{u}/U_0, \quad \boldsymbol{\zeta} = a\boldsymbol{\zeta}'/U_0.$$

Using these parameters, and taking the curl of equation (2.6) to eliminate the terms within the $\boldsymbol{\nabla}$ operator, we obtain

$$\frac{\partial \boldsymbol{\zeta}}{\partial t} - \varepsilon \boldsymbol{\nabla} \times (\boldsymbol{u} \times \boldsymbol{\zeta}) = \frac{\varepsilon}{R} \nabla^2 \boldsymbol{\zeta}, \tag{2.7}$$

where $\varepsilon = U_0/\omega a$, $R = U_0 a/\nu$, and $\boldsymbol{\nabla} \times \boldsymbol{F}$ is eliminated on account of being considered conservative.

For the purpose of illustration, we consider a simple two-dimensional case (see Riley [22, 21]) so that

$$\boldsymbol{\zeta} = \boldsymbol{\nabla} \times \boldsymbol{u} = (0, 0, \zeta) \qquad \text{with} \quad \zeta = -\nabla^2 \psi, \tag{2.8}$$

where $\psi(x, y)$ is the stream function defined by

$$\boldsymbol{u}(x, y, t) = \boldsymbol{\nabla} \times (0, 0, \psi(x, y, t)).$$

As a result, equation (2.7) becomes

$$\frac{\partial \zeta}{\partial t} + \varepsilon (\boldsymbol{u} \cdot \boldsymbol{\nabla}) \zeta = \frac{\varepsilon^2}{R_s} \nabla^2 \zeta, \tag{2.9}$$

where $R_s = \varepsilon R$ is the streaming Reynolds number.

2.2.1 Solution by Perturbation

For $\varepsilon \ll 1$, a perturbation expansion of the type

$$\begin{aligned}
\boldsymbol{u}(x, y, t) &= \boldsymbol{u}_0(x, y, t) + \varepsilon \boldsymbol{u}_1(x, y, t) + \varepsilon^2 \boldsymbol{u}_2(x, y, t) + \cdots \\
\zeta(x, y, t) &= \zeta_0(x, y, t) + \varepsilon \zeta_1(x, y, t) + \varepsilon^2 \zeta_2(x, y, t) + \cdots \\
\psi(x, y, t) &= \psi_0(x, y, t) + \varepsilon \psi_1(x, y, t) + \varepsilon^2 \psi_2(x, y, t) + \cdots
\end{aligned} \tag{2.10}$$

Since the applied force is considered conservative, the leading-order flow can be regarded as irrotational ($-\nabla^2\psi_0 = \zeta_0 = 0$). Further, considering the applied force to have an oscillatory character, $\boldsymbol{F}(\boldsymbol{x},t) = \boldsymbol{f}(\boldsymbol{x})e^{it}$, the leading-order solution may be written as $\psi_0(x,y,t) = \psi_{0f}(x,y,t)e^{it}$, where $\psi_{0f}(x,y,t)$ is the stream function corresponding the force $\boldsymbol{f}$. Near the boundary $y=0$, there is a slip velocity

$$u(x,y,t) = \frac{\partial\psi(x,y,t)}{\partial y} = U(x)e^{it} \qquad \text{at} \qquad y=0. \tag{2.11}$$

To deal with the flow field at the boundary (and satisfy the no-slip condition), we define inner variables in the Stokes layer,

$$\psi = \left(\frac{2}{R_s}\right)^{\frac{1}{2}} \varepsilon\Psi, \qquad y = \left(\frac{2}{R_s}\right)^{\frac{1}{2}} \varepsilon\eta, \tag{2.12}$$

leading to the following form of the vorticity equation (2.9),

$$\frac{\partial}{\partial t}\left(\frac{\partial^2\Psi}{\partial\eta^2}\right) - \varepsilon\frac{\partial\left(\Psi, \partial^2\Psi/\partial\eta^2\right)}{\partial(x,\eta)} = \tfrac{1}{2}\frac{\partial^4\Psi}{\partial\eta^4} + O\left(\varepsilon^2\right). \tag{2.13}$$

Upon expanding this inner variable in the same form as (2.10),

$$\Psi(x,\eta,t) = \Psi_0(x,y\eta,t) + \varepsilon\Psi_1(x,\eta,t) + \varepsilon^2\Psi_2(x,\eta,t) + \cdots, \tag{2.14}$$

we have for the leading order,

$$\frac{\partial}{\partial t}\left(\frac{\partial^2\Psi_0}{\partial\eta^2}\right) = 0, \tag{2.15}$$

with the classical Stokes-layer solution,

$$\Psi_0(x,y,t) = U(x)\left[\eta - \tfrac{1}{2}(1-i)\left\{1 - e^{-(1+i)\eta}\right\}\right]e^{it}, \tag{2.16}$$

where, as $\eta \to \infty$, the solution approaches the slip-velocity condition given in equation (2.11).

Next, to $O(\varepsilon)$, from equations (2.13) and (2.14), we obtain

$$\tfrac{1}{2}\frac{\partial^4\Psi_1}{\partial\eta^4} - \frac{\partial}{\partial t}\left(\frac{\partial^2\Psi_1}{\partial\eta^2}\right) = \frac{\partial\left(\partial^2\Psi_0/\partial\eta^2, \Psi_0\right)}{\partial(x,\eta)} \tag{2.17}$$

In spite of the oscillatory character of the flow field, we can expect nonzero time-average contribution from the term on the right-hand side when real parts of the solutions are used. This is because it involves the products leading to $\sin^2 t$ and $\cos^2 t$ types of terms which have a nonzero mean. If we are concerned only with the time-averaged part, we can decompose $\Psi_1(x,\eta,t)$ into steady ans unsteady parts, i.e.,

$$\Psi_1(x,\eta,t) = \Psi_1^{(u)}(x,\eta,t) + \Psi_1^{(s)}(x,\eta), \tag{2.18}$$

where the superscripts (u) and (s) refer to unsteady and steady parts, respectively. Taking the time-average of equation (2.17), we obtain

$$\tfrac{1}{2}\frac{\partial^4 \Psi_1^{(s)}}{\partial \eta^4} = \left\langle \frac{\partial\left(\partial^2\Psi_0/\partial\eta^2, \Psi_0\right)}{\partial(x,\eta)} \right\rangle. \tag{2.19}$$

On the right-hand side, the x-dependence will emanate from $U(x)$ in the expression for Ψ_0 in equation (2.16). This will contain terms involving $U(x)$ and $U'(x)$, as well as their complex conjugates, $U^*(x)$ and $U^{*\prime}(x)$. The solution to equation (2.19) can be written as

$$\Psi_1^{(s)}(x,\eta) = \frac{d}{dx}(UU^*)f(\eta) + U^*\frac{dU}{dx}g(\eta). \tag{2.20}$$

The successive integration of equation (2.19), requiring no-slip at the surface ($\eta = 0$) and boundedness as $\eta \to \infty$, is

$$\begin{aligned}\frac{\partial \Psi_1^{(s)}(x,\eta)}{\partial \eta} &= \frac{1}{2}\frac{d}{dx}(UU^*)\left(e^{-\eta}\sin\eta + \tfrac{1}{4}e^{-2\eta} - \tfrac{1}{4}\right)\\ &-U^*\frac{dU}{dx}\left[\left\{\tfrac{1}{2}(1+i)\eta + i - \tfrac{1}{2}\right\}e^{(1-i)\eta} - \tfrac{1}{4}ie^{-2\eta} - \tfrac{3}{2}i + \tfrac{1}{2}\right].\end{aligned} \tag{2.21}$$

This represents the x-component (i.e., tangential) of the streaming velocity within the Stokes layer. The interesting aspect here is that velocity continues beyond the Stokes layer, i.e.,

$$\lim_{\eta\to\infty}\left[\mathrm{Re}\left(\frac{\partial \Psi_1^{(s)}(x,\eta)}{\partial\eta}\right)\right] = -\tfrac{3}{2}\left[(1-i)U^*\frac{dU}{dx} + (1+i)U\frac{dU^*}{dx}\right] = u_e. \tag{2.22}$$

This slip velocity is considered to be the driving mechanism for steady streaming in the bulk. The structure of this outer streaming is considered next.

2.2.2 Stokes Drift

Again, following Riley [22, 21], and taking the perturbation expansions (2.10) together with equation (2.9), to $O(\varepsilon^2)$, we obtain

$$\frac{\partial \zeta_2}{\partial t} = -\left(\boldsymbol{u}_0\boldsymbol{\cdot}\boldsymbol{\nabla}\right)\zeta_1^{(s)}, \qquad \text{which integrates to} \qquad \zeta_2 = -\left[\left(\int^t \boldsymbol{u}_0\, dt\right)\boldsymbol{\cdot}\boldsymbol{\nabla}\right]\zeta_1^s. \tag{2.23}$$

Next, to $O(\varepsilon^3)$, we have

$$\frac{1}{R_s}\nabla^2\zeta_1^{(s)} - \left(\boldsymbol{u}_1\boldsymbol{\cdot}\boldsymbol{\nabla}\right)\zeta_1^{(s)} = \frac{\partial \eta_3}{\partial t} + \left(\boldsymbol{u}_0\boldsymbol{\cdot}\boldsymbol{\nabla}\right)\zeta_2, \tag{2.24}$$

which, upon taking the time average yields

$$\frac{1}{R_s}\nabla^2\zeta_1^{(s)} - \left(\boldsymbol{u}_1^{(s)}\boldsymbol{\cdot}\boldsymbol{\nabla}\right)\zeta_1^{(s)} = \left\langle\left(\boldsymbol{u}_0\boldsymbol{\cdot}\boldsymbol{\nabla}\right)\zeta_2\right\rangle. \tag{2.25}$$

With the use of equation (2.23) here leads to

$$\langle (\boldsymbol{u}_0 \cdot \boldsymbol{\nabla}) \, \zeta_2 \rangle = \left\langle \left(\int^t \boldsymbol{u}_0 \; dt \right) \cdot \boldsymbol{\nabla} \boldsymbol{u}_0 \right\rangle \cdot \boldsymbol{\nabla} \zeta_1^{(s)} = (\boldsymbol{u}_d \cdot \boldsymbol{\nabla}) \, \zeta_1^{(s)}, \tag{2.26}$$

where

$$\boldsymbol{u}_d = \left\langle \left(\int^t \boldsymbol{u}_0 \; dt \right) \cdot \boldsymbol{\nabla} \boldsymbol{u}_0 \right\rangle \tag{2.27}$$

is the Stokes drift velocity. Now, by defining $\boldsymbol{u}_1^{(s)} = \boldsymbol{u}_L^{(s)} + \boldsymbol{u}_d$, we may write equation (2.25) as

$$\frac{1}{R_s} \nabla^2 \zeta_1^{(s)} - \left(\boldsymbol{u}_L^{(s)} \cdot \boldsymbol{\nabla} \right) \zeta_1^{(s)} = 0, \tag{2.28}$$

where, as Riley [22] has pointed out, the vorticity on the outer region is convected with the mean Lagrangian velocity, and R_s serves as a streaming Reynolds number.

Using the development in this section, it is possible to formally obtain the results for the Rayleigh problem discussed in Chapter 1. We therefore reconsider the velocity field given earlier by equation (1.18) on page 9,

$$\boldsymbol{u} = (\sin(akx) \cos t, 0). \tag{2.29}$$

By comparing with equation (2.11), we may identify $U(x)$ as

$$U(x) = \sin akx. \tag{2.30}$$

Using this in equation (2.22), we obtain

$$u_e = -\tfrac{3}{8} \mathrm{Re} \left[(1-i) ak \sin akx \cos akx + (1+i) \sin akx \cos akx \right] = -\tfrac{3}{8} \sin 2akx \tag{2.31}$$

With this velocity applied at the wall ($y = -1$, in scaled variables), and symmetry about $y = 0$, together with $R_s \ll 1$ in (2.28), the result (1.20) can be derived.

Chapter 3

Streaming with Sound Waves Interacting with Solid Particles I

Streaming phenomenon commonly occurs when particles interact with high-frequency sound waves. This type of interaction is very common with acoustic levitation devices. Such devices are used for containerless processing, and applications include noncontact trapping of cells and particle-based assays in continuous flow microsystems. For example, an acoustic standing wave is generated in etched glass micro-channels by miniature ultrasonic transducers, and particles or cells passing the transducer can be retained and levitated in the center of the channel without any contact with the channel walls [3]. The potential of ultrasonic standing wave fields to facilitate viral transduction rate has been demonstrated by Lee & Peng [12]. Under acoustic exposure, suspended cells move to the pressure nodal planes first and form cell clusters. Then, viruses circulated between nodal planes use the pre-formed cell clusters as the nucleating sites to attach on. In the past, we have made several macroscale applications including non-contact thermophysical property measurement of liquids [16, 17]. The suspension of liquid drops is addressed in a later chapter.

3.1 Acoustic Levitators

A typical desktop levitator is shown in Figure 3.1. The main physical principle involved here is that the acoustic field provides the radiation pressure necessary to levitate a liquid drop in a gravitational field. The studies on the effects of radiation pressure on spheres and disks goes as far back as the 1930. Some of the earliest theoretical studies were King [8, 9]. With the application of this principle, ultrasound levitators have been in use for many years in ground-based experiments (as opposed to space-based). Since widespread application of levitation systems in the 1980 and the 90s, there has been an interest in understanding the fluid-flow fundamentals associated with these systems. Some of the earlier work to characterize this flow include the developments of Lee & Trinh. In one of their unreported works includes the outer streaming flow streamlines associated with a levitation system. This is

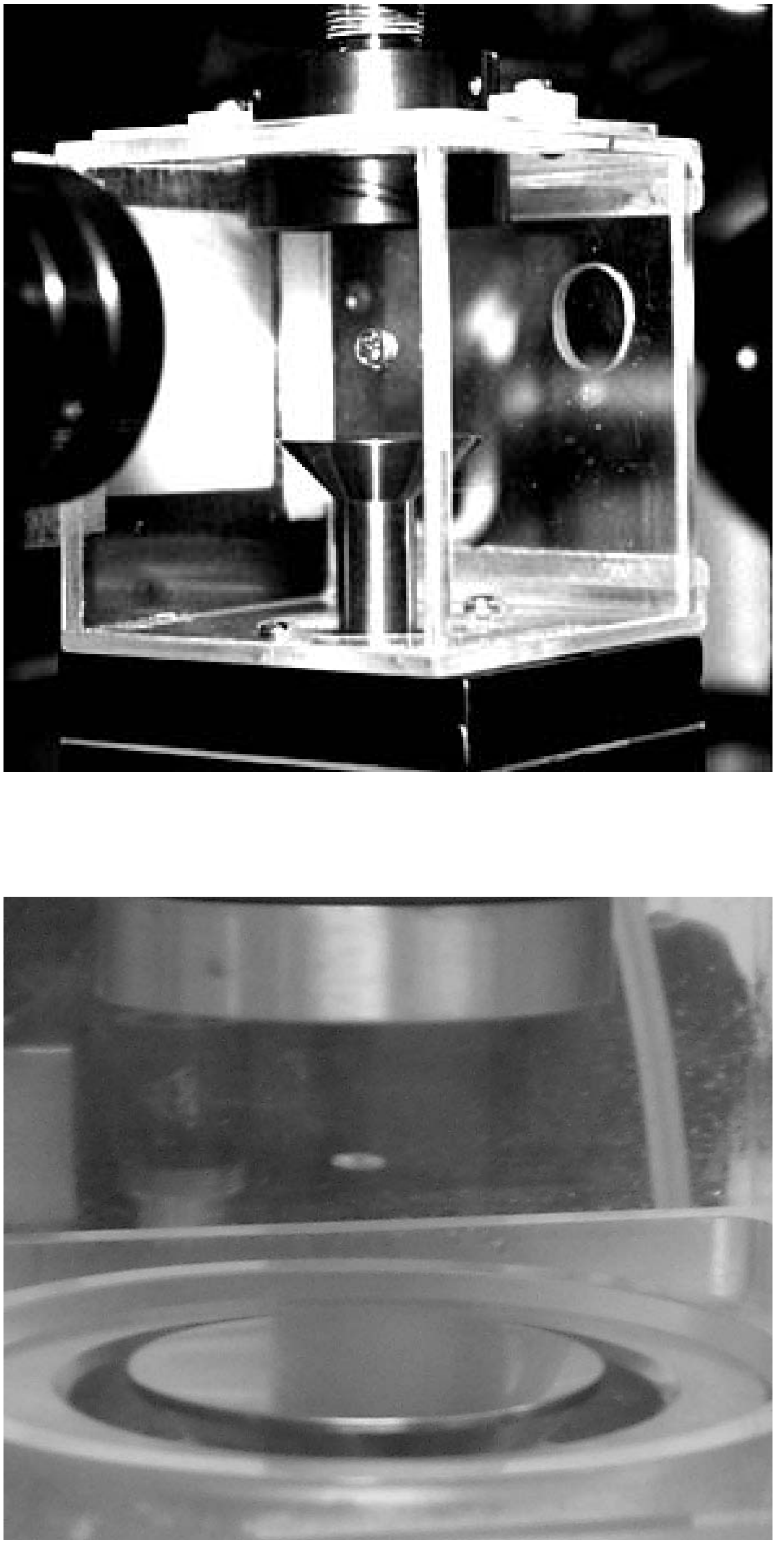

Figure 3.1: Ultrasound levitation apparatus.

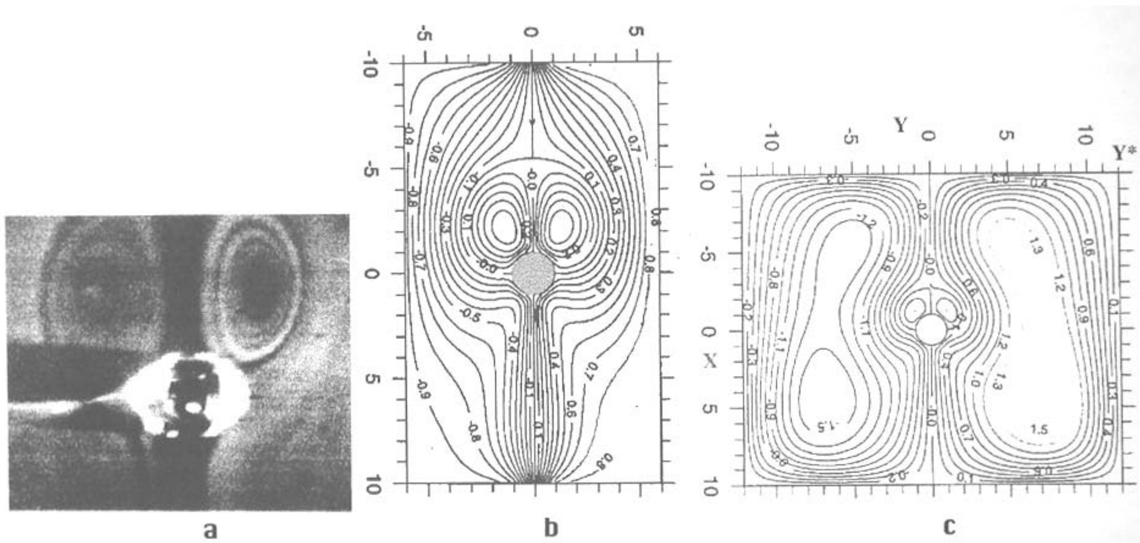

Figure 3.2: (a) Visualized streaming flow [25]; (b, c) Outer streaming calculations (enclosed levitator)

given in Figure 3.2.

As discussed in Chapters 1 and 2, if a body of typical dimension a oscillates with velocity $U_\infty \cos(\omega t)$ in a viscous fluid and $\varepsilon = U_\infty/\omega a \ll 1$, then, although the leading order solution is oscillatory, higher order terms include not only higher harmonics but steady contributions to the velocity. Following earlier discussion, this can be explained mathematically by existence of the nonlinear terms which may have steady nonzero component. For high frequency, we apply the the condition $\varepsilon \ll 1$ which implies that the amplitude of the oscillation is small compared with a. The existence of such steady streaming was first pointed out by Rayleigh [18] in his work on Kundt's dust tube and was later studied in a boundary layer context by Schlichting [23] who considered flows with the additional constraint $|M|^2 = \omega a^2/\nu \gg 1$, where ν denotes the kinematic viscosity of the fluid. Here, the parameter $|M|$ is also known as the Womersley number with the notation α. For such a flow it is now well established that the first order fluctuation vorticity is confined to a shear-wave region of thickness $O(\nu/\omega)^{1/2}$ beyond which steady velocities $O(\varepsilon U_\infty)$ persist. Riley [20] has considered the case of an oscillating sphere for both $|M| \gg 1$ and $0 < |M| < 1$. Lee & Wang [11] considered an oscillating sphere slightly displaced from the antinode of a standing wave for $|M| \gg 1$. Their analysis relied on the tangential velocity calculation based on an analytical algorithm.

One of the items of interest is the information about the characteristics of the levitation process. The theory is useful in overcoming some of experimental problems by providing suitable direction. For example, presently with acoustic levitation there is a residual flow field including solid-body rotation for drops. This problem needs

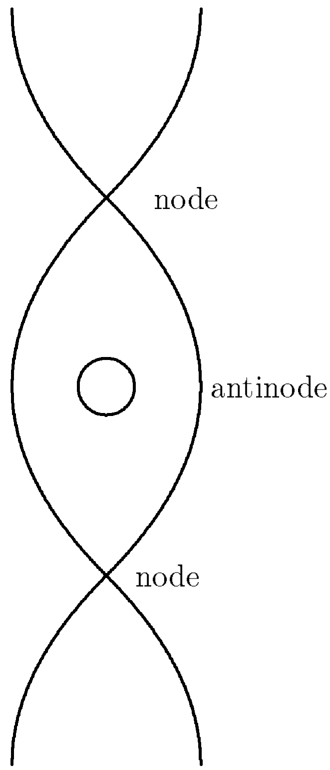

Figure 3.3: Schematic of a spherical particle positioned at the velocity antinode of a standing wave.

to be solved and detailed understanding of the flow studies would be beneficial. For levitation under zero-gravity conditions, the drop assumes an equilibrium position at the velocity antinode when the external medium is a gas. When the fluid-particle phase has higher compressibility than the external phase (e.g., a gas bubble in a liquid), the equilibrium position is at the velocity node. While the antinode solution has been available from Riley's [20] classical work, the node solution is relatively more recent. This aspect will be discussed in the next chapter.

For a levitated spherical particle positioned at the velocity antinode (see Figure 3.3), Riley's solution [20] of a vibrating sphere in an otherwise quiescent fluid can be accommodated for $a/\lambda = a\omega/c \ll 1$, i.e., when the particle size is small when compared with the wavelength of the standing wave. In the next section, we shall provide Riley's solution [20].

3.2 Solid Sphere at the Velocity Antinode: Riley's Solution

For this development, we rely on Riley [20] who gave the solution for an oscillating sphere in an otherwise quiescent infinite fluid medium. As mentioned, the solution is applicable to to a small sphere positioned at the velocity antinode of a standing wave provided $a \ll \lambda$, i.e., the size of the sphere is small compared to the wavelength. We briefly discuss Riley's [20] solution since it forms a basis for various developments in this class of problems. The following dimensionless parameters are relevant:

$$R = \frac{U_\infty a}{\nu} \quad M^2 = \frac{i\omega a^2}{\nu} \quad \text{and} \quad \frac{R}{|M|^2} = \varepsilon = \frac{U_\infty}{\omega a} \ll 1. \tag{3.1}$$

While Riley [20] considered both $|M| \ll 1$ and $|M| \gg 1$, the latter case (high frequency) is the one relevant to ultrasound levitation.

For a standing wave with velocity

$$u_z = U_\infty \cos kz e^{i\omega t}, \tag{3.2}$$

the local velocity in the neighborhood of the antinode ($z = 0$) is

$$u_z = U_\infty \left(1 - k^2 z^2 \cdots \right) e^{i\omega t}. \tag{3.3}$$

With a small particle at the antinode, the surrounding field may just be taken as the first term $u_z = U_\infty e^{i\omega t}$, whereby Riley's [20] solution is applicable.

3.2.1 Equations of Motion

By scaling the flow parameters as follows:

$$\boldsymbol{u}^* = \frac{\boldsymbol{u}}{U_\infty}, \quad \psi^* = \frac{\psi}{U_\infty a^2}, \quad \boldsymbol{x}^* = \frac{\boldsymbol{x}}{a}, \quad \text{and} \quad \tau = \omega t, \tag{3.4}$$

and dropping the asterisks, the Navier–Stokes equation of motion, in the stream function formulation may be written as

$$\frac{\partial}{\partial \tau}\left(D^2\psi\right) + \varepsilon\left[\frac{1}{r^2}\frac{\partial\left(\psi, D^2\psi\right)}{\partial(r,\bar{\mu})} + \frac{2}{r^2}D^2\psi\ L\psi\right] = \frac{1}{|M|^2}D^2\psi \tag{3.5}$$

where

$$\begin{aligned} D^2 &= \frac{\partial^2}{\partial r^2} + \frac{(1-\bar{\mu}^2)}{r^2}\frac{\partial^2}{\partial \bar{\mu}^2}, \\ L &= \frac{\bar{\mu}}{(1-\bar{\mu}^2)}\frac{\partial}{\partial r} + \frac{1}{r}\frac{\partial}{\partial \bar{\mu}}, \end{aligned}$$

and $\bar{\mu} = \cos\theta$. The Reynolds number R and frequency parameter M are defined as

$$R = U_\infty a/\nu \quad \text{and} \quad M^2 = i\omega a^2/\nu, \tag{3.6}$$

respectively.

The stream function ψ is related to the velocity components as follows

$$u_r = -\frac{1}{r^2}\frac{\partial\psi}{\partial\bar{\mu}} \qquad \text{and} \qquad u_\theta = -\frac{(1-\bar{\mu}^2)^{-\frac{1}{2}}}{r}\frac{\partial\psi}{\partial r}. \tag{3.7}$$

With this formulation the continuity condition for an incompressible fluid is satisfied.

The boundary conditions are

$$\psi = \frac{\partial\psi}{\partial r} = 0 \quad \text{on} \quad r = 1 \tag{3.8}$$

and

$$\psi \sim \tfrac{1}{2}r^2(1-\bar{\mu}^2)e^{i\tau} \quad \text{as} \quad r \to \infty. \tag{3.9}$$

Here and throughout, we have chosen $M\sqrt{2}/|M| = (1+i)$ and ε is defined as

$$\varepsilon = R|M|^{-2} \ll 1.$$

The special case $R_s = \varepsilon R \ll 1$ is considered here and Riley's [20] development is summarized next.

3.2.2 Solution

For $|M| \gg 1$, the vorticity, generated at the sphere, is confined to a thin 'shear-wave' layer of thickness $O(|M|^{-1})$. Outside this thin layer the flow field is described by

$$|M|^2\frac{\partial(D^2\psi_0)}{\partial\tau} = D^4\psi_0. \tag{3.10}$$

The solution for this is expressed by the irrotational field

$$\psi_0 \sim \left(\tfrac{1}{2}r^2 - \frac{1}{2r}\right)(1-\bar{\mu}^2)e^{i\tau}, \tag{3.11}$$

where it should be noted that both sides of (3.10) vanish independently since $D^2\psi_0 = 0$. Within the shear-wave layer, the leading-order solution is

$$\Psi_0 \sim \tfrac{3}{2}\left\{\eta - \tfrac{1}{2}(1-i)\left[1 - e^{-(1+i)\eta}\right]\right\}(1-\bar{\mu}^2)e^{i\tau}, \tag{3.12}$$

where

$$\eta = (r-1)\frac{|M|}{\sqrt{2}} \tag{3.13}$$

and

$$\Psi = \frac{R_s^{\frac{1}{2}}\psi}{\varepsilon\sqrt{2}}. \tag{3.14}$$

where $R_s = \varepsilon R$ is the streaming Reynolds number. An inner layer expansion of the type

$$\Psi = \Psi_0 + \varepsilon\Psi_1 + O(\varepsilon^2) \tag{3.15}$$

is considered. The first order term may be decomposed into steady and unsteady components in the form

$$\Psi_1 = \tfrac{9}{2}\left[\zeta_{20}(\eta) + \zeta_{22}(\eta)e^{i\tau}\right]\bar{\mu}(1-\bar{\mu}^2), \tag{3.16}$$

where ζ_{20} and ζ_{22} have been found to be

$$\zeta_{20} = \tfrac{1}{16}e^{-2\eta} + \tfrac{5}{4}e^{-\eta}\cos\eta + \tfrac{3}{4}e^{-\eta}\sin\eta - \tfrac{1}{2}\eta e^{-\eta}\sin\eta - \tfrac{21}{16} + \tfrac{5}{8}\eta, \tag{3.17}$$

$$\begin{aligned}\zeta_{22} = {} & \tfrac{9}{32}(2^{\frac{1}{2}}-1)(1+i) - \left(\tfrac{9}{32}\right)2^{\frac{1}{2}}(1+i)e^{-(1+i)\eta\sqrt{2}} + \tfrac{1}{4}(1+i)e^{-(1+i)\eta} \\ & + \tfrac{1}{32}(1+i)e^{-2(1+i)\eta} - \tfrac{1}{2}ie^{-(1+i)\eta}.\end{aligned} \tag{3.18}$$

At the edge of the shear-wave region ($\eta \to \infty$),

$$\begin{aligned}\Psi \quad \sim \quad & \tfrac{3}{2}\left[\eta\cos\tau - \left(\tfrac{1}{2}\right)\sqrt{2}\cos\left(\tau - \tfrac{1}{4}\tau\right)\right] \\ & + \tfrac{9}{32}\varepsilon\left[(-21+16\eta) + \tfrac{9}{2}\left(2-\sqrt{2}\right)\cos\left(2\tau + \tfrac{1}{4}\pi\right)\right]\bar{\mu}(1-\bar{\mu}^2) + O(\varepsilon^2).\end{aligned} \tag{3.19}$$

For the outer region where $(r-1) = O(1)$, stream function is expanded as

$$\psi = \psi_0 + \varepsilon\chi, \tag{3.20}$$

where ψ_0 is fiven by equation (3.11) and $\chi = \chi(r,\bar{\mu},\tau,\varepsilon)$ satisfies

$$\begin{aligned}+R_s\frac{\partial}{\partial\tau}\left(D^2\chi\right) + \varepsilon\left(\frac{R_s}{r^2}\right)\left[\frac{\partial}{\partial r}\left(\psi_0+\varepsilon\chi\right)\frac{\partial}{\partial\bar{\mu}}\left(D^2\chi\right) - \frac{\partial}{\partial\bar{\mu}}\left(\psi_0+\varepsilon\chi\right)\frac{\partial}{\partial r}\left(D^2\chi\right)\right. \\ \left. +2L\left(\psi_0+\varepsilon\chi\right)D^2\chi\right] = \varepsilon^2 D^4\chi.\end{aligned} \tag{3.21}$$

With the expansion of χ as

$$\chi = \chi_1 + \varepsilon\chi_2\varepsilon^2\chi_3 + \cdots, \tag{3.22}$$

and substitution into equation (3.21) yields

$$\frac{\partial D^2\chi_1}{\partial\tau} = 0. \tag{3.23}$$

This may be decomposed into steady and unsteady components in the form

$$\chi_1 = F_1(r,\bar{\mu}) + G_1(r,\bar{\mu})\phi(\tau), \tag{3.24}$$

where $G_1(r,\bar{\mu})$ satisfies

$$D^2G = 0, \tag{3.25}$$

and $\phi(\tau)$ is determined from matching as

$$\phi(\tau) = -\left(\frac{3}{2R_s^{\frac{1}{2}}}\right)\cos\left(\tau - \tfrac{1}{4}\pi\right). \tag{3.26}$$

The solution for $G_1(r, \bar{\mu})$ is found to be

$$G_1(r, \bar{\mu}) = \frac{(1 - \bar{\mu}^2)}{r}. \tag{3.27}$$

With a lot of detailed calculations [20] through the equations for χ_2 and χ_3, the differential equation for $F_1(r, \bar{\mu})$ is found to be

$$D^4 F_1 = 0, \tag{3.28}$$

with the solution

$$F_1(r, \bar{\mu}) = \frac{45}{32}\left(-\frac{1}{r^2} + 1\right). \tag{3.29}$$

The solution exhibits a typical steady streaming flow field as shown in Figure 3.4. Here the thin recirculation region (Stokes layer) is exaggerted for clarity. The important aspect of this flow is the existence of a *steady* component arising from its nonlinear character.

This development has been extended to the case of fluid sphere by Zhao et al [26] and some interesting observations have been made. This is discussed in Chapter 5. In the next chapter, we deal with a particle placed at the velocity node of the standing wave.

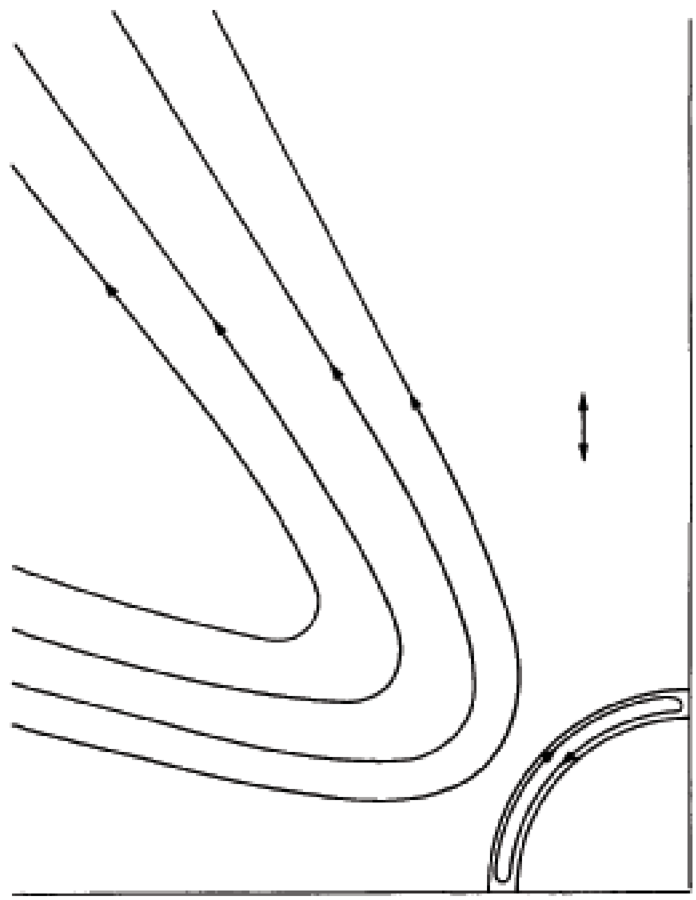

Figure 3.4: The streaming flow pattern associated with the steady flow in the case of $|M|^2 \gg 1$, and $R_s \ll 1$. The closed loop is a feature of the shear-wave layer. Reproduced from [20].

Chapter 4

Streaming with Sound Waves Interacting with Solid Particles II

In the discussion here, the focus is on the analysis of solid sphere being placed at the velocity node of the wave, which leads to an important result for calculating the streaming when the sphere is placed between the velocity node and the antinode of the wave. In this development, use will be made of the existing antinode solution of Riley [20] and the present node solution through a nonlinear combination. Although Lee & Wang [11] have considered this kind of problem, their result depends on an algorithm for calculating the tangential velocity on the edge of the recirculating shear layer. A more rigorous development of the flow field has been carried out [19]

4.1 Solid Sphere at the Velocity Node

The outer streaming around a solid sphere in plane standing wave is calculated with the following procedure. We choose axially symmetric spherical polar coordinates (r, θ) fixed in the body of the sphere such that the radial distance r is measured from the center of the sphere and $\theta = 0$ coincides with the axis of oscillation. In this case the equation governing the steady flow in the outer region is Stokes' equation.

For the standing wave described in equation (3.2), if the origin is shifted the node, the undisturbed flow is

$$u_z = -U_\infty \sin kz e^{i\omega t}, \tag{4.1}$$

and the velocity near the node $(z = 0)$ is

$$u_z = -U_\infty \left(kz - \tfrac{1}{6}k^3 z^3 \cdots \right) e^{i\omega t}. \tag{4.2}$$

For a small sphere at the node, the first term in the expansion should suffice. Thus the velocity description for the 'far field' is $U_\infty kze^{\omega t}$. With the same dimensionless parameters as in equations (3.4) and (3.6), the flow description is given by the momentum equation (3.5). At the surface of the sphere $(r = 1)$, the no-slip boundary conditions given by equation (3.8) have to be satisfied. In terms of a velocity potential, the far-field conditions take the form

$$\varphi_\infty = \frac{U_\infty}{k}\left(1 - \tfrac{1}{2}k^2 r^2 (1-\bar{\mu}^2) + \cdots\right) e^{i\omega t}, \tag{4.3}$$

4.1.1 Equations of Motion

Following equations (1.1) and (1.3) developed in Chapter 1, and applying the scaling,

$$\boldsymbol{u}^* = \frac{\boldsymbol{u}}{U_\infty}, \quad \psi* = \frac{\psi}{U_\infty a^2}, \quad \varphi* = \frac{\varphi}{U_\infty a}, \quad \boldsymbol{x}^* = \frac{\boldsymbol{x}}{a},$$
$$\tau = \omega t, \quad p^* = \frac{p}{p_0 U_\infty \omega a}, \quad \rho^* = \frac{\rho c^2}{\rho_0 U_\infty \omega a}, \quad \text{and} \quad \boldsymbol{\nabla}^* = a\boldsymbol{\nabla},$$

and dropping the asterisks, we obtain the following:
continuity:

$$(ka)^2 \frac{\partial \rho}{\partial \tau} + \boldsymbol{\nabla}\cdot\boldsymbol{u} + \varepsilon (ka)^2 \boldsymbol{\nabla}\cdot\rho\boldsymbol{u} \tag{4.4}$$

momentum:

$$\left[1 + \rho\varepsilon(ka)^2\right]\frac{\partial \boldsymbol{u}}{\partial \tau} + \varepsilon\left[1 + \rho\varepsilon(ka)^2\right]\boldsymbol{u}\cdot\boldsymbol{\nabla}\boldsymbol{u} = -\boldsymbol{\nabla}p + \frac{1}{|M|^2}\nabla^2\boldsymbol{u} \tag{4.5}$$

The boundary conditions are no-slip on the surface

$$\boldsymbol{u} = \boldsymbol{0} \quad \text{at} \quad r = 1, \tag{4.6}$$

and in the far-field,

$$u_z = -kaze^{i\tau}, \tag{4.7}$$

or equivalently, in the form of a velocity potential,

$$\varphi_\infty = \frac{1}{ka}\left[1 - \tfrac{1}{3}(ka)^2 r^2 P_2)(\bar{\mu}) - \tfrac{1}{6}(ka)^2 r^2\right] e^{i\tau}. \tag{4.8}$$

4.1.2 Solution

Once again, we apply the perturbation procedure,

$$\boldsymbol{u} = \boldsymbol{u}_0 + \varepsilon\boldsymbol{u}_1 + O(\varepsilon^2), \tag{4.9}$$
$$p = p_0 + \varepsilon p_1 + O(\varepsilon^2) \tag{4.10}$$
$$\rho = \rho_0 + \varepsilon\rho_1 + O(\varepsilon^2) \tag{4.11}$$

The Leading-Order Solution

Using the obove perturbation expansion procedure in the momentum equation (4.5), we obtain

$$\frac{\partial \boldsymbol{u}_0}{\partial \tau} = -\boldsymbol{\nabla} p_0, \tag{4.12}$$

which, according to our development in Chapter 1, corresponds to ittotational flow, and may be expressed as a velocity potential

$$\boldsymbol{u}_0 = \boldsymbol{\nabla}\varphi_0, \tag{4.13}$$

and it is not difficult to see that

$$p_0 = -\frac{\partial \varphi_0}{\partial \tau}. \tag{4.14}$$

This is applicable to the far-field so that with the use of (4.15),

$$p_\infty = \rho_\infty = -\frac{\partial \varphi_\infty}{\partial \tau} = -\frac{i}{ka}\left[1 - \tfrac{1}{3}(ka)^2 r^2 P_2)(\bar{\mu}) - \tfrac{1}{6}(ka)^2 r^2\right] e^{i\tau}. \tag{4.15}$$

From the continuity equation (4.4), the leading order solution $\boldsymbol{u}_0$ satisfies

$$(ka)^2 \frac{\partial \rho_0}{\partial \tau} + \boldsymbol{\nabla} \cdot \boldsymbol{u}_0 = 0. \tag{4.16}$$

Maintaining order in ka, it is not difficult to see that only the term $(-i/(ka))\, e^{i\tau}$ in ρ_0 is needed here. Therefore,

$$(ka)e^{i\tau} + \boldsymbol{\nabla} \cdot \boldsymbol{u}_0 = 0, \tag{4.17}$$

which may be written in the form of a potential function,

$$\nabla^2 \phi_0 + (ka) = 0, \tag{4.18}$$

where φ_0 and ϕ_0 are related by

$$\varphi_0 = \phi_0(r,\theta)e^{i\tau}. \tag{4.19}$$

Now, applying zero normal velocity on the surface of the sphere, i.e.,

$$u_{r0} = \frac{\partial \varphi_0}{\partial r} = 0 \quad \text{at} \quad r = 1, \tag{4.20}$$

together with the far-field condition (5.22), we obtain

$$\varphi_0 = \left\{\frac{1}{ka} - \tfrac{1}{3}ka\left(\tfrac{1}{2}r^2 + \frac{1}{r}\right) - \tfrac{1}{3}ka\left(r^2 + \frac{2}{3r^3}\right) P_2(\bar{\mu})\right\} e^{i\tau}, \tag{4.21}$$

and

$$p_0 = \rho_0 = -i\left\{\frac{1}{ka} - \tfrac{1}{3}ka\left(\tfrac{1}{2}r^2 + \frac{1}{r}\right) - \tfrac{1}{3}ka\left(r^2 + \frac{2}{3r^3}\right) P_2(\bar{\mu})\right\} e^{i\tau}. \tag{4.22}$$

In the boundary layer, we write the velocity field in terms of normal (radial) and tangential components,

$$\boldsymbol{u}^b = u_r^b \hat{\boldsymbol{r}} + u_\theta^b \hat{\boldsymbol{\theta}}, \tag{4.23}$$

As usual, with $|M|^2 \gg 1$, the vorticity generated at the surface of the sphere, is confined to a thin shear-wave layer of thickness $O(|M|^{-1})$, we scale the inner variables inside the shear-wave layer as

$$\eta = (r-1)\frac{|M|}{\sqrt{2}}, \qquad \text{and} \qquad u_\eta^b = \frac{|M|}{\sqrt{2}} u_r^b. \tag{4.24}$$

Again, perturbing in powers in ε,

$$\boldsymbol{u}^b = \boldsymbol{u}_0^b + \varepsilon \boldsymbol{u}_1^b + O(\varepsilon^2), \tag{4.25}$$

$$p^b = p_0^b + \varepsilon p_1^b + O(\varepsilon^2), \tag{4.26}$$

and

$$\rho^b = \rho_0^b + \varepsilon \rho_1^b + O(\varepsilon^2), \tag{4.27}$$

and using these expansions (4.25)-(4.27) in momentum equation (4.5), we have for the leading-order normal and tangential velocities,

$$\frac{\partial u_{r0}^b}{\partial \tau} = -\frac{\partial p_0^b}{\partial r} = -\frac{|M|}{\sqrt{2}}\frac{\partial p_0^b}{\partial \eta} \tag{4.28}$$

$$\frac{\partial u_{\theta 0}^b}{\partial \tau} = -\frac{\partial p_0^b}{\partial \theta} + \frac{1}{2}\frac{\partial^2 u_{\theta 0}^b}{\partial \eta^2}, \tag{4.29}$$

respectively. As we know, the frequency parameter $|M| \gg 1$, and from equation (4.28), we may deduce that the leading-order acoustic pressure p_0^b in the boundary layer is a function of θ and τ only. Therefore, $\partial p_0^b/\partial \eta = 0$, and using this information in equation (4.22), we find

$$p_0^b = \rho_0^b = p_0|_{r=1} = -\frac{i}{ka}\left[1 - \tfrac{1}{2}(ka)^2 - \tfrac{5}{9}(ka)^2 P_2(\bar{\mu})\right] e^{i\tau}. \tag{4.30}$$

With use of equation (4.30) and the boundary condition

$$u_{\theta 0}^b = 0 \quad \text{as} \quad \eta = 0, \tag{4.31}$$

in equation (4.29), we obtain the differential equation for $u_{\theta 0}^b$ which, when solved, yiels

$$u_{\theta 0}^b = \tfrac{5}{3}(ka)\sin\theta\cos\theta\left(1 - e^{-(1+i)\eta}\right) e^{i\tau}. \tag{4.32}$$

Then, from the continuity equation (4.4), we obtain the equation for the leading-order normal velocity in the boundary layer $u_{\eta 0}^b$ as

$$(ka)^2\frac{\partial \rho_0^b}{\partial \tau} + \frac{\partial u_{\eta 0}^b}{\partial \eta} + \frac{1}{\sin\theta}\frac{\partial}{\partial \theta}\left(u_{\theta 0}^b \sin\theta\right) = 0. \tag{4.33}$$

Next, the boundary condition

$$u_{\eta 0}^{b} = 0 \quad \text{at} \quad \eta = 0, \tag{4.34}$$

leads to the solution of $u_{\eta 0}^{b}$ as

$$u_{\eta 0}^{b} = \left\{-ka\eta + \tfrac{10}{3}(ka)\left[-\eta + \tfrac{1}{2}(1-i)\left(1 - e^{-(1+i)\eta}\right)\right] P_2(\bar{\mu})\right\} e^{i\tau}. \tag{4.35}$$

Here, it should be noted that the first term $-ka\eta e^{i\tau}$ represents the compressibility in the boundary layer.

The First-Order Solution $[O(\varepsilon)]$

As with most problems in this class, the first order solution is much more complex than the leading order. Since our interest lies in understanding the steady streaming outside the sphere, we only consider the steady-state solutions here. Therefore, in this section, all the first order variables are time-independent.

It is not difficult to show that the first-order velocity field is incompressible [27], i.e., $\boldsymbol{\nabla} \cdot \boldsymbol{u}_1^b = 0$. Making use of equations (4.25), (4.26) and (4.27) in the momentum equation (4.5), and equating both sides in the order of ε, we have

$$\left\langle \rho_0^b (ka)^2 \frac{\partial u_{\eta 0}^b}{\partial \tau} \right\rangle + \left\langle u_{\eta 0}^b \frac{\partial u_{\eta 0}^b}{\partial \eta} \right\rangle + \left\langle u_{\theta 0}^b \frac{\partial u_{\eta 0}^b}{\partial \theta} \right\rangle = -\frac{|M|^2}{2}\frac{\partial p_1^b}{\partial \eta} + \frac{\partial^2 u_{\eta 1}^b}{\partial \eta^2}, \tag{4.36}$$

for the first-order normal velocity in the boundary layer, and

$$\left\langle \rho_0^b (ka)^2 \frac{\partial u_{\theta 0}^b}{\partial \tau} \right\rangle + \left\langle u_{\eta 0}^b \frac{\partial u_{\theta 0}^b}{\partial \eta} \right\rangle + \left\langle u_{\theta 0}^b \frac{\partial u_{\theta 0}^b}{\partial \theta} \right\rangle = -\frac{\partial p_1^b}{\partial \theta} + \frac{1}{2}\frac{\partial^2 u_{\theta 1}^b}{\partial \eta^2}, \tag{4.37}$$

for the first-order tangential velocity in the boundary layer. Recognizing once again that $|M|^2 \gg 1$, whereby in equation (4.36), the pressure derivative term is dominant. Thus,

$$\frac{\partial p_1^b}{\partial \eta} = 0, \tag{4.38}$$

which means the first order time-independent pressure in the boundary layer is a function of θ only. Since the steady flow in the boundary layer is incompressible, the velocity field can be written in terms of the stream function ψ_1^b so that

$$u_{r1}^b = \frac{1}{r^2 \sin\theta}\left(\frac{\partial \psi_1^b}{\partial \theta}\right), \tag{4.39}$$

and

$$u_{\theta 1}^b = -\frac{1}{r \sin\theta}\left(\frac{\partial \psi_1^b}{\partial r}\right). \tag{4.40}$$

Using the stream-function form in equation (4.40) in equation (4.37), with the limit $\psi_1^b = o(\eta^2)$, together with the boundary conditions,

$$\psi_1^b = 0 \;\text{ at }\; \eta = 0, \qquad \text{and} \qquad \frac{\partial \psi_1^b}{\partial \eta} = 0 \;\text{ at }\; \eta = 0,$$

we obtain the solution for ψ_1^b as

$$\begin{aligned}\psi_1^b \;=\; & -\frac{\sqrt{2}}{|M|}(ka)^2 \Big\{ \Big(\tfrac{25}{72} e^{-2\eta} + \tfrac{10}{3} e^{-\eta} \cos\eta + \tfrac{35}{18} e^{-\eta} \sin\eta \\ & + \tfrac{5}{9} \eta e^{-\eta} \sin\eta + \tfrac{25}{12}\eta - \tfrac{265}{72} \Big) \bar{\mu}(1-\bar{\mu}^2) + \Big(-\tfrac{25}{36} e^{-2\eta} - \tfrac{100}{9} e^{-\eta}\cos\eta \\ & - \tfrac{125}{18} e^{-\eta} \sin\eta - \tfrac{25}{6}\eta e^{-\eta}\sin\eta - \tfrac{50}{9}\eta + \tfrac{425}{36} \Big) \bar{\mu}^3 (1-\bar{\mu}^2) \Big\} . \end{aligned} \tag{4.41}$$

The perturbation solution (4.41) represents an inner solution, corresponding to the shear-wave layer. For the outer region where $(r-1) = O(1)$, we need to construct another asymptotic solution. Agai, it is not difficult to demonstrate incompressibility [27] so that $\boldsymbol{\nabla} \cdot \boldsymbol{u}_1 = 0$. Once again, we introduce the stream function ψ_1, for the outer region this time, such that

$$u_{r1} = \frac{1}{r^2 \sin\theta} \left(\frac{\partial \psi_1}{\partial \theta} \right) \;\text{ and }\; u_{\theta 1} = -\frac{1}{r \sin\theta} \left(\frac{\partial \psi_1}{\partial r} \right). \tag{4.42}$$

Equating coefficients of powers of ε in the momentum equation (5.18), and using the above stream function relationship, we obtain the Stokes flow equation

$$D^4 \psi_1 = 0, \tag{4.43}$$

where D^2 is the standard Stokes operator. After asymptotic matching, we obtain the following expression for ψ_1:

$$\begin{aligned}\psi_1 \;=\; & (ka)^2 \tfrac{25}{168} \left(-r^{-2} + 1 \right) \bar{\mu}(1-\bar{\mu}^2) \\ & + (ka)^2 \tfrac{25}{63} \left(-r^{-4} + r^{-2} \right) (7\bar{\mu}^3 - 3\bar{\mu})(1-\bar{\mu}^2), \end{aligned} \tag{4.44}$$

again demonstrating the persistence of streaming outside the shear-wave layer.

Discussion

The streaming flow field in the outer region is depicted in Figure 4.1. Here, unlike the sphere at the velocity antinode, the outer region has closed vortex around the equatorial region. The recirculating part of the Stokes layer does not cover the entire sphere but just the equatorial belt. Over the remaining region in the Stokes layer, the outer flow continues into the Stokes layer. In order to see this detail, we have shown the Stokes-layer region on a stretched scale. This is shown in Figure 4.2.

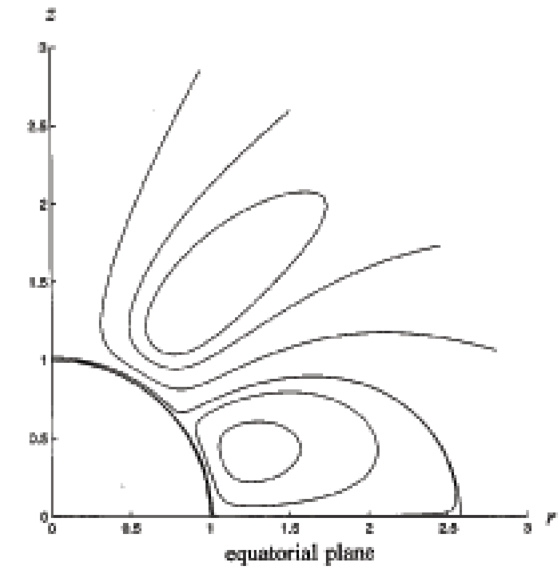

Figure 4.1: Streaming in the outer region for a sphere placed at the velocity node [27]

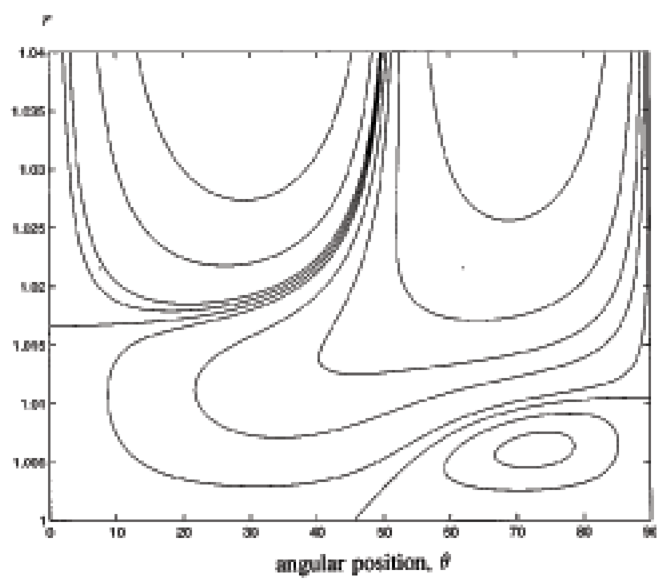

Figure 4.2: Detailed flow field in the Stokes layer on the surface with a stretched radial scale. The fluid motion is clockwise in the upper left region and the lower closed vortex, and counterclockwise elsewhere [27]

4.2 Streaming Around a Sphere Placed Between Nodes

A particle levitated in a gravity field would position itself between the velocity node and the antinode. The analysis of a solid sphere present between nodes has also been carried out. However, the details of calculation will not be presented since these can be easily derived from the liquid-drop cases (discussed in the next chapter) when the infinite-viscosity limit is taken. The basis of the analysis is the expansion of the standing wave for which we expand the velocity u_z^* such that [19]

$$\begin{aligned} u_z^* &= U_\infty \cos(kz^*)e^{i\omega t^*} = U_\infty \cos(\bar{k}z)e^{it} \\ &= U_\infty \left[\cos \bar{k}z_0 - \bar{k}(z - z_0)\sin \bar{k}z_0 + O(\bar{k}^2(z-z_0)^2)\right] e^{it}, \end{aligned} \tag{4.45}$$

where $\bar{k} = ka$ is the dimensionless wavenumber. This right-hand side represents the local velocity in the neighborhood of the sphere centered at $z = z_0$, the dimensionless displacement of the center of the sphere from the velocity antinode. The expansion splits the far-field velocity into a solution about the velocity node and the antinode. While this combines linearly, the streaming part is nonlinear and there are terms in addition to the node and the antinode solution. This procedure is detailed in the next chapter for the liquid drop. However, the solid-sphere results are relevant here, and some of them are presented.

We have found that the results obtained for solid-sphere case are consistent with the outer solution of Lee & Wang [11] which allows for a slip velocity on the solid surface. In Figures 4.3 through 4.7, we can see the streamlines for a solid sphere with $\bar{k} = 0.3$. It is apparent that the asymmetry about the equator in the streaming pattern when the sphere is away from the velocity antinode is because of the asymmetric distribution of the undisturbed flow. There is stronger streaming on the velocity antinode side where the fluid velocity tends to be higher. Away from the surface of the sphere, the flow pattern does not depend on M of course, but on the displacement $\bar{k}z_0$. It is noted that there is a transition value $\bar{k}z_0 = K_0$ (with $5\pi/16 < K_0 < 3\pi/8$) in the flow pattern between. When $\bar{k}z_0 < K_0$, there exists a thin recirculating region, limited to the Stokes layer adjacent to the surface, quite similar to that for a solid particle at the velocity antinode. This region is quite thin and not clearly visible in the Figures 4.3 through 4.5. However, when $\bar{k}z_0 > K_0$, larger vortices appear around the north-pole region as shown in Figures 4.6 and 4.7.

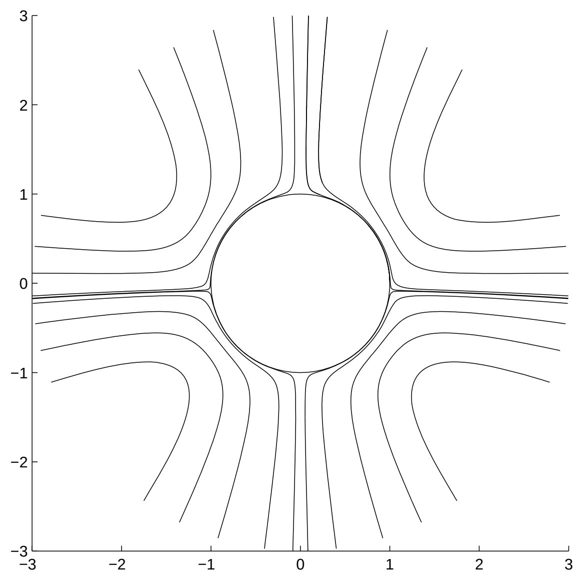

Figure 4.3: Streaming about a solid sphere displaced between velocity node and antinode for $\bar{k}z_0 = \pi/8$, $\bar{k} = 0.3$, and $M = 800$ [19].

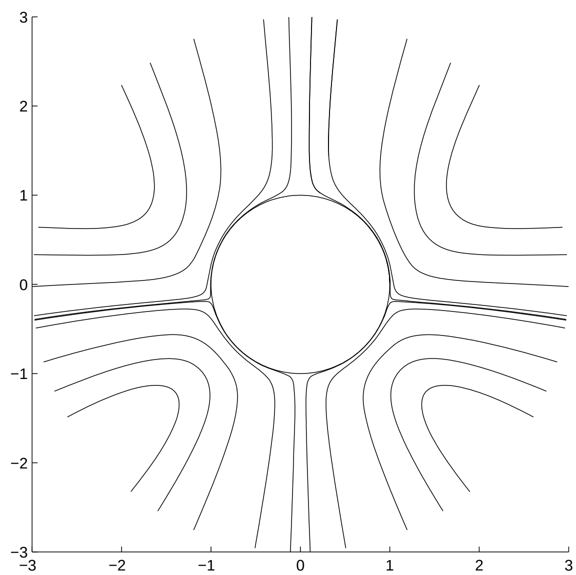

Figure 4.4: Streaming about a solid sphere displaced between velocity node and antinode for $\bar{k}z_0 = \pi/4$, $\bar{k} = 0.3$, and $M = 800$ [19].

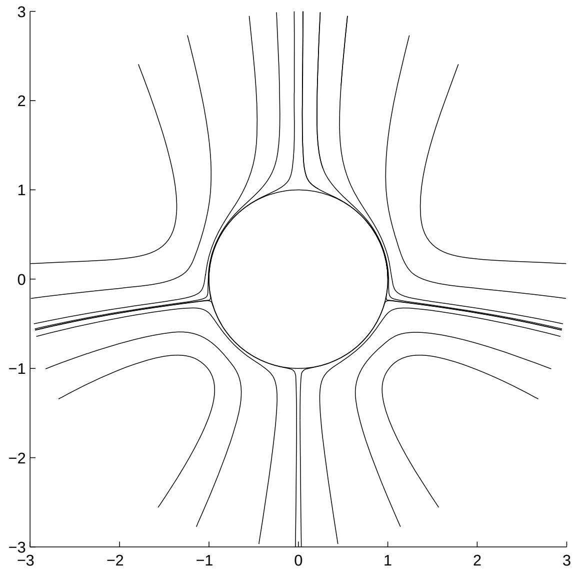

Figure 4.5: Streaming about a solid sphere displaced between velocity node and antinode for $\bar{k}z_0 = 5\pi/16$, $\bar{k} = 0.3$, and $M = 800$ [19].

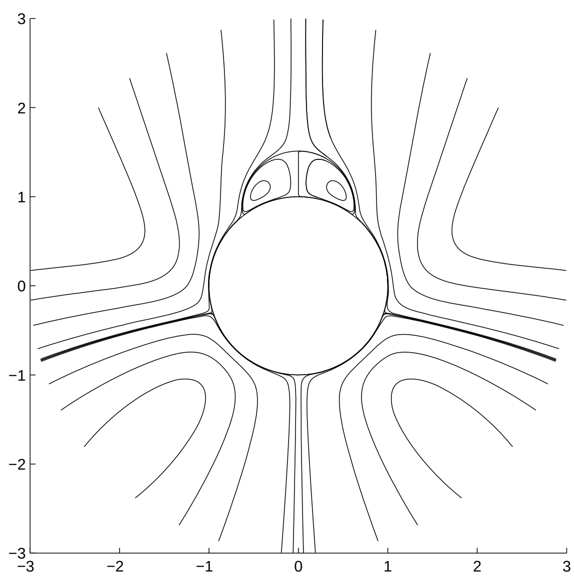

Figure 4.6: Streaming about a solid sphere displaced between velocity node and antinode for $\bar{k}z_0 = 3\pi/8$, $\bar{k} = 0.3$, and $M = 800$ [19].

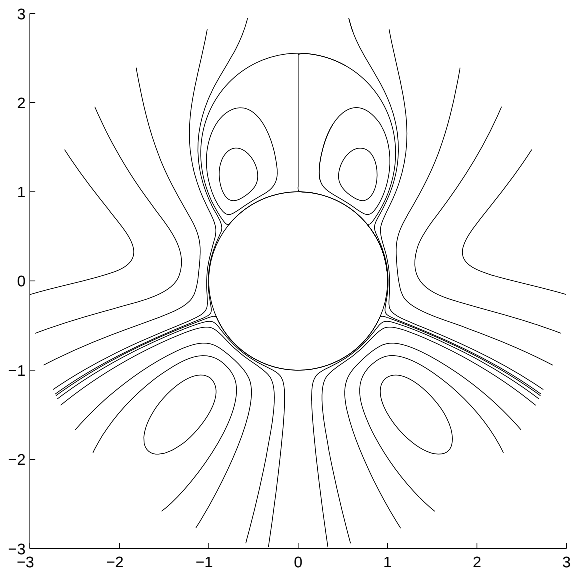

Figure 4.7: Streaming about a solid sphere displaced between velocity node and antinode for $\bar{k}z_0 = 7\pi/16$, $\bar{k} = 0.3$, and $M = 800$ [19].

Chapter 5

Acoustic Streaming with Drops and Bubbles

So far our discussions have been on the streaming phenomenon coming about as an oscillating fluid interacts with solid surface. From a fundamental standpoint, as well as application to levitated drops, there is interest in studying the streaming phenomenon when a standing wave interacts with a fluid-fluid interface. The results are very interesting and show that there can be a marked difference in the characterization of the streaming by simply allowing some degree of interfacial mobility. We consider here first the case of a liquid drop placed at the velocity antinode. This result is derived by generalizing Riley's [20] classical results to a liquid drop. Since the derivation closely follows Riley [20] whose results are repeated here in Chapter 2, we shall focus on just the results of liquid-drop case. Furthermore, the more general case of a liquid drop between nodes (given later in this chapter) covers the antinode case as a limit.

5.1 Liquid Drop at the Velocity Antinode

In this analysis, we present the internal flow in a liquid drop at the antinode of a standing wave. The set of governing equation for calculating streaming around a liquid sphere is the same as that for calculating streaming around a solid sphere. However, at the interface, the continuity of velocity and shear stress have been applied. We assume that medium outside the sphere is a gas. Parameters with ($\hat{}$) represent properties of liquid inside the sphere, and parameters without ($\hat{}$) represent properties of gas outside the drop.

Since

$$\frac{R}{\hat{R}} = \frac{\hat{\nu}}{\nu}, \quad \text{and} \quad \frac{|M|^2}{|\hat{M}|^2} = \frac{\hat{\nu}}{\nu},$$

we have

$$\frac{|M|^2}{R} = \frac{|\hat{M}|^2}{\hat{R}},$$

With $|M|^2 \gg R$, we may deduce that $|\hat{M}|^2 \gg \hat{R}$. Thus the leading-order stream function for the liquid-drop region must also satisfy equation (3.10). In the notation for the dispersed-phase variables, this is

$$|\hat{M}|^2 \frac{\partial(D^2\hat{\psi}_0)}{\partial\tau} = D^4\hat{\psi}_0. \tag{5.1}$$

5.1.1 Solution by Singular Perturbation

Here we consider the case, where $|M|^2 \gg 1$ and the liquid sphere is placed at the velocity antinode of the wave, which is quite similar to that of Riley's [20] problem. We apply the perturbation expansions of the type given in equations (4.9)-(4.11). After a lot of lengthy calculations, the results are obtained to the leading order and $O(\varepsilon)$.

Leading Order

$$\begin{aligned}
\psi_0 &= \tfrac{1}{2}\left(r^2 - \frac{1}{r}\right)(1-\bar{\mu}^2)e^{i\tau} && (5.2)\\
\Psi_0 &= \left[C + \tfrac{3}{2}\eta + Fe^{-(1+i)\eta}\right](1-\bar{\mu}^2)e^{i\tau}, && (5.3)
\end{aligned}$$

for the gas region, and

$$\hat{\psi}_0 = [A^*r^2 + C^*(\frac{1}{\hat{M}r} - 1)e^{\hat{M}r} - C^*(\frac{1}{\hat{M}r} + 1)e^{-\hat{M}r}](1-\bar{\mu}^2)e^{i\tau}. \tag{5.4}$$

where the standard notation for the outer and inner stream functions are used. The 'hat' ($\hat{}$) refers to liquid-phase quantities. The following interface conditions apply:

- Velocity continuity:

$$\hat{\psi}_0|_{r=1} = \Psi_0|_{\eta=0} = 0 \tag{5.5}$$

$$\frac{\partial\hat{\psi}_0}{\partial r}|_{r=1} = \frac{\partial\Psi_0}{\partial\eta}|_{\eta=0} \tag{5.6}$$

- Shear stress continuity:

$$[\tau_{r\theta} - \hat{\tau}_{r\theta}]_{r=1} = -\left[\mu\frac{r}{\sin\theta}\frac{\partial}{\partial r}(\frac{1}{r^2}\frac{\partial\Psi_0}{\partial\eta}) - \hat{\mu}\frac{r}{\sin\theta}\frac{\partial}{\partial r}(\frac{1}{r^2}\frac{\partial\hat{\psi}_0}{\partial r})\right]_{r=1} = 0, \tag{5.7}$$

  where μ is the dynamic viscosity for gas and $\hat{\mu}$ is that for liquid.

Upon satisfying the boundary conditions (5.5), (5.6), and (5.7), we have

$$\begin{aligned}
F &= -C\\
A^* &= C^*\left[\left(\tfrac{1}{\hat{M}} + 1\right)e^{-\hat{M}} - \left(\tfrac{1}{\hat{M}} - 1\right)e^{\hat{M}}\right]\\
C^* &= \frac{\frac{3}{2} + C(1+i)}{e^{-\hat{M}}(\frac{3}{\hat{M}} + 3 + \hat{M}) + e^{\hat{M}}(-\frac{3}{\hat{M}} + 3 - \hat{M})}
\end{aligned}$$

where

$$C = \frac{\left\{ \begin{array}{l} -3\lambda[e^{-\hat{M}}(\frac{3}{\hat{M}}+3+\hat{M})+e^{\hat{M}}(-\frac{3}{\hat{M}}+3-\hat{M})] \\ -\frac{3}{2}[e^{-\hat{M}}(-\frac{6}{\hat{M}}-6-3\hat{M}-\hat{M}^2)+e^{\hat{M}}(\frac{6}{\hat{M}}-6+3\hat{M}-\hat{M}^2)] \end{array} \right\}}{\left\{ \begin{array}{l} (1+i)[e^{-\hat{M}}(-\frac{6}{\hat{M}}-6-3\hat{M}-\hat{M}^2)+e^{\hat{M}}(\frac{6}{\hat{M}}-6+3\hat{M}-\hat{M}^2)] \\ +\lambda(1+i)(2+M)[e^{-\hat{M}}(\frac{3}{\hat{M}}+3+\hat{M})+e^{\hat{M}}(-\frac{3}{\hat{M}}+3-\hat{M})] \end{array} \right\}}$$

and $\lambda = \mu/\hat{\mu}$.

Solutions of inner and outer flow fields are obtained as follows:

$$\begin{aligned} \hat{\psi}_0 &= C^* \Big[r^2(\tfrac{1}{\hat{M}}+1)e^{-\hat{M}} - r^2(\tfrac{1}{\hat{M}}-1)e^{\hat{M}} \\ &\qquad + (\tfrac{1}{\hat{M}r}-1)e^{\hat{M}r} - (\tfrac{1}{\hat{M}r}+1)e^{-\hat{M}r} \Big](1-\bar{\mu}^2)e^{i\tau} \qquad (5.8) \\ \Psi_0 &= (C + \frac{3}{2}\eta - Ce^{-(1+i)\eta})(1-\bar{\mu}^2)e^{i\tau} \qquad (5.9) \\ \psi_0 &= \frac{1}{2}(r^2 - \frac{1}{r})(1-\bar{\mu}^2)e^{i\tau} \qquad (5.10) \end{aligned}$$

The result of ψ_0 is the same as that of Riley's solution for solid sphere.

Usually μ is much smaller than $\hat{\mu}$, and in this case $\lambda \ll 1$. With $\hat{M} \gg 1$, we can simplify C as

$$\begin{aligned} C &\approx \frac{3\lambda\hat{M} - \frac{3}{2}(3\hat{M} - \hat{M}^2)}{(1+i)(3\hat{M}-\hat{M}^2) - \lambda(1+i)(2+M)\hat{M}} \\ &\approx \frac{\frac{3}{2}\hat{M}}{-(1+i)(\hat{M}+\lambda M)} \qquad (5.11) \end{aligned}$$

and

$$C^* \approx -\frac{\frac{3}{2}(\frac{1}{\hat{M}} - \frac{1}{\hat{M}+\lambda M})}{e^{\hat{M}}} \qquad (5.12)$$

According to our assumption, if $M \gg 1$ and $\hat{M} \gg 1$, we may see from equation (5.12) that C^* is quite small. In this case $\hat{\psi}_0 \to 0$. That means flow inside the sphere is very weak. This is owing to the recirculating Stokes layer in which there are opposing velocities that require a very large shear in order to sustain substantial motion. Since the system cannot afford sufficiently large shear stresses, the result is that the motion remains weak.

In the solid-sphere limit, $|\hat{M}| = 0$, $\lambda = \mu/\hat{\mu} = 0$, and

$$C = -\tfrac{3}{4}(1-i)$$

and

$$\Psi_0 = \tfrac{3}{2}\left\{ \eta - \tfrac{1-i}{2}(1-e^{-(1+i)\eta}) \right\}(1-\bar{\mu}^2)e^{i\tau}.$$

Thus, for the solid sphere limit ($\hat{\mu}/\mu \to \infty$), we recover Riley's[20] solution of stream function in the shear-wave layer.

Solutions to $O(\varepsilon)$

To $O(\varepsilon)$, we obtain only the time-independent parts of the flow field. These are

$$\begin{aligned}\Psi_{1(\tau-indep)} \quad &= \quad \frac{9}{2}\left[\frac{5}{8}\eta - \frac{|M|\kappa\eta}{\sqrt{2}(20+8\kappa)} - \frac{21}{16} + \frac{1}{16}e^{-2\eta} + \frac{5}{4}e^{-\eta}\cos\eta \right. \\ &\quad \left. + \frac{3}{4}e^{-\eta}\sin\eta + \frac{1}{2}\eta e^{-\eta}\sin\eta\right]\bar{\mu}(1-\bar{\mu}^2), \qquad (5.13)\end{aligned}$$

and

$$\hat{\psi}_{1(\tau-indep)} = \frac{9|M|\kappa}{\sqrt{2}(80+32\kappa)}\left(r^3 - r^5\right)\bar{\mu}(1-\bar{\mu}^2). \qquad (5.14)$$

$$\psi_{1(\tau-indep)} = \left(-\frac{45}{32} + \frac{9|M|\kappa}{\sqrt{2}(80+32\kappa)}\right)\left(\frac{1}{r^2} - 1\right)\bar{\mu}(1-\bar{\mu}^2). \qquad (5.15)$$

Discussion

The flow descriptions given by equation (5.13) and equation (5.15) show that these inner and outer fields depend on the frequency parameter M. At the macroscale, many of the levitation experiments, the wave frequency is $20-40$kHz, and the diameter of the sphere is $3-8$mm. For a gaseous medium outside the liquid drop, $\kappa = 1/\lambda$ is $O(10^{-2})$. In this case, $|M|$ ranges from 140 to 600, and we find that

$$\frac{9|M|\kappa}{\sqrt{2}(80+32\kappa)} < \frac{45}{32} \quad \text{or} \quad |M| < \frac{5\sqrt{2}(5+2\kappa)}{2\kappa}.$$

The steady-state flow pattern outside the liquid sphere is quite similar to that of the solid sphere obtained by Riley [20]. The shear layer in this case has recirculation (see Figure 5.1 and 5.2). With increasing $|M|$, the parameter

$$B_1 = -\frac{45}{32} + \frac{9|M|\kappa}{\sqrt{2}(80+32\kappa)} \qquad (5.16)$$

in equation (5.15) vanishes and then reverses sign. At that point, the recirculation in the shear layer ceases. The streamlines inside the layer merge with the outer ones (see Figure 5.2).

While this theory that predicts the cessation of recirculation in the shear-wave layer has been reported for over ten years now, there is still need for conclusive experimental verification. In recent experiments [7], the strong dependence of the internal and external flow characteristics on the liquid viscosity have been reported. While we are still seeking detailed theoretical explanations for this phenomenon, we should mention that the vorticity generated by the acoustic field interacting with an interface is manifested in the form of recirculation (see Schlichting [23]). This takes place when an acoustic field interacts with a solid surface. However, in the case of a fluid surface, interfacial mobility is likely to reduce this effect. With decreasing

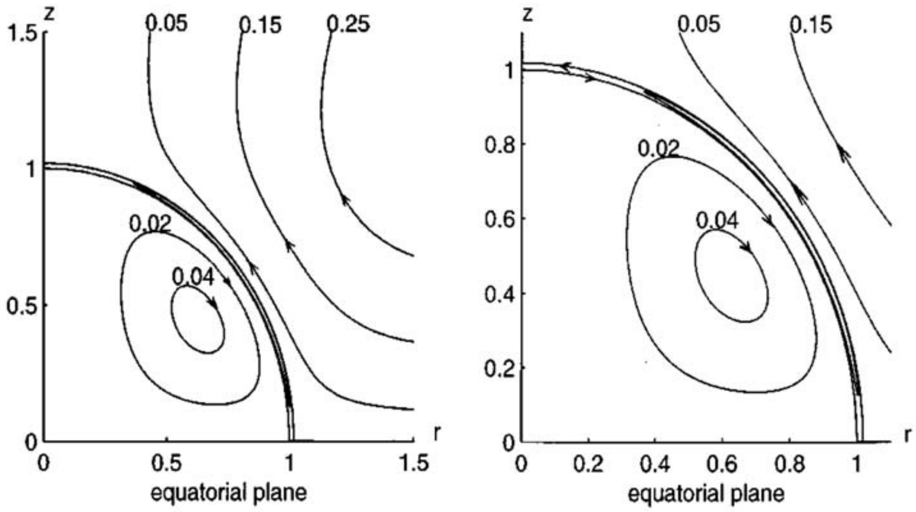

Figure 5.1: Streaming about a drop at the velocity antinode with $B_1 < 1$, for $|M| = 200$ and $\kappa = 0.0156$[26]

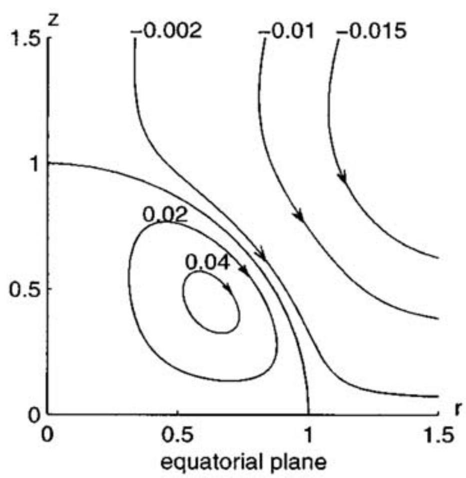

Figure 5.2: Streaming about a drop at the velocity antinode for $B_1 > 1$, with $|M| = 200$ and $\kappa = 0.0156$ [26]

drop-phase viscosity, the strength of the shear-wave layer recirculation diminishes and could vanish when the parameter B_1 in equation (50) is zero. The effect is particularly pronounced because the thinness of the recirculating layer affords a great deal of shear, and fluidity at the interface appears to mitigate that effect. It should be remarked that at the cessation point, ψ_1 also vanishes, and higher-order solutions are needed for a valid description.

5.2 Liquid Drop Between Nodes

In this section, we discuss the flow field dealing with a liquid sphere in gas medium displaced between the velocity node and the antinode in acoustic levitation. The analysis is carried out for a high-frequency standing acoustic wave which is useful to levitate particles in Earth gravity or to stabilize particles in low-gravity situations. The drop is considered to have sufficient mass so that it occupies a stable position in the acoustic field and it does not experience significant body oscillations. As in previous chapters, we depend a great deal on the perturbation procedure based on small-amplitude and high-frequency assumptions for the acoustic fields. We choose axially symmetric spherical polar coordinates (r, θ) with the origin at the center of the sphere. The z-axis passes through the center of the sphere and points along the direction of vibration, and $z = 0$ represents the velocity antinode closest to the sphere, while $z = z_0$ is the center of the sphere. The following dimensionless parameters are used:

$$|M|^2 = \omega a^2/\nu \gg 1, \quad \varepsilon = \frac{U_\infty}{\omega a} \ll 1, \quad \bar{k} = ka \text{ and } R_s = \varepsilon^2 |M|^2 \ll 1,$$

where U_∞ is the velocity amplitude of the standing wave, ω is the frequency, ν is the kinematic viscosity of the gas medium, a is the drop radius, $k = \omega/c$ is the acoustic wavenumber, M is the frequency parameter, ε is the amplitude parameter which is actually the reciprocal of the Strouhal number. The high-frequency and small-amplitude case corresponds to $M \gg 1$ and $\varepsilon \ll 1$, respectively. Besides, we assume that the particle size is much smaller than the acoustic wavelength, i.e., $\bar{k} \ll 1$. Furthermore, R_s, the expected value of the Reynolds number for the resulting steady streaming (the streaming Reynolds number [20]), is also assumed to be small. Since the development closely follows the solid-sphere analysis, we shall dispense with much of the details which are available in [19].

The flow parameters are scaled as follows:

$$\boldsymbol{u} = \frac{\boldsymbol{u}^*}{U_\infty}, \quad \psi = \frac{\psi^*}{U_\infty a^2}, \quad r = \frac{r^*}{a}, \quad z = \frac{z^*}{a}, \quad \varphi = \frac{\varphi^*}{U_\infty a},$$
$$t = \omega t^*, \quad p = \frac{p^*}{\rho_0^* U_\infty \omega a}, \text{ and } \rho = \frac{\rho^* c^2}{\rho_0^* U_\infty \omega a},$$

where ρ_0^* is the unperturbed medium density, c is the speed of sound, ρ^* is the density perturbation due to the acoustic wave, and p^* is the acoustic pressure. The flow field will be described by the stream function ψ^* and the velocity potential φ^*. The asterisks denote dimensioned variables while the dimensionless variables are without asterisks. The dimensioned constants do not, however, have asterisks. The dimensionless continuity and momentum equations are the same as equations (4.4) and (4.5) but are repeated here with a slightly different notation.

$$\bar{k}^2 \frac{\partial \rho}{\partial t} + \boldsymbol{\nabla} \cdot \boldsymbol{u} + \varepsilon \bar{k}^2 \boldsymbol{\nabla} \cdot (\rho \boldsymbol{u}) = 0, \tag{5.17}$$

and

$$\left(1 + \rho\varepsilon\bar{k}^2\right) \frac{\partial \boldsymbol{u}}{\partial t} + \varepsilon \left(1 + \rho\varepsilon\bar{k}^2\right) \boldsymbol{u} \cdot \boldsymbol{\nabla} \boldsymbol{u} = -\boldsymbol{\nabla} p + \frac{1}{M^2} \nabla^2 \boldsymbol{u}, \tag{5.18}$$

respectively. By using adiabatic relation $\rho^* = p^*/c^2$ with c as the speed of sound, the dimensionless acoustic pressure and density can be shown to be equal for $\gamma = c_p/c_v \simeq 1$, i.e.,

$$p = \rho \tag{5.19}$$

to the leading order.

As discussed in Section 4.2, a particle levitated in a gravity field would position itself between the velocity node and the antinode. To consider such a problem, we need to expand the standing wave velocity u_z^* such that

$$\begin{aligned} u_z^* &= U_\infty \cos(kz^*) e^{i\omega t^*} = U_\infty \cos(\bar{k}z) e^{it} \\ &= U_\infty \left[\cos \bar{k}z_0 - \bar{k}(z - z_0) \sin \bar{k}z_0 + O(\bar{k}^2(z - z_0)^2)\right] e^{it}, \end{aligned} \tag{5.20}$$

represents the local velocity in the neighborhood of the sphere centered at $(z = z_0)$. The first term in the expanded version of equation (5.20) is just the far-field velocity for the situation when the sphere is at velocity antinode of a standing wave, and the second term is the far-field velocity for the case when the sphere is positioned at the node. The cases $\bar{k}z_0 = 0$ and $\bar{k}z_0 = \frac{1}{2}\pi$ would correspond to cases of a sphere placed at the velocity antinode and node, respectively. The displaced sphere problem is a combination of the solutions about the node and the antinode, together with additional nonlinear terms.

While the fluid within the Stokes layer near the surface of the sphere has vorticity to meet the continuity conditions on the interface, the flow outside the layer behaves irrotationally as in a sound field. This outer flow field can therefore be expressed as a velocity potential,

$$\boldsymbol{u} = \boldsymbol{\nabla} \varphi. \tag{5.21}$$

The dimensionless far-field potential function, corresponding to equation (4.45), takes the form

$$\begin{aligned} \varphi_\infty &= \left[\frac{1}{\bar{k}} \sin \bar{k}z_0 + (z - z_0) \cos \bar{k}z_0 - \tfrac{1}{2}\bar{k}(z - z_0)^2 \sin \bar{k}z_0 + O\left(\bar{k}^2\right)\right] e^{it} \\ &= \left[\frac{1}{\bar{k}} \sin(\bar{k}z_0) + r \cos(\bar{k}z_0) P_1(\bar{\mu}) - \tfrac{1}{6}\bar{k}r^2 \sin(\bar{k}z_0) \right. \\ &\quad \left. - \tfrac{1}{3}\bar{k}r^2 \sin(\bar{k}z_0) P_2(\bar{\mu}) + O\left(\bar{k}^2\right) \right] e^{it}, \end{aligned} \tag{5.22}$$

where $P_n(\bar{\mu})$ denotes Legendre polynomials, and $\bar{\mu} = \cos\theta$. With the spherical coordinate system centered at $z = z_0$, it should be noted that $z - z_0 = r\bar{\mu}$. From momentum equation (5.18), we have as before

$$\frac{\partial \boldsymbol{u}_\infty}{\partial t} = -\boldsymbol{\nabla} p_\infty, \tag{5.23}$$

and using equation (5.21), we obtain

$$\begin{aligned} p_\infty = \rho_\infty &= -i\left[\frac{1}{\bar{k}}\sin(\bar{k}z_0) + r\cos(\bar{k}z_0)P_1(\bar{\mu})\right. \\ &\left. -\tfrac{1}{6}\bar{k}r^2\sin(\bar{k}z_0) - \tfrac{1}{3}\bar{k}r^2\sin(\bar{k}z_0)P_2(\bar{\mu})\right]e^{it}, \end{aligned} \tag{5.24}$$

where the real part applies.

5.2.1 Solution

In this section, the flow-field results of the analysis by singular perturbation using $\varepsilon = U_\infty/(\omega a) \ll 1$. As in the earlier section of this chapter, parameters with $(\hat{\ })$ represent properties of liquid inside the drop, and parameters without $(\hat{\ })$ correspond to the gas region outside the drop.

By applying the perturbation method, we expand the velocity, acoustic pressure and density outside the boundary layer in powers of ε as follows:

$$\boldsymbol{u} = \boldsymbol{u}_0 + \varepsilon\boldsymbol{u}_1 + O(\varepsilon^2), \tag{5.25}$$

$$p = p_0 + \varepsilon p_1 + O(\varepsilon^2), \tag{5.26}$$

and

$$\rho = \rho_0 + \varepsilon\rho_1 + O(\varepsilon^2). \tag{5.27}$$

These expansions are substituted into equations (5.17) and (5.18) to form a hierarchy of equations in orders of ε. We treat here the leading order ($O(1)$) and $O(\varepsilon)$.

Leading-Order Solutions

Outer Region The leading-order velocity potential φ_0 takes the form

$$\begin{aligned} \varphi_0 = &\left\{\frac{1}{\bar{k}}\sin(\bar{k}z_0) + \cos(\bar{k}z_0)\left(r + \tfrac{1}{2}r^{-2}\right)P_1(\bar{\mu})\right. \\ &\left. -\tfrac{1}{3}\bar{k}\sin(\bar{k}z_0)\left[\left(r^{-1} + \tfrac{1}{2}r^2\right) + \left(r^2 + \tfrac{2}{3}r^{-3}\right)P_2(\bar{\mu})\right] + O(\bar{k}^2)\right\}e^{it}. \end{aligned} \tag{5.28}$$

The leading-order acoustic pressure p_0 and density ρ_0 are then given by

$$\begin{aligned} p_0 = \rho_0 = -\frac{\partial\varphi_0}{\partial t} = -i&\left\{\frac{1}{\bar{k}}\sin(\bar{k}z_0) + \cos(\bar{k}z_0)\left(r + \tfrac{1}{2}r^{-2}\right)P_1(\bar{\mu})\right. \\ &\left. -\tfrac{1}{3}\bar{k}\sin(\bar{k}z_0)\left[\left(r^{-1} + \tfrac{1}{2}r^2\right) + \left(r^2 + \tfrac{2}{3}r^{-3}\right)P_2(\bar{\mu})\right]O(\bar{k}^2)\right\}e^{it}. \end{aligned} \tag{5.29}$$

In the liquid phase, the leading-order solution os

$$\hat{\psi}_0 = 0, \tag{5.30}$$

implying no flow at all to the leading order. This also means that the boundary layer, to this order, will satisfy the no-slip conditions as for a solid sphere.

Gas-Phase Stokes Layer In the boundary layer, we express the velocity as

$$\boldsymbol{u}^b = u_r^b \hat{\boldsymbol{r}} + u_\theta^b \hat{\boldsymbol{\theta}}, \tag{5.31}$$

where u_r^b is the normal velocity, u_θ^b is the tangential velocity, and $(\hat{\boldsymbol{r}}, \hat{\boldsymbol{\theta}})$ are unit vectors. The solution is

$$u_{\theta 0}^b = \left\{-\tfrac{3}{2}\cos(\bar{k}z_0)\sin\theta + \tfrac{5}{3}\bar{k}\sin(\bar{k}z_0)\sin\theta\cos\theta\right\}\left(1 - e^{-(1+i)\eta}\right)e^{it}. \tag{5.32}$$

and

$$\begin{aligned} u_{\eta 0}^b \;=\; & \left\{3\cos(\bar{k}z_0)\left[\eta - \tfrac{1}{2}(1-i)\left(1 - e^{-(1+i)\eta}\right)\right]P_1(\bar{\mu})\right. \\ & \left. - \bar{k}\sin(\bar{k}z_0)\left(\eta + \tfrac{10}{3}\left[\eta - \tfrac{1}{2}(1-i)\left(1 - e^{-(1+i)\eta}\right)\right]P_2(\bar{\mu})\right)\right\}e^{it}. \end{aligned} \tag{5.33}$$

Here, we notice that all the leading-order solutions, including velocity, pressure and density, are just the linear combination of two groups of results, one is when the sphere is placed at the velocity antinode, and the other one is at the node.

First-Order Solutions

Our interest is mainly in understanding the steady streaming outside the sphere. We therefore consider here only the steady-state components of the solutions. The results are

$$\begin{aligned} u_{\theta 1}^b \;=\; & \bar{k}\sin(\bar{k}z_0)\cos(\bar{k}z_0)\left\{\sin\theta\left[\tfrac{5}{8}e^{-2\eta} + \tfrac{5}{4}e^{-\eta}\cos\eta + \tfrac{17}{4}e^{-\eta}\sin\eta\right.\right. \\ & \left. + \tfrac{1}{2}\eta e^{-\eta}(\sin\eta - \cos\eta) + Q_1\right] + \sin\theta\cos^2\theta\left[-\tfrac{15}{8}e^{-2\eta}\right. \\ & \left.\left. -20e^{-\eta}\sin\eta + \tfrac{25}{4}e^{-\eta}(\eta\cos\eta - \eta\sin\eta - \sin\eta) + Q_3\right]\right\} \\ & + \cos^2(\bar{k}z_0)\sin\theta\cos\theta\left\{\tfrac{9}{16}e^{-2\eta} + \tfrac{27}{4}e^{-\eta}\sin\eta\right. \\ & \left. + \tfrac{9}{4}e^{-\eta}(\eta\sin\eta - \eta\cos\eta + \cos\eta) + Q_2\right\} + O(\bar{k}^2), \end{aligned} \tag{5.34}$$

where Q_1, Q_2, and Q_3 are constants found to be

$$Q_1 = \tfrac{23}{168}\sqrt{2}M_\mu - \tfrac{15}{8}, \quad Q_2 = \tfrac{9}{80}\sqrt{2}M_\mu - \tfrac{45}{16}, \quad \text{and} \quad Q_3 = -\tfrac{15}{56}\sqrt{2}M_\mu + \tfrac{65}{8}, \tag{5.35}$$

Inside the drop, assuming that the Reynolds number is small, the steady streaming satisfies Stokes equation, i.e.,

$$D^4\hat{\psi}_1 = 0. \tag{5.36}$$

Here, $\hat{\psi}_1$ is the stream function s inside the drop is given by

$$\begin{aligned}\hat{\psi}_1 &= \bar{k}\sin(\bar{k}z_0)\cos(\bar{k}z_0)\tfrac{1}{24}\sqrt{2}M_\mu\left(r^2-r^4\right)(1-\bar{\mu}^2)\\ &\quad+\cos^2(\bar{k}z_0)\tfrac{9}{160}\sqrt{2}M_\mu\left(r^3-r^5\right)\bar{\mu}(1-\bar{\mu}^2)\\ &\quad-\bar{k}\sin(\bar{k}z_0)\cos(\bar{k}z_0)\tfrac{3}{112}\sqrt{2}M_\mu\left(r^4-r^6\right)(5\bar{\mu}^2-1)(1-\bar{\mu}^2)+O(\bar{k}^2)\end{aligned}\tag{5.37}$$

It should be noted that this solution in the drop region is uniformly valid as there is no internal Stokes layer.

The stream function in the boundary layer may be expressed as

$$\begin{aligned}\psi_1^b &= -\Big\{\bar{k}\sin(\bar{k}z_0)\cos(\bar{k}z_0)\Big[\Big(-\tfrac{5}{16}e^{-2\eta}-3e^{-\eta}\cos\eta-\tfrac{7}{4}e^{-\eta}\sin\eta\\ &\quad-\tfrac{1}{2}\eta e^{-\eta}\sin\eta+\tfrac{23}{168}\sqrt{2}M_\mu\eta-\tfrac{15}{8}\eta+\tfrac{53}{16}\Big)(1-\bar{\mu}^2)\\ &\quad+\Big(\tfrac{15}{16}e^{-2\eta}+\tfrac{65}{4}e^{-\eta}\cos\eta+10e^{-\eta}\sin\eta\\ &\quad+\tfrac{25}{4}\eta e^{-\eta}\sin\eta+\tfrac{65}{8}\eta-\tfrac{15}{56}\sqrt{2}M_\mu\eta-\tfrac{275}{16}\Big)\bar{\mu}^2(1-\bar{\mu}^2)\Big]\\ &\quad+\cos^2(\bar{k}z_0)\Big(-\tfrac{9}{32}e^{-2\eta}-\tfrac{45}{8}e^{-\eta}\cos\eta-\tfrac{27}{8}e^{-\eta}\sin\eta-\tfrac{9}{4}\eta e^{-\eta}\sin\eta\\ &\quad+\tfrac{9}{80}\sqrt{2}M_\mu\eta-\tfrac{45}{16}\eta+\tfrac{189}{32}\Big)\bar{\mu}(1-\bar{\mu}^2)\Big\}+O(\bar{k}^2).\end{aligned}\tag{5.38}$$

This inner solution is valid only in the shear-wave layer, and to complete the analysis, we must seek the steady streaming in the outer region as well, where

$$r-1=O(1).$$

In the limit of small streaming Reynolds number ($R_s \ll 1$) the outer streaming satisfies the Stokes equation,

$$D^4\psi_1=0,\tag{5.39}$$

To obtain the solution to this equation, the angular eigenfunctions are chosen to be the same as the inner solution, ψ_1^b, given by equation (5.38). The far-field behavior of the solution requires the flow velocity to fade away. At the surface we require matching with the Stokes-layer solution (5.38). Thus, we obtain

$$\begin{aligned}\psi_1 &= \bar{k}\sin(\bar{k}z_0)\cos(\bar{k}z_0)\Big[\left(\tfrac{1}{8}-\tfrac{1}{24}\sqrt{2}M_\mu\right)\left(r-\frac{1}{r}\right)(1-\bar{\mu}^2)\\ &\quad-\left(\tfrac{13}{16}-\tfrac{3}{112}\sqrt{2}M_\mu\right)\left(\frac{1}{r}-\frac{1}{r^3}\right)(5\bar{\mu}^2-1)(1-\bar{\mu}^2)\Big]\\ &\quad+\cos^2(\bar{k}z_0)\left(\tfrac{45}{32}-\tfrac{9}{160}\sqrt{2}M_\mu\right)\left(1-\frac{1}{r^2}\right)\bar{\mu}(1-\bar{\mu}^2)+O(\bar{k}^2).\end{aligned}\tag{5.40}$$

To sum it up, the internal circulation within the drop is defined by equation (5.37), while the steady streaming in the gas medium is given by (5.38) for the Stokes layer, and by (5.40) for the outer region. We note that the case of the solid sphere is recovered in all these expressions by letting the liquid-phase viscosity go to infinity, i.e., setting $M_\mu = 0$.

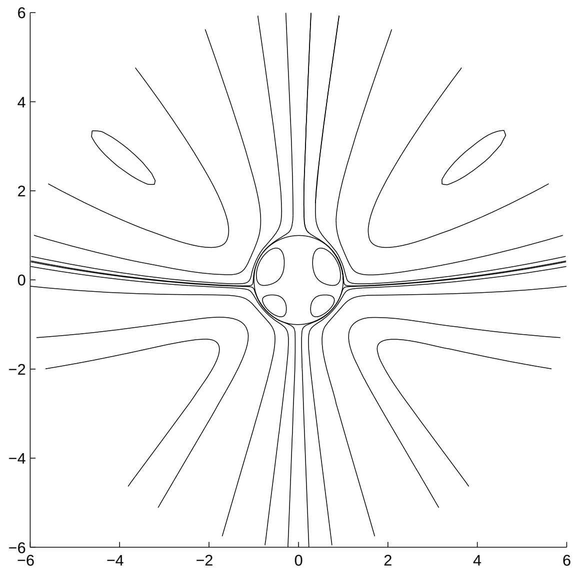

Figure 5.3: Streaming about a drop displaced between velocity node and antinode for $\bar{k}z_0 = \pi/4$, $\bar{k} = 0.3$, and $M_\mu = 3.12$,

5.2.2 Discussion

In the above analysis, we find that the leading-order solution is a linear combination of the two groups of fundamental solutions corresponding to the sphere being placed at the node and antinode, respectively, of a standing wave. At higher orders, nonlinear effects become important and additional terms besides the two fundamental solutions are needed for the proper description of the flow.

The leading-order oscillatory flow for a liquid sphere is essentially the same as for a solid one, in view of the high inertia of the liquid as compared to the surrounding gas medium. However, this is not the case for the steady streaming, when the difference between the liquid and the solid spheres may be appreciable. The effect of the 'liquidity' on the streaming is measured by the parameter M_μ. Typical flow patterns associated with the steady streaming of liquid sphere displaced between velocity node and antinode are displayed in Figure 5.3 through Figure 5.11. In these figures, we plot the streamlines for $\bar{k} = 0.3$, and $\bar{k}z_0 = \pi/4$. Equation (5.38) contains three terms that are linear in η, with coefficients a_1, a_2 and a_3, identified as

$$a_1 = \tfrac{23}{168}\sqrt{2}M_\mu - \tfrac{15}{8}, \tag{5.41}$$

$$a_2 = \tfrac{9}{80}\sqrt{2}M_\mu - \tfrac{45}{16}, \tag{5.42}$$

and

$$a_3 = \tfrac{15}{56}\sqrt{2}M_\mu - \tfrac{65}{8}. \tag{5.43}$$

These three factors divide the range of M_μ into four smaller ones. Each of these is discussed next.

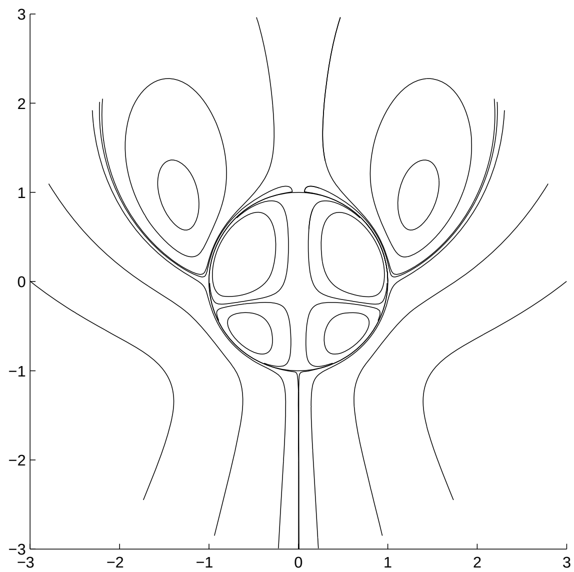

Figure 5.4: Streaming about a drop displaced between velocity node and antinode for $\bar{k}z_0 = \pi/4$, $\bar{k} = 0.3$, and $M_\mu = 9.36$

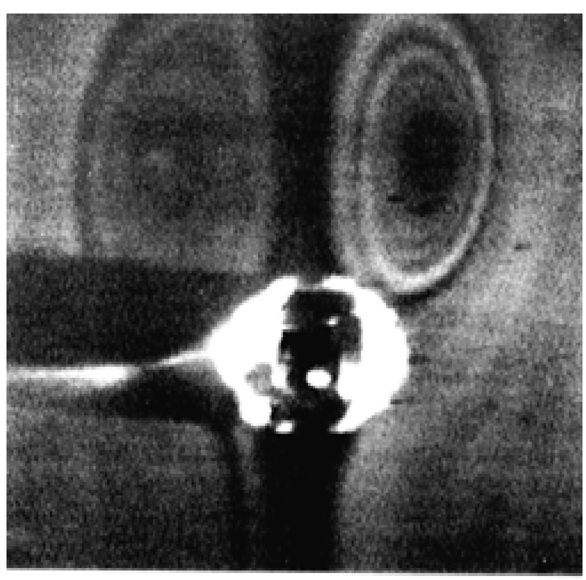

Figure 5.5: An experimental result. The tested particle is a drop of water with diameter 1.8-1.85mm. The acoustic frequency is 37kHz, corresponding to $M \simeq 110$ and $M_\mu \simeq 2.3$

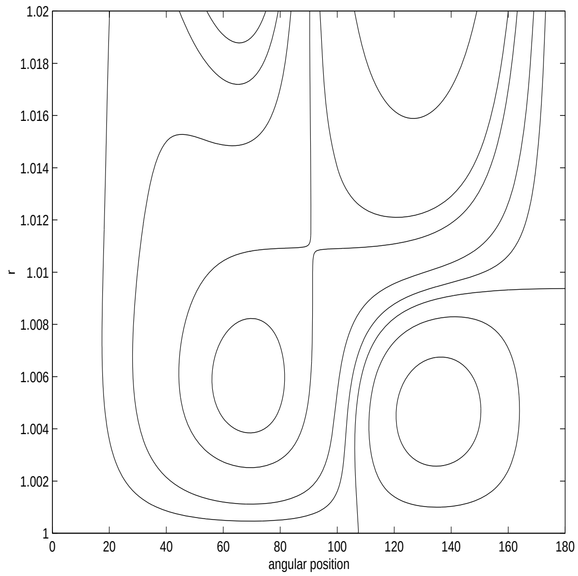

Figure 5.6: Detailed streaming near the surface of drop stretched in the $\theta - r$ plane for $\bar{k}z_0 = \pi/4$, $\bar{k} = 0.3$, and $M_\mu = 9.36$

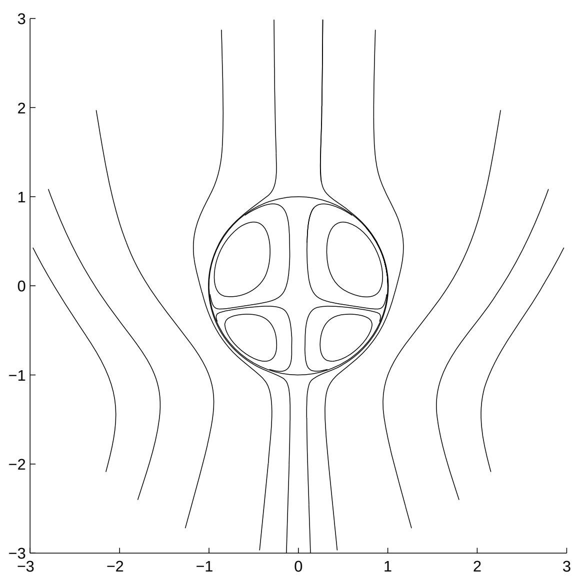

Figure 5.7: Streaming about a drop displaced between velocity node and antinode for $\bar{k}z_0 = \pi/4$, $\bar{k} = 0.3$, and $M_\mu = 12.48$

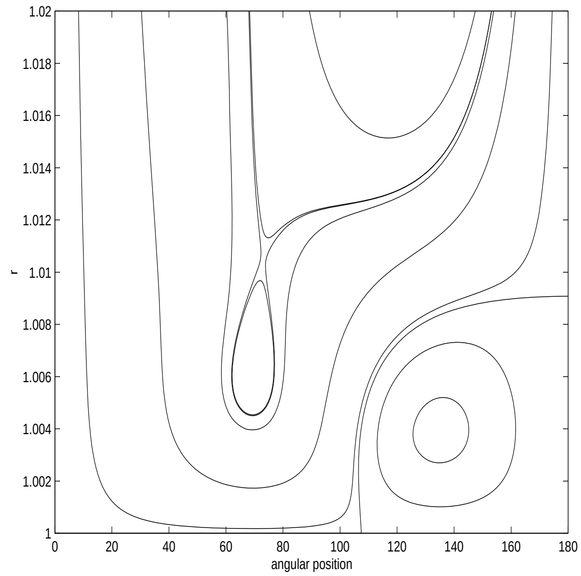

Figure 5.8: Detailed streaming near the surface of drop stretched in $\theta - r$ plane for $\bar{k}z_0 = \pi/4$, $\bar{k} = 0.3$, and $M_\mu = 12.48$

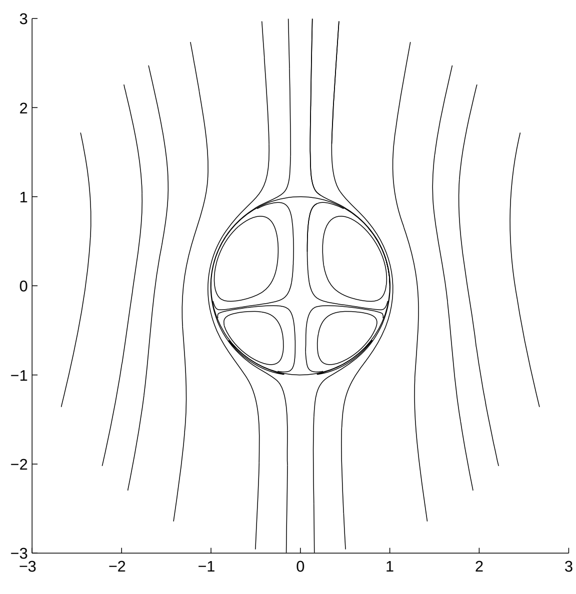

Figure 5.9: Streaming about a drop displaced between velocity node and antinode for $\bar{k}z_0 = \pi/4$, $\bar{k} = 0.3$, and $M_\mu = 19.5$

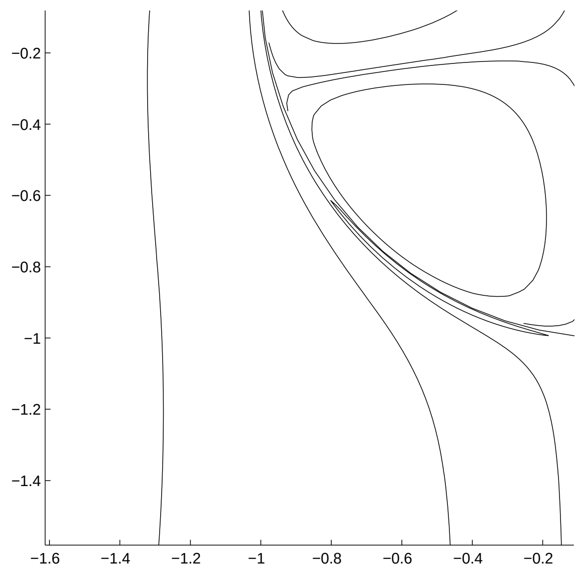

Figure 5.10: Detailed streaming about the drop for $\bar{k}z_0 = \pi/4$, $\bar{k} = 0.3$, and $M_\mu = 19.5$

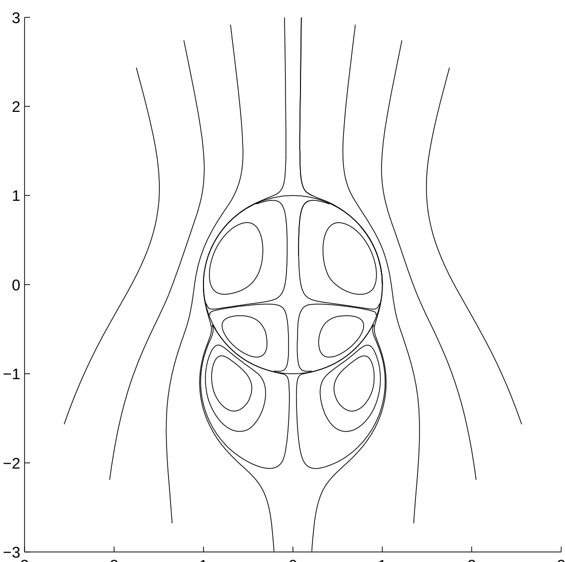

Figure 5.11: Streaming about a drop displaced between velocity node and antinode for $\bar{k}z_0 = \pi/4$, $\bar{k} = 0.3$, and $M_\mu = 28.08$

For

$$a_1 < 0 \quad \text{or} \quad M_\mu < \tfrac{315}{46}\sqrt{2},$$

there are vortices near the surface of the drop on the side of velocity node, as shown in Figures 5.3 and 5.4. Here there is a large recirculatory region on the 'front side' of the drop with respect to the outer streaming which is downward. This may appear to be unusual from the standpoint of flows past obstacles that have a rear-side wake. However, with levitation, there is a low-pressure region on the top, and therefore it is possible for recirculation in that region. An experimental result is shown in Figure 5.5 which is qualitatively consistent with the theoretical prediction. While the experiment corresponds to $M = 113$, theoretical calculations at such low value of M_μ do not show a 'front-side' recirculatory region. However, in the experiment, there are some effects such as those from the chamber walls that are not accounted for. There are some other interesting features in this flow field. There exist very thin recirculatory regions in the gas phase on the lower side of the drop. These are difficult to resolve graphically, except on a stretched scale (see Figure 5.6). With an increase in M_μ, when

$$a_1 > 0 \quad \text{and} \quad a_2 < 0, \quad \text{or} \quad \tfrac{315}{46}\sqrt{2} < M_\mu < \tfrac{25}{2}\sqrt{2},$$

the vortices disappear. While the streamlines inside the shear-wave layer join the outside ones smoothly, as shown in Figure 5.7, the small recirculatory region still persists. With further increase in M_μ, when

$$a_2 > 0 \quad \text{and} \quad a_3 < 0, \quad \text{or} \quad \tfrac{25}{2}\sqrt{2} < M_\mu < \tfrac{91}{6}\sqrt{2},$$

the thin layer of recirculation becomes apparent near the surface on the lower side of the drop, as shown in Figures 5.9 and 5.10. When M_μ is very large, corresponding to

$$a_3 > 0 \quad \text{or} \quad M_\mu > \tfrac{91}{6}\sqrt{2},$$

the thin layer of recirculation becomes enlarged and vortices are created on the side of the velocity antinode as shown in Figure 5.11.

One of the important findings of the present study is the marked difference in the streaming flow behaviour about a liquid drop from that about a solid sphere. This is the case even when the liquid viscosity is quite high. It is apparent that the flow characterization is sensitive to surface mobility which affects the interaction of the acoustic wave with that surface. As shown by Schlichting [23] and by Riley [20], the interaction with a solid surface produces recirculating regions adjacent to the surface. However, as argued earlier by Zhao, Sadhal & Trinh [26], the flow behavior resulting from vorticity generated at the interface by this interaction is affected by the surface mobility.

5.3 Bubbles in Acoustic Fields

In this section, we shall examine the phenomenon of microstreaming that happens due to a bubble when its surrounding liquid is undergoing steady vibrations. We shall not discuss other phenomena such as sonoluminescence. The early experiments by Elder [2] demonstrated that the streaming observed around the bubble is opposite to that for a solid particle. This is indeed consistent with the absence of the recirculating layer for the bubble. In fact, for a surface-contaminated bubble which behaves like a rigid particle, the recirculating layer was observed. Interestingly, when the driving amplitude was increased, the surface skin broke and the streaming changed sign. The analysis of this type of flow was conducted by Davidson & Riley [1] based on Riley's [20] basic development. Among the solutions obtained were cases for $|M|^2 = \omega a^2/\nu \gg 1$, and $|M|^2 = \omega a^2/\nu \ll 1$. Since the groundwork for the basic perturbation procedure is similar to Riley's [20] classical solution (see also pages 20 -24 in Section 3.2), we shall give only the results. The analysis was carried out for a bubble at the velocity antinode. The flo-field description can be given by equation (3.5) on page 21 in Section 3.2.1, together with the far-field condition (3.9). As with the the solid sphere case, the zero normal velocity at the surface surface is maintained. However, in place of the zero tangential velocity, we have the shear-free condition. Therefore, instead of (3.8), we have

$$\psi = 0 \qquad \text{and} \qquad \frac{\partial^2 \psi}{\partial r^2} - \frac{\partial \psi}{\partial r} = 0 \qquad \text{at} \qquad r = 1. \tag{5.44}$$

The perturbation expansion used in this analysis employed both $\varepsilon = U_\infty/\omega a \ll 1$ and $|M|^{-1} \ll 1$, i.e.,

$$\begin{aligned} \psi = {} & \psi_{00} + (1/|M|)\psi_{01} + (1/|M|^2)\psi_{02} + O(1/|M|^3) \\ & +\varepsilon \left[\psi_{10} + (1/|M|)\psi_{11} + (1/|M|^2)\psi_{12} + O(1/|M|^3)\right] \end{aligned} \tag{5.45}$$

for the outer region. The solution was found to be

$$\begin{aligned} \psi_{00} &= \tfrac{1}{2} r^2 (1 - 1/r^3)(1 - \bar{\mu}^2) e^{i\tau}, \\ \psi_{01} &= 0, \\ \psi_{02} &= \frac{3i}{r}(1 - \bar{\mu}^2) e^{i\tau}, \end{aligned} \tag{5.46}$$

where the set of boundary conditions (5.44) cannot be fully satisfied since highest derivatives in (3.5) are lost in the outer expansion with $1/|M| \ll 1$. Using inner variables as defined in equations (3.13) and (3.14) on page 22, and noting that $R_s = \varepsilon^2 |M|^2$, the expansion procedure

$$\begin{aligned} \Psi = {} & \Psi_{00} + (1/|M|)\Psi_{01} + (1/|M|^2)\Psi_{02} + O(1/|M|^3) \\ & +\varepsilon \left[\Psi_{10} + (1/|M|)\Psi_{11} + (1/|M|^2)\Psi_{12} + O(1/|M|^3)\right] \end{aligned} \tag{5.47}$$

is used. The result is given as [1]

$$\begin{aligned} \Psi_{00} &= \tfrac{3}{2}\eta(1 - \bar{\mu}^2) e^{i\tau} \\ \Psi_{01} &= \tfrac{3}{2}\sqrt{2}\left(1 - e^{-(1+i)\eta}\right)(1 - \bar{\mu}^2) e^{i(\tau + \pi/2)} \\ \Psi_{02} &= \left[\eta^3 - 3i\eta - 3(1+i)\left(1 - e^{-(1+i)\eta}\right)\right](1 - \bar{\mu}^2) e^{i\tau} \end{aligned} \tag{5.48}$$

To $O(\varepsilon)$, the steady components are given as

$$\begin{aligned}
\psi_{11}^{(s)} &= -\tfrac{27}{40}\sqrt{2}\left(1-\frac{1}{r^2}\right)\bar{\mu}(1-\bar{\mu}^2) \\
\Psi_{11}^{(s)} &= -18\sqrt{2}\left\{1-\tfrac{3}{20}-\tfrac{1}{4}\left[4\cos\eta e^{-\eta}+\eta e^{-\eta}\left(\cos\eta+\sin\eta\right)\right]\right\}\bar{\mu}(1-\bar{\mu}^2)
\end{aligned} \tag{5.49}$$

with $\psi_{10}^{(s)} = \psi_{12}^{(s)} = \Psi_{10}^{(s)} = \Psi_{12}^{(s)} = 0$. As with the case of the solid sphere, the nonzero expression for $\psi_{11}^{(s)}$ indicates the persistence of the streaming outside the shear-wave layer. The order of the streaming vortices in this case are $O(\varepsilon U_\infty/|M|)$ as compared with $O(1/|M|)$ for the solid sphere. The outer streaming pattern is shown in Figure 5.12. Of course, with the absence of closed streamlines in the shear-wave layer (see Figure 3.4 on page 25), the outer streaming pattern is the reverse of the solid-sphere case.

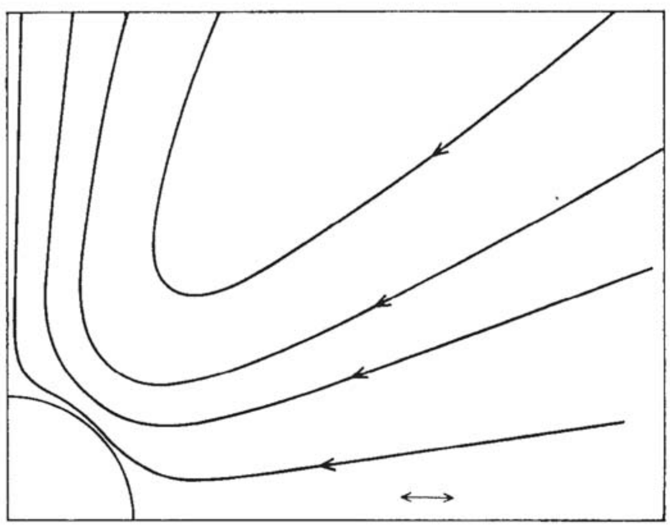

Figure 5.12: The outer steady streaming pattern for a bubble with $|M| \gg 1$. Reproduced from [1].

5.3.1 Radial and Transverse Oscillations of Bubbles

If we include radial oscillations besides the transverse ones, interesting streaming patterns emerge [13, 14]. This happens, for example, in the case of a bubble undergoing sonoluminescence. We shall not discuss the details but just examine the results. While simple transverse oscillations, and purely radial oscillations do not produce any drift, the combination of these leads to the dipole potential,

$$\Phi = \frac{S\cos\theta}{2r^2}, \tag{5.50}$$

where the diploe strength S is related to the oscillatory parameters by [13]

$$S = 1.5\left(\frac{\omega}{2\pi}\right)a^3 b\sin\gamma. \tag{5.51}$$

Here, a is the mean radius of the sphere, b is the amplitude of the transverse oscillations, and γ is the phase difference between the two modes of oscillations.

Chapter 6

Interaction of Oscillatory Thermal Fields in Tune with Acoustic Fields

6.1 Introduction

In this chapter, we shall examine the process of convective heat transfer due to acoustic streaming induced by a sound field about an isolated sphere which is subject to time-periodic temperature fluctuations. In order to illustrate the ideas, we consider the problem studied by Gopinath & Sadhal [6] several years back.

The principal feature of interest in the present study is the energy transport phenomenon emanating from the time-independent contribution of the convective term due to the interactions of the thermal oscillations with the acoustic field.

In previous studies [4, 5], the steady heat transport due to the streaming motion was examined for the case of an isothermal sphere exchanging heat with an isothermal fluid. However, in the development reported here, although the ambient fluid is considered isothermal, the temperature of the sphere is taken to be time-periodic. The basic problem of the sphere considered here would help address the larger issue of the influence of acoustic fields on such processes. The discussion here deals principally with the *convective* transport of heat due to steady streaming effects in the fluid around the sphere.

The steady streaming motion in the fluid is taken to be induced around a rigid sphere of radius, a, by a standing acoustic field with a velocity distribution of the form,

$$U_\infty \cos(\omega t) \sin(2\pi z/\lambda) \tag{6.1}$$

Here we treat the parameter ranges of $a\omega/c \ll 1$ and $\varepsilon = U_\infty/a\omega \ll 1$, for which the flow induced around the sphere can be assumed to be laminar and unseparated, with negligible compressibility effects. This also allows the governing equations to be treated by the method of matched asymptotic expansions with ε playing the role of a small perturbation parameter. Furthermore, only the high frequency range, $M^2 = a^2\omega/\nu \gg 1$, is considered, for which the streaming effects are most significant. Here again, we use the flow field solution developed by Riley [20] in which the steady flow field of interest has a thin, inner recirculating Stokes layer region in which an $O(\varepsilon U_\infty)$ streaming velocity originates to drive the steady flow in an outer region making up of the remainder of the domain. In the analysis reported here, the acoustic signal is taken to be sufficiently strong so as to give rise to a large streaming Reynolds number ($R_s = \varepsilon^2 M^2$), for which the steady transport effects due to the streaming motion are most pronounced. Particular attention is given to cases in which the surrounding fluid is a gas with $Pr = O(1)$. For large R_s, the outer steady flow has a boundary layer structure, the behavior of which has been obtained in [5].

For purposes of simplicity the periodic temperature excursions of the sphere are taken to be harmonic (at a single frequency) and of the form, $T_\infty + (\Delta T)_a \cos(\omega t + \gamma)$. It is assumed that the amplitude of these oscillations, $(\Delta T)_a$, is small enough to neglect (as a first approximation) any interaction of the thermal and acoustic fields. Furthermore, it is also assumed that any high-intensity thermoacoustic effects as discussed by Gopinath [4] are small. The validity of this assumption can be ensured if a suitably defined Eckert number is maintained small. More importantly, it must be noted that the angular frequency of the acoustic field, ω, is taken to be "tuned" to match that of the temperature oscillations, with allowance made for a possible difference in phase, γ. Such isoharmonic situations are of principal interest since the magnitude of the expected steady heat transport resulting from the interactions of these oscillations is the strongest for such cases. In general however, the procedure followed in this study can be extended to any arbitrary periodic temperature disturbance, after it is Fourier decomposed into its constituent frequencies.

6.2 Governing Equations

For this axisymmetric problem, we describe the fluid motion by the Stokes stream function ($\psi \equiv \psi^*/U_\infty a^2$) in a spherical coordinate system. It is related to the velocity components by equation (3.7). The momentum equation is given by (3.5) and the dimensionless energy equation is as follows

$$\frac{\partial \phi}{\partial \tau} + \frac{\varepsilon}{r^2}\left[\frac{\partial(\psi, \phi)}{\partial(r, \bar{\mu})}\right] = \frac{1}{Pr \cdot M^2}\nabla^2 \phi, \tag{6.2}$$

where

$$\nabla^2 = \frac{1}{r^2}\frac{\partial}{\partial r}\left[r^2 \frac{\partial}{\partial r}\right] + \frac{1}{r^2}\frac{\partial}{\partial \bar{\mu}}\left[(1-\bar{\mu}^2)\frac{\partial}{\partial \bar{\mu}}\right] \tag{6.3}$$

The boundary conditions are

$$\phi = \cos(\tau + \gamma) \quad \text{and} \quad \psi = \frac{\partial \psi}{\partial r} = 0 \quad \text{at } r = 1 \tag{6.4}$$

$$\left.\begin{array}{lcl} \psi & \to & \frac{1}{2}r^2(1-\bar{\mu}^2)\cos\tau \\ \phi & \to & 0 \end{array}\right\} \quad \text{as } r \to \infty \tag{6.5}$$

As with the previous discussion, we are concerned with the cases of $\varepsilon \ll 1$ and $M \gg 1$. Following Riley's [20] for small ε and $1/M$, together with the treatment of Gopinath

& Mills [5], we focus on determining the additional steady thermoacoustic streaming phenomena introduced by the interaction of the oscillating thermal and acoustic fields. These methods call for perturbation expansions in the inner and outer regions.

6.3 The Inner Region

For the frequency parameter, $|M| \gg 1$, the oscillatory flow has a Stokes boundary layer on the surface of the sphere with an irrotational exterior region. The dynamics of this inner oscillatory shear layer region of dimensional thickness of $O(\delta)$ can be described in terms of the boundary layer variables, η and Ψ, given by equations (3.13)–(3.14), together with $\Phi(\eta, \bar{\mu}, \tau) \equiv \phi(r, \bar{\mu}, \tau)$. In these variables, Ψ satisfies the equation for the temperature distribution given by

$$\frac{\partial \Phi}{\partial \tau} + \varepsilon \left[\frac{\partial(\Psi, \Phi)}{\partial(\eta, \bar{\mu})} \right] + O(\varepsilon M^{-1}) = \frac{1}{2\ Pr} \left[\frac{\partial^2 \Phi}{\partial \eta^2} + \frac{2\sqrt{2}}{M} \frac{\partial \Phi}{\partial \eta} + O(M^{-2}) \right] \tag{6.6}$$

These equations can satisfy only the inner boundary conditions on the sphere surface, i.e.,

$$\Psi = \frac{\partial \Psi}{\partial \eta} = 0 \quad \text{and} \quad \Phi = \cos(\tau + \gamma) \quad \text{at } \eta = 0 \tag{6.7}$$

The solution for the stream function, Ψ, has been presented earlier, and the leading order term, Ψ_0 is given by equation (3.12). This may be expressed in real variables as

$$\Psi_0 \;=\; \frac{3\sqrt{2}}{4}(1 - \bar{\mu}^2) \left[\sqrt{2}\, \eta \cos \tau - \cos(\tau - \frac{\pi}{4}) + e^{-\eta} \cos(\tau - \eta - \frac{\pi}{4}) \right] \tag{6.8}$$

Although the above form for Ψ_0 will suffice for the present illustration, it is important to note that it is the time-independent part of the $O(\varepsilon)$ contribution which explains the behavior of the acoustic streaming motion in the inner region and provides a description of the slip-like velocity which drives the steady flow in the outer region.

For the temperature distribution also, a perturbation expansion of the form

$$\Phi = \Phi_0 + \varepsilon(\Phi_{1s} + \Phi_{1u}) + \ldots \tag{6.9}$$

is sought. Here it can be shown from a solution of equation (6.2) subject to equations (6.4)–(6.5) that the leading order solution, Φ_0, is given by

$$\Phi_0 = e^{-\eta Pr^{1/2}} \cos(\tau + \gamma - \eta\sqrt{Pr}) \tag{6.10}$$

and represents an oscillatory temperature wave in the Stokes layer region. Since the variation of Φ_0 is time-periodic, there is no net time averaged transfer of heat at this level. Of greater interest is the $O(\varepsilon)$ contribution to the temperature distribution in the fluid which arises only due to the presence of the acoustic field. An analysis of the $O(\varepsilon)$ terms of equation (6.6) using equation (6.9) shows that in addition to an $O(1)$ second harmonic and an $O(1/\sqrt{R_s})$ first harmonic contained in Φ_{1u}, there also arises from the convective term a non zero steady part, Φ_{1s}, resulting from the time-averaged interaction of the leading order oscillatory temperature and flow fields in the fluid. The behavior of this steady part is governed by

$$\frac{1}{2\,Pr}\frac{\partial^2 \Phi_{1s}}{\partial \eta^2} = \left\langle \frac{\partial(\Psi_0, \Phi_0)}{\partial(\eta, \bar{\mu})} \right\rangle, \tag{6.11}$$

where the angle-brackets, $\langle\ \rangle$, denote a time-average of the enclosed quantities. This equation is subject to the inner boundary condition

$$\Phi_{1s} = 0 \qquad \text{at } \eta = 0 \tag{6.12}$$

and appropriate matching with the outer region. Although the details of the analysis have been excluded, it can be shown that the resulting variation of Φ_{1s} can be obtained from a solution of the above equations as,

$$\begin{aligned}
\Phi_{1s} &= \frac{3\bar{\mu}}{2}\, e^{-\eta\sqrt{Pr}}\, \Big[\sqrt{Pr}\,(1-\eta)\cos(\gamma - \eta\sqrt{Pr}) \\
&- (2+\eta\sqrt{Pr})\,\sin(\gamma - \eta\sqrt{Pr}) \\
&+ \frac{Pr\sqrt{Pr}}{(1+Pr)^2} e^{-\eta}\Big\{(1-Pr)\cos(\gamma + \eta - \eta\sqrt{Pr}) \\
&+ 2\sqrt{Pr}\,\sin(\gamma + \eta - \eta\sqrt{Pr})\Big\}\Big] \\
&+ \bar{\mu}\,\Phi_{1\infty}(Pr, \gamma)
\end{aligned} \tag{6.13}$$

where

$$\begin{aligned}
\Phi_{1\infty}(Pr, \gamma) &= \frac{3}{2}\frac{\sqrt{9Pr+4}}{(1+Pr)}\,\sin(\gamma - \gamma_0) \\
\text{with} \quad \tan\gamma_0 &= \frac{\sqrt{Pr}(1+3Pr)}{2(1+2Pr)}
\end{aligned} \tag{6.14}$$

There are two important implications of this steady temperature variation, both of which depend strongly on the phase difference, γ, namely:

6.4 The Outer Region, $R_s \gg 1$

For the related problem of the steady variation of velocity and temperature in the outer region, the solution in the form of series expansion similar to equation (6.9) is sought. Therefore, the following expansions are used

$$\psi = \psi_0 + \varepsilon\,(\psi_{1s} + \psi_{1u}) + \cdots \tag{6.15}$$

$$\phi = \phi_0 + \varepsilon\,(\phi_{1s} + \phi_{1u}) + \cdots \tag{6.16}$$

with particular interest in the dominant contributions of the time–independent portions of each, namely the steady component of the $O(\varepsilon)$ term, ψ_{1s}, in equation (6.15) for the stream function and the $O(\varepsilon)$ term, ϕ_{1s}, in (6.16) for the temperature. For completeness it is also useful to quote the solution for the basic leading order contribution to the stream function, ψ_0 in equation (6.15), obtained by Riley [see equation (3.11)]. For the leading order temperature, ϕ_0 in eqiation (6.16), matching (as $\eta \to \infty$) with the exponentially decaying oscillatory behavior of the inner region in equation (6.10) shows that in the outer region $\phi_0 \equiv 0$.

Stuart [24] showed that the nature of the steady transport effects in the outer region is governed by the magnitude of the streaming Reynolds number, R_s. This parameter can be determined from the acoustic signal and the fluid properties as described (for the case of air) in [5]. In general, for a plane standing acoustic field in an ideal gas, R_s can be expressed as

$$R_s = \frac{c^2}{\omega \nu \gamma_r^2} \left(\frac{p_0}{p_m} \right)^2 \tag{6.17}$$

where (p_0/p_m) is the pressure amplitude ratio, which is oftentimes the measured parameter used to characterize strong acoustic fields.

For large values of R_s and $Pr = O(1)$ being considered here, the variation of the steady terms ψ_{1s} and ϕ_{1s} in this outer region exhibits a boundary layer behavior as mentioned before. Although this boundary layer region is thin on the scale of the sphere radius, it is much thicker than the inner Stokes layer. This region has to be analyzed by a *numerical* solution of the governing equations subject to suitable matching conditions from the inner region. These equations themselves have to be obtained in a not entirely trivial manner as described by Riley [20]; the procedural details have been omitted here and the relevant equations as developed in [5]have simply been summarized below in their final forms. The outer boundary layer variables are defined as,

$$\bar{\eta} = (r-1)\sqrt{R_s} \tag{6.18}$$

and

$$\bar{\psi}_{1s}(\bar{\eta}, \bar{\mu}) = \psi_{1s}(r, \bar{\mu})\sqrt{R_s}, \quad \bar{\phi}_{1s}(\bar{\eta}, \bar{\mu}) \equiv \phi_{1s}(r, \bar{\mu}). \tag{6.19}$$

For convenience these are expressed in terms of commonly used symbols for the coordinates and suitably defined "artifical" velocities,

$$y \equiv \bar{\eta} \ , \ x \equiv \bar{\mu} \ , \ u = \frac{\partial \bar{\psi}_{1s}}{\partial \bar{\eta}} \ , \ v = -\frac{\partial \bar{\psi}_{1s}}{\partial \bar{\mu}} \tag{6.20}$$

along with

$$t(x, y) \equiv \bar{\phi}_{1s}(\bar{\mu}, \bar{\eta}). \tag{6.21}$$

The governing equations in these variables are,

$$\frac{\partial u}{\partial x} + \frac{\partial v}{\partial y} = 0 \tag{6.22}$$

$$u\frac{\partial u}{\partial x} + v\frac{\partial u}{\partial y} + \frac{xu^2}{(1-x^2)} = \frac{\partial^2 u}{\partial y^2} \tag{6.23}$$

$$u\frac{\partial t}{\partial x} + v\frac{\partial t}{\partial y} = \frac{1}{Pr}\frac{\partial^2 t}{\partial y^2} \tag{6.24}$$

with boundary conditions

$$u = \frac{45}{16}\,x\,(1-x^2), \quad v = 0, \quad t = x\,\Phi_{1\infty} \;\text{ at } y = 0 \tag{6.25}$$

$$u \to 0, \quad t \to 0 \qquad \text{as } y \to \infty \tag{6.26}$$

It may be recalled from the brief discussion at the end of §3, that the limiting value of the temperature from the inner region, $\Phi_{1\infty}$ in equation (6.14), prescribes the driving temperature for the outer region as is clear from the temperature boundary condition in equation (6.25).

The governing equations are now completely defined and can be solved with the help of a suitable numerical method. The coupled set of nonlinear partial differential equations for u and v are first solved using an implicit finite-difference scheme with marching of the solution from the equator ($x = 0$) to the poles ($x = \pm 1$). All the derivatives are approximated by central differences and the nonlinearity is handled by quasi-linearization and iteration at each x-station along the periphery. Owing to the decoupled nature of the momentum and energy equations, once u and v have been determined, the temperature, t, can be found in a relatively straightforward non–iterative manner using triangular resolution and backward substitution. The symmetry about the equatorial plane is exploited to carry out the procedure over only one hemisphere. Further details of the discretization scheme and the grid parameters as well as an account of the means of accomodating the converging flow in the polar regions may be found in [5].

It must be emphasized that the system of governing equations and boundary conditions presented above for the outer region, is strictly valid only for cases of strong streaming motion ($R_s \gg 1$) in moderate Prandtl number fluids ($Pr \sim 1$).

1. Equation (6.13) predicts a nonzero fluid temperature gradient at the sphere wall given by

   $$\left.\frac{\partial \Phi_{1s}}{\partial \eta}\right|_{\eta=0} = \frac{3\bar{\mu}}{\sqrt{2}}\,\sin(\gamma_1 + \tfrac{1}{4}\pi)\,\sin(\gamma - \gamma_1)$$

   with

   $$\tan\gamma_1 = \frac{\sqrt{Pr}-1}{\sqrt{Pr}+1}. \tag{6.27}$$

   This yields an average *inner* Nusselt number (based on the sphere diameter) for the corresponding heat transfer rate over each hemisphere.

2. The variation in equation (6.14) also prescribes a temperature at the outer edge of the inner Stokes region ($\Phi_{1s}(\eta \to \infty) \to \bar{\mu}\,\Phi_{1\infty}$) which in turn determines the steady temperature distribution in the outer region.

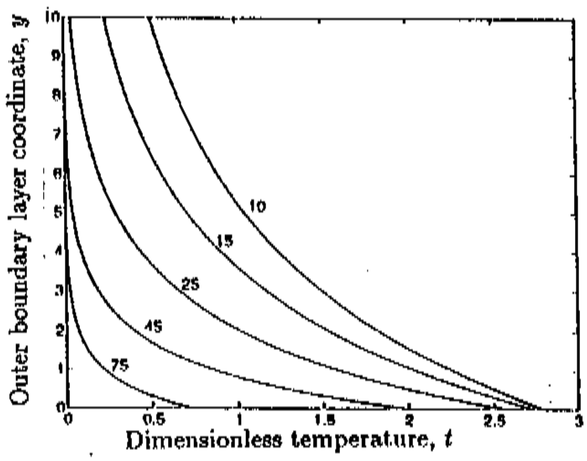

Figure 6.1: Outer boundary-layer temperature profiles for air ($Pr = 0.7$) for the case $(\gamma - \gamma_0) = \frac{1}{2}\pi$ and $R_s \gg 1$. The corresponding angular locations are degrees [6].

6.5 Discussion

It should be noted at the outset that the results for the steady flow field, ψ_{1s}, are known and a representative plot of the boundary layer velocity profiles may be found [5]. It is the variation of the steady temperature and the related heat transfer effects which will be of special interest in this study.

A representative plot of the numerically determined outer boundary layer temperature profiles for air ($Pr = 0.7$) is given in Fig. 6.1 for the case of $(\gamma - \gamma_0) = \pi/2$ and $0° < \theta \leq 90°$. For the other hemisphere ($90° \leq \theta < 180°$), the sign on the temperature values is reversed and the corresponding distribution may be simply obtained by a reflection about the y–axis.

Also of interest, is the variation of the local heat flux over the periphery of the sphere. This is characterized by the local driving temperature gradient for the outer region, $(-\partial t/\partial y)_{y=0}$, which is plotted in Fig. 6.2, also for $Pr = 0.7$ and $(\gamma - \gamma_0) = \pi/2$. The observed trend in this figure may be explained as follows: since, according to equation (6.25), $t \sim x$, the magnitude of the temperature and its gradient increase with $|x|$ as the flow progresses from the equator to the poles. However, as the flow converges towards the poles ($x = \pm 1$), continuity dictates a thickening of the boundary layers. This in turn reduces the driving fluid temperature gradient, which becomes negligible as $x \to \pm 1$, where there is a breakdown of the boundary layer structure of the flow. The temperature gradient thus reaches a maximum at some intermediate angular location, which for air ($Pr = 0.7$), occurs at $\theta \approx 45°, 135°$. The resulting heat transfer rate with the fluid (over each hemisphere) can be characterized by an average *outer* Nusselt number (based on the sphere diameter) by numerically integrating this

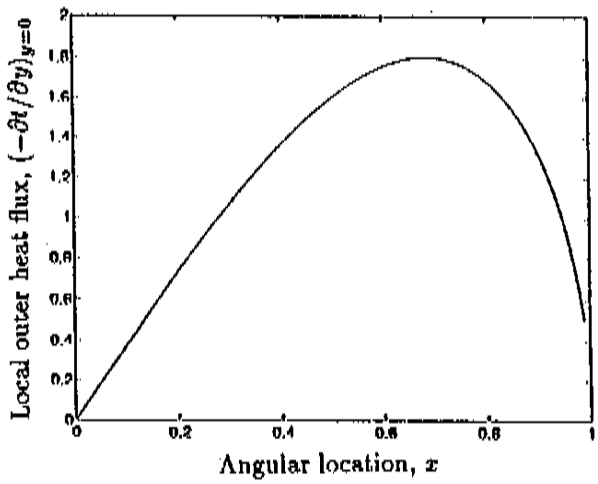

Figure 6.2: Distribution of the local heat flux for air ($Pr = 0.7$) over the upper hemisphere for $(\gamma - \gamma_0) = \frac{1}{2}\pi$ and $R_s \gg 1$ [6].

driving temperature gradient. For air ($Pr = 0.7$) this gives

$$\frac{Nu_0}{\varepsilon\sqrt{R_s}} = \int_0^1 \left(-\frac{\partial t}{\partial y}\right)_{y=0} dx \approx 1.20\ \sin(\gamma - \gamma_0) \tag{6.28}$$

An observation of the $\bar{\mu}$–dependence of the temperature in equations (6.13)–(6.27) (and hence in equation (6.25)) shows that the driving temperature and its gradient in both the inner and outer regions, are antisymmetric about the plane of the equator. This indicates that the Nusselt number result in (6.28) is only valid for each hemisphere, and there is no net exchange of heat between the entire sphere and the fluid. Such a situation is physically realized in the *fluid* by an equal amount of cooling and heating in each hemispherical portion of the domain, while within the *solid* sphere it takes the form of a steady flow of heat into a hemisphere and out the other, across the equatorial plane. Thus in the sphere, this time averaged heat flow rate is capable of inducing a steady temperature gradient across its poles. It is also clear from these Nusselt number results that the magnitude and direction of this heat flow strongly depend on the relation between the imposed phase difference, γ, and the innate phasing provided by the fluid via γ_0 and γ_1, which is a characteristic feature of such thermoacoustic flows.

In concluding, it is emphasized that this fundamental problem serves to underline the importance of the ability to induce steady heat transfer rates to/from a body subject to time–periodic temperature fluctuations. A suitably chosen acoustic field is an important participant here and without it, the body *does not* experience a *steady* exchange of heat with the surrounding fluid.

Bibliography

[1] B.J. Davisdson and N. Riley. Cavitation microstreaming. *J. Sound Vib.*, **15**:217–233, 1971.

[2] S.A. Elder. Cavitation microstreaming. *J. Acoust. Soc. Amer.*, **31**:54–, 1959.

[3] M. Evander, L. Johansson, T. Lilliehorn, J. Piskur, M. Lindvall, S. Johansson, M. Almqvist, T. Laurell, and J. Nilsson. Noninvasive acoustic cell trapping in a microfluidic perfusion system for online bioassays. *Anal. Chem.*, **79**:2984–2991, 2007.

[4] A. Gopinath. Steady streaming due to a small-amplitude torsional oscillations of a sphere in a viscous fluid. *Quart. J. Mech. Appl. Math.*, **46**:501–520, 1993.

[5] A. Gopinath and A.F. Mills. Convective heat transfer from a sphere due to acoustic streaming. *ASME J. Heat Transfer*, **115**:332–341, 1993.

[6] A. Gopinath and S.S. Sadhal. Thermoacoustic streaming effects from a sphere subject to a time-periodic temperature disturbance. In *Heat Transfer 1994*, Brighton, UK, August 1994. Tenth International Heat and Mass Transfer Conference.

[7] K. Hasegawa, Y. Abe, A. Kaneko, and K. Aoki. PIV measurement of internal and external flow of an acoustically levitated droplet. In *Sixth Interdisciplinary Transport Phenomena Conference*, 2009. Paper 24.

[8] Louis V. King. On the acoustic radiation pressure on spheres. *Proceeding of the Royal Society of London*, A147:212–240, 1934.

[9] L.V. King. On the acoustic radiation pressure on circular discs: Inertia and diffraction corrections. *Proc. Roy. Soc. Lond. A*, **153**:1–16, 1935.

[10] L.D. Landau and E.M. Lifshitz. *Fluid Mechanics* (English Edition). Pergamon Press, 1959.

[11] C.P. Lee and T.G. Wang. Outer acoustic streaming. *Journal of the Acoustical Society of America*, 88:2367–2375, 1990.

[12] Y.-H. Lee and C.-A. Peng. Enhanced retroviral gene delivery in ultrasonic standing wave fields. *Gene Therapy.*, **12**:625–633, 2005.

[13] M.S. Longuet-Higgins. Particle drift near an oscillating bubble. *Proc. Roy. Soc. Lond. A*, **453**:1551–1568, 1997.

[14] M.S. Longuet-Higgins. Viscous streaming from an oscillating spherical bubble. *Proc. Roy. Soc. Lond. A*, **454**:725–742, 1998.

[15] B.R. Lutz, J.Chen, and D.T. Schwartz. Microfluidics without microfabrication. *PNAS*, **100**:4395 4398, 2003.

[16] K. Ohsaka, A. Rednikov, S.S. Sadhal, and E.H. Trinh. Noncontact technique for determining viscosity from shape relaxation of ultrasonically levitated and initially elongated drops. *Rev. Sci. Instrum.*, **75**:2091–2095, 2002.

[17] K. Ohsaka, S.S. Sadhal, and A. Rednikov. Thermocapillary flow induced by laser-heating of an acoustically levitated flattened glycerin drop. *J. Heat Transfer.*, **124**:599, 2002.

[18] Lord Rayleigh. On the circulation of air observed in Kundt's tubes and some allied acoustical problems. *Phil. Trans. Roy. Soc. Lond. A*, **175**:1–21, 1884.

[19] A. Rednikov, H. Zhao, S.S. Sadhal, , and E.H. Trinh. Steady streaming around a spherical drop displaced from the velocity antinode in an acoustic levitation field. *Quart. J. Mech. Appl. Math.*, **59**:377 397, 2006.

[20] N. Riley. On a sphere oscillating in a viscous liquid. *Quart. J. Mech. Appl. Math.*, **19**:461–472, 1966.

[21] N. Riley. Acoustic streaming. *Theoret. Comput. Fluid Dynamics*, **10**:349–356, 1998.

[22] N. Riley. Steady streaming. *Ann. Rev. of Fluid Mech.*, **33**:43–65, 2001.

[23] H. Schlichting. Berechnung ebener periodischer Grenzchichtströmungen. *Physik Zeitschr.*, **23**:327–335, 1932.

[24] J.T. Stuart. Double boundary layers in oscillatory viscous flows. *J. Fluid Mech.*, **24**:673–687, 1966.

[25] E.H. Trinh and J.L. Robey. Experimental study of streaming flows associated with ultrasonic levitators. *Phys. Fluids*, **6**:3567–, 1994.

[26] H. Zhao, S.S. Sadhal, and E.H. Trinh. Internal circulation in a drop in an acoustic field. *J. Acoust. Soc. Amer.*, **106**:3289–3295, 1999.

[27] H. Zhao, S.S. Sadhal, and E.H. Trinh. Singular perturbation analysis of an acoustically levitated sphere: Flow about the velocity node. *J. Acoust. Soc. Amer.*, **106**:589–595, 1999.

M8 Applications

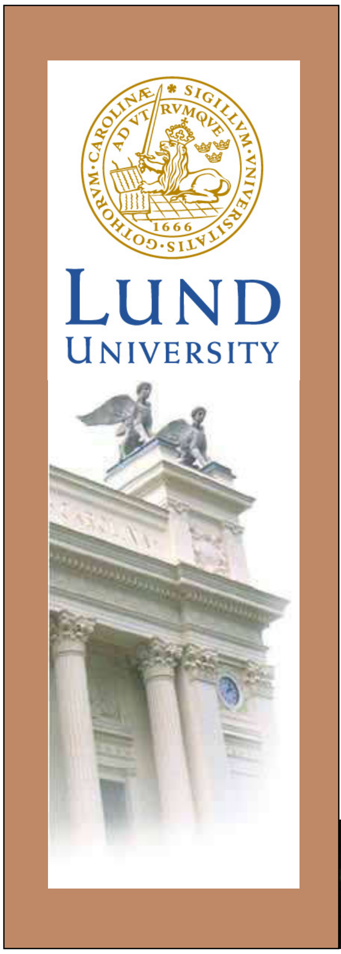

LUND UNIVERSITY

Acoustic valving and mixing in chemical microcreactors

Thomas Laurell

Dept. Measurement Technology & Industrial Electrical Engineering
Div. Nanobiotechnology
Lund Luniversity
Sweden

thomas.laurell@elmat.lth.se
www.elmat.lth.se/english/research

Valving in microscale

LUND UNIVERSITY

Moving parts

- Check valves
    - Active
    - Passive

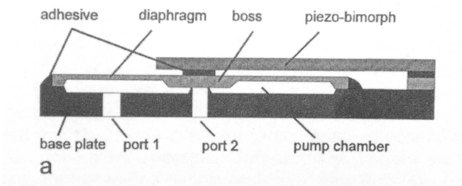

Zengerle MicroTAS 1996

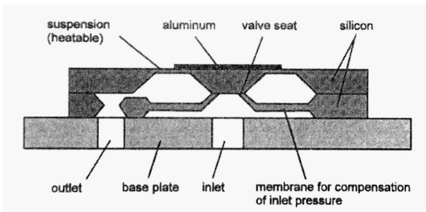

Zengerle MicroTAS 1996

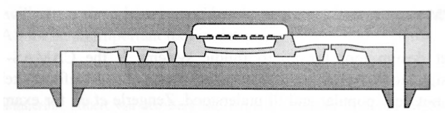

Fluitman J., MicroTAS 1994

Valving in microscale

Pneumatically actuated
Glass / PDMS-valves

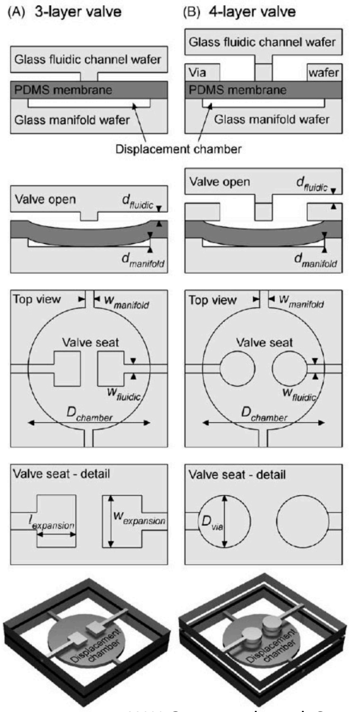

W.H.Groveretal. et al, SensorsandActuatorsB89(2003)315±323

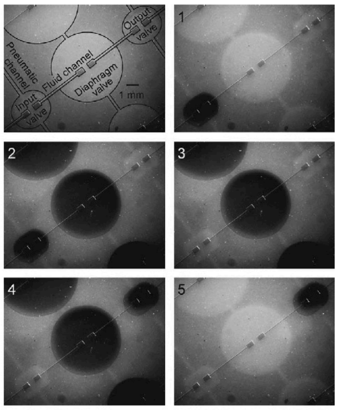

Pneumatically actuated
all PDMS-valves

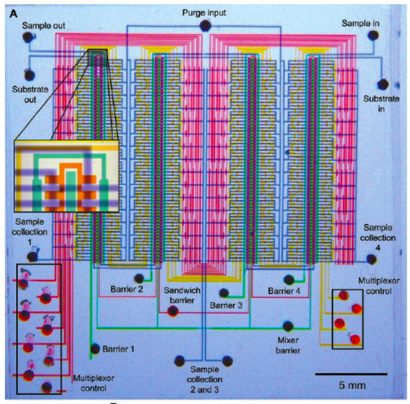

T. Thorsen. Et.al.
"Microfluidic Large Scale Integration",
Science 298: 580-584 (2002)

Hydrodynamic switching

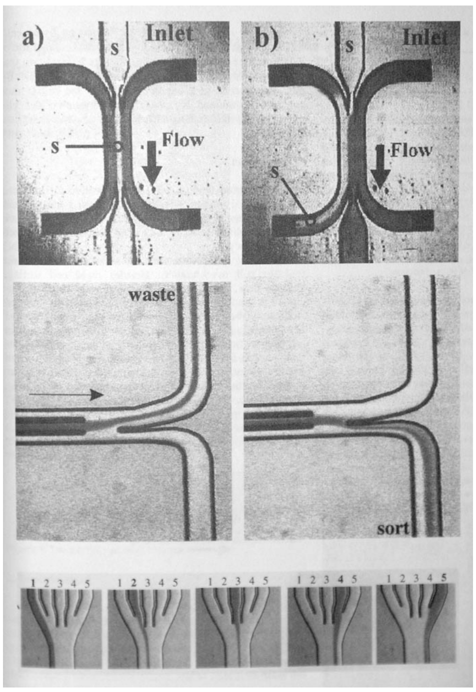

Branebjerg et al. MicroTAS 1996

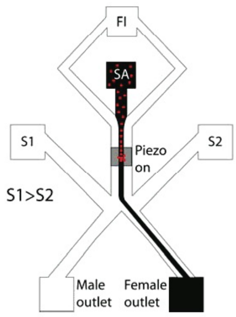

Vorehees J. et al. Anal Chem 2009, 81, 6089

Valving/switching by means of no moving parts

Preferred when fluid contains particulate or cellular matter

Avoids

- Mechanical wear
- Cell/particle loss
- Improved switching speed e.g. Flow cytometry

- Hydrodynamic switching
- Surface acoustic wave switching
- Optical switching
- Magnetic switching
- Dielectrophoretic
- USW wave switching/valving

Benefits

Simple
Non contact
No moving parts
Independent of pH & ionic properties etc
(not DEP)

Surface acoustic wave valving

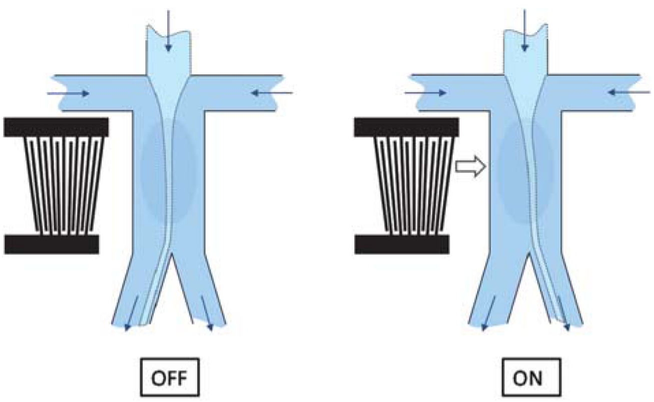

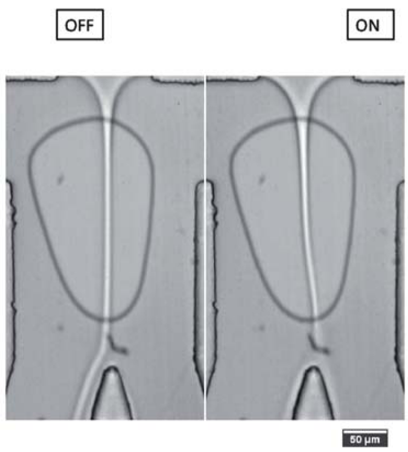

Franke et al., Lab Chip, 2010, 10, 789–794

Surface acoustic vave valving

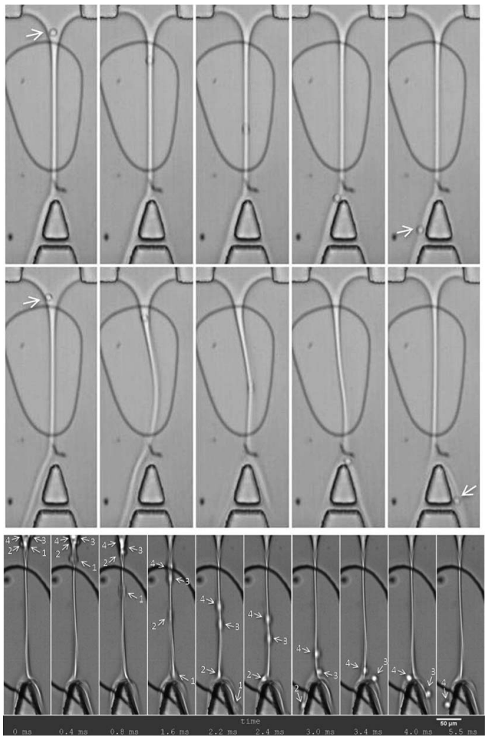

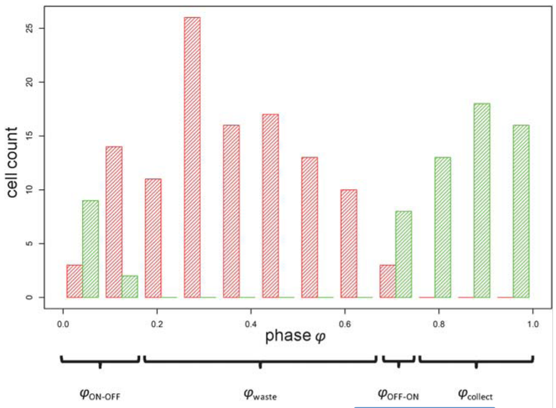

Frequency	$\varphi_{collect}$	φ_{waste}	$\varphi_{ON\text{-}OFF}$	$\varphi_{OFF\text{-}ON}$	collect	waste	# cells
MV3 cells (25 dBm)							
200 Hz	0.45	0.40	0.10	0.05	100 %	100 %	175
400 Hz	0.60	0.20	0.08	0.12	100 %	100 %	90
400 Hz	0.30	0.44	0.08	0.18	100 %	100 %	91
1000 Hz	(0.50)	(0.50)	--	--	78 %	81 %	149
2000 Hz	(0.60)	(0.40)	--	--	76 %	69 %	315
Mouse Fibroblast cells (33 dBm)							
2000 Hz	0.28	0.56	0.04	0.12	100 %	100 %	179
4000 Hz	(0.60)	(0.40)	--	--	79 %	64 %	87
HaCat cells (28 dBm)							
1000 Hz	0.08	0.17	0.33	0.42	100 %	100 %	136
2000 Hz	(0.67)	(0.33)	--	--	76 %	57 %	208

Franke et al., Lab Chip, 2010, 10, 789–794

Optical valving/switching

Optical tweezer

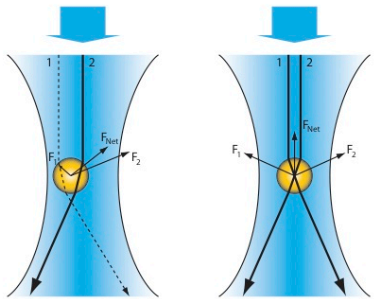

Different index of refraction
for live and dead cells

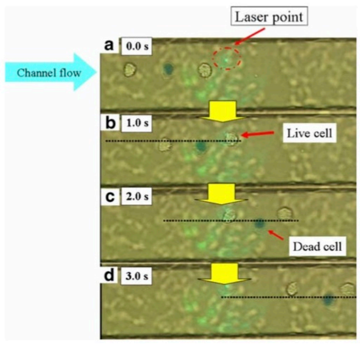

Murata M. Et al
Anal Bioanal Chem
(2009) 394:277–283

Interferometric optical lattices

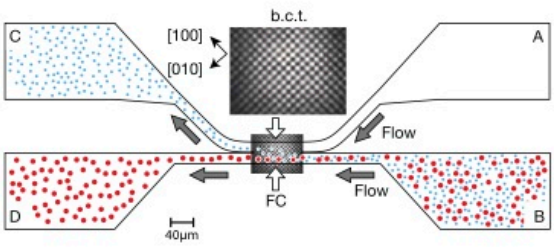

. P. MacDonald, G. C. Spalding and K. Dholakia, Nature,2003, 426, 421–424

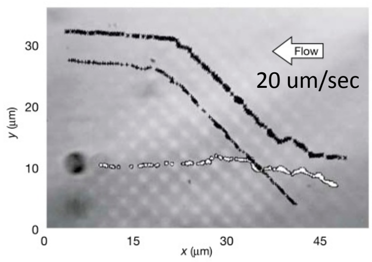

White dots trajectory 4 um capsle
Balck dots trajectory 8 um capsle

Multiple length-scale separation

$$\mathbf{F}_{mag} = \mathrm{m}\nabla\mathrm{B}$$

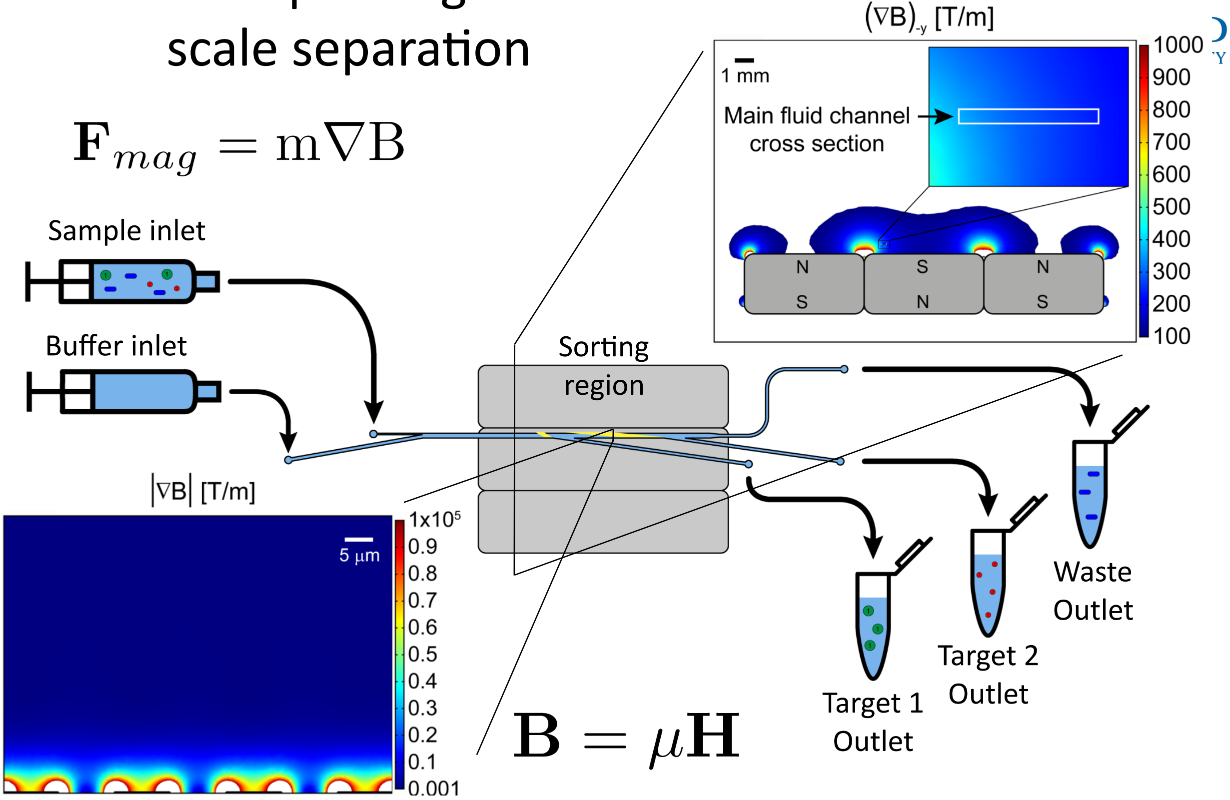

$$\mathbf{B} = \mu\mathbf{H}$$

Courtesy of Jonathan Adams, Tom Soh Lab, UC St. Barbara

Multitarget Magnetic Activated Cell Sorter

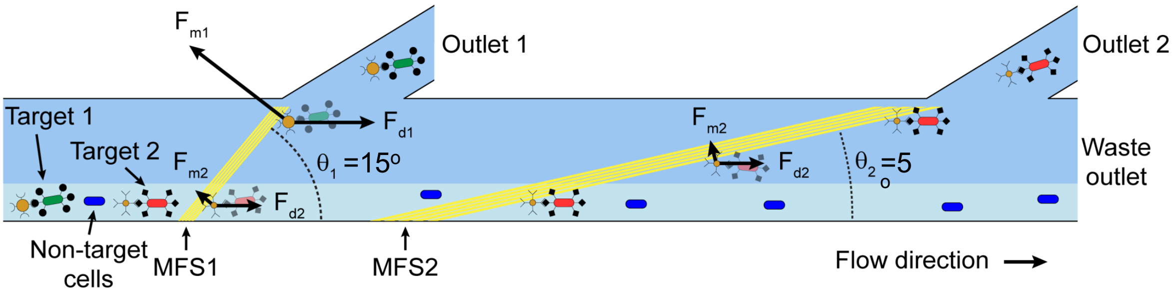

$$F_{mag} > F_{hyd}\sin(\theta)$$

$$F_{mag} \propto r^3$$

$$F_{hyd} \propto r$$

$$\approx C_1 r^2 > \sin(\theta)$$

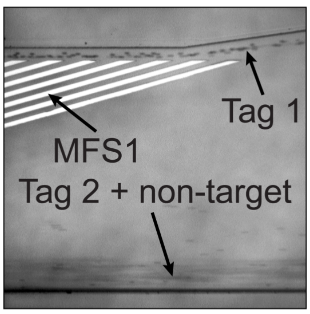

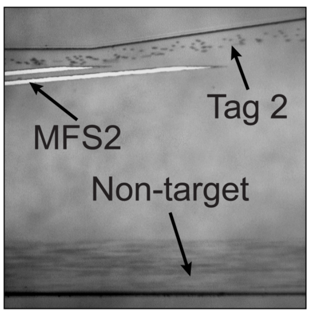

JD Adams, U Kim, HT Soh, *PNAS* **105**, 18165-18170 (2008)

Dielectrophoretic valving/switching

Tornay R.L. & Renaud P. et al, 08 LOC

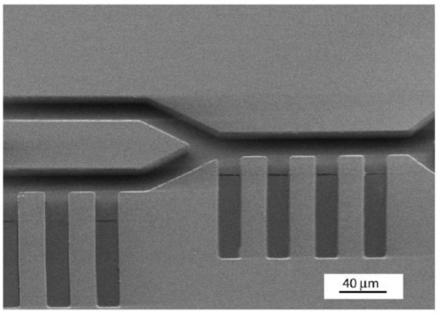

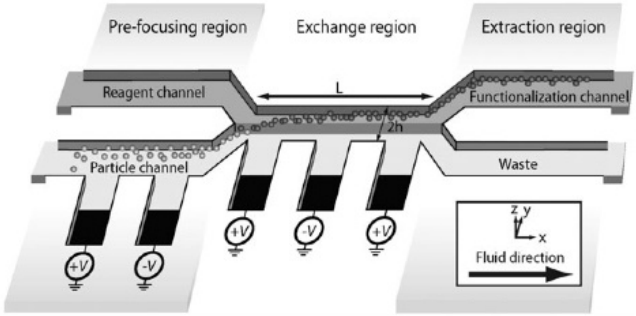

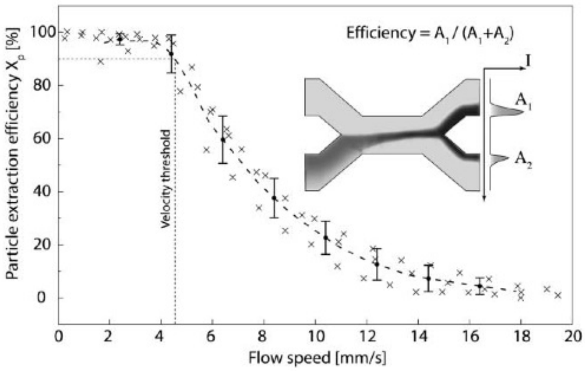

Acoustc valving
or
Harmonic switching

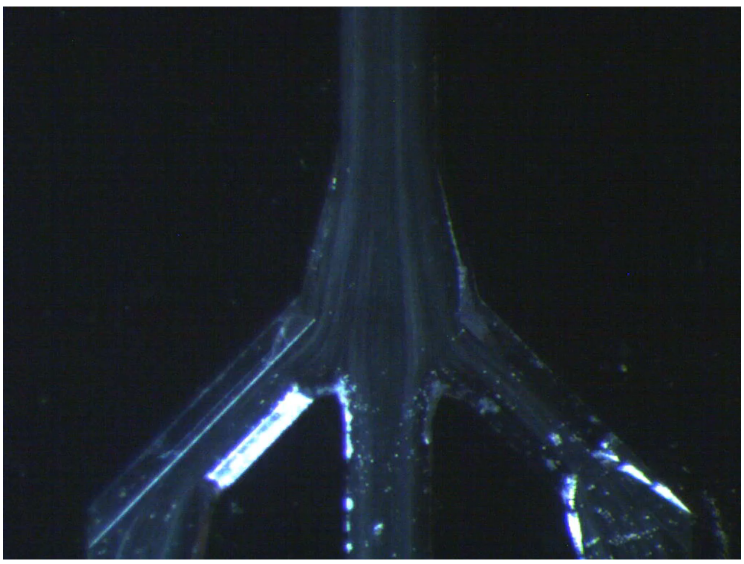

Binary valving

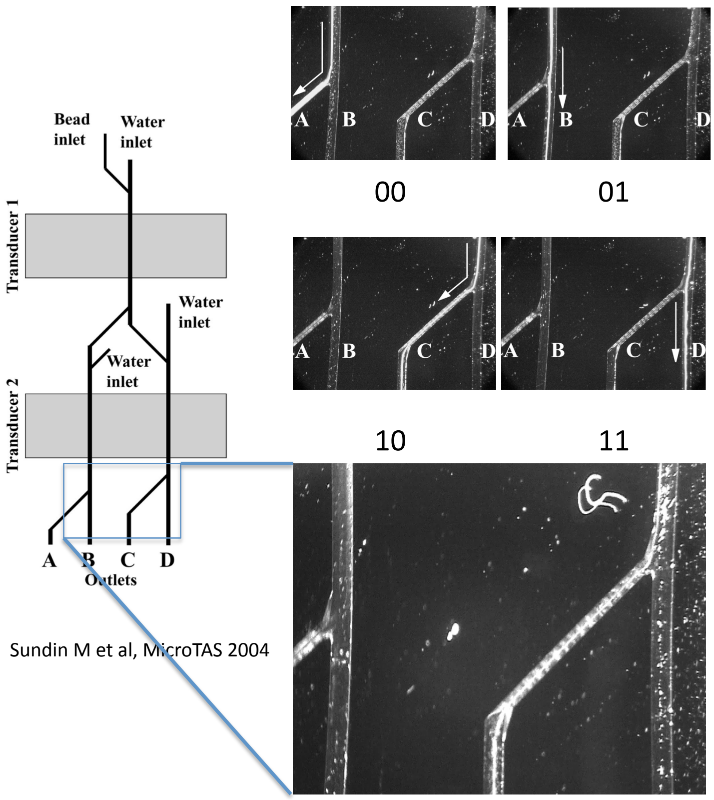

Sundin M et al, MicroTAS 2004

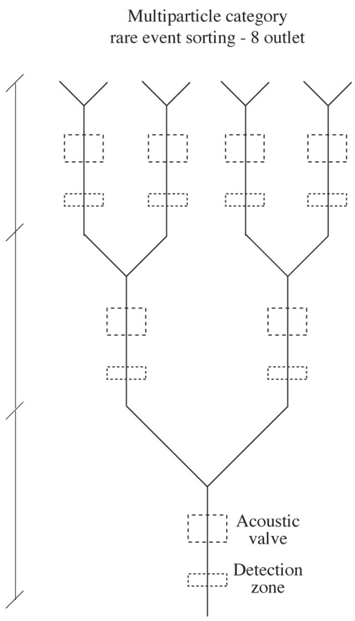

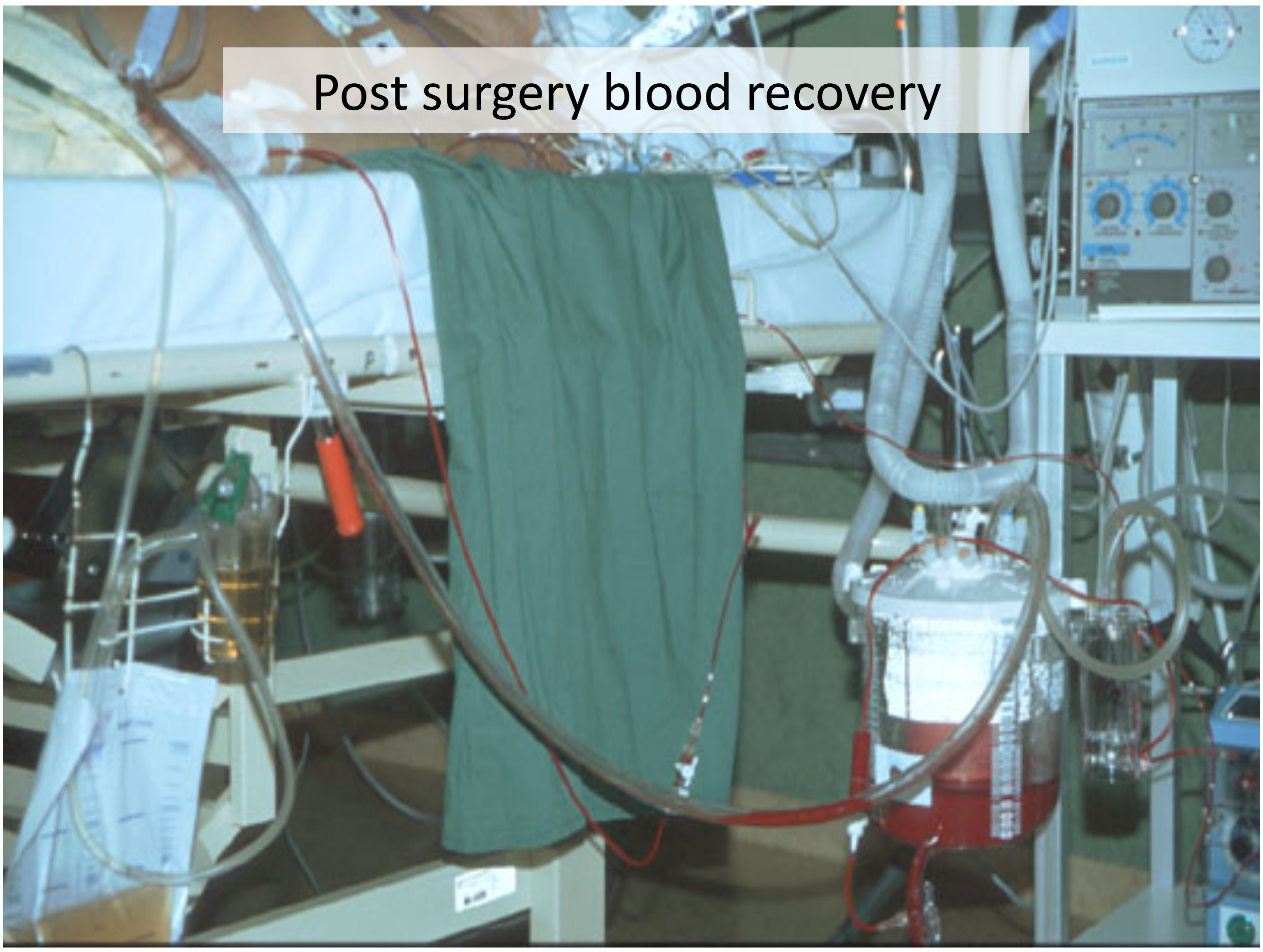

Blood constituents recovered post surgery

LUND UNIVERSITY

Substance	Normal range	Amount in shed blood	Times normal range	Possible effects
Il-6*	ca 10	27210	2700	Opens BBB, Neurotoxic Neuroprotective, fever, lowers SVR
Il-8*	<30	2321	80	Fever
TCC**	4,0	110	27	
C3b**	9,0	110	12	
TAT**	3,5	21000	6000	”harmless”
Protrombin**	1,0	430	400	Coagulation

** Unpublished data*

*** Flom-Halvorsen et al J Thorac Cardiovasc Surg 1999;118:610-7.*

Acoustic valving/washing of cells and particles

LUND UNIVERSITY

- clean medium enters in the centre lower inlet
- contaminated medium with particles enters on each side, lower inlet
- when the ultrasound is turned on the particles are shifted from the contaminated medium to the clean medium

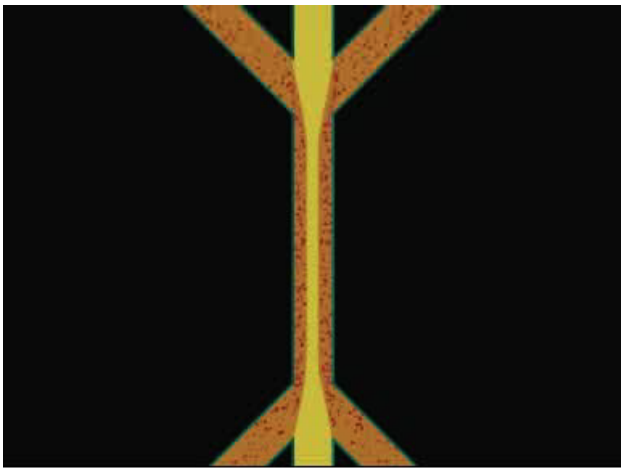

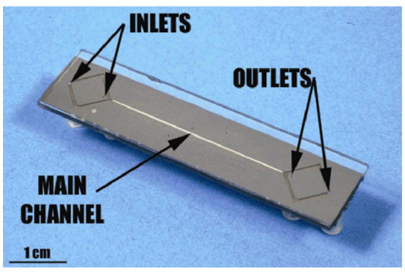

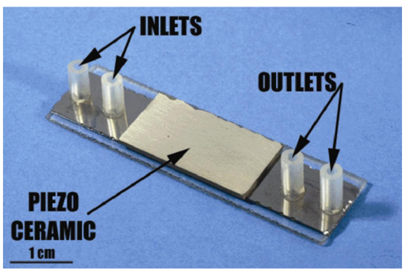

Buffer exchange/washing of cells

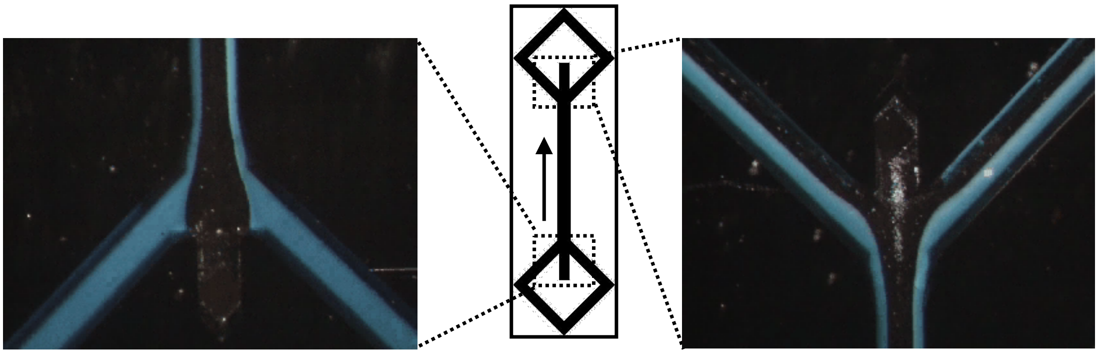

Ultrasound ON/OFF

Ultrasound ON

Contaminated fluid
- distilled water
- 5 µm white latex particles (5%)
- glycerol (1%)
- Evans blue (300 mg/L)

Clean fluid
- distilled water
- glycerol (1%)

Petersson F., Nilsson A., Holm C., Jönsson H., and Laurell T, Anal. Chem., 2005, 77, 5, 1216-1221

Carrier medium exchange efficency

Medium exchange effiency
vs.
contaminant concentration

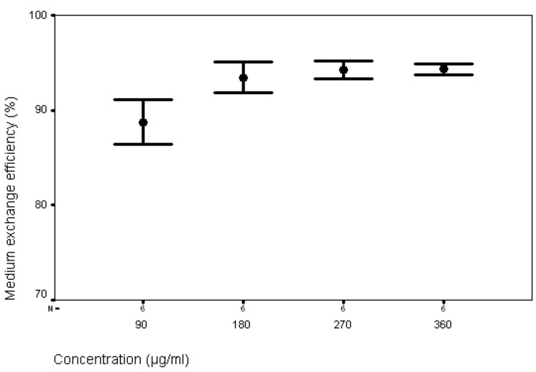

Activation voltage: 10 V_{pp}
Particle concentration: 1.5% by volume

Flow rate: 0.1 ml/min side inlets and centre outlet, 0.17 ml/min through centre inlet and side outlets

Medium exchange effiency
vs.
particle concentration

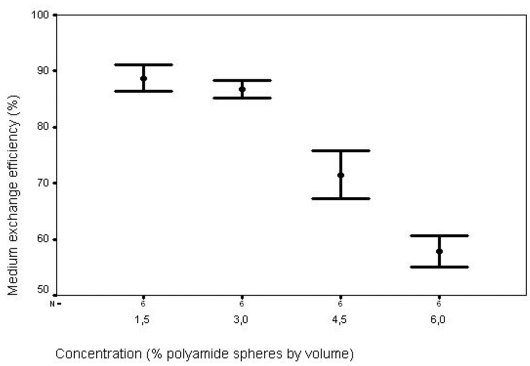

Activation voltage: 10 V_{pp}
Evans blue concentration: 90 µg/ml

Flow rate: 0.1 ml/min side inlets and centre outlet, 0.17 ml/min through centre inlet and side outlets

Chip integrated
Fluorescence Activated Acoustic Cell Sorting

- rare event multiplex sorting and acoustic enrichment -

Acoustic switching

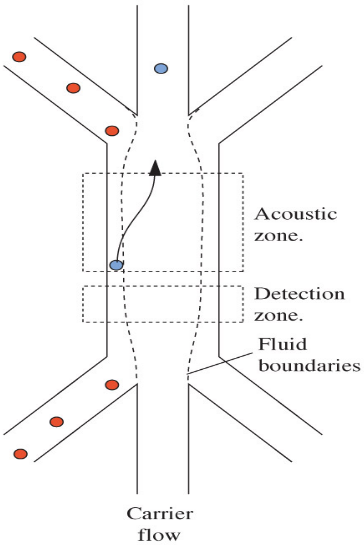

Acoustic trapping

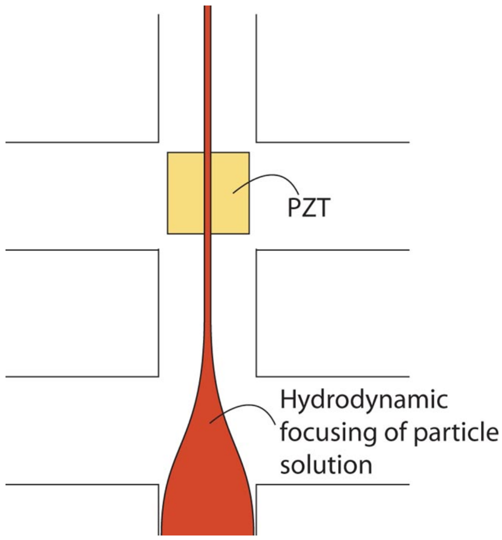

Fluorescence activated acoustic cell sorting FAACS

Photo Multiplier Tube (PMT) activated US-transducer

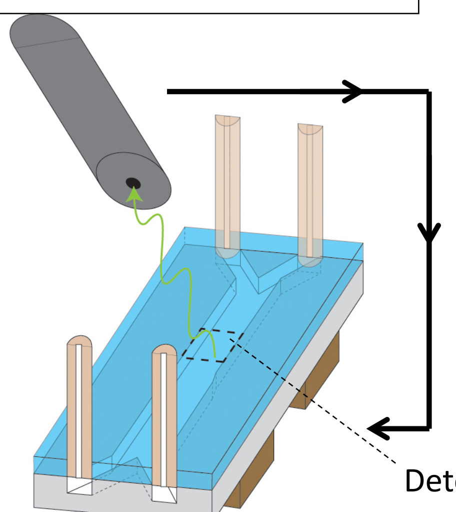

The PMT detects fluorescence and triggers the 2MHz acoustic transducer which switch the cells into the desired outlet

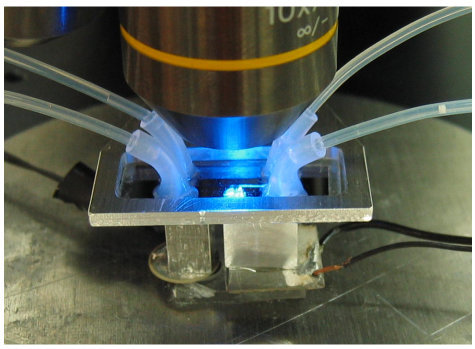

Grenvall C. et al. MicroTAS 2007

2D-acoustic focusing of particles

- Simultaneous **vertical and lateral** acoustic focusing
  - Uniform particle velocities
  - Particles migrate to the closest of the three common nodes

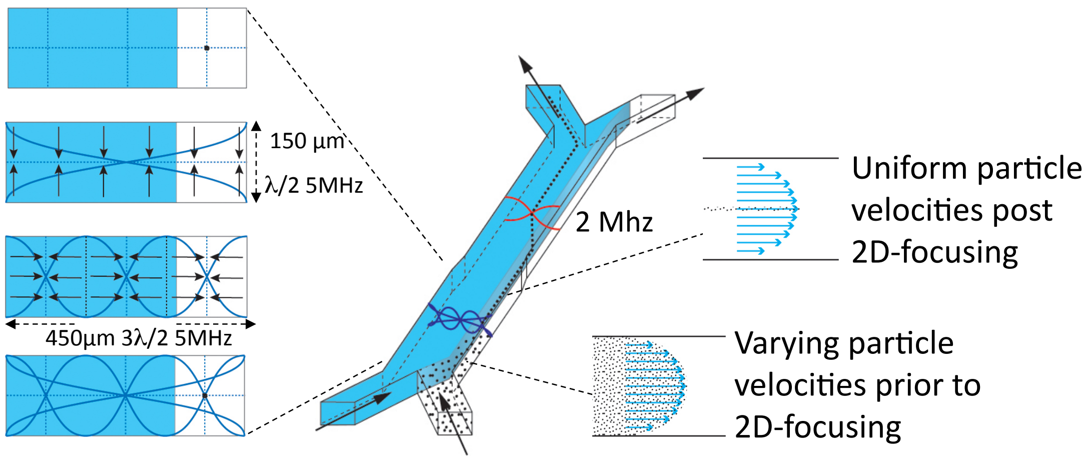

Grenvall C. et al. MicroTAS 2007

2D-acoustic focusing of particles

Uniform speed thanks to precise vertical and lateral positioning

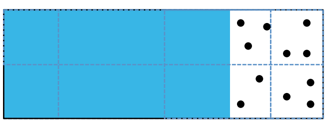

Side wall lamination
- varying particle speeds -

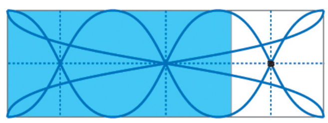

2D acoustic standing wave focusing
- uniform particle speeds -

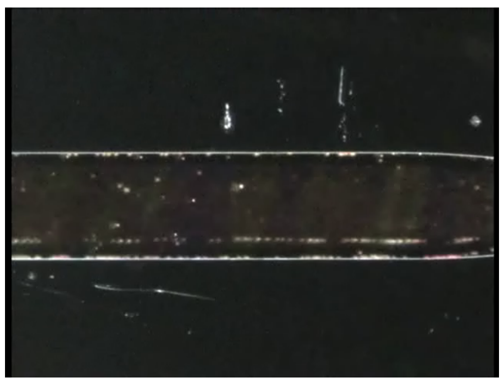

Grenvall C. et al. MicroTAS 2007

2D-focusing and acoustophoretic valving

Confined positioning in the vertical parabolic flow profile allows rapid on/off switching

Without 2D focusing	With 2D focusing	2D focusing &
Varying particle velocities - tailing of particles-	Uniform particle velocities – no tailing -	acoustic switching

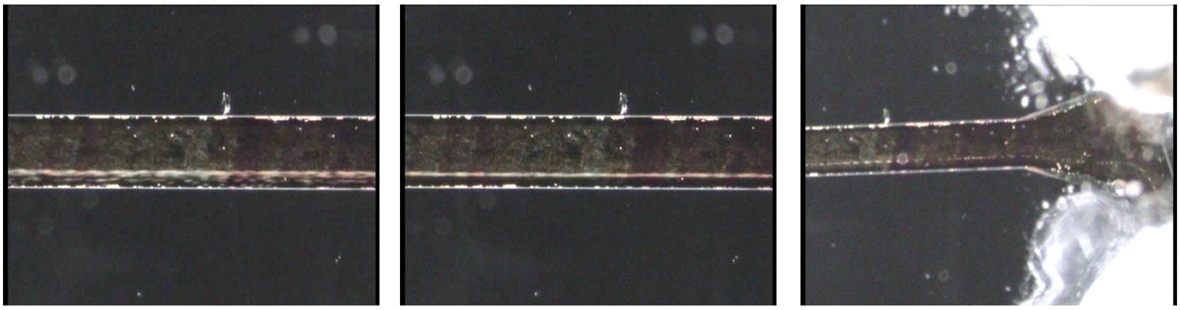

Grenvall C. et al. MicroTAS 2007

Fluorescence activated acoustophoretic particle sorting

µFAACS evaluation
- 100 particles/s
- 1:5000 6µm FITC / 8µm unmarked particle ratio

>95% of the FITC particles go into the collection channel

>99% of the unmarked particles go into the waste channel

== >100-fold increase in FITC vs unlabelled particle ratio

Collection outlet

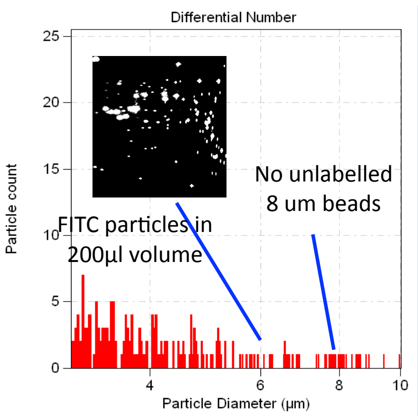

Waste outlet

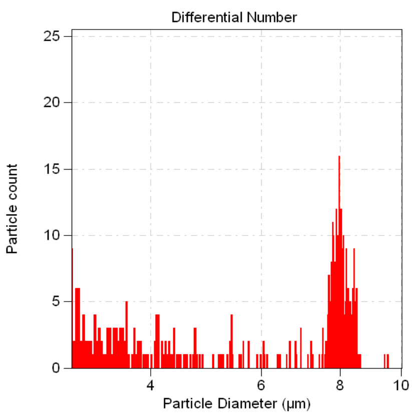

Grenvall C. et al. MicroTAS 2007

Acoustic switching of fluids

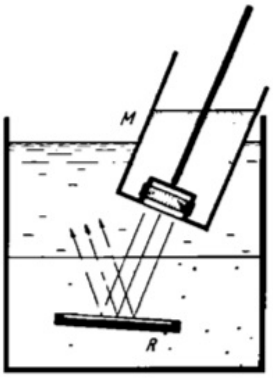

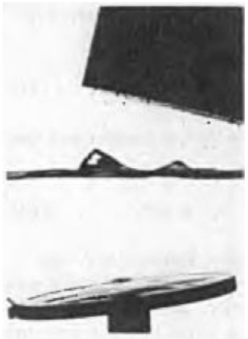

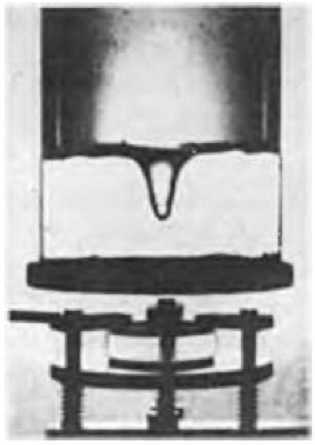

Hertz & Mende, Phys. 1939

Acoustic switching of fluids

Johansson L. et al, Anal Chem, 2009, 81, pp. 5188

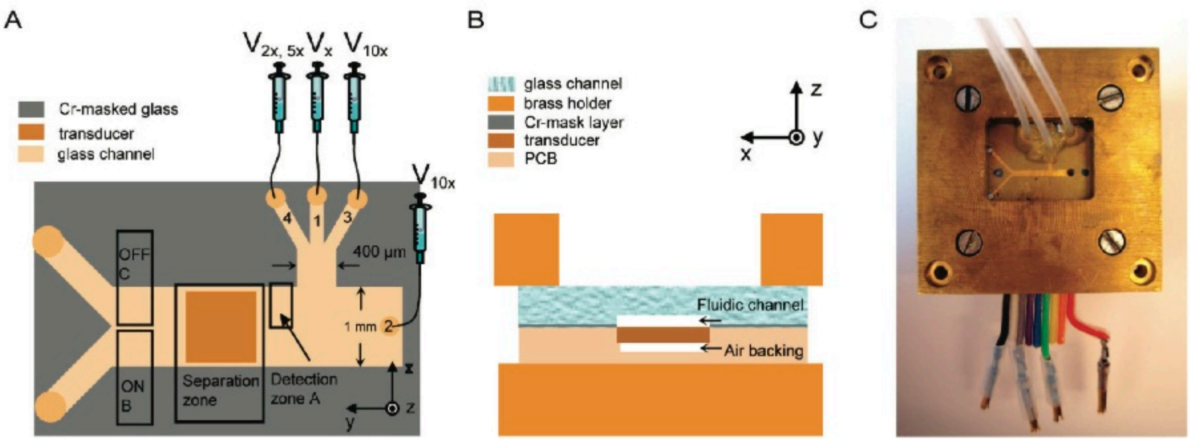

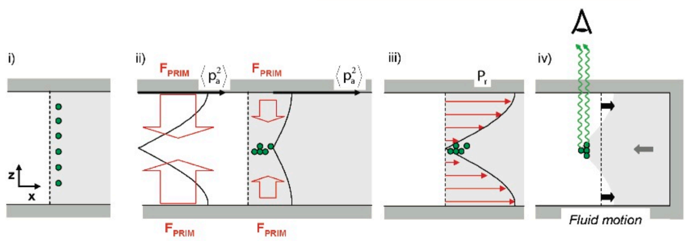

Acoustic switching of fluids

Johansson L. et al, Anal Chem, 2009, 81, pp. 5188

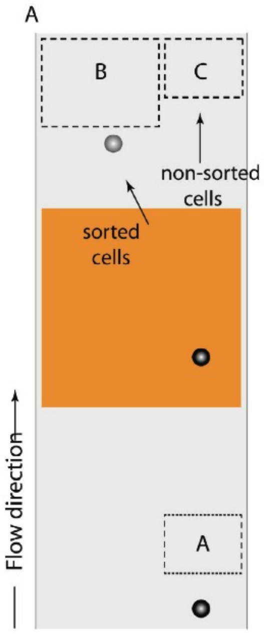

Table 1. Evaluation of the Automatic Detection and Sorting in Terms of Number of Beads (i) without Transducer Activation, (ii) Displacement of Every Bead, and (iii) Displacement of Every Second Bead[a]

manually counted	sorting algorithm	detection zone A	detection zone B	detection zone C
100 (19.6 beads min^{-1})	no sorting	99	0	94
100 (28.0 beads min^{-1})	all sorted	99	100	7
100 (22.0 beads min^{-1})	every second sorted	98	50	49

[a] The fluid flow is 3.4 mm s^{-1}.

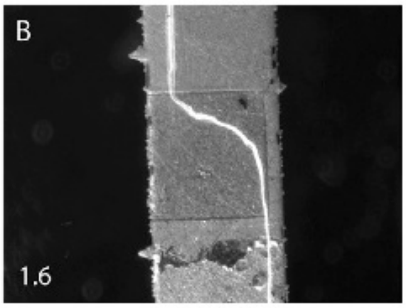

Direct ejection from well plates

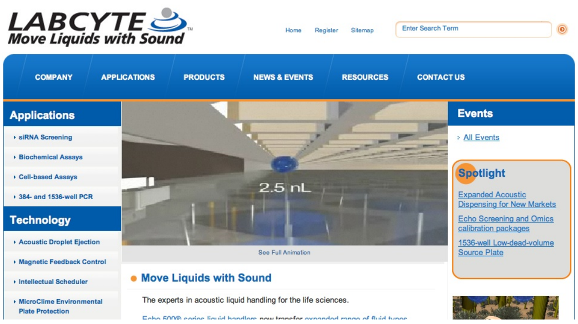

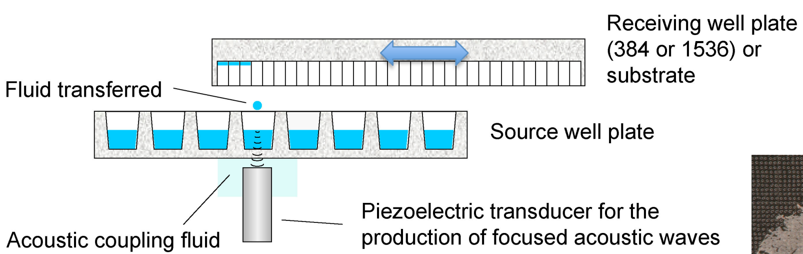

Drug screening
Genotyping assays
Imaging mass spectrometry

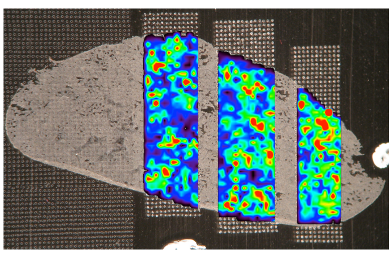

- 1 MHz - 200 nl
- 100 MHz - 10 pl

Miniaturisation
==>
Increased surface area to volume ratio
==>
Surface bound chemistry becomes beneficial
==>
Look for more surface area

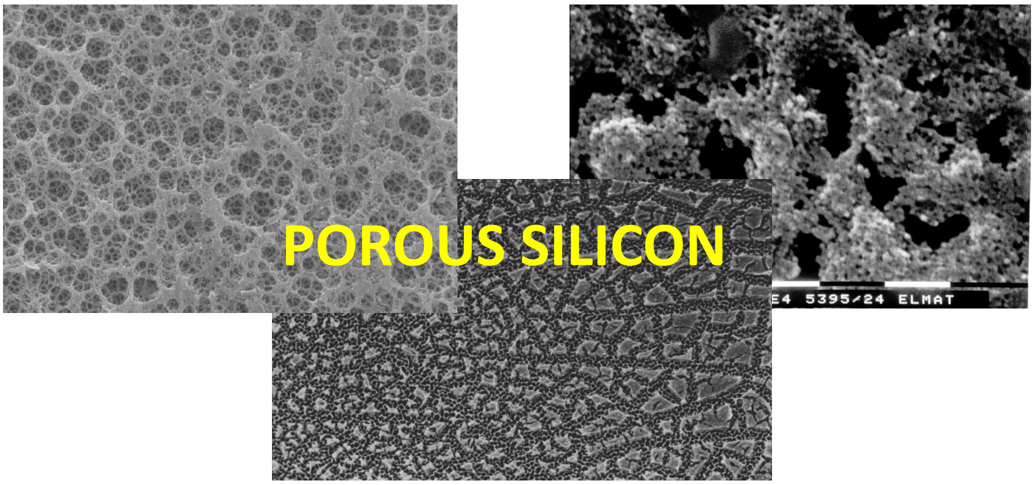

Porous silicon proteolytic microreactors

Typical dimensions:

Channel width: 50 μm
Channel depth: 250 μm
Channel length: ≈10 mm
Internal volume: 1-6 μl

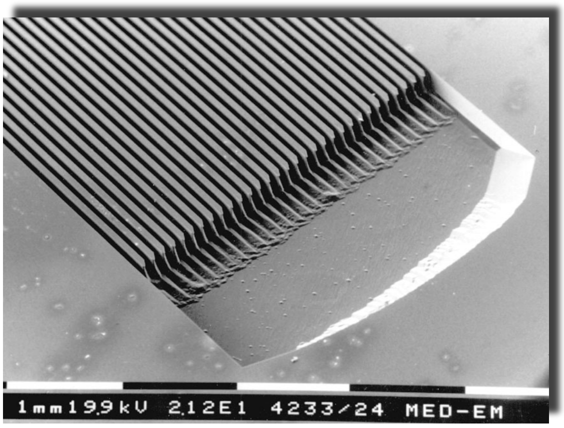

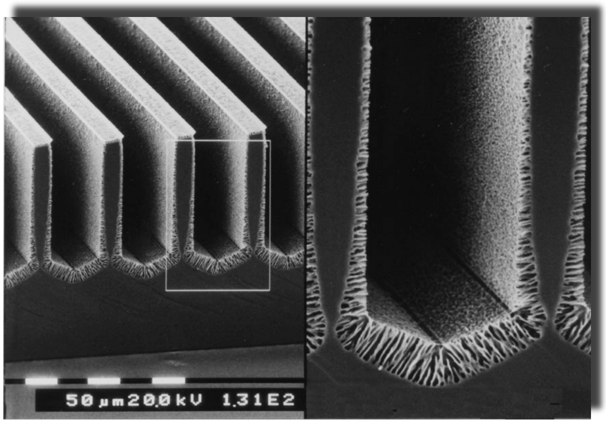

J. Micromech. Microeng., 7, No. 1, 1997, 14-23

Protein analysis by means of MALDI-TOF MS

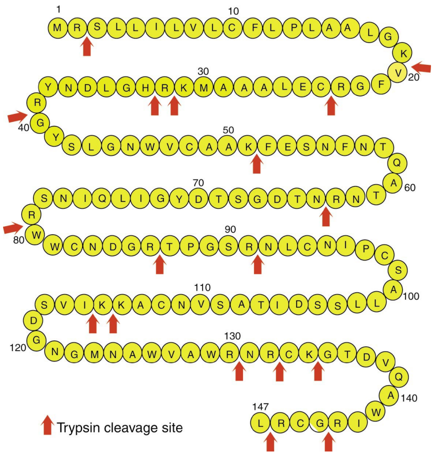

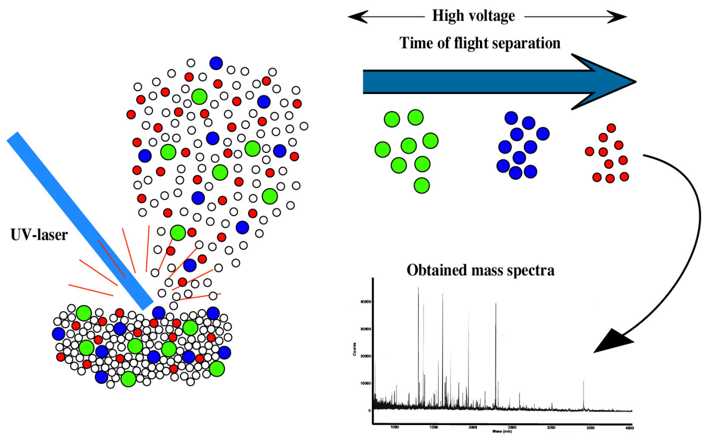

On-line protein digest in porous silicon microreactors

Digestion of 1 pmol Lysozyme
Sample volume 1 μl
Digestion time: 1 min

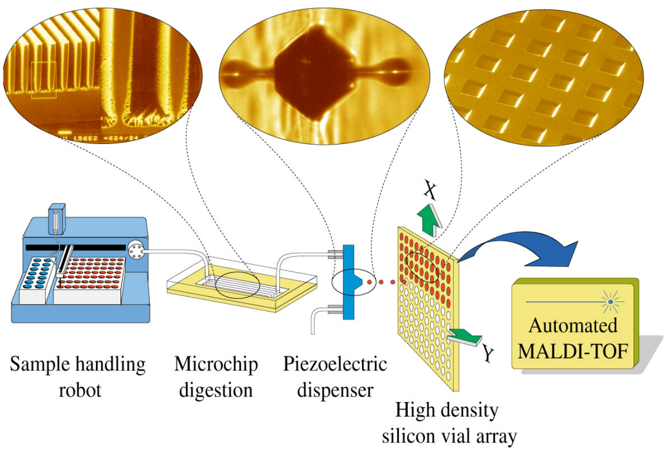

Trypsin microreactor
91 % sequence coverage

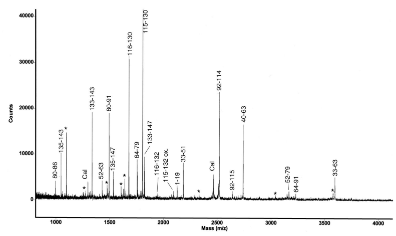

Chymotrypsin microreactor
64% sequence coverage

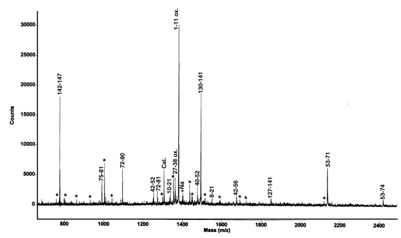

Ekström S. et al. Anal. Chem. 72 (2) 2000, 286-293

Open tubular microreactors substrate diffusion limited

AB + Enzyme ➔ A + B

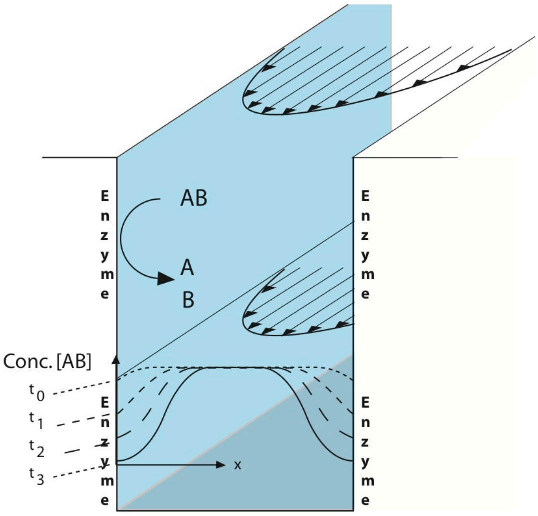

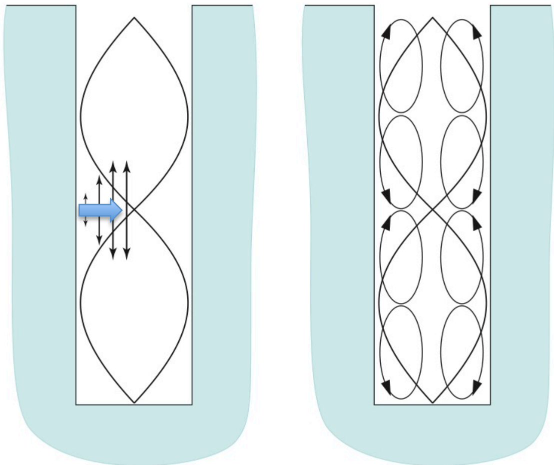

Validating Rayleigh mixing in deep open tubular reactor

Test channel

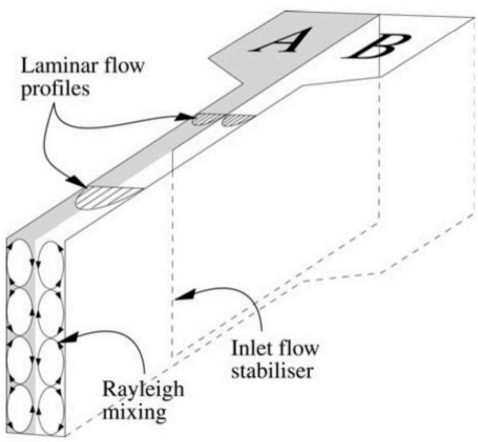

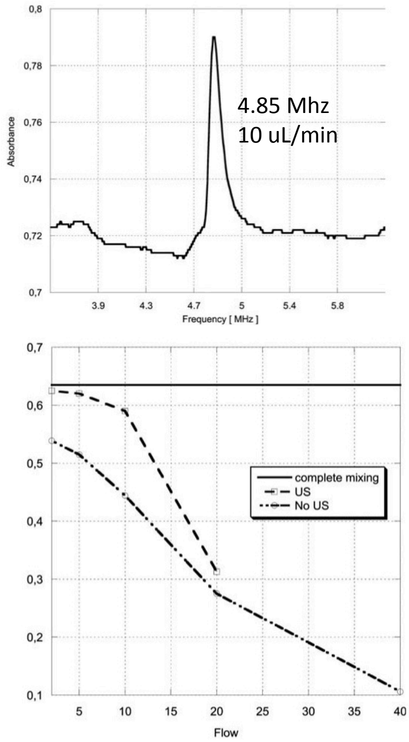

Enzymatic colourimetric test
Absorbancemesurement at 261 nm

Channel depth: 300 um
4.85 MHz in water => $\lambda/2$=305 um

Bengtsson M., **Laurell T.,** Ultrasonic agitation in microchannels, **Analytical and Bioanalytical Chem**, 2004, 378 (7):1716-1721

Rayleigh mixing in porous silicon parallel channel reactor

Manifold for Rayleigh mixing enhanced Proposu silcion enzyme reactor

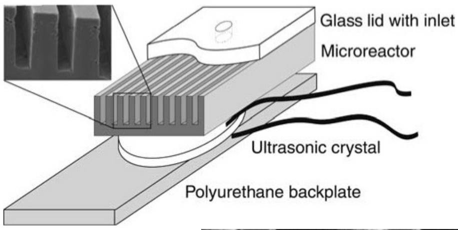

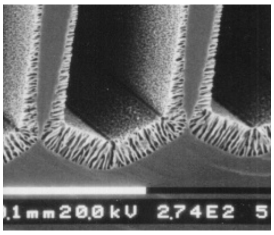

Colourimetric readout of the catalytic efficiency

Band broadening

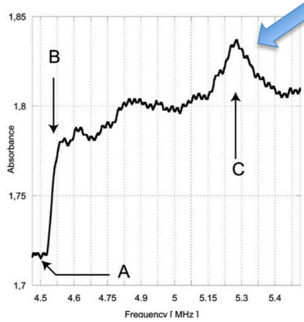

A – No Ultrasound
B – Ultrasound on
C – Resonance

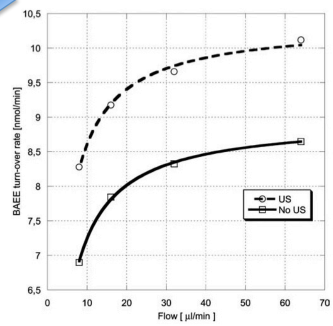

≈ 20% increase

Bengtsson M., **Laurell T.,** Ultrasonic agitation in microchannels, **Analytical and Bioanalytical Chem**, 2004, 378 (7):1716-1721

Acoustic switching of fluids

Coloured salt solution in side inlets with high density

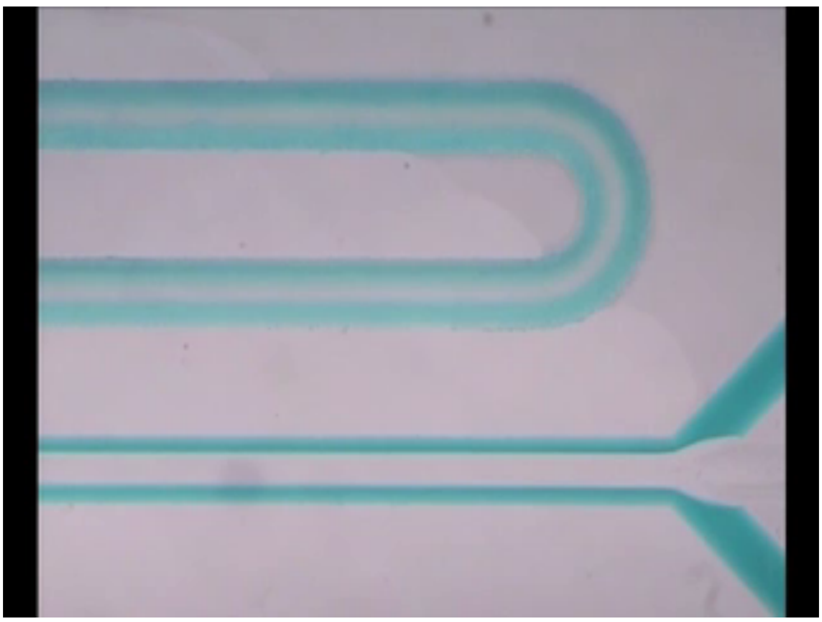

USWNet
Ultrasonic Standing Wave Network

LUND UNIVERSITY

USWNet 2010 Conference
2-3 October 2010
www.USWNet.com
Groningen
The Netherlands

Abstract deadline
June 25!!!!

Free flow acoustophoresis and binary acoustic separation

Thomas Laurell

Dept. Measurement Science & Industrial Electrical Engineering
Div. Nanobiotechnology
Lund Luniversity
Sweden

thomas.laurell@elmat.lth.se
www.elmat.lth.se/english/research

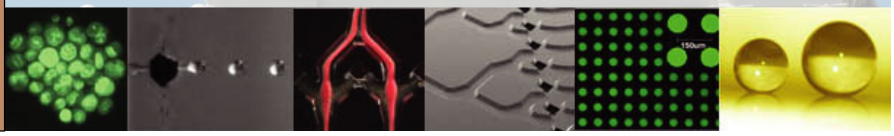

Particle separation

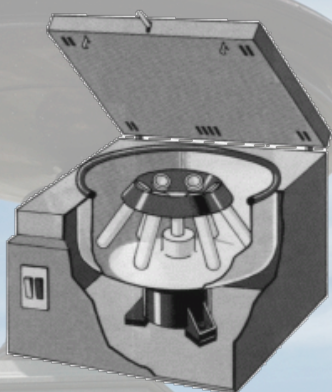

Ruled by centrifugation – density

Regular pelleting

Gradient centrifugation

Field flow fractionation - Pioneered by Giddings
Science 1993, 260, 5113, 1456-1465

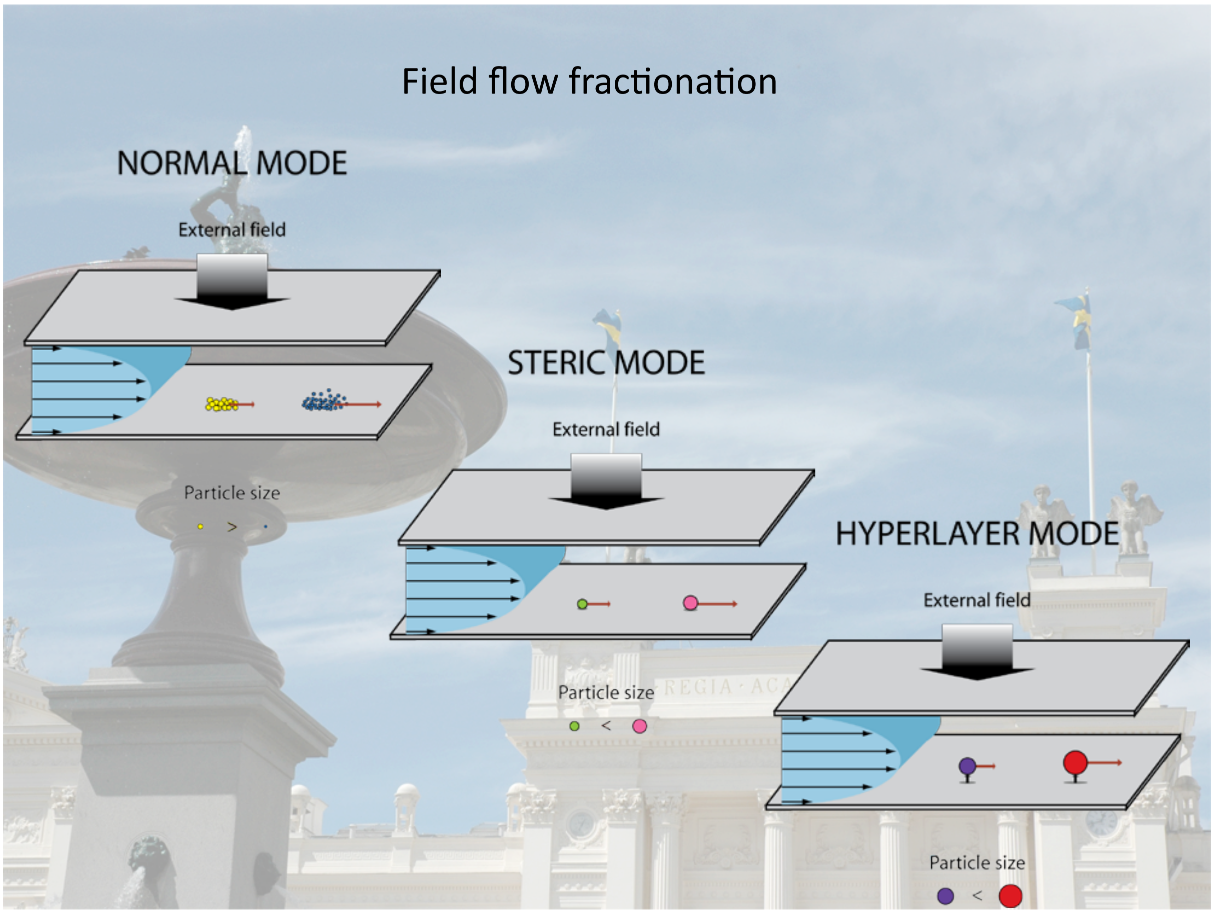
Field flow fractionation
NORMAL MODE
External field
Particle size
>
STERIC MODE
External field
Particle size
<
HYPERLAYER MODE
External field
Particle size
<

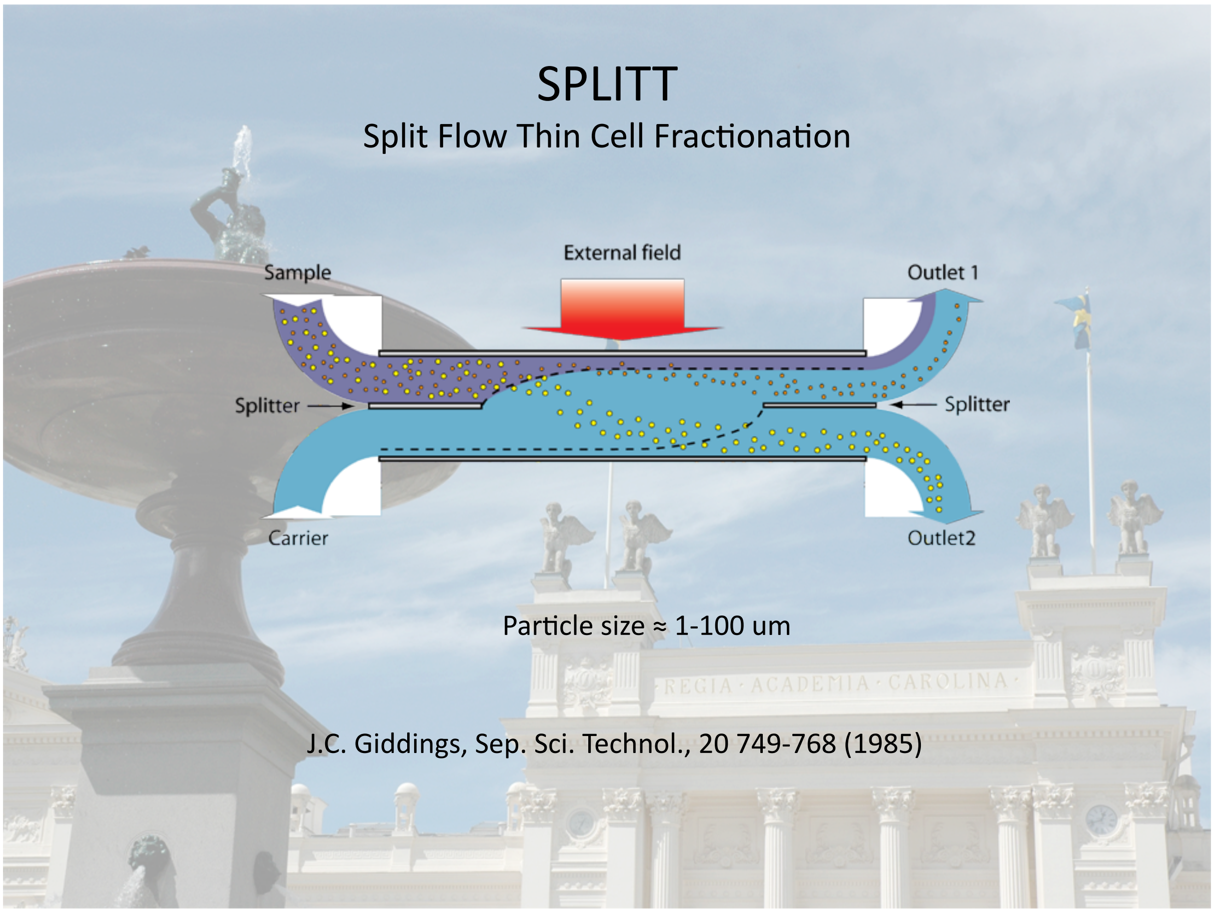
SPLITT
Split Flow Thin Cell Fractionation
External field
Sample
Outlet 1
Splitter
Splitter
Carrier
Outlet2
Particle size ≈ 1-100 um
J.C. Giddings, Sep. Sci. Technol., 20 749-768 (1985)

Feke, Separations Technology, 1995

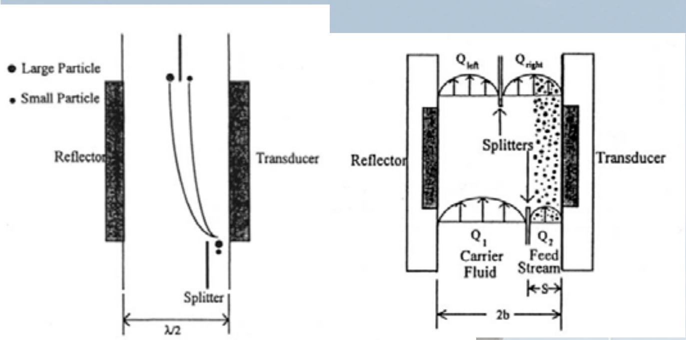

Kapishnikov,
J. Stat. Mech. 2006

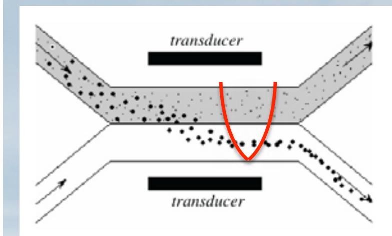

SU8-based
λ/4 channel

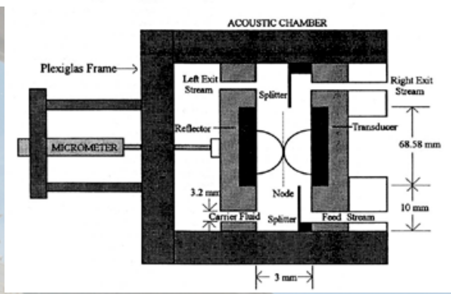

Red particels 170 um
Blue particles 100 um

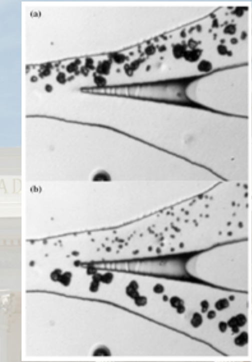

2.5 um
&
10 um
Particles

162 nl/sec

Q (mm²/s)	E_{ac} (J/m³)	N^*_{red} theory	N^*_{red} experiment	N^*_{blue} theory	N^*_{blue} experiment
12.82	0.0162	100%	98.05%	0.00%	3.10%
12.82	0.0162	100%	99.14%	0.00%	0.00%
12.82	0.0149	100%	85.23%	0.00%	8.12%
12.825	0.0149	100%	92.87%	0.00%	9.47%
7.28	0.0142	100%	94.48%	0.00%	1.40%

Acoustic standing wave particle focusing

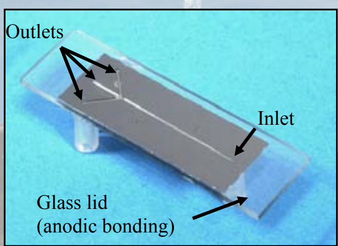

- wet etched in <100>-silicon
- channel width: 350 µm
- channel depth: 125 µm
- piezoelectric actuation
- fundamental frequency: ~ 2 MHz
- capacity: 0.1 ml/min

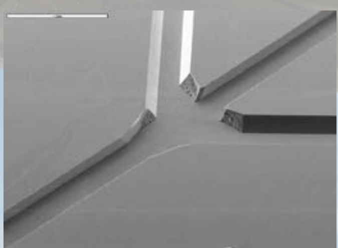

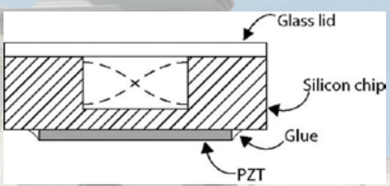

Nilsson A., Petersson F., Jönsson H. and Laurell T., Lab On A Chip, 2004, 4, 131 – 135

Shed blood during thoracic surgery cause lipid microembolisation of the brain

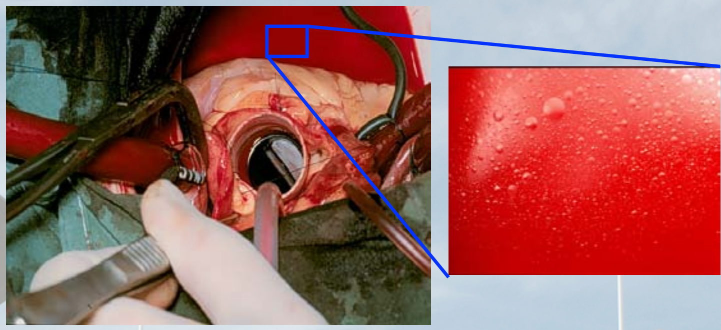

Lipid microemboli in dog brain

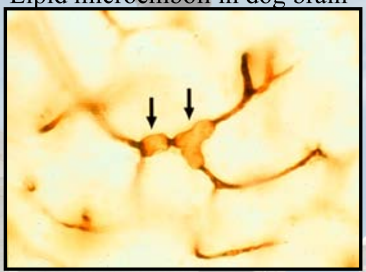

Picture by courtesy of Dr Dixon Moody

Incidence of cognitive decline after cardiac surgery

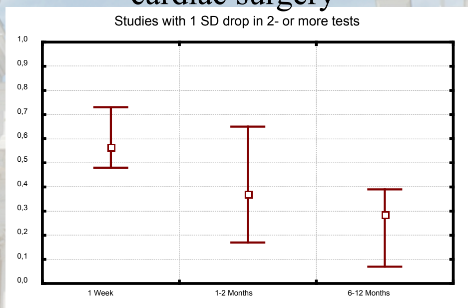

Acoustic parameters of blood

	Density [kg/m^3]	Compressibility [ms^2/kg]	Velocity [m/s]	Φ
fat	1,09E+03	3,58E-10	1,60E+03	**1,84E-01**
erythrocyte	9,20E+02	5,20E-10	1,45E+03	**-3,85E-01**
plasma	1,03E+03	4,09E-10	1,54E+03	

$$F_r = -\left(\frac{\pi P_0^2 V_c \beta_w}{2\lambda}\right)\cdot\Phi(\beta,\rho)\cdot\sin\left(\frac{4\pi z}{\lambda}\right) \qquad (1)$$

$$\Phi = (5\rho_{erythrocyte} - 2\rho_{plasma})/(2\rho_{erythrocyte} + \rho_{plasma}) - (\beta_{plasma}/\beta_{erythrocyte})$$

β_{plasma} = compressibility of the liquid
$\beta_{erythrocyte}$ = compressibility of the particle
ρ_{plasma} = density of the liquid
$\rho_{erythrocyte}$ = density of the particle
c = sound velocity

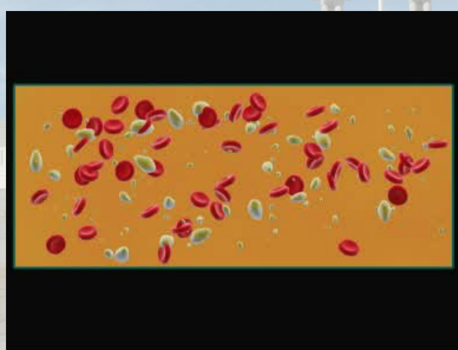

Lipid emboli elimination in blod

Cream and blood mixture

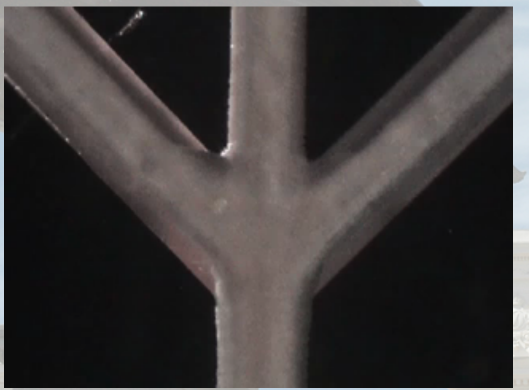

Patient blood from throacic surgery

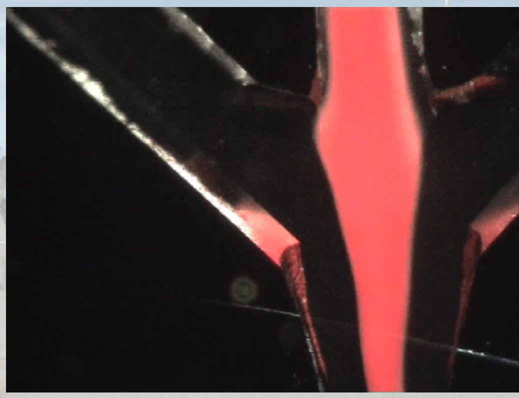

Petersson F., Nilsson A., Holm C., Jönsson H., and Laurell T., Lab Chip 2005

Bifurcation structure for increased throughput

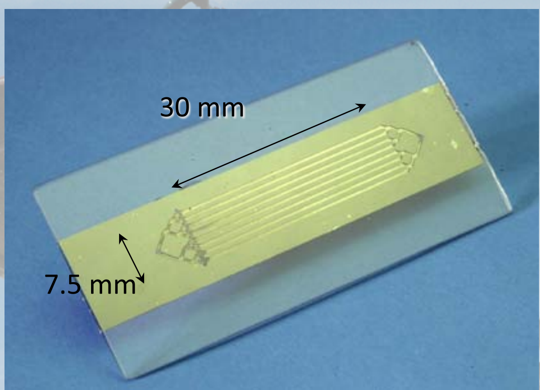

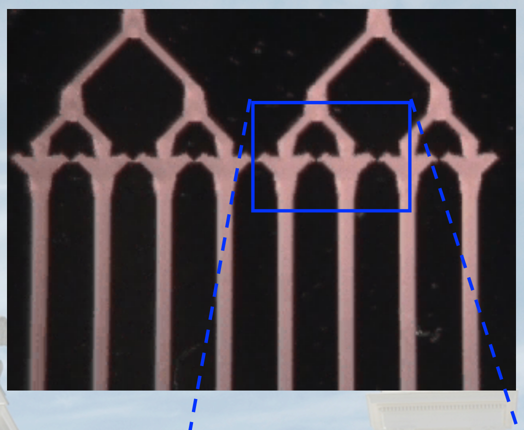

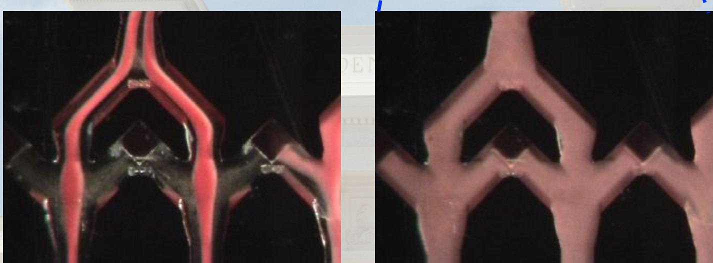

8 Channels = 48-96 ml/h
=>
10 to 20 multi channel structures needed for a clinical application (1000 ml/h)

Fat emboli reduction ratio - FERR

Real shed blood

100% FERR (Fat Emboli Reduction Ratio) - visual

Model with radioactive labelled fat

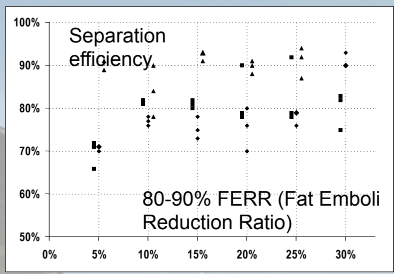

Erythrocyte recovery

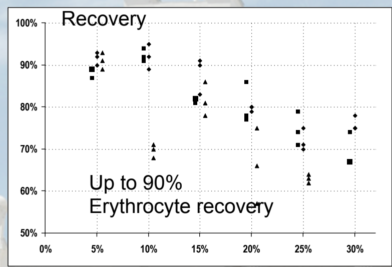

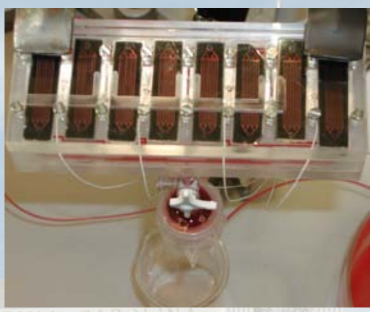

Free Flow Acoustophoresis - FFA

- continuous multiplex separation -

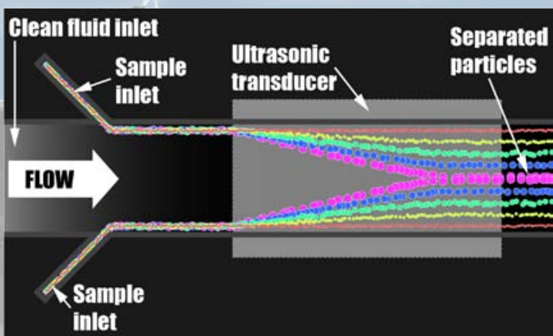

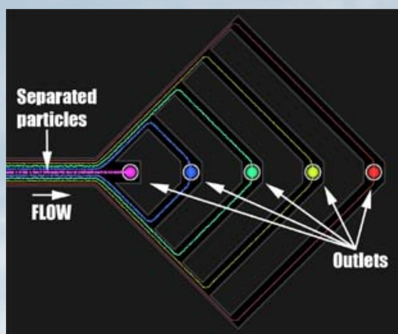

$$F_r = -\left(\frac{\pi P_0^2 V_p \beta_m}{2\lambda}\right) \cdot \Phi(\beta, \rho) \cdot \sin\left(\frac{4\pi x}{\lambda}\right)$$

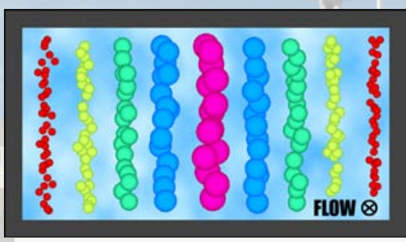

Cross-section of the channel after the piezoceramic

Petersson F. T., Åberg L. B., Swärd-Nilsson A.-M. S. and Laurell T., Analytical Chemistry, 2007, 79, 14, 5117-5123.

Free Flow Acoustophoresis - FFA - chip design

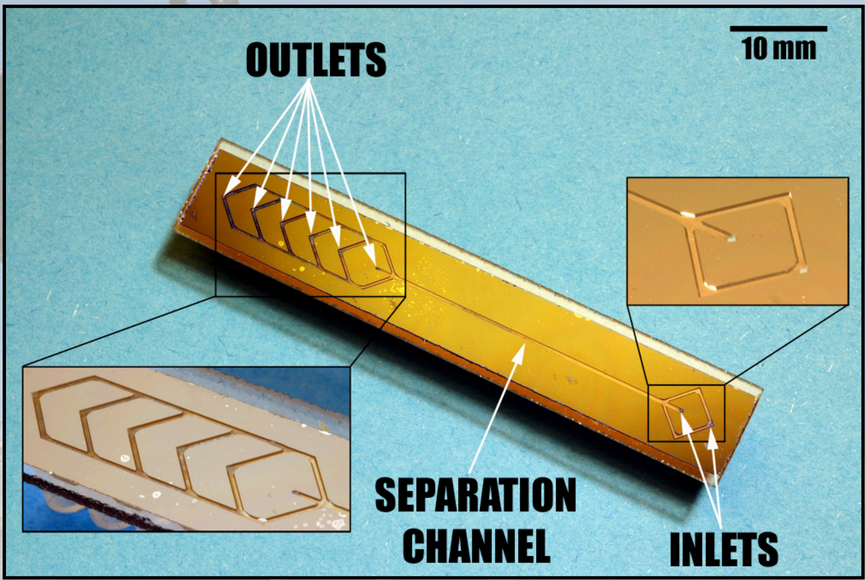

- channel width: 350 µm
- channel depth: 125 µm
- actuation: piezoceramic
- frequency: ~ 2 MHz
- capacity: ~0.5 ml/min (1/10 sample)
- power: 0.5 - 2.0 W

FFA-separation of three particle sizes

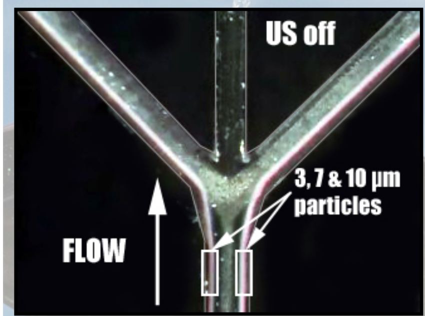

PS particles

3 µm (red)
7 µm (white)
10 µm (blue)

Ultrasound OFF

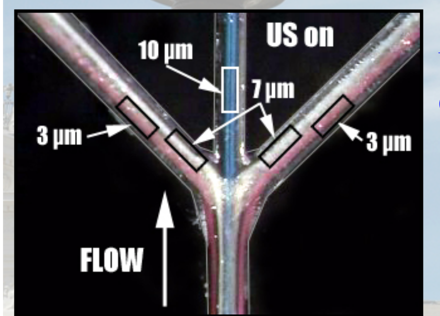

Ultrasound ON

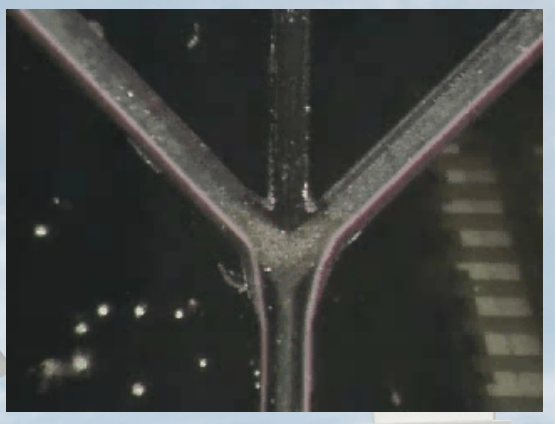

Ultrasound ON/OFF

- three active outlets
- total flow rate: 0.4 ml/min
- sample flow rate: 0.04 ml/min
- ~ 2% by volume of each

FFA – Separation of 3, 7 & 10 um particles

- total flow 0.4 ml/min
- sample flow 0.04 ml/min
- sample conc. 3x2% by vol.

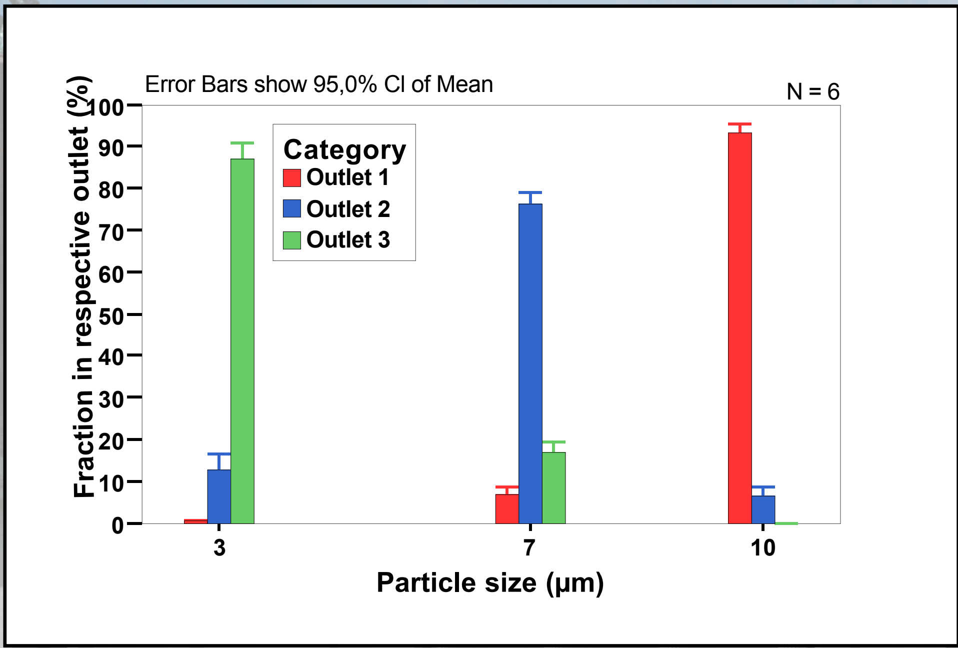

FFA – separation of four particle sizes

- total flow 0.4 ml/min
- sample flow 0.04 ml/min
- sample conc. 4x1% by vol.

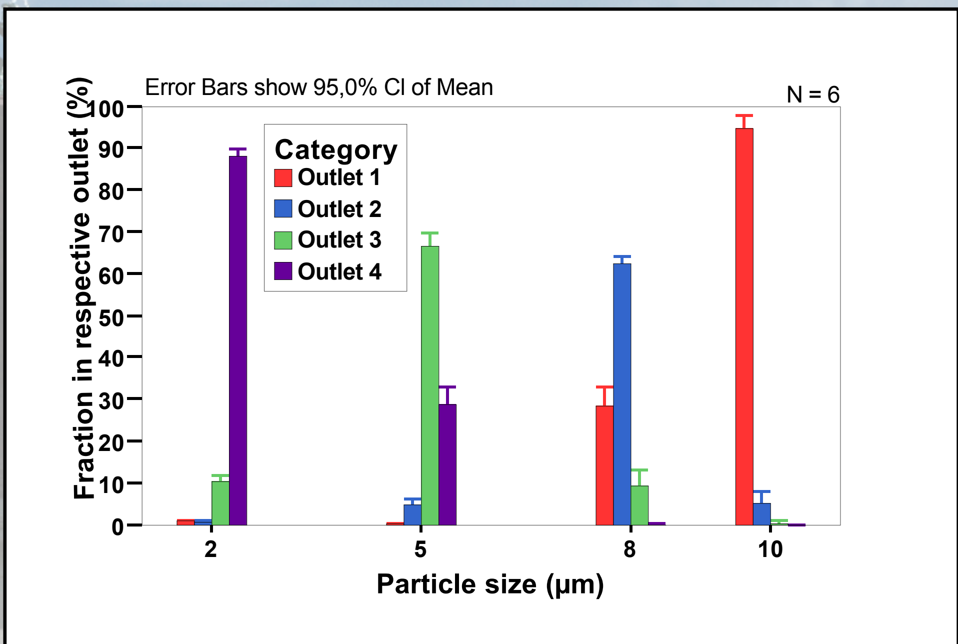

Medium manipulation - Blood cell buffy coat

- Red Blood Cells (RBC) (~2.5×10e11 /L)
- Platelets (PLT) (~1.0×10e11 /L)
- White Blood Cells (WBC) (~1.5×10e9 /L)
- CsCl: 0.22 g/ml

- total flow 0.4 ml/min
- sample flow 0.04 ml/min
- tot. cell conc. 2% by vol.

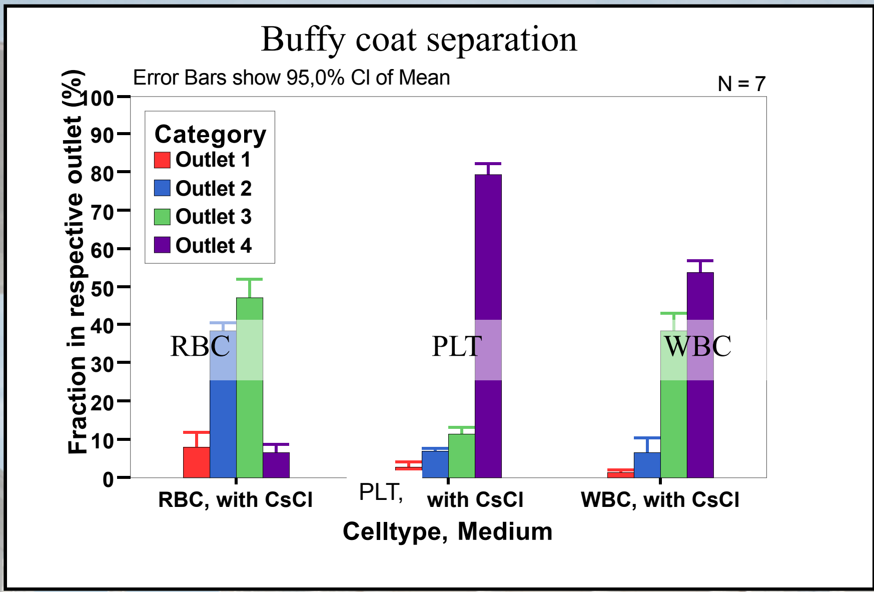

Band broadening

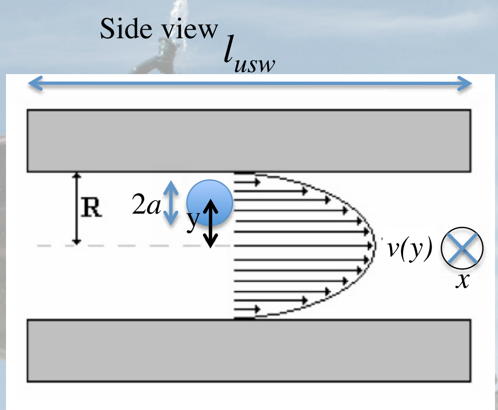

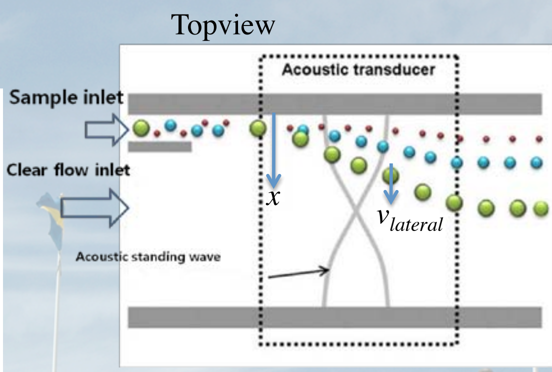

$$t_{usw} = \frac{l_{usw}}{v(y)} \approx \frac{1}{R^2 - y^2}$$

$$v(y) = \frac{\Delta p}{4\eta L} \cdot \left(R^2 - y^2\right)$$

$$F_{usw} = F_{stoke} = 6\pi\eta a v_{lateral}$$

$$x = v_{lateral} t_{usw} \approx \frac{1}{y^2}$$

Free flow acoustophoresis (FFA) with prefocusing

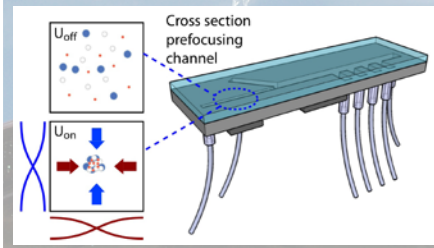

No prefocusing

With prefocusing

No prefocusing

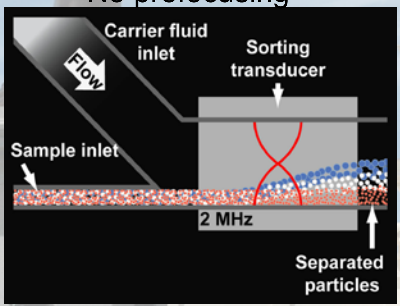

With prefocusing

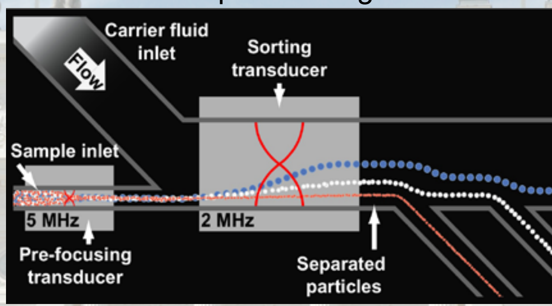

Free flow acoustophoresis (FFA) with prefocusing

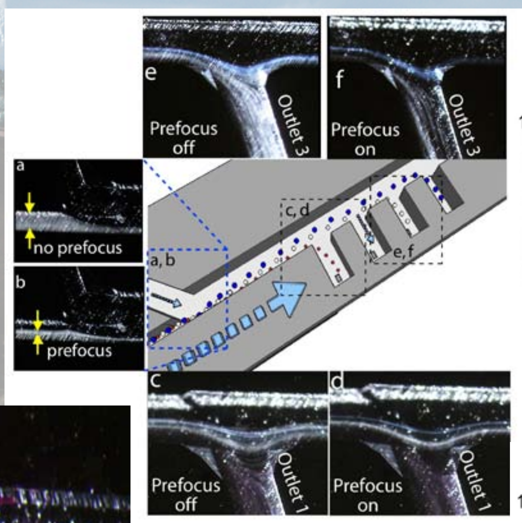

No prefocusing

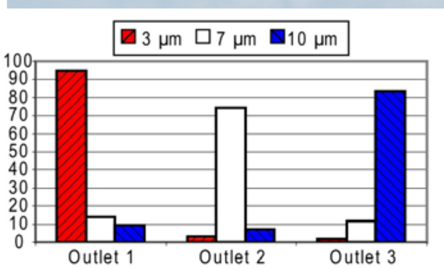

With prefocusing

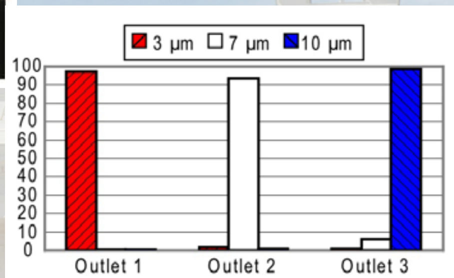

Buffer medium manipulation

$$F_r = -\left(\frac{\pi P_0^2 V_p \beta_m}{2\lambda}\right) \cdot \Phi(\beta,\rho) \cdot \sin\left(\frac{4\pi x}{\lambda}\right)$$

$$\Phi = (5\rho_p - 2\rho_m)/(2\rho_p + \rho_m) - (\beta_p/\beta_m)$$

F_r = primary acoustic radiation force
P_0 = acoustic pressure amplitude
V_p = particle volume
β_m = compressibility of the medium
β_p = compressibility of the particle
λ = acoustic wavelength
x = particle distance from a pressure node
ρ_m = density of the medium
ρ_p = density of the particle

Changing the properties of the suspending medium
Density manipulation ρ_m
==>
a difference in acoustic force on similar particle types can be obtained

Normally acoustically unseparable particles can be separated!

Medium manipulation - PS & PMMA

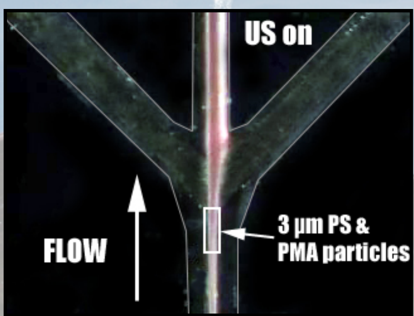

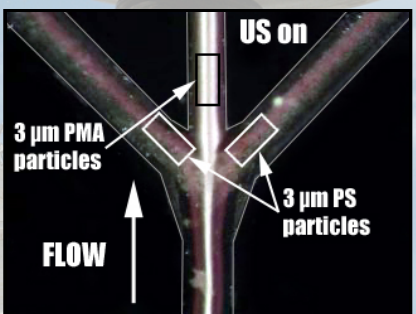

3 µm PS particles (red, 1.05 g/cm³)
&
3 µm PMMA particles (white, 1.22 g/cm³)
in distilled water

- two active outlets
- total flow rate: 0.4 ml/min
- sample flow rate: 0.04 ml/min
- ~ 2.5% by volume of each particle type

With CsCl (0.22 g/ml) added:
~96 % PMMA - middle
~ 88 % PS - side

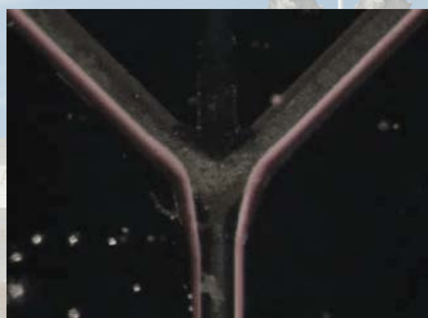

Medium manipulation - Blood cells

- total flow 0.2 ml/min
- sample flow 0.02 ml/min
- sample conc. 2x1% by vol.
- CsCl 0.22 g/ml

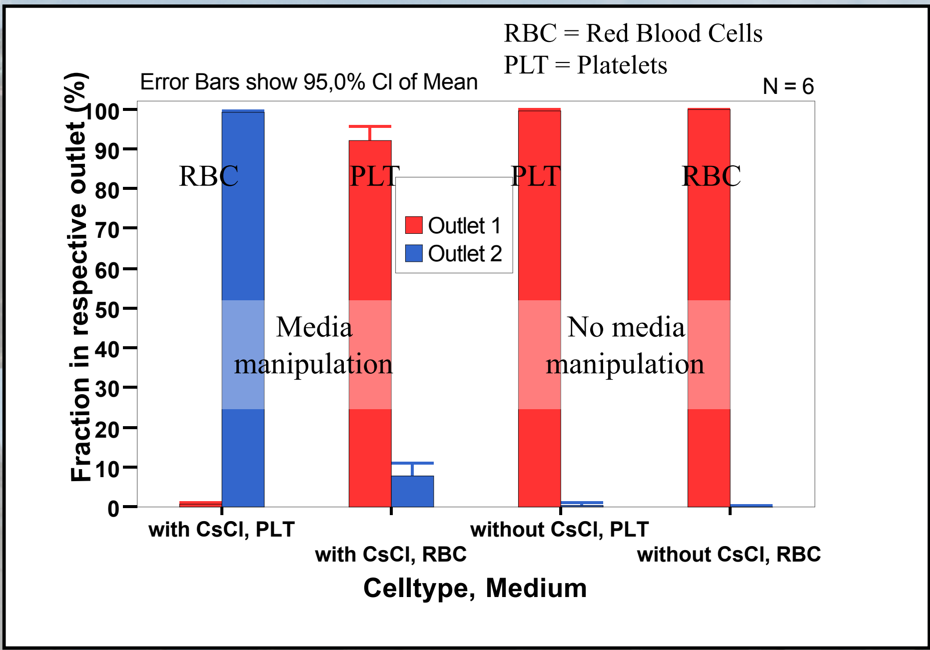

Raw milk quality control by means of acoustophoresis

- Rapidly growing dairy sector with great demands on quality control
- Current QC techniques => manual sample processing prior to analysis
- Acoustophoretic pre-processing of raw milk enbales rapid and sampl automated analysis without the need for chemical additives

In collaboration with:
Prof. Hideaki Matsuoka, Tokyo Univ. Agriculture & Technology
and
Jacob Riis-Volkenberg, Foss, Hilleröd, Denmark

Raw milk quality control by means of acoustophoresis

Needs: Remove and concentrate lipids
Idea: Move lipids to anti nodes

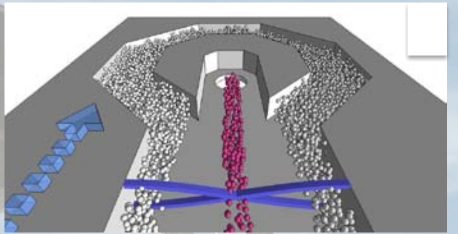

The problem

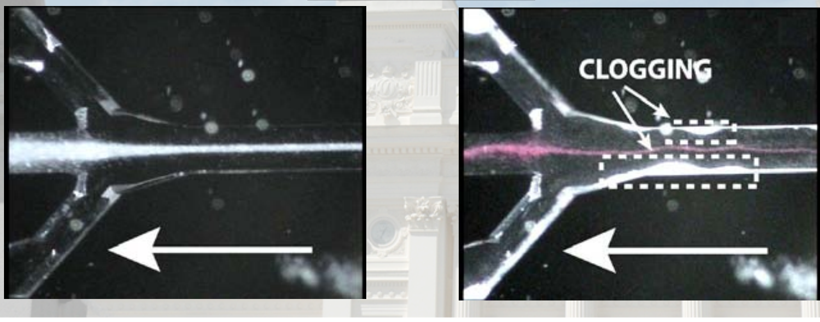

Lipid enrichment mode 2λ/2 facilitate fatty acid conent analysis by FTIR

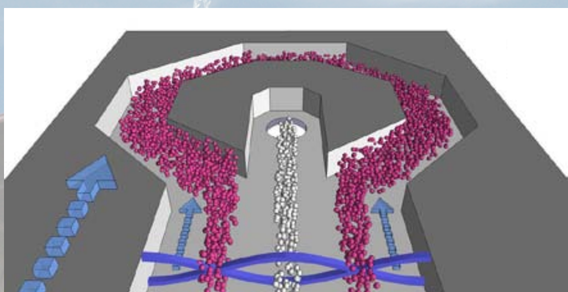

750 µm
(2*λ/2 @ 2 MHz)

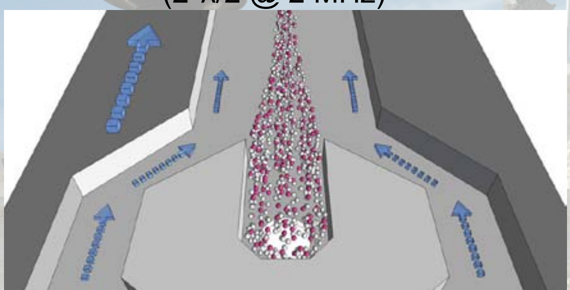

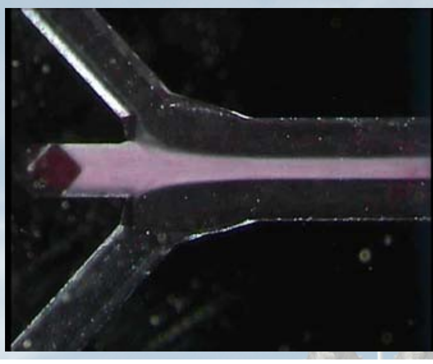

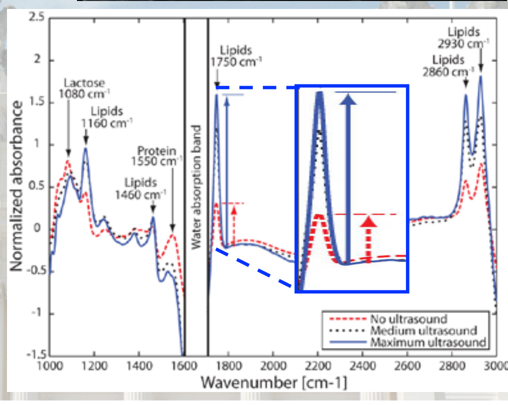

Lipid depletion mode 3λ/2 enables label free cell count in milk

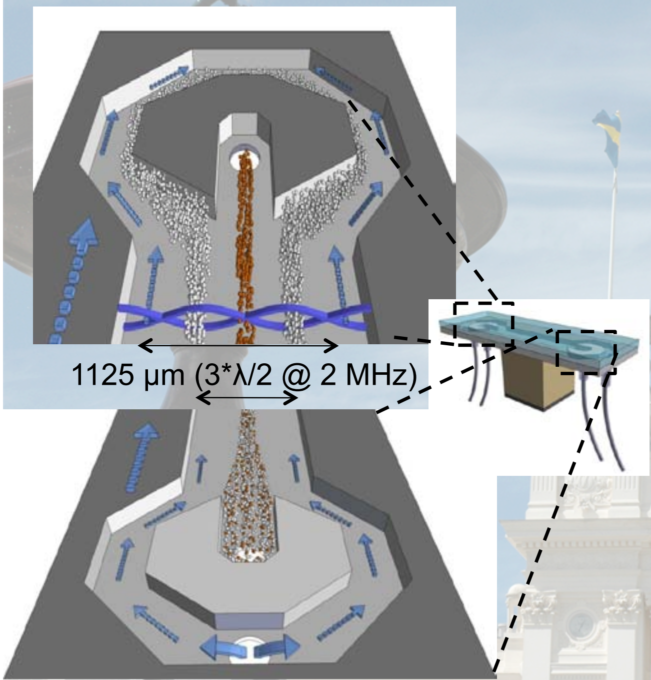

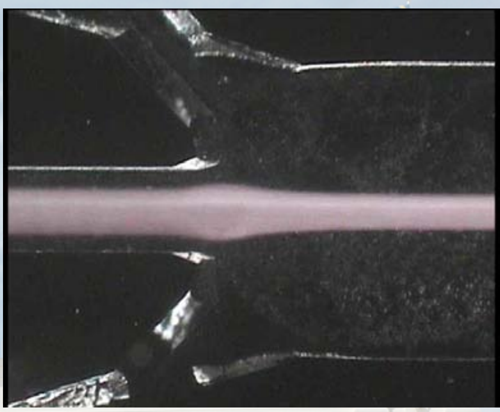

Lipid depletion mode 3λ/2

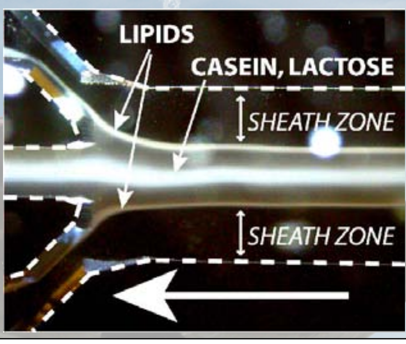

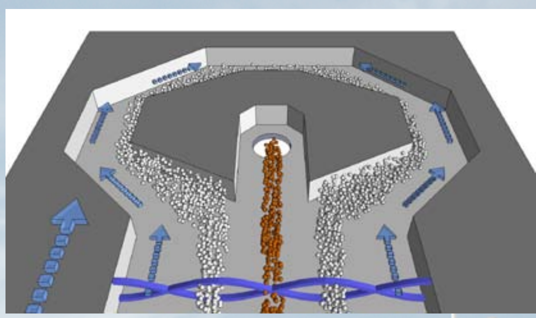

- Acoustophoretic removal of lipids in raw milk allows immediate FTIR-analysis
  - lactose and protein
  - No lipid dissolving chemicals

- Lactose and protein levels remain unchanged while >90% of lipids are removed

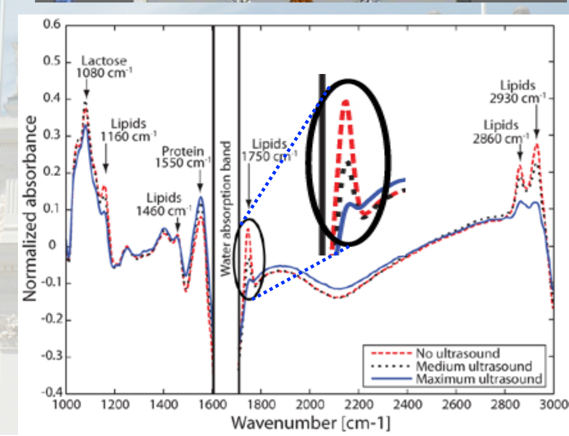

Lipid depletion mode 3λ/2 enables label free milk cell count

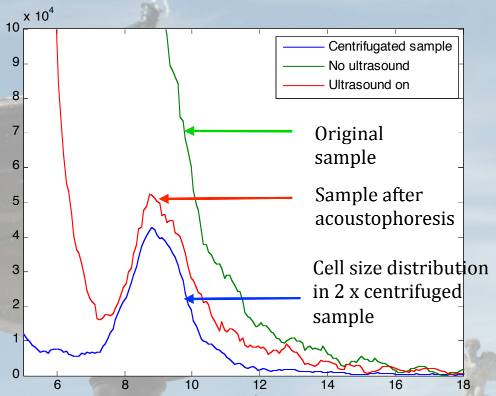

Sample : approx. 4×10^6 cells/mL
- flow cytometry & by coulter counter

Raw sample

Fluorescence mode | Phase contrast

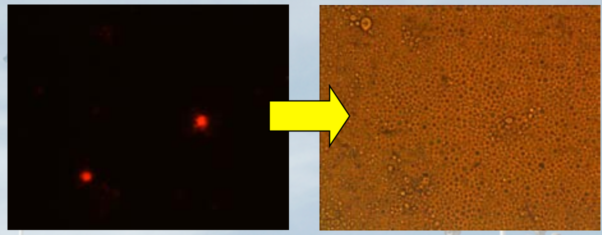

Sample after acoustophoresis

Fluorescence mode | Phase contrast

Acoustophoretic sample preparation
- Cells visible in normal microscope
- Requires no staining to count cells

Acoustophoretic Cell Synchronization device

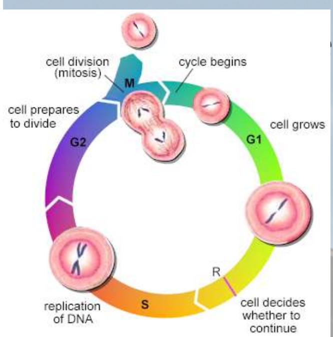

www.teachline.ls.huji.ac.il

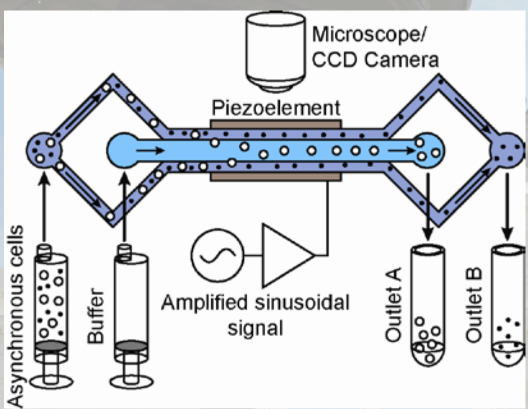

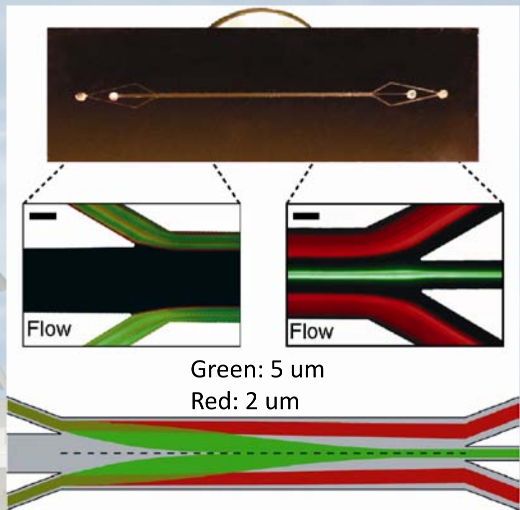

P Thévoz, JD Adams, H Shea, H Bruus, HT Soh, *Anal. Chem.* **82**, 3094-3098 (2010).

Acoustic separation of G1-phase mammalian cells

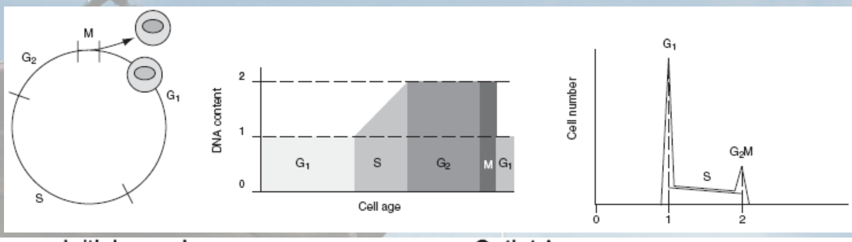

Z Darzynkiewicz, G Juan, E Bedner, *Curr. Prot. Cell. Bio.* 8.4.1-8.4.18 (1999)

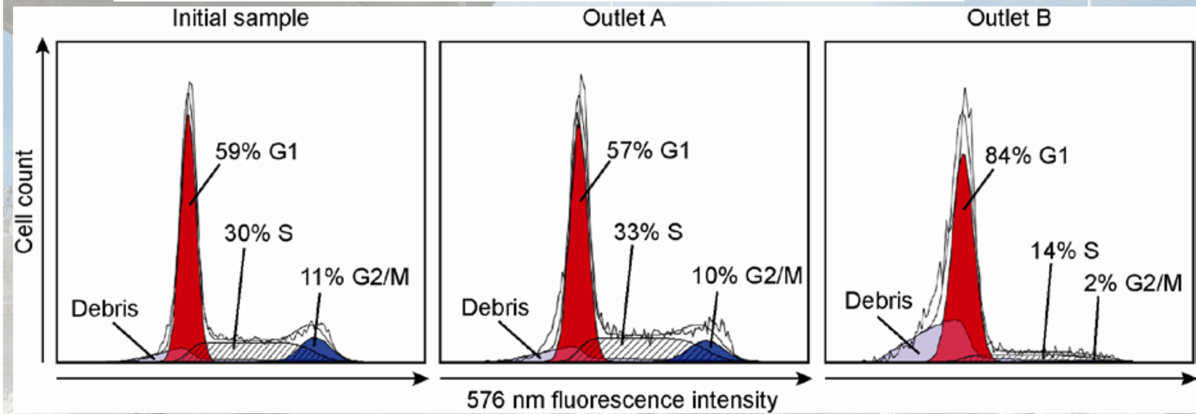

P Thévoz, JD Adams, H Shea, H Bruus, HT Soh, *Anal. Chem.* **82**, 3094-3098 (2010).

~3 mL/h, ~3×10^6 cells/h

Separation does not affect short- or long-term viability

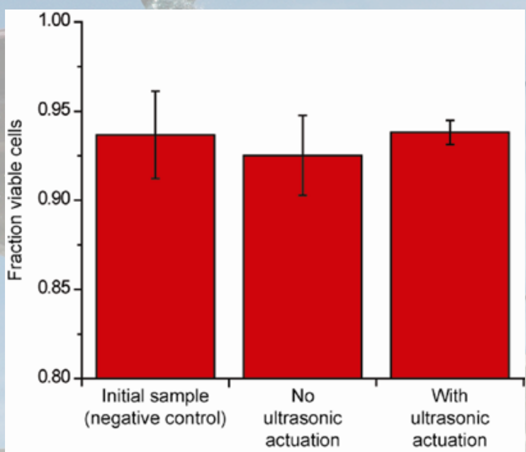

Trypan blue live/dead assay

Proliferation study of separated cells →

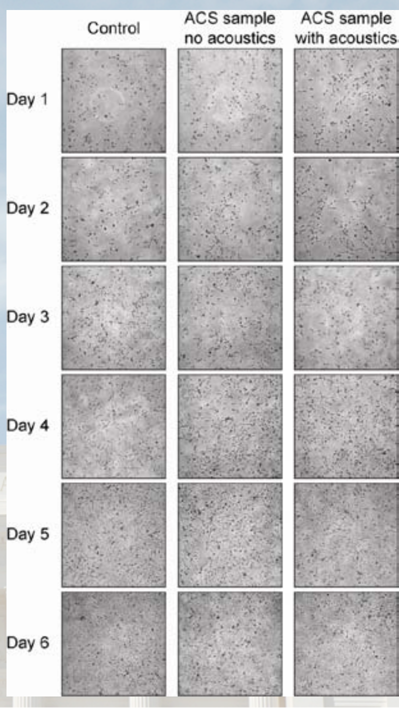

P Thévoz, JD Adams, H Shea, H Bruus, HT Soh, *Anal. Chem.* **82**, 3094-3098 (2010).

Integrated Acoustic-Magnetic Separation device

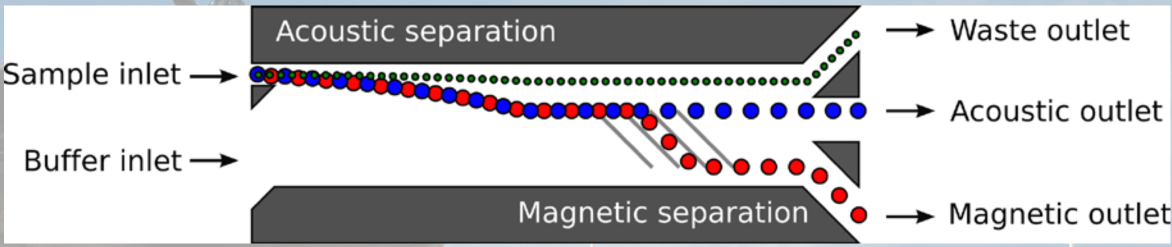

- Integration of label-based and label-free techniques
- Both separation forces are independent of pH, buffer conditions

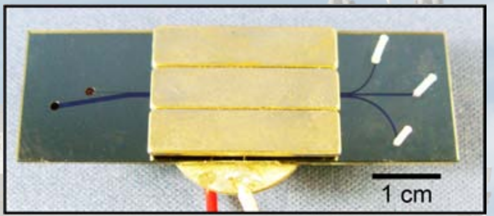

JD Adams, P Thévoz, H Bruus, HT Soh, *Appl. Phys. Lett.* **95**, 254103 (2009)

Integrated acoustic and magnetics

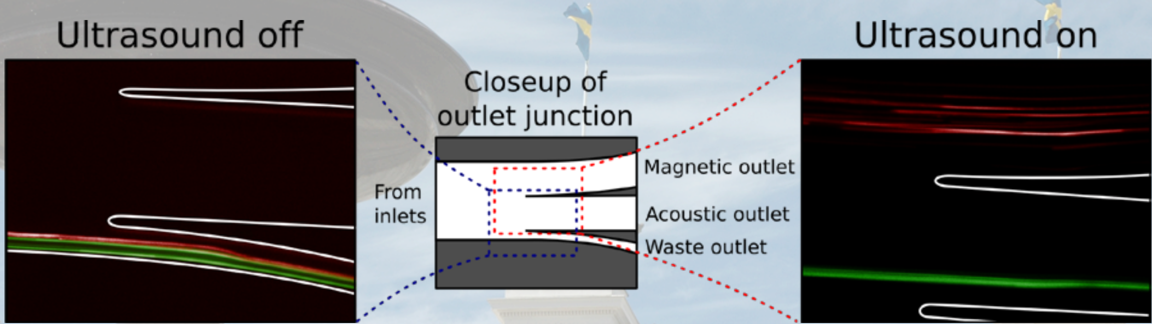

Simultaneous rare target enrichment

- 10^8 particles/h
- Initial target purities <1%
- Acoustic target purity 89%
- Magnetic target purity 95%
- Separation of 91% of all targets

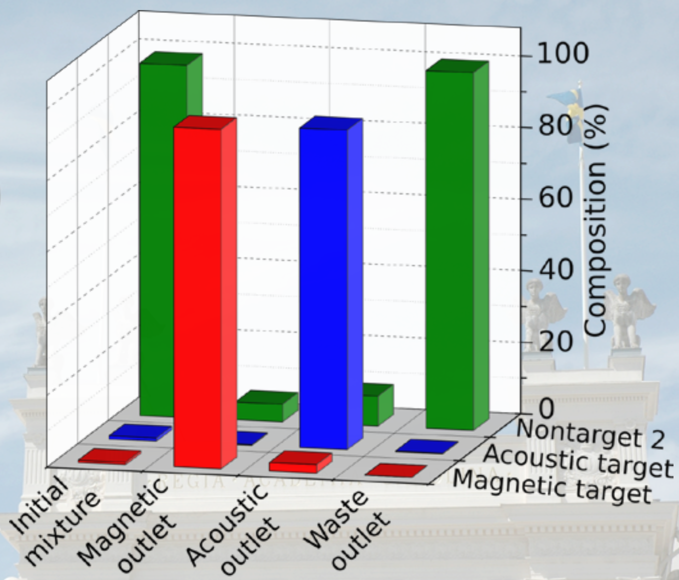

Acoustic target: large acoustic + no magnetic response
Magnetic target: large acoustic + large magnetic response
Nontarget 2: small acoustic + no magnetic response

Plasmapheresis

- Sequential removal of cells lowers concentration gradually

Whole blood ≈ 45% cellular content

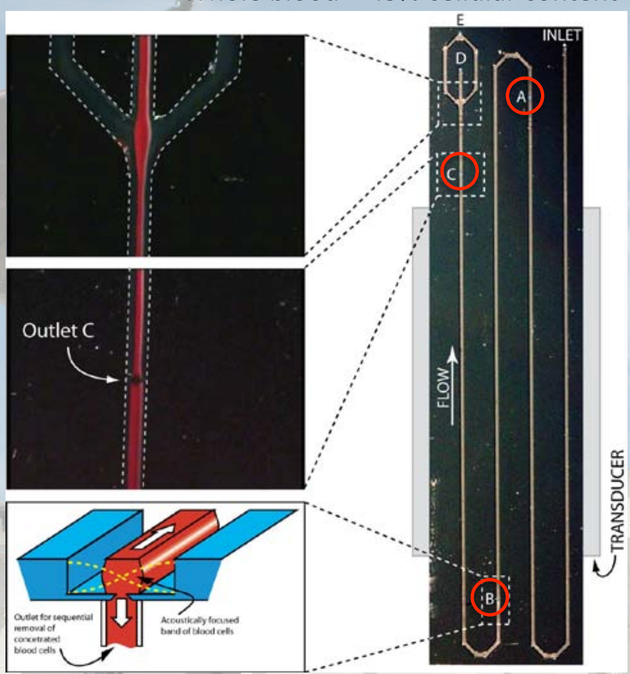

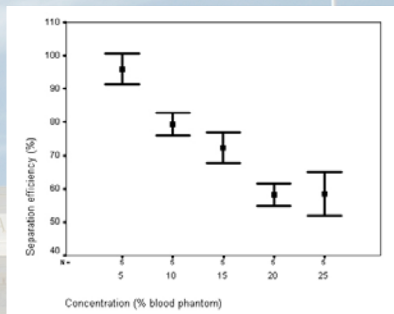

High particle concentrations => poor separation!

Lenshof A. et al, **Analytical Chemistry**, 2009, 81, 15, 6030-6037

Sequential RBC removal – 4M

Separation results using whole blood (40%)

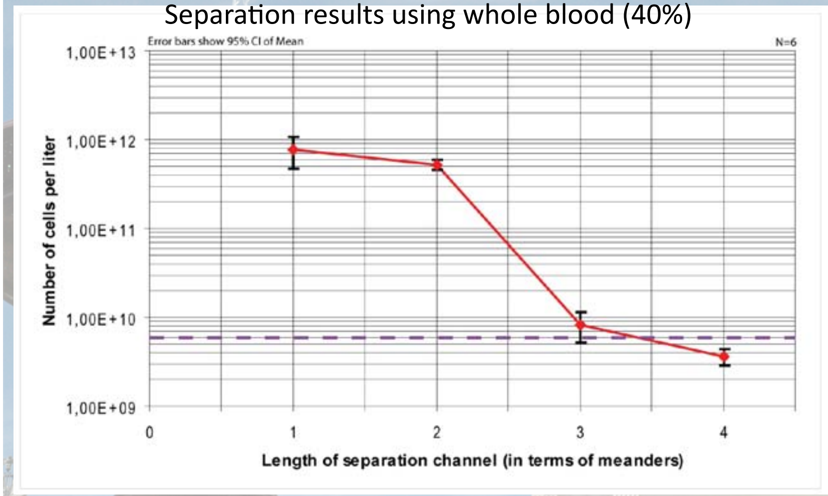

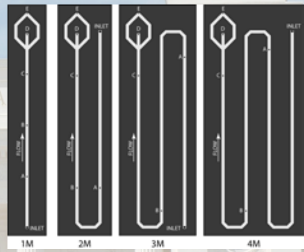

Purple line - 6E+9 erythrocytes / liter plasma - Limit recommended for transfusion by The Council of Europe

Lenshof A. et al, **Analytical Chemistry**, 2009, 81, 15, 6030-6037

Plasmapheresis linked to PSA microarray diagnostics

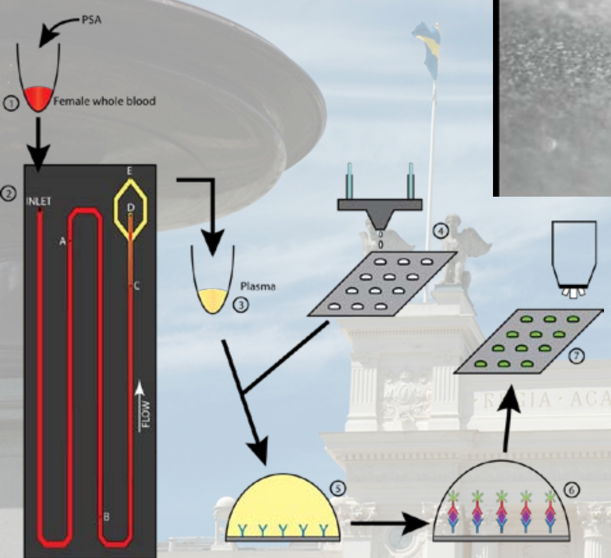

Lenshof A. et al, **Analytical Chemistry**, 2009, 81, 15, 6030-6037

Results – PSA microarray

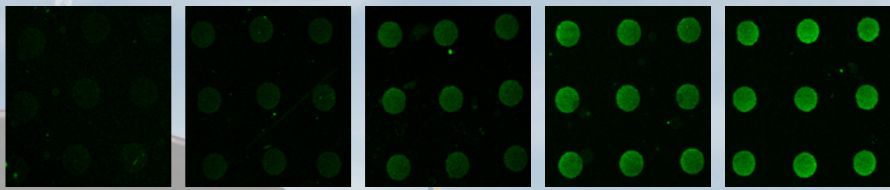

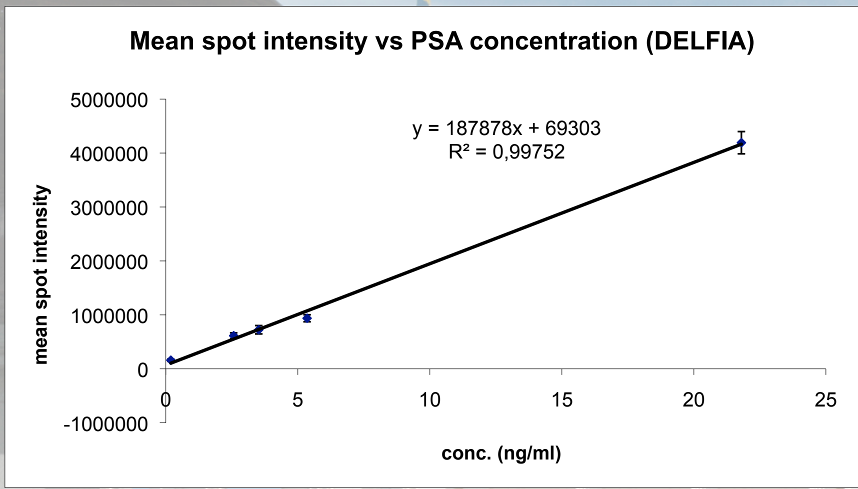

Lenshof A. et al, **Analytical Chemistry**, 2009, 81, 15, 6030-6037

L2: Designing multi-frequency force fields in microsystems

Martin Wiklund

Dept. of Applied Physics

Royal Institute of Technology

Stockholm, Sweden

CISM course ”*Ultrasound standing wave action on suspensions and biosuspensions in micro- and macro fluidic systems*”, June 7-11, 2010

KTH Physics

M. Wiklund

-1-

Outline

- Single-frequency force fields in microsystems
- Multiple-frequency force fields in microsystems
- Actuation strategies using more than one frequency

KTH Physics

M. Wiklund

-2-

Starting point

- Our experimental observations from 2004 until today (Wiklund group)

- Our attempts to predict the observations by numerical modelling from 2007 until today (Wiklund group, collab. with the Bruus group)

- Review of different strategies involving more than one actuation frequency (all groups):
  - Superimposed orthogonal fields, small Δf (Dual group)
  - Superimposed orthogonal fields, large Δf (Wiklund group)
  - Frequency modulation techniques (Hill group, Wiklund group)

KTH Physics

M. Wiklund

-3-

Single-frequency approaches

KTH Physics

M. Wiklund

Transducer – chip platform

M. Wiklund

glass-silicon-glass chip

fluid channel

wedge transducers

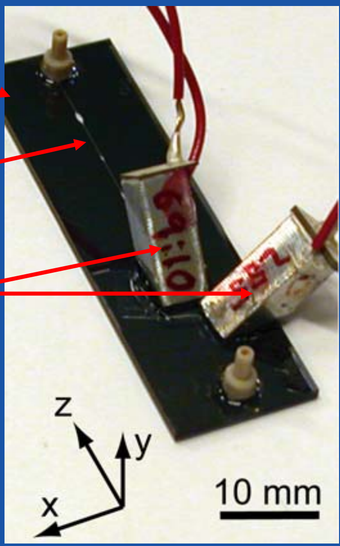

Wiklund *et al.*, Lab Chip 6, 1537 (2006)

Transducer – chip platform

M. Wiklund

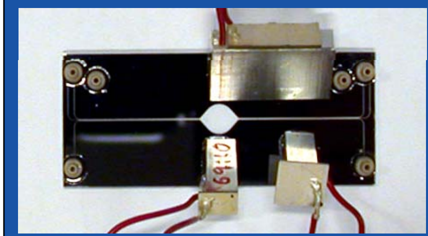

- 1 – 5 transducers
- < 10 V_{pp} actuation voltage
- 1 – 10 MHz actuation frequency

Radiation force: Numerical modelling

Gorkov equation: Force F depends on particle volume V and material constans f_1 and f_2:

$$U = V\left(f_1 \cdot E_{pot} - \frac{3}{2} f_2 \cdot E_{kin} \right) \quad \text{where} \quad E_{pot} = \frac{<p^2>}{2\rho_0 c_0^2}$$

$$\mathbf{F} = -\nabla U \qquad E_{kin} = \frac{\rho_0 <v^2>}{2}$$

- $\mathbf{F}$ can be expressed as a function of the pressure field only:

$$\mathbf{F} = -V\left[f_1\, p \nabla p - f_2 \left(\nabla p \cdot \nabla \right) \nabla p \right]$$

M. Wiklund

KTH Physics

Radiation force: Numerical modelling

- Simulations of displacement field in Comsol (in 2D)

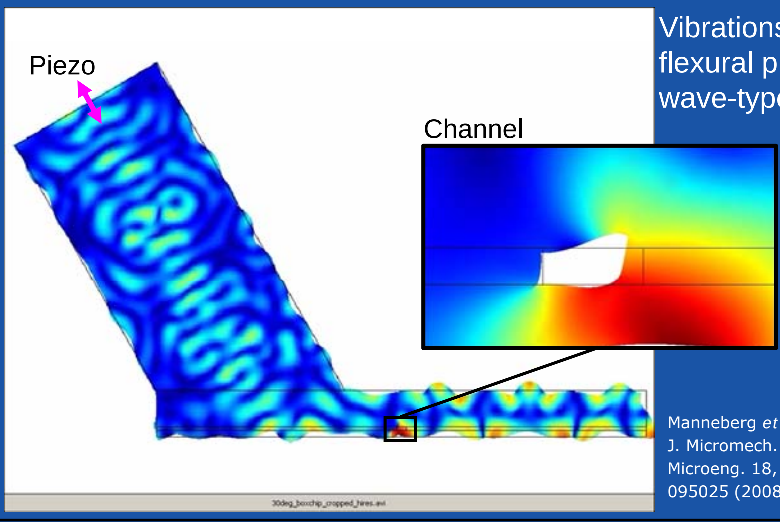

Vibrations: flexural plate wave-type!

Manneberg *et al.*, J. Micromech. Microeng. 18, 095025 (2008)

M. Wiklund

KTH Physics

Radiation force: Numerical modelling

- The displacement field in the solid structure couple to a pressure field in the fluid channel:

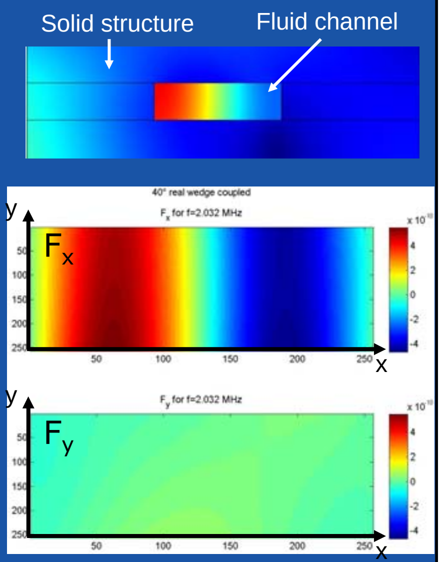

- Calculation of the radiation force:

$$\mathbf{F} = -V\left[f_1\, p\nabla p - f_2 (\nabla p \cdot \nabla)\nabla p \right]$$

KTH Physics

M. Wiklund

Radiation force: Numerical modelling

- What about the z direction? (along the channel)

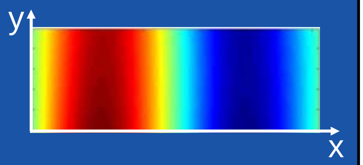

- x-z simulations:

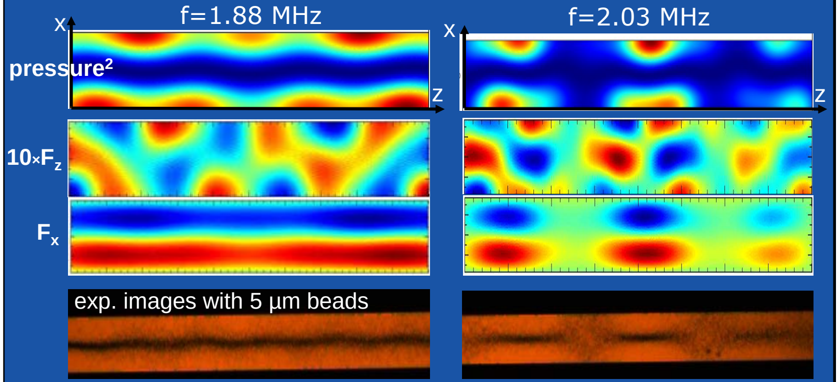

- Note: In flow-through, these are ”identical”!

KTH Physics

M. Wiklund

M. Wiklund

Origin of the spurious cavity modes?

M. Wiklund

Spurious cavity modes

- A microchannel is part of a complex 3D resonator (including its solid support = chip)

Pure 1D channel resonances impossible:

Sometimes very complex patterns are obtained:

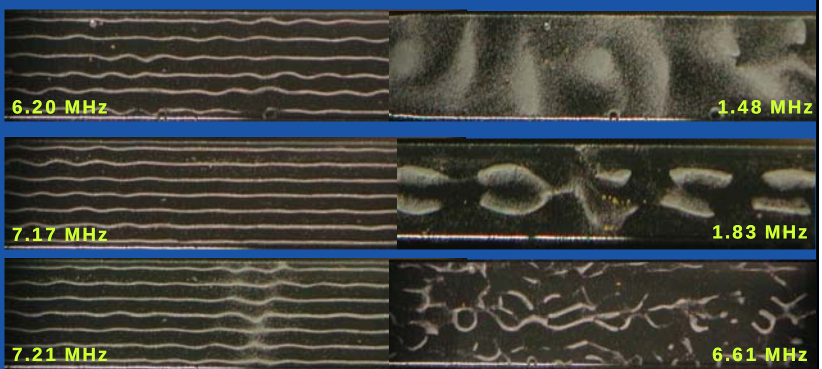

No-flow manipulation of 2 μm beads at different actuation frequencies

Compare: Chladni plates

KTH Physics

M. Wiklund

Plate vibration modes visualized by particles (sand, powder)

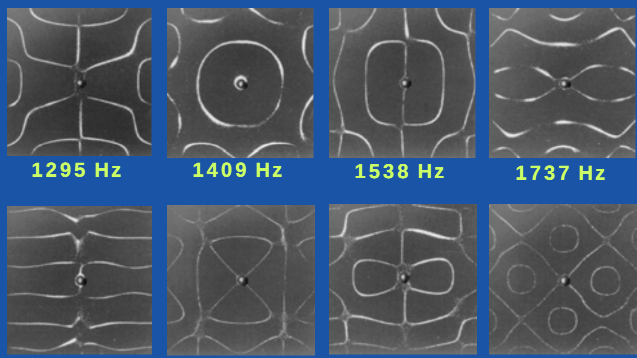

Compare: Chladni plates

KTH Physics

M. Wiklund

- Similar phenomenon in a microfluidic chip?

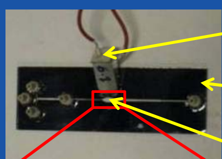

Operation from 1 to 6 MHz:

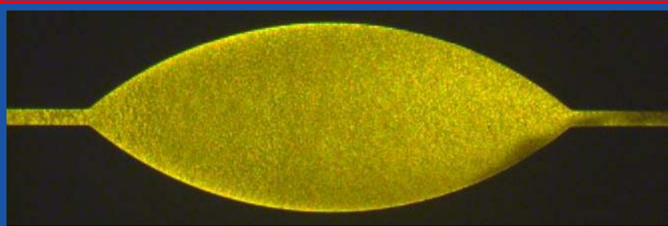

Prediction of spurious cavity modes?

Theoretical work in the 80s:
Barmatz and Collas (J. Acoust. Soc. Am. 77, 928 (1985))

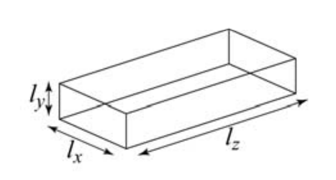

Resonance frequencies:

$$f_{n_x,n_y,n_z} = \frac{c_{med}}{2}\sqrt{\frac{n_x^2}{l_x^2}+\frac{n_y^2}{l_y^2}+\frac{n_z^2}{l_z^2}}$$

Gorkov equation:

$$\begin{aligned}\tilde{U} = {} & (f_1/3)\cos^2 k_x x \cos^2 k_y y \cos^2 k_z z \\ & - (f_2/2)[(k_x/k)^2 \sin^2 k_x x \cos^2 k_y y \cos^2 k_z z \\ & + (k_y/k)^2 \cos^2 k_x x \sin^2 k_y y \cos^2 k_z z \\ & + (k_z/k)^2 \cos^2 k_x x \cos^2 k_y y \sin^2 k_z z].\end{aligned}$$

KTH Physics

M. Wiklund

Prediction of spurious cavity modes?

Theoretical work in the 80s:
Barmatz and Collas (J. Acoust. Soc. Am. 77, 928 (1985))

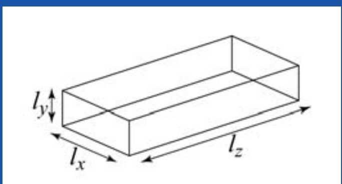

Resonance frequencies:

$$f_{n_x,n_y,n_z} = \frac{c_{med}}{2}\sqrt{\frac{n_x^2}{l_x^2}+\frac{n_y^2}{l_y^2}+\frac{n_z^2}{l_z^2}}$$

Potential minimas (”nodal force surfaces”):

Mode	x	y	z
axial $(00n_z)$	...	...	$\cos k_z z = 0$
tangential $(n_x 0 n_z)$	$\sin k_x x = 0$	...	$\cos k_z z = 0$
	$\cos k_x x = 0$	...	$\sin k_z z = 0$
oblique $(n_x n_y n_z)$	$\cos k_x x = 0$	$\sin k_y y = 0$	$\sin k_z z = 0$
	$\sin k_x x = 0$	$\cos k_y y = 0$	$\sin k_z z = 0$
	$\sin k_x x = 0$	$\sin k_y y = 0$	$\cos k_z z = 0$

KTH Physics

M. Wiklund

Prediction of spurious cavity modes?

Application to a microfluidic channel:
Henrik Bruus et al (Lab Chip, 2010)

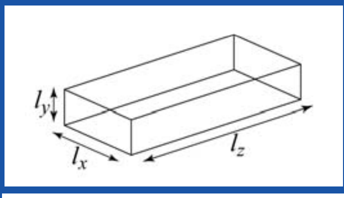

Resonance frequencies:

$$f_{n_x,n_y,n_z} = \frac{c_{med}}{2}\sqrt{\frac{n_x^2}{l_x^2}+\frac{n_y^2}{l_y^2}+\frac{n_z^2}{l_z^2}}$$

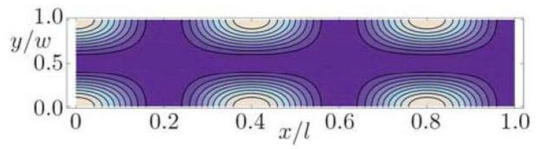

Fig. 2 Contour plot with 10% contour lines from low (dark) to high (light) of the normalized acoustic potential U_{ac}/U_o from eqn (12) for a polystyrene sphere in water given the pressure field p_1 of eqn (10a) with $(k_x, k_y) = (\pi/(2w), \pi/w)$ so that $\theta \approx 63°$. Further parameter values used in the simulation are given in Table 1.

Bruus/Laurell groups, Lab Chip **10**, 563 (2010)

M. Wiklund

Prediction of spurious cavity modes?

Compare the analytical solution (Bruus) with
Comsol simulations and experimental verification (Wiklund):

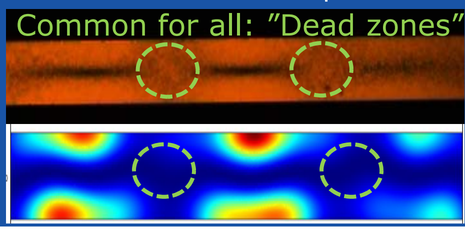

Manneberg, Wiklund et al, J. Micromech. Microeng. **18**, 095025 (2008)

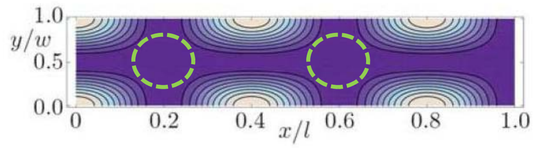

Bruus/Laurell groups, Lab Chip **10**, 563 (2010)

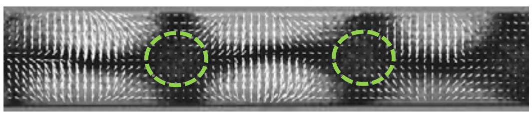

Bruus/Laurell groups, Lab Chip **8**, 1178 (2008)

Same results were found earlier by Townsend/Hill in Ultrasonics **44**, e467 (2006)

M. Wiklund

M. Wiklund

Prediction of spurious cavity modes?

Theoretical work in the 80s:

Barmatz and Collas (J. Acoust. Soc. Am. 77, 928 (1985))

See also Kinsler, Frey et al, Chapter 9 (”Cavities and Waveguides”)

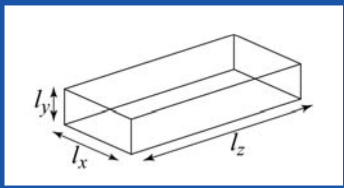

Resonance frequencies:

$$f_{n_x,n_y,n_z} = \frac{c_{med}}{2}\sqrt{\frac{n_x^2}{l_x^2}+\frac{n_y^2}{l_y^2}+\frac{n_z^2}{l_z^2}}$$

Simple 2D example, l_x x l_y = 200 x 300 µm rectangle:

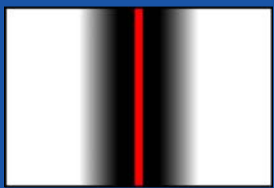

$$f_{n_x,n_y} = \frac{c_{med}}{2}\sqrt{\frac{n_x^2}{l_x^2}+\frac{n_y^2}{l_y^2}} =$$

$$\{n_x, n_y = 1,0\} = 2.50 \text{ MHz}$$

M. Wiklund

Prediction of spurious cavity modes?

Theoretical work in the 80s:

Barmatz and Collas (J. Acoust. Soc. Am. 77, 928 (1985))

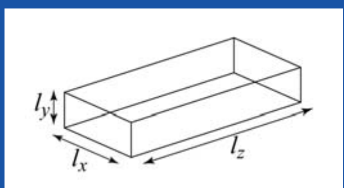

Resonance frequencies:

$$f_{n_x,n_y,n_z} = \frac{c_{med}}{2}\sqrt{\frac{n_x^2}{l_x^2}+\frac{n_y^2}{l_y^2}+\frac{n_z^2}{l_z^2}}$$

Simple 2D example, l_x x l_y = 200 x 300 µm rectangle:

$$f_{n_x,n_y} = \frac{c_{med}}{2}\sqrt{\frac{n_x^2}{l_x^2}+\frac{n_y^2}{l_y^2}} =$$

$$\{n_x, n_y = 0,1\} = 2.75 \text{ MHz}$$

M. Wiklund

Prediction of spurious cavity modes?

Theoretical work in the 80s:

Barmatz and Collas (J. Acoust. Soc. Am. 77, 928 (1985))

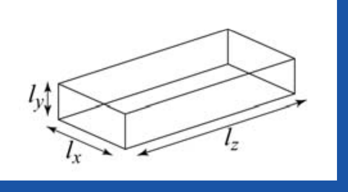

Resonance frequencies:

$$f_{n_x,n_y,n_z} = \frac{c_{med}}{2}\sqrt{\frac{n_x^2}{l_x^2}+\frac{n_y^2}{l_y^2}+\frac{n_z^2}{l_z^2}}$$

Simple 2D example, l_x x l_y = 200 x 300 µm rectangle:

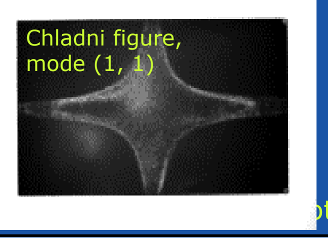

$$f_{n_x,n_y} = \frac{c_{med}}{2}\sqrt{\frac{n_x^2}{l_x^2}+\frac{n_y^2}{l_y^2}} =$$

$$\{n_x, n_y = 1,1\} = 4.51\ \mathrm{MHz}$$

ote: No trapping in the center!

M. Wiklund

Prediction of spurious cavity modes?

Experimental verification:

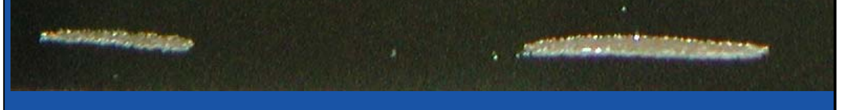

Simple 2D example, l_x x l_y = 200 x 300 µm rectangle:

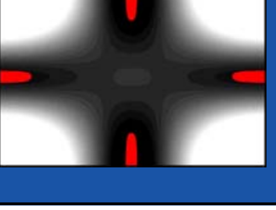

$$f_{n_x,n_y} = \frac{c_{med}}{2}\sqrt{\frac{n_x^2}{l_x^2}+\frac{n_y^2}{l_y^2}} =$$

$$\{n_x, n_y = 1,1\} = 4.51\ \mathrm{MHz}$$

Prediction of spurious cavity modes?

Typical microchannel (top-view):
l_x x l_y = 0.75 x 8 mm

$$f_{n_x,n_y} = \frac{c_{med}}{2}\sqrt{\frac{n_x^2}{l_x^2}+\frac{n_y^2}{l_y^2}} =$$

$$\{n_x, n_y = 2,3\} = 1.997 \text{ MHz}$$

Experimental verification:

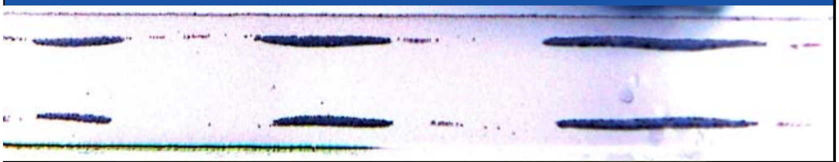

M. Wiklund

Prediction of spurious cavity modes?

Back to this mode again:

Simple 2D example, l_x x l_y = 200 x 300 µm rectangle:

$$f_{n_x,n_y} = \frac{c_{med}}{2}\sqrt{\frac{n_x^2}{l_x^2}+\frac{n_y^2}{l_y^2}} =$$

$$\{n_x, n_y = 1,1\} = 4.51 \text{ MHz}$$

Another approach by Oberti, Dual et al (JASA, 2007):

Superposition of two orthogonal standing waves (same f and ampl.)

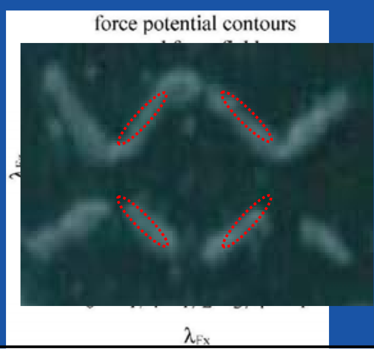

M. Wiklund

Prediction of spurious cavity modes?

More reasons for the occurance of non-uniform nodal lines?

Streaming vortices (400 nm beads)

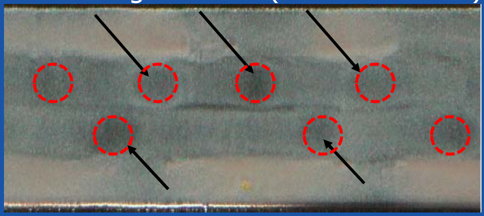

Streaming may add further complexity to the trapping pattern!

M. Wiklund

KTH Physics

Multiple-frequency approaches

M. Wiklund

KTH Physics

Multi-frequency approaches

Approach 1 (Dual group, 2007) - superposition:
Slight frequency difference ($\Delta f/f = 10^{-5}$) between two superimposed orthogonal fields
From: [Oberti et al, JASA **121**, 778 (2007)]

Same frequency | Small frequency shift

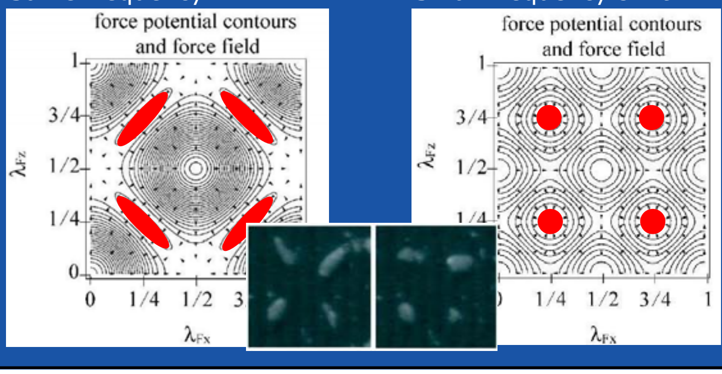

KTH Physics

M. Wiklund

Multi-frequency approaches

Approach 2 (Wiklund group, 2007) - superposition:
Two frequencies (f_1, f_2) with larger diff. (f_1 - f_2)

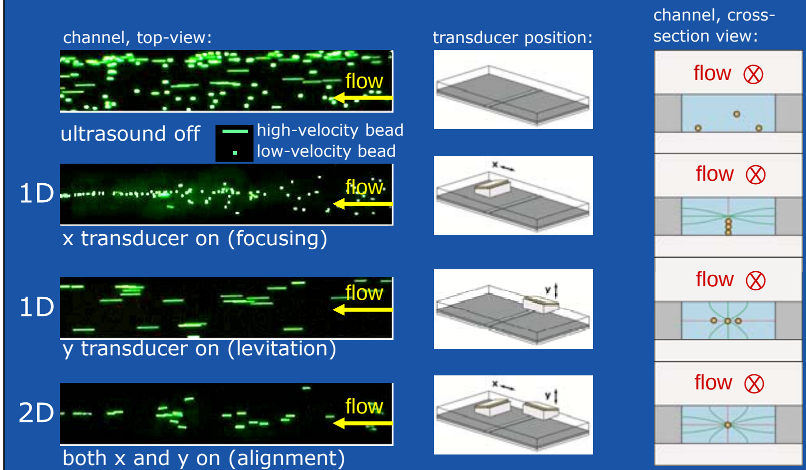

Manneberg *et al.*, Proc. of Nanotech Montreux, 2007

KTH Physics

M. Wiklund

Multi-frequency approaches

Approach 2 (Wiklund group, 2007) - superposition:
Two frequencies (f_1, f_2) with larger diff. (f_1 - f_2)

Compare with single-frequency 2D field!
(No trapping in center)

Analytical solution, mode (1, 1)

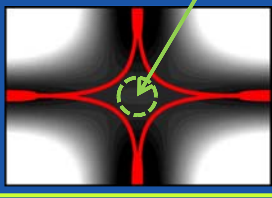

Chladni figure, mode (1, 1)

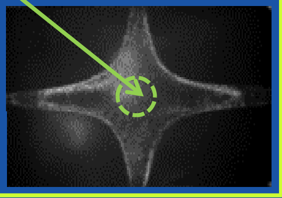

2D

both x and y on (alignment)

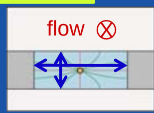

Manneberg *et al.*, Proc. of Nanotech Montreux, 2007

KTH Physics

M. Wiklund

Multi-frequency approaches

Approach 3 (Wiklund group, 2008) - localization:
Several frequencies (f_1, f_2, ...) matching ***local*** channel resonances

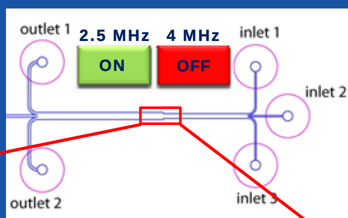

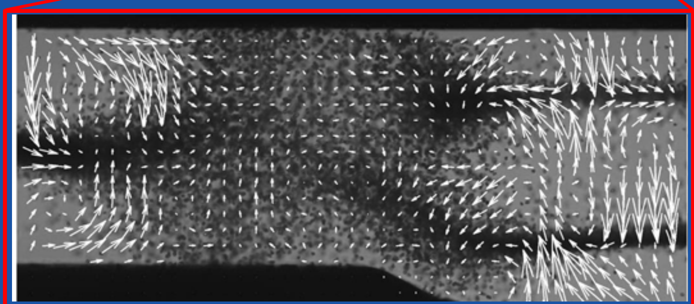

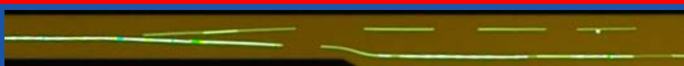

Manneberg *et al.*, Ultrasonics, **49**, 112, 2009

KTH Physics

M. Wiklund

M. Wiklund

Multi-frequency approaches

Approach 4 (Wiklund group, 2008) – superposition and localization:

Many frequencies (f_1, f_2, …) with larger diff. (f_1 - f_2, …) combined with geometrical channel features (”cages”) of λ/2-widths in x, y and z directions

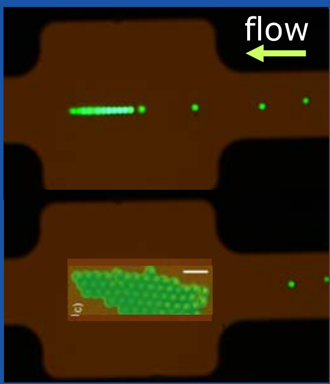

Manneberg *et al*, Appl. Phys. Lett. 2008

1) 2D pre-alignment
   6.9 MHz
2) Initially: 1D aggregation
   2.5 MHz and 6.9 MHz
3) Later: 3D aggregation
   2.5 MHz and 6.9 MHz
4) 3D ⇔ 2D aggregation
   tuning the ampl. ratio of 2.5 and 6.9 MHz

M. Wiklund

Multi-frequency approaches

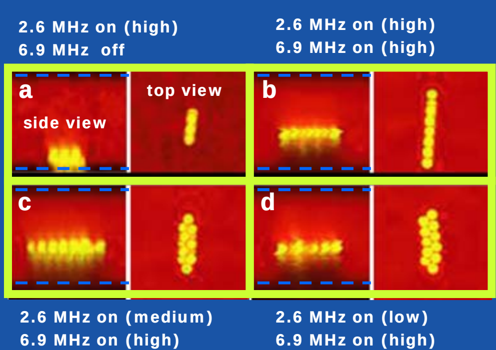

Manneberg *et al*, Appl. Phys. Lett. 2008

a) Vertical 2D monolayer on the bottom
b) Vertical 2D monolayer, levitated
c) Compact 3D spheriod, levitated
d) Horizontal 2D monolayer, levitated

4) 3D ⇔ 2D aggregation
   tuning the ampl. ratio of 2.5 and 6.9 MHz

Multi-frequency approaches

Video example of cage in action

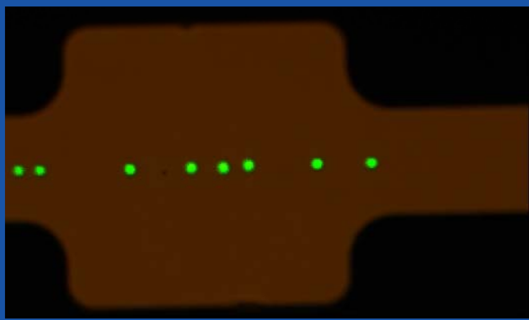

M. Wiklund

-33-

Multi-frequency approaches

Another example (round ”confocal” cage)

Single-frequency operation

Levitation mode @ 6.93 MHz

Focusing mode @ 2.55 MHz

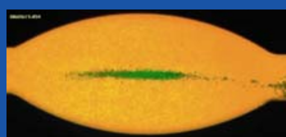

Dual-frequency operation

All three below: 6.93 @ 6 V (constant level) + 2.55 MHz @ varying levels

2.55MHz @ 2 V

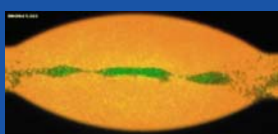

2.55MHz @ 6 V

2.55MHz @ 10 V

M. Wiklund

-34-

Multi-frequency approaches

Rectangular cage

Confocal cage, large radius of curvature

Confocal cage, small radius of curvature

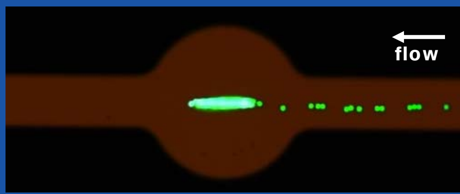

KTH Physics

M. Wiklund

Multi-frequency approaches

Approach 4, another example (Wiklund group, 2009) – superposition and localization:

Many frequencies (f_1, f_2, …) with larger diff. ($f_1 - f_2$, …) combined with geometrical channel features (”cages”) of different widths (both ~λ and >>λ widths)

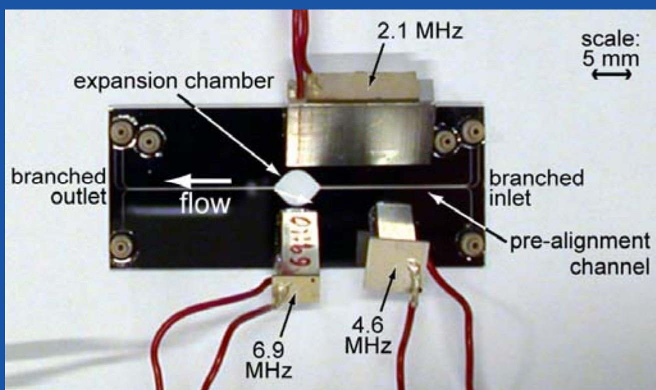

Svennebring *et al.*, Biotech. Bioeng. **103**, 323, 2009

KTH Physics

M. Wiklund

M. Wiklund

Multi-frequency approaches

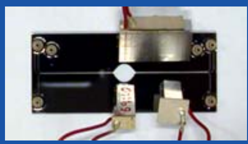

Cage with >>λ width:
(5 mm width @ 6.9 MHz ⇨ >20×λ)
Idea: Localization of forces by focusing

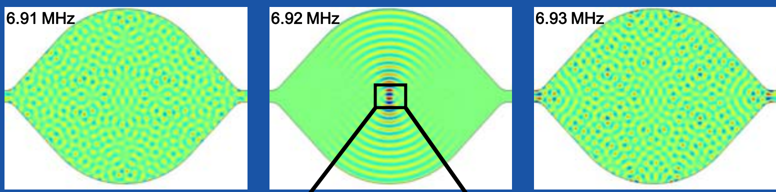

Simulation (Henrik Bruus group, DTU, Denmark)

Experiments

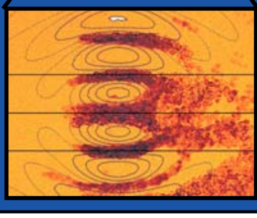

flow

M. Wiklund

Multi-frequency approaches

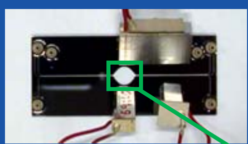

Cage with >>λ width:
(5 mm width @ 6.9 MHz ⇨ >20×λ)
Idea: Localization of forces by focusing

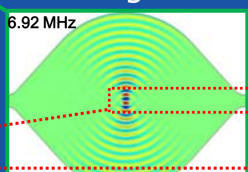

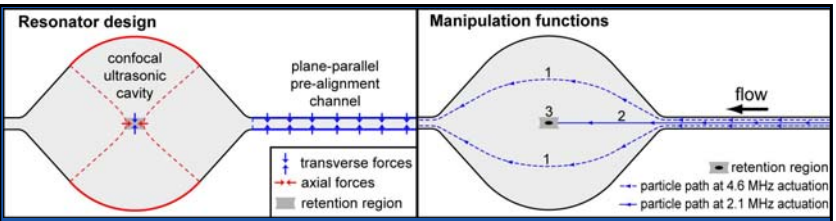

Approach 3, another example (Wiklund group, 2009) – superposition and localization:

Principle of operation:
Resonator design and manipulation functions

KTH Physics

M. Wiklund

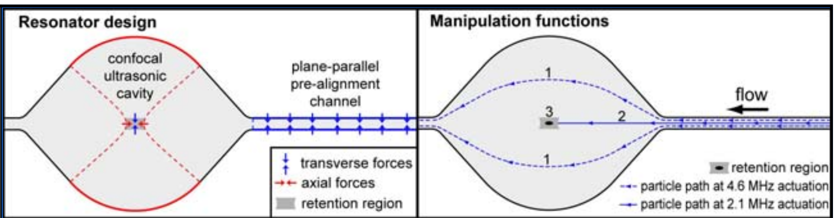

- Bypass
- Injection
- Bypass
- Retention

TRANSDUCER ON
TRANSDUCER OFF

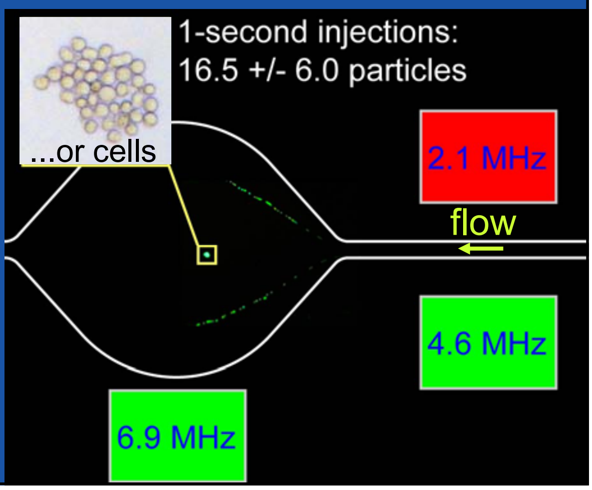

KTH Physics

M. Wiklund

Multi-frequency approaches

Approach 5 (Hill group, 2007-2010):
Frequency modulation
(switching between two frequencies, ”mode switching”)

P. Glynne-Jones, Ultrasonics **50**, 68, 2010

ARTICLE INFO

Article history:
Received 15 January 2008
Received in revised form 20 July 2009
Accepted 29 July 2009
Available online 4 August 2009

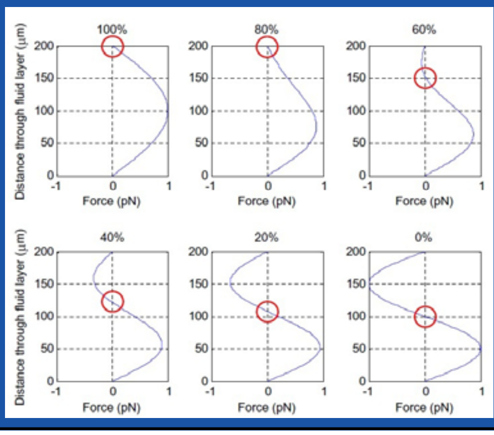

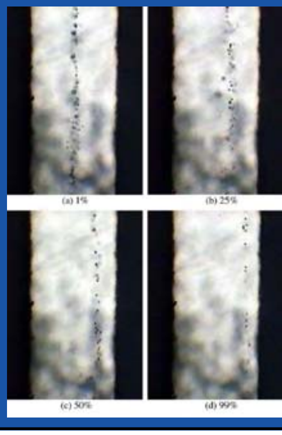

KTH Physics

M. Wiklund

Multi-frequency approaches

Approach 5 (Wiklund group, 2009):

Frequency modulation (cycling linear frequency sweeps)

Single frequencies:
From 6.85 to 6.95 MHz

”Dead zones” at different locations for different freq.

”Negative alignment” at different locations for different freq.

Frequency modulation:
6.85-6.95 MHz at the rate 1 kHz

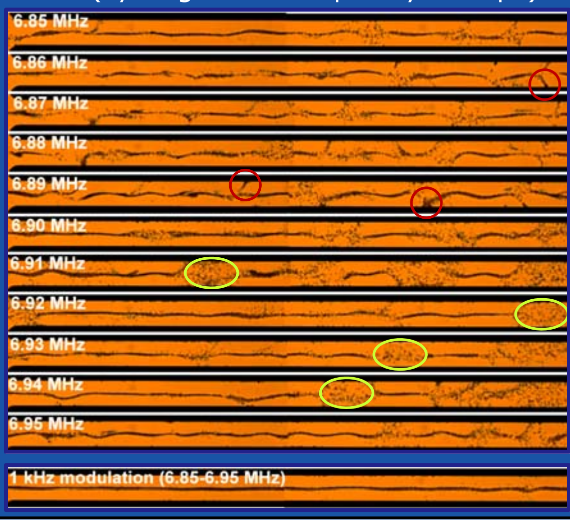

KTH Physics

M. Wiklund

Multi-frequency approaches

Approach 5 (Wiklund group, 2009):

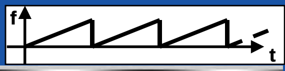

Slow rate of modulation (<1 Hz):

Particle transport!

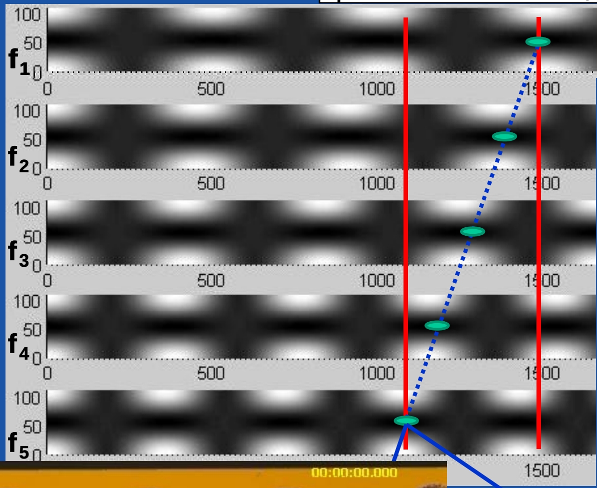

Video clip:

M. Wiklund

Multi-frequency approaches

Combine caging (approach 4)
with frequency modulation (approach 5): Transport + caging!

f_1: 6.9±0.05 MHz, rate 1 kHz

f_2: 2.6±0.05 MHz, rate <1 Hz

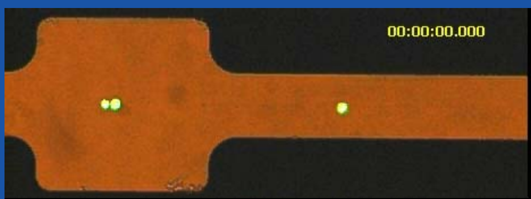

Immune cells

5 µm beads

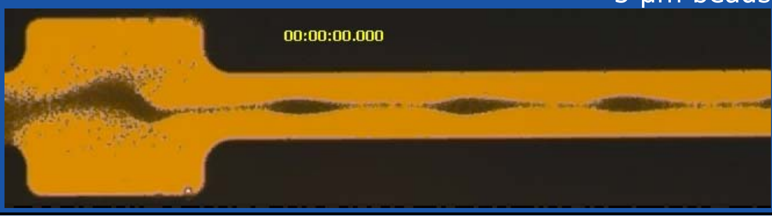

M. Wiklund

M. Wiklund

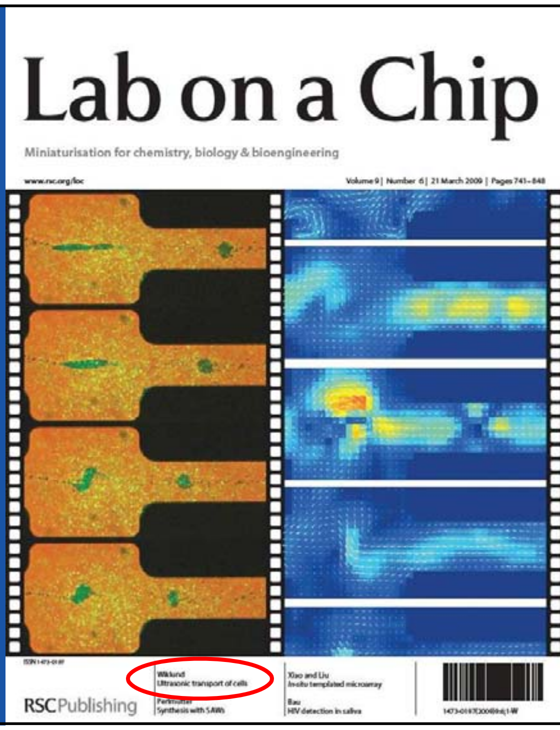

Vol. 9, No. 6, March 2009

M. Wiklund

Multi-frequency approaches

Parallelization?

10 x 10 cages of the 300 µm format:

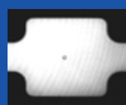

Schematic of the multi-well

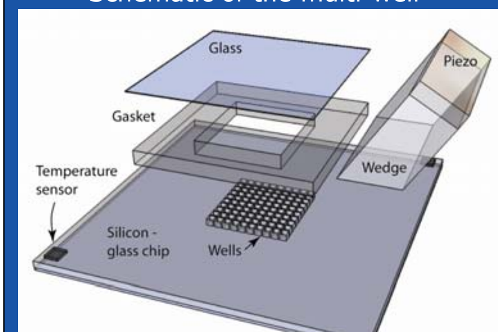

22 x 22 mm

Experimental Platform

Multi-frequency approaches

Multi-well plate:
Compare theory and experiments (beads)

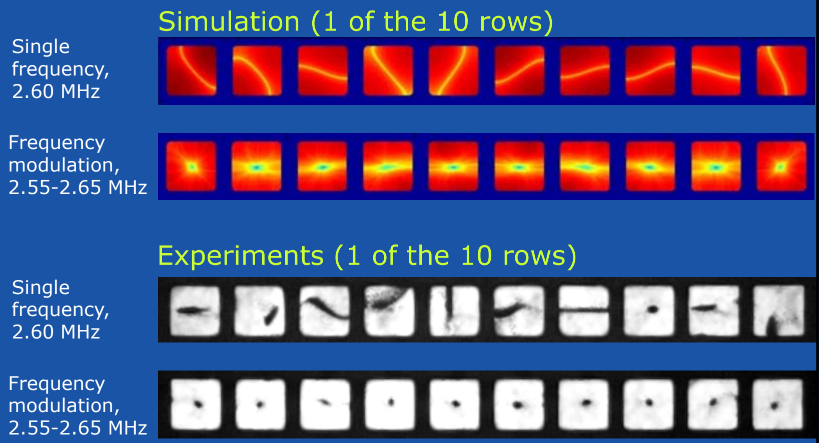

Vanherberghen *et al*, submitted manuscript

KTH Physics

M. Wiklund

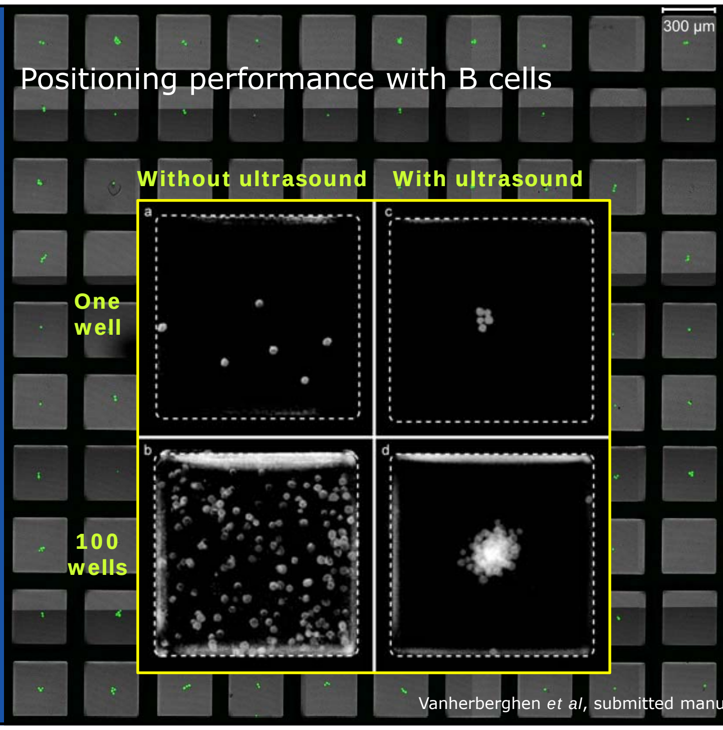

Vanherberghen *et al*, submitted manuscript

KTH Physics

M. Wiklund

KTH Physics

M. Wiklund

Video demo

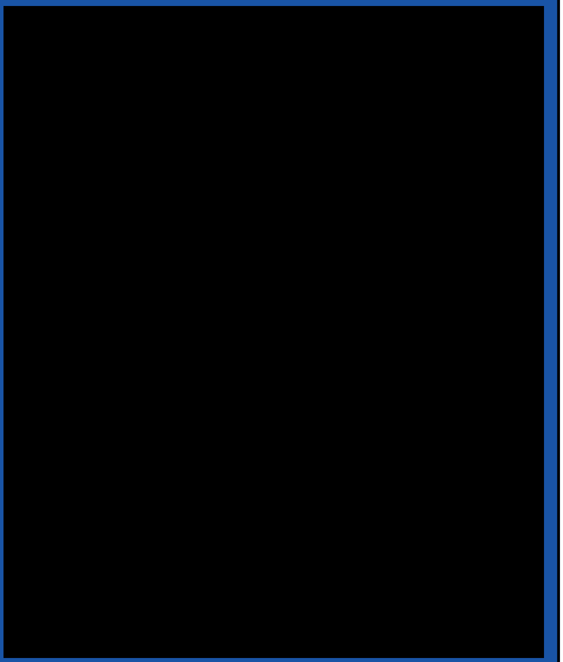

Vanherberghen *et al*, submitted manuscript

KTH Physics

M. Wiklund

-50-

Summary

- Multi-frequency approaches are useful for creating advanced manipulation functions:
  - Superimposed (orthogonal) fields
  - Localized fields
  - Both superimposed and localized fields
  - Frequency-modulated fields
    1. Averaged fields over many frequencies
    2. Moving nodes

Ultrasonic trapping, cell culturing and coupling to bioanalysis

Johan Nilsson

Dept. Measurement Technology and
Industrial Electrical Engineering
Div. Nanobiotechnology/Electrical Measurements
Lund University
Sweden

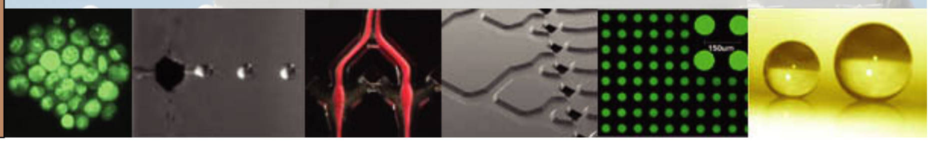

Non-contact acoustic trapping

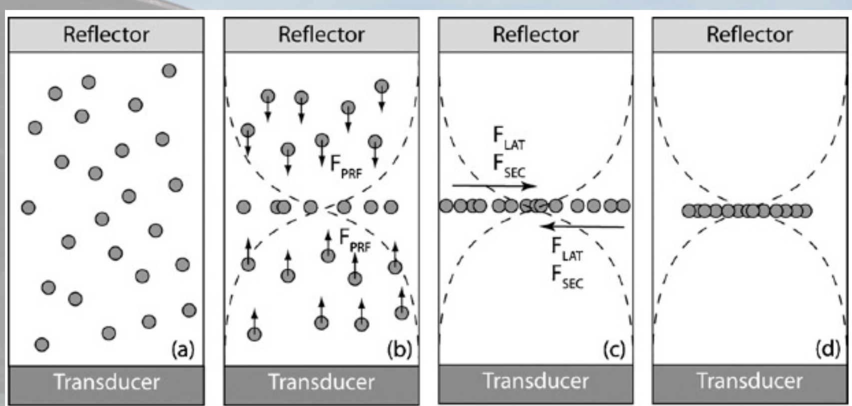

Transversal acoustic standing wave forces

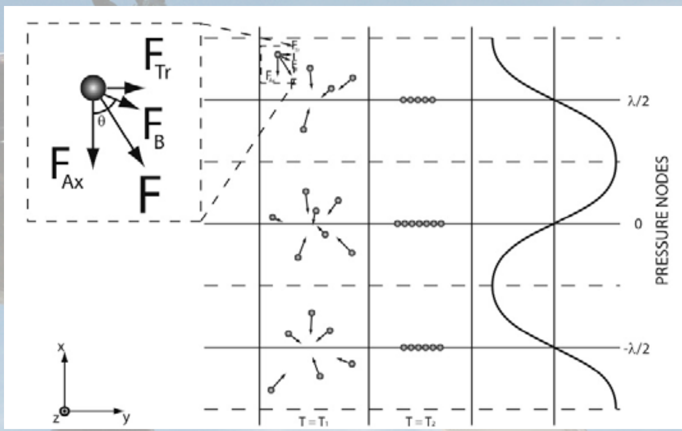

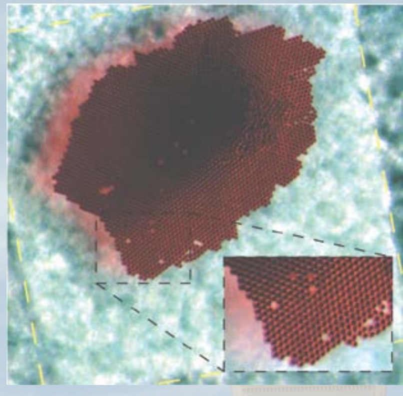

Hammarström et al.
Lab. Chip. 2010 accepted

$$F_{Tr} = V_p \nabla \bar{E} \left(\frac{3(\rho_p - \rho_f)}{\rho_f + \rho_p} \cos^2\left(\frac{2\pi x}{\lambda}\right) - \frac{\beta_f - \beta_p}{\beta_f} \sin^2\left(\frac{2\pi x}{\lambda}\right) \right)$$

Gradient in energy density required!

Secondary radiation force

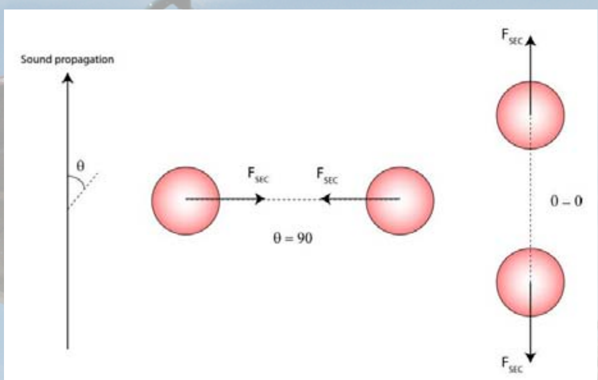

$$F_B(x) = 4\pi R^6 \left[\frac{(\rho_p - \rho_f)^2 (3\cos^2\theta - 1)}{6\rho_f d^4} v^2(x) - \frac{\omega^2 \rho_f (\beta_p - \beta_f)^2}{9d^2} p^2(x) \right]$$

F_B is the secodary acosutic force, also called Bjerknes force, F_B
d is the distance between the particles
Φ is the angle between the center line of the particles and the direction of propagation of the incident acoustic wave

Bjerknes, V.F.K., *Die Kraftfelder. 1909, Vieweg und Sohn: Braunschweig,Germany.*

Non-contact acoustic trapping

Multinode trap

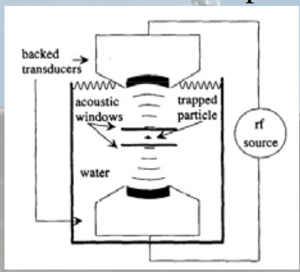

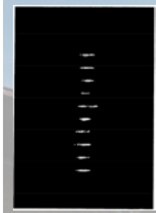

Hertz. J. Appl. Phys. 78 (8) 1995

λ/2 cage trap

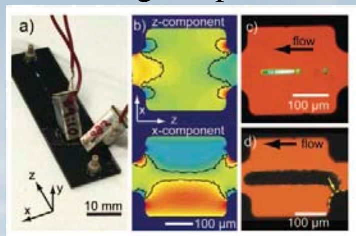

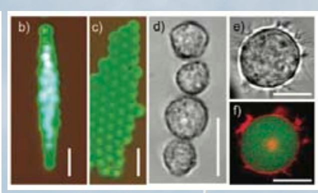

Manneberg et al. Appl. Phys. Lett. 93, 063901, 2008.

λ/2 trap

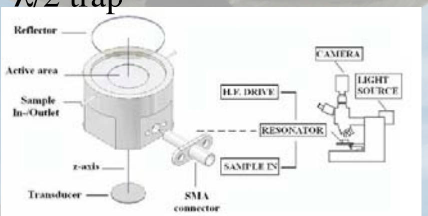

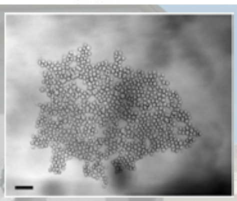

Multinode trap

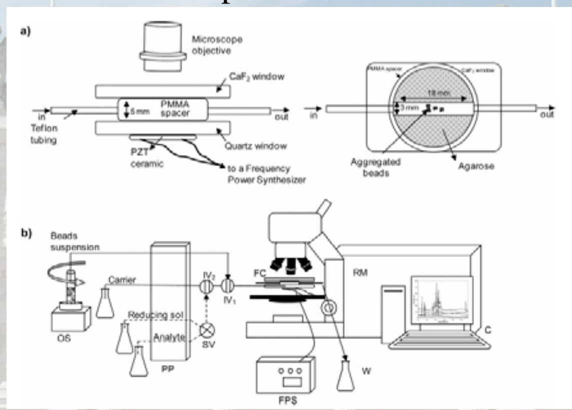

Bazou et al. Ultrasound in Med. & Biol. 31 (3) 2005   Ruedas-Rama et al. Anal. Chem. 2007, 79, 7853-7857

Non-contact acoustic trapping

Normally the limit in particle size for trapping is found around 1 μm due to acoustic streaming

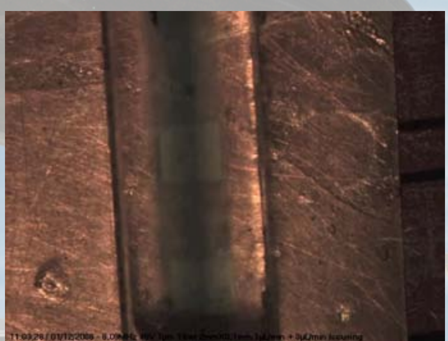

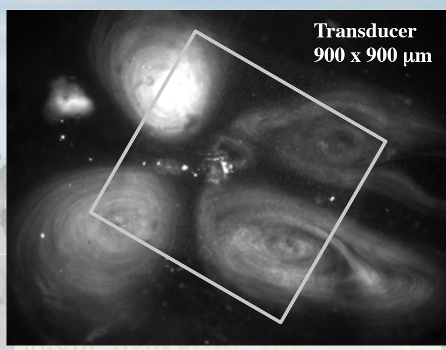

Trapping 1 μm particles

Acoustic streaming
240 nm fluorescentparticles

Our vision

- Dynamic array trapping -

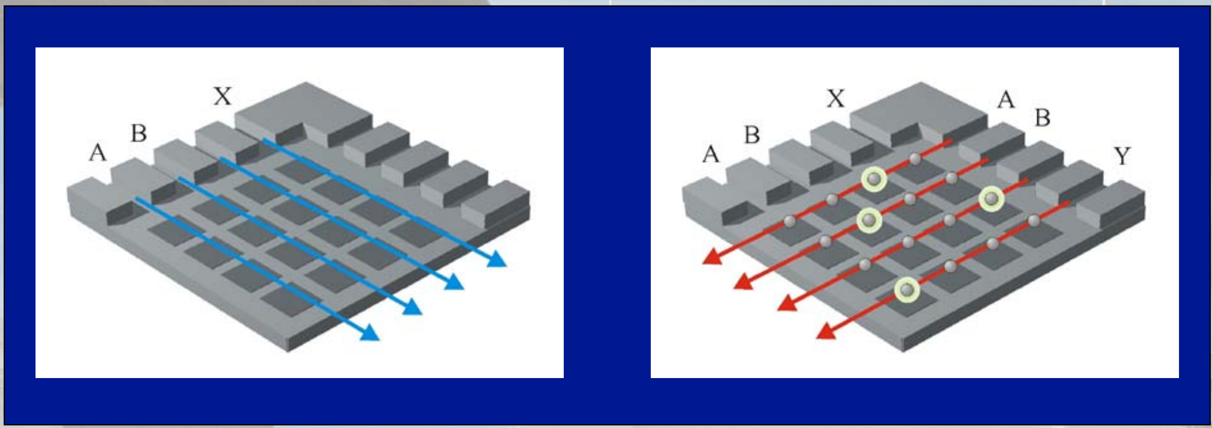

Lilliehorn et al. Sens. Act. B 106 (2005) 851

System set-up for acoustic trapping

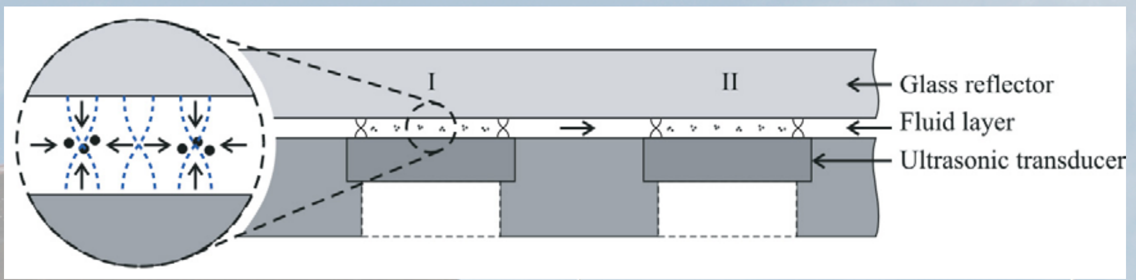

- Reflector, (2n+1) λ/4
- Channel, λ/2
- Transducer, λ/2

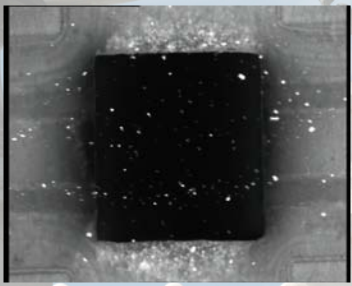

Trapping over a single transducer

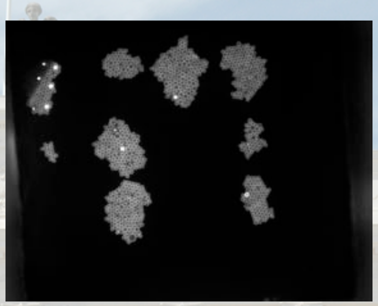

Monolayered bead clusters

Lilliehorn et al. Sens. Act. B 106 (2005) 851

Resonator design

To achieve particle trapping in the center of the channel

Transducer: $\lambda/2$

Channel height: $\lambda/2$

Cover thickness: $(2n+1) \lambda/4$

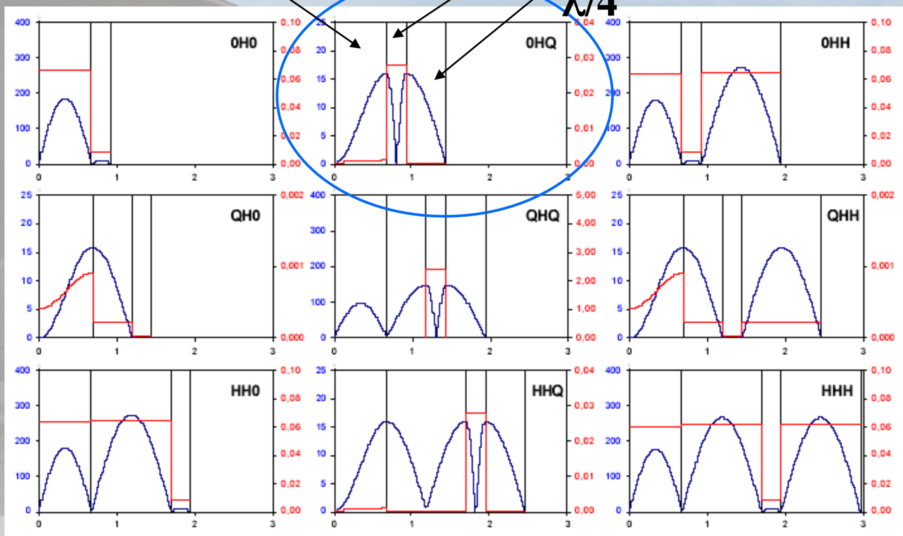

[Hawkes et al., Proc. Forum Acusticum 2002 Sevilla, Spain, 2002]

Microfluidic platform

- Transducer plate -

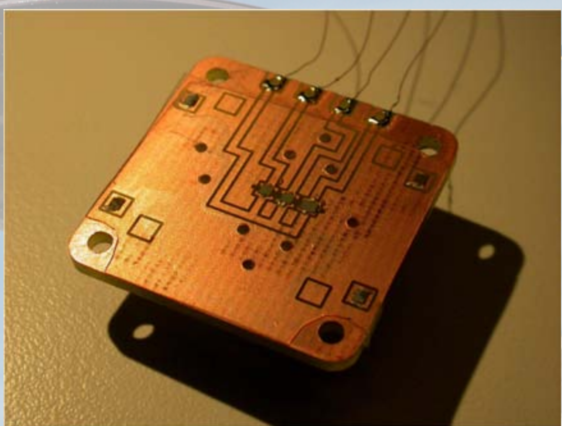

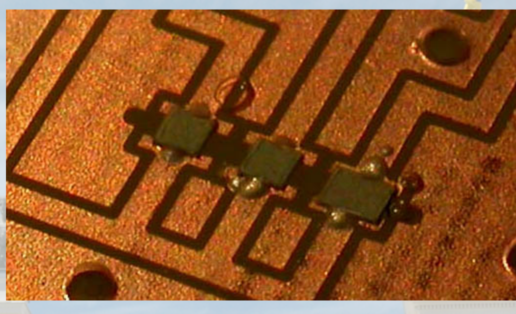

Printed circuit board with 3 miniaturized 10 MHz ultrasonic transducers (PZT, 600 x 600 μm)

Lilliehorn et al. Sens. Act. B 106 (2005) 851

Microfluidic platform

- Channel structure -

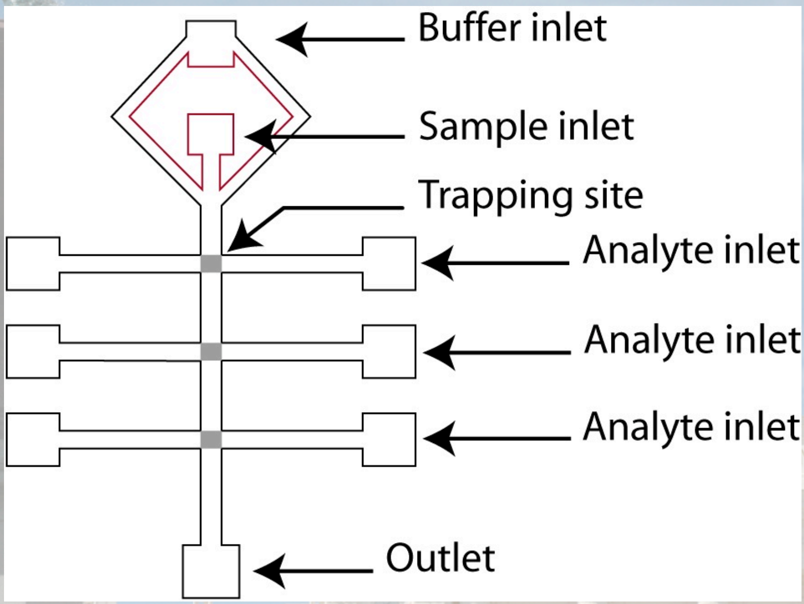

Lilliehorn et al. Sens. Act. B 106 (2005) 851

Microfluidic platform

- Transducer and channel structure joined -

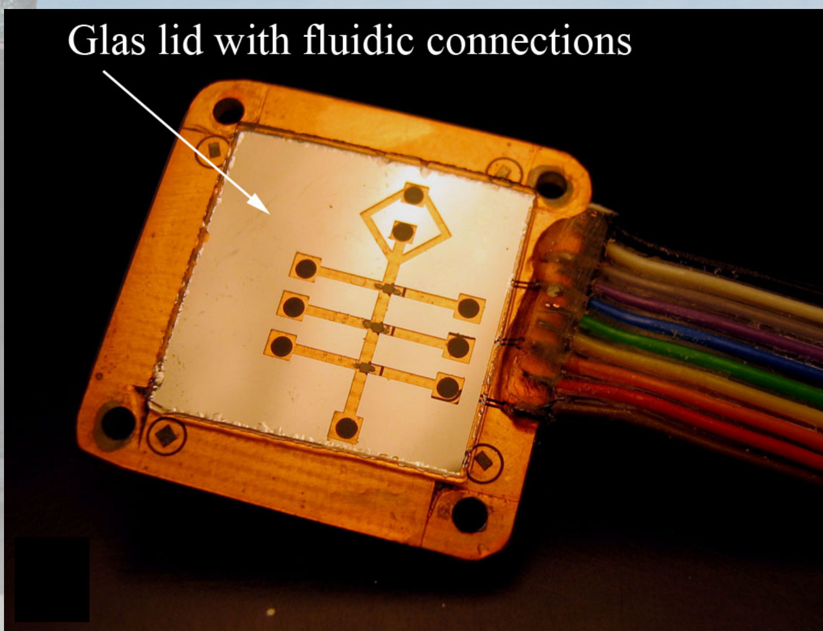

Lilliehorn et al. Sens. Act. B 106 (2005) 851

Microfluidic platform

- Complete unit in brass fixture -

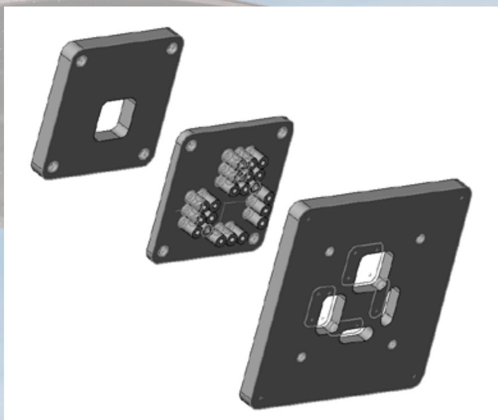

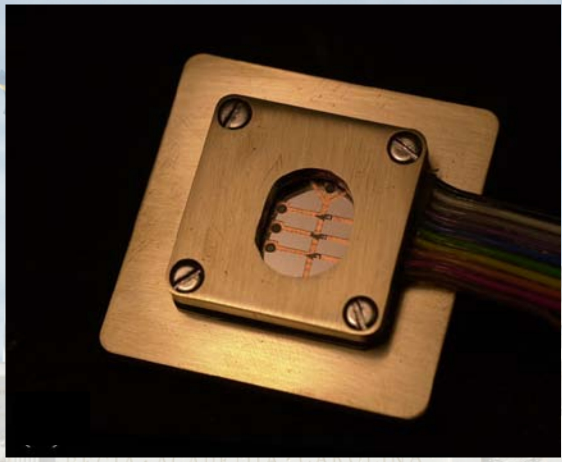

• Glass lid - Optical access

Lilliehorn et al. Sens. Act. B 106 (2005) 851

Capture and release of particles

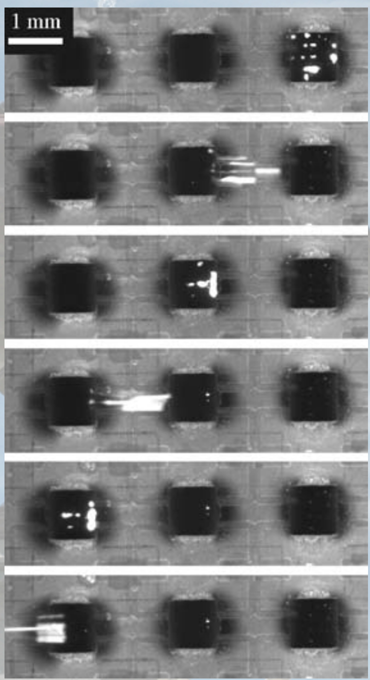

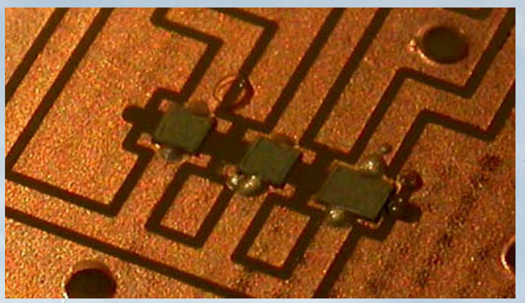

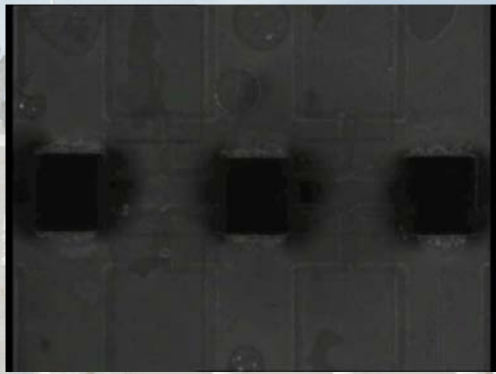

Lilliehorn T. et al, Ultrasonics 43(5) (2005) 289-299

Lilliehorn et al. Sens. Act. B 106 (2005) 851

Temperature control

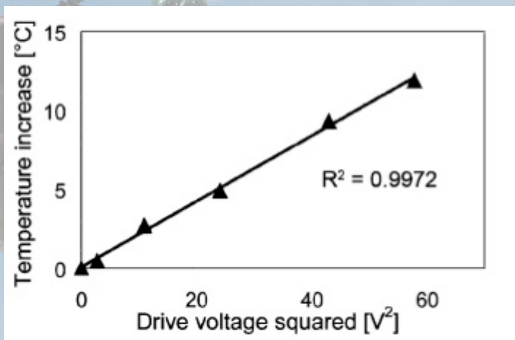

- The temperature was measured using the temperature dependent fluorescence of 0.1 mM Rhodamine B
- The temperature increase above room temperature is plotted against (Piezo drive voltage)^2

Nilsson M. et al Anal.Chem. 2007, 79, 2984-2991

On-line yeast culturing in the acoustic trap

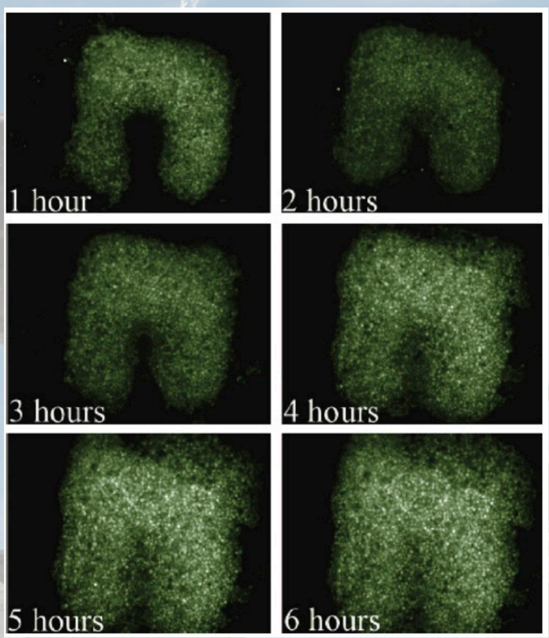

- Culturing temperature stability is controlled by acoustic input power
- Continuous supply of fresh media
- Proliferation during 6 hours

Nilsson, M. et al Analytical Chemistry, 2007, 79, 2984-2991

Neural stem cell viability

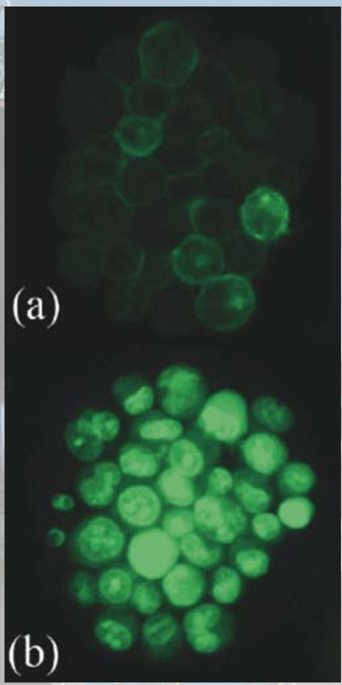

GFP Neural stem cell viability test,
(a) 0 min (b) 15 min cultivation and then supply of acridine orange through side channels. The transport of acridine orange into cells indicates viability.

Nilsson, M. et al Analytical Chemistry, 2007, 79, 2984-2991

Erythrocyte ATP release

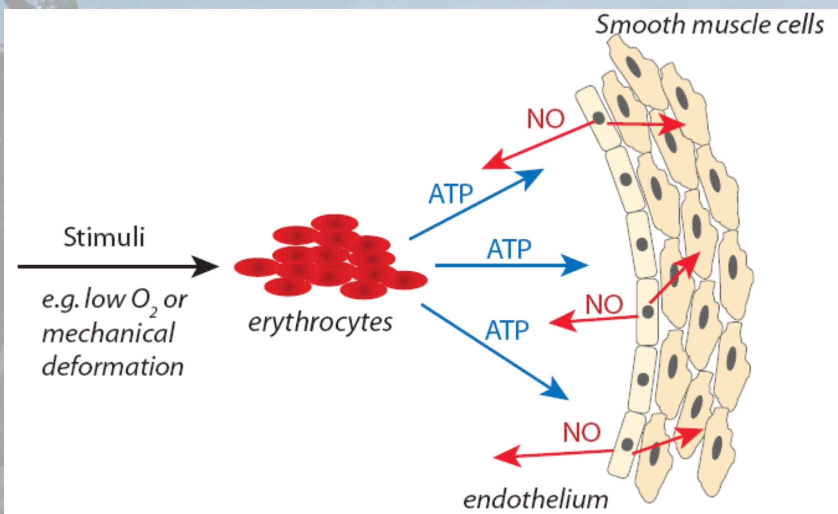

- ATP in the blood mediates vascular diameter
- Erythrocytes (Red blood cells) make up 45 % of blood volume

Erythrocyte perfusion and detection system

- Acoustic non-contact trapping and continuous perfusion
- Chemiluminescent Luciferin/ Luciferase reaction for ATP detection

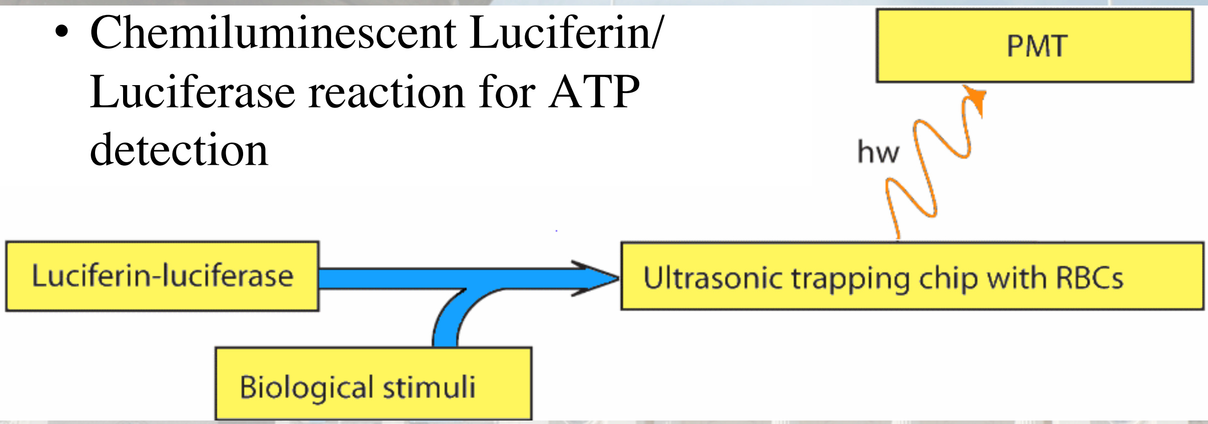

Capture of particles

- Hydrodynamic focusing -

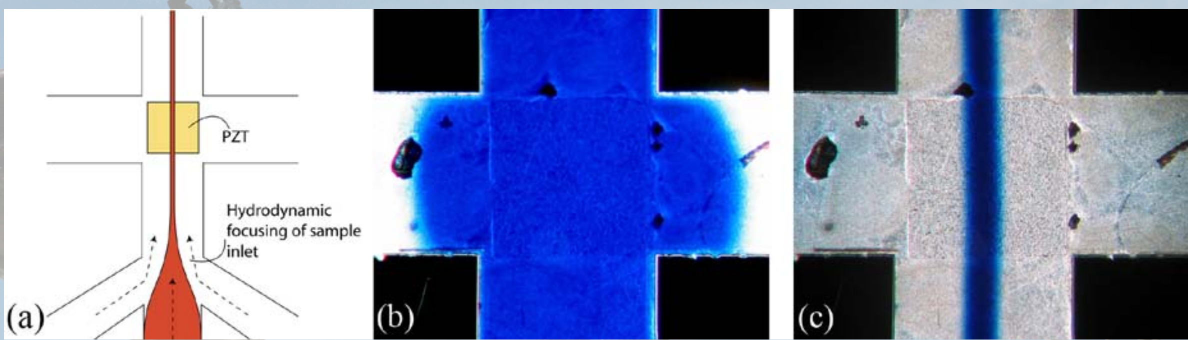

- Eliminate loss of material to the side channels

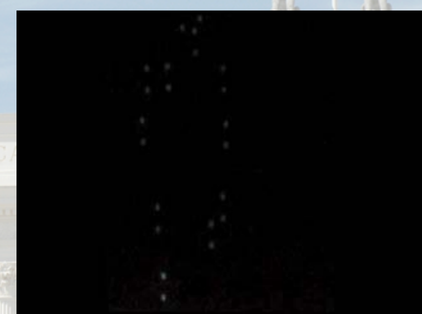

Nilsson, M. et al Analytical Chemistry, 2007, 79, 2984-2991

Microfluidic layout

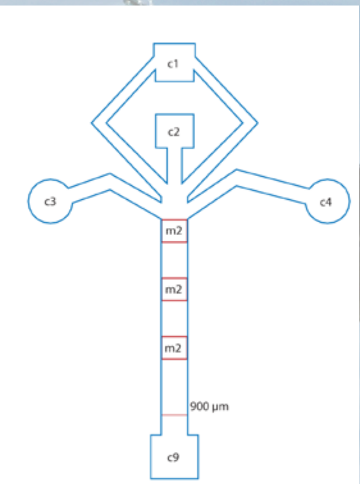

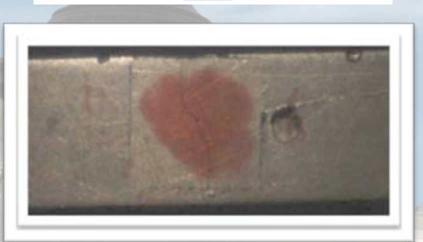

- 1 μl/min flow rate
- Trapping phase
  - Centre stream: isolated RBCs
  - Hydrodynamic focusing with PSS (Physiological saline solution)
- PSS wash phase
- Luciferin/Luciferase (L/L) phase
  - L/L stream from side inlet
  - Stimuli injected to L/L stream (off-chip)

Experimental set-up

- Rotating holder for PMT and USB-microscope
- Chip mounted in holder underneath
- Light screening

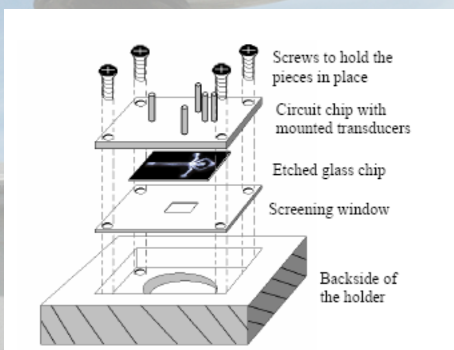

Response curves: RBC lysis

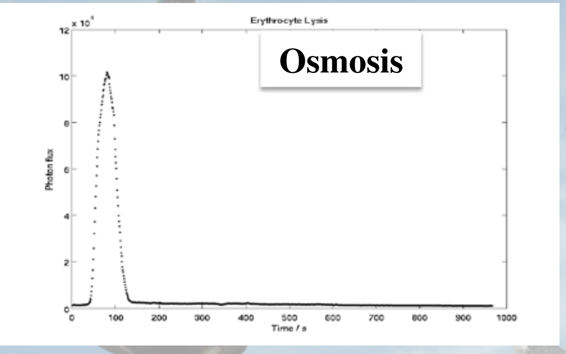

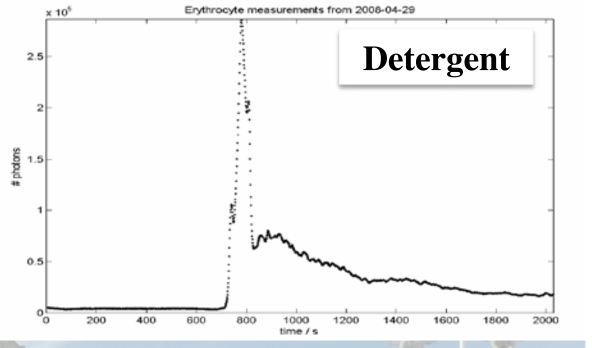

- On lysis the RBCs release all ATP
- Evaluates system sensitivity
- L/L mixed with MilliQ water (osmosis)
- L/L injected with 1 % TritonX-100 (detergent)
- Intensity dependent on age of the erythrocytes and size of cluster

Response curves: Adrenaline

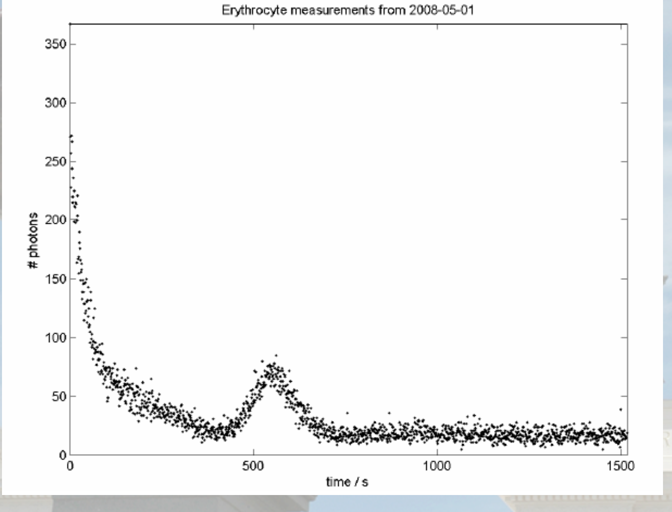

- 10 μM adrenaline injected
- Hormone and neurotransmitter
- Fight or escape situations - boosts oxygen supply and increases heart rate
- High but physiologically relevant concentration

Acoustic Differential Extraction (ADE) for DNA analysis of sexual assault evidence

- Almost all states in the USA require that convicted offenders are DNA-typed (STR typing)
- Huge sample backlog of sexual assault cases in the US
  - **~ 350 000**

United States Cong. House. 107th Cong. H. R. 3961, 2002.
Report to the Attorney General on Delays in Forensic DNA Analysis. NIJ. 2003.
Lovrich NP, et al. National Forensic DNA Study Report. 2004.

The sample

- The sexual assault sample collected from the victim consists of
  - Male sperm cells (Perpetrator)
  - Female epithelial cells (victim)
  - Female cell lysate (free female DNA)
- The male and female DNA is isolated
  - Purification and enrichment of the male fraction is necessary to obtain a DNA profile of the suspect

Laminar flow valving

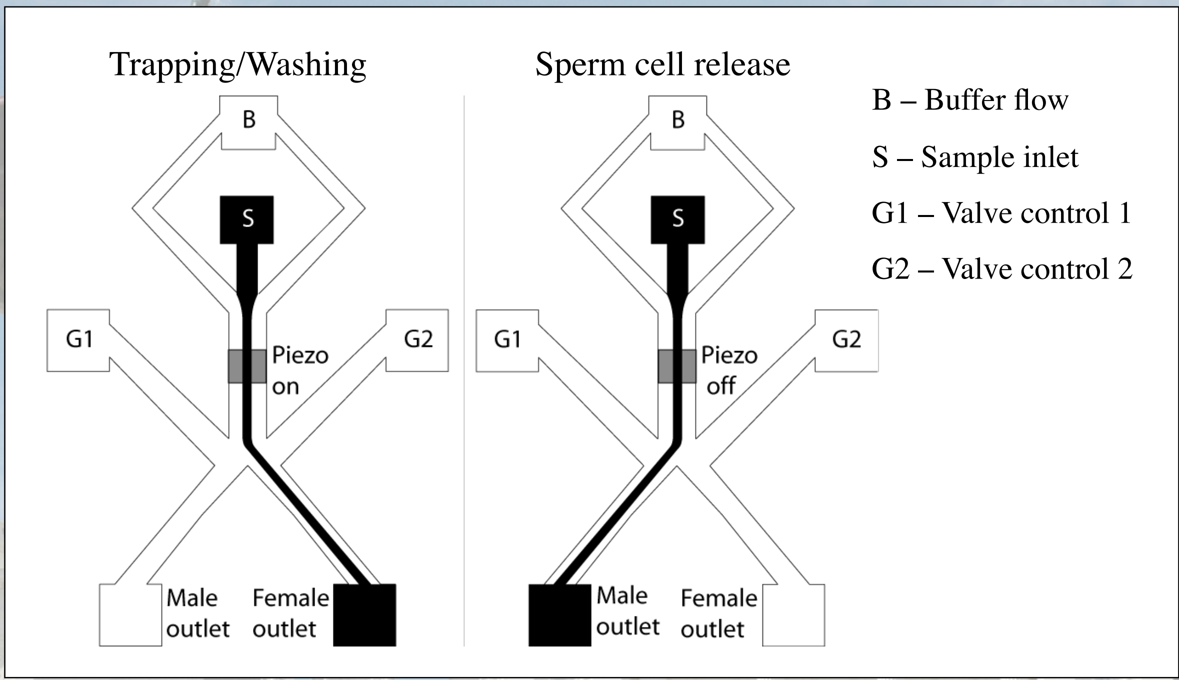

Norris, Evander et al. Anal. Chem. 2009, 81, 6089 Evander et al. MicroTAS Conf. 2006

Flow simulations

- COMSOL simulations was used to find the velocities to control the valves.

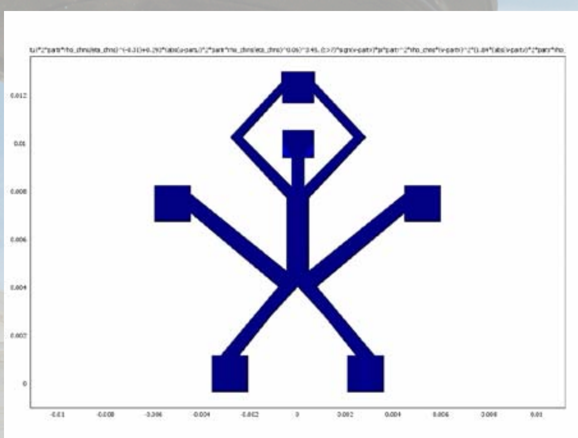

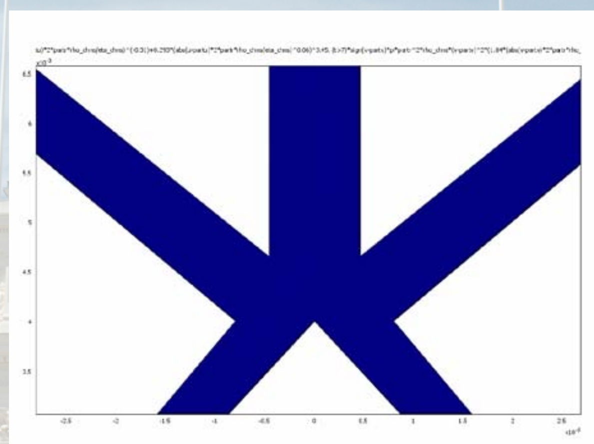

Norris, Evander et al. Anal. Chem. 2009, 81, 6089 Evander et al. MicroTAS Conf. 2006

Acoustic trapping, washing and hydrodynamic valving

Evan's blue (dye) = female DNA
Polystyrene beads (10 μm) = sperm cells

Norris, Evander et al. Anal. Chem. 2009, 81, 6089 Evander et al. MicroTAS Conf. 2006

Purifying the sample

Flow direction

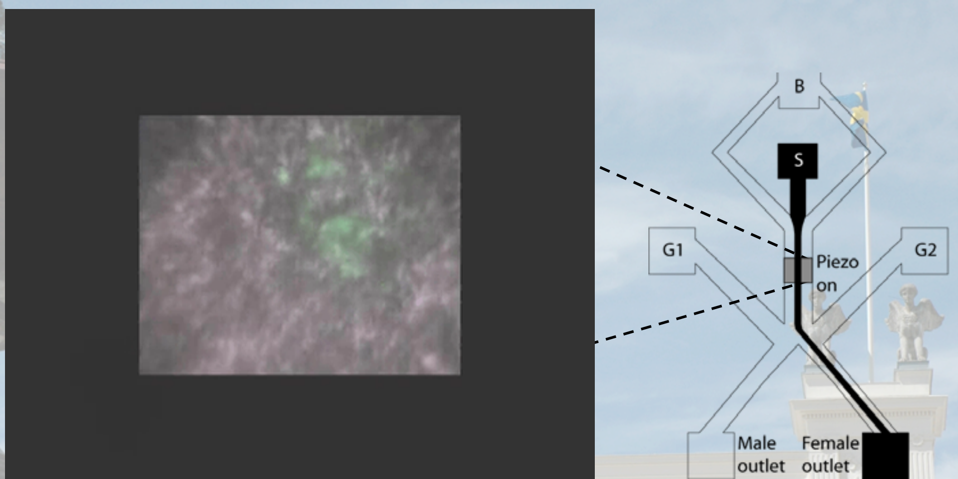

Video of sperm cell capture and release

Norris, Evander et al. Anal. Chem. 2009, 81, 6089 Evander et al. MicroTAS Conf. 2006

Purity of Recovered Product

- Highly enriched male and female fractions

	Percent Male	Percent Female
Original Sample:	5.1 ± 0.5 %	94.9 ± 9.3 %
Enriched male fraction:	**85.4 ± 5.7 %**	14.6 ± 1.0 %
Enriched female fraction:	0.5 ± 0.04 %	**99.5 ± 8.0 %**

[1]**Horsman KM, Hickey JA, Cotton RW, Landers JP, and LO Maddox, *Journal of Forensic Sciences.*, 2006, *4*, 131-5.**

Norris, Evander et al. Anal. Chem. 2009, 81, 6089 Evander et al. MicroTAS Conf. 2006

Capillary trapping

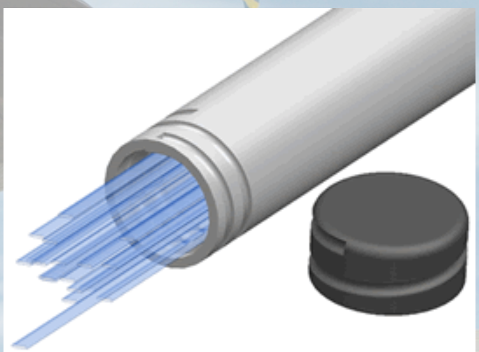

Off-the-Shelf capillaries for acoustic trapping

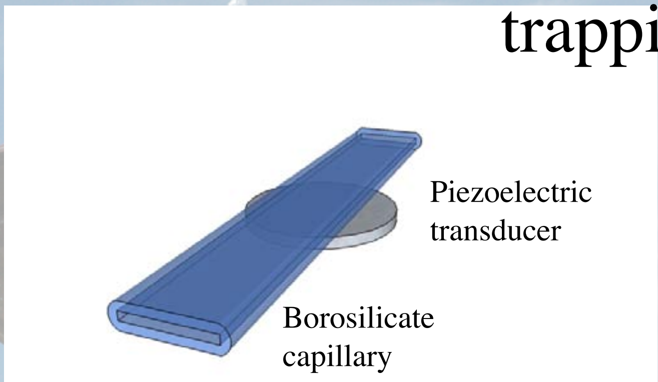

- No clean-room fabrication
- Single-use applications
- Trapping occurs over the transducer
- Damping localize the field in the flow direction

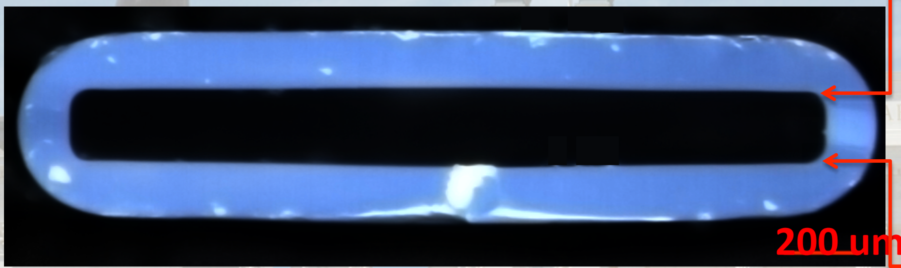

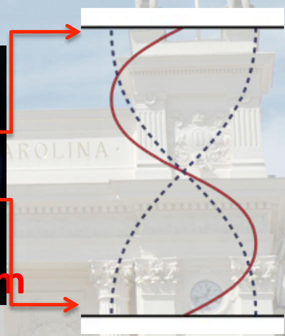

Cross-sectional optical image

Hammarström et al. Lab. Chip. 2010 accepted

Single – multinode trapping

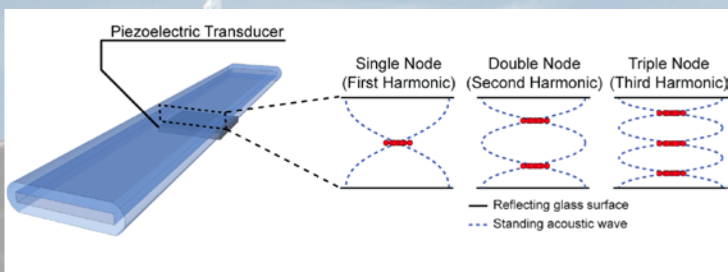

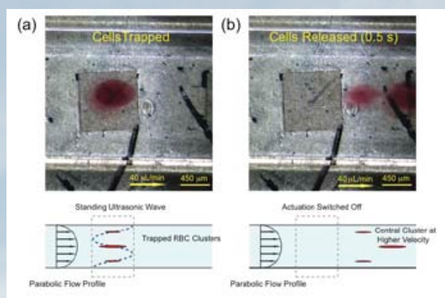

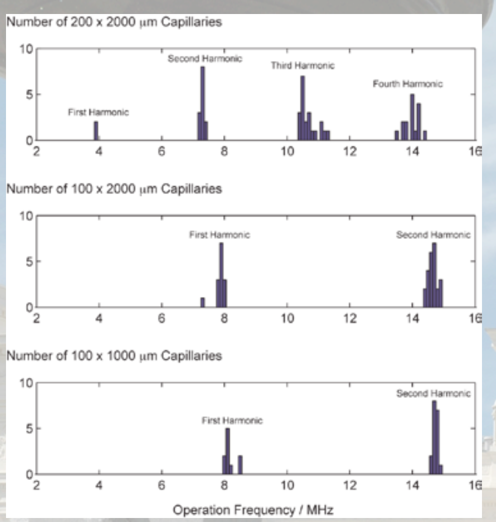

200 x 2000 μm

100 x 2000 μm

100 x 1000 μm

- Large number of capillaries evaluated
- Note: Manufacturer states ± 10% dimensional variation

Hammarström et al. Lab. Chip. 2010 accepted

Single – multinode trapping
Simulation

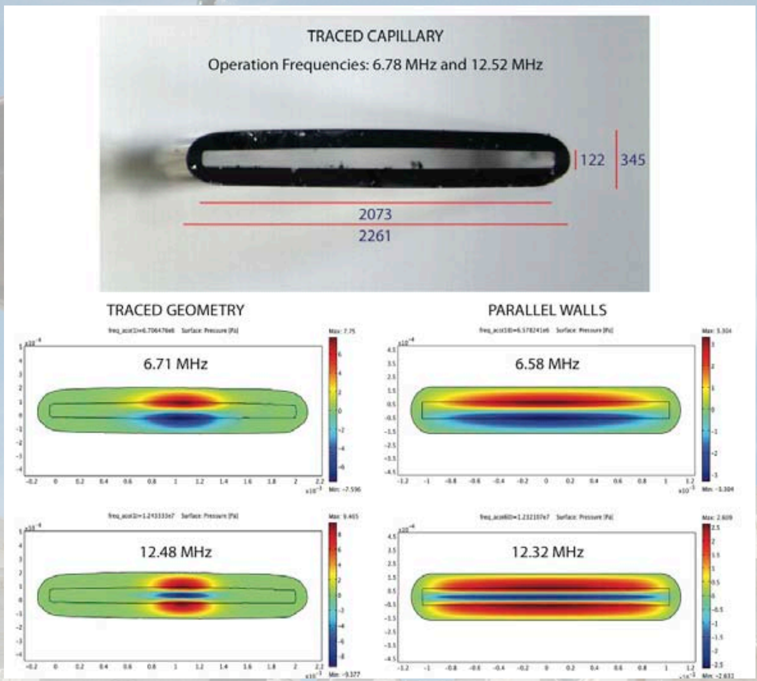

- COMSOL simulation
- The slightly bulging walls should be taken into consideration (left)
- In excellent agreement with experiments

Hammarström et al. Lab. Chip. 2010 accepted

200 x 200

100 x 200

100 x 100

The trapping pipette
(Trapipette™, Trapette™, Pipettrap™ or TripTrap™?:-)

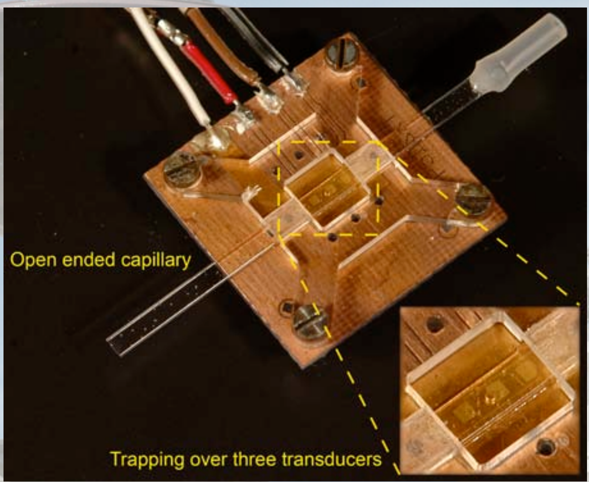

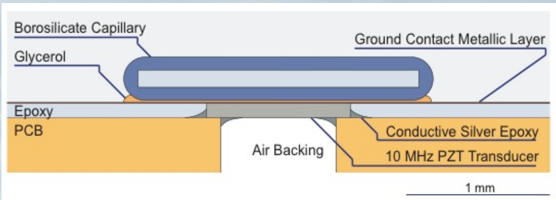

- Multiple transducers
- Aspirate/dispense

Hammarström et al. Lab. Chip. 2010 accepted

Volume reconstruction from confocal microscopy shows cluster conformation

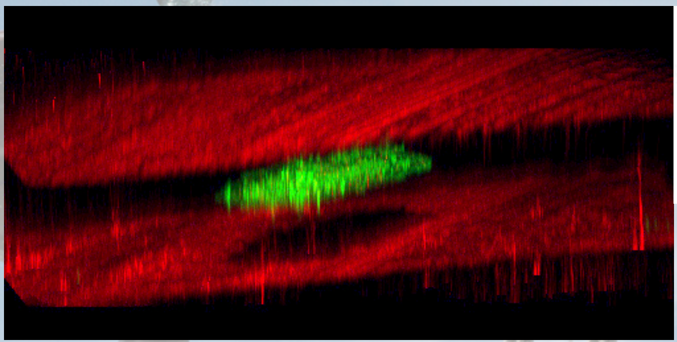

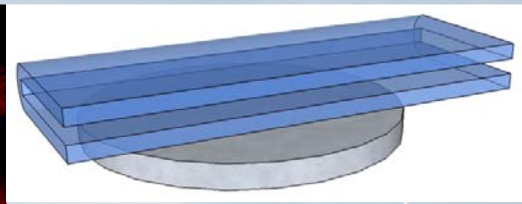

Confocal volume scan:
Green channel – 4.2 um FITC (bead cluster)
Red channel – reflective data (capillary walls)

- Beads collected in channel centre
- Volumetric calculation gives ~500 000 cells

Hammarström et al. Lab. Chip. 2010 accepted

System Workflow

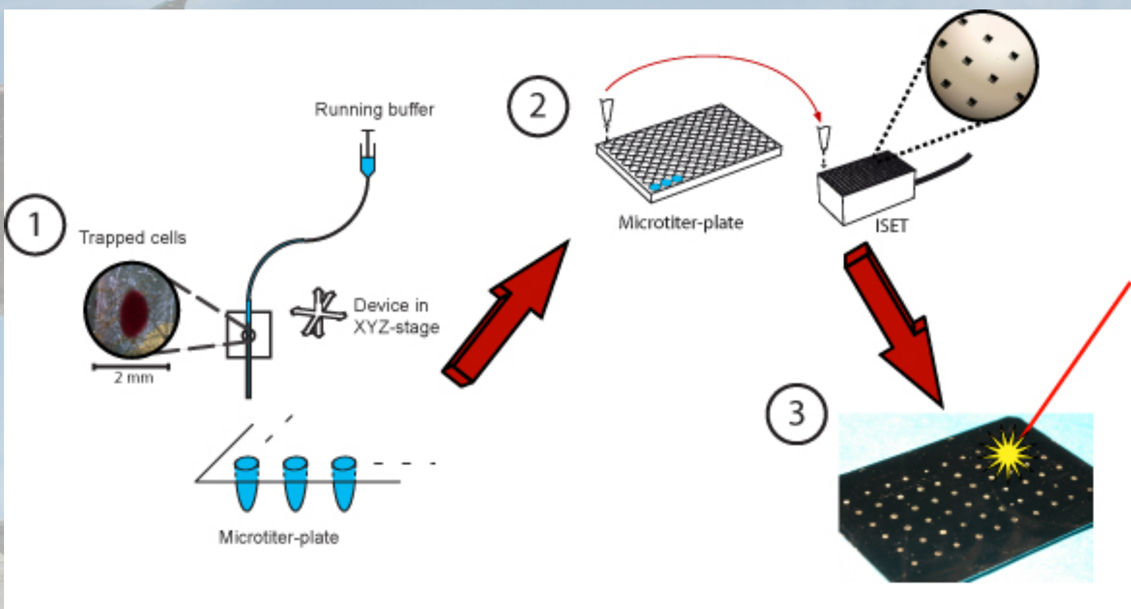

Automated trapping of cells

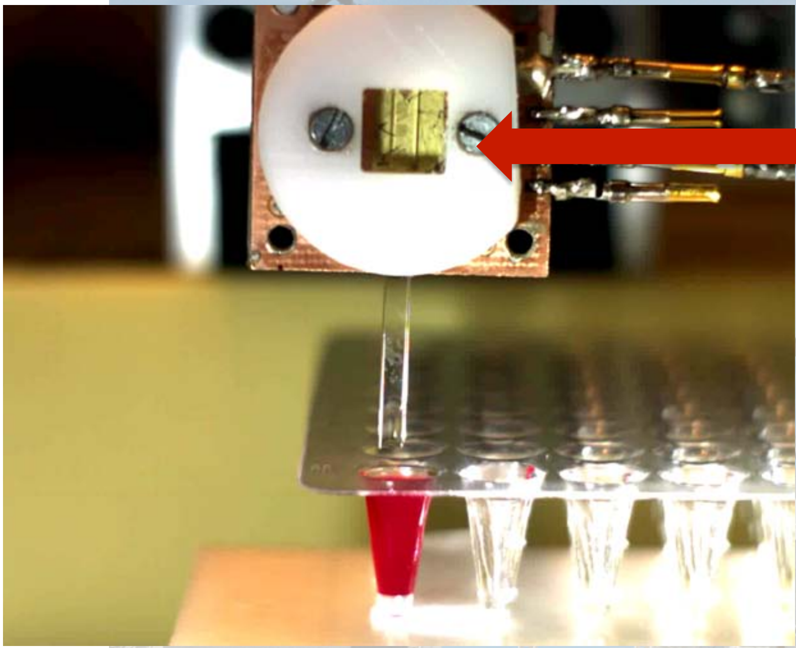

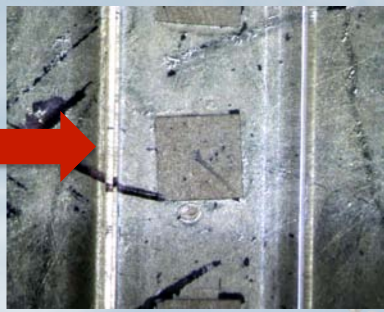

- **Automation**
- **Aspiration perfusion**
- **Defined number of cells**
- **Temporal resolution**

Proof of principle experiment

- 10 uL Blood diluted x 10 PBS
- Impermeable peptide at 40 uM
- Membrane binding small molecule at 2 uM

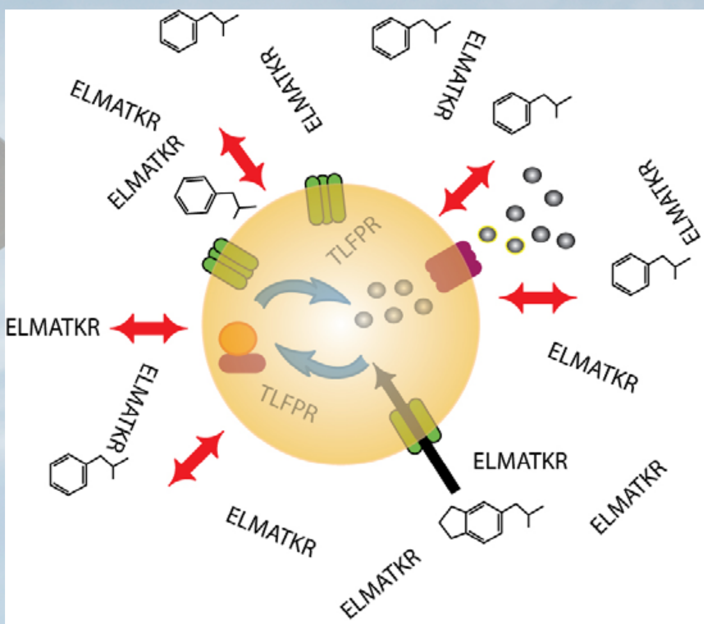

Acoustic trapping -> wash -> lysis -> ISET -> MALDI MS

MALDI MS read-out

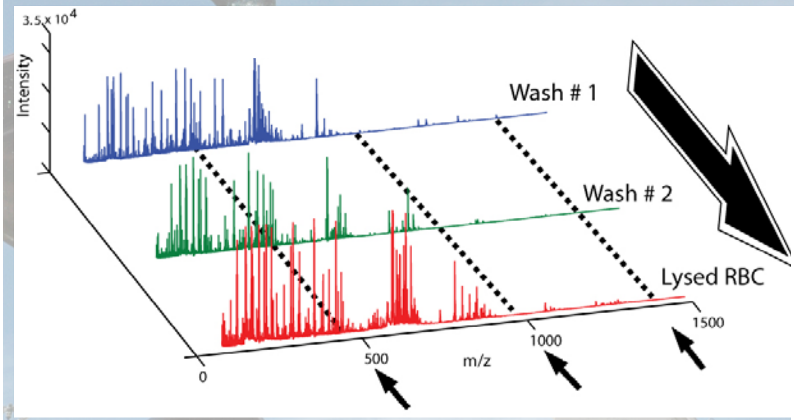

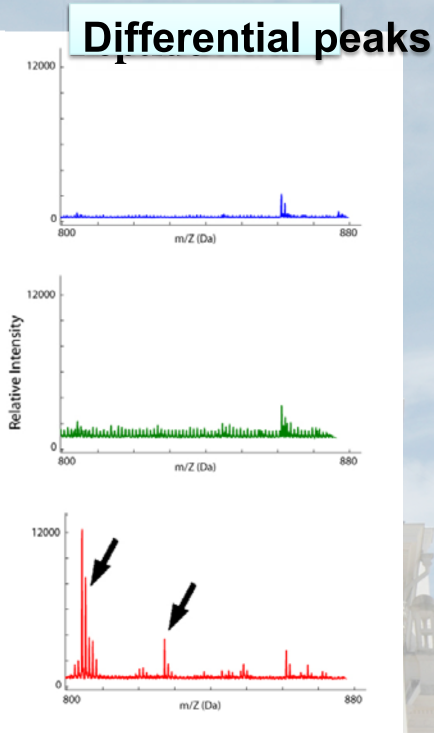

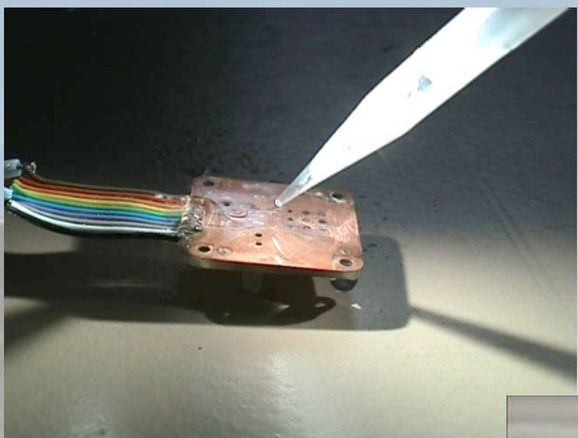


Questions?
REGIA · ACADEMIA · CAROLINA ·

Affinity probing and biospecific extraction in acoustic standing wave chips

Thomas Laurell

Dept. Measurement Science & Industrial Electrical Engineering
Div. Nanobiotechnology
Lund Luniversity
Sweden

thomas.laurell@elmat.lth.se
www.elmat.lth.se/english/research

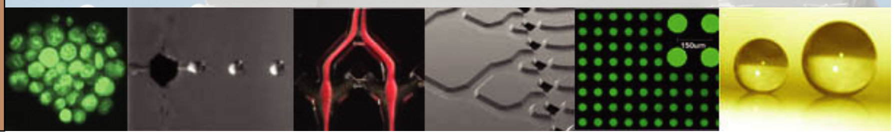

Acoustic buffer exchange strategies

Aspirate – trap – wash - dispense

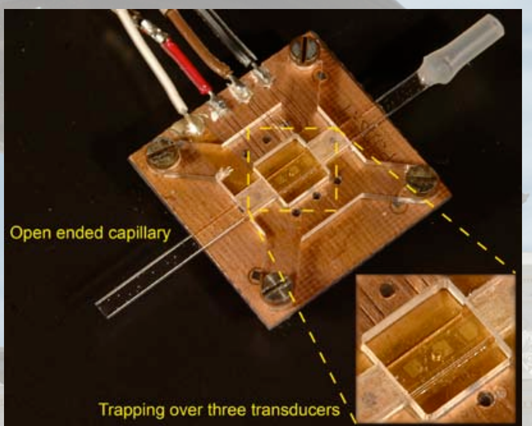

Translate into new buffer

Washing by sequential buffer shifting

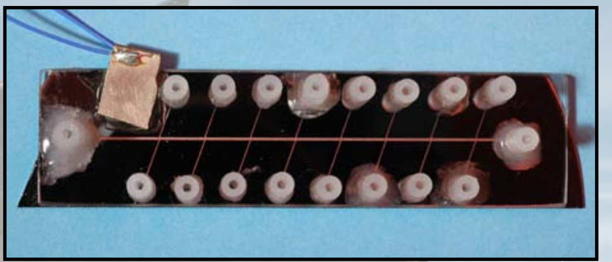

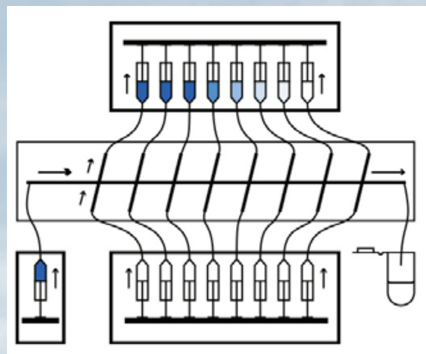

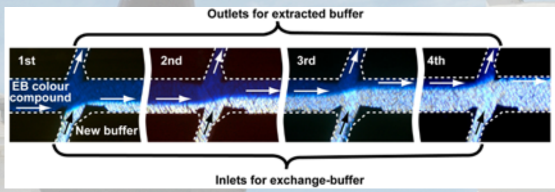

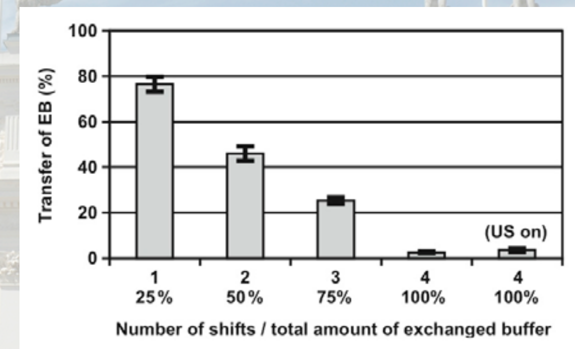

Augustsson P. et al Microchim Acta (2009) 164:269–277

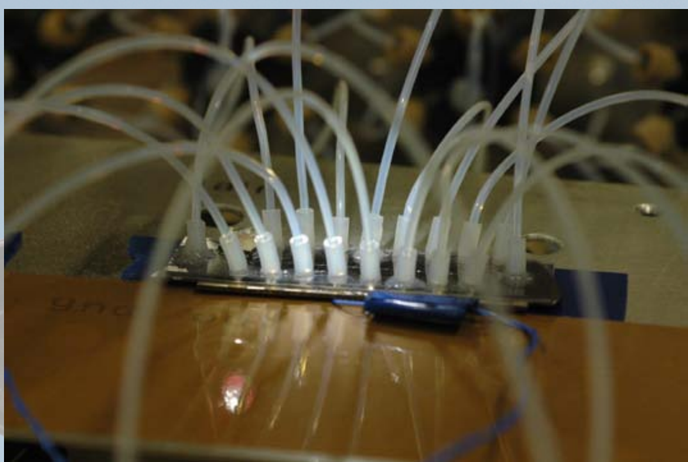

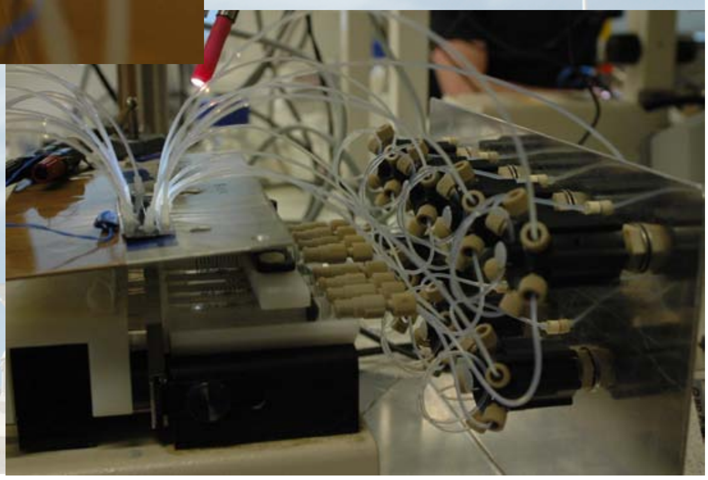

Washing by sequential buffer shifting

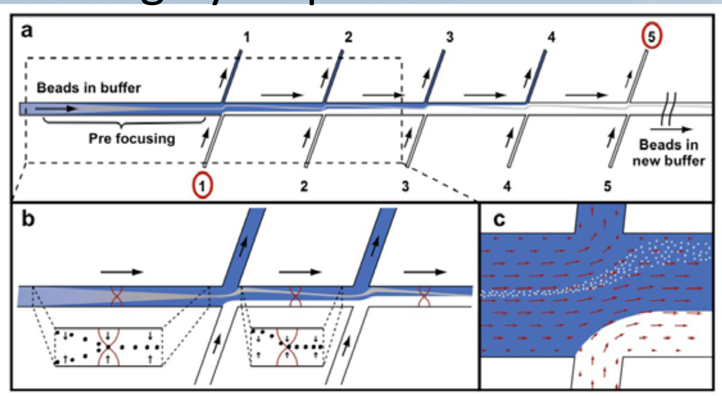

80 uL/min; 2% bead content/vol; 500*10^6 beads/mL
Each lateral shift = 25% of total flow => 4 shifts = 100%

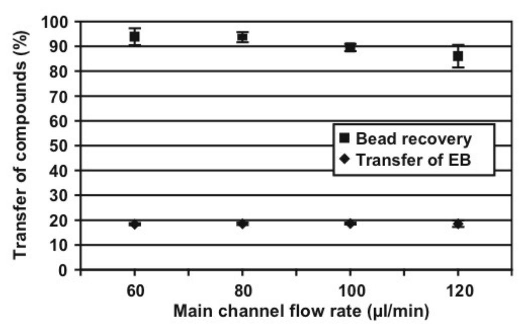

80 uL/min; 2% bead content/vol
Each lateral shift 25% of total flow

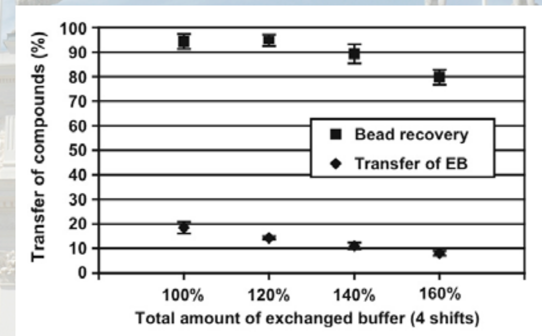

Augustsson P. et al Microchim Acta (2009) 164:269–277

Washing by sequential buffer shifting

Washing efficiency vs. High/low bead conc.

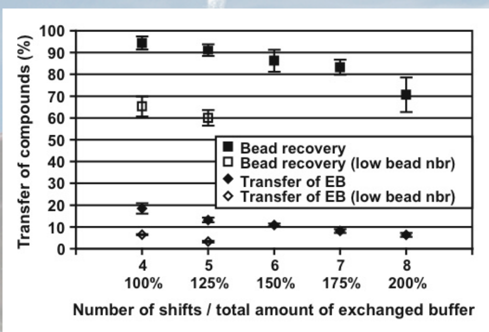

Washing efficiency vs. bead conc.

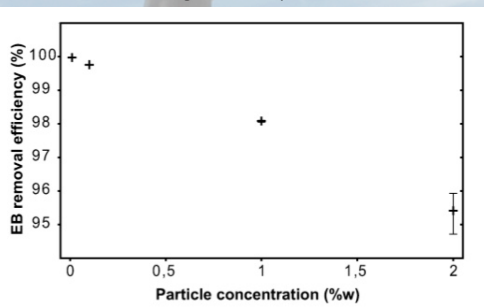

RBC washing efficiency

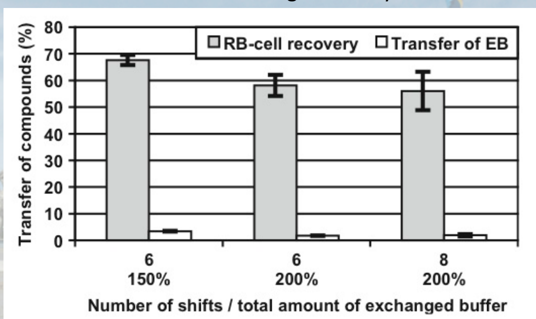

Augustsson P. et al Microchim Acta (2009) 164:269–277

Augustsson P. et al, Lab Chip, 2009, 9, 810–818

Washing and sequential elution

Beads/cells are focused and retained in the centre of the channel by means of an acoustic radiation while the buffer is sequentially exchanged along the flow path

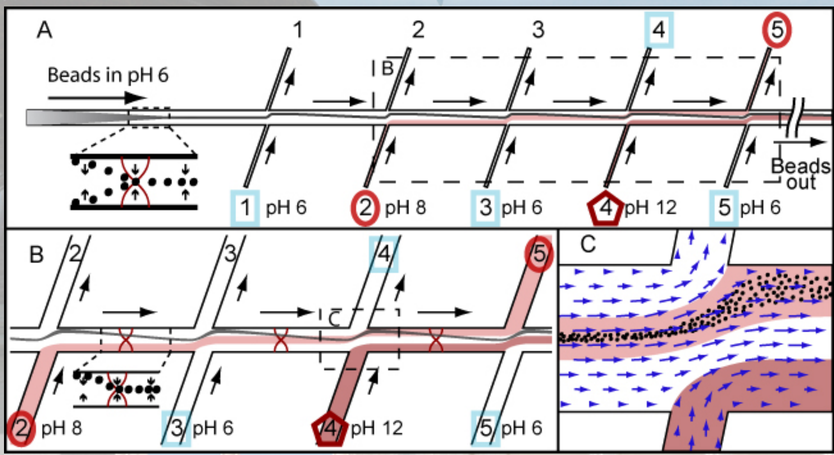

Augustsson P., Åberg L. B., Swärd-Nilsson A-M. K., and Laurell T., Microchim Acta (2009) 164:269–277

Workflow

1. Acustophoretic sample preparation

2. Microfluidic solid-phase extraction

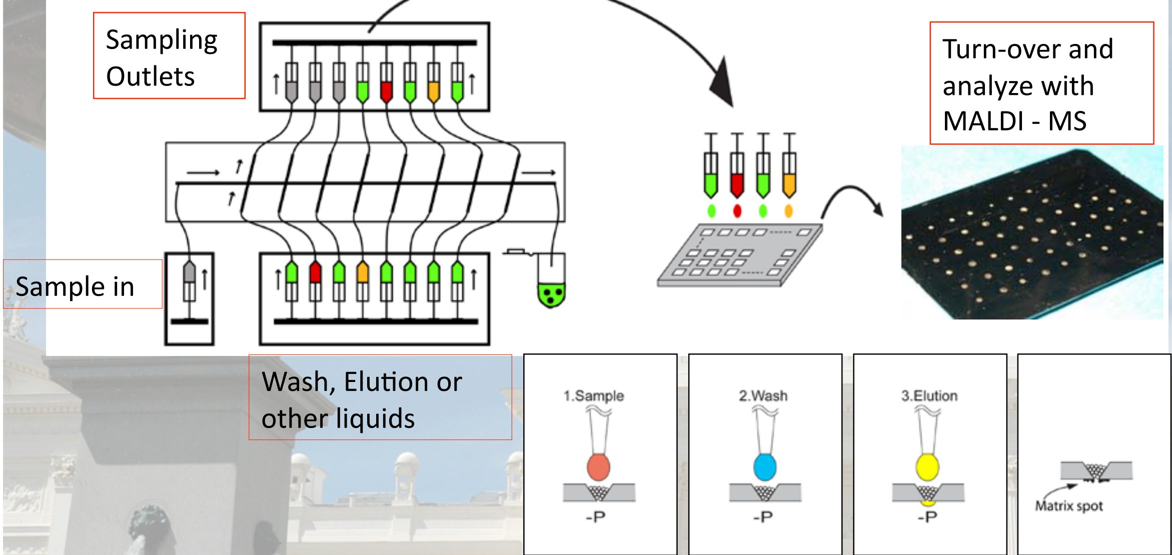

Principle of ISET- sample preparation and MALDI readout

1. Sample
2. Wash
3. Elute & matrix
4. MALDI

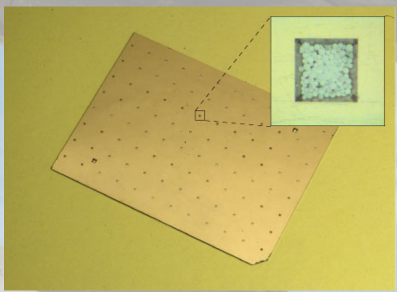

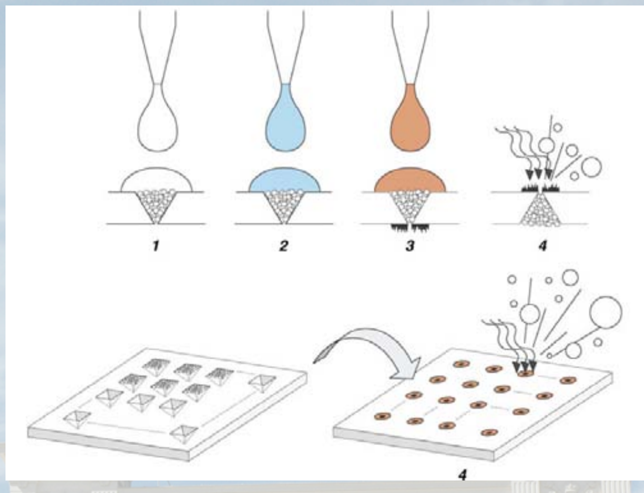

Frontside of ISET

Backside of ISET with MALDI spots

Adapted for standard MALDI-target

Prototypes by GeSIM mbH

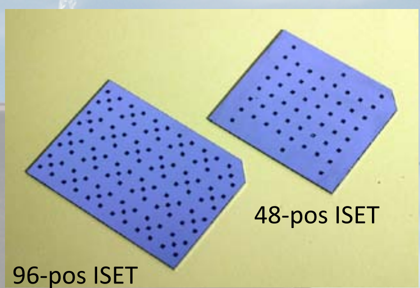

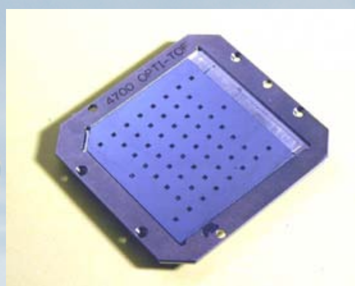

Standard u-titre plate vacuum interface

MALDI-platform independent interfaces

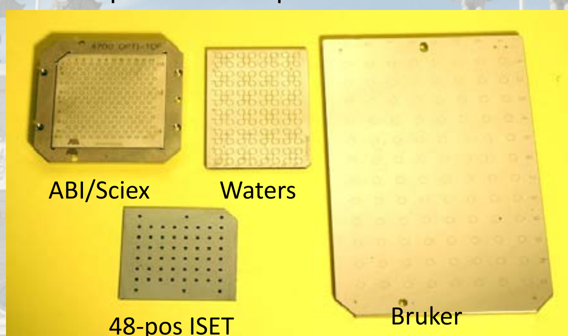

Comparison ISET vs. Commercial standards

SPE processing of a 2D-gel spot digest (Annexin)
10 ul processed with each preparation technique

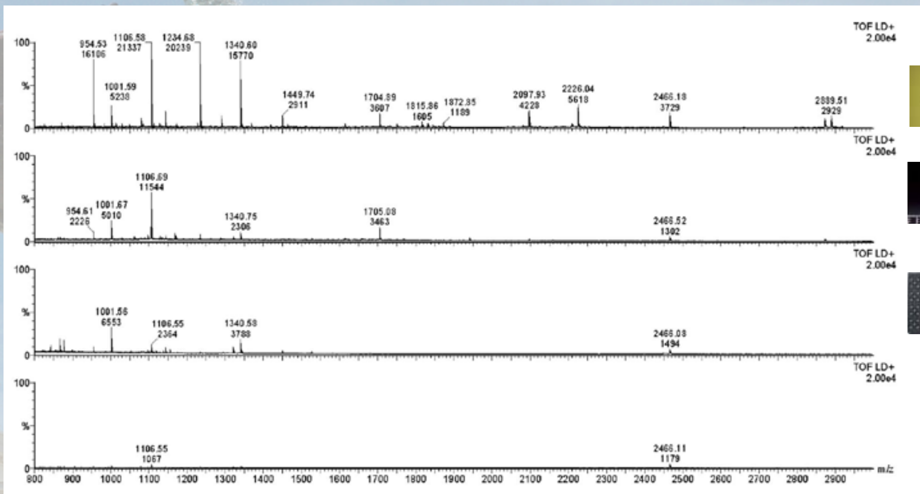


ISET

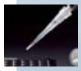
ZipTip


MassPREP


Dried droplet

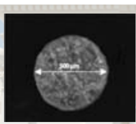

ISET MALDI-spot confinement

Standard robotic sample processing on ISET

- bead loading -> sample loading -> wash -> elute & crystalise

Carry over control

Peptide P1 spiked in inlet 1 and Peptide P2 in inlet 3

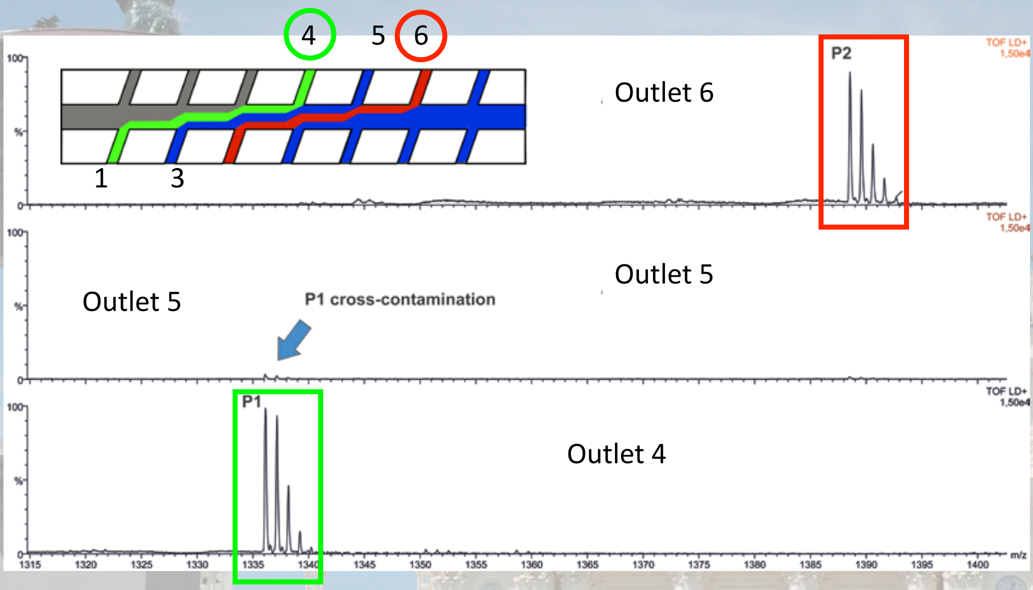

Note that y-axis scaling is normalized to 15000 counts.

Reduction of complexity

Sequential elution of Human plasma peptides captured on the surface of ion-exchange (SAX) beads

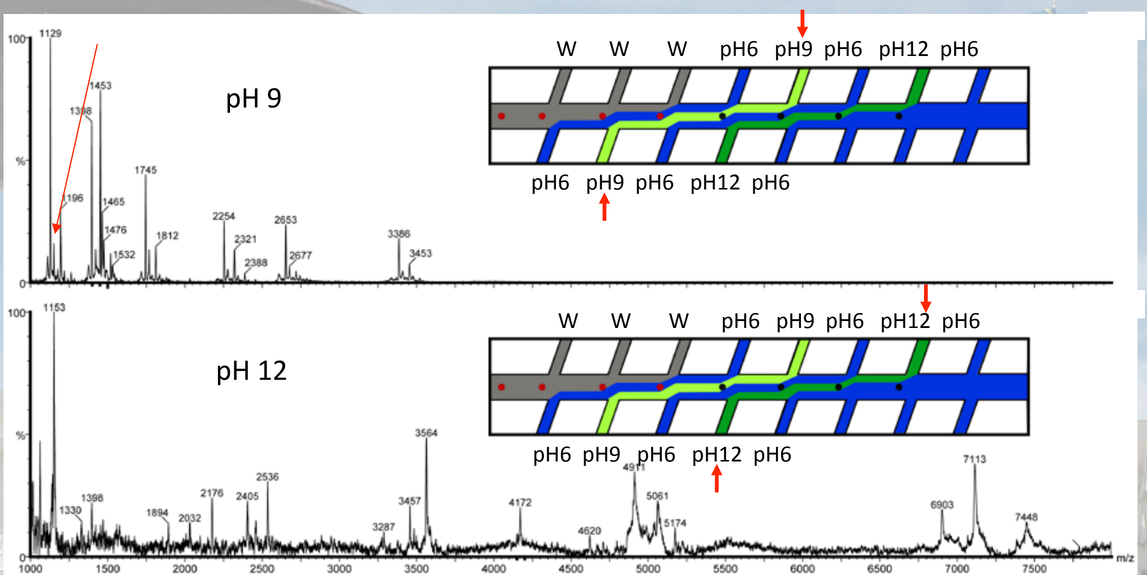

Very few common peptides present in the fractions!

Wash of antibody covered beads

- Continous flow with wetting in all steps, limits unspecific background
- Offers the possibility for continous reuse of the antibody covered beads

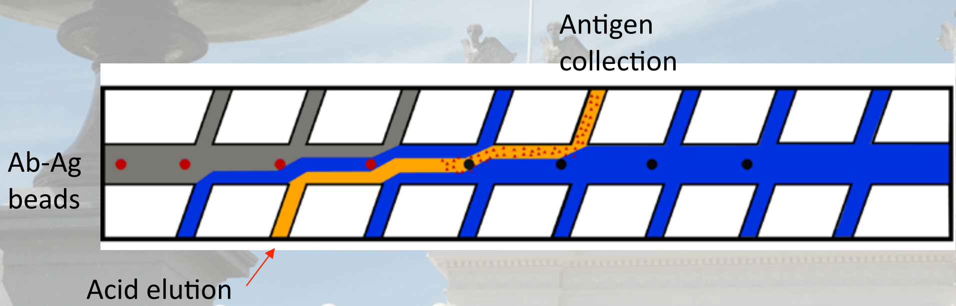

Cell washing by sequential buffer shifting

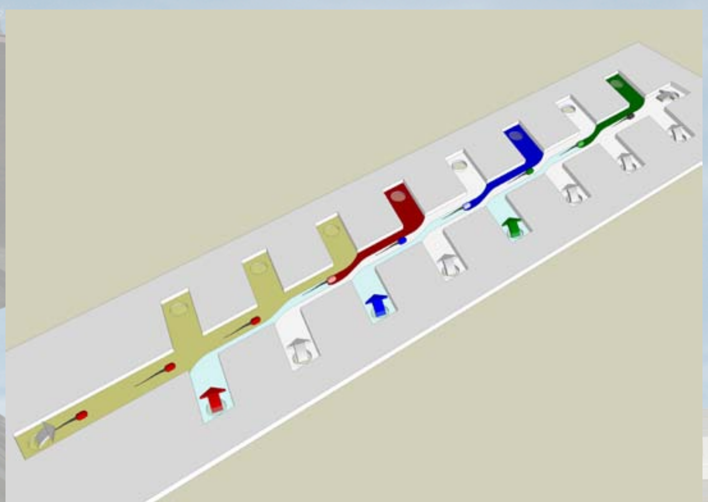

Elution of surface bound peptides from spermatozoa

- Infertility, affects approximately one in seven couples and in 50% of these cases it is defects in the male that cause the failure to conceive.
- The underlying biochemical, molecular and genetic causes are poorly understood.
- Dropping birth numbers is a huge societal problem.
- The symptomatic treatment (i.e. assisted reproduction) is very expensive

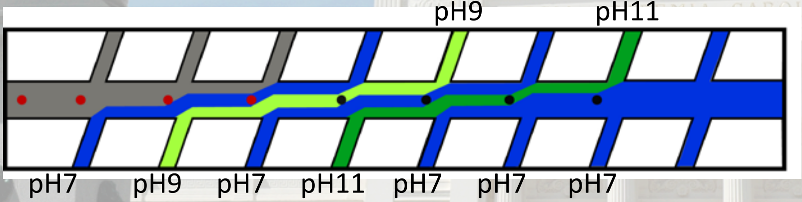

Mass spectra obtained after processing Human spermatozoa

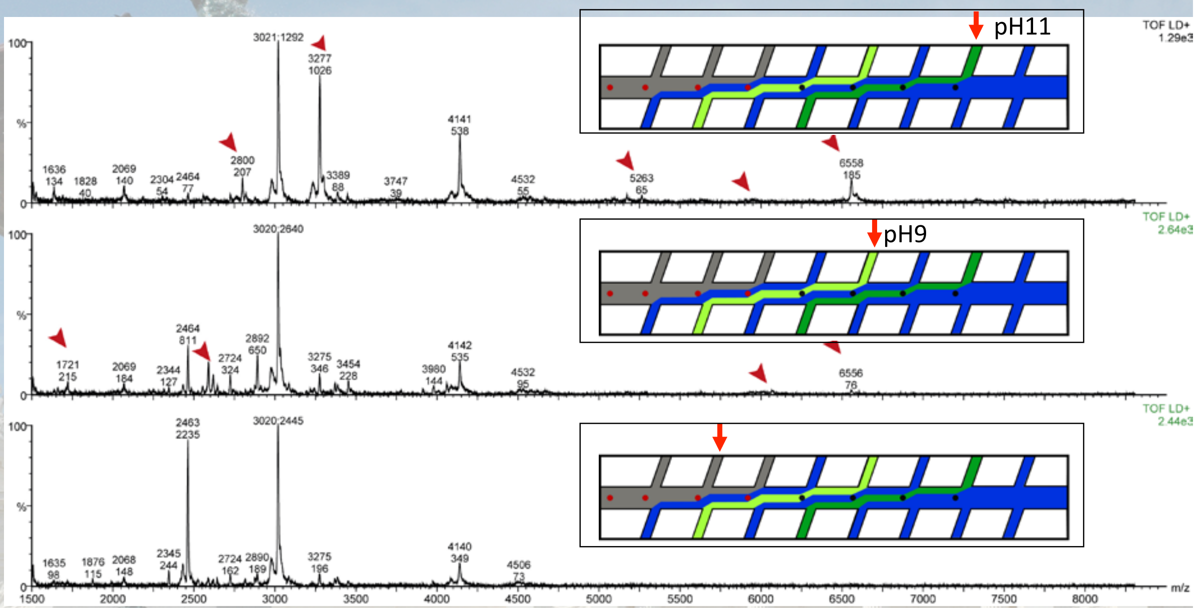

Acoustic 2-step buffer exchange

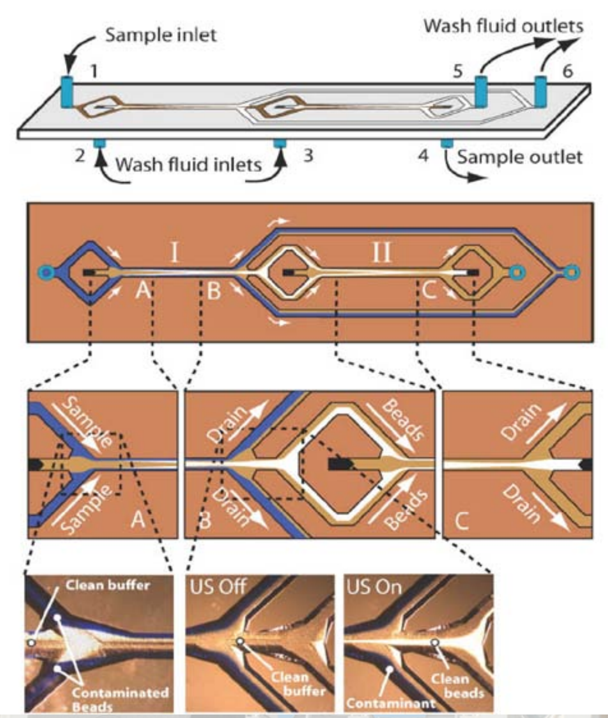

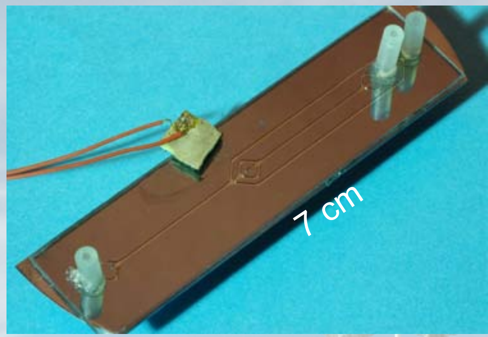

Flow rates:
Sample in and out 50 µl/min
Wash fluid: 100 to 200 µl/min
Reynolds number: ~10

P. Augustsson, J. Persson, S. Ekstrom, M. Ohlin and T. Laurell
Lab On A Chip, 2009, 9, 810–818

Bead wash efficiency

- Evaluated using Evans Blue colour compound -1

Wash efficiency vs. Particle conc

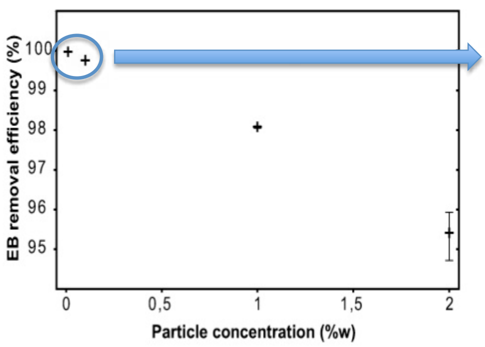

Chip wash efficiency vs. Manual magnetic bead.

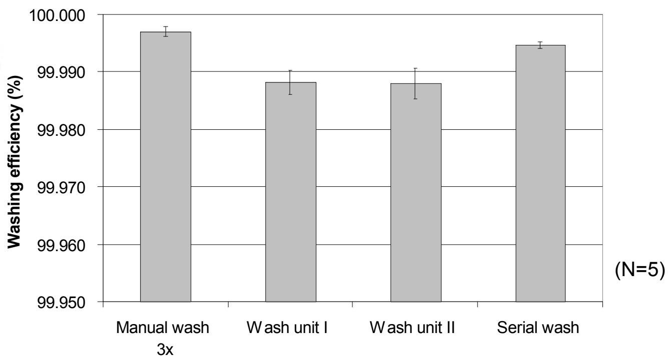

Efficiency: (In-Out)/In
Evans blue: 30 mg/ml
Bead number: ~6M/ml
Bead diameter: ~5µm
Solid content: ~0.05 %

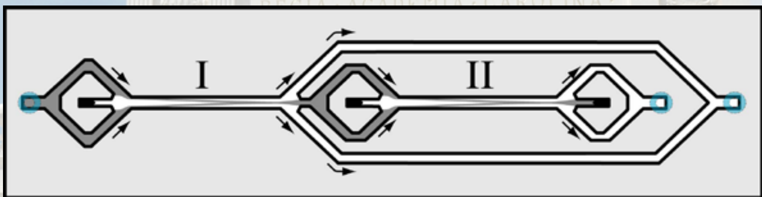

Phosphopeptide capture and acoustophoretic buffer exchange

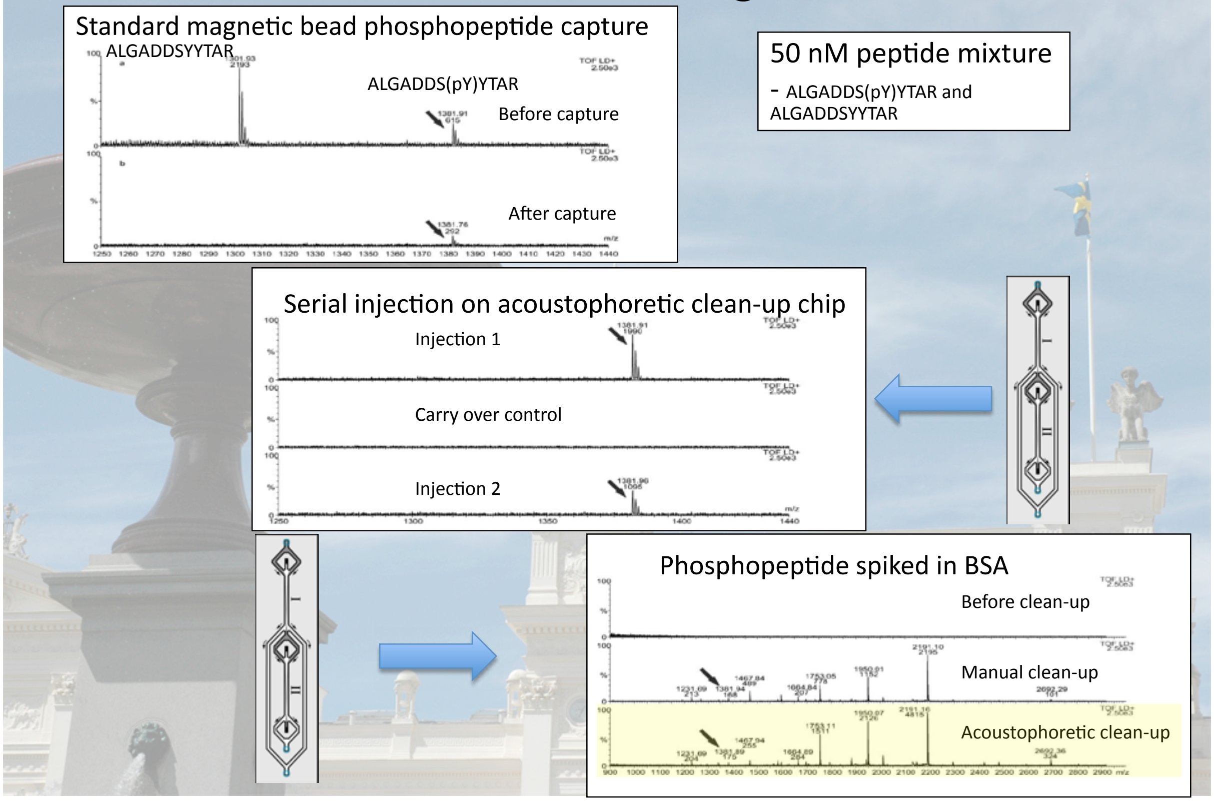

Protein microarrays for disease diagnostics

Protein microarray

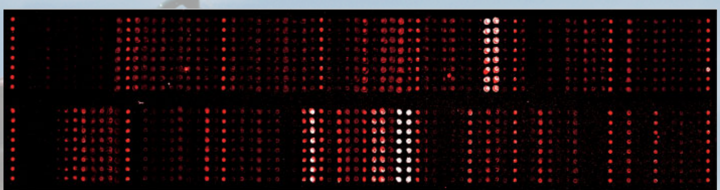

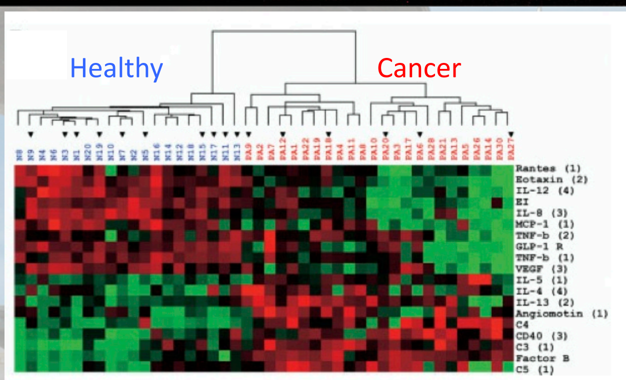

Antigen (no. of clones)	Antigen (no. of clones)
IL-1α (3)	GLP-1 (1)
IL-1β (3)	GLP-1R (1)
IL-1-ra (3)	C1q (1)
IL-2 (3)	C1s (1)
IL-3 (3)	C3 (2)
IL-4 (4)	C4 (1)
IL-5 (3)	C5 (2)
IL-6 (4)	Factor B (1)
IL-7 (2)	B (1)
IL-8 (3)	Properdin (1)
IL-9 (3)	C1-INH (1)
IL-10 (3)	CD40L (1)
IL-11 (3)	PSA (1)
IL-12 (4)	Leptin (1)
IL-13 (3)	LDL (2)
IL-16 (3)	Integrin α10 (1)
IL-18 (3)	Integrin α11 (1)
TGF-β1 (3)	Procathepsin (1)
TNF-β (3)	Tyrosine-protein kinase BTK (1)
TNF-β (4)	Tyrosine-protein kinase JAK3 (1)
INF-γ (3)	B-lactamase (1)
VEGF (4)	Lewis[x] (2)
Angiomotin (2)	Lewis[y] (1)
MCP-1 (3)	B cell lymphoma ag (1)
MCP-3 (3)	Sialo Lewis[x] (1)
MCP-4 (3)	MUC-1 (1)
Eotaxin (3)	Streptavidin (control) (1)
RANTES (3)	Digoxin (control) (1)
GM-CSF (3)	FITC (control) (1)
CD40 (4)	TAT (control) (2)

Ingvarsson J. et al, Proteomics, 2008

The challenge and the opportunity

-Discovery of new biomarkers (proteins) that correlate to disease

- New affinity probes (antibodies) requested

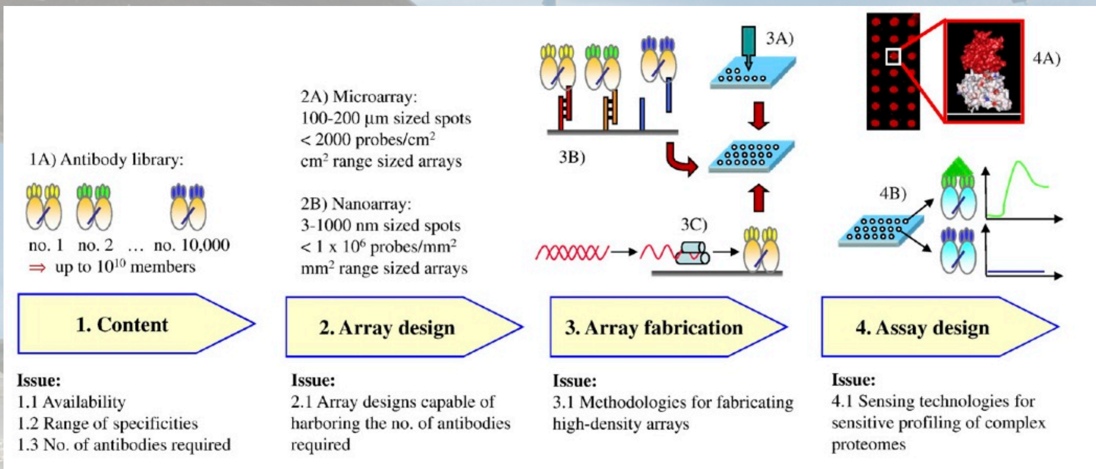

Borrebaeck CA, J. Proteomics, 2009

Phage display and antibody libraries

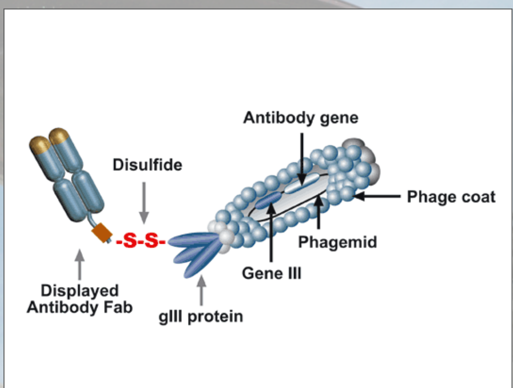

www.abdserotec.com

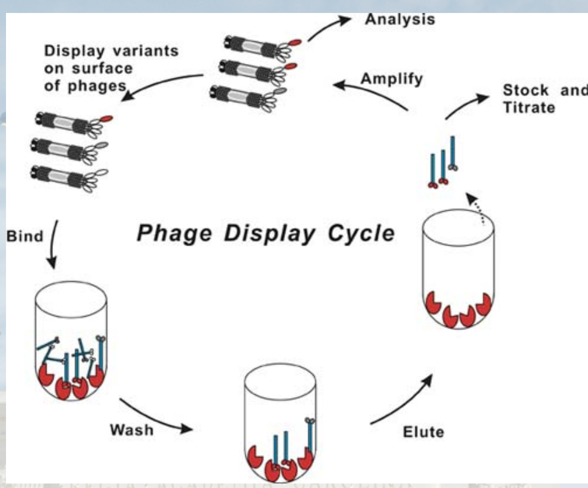

www.creative-biolabs.com

Phage display selection procedure

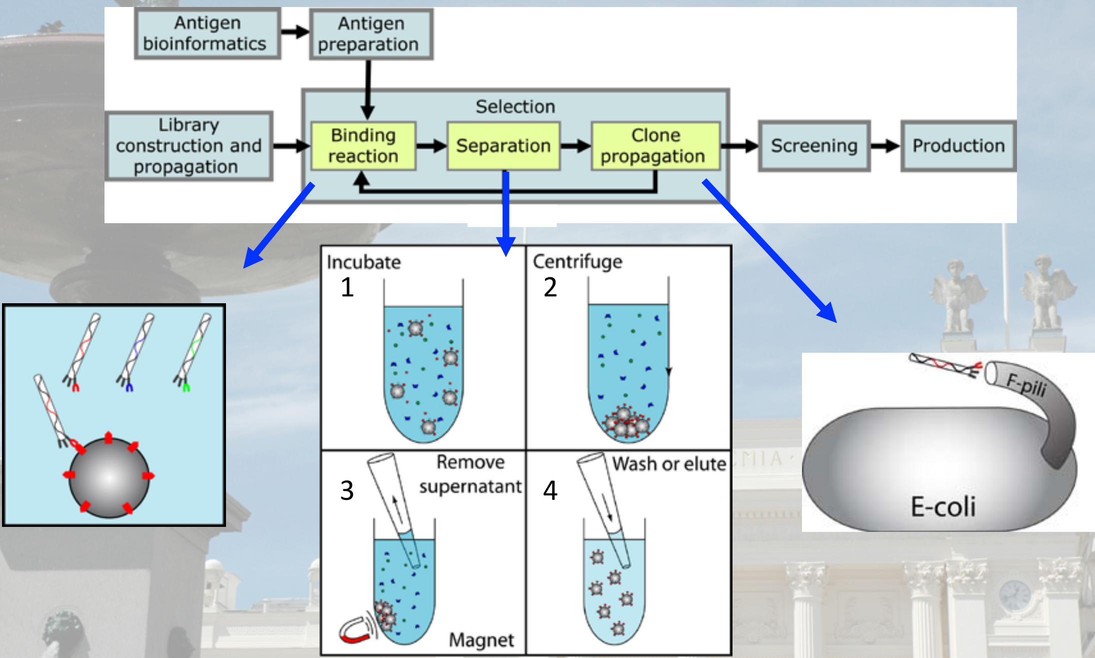

Affinity acoustophoresis

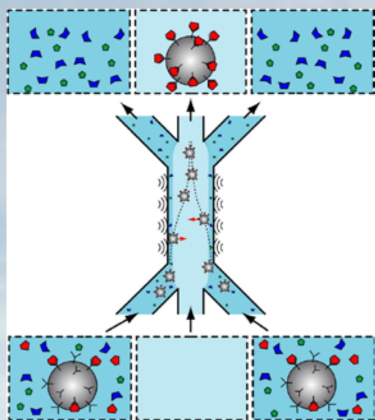

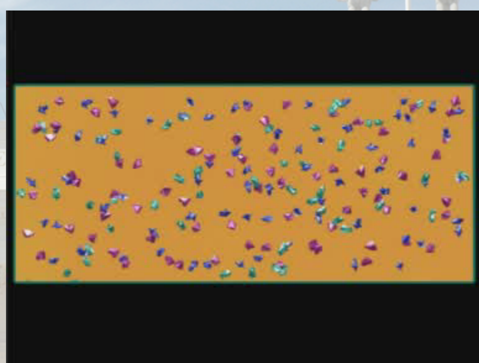

Persson, Augustsson, Laurell, Ohlin, FEBS Journal, 275 (2008) 5657-5666

Affinity bead based phage selection

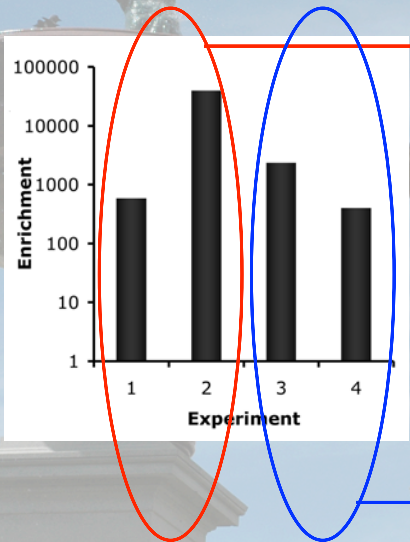

Enrichment factor of an antibody A in the presence of a 1000-fold excess of phages displaying an antibody B.

Enrichment factor of B in the presence of a 1000-fold excess of phages displaying A.

Acoustic 2-step buffer exchange

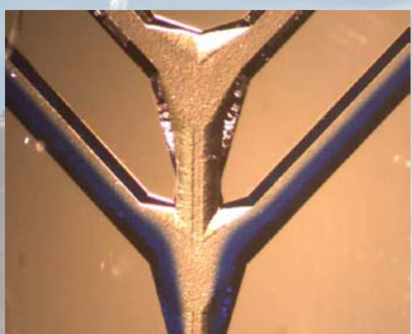

Phage washing
Specific vs. unspecific

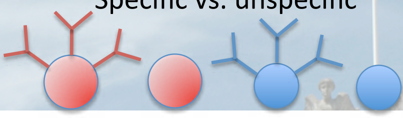

Phage transfer in wash chip vs. manual

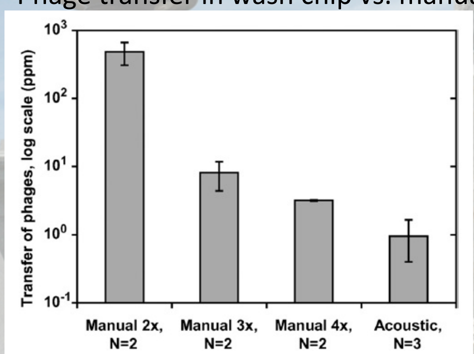

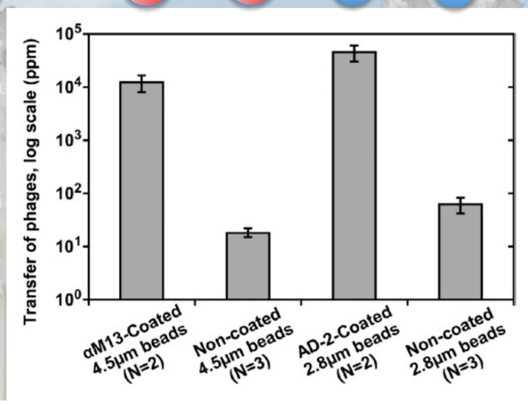

Enrichment and selectivity

Assay sensitivity after acoustophoretic selection

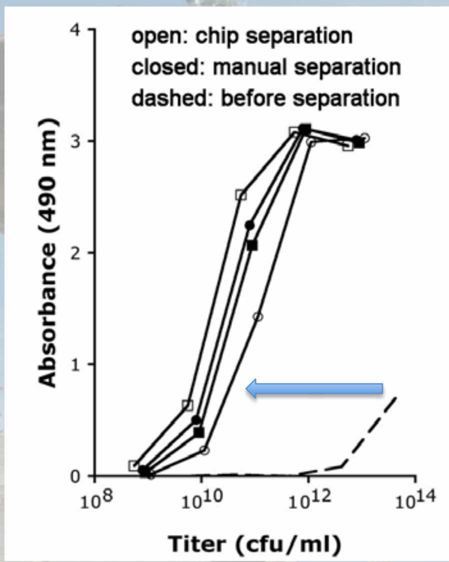

Antigen-specificity of selected binders (10*9 allergen library) for the grass pollen allergen Phl p 5

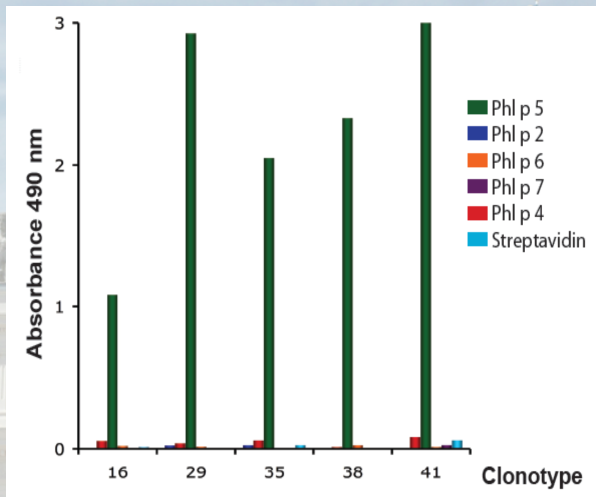

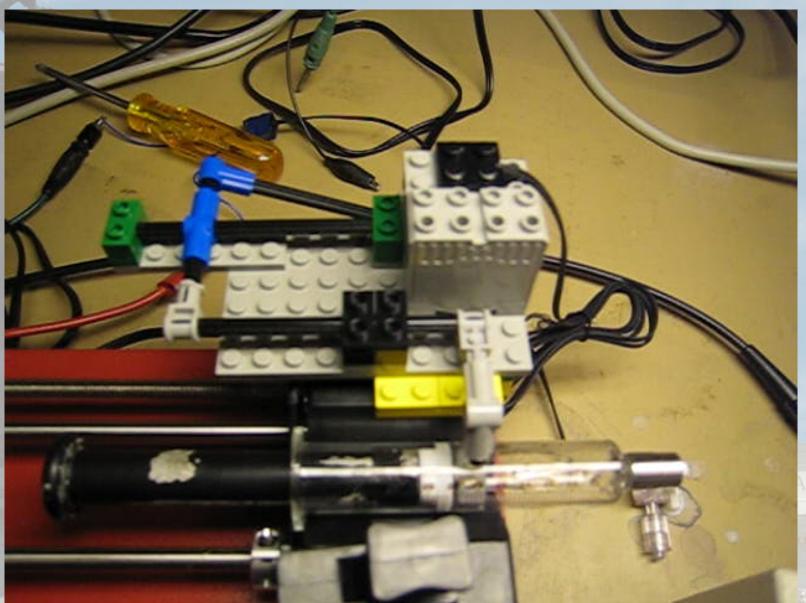

20th century centrifugation

21st century centrifugation

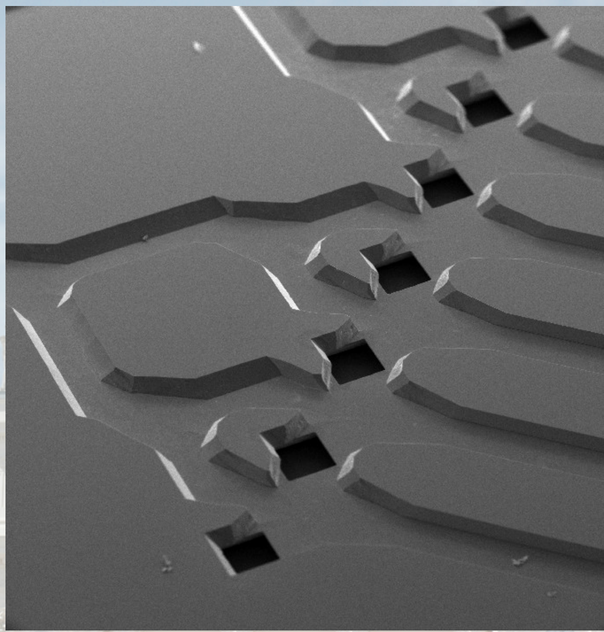

USWNET

USWNet

Ultrasonic Standing Wave Network

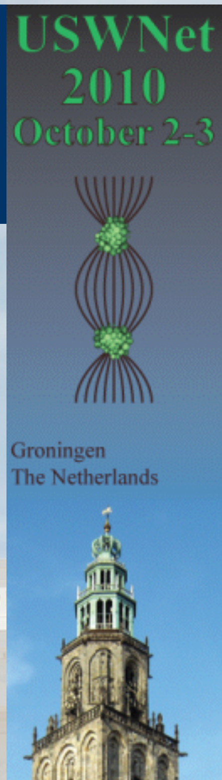

USWNet 2010 Conference

2-3 October 2010

www.USWNet.com

Groningen

The Netherlands

Abstract deadline June 25!!!!


REGIA · ACADEMIA · CAROLINA

L6: Bioanalysis: Enhanced immunoassays and agglutination assays

Martin Wiklund

Dept. of Applied Physics
Royal Institute of Technology
Stockholm, Sweden

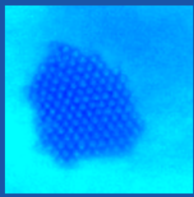

CISM course ”*Ultrasound standing wave action on suspensions and biosuspensions in micro- and macro fluidic systems*”, June 7-11, 2010

M. Wiklund

-1-

Outline

1. **Agglutination-based methods**
2. **Fluorescence-based methods**

M. Wiklund

-2-

What is an immunoassay?

- A method for identification and/or quantification of specific proteins or other biomolecules
- The method uses the interaction/binding of antibodies to antigens (often proteins)
- The assay is often designed to bind the analyte (the target protein) onto a solid support
- The solid support can be a surface (functionalized surface = antibody-coated surface)
- Or, the solid support can be beads (functionalized polymer microspheres)

Building blocks of an immunoassay

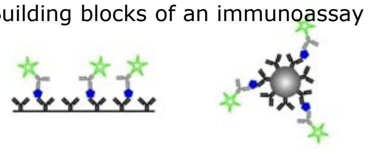

M. Wiklund

-3-

Agglutination-based bead assays

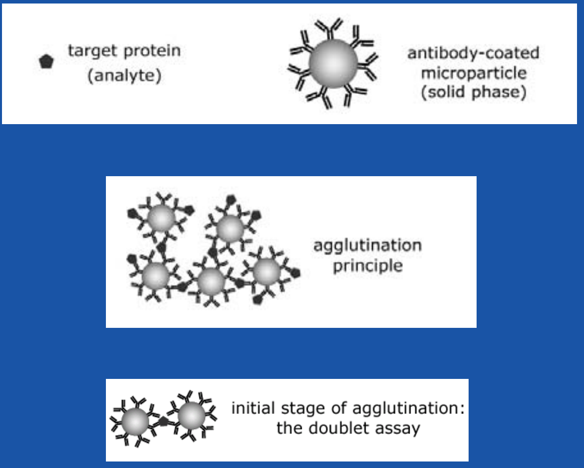

M. Wiklund

2004-04-23

-4-

The Latex Agglutination Test (LAT): History

First LAT in 1956 (Singer and Plotz):

0.8 μm polystyrene latex particles (beads) coated with human gamma globulin (HGG) were clumped when mixed with serum from patients having rheumatoid arthritis

Today, same or smaller bead sized are used (0.01-0.8 μm)

KTH Physics

M. Wiklund

2004-04-23

-5-

The Latex Agglutination Test (LAT): Principles

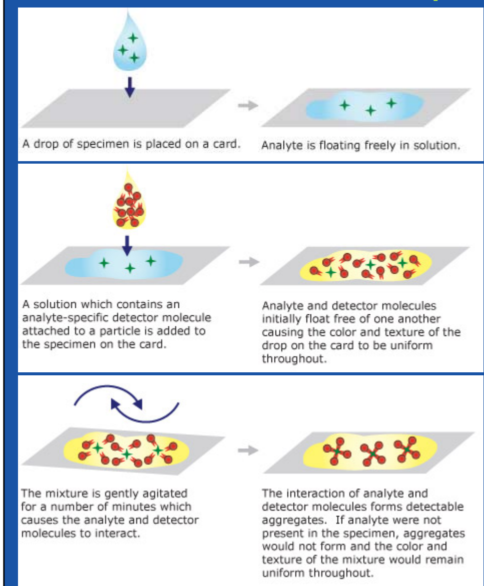

From: http://www.rapid-diagnostics.org/tech-agglut.htm

Detection (yes/no): Visual

A: Positive, B-G: Negative

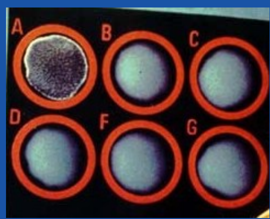

KTH Physics

M. Wiklund

2004-04-23

-6-

The Latex Agglutination Test (LAT): Quantification?

Quantification methods (except for the visual ”yes/no”):

-Turbidimetry (*forward scattered light*), <1 µm beads
(Litchfield et al., Clin. Chem. **30**, 1489, 1984)

-Nephelometry (*side scattered light*), <1 µm beads
(Kapmeyer et al., J. Clin. Lab. Anal. **2**, 76, 1988)

-Particle counting detectors (decrease in counting rate), >1 µm beads
(Masson, J. Pharmaceut. Biomed. **5**, 113, 1987)

-Flow cytometry, >1 µm beads
(Wiklund et al, Anal. Biochem. **338**, 90, 2005)

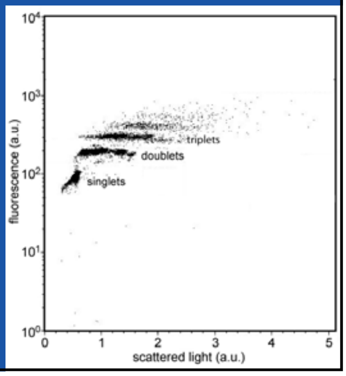

M. Wiklund
2004-04-23
-7-

The Latex Agglutination Test (LAT): Performance, limitations

Typical detection limit: nM-range

Why?

- Relatively high particle concentrations are needed for sufficiently high particle collision rates

- Relatively small particles (<1 µm) are needed for sufficiently high diffusion rates

- Small particles are associated with spontaneous agglutination (non-specific agglutination)

M. Wiklund
2004-04-23
-8-

The Latex Agglutination Test (LAT): Ultrasonic enhancement

What can be enhanced with USW technology?

We can increase the probability of bead collisions!

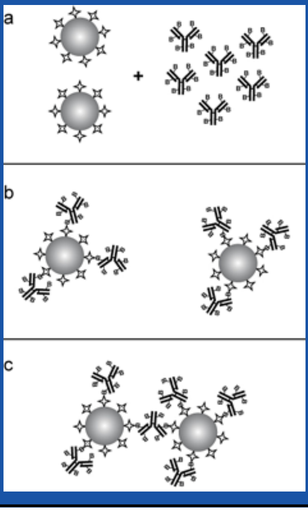

- Enhanced speed (~min)
  (Grundy et al., J. Immunol. Methods **165**, 47, 1993)
- Enhanced sensitivity (~0.1 nM)
  (Grundy et al., J. Immunol. Mehtods **176**, 169, 1994)

KTH Physics

M. Wiklund

-9-

The Latex Agglutination Test (LAT): Ultrasonic enhancement

What can be enhanced with USW technology?

We can increase the probability of bead collisions!

Device (developed in the Coakley group):

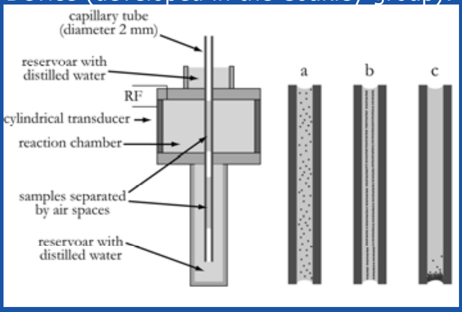

REVIEW: M. Wiklund et al., Lab Chip **6**, 1279 (2006)

Commercial device: "Immunosonic" from EMS

Target application: Bacterial Meningitis

KTH Physics

M. Wiklund

-10-

M. Wiklund

-11-

The Latex Agglutination Test (LAT): Ultrasonic enhancement

What can be enhanced with USW technology?

We can increase the probability of bead collisions!

The trick is to reduce the concentration of beads!

How?

- Enhanced speed (~min)
  (Grundy et al., J. Immunol. Methods **165**, 47, 1993)
- Enhanced sensitivity (~0.1 nM)
  (Grundy et al., J. Immunol. Mehtods **176**, 169, 1994)

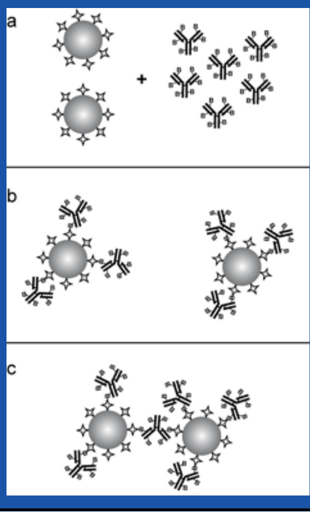

M. Wiklund

-12-

Ambient analyte conditions in immuno-agglutination assays

Trick:

Increase the sensitivity by decreasing the number of available binding receptors (=capture antibodies)

The term ”ambient analyte conditions” was first proposed by Roger Ekins

(R. P. Ekins, J. Pharm. Biomed. Anal. **7**, 155, 1989)

Ekins used the concept in microspot array technology

(R. Ekins, Ann. Biol. Clin. **50**, 337, 1992)

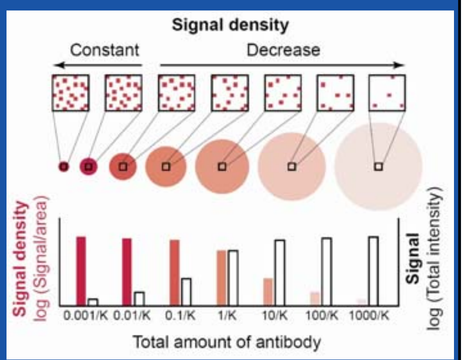

Modelling of the reaction kinetics

Antibody (A) – antigen (Y) interaction:

$$A + Y \underset{k_-}{\overset{k_+}{\Leftrightarrow}} AY \qquad K = k_- / k_+$$

Amount of A-Y complexes on particle surface:

$$N_{AY} = \frac{Y\, N_A}{K}$$

Concentration of free analyte (antigen), Y, in the medium:

$$Y = -\frac{1}{2}\left(I_0 - Y_0 + K\right) + \frac{1}{2}\sqrt{\left(I_0 - Y_0 + K\right)^2 + 4KY_0}$$

with $I_0 = n_1(0)\, N_{max}$

binding capacity of the particle

initial conc. of receptors

initial conc. of singlets

M. Wiklund

2004-04-23

-13-

Modelling of the reaction kinetics

- Initial stage of immunoagglutination (”doublet formation”)

Particle – particle interaction:

$$L_i + L_j \overset{k_{ij}}{\Rightarrow} L_{i+j}$$

rate constant of agglutination
(assumed to be irreversible)

von Smoluchowski kinetics (coagulation theory):

$$\frac{dn_i}{dt} = -\sum_{j=1}^{\infty} k(i,j)\, n_i n_j + \frac{1}{2}\sum_{j=1}^{i-1} k(j, i-j)\, n_j n_{i-j}$$

where $n_i(t)$ is the concentration of a cluster containing i particles

M. Wiklund

2004-04-23

-14-

Modelling of the reaction kinetics

- Initial stage of immunoagglutination (”doublet formation”)

Particle – particle interaction:

$$L_i + L_j \overset{k_{ij}}{\Rightarrow} L_{i+j}$$

rate constant of agglutination
(assumed to be irreversible)

Cluster kinetics (singlets, doublets, triplets):

$$\frac{dn_1}{dt} = -k(1,1)n_1^2 - k(1,2)n_1 n_2 - k(1,3)n_1 n_3$$

$$\frac{dn_2}{dt} = \frac{1}{2}k(1,1)n_1^2 - k(1,2)n_1 n_2 - k(2,2)n_2^2 - k(2,3)n_2 n_3$$

$$\frac{dn_3}{dt} = k(1,2)n_1 n_2 - k(1,3)n_1 n_3 - k(2,3)n_2 n_3 - k(3,3)n_3^2$$

M. Wiklund
2004-04-23
-15-

Modelling of the reaction kinetics

- Initial stage of immunoagglutination (”doublet formation”)

Particle – particle interaction:

$$L_i + L_j \overset{k_{ij}}{\Rightarrow} L_{i+j}$$

rate constant of agglutination
(assumed to be irreversible)

The rate constants, k_{ij}:

$$\frac{1}{k(i,j)} = \frac{1}{k_D(i,j)} + \frac{1}{k_r(i,j)} \qquad k_D(i,j) \approx k_D(1,1)$$

probability of agglutination per one collision

$$k_D(1,1) = \frac{8k_B T}{3\eta} \qquad k_r(i,j) = ijc_h(i,j)\beta\, k_D(i,j)$$

rate of collision (diffusion-limited)

rate of binding

steric hindrance coefficient

M. Wiklund
2004-04-23
-16-

Modelling of the reaction kinetics

The beta parameter (probability of agglutination per one collision):

$$\beta = N_{1A} N_{1AY} f^{3/2}$$

N_{1AY}: amount of occupied binding sites per particle

N_{1A}: amount of free binding sites per particle

with

$$N_{1A} N_{1AY} = \frac{K/Y}{(1+K/Y)^2} N_{\max}^2$$

$$f = \frac{b^2}{4R^2}$$

b: radius of a binding site

R: radius of the particle

f: surface fraction of a binding site

$$N_{\max} = N_A + N_{AY}$$

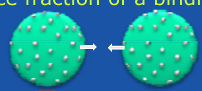

Max. analyte conc:

$$Y_{0\max} = \frac{1}{2} I_{0\max} + K$$

probability of agglutination per one collision

$$k_r(i,j) = ij c_h(i,j) \beta k_D(i,j)$$

k_r: rate of binding

c_h: steric hindrance coefficient

M. Wiklund

2004-04-23

-17-

Agglutination probability: Plot the beta parameter vs. Y_0

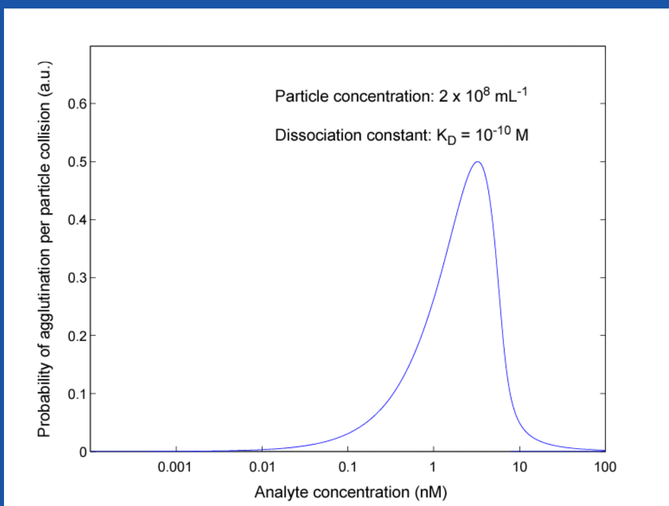

M. Wiklund

2004-04-23

-18-

Agglutination probability: Plot the beta parameter vs. Y_0

Varying the affinity of the immunoassay

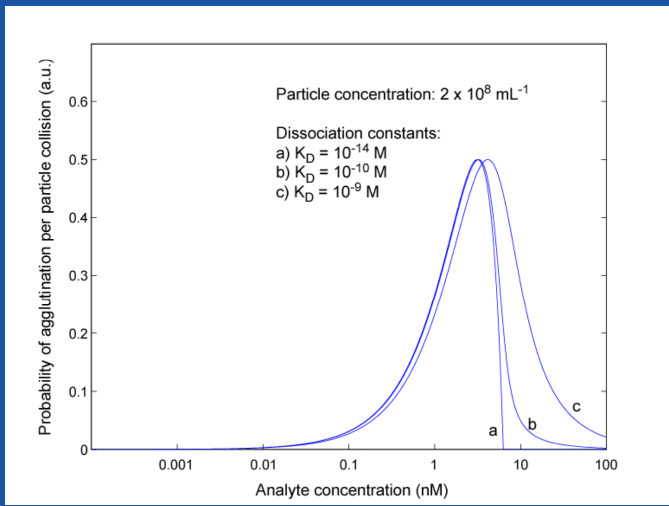

M. Wiklund

2004-04-23

-19-

Agglutination probability: Plot the beta parameter vs. Y_0

Varying the particle (=receptor) concentration

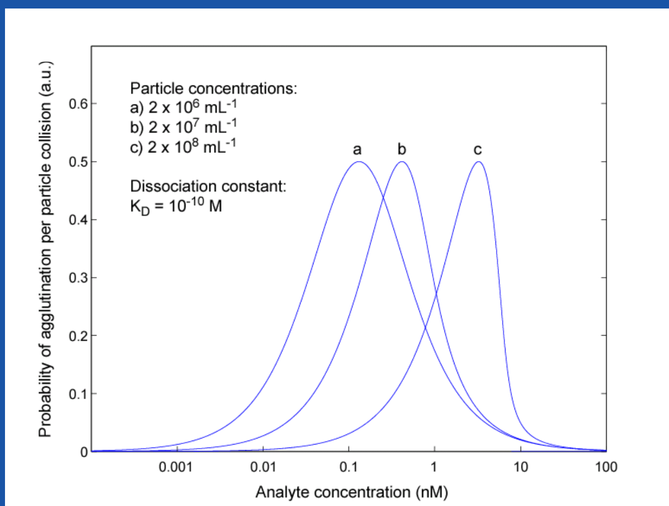

M. Wiklund

2004-04-23

-20-

Detection limit

What about the detection limit?

Is typically defined by the amount of non-specific agglutination (background noise)

Let's expand the model to include non-specific agglutination:

$$k(i,j) = \left(\frac{1}{\alpha + ijc_h(i,j)\beta} + 1 \right)^{-1} k_D(1,1)$$

where α is the probability of **non-specific** agglutination (assume constant)

and β is the probability of **specific** agglutination (as previously defined)

M. Wiklund

2004-04-23

-21-

Agglutination probability: Non-specific (α) and specific (β) vs. Y_0

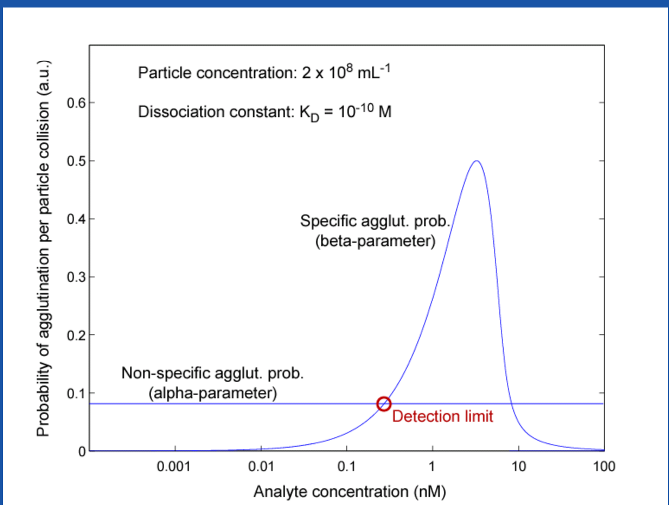

M. Wiklund

2004-04-23

-22-

Using the model to fit experimental data

Purpose:

To optimize an agglutination assay in terms of sensitivity, dynamic range, etc.

- Particles: 0.9 µm fluorescent, streptavidin coated
- Analyte: Biotinylated monoclonal antibody, 6.2 biotin molecules per antibody

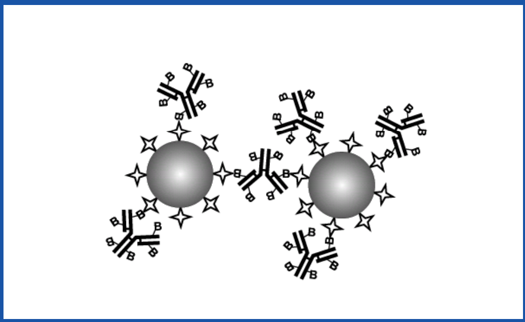

M. Wiklund

2004-04-23

-23-

Analyte concentration dependence on immunoagglutination

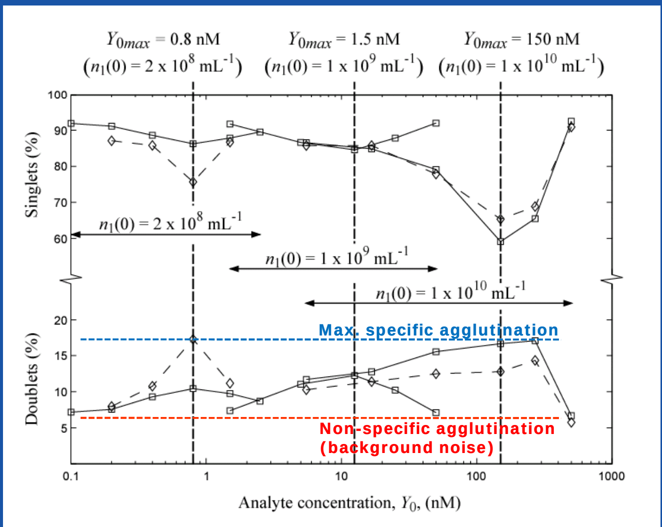

(Wiklund et al, Anal. Biochem. **338**, 90, 2005)

M. Wiklund

2004-04-23

-24-

Fitting the exp. data to the model

- Compare the particle and analyte concentrations at maximum agglutination rate with the number of receptors on the particles

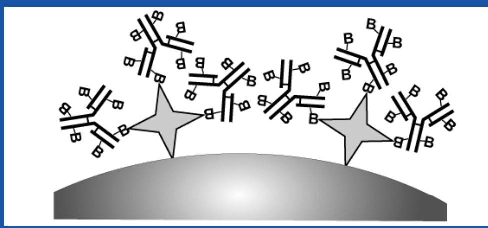

Maximum three antibodies per particle-immobilized streptavidin molecule
(fourth site unavailable due to steric hindrance)

M. Wiklund
2004-04-23
-25-

Compare the non-specific and specific agglutinations

- Results: beta / alpha ≈ 10 (or even less)
  biotin-binding site (on streptavidin molecule) = 0.4 nm

  Steric hindrances of biotin at particle-particle interaction

Typical detection limit of an immuno-agglutination assay: 100 pM (M. Wiklund et al., Lab Chip **6**, 1279, 2006)

M. Wiklund
2004-04-23
-26-

Enhanced particle sensors

- Driving cells/spores to a surface in a λ/4-channel
- Antibody-coated surface

J. J. Hawkes et al., Biosens. Bioelectron. **19**, 1021, 2004

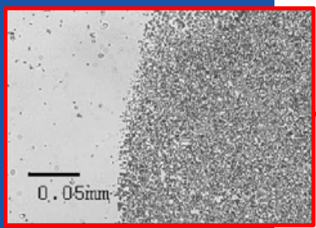

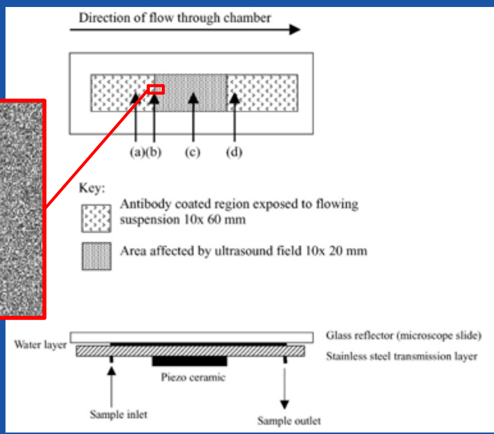

KTH Physics

M. Wiklund
2004-04-23
-27-

Enhanced particle sensors

Potential:
- Separate specific / non-specific interactions
- Measure the binding strength

P. Glynne-Jones et al., Ultrasonics **50**, 235, 2010

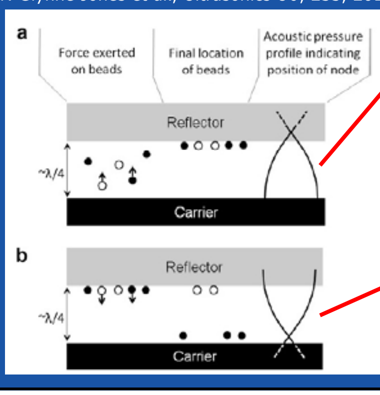

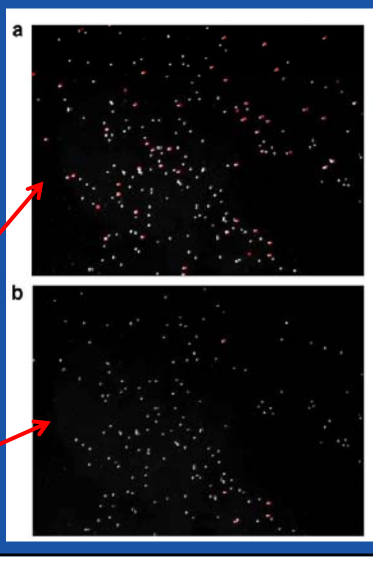

KTH Physics

M. Wiklund
2004-04-23
-28-

Outline

1. **Agglutination-based methods**

2. **Fluorescence-based methods**

M. Wiklund

-29-

Fluorescence-based bead assays

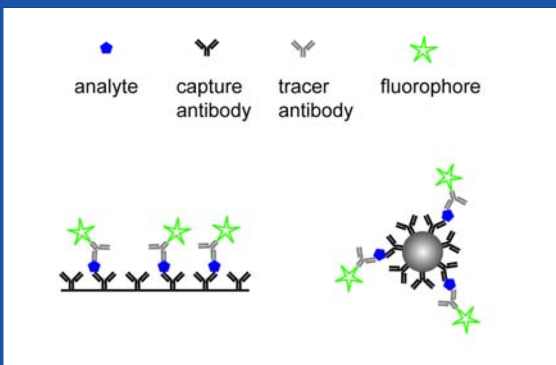

Traditional surface-based assay

Alternative bead-based assay

M. Wiklund

-30-

Ambient analyte conditions

Valid for both agglutination assays and fluorescence assays!

Microspot fluorescence assay

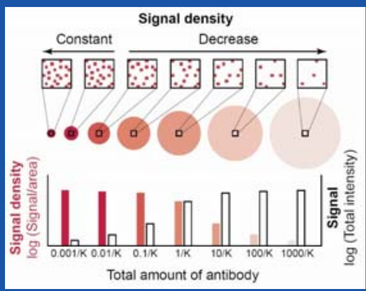

Decrease the spot size

Agglutination assay

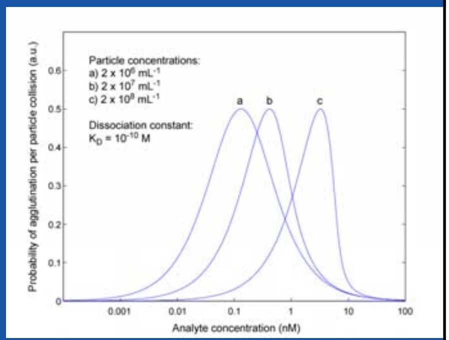

Decrease the bead conc.

M. Wiklund

-31-

Fluorescence-based bead assays

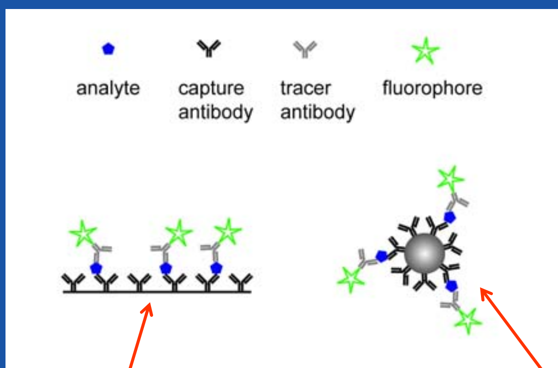

Problem with microspot assays:
- Expensive
- Inefficient surface reactions
- Limited sample volumes

Advantage with bead assays:
- Cost-effective
- Fast solution-phase kinetics
- Easy to scale (reagents)

High sensitivity?

Few capture antibodies
⇒ few beads!

M. Wiklund

-32-

Fluorescence-based bead assays: Ultrasonic enhancement

- Increased sensitivity by reducing the concentration of particle-immobilized receptors
- Developed for screening of microtiter plates

Idea:
Enrich microparticles into the scanning plane of the laser focus

Test assay:
Thyroid stimulating hormone (TSH) assay

M. Wiklund

-33-

Fluorescence-based bead assays: Two-photon (TPX) or confocal fluorescence detection

Fluorescence detection – confocal or two-photon excitation (TPX)

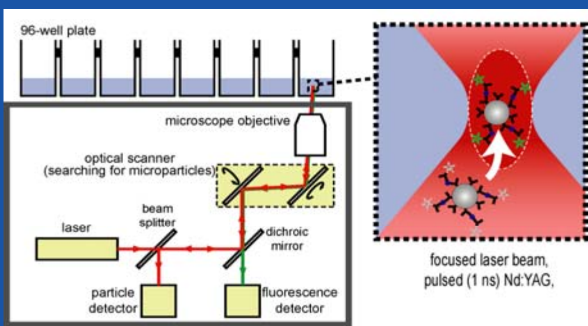

Typical sensitivity: ~pM

Hänninen et al, Biophys. Chem. **105**, 23 (2003)

M. Wiklund

-34-

Fluorescence-based bead assays: Ultrasonic enhancement

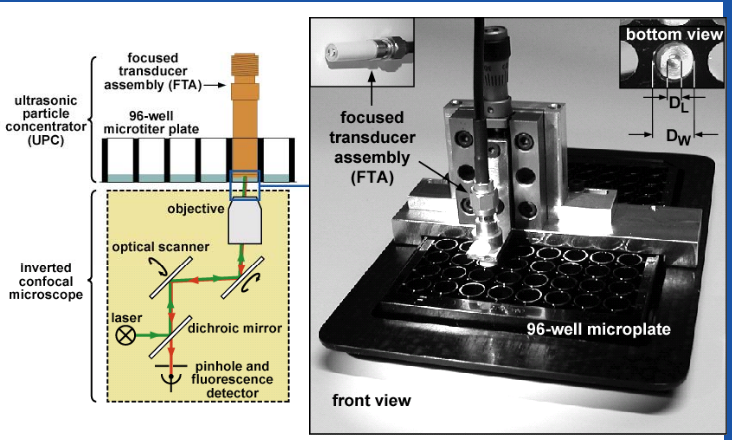

(M. Wiklund et al., J. Appl. Phys. **96**, 1242, 2004)

M. Wiklund

-35-

Fluorescence-based bead assays: Ultrasonic enhancement

Motivation

- Re-arrangement of the suspended particles into single layers
- Horizontal scanning of a confocal laser focus on this layer

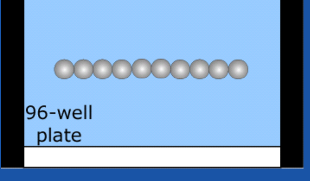

M. Wiklund

-36-

Fluorescence-based bead assays: Ultrasonic enhancement

Model assay: Thyroid-stimulating hormone (TSH)-assay

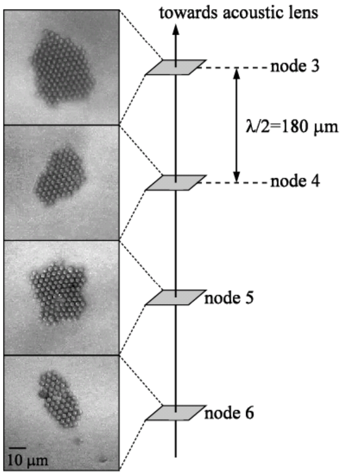

Sensitivity:

20 fM

Wiklund *et. al.*
(J. Appl. Phys. 2004)

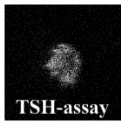

KTH Physics

M. Wiklund

-37-

Optimizing sensitivity

Trick: low conc. of analyte ⇒ low conc. of capture antibody
(R. Ekins *et al.* Anal. Chim. Acta, **227**, 73-96, 1989)

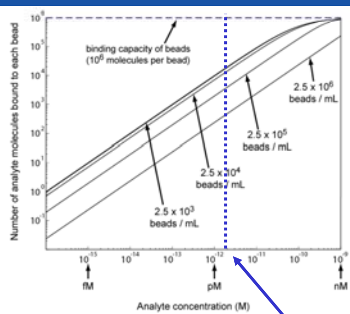

Measure for a fixed analyte concentration, vary the bead concentration

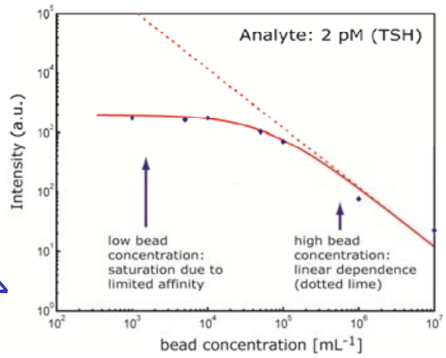

KTH Physics

M. Wiklund

-38-

Optimizing sensitivity

- 20 fM analyte, 2.5×10^4 mL^{-1} bead concentration
  => ~480 molecules per bead in sample
- Theory: K_a ~10^{10} M^{-1}, 10^6 receptors per bead
  => ~140 bound molecules per bead (~30%)
- Detection limit, confocal fluorescence system:
  100 fluorophores per bead

KTH Physics

M. Wiklund

-39-

Optimizing sensitivity

How does it work in practice?
Example 1: - high analyte concentration
- normal reagent concentration

- Sample of proteins
- Add capture beads
- Add fluorescent tracer
- Incubate
- Enrich beads with ultrasound
- Read out (confocal micr.)

KTH Physics

M. Wiklund

-40-

Optimizing sensitivity

How does it work in practice?
Example 2: - low analyte concentration
- normal reagent concentration

- Sample of proteins
- Add capture beads
- Add fluorescent tracer
- Incubate
- Enrich beads with ultrasound
- Read out (confocal micr.)

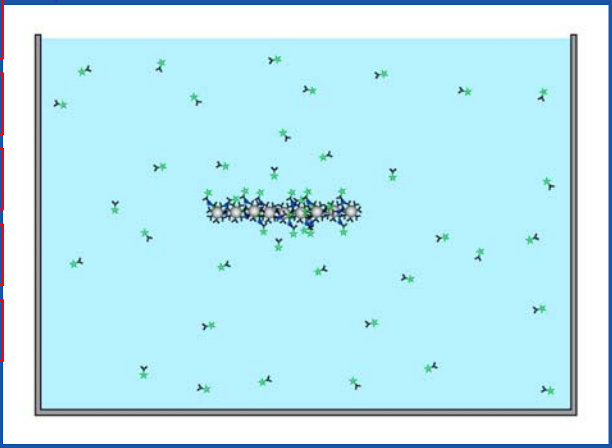

KTH Physics

M. Wiklund

-41-

Optimizing sensitivity

How does it work in practice?
Example 3: - low analyte concentration
- low reagent concentration

- Sample of proteins
- Add capture beads
- Add fluorescent tracer
- Incubate
- Enrich beads with ultrasound
- Read out (confocal micr.)

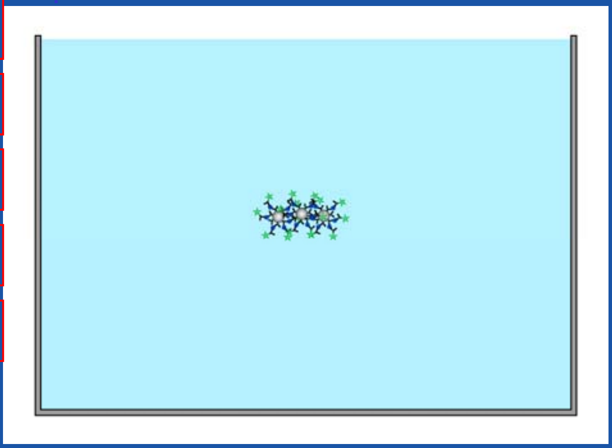

KTH Physics

M. Wiklund

-42-

Summary

- The immuno-agglutination assay
  Detection limit: **>1 nM** without ultrasonic enrichment
  ~100 pM with ultrasonic enrichment

- The fluorescence-based bead assay
  Detection limit: **2 pM** without ultrasonic enrichment
  ~20 fM with ultrasonic enrichment

KTH Physics

M. Wiklund
2004-04-23
-43-

CISM course on Ultrasound Standing Wave Action on Suspensions and Biosuspensions
Lecture 6, Dual

Particle Manipulation Using Acoustic Radiation Forces in Micromachined Devices

Institute for Mechanical Systems
ETH Zürich /
Swiss Federal Institute of Technology Zürich

Jürg Dual

Contents

ETH Eidgenössische Technische Hochschule Zürich Swiss Federal Institute of Technology Zurich

Acknowledgement

IMES

- The work presented is based on about 10 years of research by
- Dr. A. Haake, now at Bucherer, Watch Company, Switzerland
- Dr. A. Neild, now at Monash University in Australia
- Dr. S. Oberti, now with the Federal Aviation Office
- Dr. J. Wang, Postdoc, ETHZ
- D. Möller, doctoral student, ETHZ
- T. Schwarz, doctoral student, ETHZ
- a number of student coworkers
- Collaboration with other institutes: Dr. G. Radziwill, USZ
  Dr. L. Bestmann, USZ, now with Unilabs
  Prof. Dr. Brad Nelson's group, F. Beyeler, ETH Zurich

ETH Eidgenössische Technische Hochschule Zürich Swiss Federal Institute of Technology Zurich

Theory

IMES

- Gor'kov's* theory:
  - time-averaged acoustic force acting on a compressible, spherical suspended particle in an arbitrary acoustic field
  - Force: $\langle F \rangle = -\nabla \langle U \rangle$
  - Force potential: $\langle U \rangle = 2\pi r_S{}^3 \rho_F \left(\frac{1}{3} \frac{\langle p^2 \rangle}{\rho_F{}^2 c_F{}^2} f_1 - \frac{1}{2} \langle v^2 \rangle f_2 \right)$

where $\langle p^2 \rangle, \langle v^2 \rangle$ mean square fluctuation of fluid pressure and velocity

$$f_1 = 1 - \frac{\rho_f c_f^2}{\rho_s c_s^2} \qquad f_2 = \frac{2(\rho_s - \rho_f)}{(2\rho_s + \rho_f)}$$

L.P. Gor'kov, Doklady Akademii Nauk Sssr, 140, pp.88-92, 1961

ETH Eidgenössische Technische Hochschule Zürich
Swiss Federal Institute of Technology Zurich

Numerical Modelling
J. Wang et al.

IMES

- The existing analytical solutions cannot determine the acoustic forces under more complex system conditions such as
  - proximity to the chamber wall,
  - complex viscous function,
  - acoustic streaming and
  - complicated particle shapes.
- Numerical modelling may become a powerful tool.

Ref. Numerical simulations for the time-averaged acoustic forces acting on rigid cylinders in ideal and viscous fluids, Wang JT, Dual J, **JOURNAL OF PHYSICS A-MATHEMATICAL AND THEORETICAL** Volume: **42** Issue: **28**, **JUL 17 2009**

ETH Eidgenössische Technische Hochschule Zürich
Swiss Federal Institute of Technology Zurich

Governing equations

IMES

- Equations for the host fluid (N-S equations)

$$\frac{\partial \rho}{\partial t} + \frac{\partial \rho u_i}{\partial x_i} = 0$$

$$\frac{\partial \rho u_i}{\partial t} + \frac{\partial (\rho u_i u_j + \sigma_{ij})}{\partial x_j} = 0$$

$$\sigma_{ij} = p\delta_{ij} - \left[\eta \left(\frac{\partial u_i}{\partial x_j} + \frac{\partial u_j}{\partial x_i} - \frac{2}{3}\frac{\partial u_k}{\partial x_k}\delta_{ij} \right) + \xi \frac{\partial u_k}{\partial x_k}\delta_{ij} \right]$$

$$p = p_0 + c_0^2(\rho - \rho_0)$$

- Time-averaged force

$$F_i = < \int_{S_0} -\sigma_{ij} n_j \mathrm{d}S_0 >$$

The angular bracket means average over one or several periods of the sound wave

Our numerical method: 2D - implementation

- Solve an initial value problem with given boundary conditions.
- FVM (Finite Volume Method) based on triangular meshes with Jameson difference method (AIAA paper 85-0435). (space discretization)
- Fourth-order Runge-Kutta algorithm. (time discretization)

- Comparison with
  - Haydock's theoretical solution
    - No viscosity, no boundaries, Only cylinder particle, $R/\lambda << 1$.
  - Haydock's Lattice Boltzmann method (LB)
    - Only for viscous fluid, difficulties on boundary conditions,
    - Very high computational effort, sometimes not very accurate.
  - COMSOL
    - Inviscid/viscous fluid, arbitrary particle shape, **only reflecting boundary**
    - High computational effort.

Numerical simulations

- Simulations for inviscid fluid

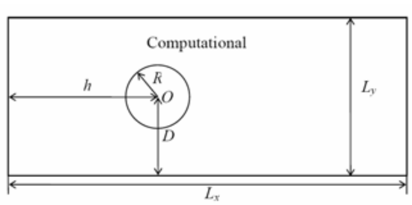

Geometrical configuration

The length of the computational region is $L_x = \lambda$ (wavelength)

Initial conditions: The wave is initialized as $\rho = \rho_0 + d\rho\cos(kx)$ and zero fluid velocity field $\mathbf{u} = 0$, where k is the wave vector, ρ_0=1.0 and $d\rho$ = 0.01.

Boundary conditions: Left: $\rho = \rho_0 + d\rho\cos(\omega t)$
Right: reflecting condition $u_x = 0$
Top and bottom: $u_y = 0$

•Results

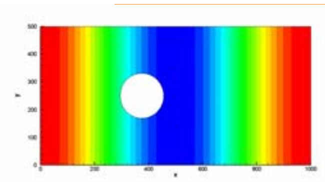

Density varying in first 5 cycles

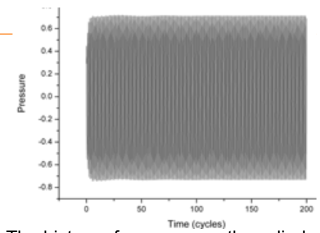

The history of pressure on the cylinder for 200 cycles

R	L_x	L_y	h	F_{th} (10^{-5})	F_{LB} (10^{-5})	F_{COM} (10^{-5})	F_{FVM} (10^{-5})
5	1000	100	375	-1.24	-3.04	-1.22	-1.25
10	1000	100	375	-4.95	-8.20	-5.13	-5.17
20	1000	200	375	-19.79	-25.12	-21.13	-21.17
40	1000	200	375	-77.85	-81.02	-108.41	-105.15
80	1000	500	375	-265.70	-247.20	-384.22	-375.30

F_{th}: analytical solutions (Haydocks, Journal of Physics A (**38**), 2005, pp. 3279), F_{LB}: calculated by LB method (Haydocks, Journal of Physics A (**38**), 2005, pp. 3265), F_{COM}: calculated by COMSOL (a commercial FEM software package), F_{FVM}: calculated by our FVM program

•Perfectly Matched Layers

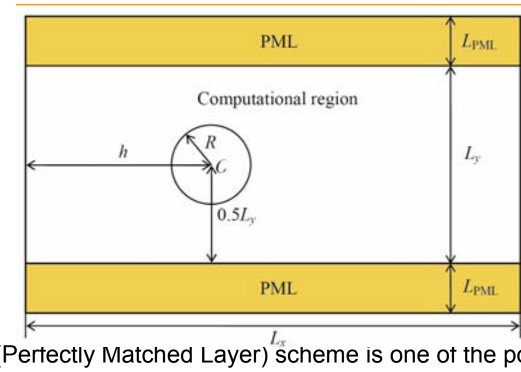

The PML (Perfectly Matched Layer) scheme is one of the popular artificial non-reflecting boundary conditions. The key idea of PML is to add an extra region (PML) outside the original computational region, into which the outgoing waves are allowed to propagate without any reflections and then dissipated entirely.

ETH
Eidgenössische Technische Hochschule Zürich
Swiss Federal Institute of Technology Zurich

•Viscosity

IMES

Ratio of forces with/without viscosity versus viscosity at the cylinder position h = 375 and L_x = 1000 with PML.

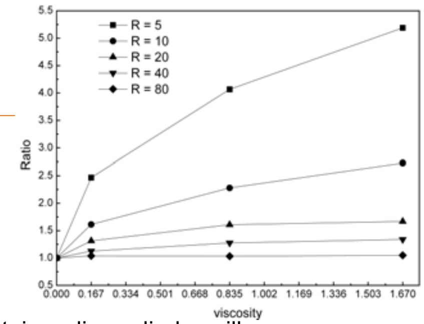

- ❖ The mean force on a certain radius cylinder will increase due to the fluid viscosity as described by Dojnikov.
- ❖ The viscosity influences the mean forces more significantly for small cylinders at a certain wave frequency, which is also described by analytical works.

acoustic boundary layer
$\delta = (2\nu/\omega)^{1/2}$

The reason is that the larger value of δ/R implies more significant viscous effects. The value of the variable δ/R reaches 6.07 when ν = 1.67 and R = 5, whereas it is merely 0.38 for R = 80

ETH
Eidgenössische Technische Hochschule Zürich
Swiss Federal Institute of Technology Zurich

Calculations for acoustic radiation force acting on a cylinder near a flat wall in a standing wave excitation in an ideal fluid

IMES

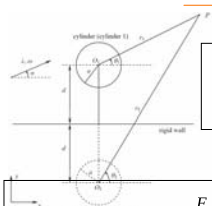

$$\mathbf{u} = \nabla\varphi$$
$$p = -\rho_0\dot{\varphi}$$
$$\nabla^2\varphi + k^2\varphi = 0$$

Expand with Bessel functions in the two coordinates respectively

$$\varphi_{\mathrm{I}} = A\cos[kr_1\cos(\theta_1-\alpha)+kh] = \sum_{m=-\infty}^{+\infty} C_m J_m(kr_1)e^{im\theta_1}$$ *Standing wave*

$$\varphi_{\mathrm{S}}^{(11)} = \sum_{m=-\infty}^{+\infty} a_m^{(11)} H_m^{(1)}(kr_1)e^{im\theta_1} \quad \varphi_{\mathrm{S}}^{(22)} = \sum_{m=-\infty}^{+\infty} a_m^{(22)} H_m^{(1)}(kr_2)e^{im\theta_2}$$

With Graf's additional theorem

Total acoustic field

$$\varphi_{\mathrm{T}}^{(1)} = \varphi_{\mathrm{I}} + \varphi_{\mathrm{S}}^{(11)} + \varphi_{\mathrm{S}}^{(21)}$$
$$= \sum_{m=-\infty}^{+\infty} b_m^{(22)} J_m(kr_1)e^{im\theta_1} + \sum_{m=-\infty}^{+\infty} a_m^{(11)} H_m^{(1)}(kr_1)e^{im\theta_1}$$
$$b_m^{(22)} = C_m + \sum_{n=-\infty}^{+\infty} i^{m-n} H_{m-n}^{(1)}(2kd)a_n^{(22)}$$

Final solutions

$$F_x = -\frac{\rho\pi a}{4}\mathrm{Re}\left[\frac{\omega^2}{c^2}(I_1^+ + I_1^-) - \frac{1}{a^2}(I_2^+ + I_2^-)\right]$$
$$F_y = -\frac{\rho\pi a}{4}\mathrm{Im}\left[\frac{\omega^2}{c^2}(I_1^+ - I_1^-) - \frac{1}{a^2}(I_2^+ - I_2^-)\right]$$
$$I_1^{\pm} = \sum_{m=-\infty}^{+\infty} a_m^{(11)}a_{m\pm1}^{(11)*}H_m^{(1)}H_{m\pm1}^{(2)} + a_m^{(11)}b_{m\pm1}^{(22)*}H_m^{(1)}J_{m\pm1} + b_m^{(22)}a_{m\pm1}^{(11)*}J_m H_{m\pm1}^{(2)} + b_m^{(22)}b_{m\pm1}^{(22)*}J_m J_{m\pm1}$$
$$I_2^{\pm} = m(m\pm1)\sum_{m=-\infty}^{+\infty} a_m^{(11)}a_{m\pm1}^{(11)*}H_m^{(1)}H_{m\pm1}^{(2)} + a_m^{(11)}b_{m\pm1}^{(22)*}H_m^{(1)}J_{m\pm1} + b_m^{(22)}a_{m\pm1}^{(11)*}J_m H_{m\pm1}^{(2)} + b_m^{(22)}b_{m\pm1}^{(22)*}J_m J_{m\pm1}$$

Comparisons of the exact, approximate and numerical results ka = 0.063

ρ_0 = 1.0 , ν = 0.0167 ,
λ= 1000, h=375, dρ = 0.01,
c_0 =1/sqrt(3) and R = 20.

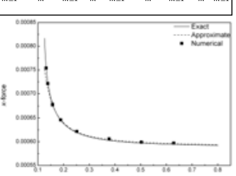

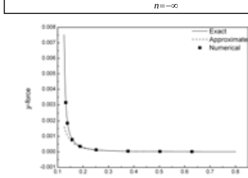

Experiments: Glass plate device
A. Haake et al.

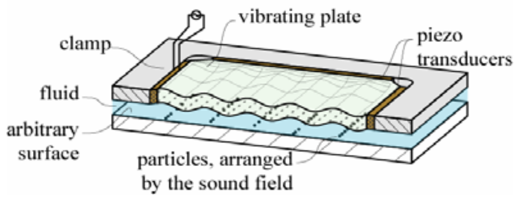

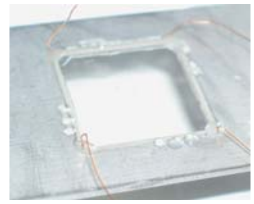

- Piezo transducers are used to excite a glass plate
- This results in a bending mode of vibration
- A pressure field results in the fluid layer
- One or two elements can be excited

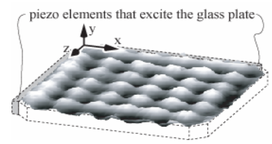

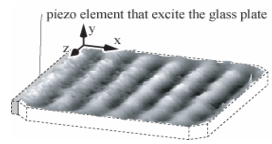

Glass plate device
Single Particle Motion, side view

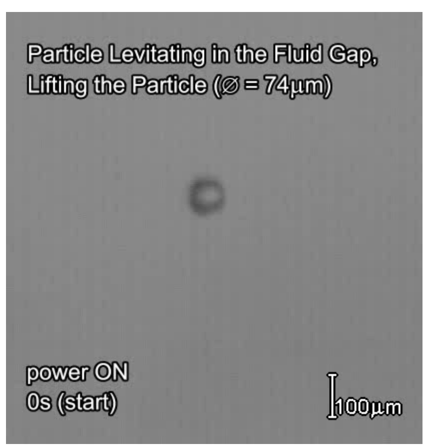

Glass plate device - Line forming, 1-D

with G. Radziwill, Medical Virology, USZ

Field of view: 0.67 × 0.56 mm
MCF10A cells
Real time

View of whole device
HL60 cells
After 48 seconds

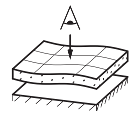

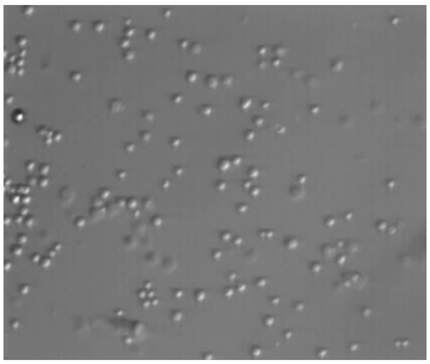

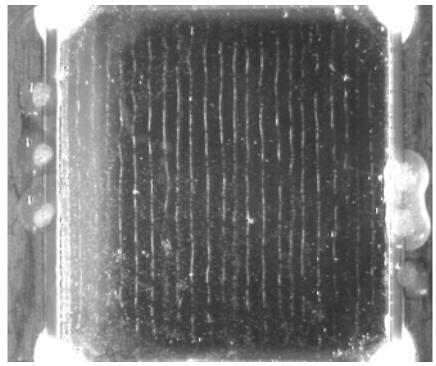

Flexural plate device - Clump forming, 2-D

Field of view: 1.75 × 1.5 mm
HL60 cells
Real time

View of whole device
HL60 cells
After 110 seconds

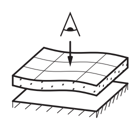

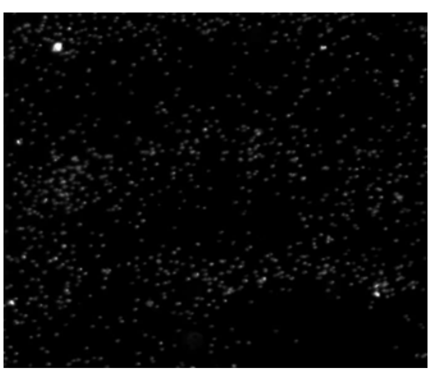

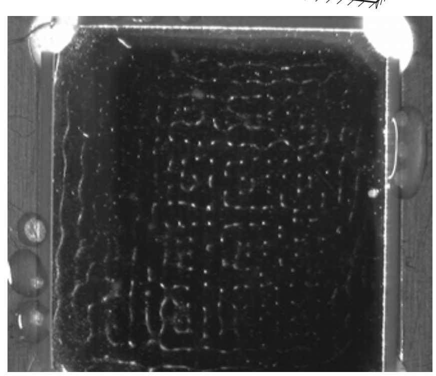

Moving Particles

- 3 Possibilities:

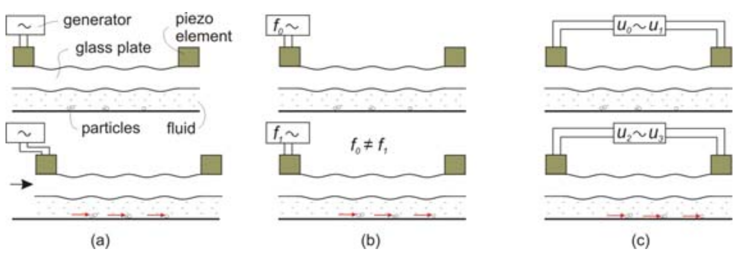

- Moving plate device
- Ramping frequency
- -> Bead Sweeper
- Changing relative voltages on opposite electrodes

Miniaturization
S. Oberti, A. Neild et al.

- Motivation for miniaturization
  - Most applications require a closed system (Cell sorting, Cell fusion, 2-D testing array for reaction analysis)
  - If focus on cells, large magnification limits field of view
  - Possibility of integration into Lab-on-a-chip devices
  - Higher repeatability is needed and is obtainable through better defined boundary conditions, thus more accurate manufacturing is needed

- Characteristics which ought to be retained
  - Possibility to collect particles in lines in either of two directions or clumps depending on actuation
  - The device should be able to operate in a no-flow condition

Microfluidic channel device - Description

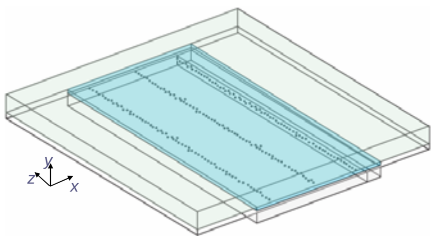

3 layers:
Upper – Glass 1mm thick
Middle – Si 0.3 mm thick, 12 mm wide
Lower – Piezo, 0.5 mm thick, 5mm wide, polarized in the vertical direction, electrodes on upper and lower surfaces

The structure is 25 mm long, and supported at each end.

Fluid Channel etched in Si, 200 μm deep, 5mm wide.

The lower electrode of the piezo is cut so that a strip is created at one end which is 700 μm wide

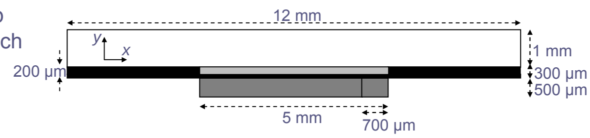

Microfluidic channel device - Modeling

Femlab: commercial partial differential equation solver with meshing facilities
Boundary conditions used were:
-Free displacement at all external edges
-Fluid structure interaction
Variables are: pressure (p, fluid) and displacement vector (u, solid)

Force balance

$$F_n = -A\rho_f \left.\frac{\partial \phi}{\partial t}\right|_s$$

Solid module
Area Load can be applied

$$F_n / A = -n_s p$$

Equate velocities

$$v_n = -\nabla\phi|_s . n_s$$

Fluid module
Normal Acceleration can be applied

$$\left(-\omega^2 u\right) n_s = -\frac{\nabla p}{\rho_f} . n_s = a_n$$

-Electrical
upper electrode: ground
lower larger electrode: ground
lower strip electrode: a.c. voltage

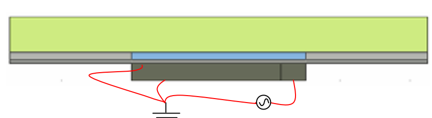

Damping was applied using complex stiffness parameters for solids, and wave speed for the fluid.

A mesh of 6000 triangular elements was found to be sufficient.

Microfluidic channel device - Result at 1.25MHz

This is done within Femlab by using the equations given by Gor'kov.

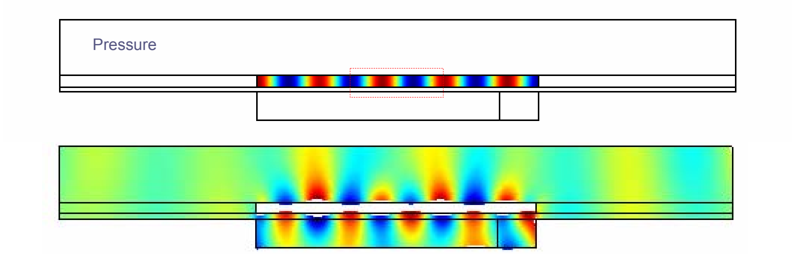

Force field (Zoomed)

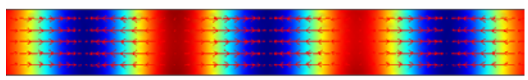

Microfluidic channel device - Pressure field

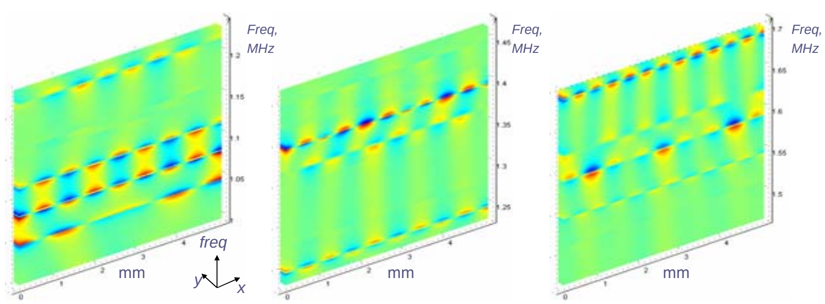

Pressure plotted over a range of frequencies, across the area of the device

- Pressure amplitude: 0.8 MPa
- Displacement amplitude: 20 nm
- Force amplitude: 0.2 nN

Frequency range:
1 to 1.7 MHz
0.002 MHz steps

Microfluidic channel device - Simulation vs Experimentation

Major resonances (1.0 to 1.7 MHz)

Experiments used 26 μm diameter copolymer beads.
Frequency steps of 0.01 MHz. Fluid flow used.
No reference was made to simulation results.

Simulation			Experiment	
Frequency (MHz)	No. of lines		Frequency (MHz)	No. of lines
1.05	4			
1.08	8		1.08	8
1.12	8		1.12	8
1.22	7		1.20	9 Static
1.25	9		1.24	9 Static
1.40	10		1.42	10
1.54	11		1.52	11 Static
1.58	10		1.59	10
1.69	12		1.69	12

If a signal is applied across the whole plate the three frequencies which worked under static conditions do not occur

Microfluidic channel device - Example experimental results 1

Lines of 26 μm diameter copolymer beads, formed in a non-flowing fluid.

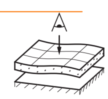

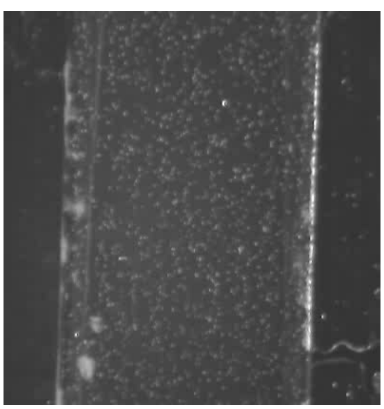

1.24 MHz

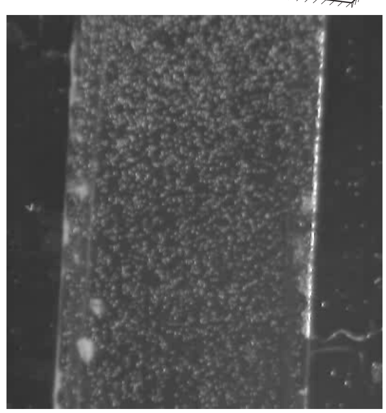

1.52 MHz

1 mm Open ended channel

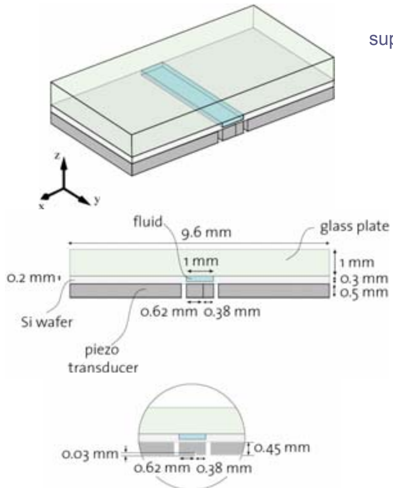

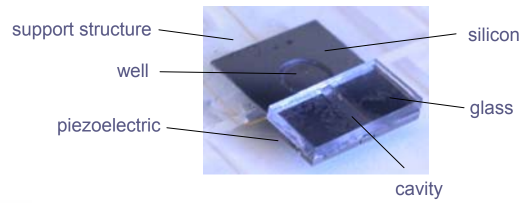

Requirements:

- concentration of particles in a single line along the center of the channel
- allow access to the positioned particles
- operate with non-flowing fluid

2D Modeling

Frequency sweep 0.5 to 3 MHz

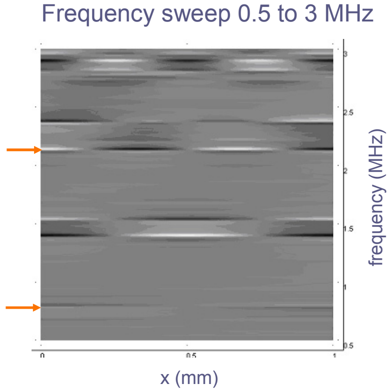

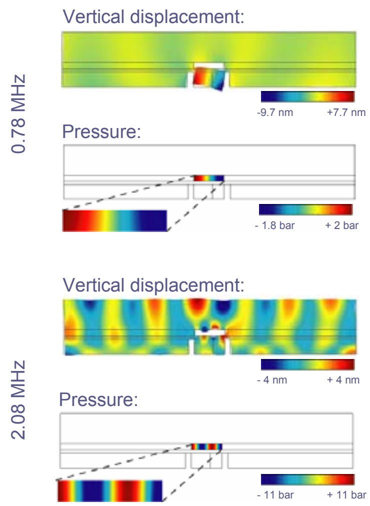

Cell positioning

- MCF10A cells

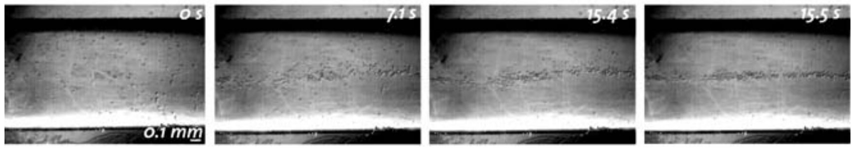

Positioning into 1 line. First, at 0.78MHz to make the cells roughly collect along the centerline of the channel, then at 2.08 MHz for more accurate positioning

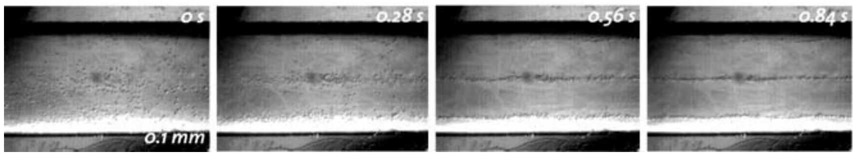

Positioning into 3 lines at 2.08 MHz.

S. Oberti et al, Nanotech 05

Experimental setup

Nelson, et al., IRIS, ETHZ
Dual, et al. IMES, ETHZ

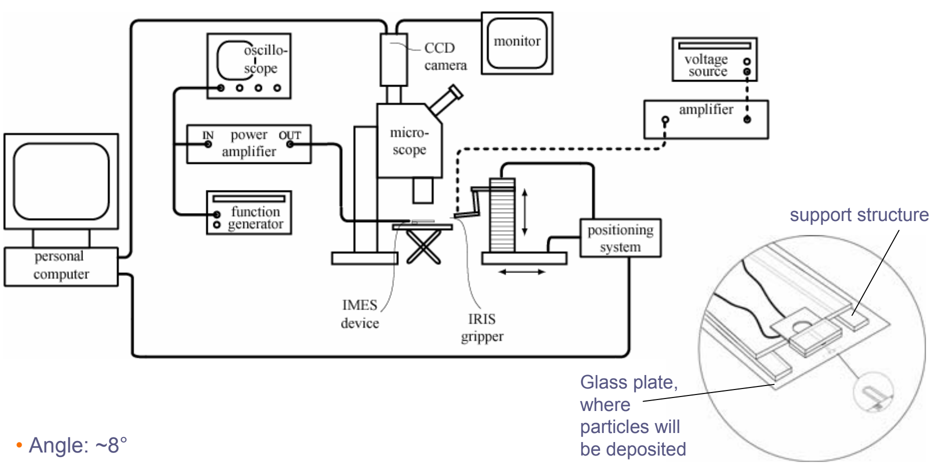

- Angle: ~8°

ETH
Eidgenössische Technische Hochschule Zürich
Swiss Federal Institute of Technology Zurich

US positioning + pick and place

IMES
Institut für Mechanische Systeme

1) Random particles

2) Ultrasound (US) ON, 0.78MHz, particles approximately in 1 line

3) US ON, 2.08MHz, so particles more accurately aligned

4) US OFF

5) Gripper in, grab particle, and remove

6) Drop gripper down to a glass slide 2mm under the device, and change focus

7) Release particle

8) Go up with gripper, change focus back, US ON and OFF to realign the particles, and grip again etc.

74 μm copolymer particles
Speed: 6x

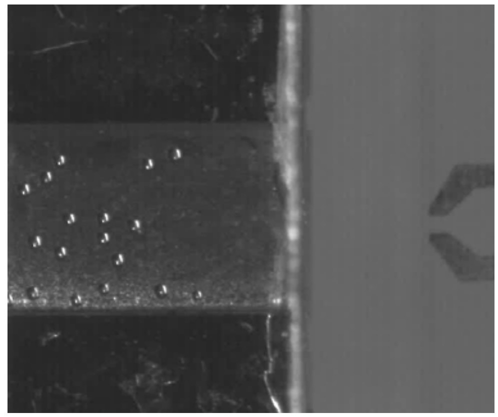

ETH
Eidgenössische Technische Hochschule Zürich
Swiss Federal Institute of Technology Zurich

2D manipulation in micromachined chamber

IMES
Institut für Mechanische Systeme

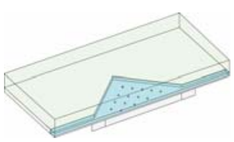

26 µm diameter copolymer beads
5 mm x 5mm x 0.2 mm chamber
Operation at 1.971 MHz

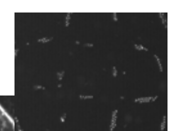

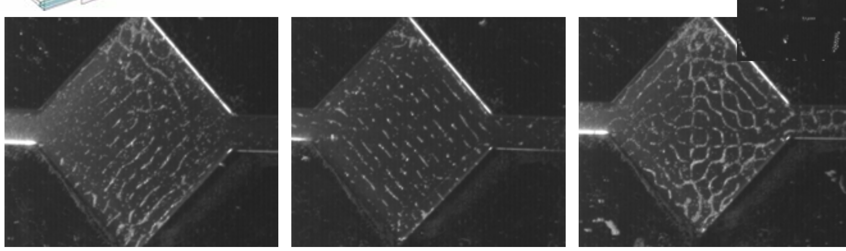

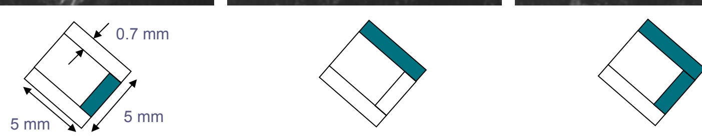

Diagonal orientation

Two identical frequencies $\omega = \omega_x = \omega_z \quad k = k_x = k_z$

Express pressure as:

$$p_x = p_{x0}\cos\left(k_x x\right)\cos\left(\omega_x t\right) \qquad p_z = p_{z0}\cos\left(k_z z\right)\cos\left(\omega_z t\right)$$

Force equation from Gor'kov:

$$\langle U\rangle = 2\pi r_S^3 \rho_F \left(\frac{1}{3}\frac{\langle p^2\rangle}{\rho_F^2 c_F^2} f_1 - \frac{1}{2}\langle q^2\rangle f_2\right)$$

Time averaged pressure squared term:

$$\langle p^2\rangle = \left\langle \left(p_x + p_z\right)^2\right\rangle = \frac{p_{x0}^2\cos^2(kx)}{2} + \frac{p_{z0}^2\cos^2(kz)}{2} + p_{x0}p_{z0}\cos(kx)\cos(kz)$$

Time averaged velocity squared term:

$$\langle q^2\rangle = \left\langle v_x^2 + v_z^2\right\rangle = \frac{k^2}{\rho_F^2\omega^2}\left[\frac{p_{x0}^2\sin^2(kx)}{2} + \frac{p_{z0}^2\sin^2(kz)}{2}\right]$$

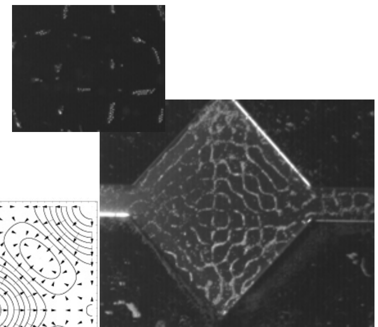

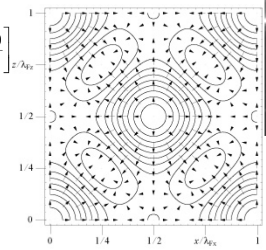

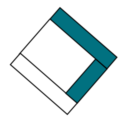

Lines and Diagonal orientation

9.6 µm diameter copolymer beads

Operation at 2.562 MHz

Real time

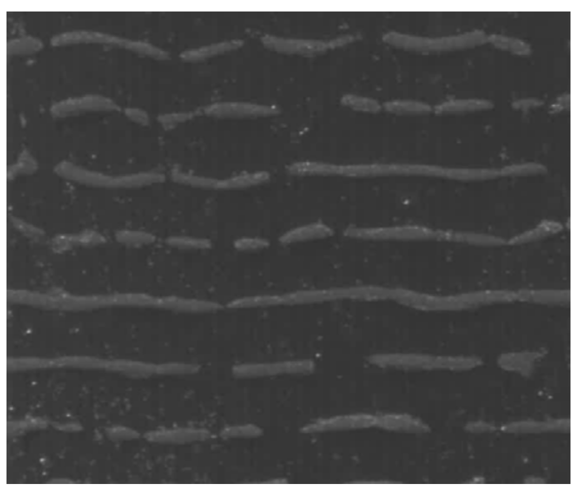

ETH Eidgenössische Technische Hochschule Zürich Swiss Federal Institute of Technology Zurich

Orientation in points

IMES

Two different frequencies

Express pressure as:

$$p_x = p_{x0}\cos\left(k_x x\right)\cos\left(\omega_x t\right) \qquad p_z = p_{z0}\cos\left(k_z z\right)\cos\left(\omega_z t\right)$$

Force equation from Gor'kov:

$$\langle U\rangle = 2\pi r_S^{\ 3}\rho_F\left(\frac{1}{3}\frac{\langle p^2\rangle}{\rho_F^{\ 2}c_F^{\ 2}}f_1 - \frac{1}{2}\langle q^2\rangle f_2\right) \qquad \partial\phi/\partial t = p/\rho_F \qquad v = \left[-\partial\phi/\partial x, -\partial\phi/\partial z\right]$$

Time averaged pressure squared term:

$$\langle p^2\rangle = \left\langle (p_x + p_z)^2\right\rangle = \frac{p_{x0}^{\ 2}\cos^2(k_x x)}{2} + \frac{p_{z0}^{\ 2}\cos^2(k_z z)}{2} + \cancel{p_{x0}p_{z0}\cos(k_x x)\cos(k_z z)}$$

Time averaged velocity squared term:

$$\langle q^2\rangle = \left\langle v_x^{\ 2} + v_z^{\ 2}\right\rangle = \frac{1}{2\rho_F^{\ 2}}\left[\frac{k_x^{\ 2}p_{x0}^{\ 2}\sin^2(k_x x)}{\omega_x^{\ 2}} + \frac{k_z^{\ 2}p_{z0}^{\ 2}\sin^2(k_z z)}{\omega_z^{\ 2}}\right]$$

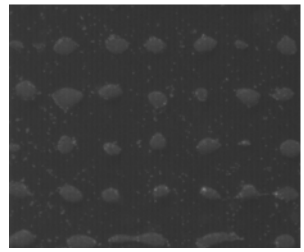

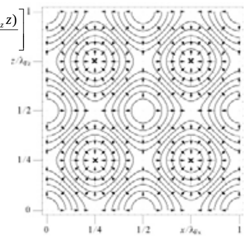

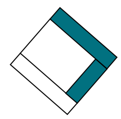

ETH Eidgenössische Technische Hochschule Zürich Swiss Federal Institute of Technology Zurich

Lines to Points

IMES

9.6 µm diameter copolymer beads

Operation at 2 frequencies around 2.562 MHz, differing by 25 Hz

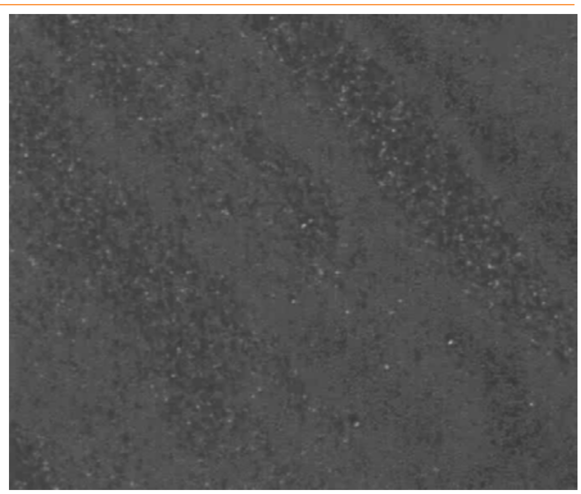

CISM2010, Lecture 6 Dual

Applications

- Pharmaceutical screening

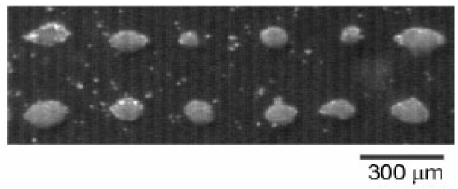

e.g. Subjecting cells to sequences of drugs

Applications: Bead Sweeping

Ultrasonic Bead Sweeper:

Collecting Chemicals from fluids

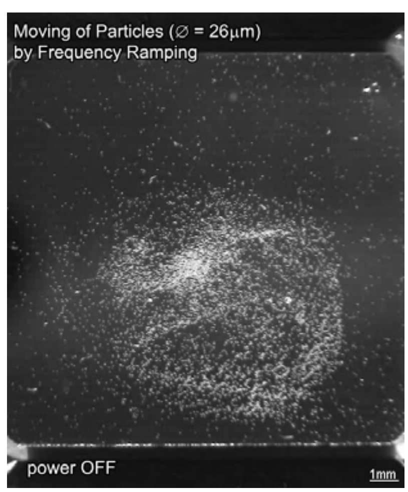

ETH
Eidgenössische Technische Hochschule Zürich
Swiss Federal Institute of Technology Zurich

Manipulation of Protein crystals in channels using ultrasonics and nylon loop

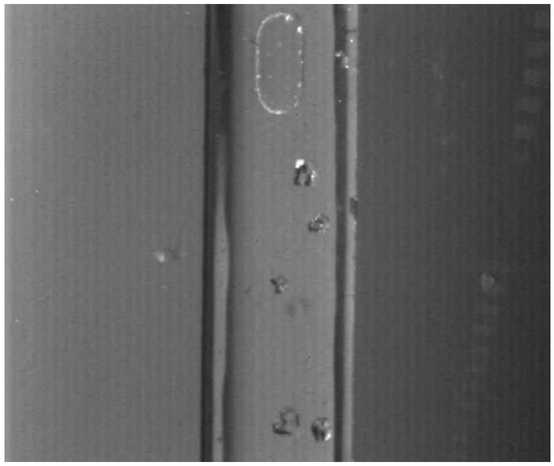

ETH
Eidgenössische Technische Hochschule Zürich
Swiss Federal Institute of Technology Zurich

•Concentration of particles
•D. Möller

- Conventional: sedimentation, centrifugation, magnetic
- Acoustics:
  - Advantages: Contactless, can be miniatuized, fast
  - Methods:
    - Exciting a plate to vibration
    - Longitudinal excitation
    - Mixture of excitation
  - Longitudinal excitation
    - Frequency sweep (discrete and continuous)
    - Pseudo standing wave

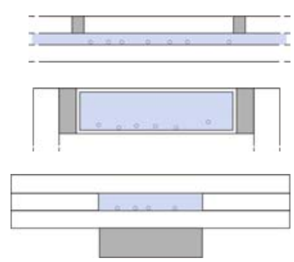

A. Haake, Micromanipulation of Small Particles with Ultrasound, Diss. ETH No. 15681
M. Saito, N. Kitamura and M. Terauchi, Jour. Of Appl. Physics, vol 92, no 12, 12 (2002), pp. 7581-7586
G. Whiteworth, M.A. Grundy and W.T. Coakley, Ultrasonics, vol 29 ,12 (1991), pp. 439-444

Setup and Simulation

- Device for longitudinal, continuous and asymmetric excitation
  - Enables to move particles close to chamber wall
- 2D simulation
  - significant influence of boundaries
  - Potential field at off resonance frequencies can't be neglected

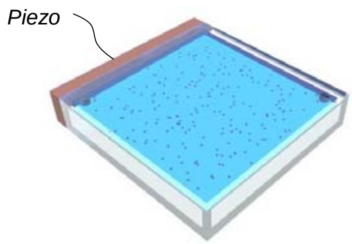

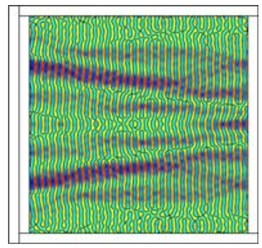

Pressure field 2.5*MHz*

dirk.moeller@imes.mavt.ethz.ch

Experimental

- Macro scale chamber
  - 25x25x5mm
  - Different materials (here: Al)
  - Rapid movement with larger particles (26µm copolymer)
  - Streaming visible with smaller particles
  - 1.5 – 2.5MHz at 0.05Hz sweeping rate
- Modularity
  - Extendable to 2D excitation
  - Introduction of waveguides
  - Symmetric and asymmetric excitation possible

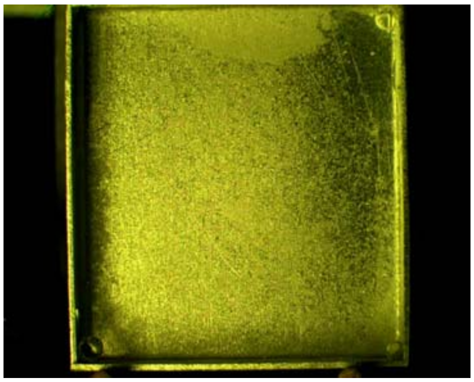

dirk.moeller@imes.mavt.ethz.ch

ETH
Eidgenössische Technische Hochschule Zürich
Swiss Federal Institute of Technology Zurich

Rotation of Objects
T. Schwarz

IMES

Viscous torque

- rotation of spherical and non-spherical particles (axisymmetric)
- Torque results from viscous effect (acoustic near boundary streaming)

Torque on an object subjected to the influence of two orthogonal acoustic waves with phase lag

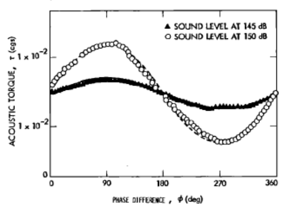

Acoustic torque as a function of the phase difference between the x and y components of the pressure oscillation [1]

- Maximal torque at 90° or 270° phase lag
- No torque at 0° and 180° phase lag

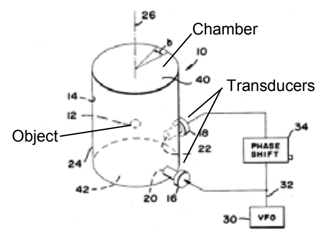

cylindrical chamber for controlling an object [2]

[1] Busse, Wang; Torque generated by orthogonal acoustic waves-Theory; J. Acoust. Soc. Am. 96(6), 1981
[2] US Patent 4,800,756; Barmatz et al.; Acoustic Controlled Rotation and Orientation (1989-01-31)

ETH
Eidgenössische Technische Hochschule Zürich
Swiss Federal Institute of Technology Zurich

Rotation of Objects

IMES

Acoustic radiation torque

- Non-spherical particles (fiber), shorter λ/4
- Torque aligns object parallel to nodal pressure planes
- Torque originates from the acoustic force gradient between the node and the antinode

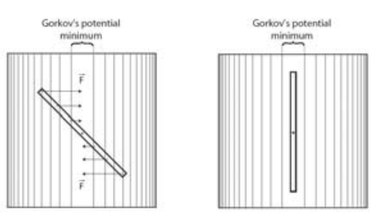

- modification of potential field leads to movement (rotation) of object

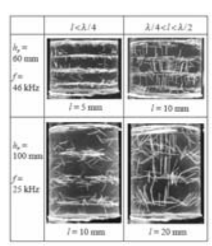

Alignment of polystyrene fibers of different length [2]

Yamahira:
- Orientation of fibers in a liquid irradiated with ultrasound
- reinforcing fibers in the molten matrix of a composite material (enhance mechanical properties)

[1] Brodeur; Motion of fluid-suspended fibres in a standing wave field; Ultrasonics 1991; Vol.29
[2] Yamahira; Orientation of Fibers in Liquid by Ultrasonic Standing Waves; Jpn.J.Appl.Phys 2000; Vol.39

ETH
Eidgenössische Technische Hochschule Zürich
Swiss Federal Institute of Technology Zurich

Rotation of Objects – Amplitude Modulation

IMES

Motivation:

- Generate and control the rotation of micro fibers using ultrasonic standing waves
- Control direction, speed of rotation or angular position

Device:

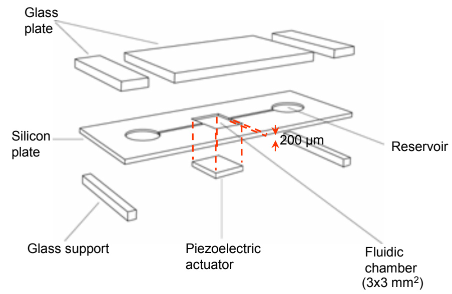

Piezoelectric actuator:
bottom electrode

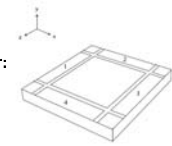

Fluidic chamber with Copolymer particles (Ø = 17 µm); red area symbolizes the active electrode; f = 1698 kHz

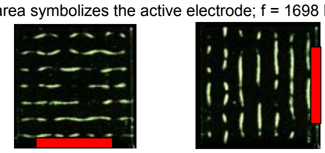

Orthogonal superposition of standing waves (x and z direction)

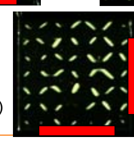

Schwarz@imes.mavt.ethz.ch

ETH
Eidgenössische Technische Hochschule Zürich
Swiss Federal Institute of Technology Zurich

Rotation of Objects – Amplitude Modulation

IMES

- Use of acoustic radiation torque
- Two standing pressure waves in x and z direction
- Control of the rotation based on the modulation of the amplitude of two superposed orthogonal standing waves

$$P_x = A_x \cos(k_x x)\cos(\omega_x t)$$
$$P_z = A_z \cos(k_z z)\cos(\omega_z t)$$

A...amplitude
ω...angular frequency
k...wave vector

$$\omega_x = \omega_z$$

$$U = 2\pi r_s^3 \rho_f \left(\frac{f_1}{3\rho_f^2 c_f^2}\langle p^2\rangle - \frac{f_2}{2}\langle v^2\rangle \right)$$

Visualization of Gorkov's potential U for one wavelength in x and z direction

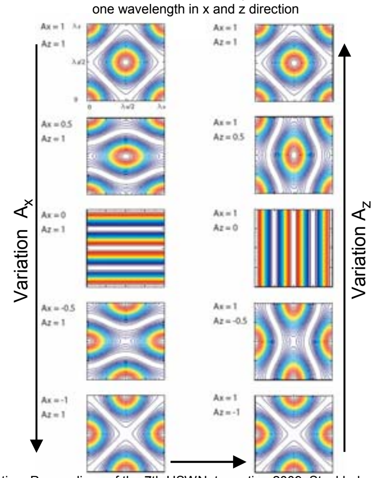

Schwarz@imes.mavt.ethz.ch

Schwarz, Petit-Pierre, Dual; Rotation of non spherical particles with amplitude modulation, Proceedings of the 7th USWNet meeting 2009, Stockholm

ETH
Eidgenössische Technische Hochschule Zürich
Swiss Federal Institute of Technology Zurich

Rotation of Objects – Amplitude Modulation

IMES

- Copolymer particles (Ø = 17 µm)
- Frequency f=1689kHz ; max. Voltage 30V

- Glass-fiber Ø= 9 µm ; length = 250 µm
- Frequency f=1085kHz ; max. Voltage 30V

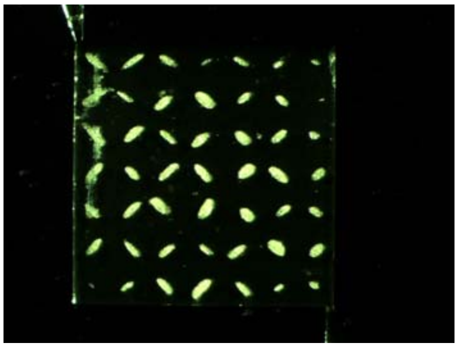

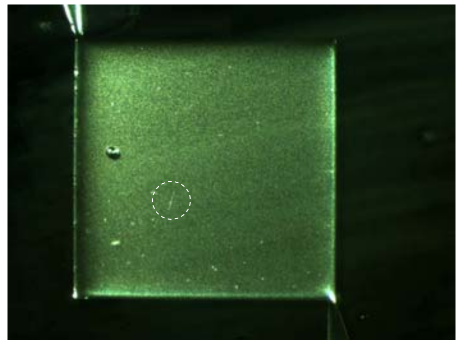

λ

- Change of direction possible
- Speed of rotation up to 30 rpm

λ

Schwarz@imes.mavt.ethz.ch

ETH
Eidgenössische Technische Hochschule Zürich
Swiss Federal Institute of Technology Zurich

Conclusions

IMES

- Numerical Model
- Glass Plate Device
  - Lines and Clumps of cells formed
- Microfluidic devices
  - Actuation method suitable for miniaturization found, by use of piezo plate with a strip electrode
  - Femlab model, Comparison of simulated pressure fields with experimental work
  - Chamber device: Positioning in points, lines, Rotation, etc.
- Fascinating field with a combination of basic questions, exciting features and possible applications
- Applications: Cell sorting, Drug screening, Bead Sweeping, …

Literature by the Particle Manipulation Group at ETHZ

J. Dual et al.

1.Monolithically fabricated microgripper with integrated force sensor for manipulating microobjects and biological cells aligned in an ultrasonic field
Author(s): Beyeler F, Neild A, Oberti S, et al.
Source: **JOURNAL OF MICROELECTROMECHANICAL SYSTEMS** Volume: **16** Issue: **1** Pages: **7-15** Published: **FEB 2007**

2. Positioning, displacement, and localization of cells using ultrasonic forces
Author(s): Haake A, Neild A, Radziwill G, et al.
Source: **BIOTECHNOLOGY AND BIOENGINEERING** Volume: **92** Issue: **1** Pages: **8-14** Published: **OCT 5 2005**

3. A micro-particle positioning technique combining an ultrasonic manipulator and a microgripper
Author(s): Neild A, Oberti S, Beyeler F, et al.
Source: **JOURNAL OF MICROMECHANICS AND MICROENGINEERING** Volume: **16** Issue: **8** Pages: **1562-1570** Published: **AUG 2006**

4. Manipulation of micrometer sized particles within a micromachined fluidic device to form two-dimensional patterns using ultrasound
Author(s): Oberti S, Neild A, Dual J
Source: **JOURNAL OF THE ACOUSTICAL SOCIETY OF AMERICA** Volume: **121** Issue: **2** Pages: **778-785** Published: **FEB 2007**

5. Positioning of small particles by an ultrasound field excited by surface waves
Author(s): Haake A, Dual J
Conference Information: Ultrasonics International 2003 Meetng, JUN 30-JUL 03, 2003 Granada, SPAIN
Source: **ULTRASONICS** Volume: **42** Issue: **1-9** Pages: **75-80** Published: **APR 2004**

6. Micro-manipulation of small particles by node position control of an ultrasonic standing wave
Author(s): Haake A, Dual J
Conference Information: 1st Ultrasonics International Conference, JUL 03-05, 2001 DELFT, NETHERLANDS
Source: **ULTRASONICS** Volume: **40** Issue: **1-8** Pages: **317-322** Published: **MAY 2002**

7. Manipulation of cells using an ultrasonic pressure field
Author(s): Haake A, Neild A, Kim DH, et al.
Source: **ULTRASOUND IN MEDICINE AND BIOLOGY** Volume: **31** Issue: **6** Pages: **857-864** Published: **JUN 2005**

8. Design, modeling and characterization of microfluidic devices for ultrasonic manipulation
Author(s): Neild A, Oberti S, Dual J
Source: **SENSORS AND ACTUATORS B-CHEMICAL** Volume: **121** Issue: **2** Pages: **452-461** Published: **FEB 20 2007**

9. Simultaneous positioning of cells into two-dimensional arrays using ultrasound
Author(s): Neild A, Oberti S, Radziwill G, et al.
Source: **BIOTECHNOLOGY AND BIOENGINEERING** Volume: **97** Issue: **5** Pages: **1335-1339** Published: **AUG 1 2007**

10. Contactless micromanipulation of small particles by an ultrasound field excited by a vibrating body
Author(s): Haake A, Dual J
Source: **JOURNAL OF THE ACOUSTICAL SOCIETY OF AMERICA** Volume: **117** Issue: **5** Pages: **2752-2760** Published: **MAY 2005**

11. Finite element modeling of a microparticle manipulator
Author(s): Neild A, Oberti S, Haake A, et al.
Conference Information: Ultrasonics International (UI 05)/ World Congress on Ultrasonics (WCU 2005), AUG 29-SEP 01, 2005 Beijing, PEOPLES R CHINA
Source: **ULTRASONICS** Volume: **44** Pages: **E455-E460** Supplement: **Suppl. 1** Published: **DEC 22 2006**

12. Towards the automation of micron-sized particle handling by use of acoustic manipulation assisted by microfluidics
Author(s): Oberti S, Neild A, Moller D, et al.
Conference Information: Inaugural Meeting of the International Congress on Ultrasonic, APR 09-12, 2007 Vienna, AUSTRIA
Source: **ULTRASONICS** Volume: **48** Issue: **6-7** Pages: **529-536** Published: **NOV 2008**

13. The use of acoustic radiation forces to position particles within fluid droplets
Author(s): Oberti S, Neild A, Quach R, et al.
Source: **ULTRASONICS** Volume: **49** Issue: **1** Pages: **47-52** Published: **JAN 2009**

14. Novel sample preparation technique for protein crystal X-ray crystallographic analysis combining microfluidics and acoustic manipulation
Author(s): Oberti S, Moller D, Gutmann S, et al.
Source: **JOURNAL OF APPLIED CRYSTALLOGRAPHY** Volume: **42** Pages: **636-641** Part: **Part 4** Published: **AUG 2009**

15. Numerical simulations for the time-averaged acoustic forces acting on rigid cylinders in ideal and viscous fluids
Author(s): Wang JT, Dual J
Source: **JOURNAL OF PHYSICS A-MATHEMATICAL AND THEORETICAL** Volume: **42** Issue: **28** Article Number: **285502** Published: **JUL 17 2009**

16. Strategies for single particle manipulation using acoustic radiation forces and external tools
Author(s): Oberti S, Neild A, Moller D, et al.
Conference Information: International Congress on Ultrasonics, JAN 11-17, 2009 Univ Santiago Chile, Santiago, CHILE
Source: **INTERNATIONAL CONGRESS ON ULTRASONICS, PROCEEDINGS** Book Series: **Physics Procedia** Volume: **3** Issue: **1** Pages: **255-262** Published: **2010**

17. Strategies for single particle manipulation using acoustic and flow fields
Author(s): Oberti S, Moller D, Neild A, et al.
Conference Information: International Congress on Ultrasonics 2009, JAN 11-17, 2009 Univ Santiago Chile, Santiago, CHILE
Source: **ULTRASONICS** Volume: **50** Issue: **2** Pages: **247-257** Published: **FEB 2010**

Posters

INTEGRATED MAGNETOPHORETIC-ACOUSTOPHORETIC SEPARATION DEVICE FOR RAPID MULTITARGET CELL SORTING

Jonathan D Adams[1], Patrick Thévoz[1,2], Unyoung Kim[1], Henrik Bruus[3], H Tom Soh[1]
[1]University of California, Santa Barbara, USA [2]Ecole Polytecnique Fédérale de Lausanne, Switzerland [3]Technical University of Denmark, Denmark

INTRODUCTION

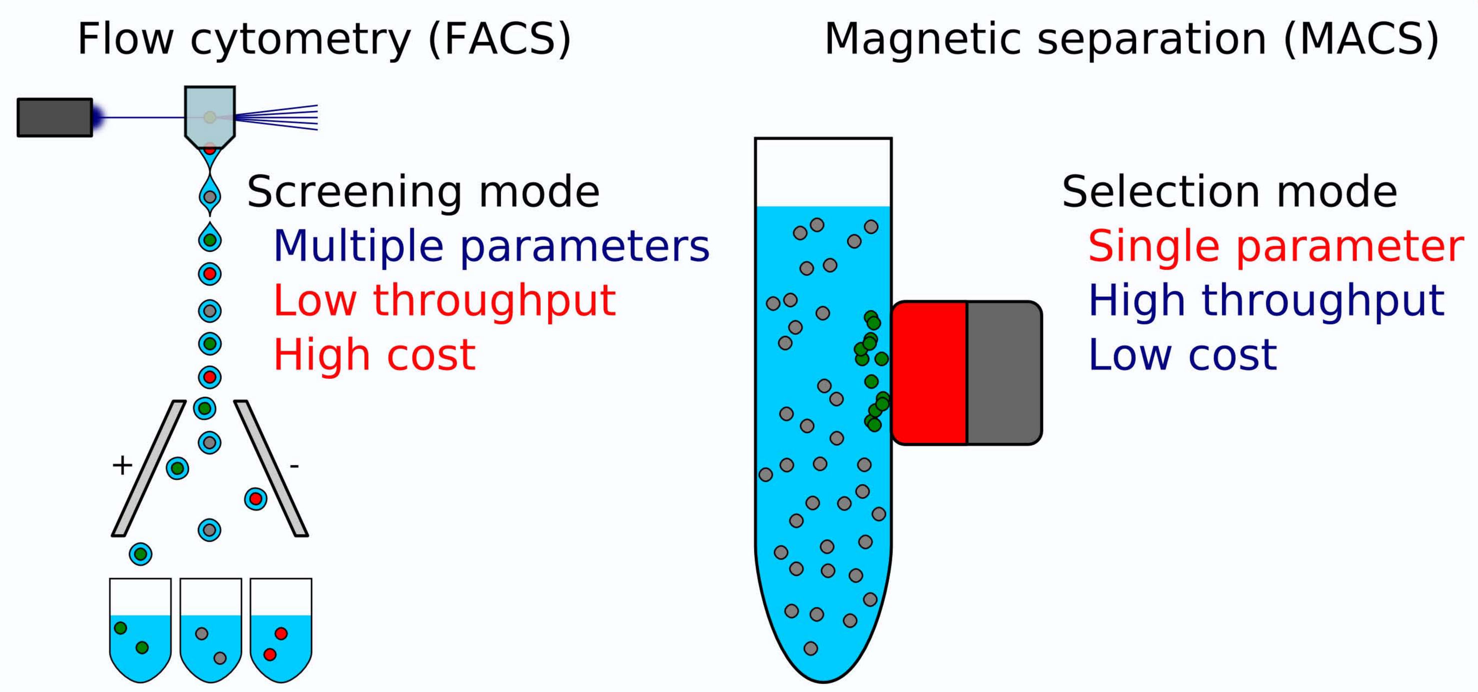

Can we create a single technology that has the benefits of both to achieve rapid, multiparameter separation?

We present the first integrated device that combines two complementary separation techniques, continuous-flow acoustophoresis [1] and magnetophoresis [2].

INTEGRATED SEPARATION FORCES

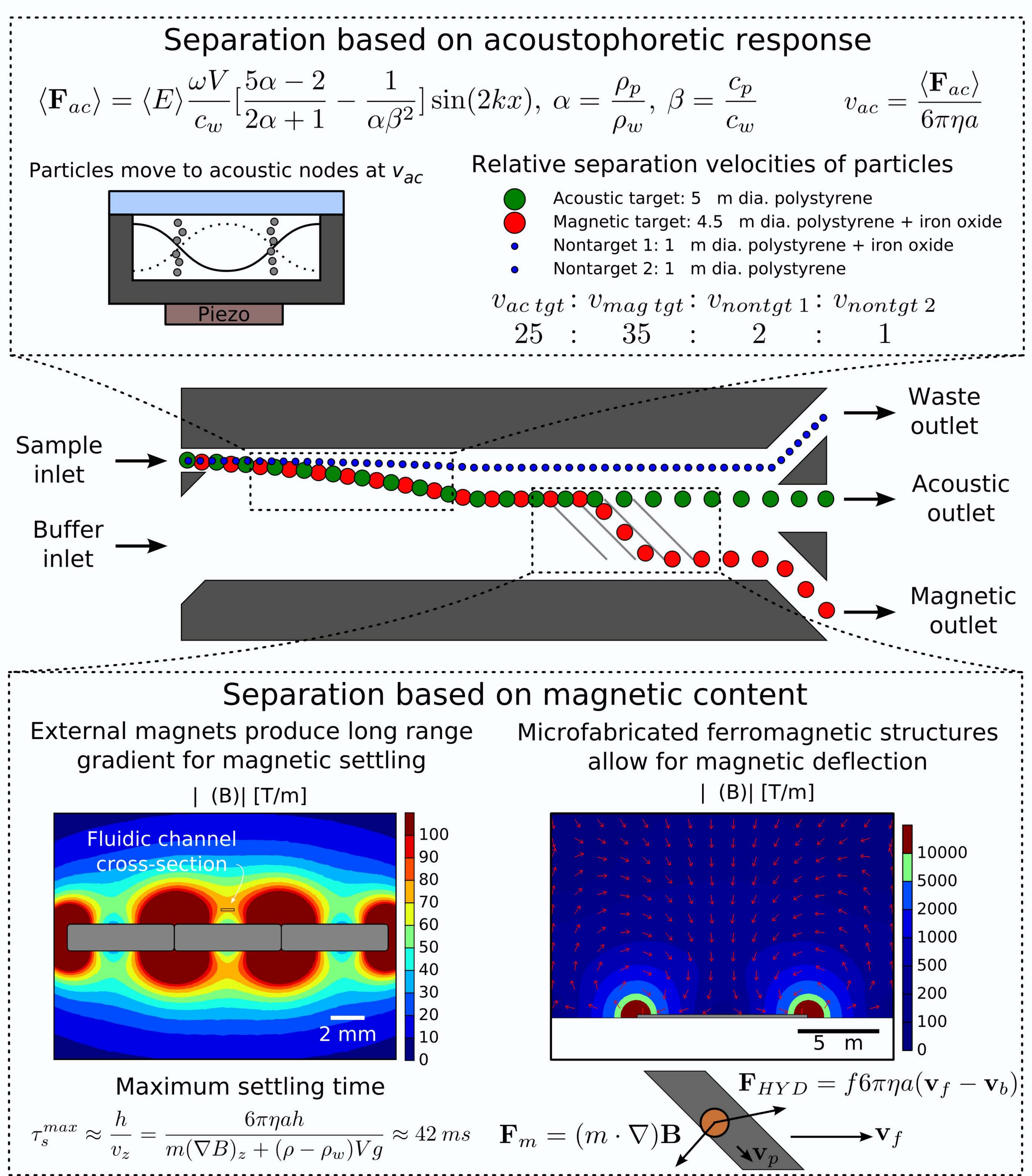

FLUIDIC CHANNEL DESIGN

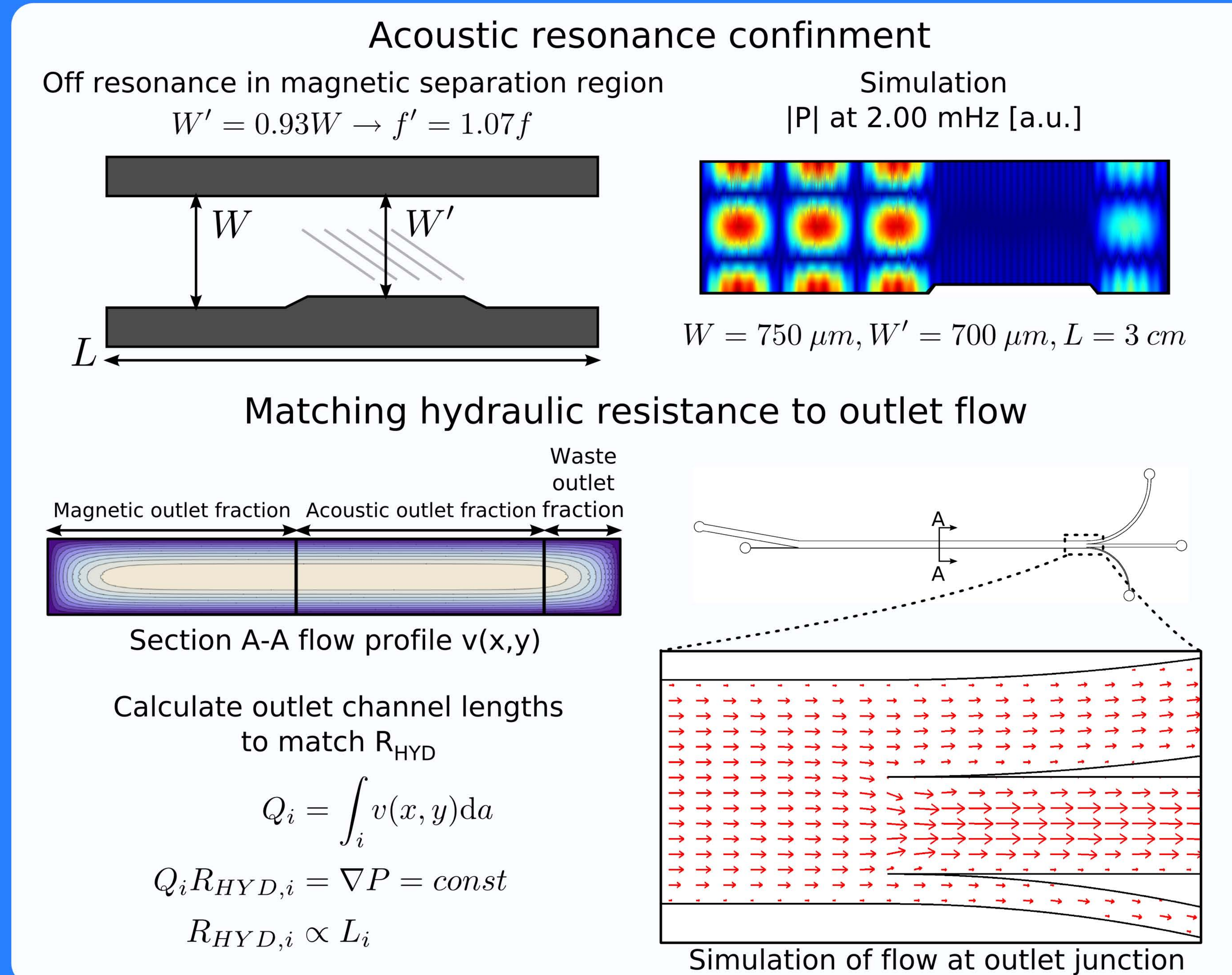

FABRICATION

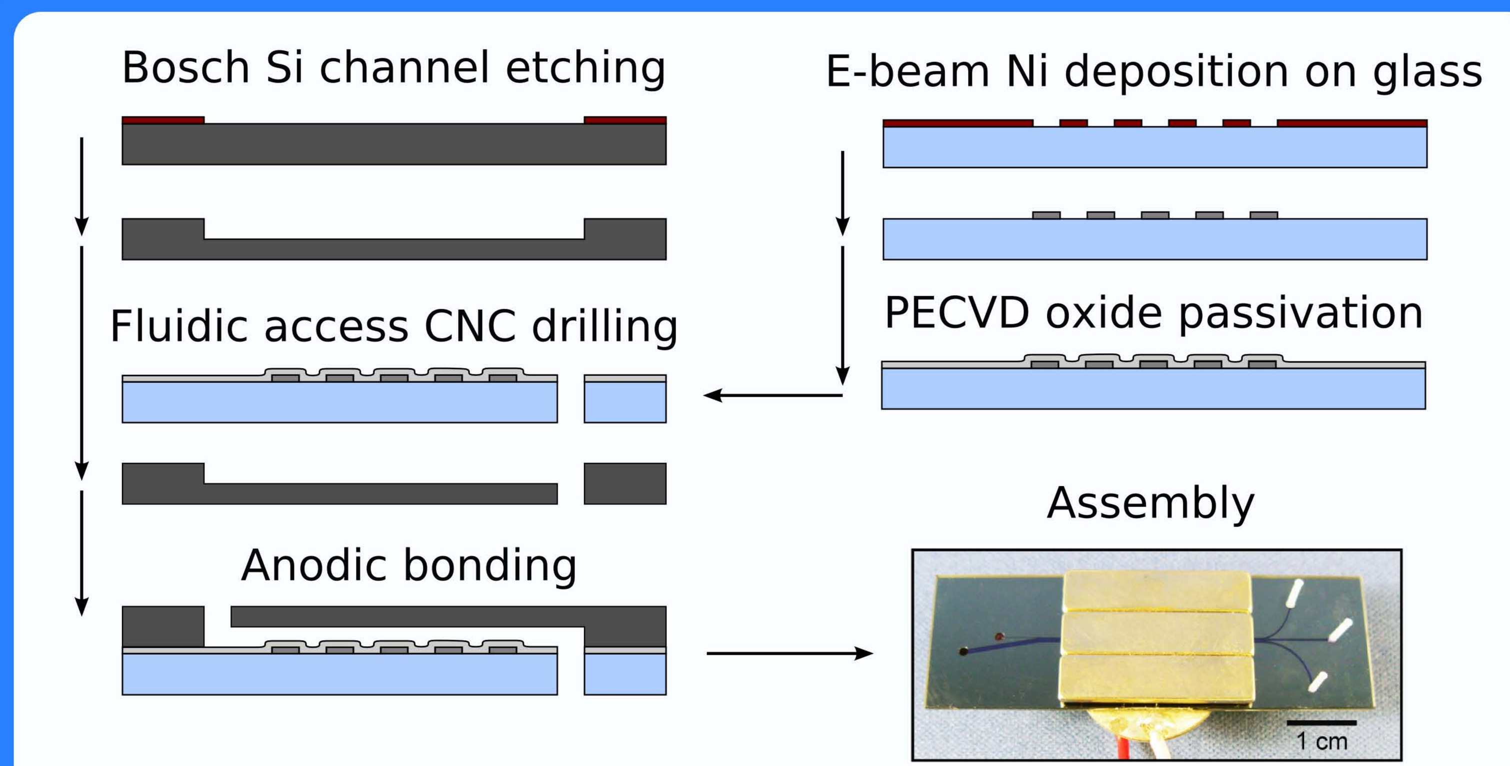

EXPERIMENTAL SETUP

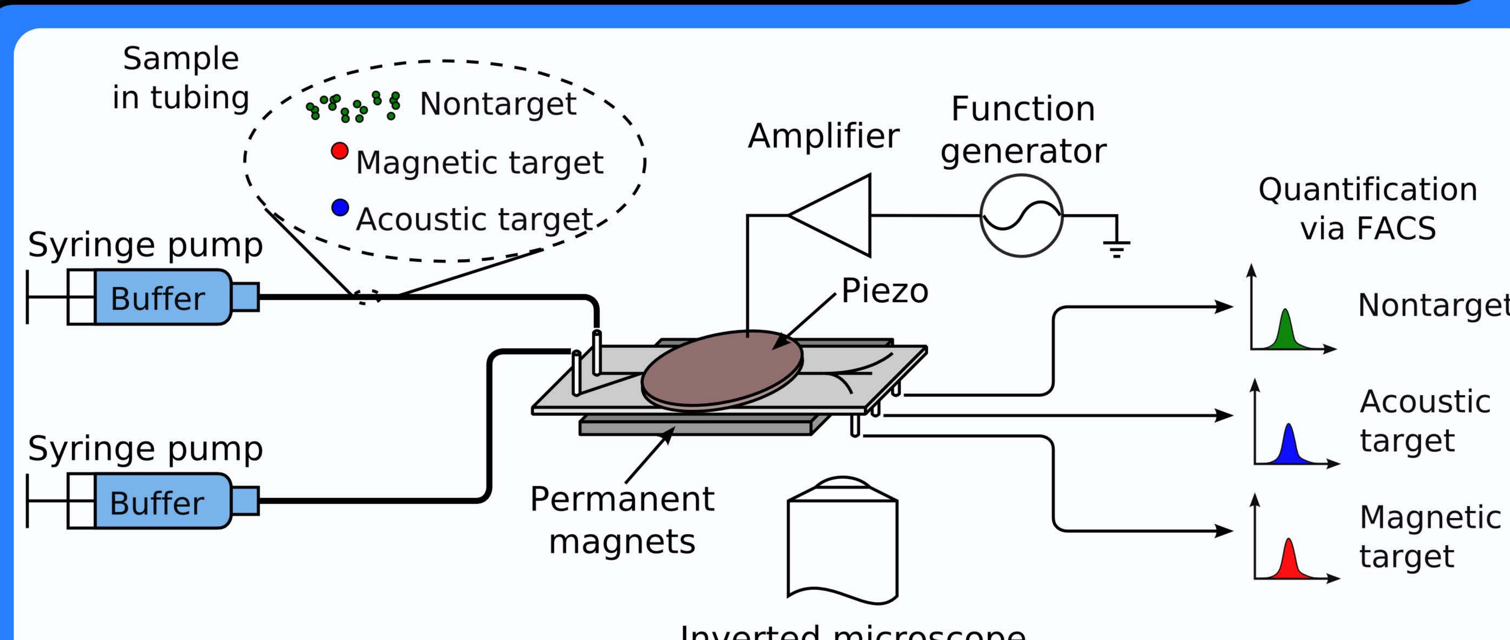

RESULTS

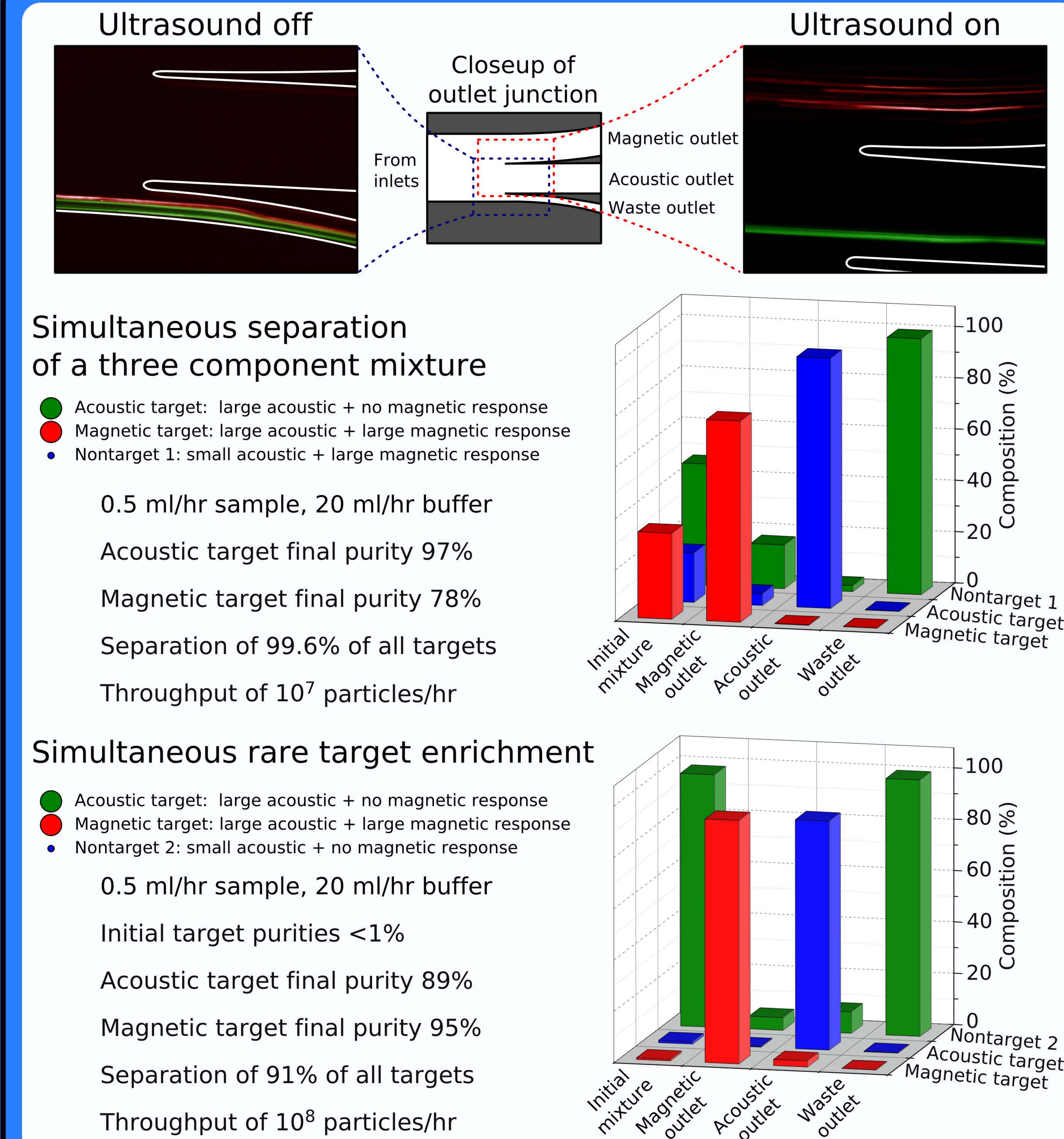

CONCLUSIONS

We present the first integration of acoustophoresis and magnetophoresis in a single microfluidic chip format, and demonstrate separation of three-component complex mixtures at high throughput and purity. By optimizing the geometry of the device, we believe our approach can be extended to sorting a wide variety of targets, including bacteria, viruses and mammalian cells.

ACKNOWLEGMENTS AND REFERENCES

We thank the ARO Institute for Collaborative Biotechnologies (DAAD1903D004) and Office of Naval Research (N00014-08-1-0469) for their financial support. Microfabrication was carried out in the Nanofabrication facility at UC Santa Barbara.

[1] A. Nilsson, F. Petersson, H. Jonsson, T. Laurell. "Acoustic control of suspended particles in micro fluidic chips", *Lab Chip*, **4**, 131-135 (2004).

[2] D.W. Inglis, R. Riehn, R.H. Austin, J.C. Sturm. "Continuous microfluidic immunomagnetic cell separation", *Appl Phys Lett*, **85**, 5093-5095 (2004).

MICROCHANNEL ACOUSTOPHORESIS FOR MANIPULATION OF CELLS AND PARTICLES

Andreas Lenshof, Per Augustsson, Carl Grenvall and Thomas Laurell

Lund University, SWEDEN

Acoustic forces on particles in suspension

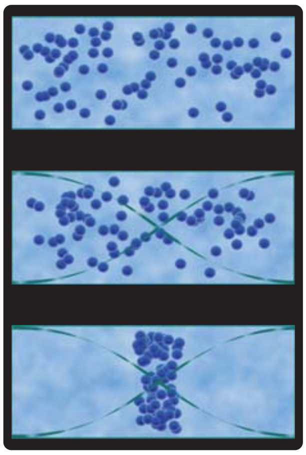

An acoustic resonant pressure field causes particles to move towards either the pressure node or the antinodes depending on the physical properties of the particles.

$$F_r = -\left(\frac{\pi p_0^2 V_c \beta_w}{2\lambda}\right)\cdot \phi(\beta,\rho)\cdot \sin(2kx)$$

$$\Phi = (5\rho_c - 2\rho_w)/(2\rho_c + \rho_w) - (\beta_c/\beta_w)$$

- $\mathbf{F_r}$ = acoustic radiation force
- $\mathbf{P_0}$ = applied acoustic pressure amplitude
- $\mathbf{V_c}$ = particle volume
- β_w = compressibility of the liquid
- β_c = compressibility of the particle
- λ = acoustic wavelength
- $\mathbf{z}$ = particle distance to the node
- ρ_c = density of the particle
- ρ_w = density of the liquid

Nilsson A. et al., Lab. Chip. 2004, 4, 131-135

Laurell T. et al., Chem. Soc. Rev. 2007, 36, 492-506

Blood wash

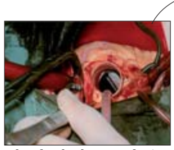

Blood leakage during cardiac surgery.

The blood is contaminated with lipid particles.

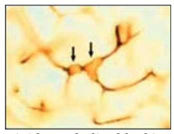

Lipid emboli blocking capillaries in the brain.

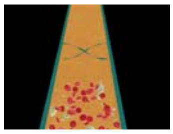

Red blood cells and lipid particles are exposed to an USW.

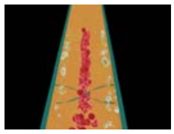

RBC are separated from lipid particles by acoustophoresis.

The laminar flow enables discrete collection of RBCs and lipids.

Photo of the RBC wash. Lipids are exiting through the side outlets.

A mixture containing bovine blood and tritium labeled trigrycerides was used to mimic human shed blood. The acoustic blood wash system was able to remove ~90% of the lipid patricles while retaining ~90% of the erythrocytes.

Petersson F. et al., *The Analyst*, 2004, 129, 938-943

Jönsson H. et al., *Ann. Thorac. Surg.*, 2004, 78, 1572-1578

Plasmapheresis for PSA analysis

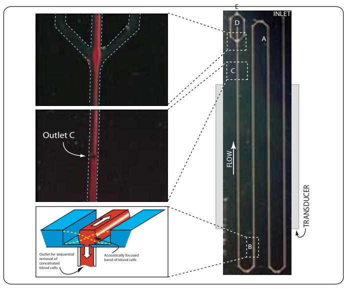

Acoustic standing waves gather blood cells in the pressure node located in the middle of the separation channel. Enriched blood cell fractions are removed through outlets A-C, thus decreasing the hematocrit gradually in the channel. The remaining focused blood cells exit through outlet D while the clean plasma fraction is withdrawn from exit E.

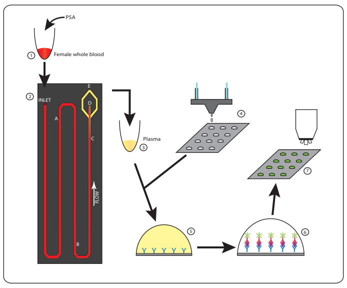

Schematic of the chip based whole blood plasmapheresis and PSA diagnostics: (1) spiking of PSA in female whole blood, (2) ultrasonic standing wave driven plasmapheresis, (3) plasma collected via injector sample loops, (4) microarraying of PSA antibody, (5) microchip incubation in obtained plasma, (6) sandwich assay, and (7) fluorescence readout.

The quality of the plasma fulfilled the standard defined by the Council of Europe for plasma transfusion. Obtained PSA microarray data showed good linearity to a well-documented commercial PSA assay.

Lenshof A. et al., Anal. Chem., 2009, 81, 6031-6037

Free Flow Acoustophoresis (FFA)

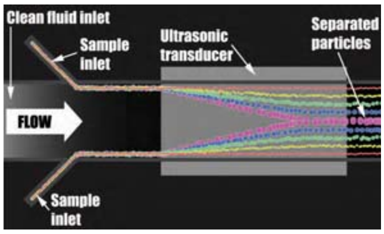

Suspended particles of different sizes entering an acoustic field. Particles move towards the central pressure node in the channel at a rate determined by their acoustic properties and size.

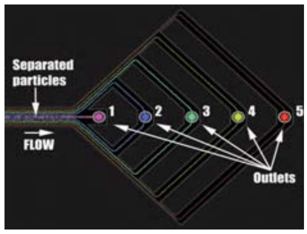

At the end of the separation channel the flow is branched off into 5 consecutive outlets, each containing a direte subset of the initial particle mixture.

The FFA separation strategy (described above) has been successfully applied to polystyrene particles in the 3-10 µm range. A first attempt at separating samples of whole blood into fractions of RBCs, platelets and WBCs revealed that blood cell fractionation is indeed feasible even though complete separation was not achieved. A modified version of the device that will dramatically increase the resolution is under development.

Petersson F. et al., Anal. Chem., 2007, 79, 5117-5123

Affinity extraction on a chip

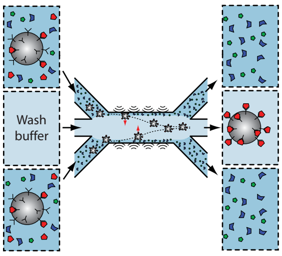

Acoustophoresis based extraction. Beads are transferred from one laminar flow path into a stream of clean wash fluid.

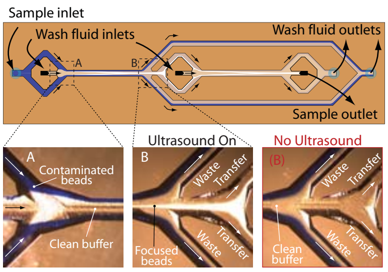

System schematic and images of the trifurcation inlet (A) and outlet (B) of one wash unit. Two sequential buffer exchanges are carried out in one passage through the device.

Acoustophoresis microchip for bead based extraction of specific binders from antibody libraries was developed. Beads, carrying bound species, are transfered into clean buffer, reducing the high background of non specific material. The chip performance compete well with standard manual protocols regarding washing efficiency.

Augustsson P. et al., Lab. Chip., 2009, 9, 810–818

Persson J. et al., FEBS J, 2008, 275, 5657–5666

Raw milk quality control using acoustophoresis

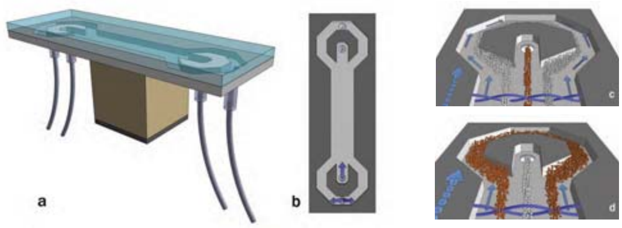

(a) Schematic of the device. Channel structure etched in Silicon with a bonded piece of glass on top. An aluminium distance is placed between the chip and a piezoceramic transducer (dark grey). Fluid connections are attached to the bottom side of the chip. (b) A top view of the channel along with flow directions. (c) Lipid depletion mode where lipids are translated into the side flows while retaining cells and supernatant in the center outlet. (d) Lipid enrichment mode where lipids are fo-cused and extracted via the center outlet in a minimized fraction of the volume flow.

Milk solids are normally impossible to detect without appropriate staining protocols due to overlapping size distributions of cells and lipid particles. Acoustophoretic removal of lipid particles allows for in line optical measurement strategies not involving any form of staining. Similarly, enriched lipid samples allow direct lipid analysis without chemicals.

Grenvall C. et al., Anal. Chem., 2009, 81, 6195-6200

CISM Posters 7th-11th June 2010

Ultrasound standing wave action on suspensions and biosuspensions in micro- and macro fluidic devices

Jonathan D. Adams
adams@physics.ucsb.edu
University of California, Santa Barbra
Integrated magnetophoretic-acoustophoretic separation device for rapid multitarget cell sorting

Per Augustsson
per.augustsson@gmail.com
Lund University, SWEDEN
Microchannel Acoustophoresis for manipulation of cells and particles

Rune Barnkob
Rune.Barnkob@nanotech.dtu.dk
Department of Micro- and Nanotechnology, Technical University of Denmark, Kongens Lyngby, Denmark, / Department of Electrical Measurements, Lund University, Lund, Sweden
Microchannel acoustophoresis: Resonances, particle tracking, and PIV

Carl Grenvall
carl.grenvall@gmail.comcarl.grenvall@gmail.com
Department of Electrical Measurements, Elmat, Sweden
Reduced particle size dispersion in free flow acoustophoresis using 2D acoustic prefocusing

Björn Hammarström
bjorn.hammarstrom@elmat.lth.se
Electrical Measurements, Lund University, SWEDEN
Label-Free Cell Population Studies In Disposable Acoustic Trapping Capillaries With ISET Enhanced MALDI- MS Analysis

Cosima Koch
cosima.koch@gmx.at
Vienna University of Technology
Ultrasonic particle manipulation for mid-infrared spectroscopy of suspensions

Philippe Marmottant
philippe.marmottant@ujf-grenoble.fr
Laboratoire de Spectrométrie Physique, CNRS and Université de Grenoble, 140 Avenue de la Physique, BP87 38402 Saint Martin d'Hères
Acoustically-bound crystals: when pulsating microbubbles self- organize

Dirk Möller
dirk.moeller@imes.mavt.ethz.ch
Institute of Mechanical Systems, ETH Zurich, Switzerland
Flow-free transport of particles in a macro scale chamber

Thomas Schwarz
schwarz@imes.mavt.ethz.ch
Institute of Mechanical Systems, ETH Zurich, Switzerland, schwarz@imes.mavt.ethz.ch
Rotation of non spherical particles with amplitude modulation

Francisco Trujillo
Francisco.Trujillo@csiro.au
CSIRO Food and Nutritional Sciences, North Ryde, New South Wales, 2113, Australia
CFD modelling of the acoustic streaming induced by an ultrasonic horn reactor

Microchannel acoustophoresis: Resonances, particle tracking, and PIV

Rune Barnkob[a], Per Augustsson[b], Thomas Laurell[b], and Henrik Bruus[a]

[a] Department of Micro- and Nanotechnology, Technical University of Denmark, Kongens Lyngby, Denmark.
[b] Department of Electrical Measurements, Lund University, Lund, Sweden

Abstract

A new method is reported on how to measure the local pressure amplitude and the Q factor of ultrasound resonances in microfluidic chips designed for acoustophoresis of particle suspensions. The method relies on tracking individual polystyrene tracer microbeads undergoing acoustophoresis in straight water-filled silicon/glass microchannels and on a fully automated PIV system. The tracks are recorded and fitted to a theoretical expression for the acoustophoretic motion of the microbeads. From the curve fits we obtain the acoustic energy density, and hence the pressure amplitude as well as the acoustophoretic force. By plotting the obtained energy densities as a function of applied frequency, we obtain Lorentzian line shapes, from which the resonance frequency and the Q factor for each resonance peak are derived. PIV measurements yield the acoustic velocity amplitude. Both measurements yield same results: acoustic energy densities of the order of 10 J/m^3, pressure amplitudes of 0.2 MPa, and Q factors around 500.

Experimental setup

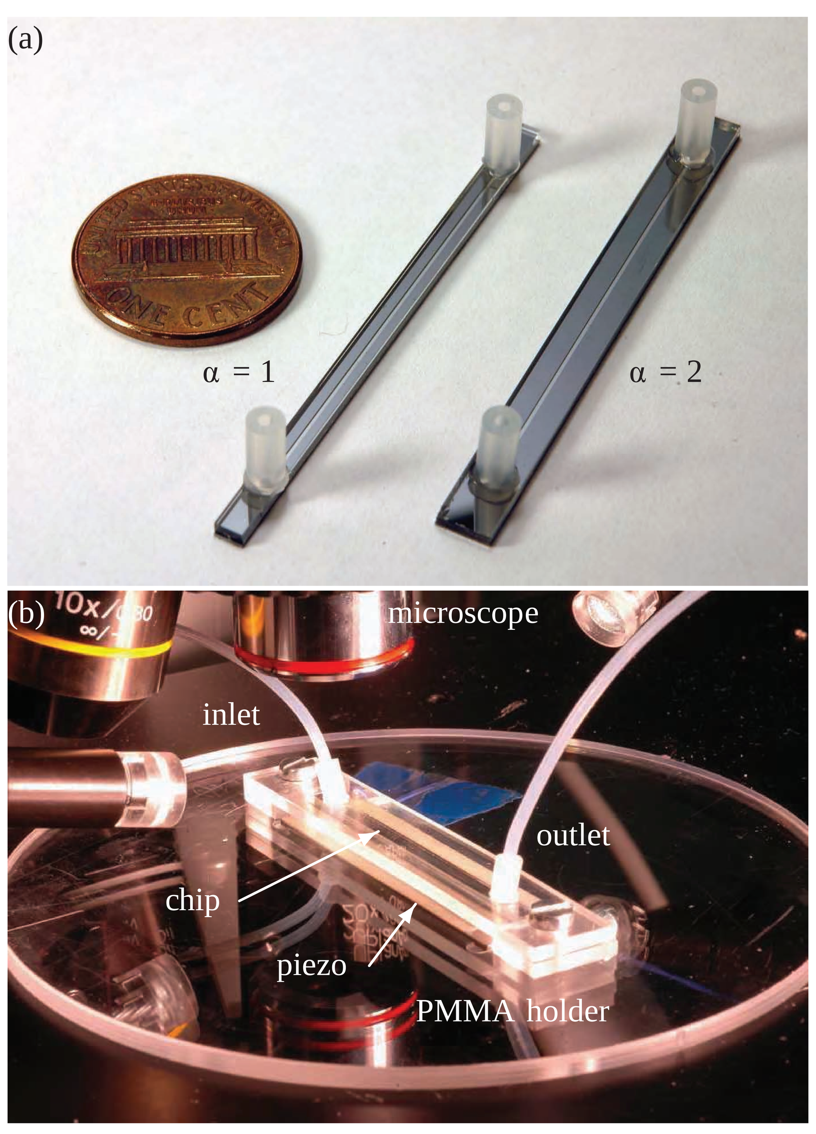

(a) Silicon/glass chips containing straight channels of length l = 40 mm, width w = 377 mm, and height h = 157 mm.
(b) Photograph of the experimental setup: chip mounted on PZT piezo crystal in PMMA holder under microscope with attached camera.

Theory

Acoustic radiation force $\boldsymbol{F}_{ac}$ acts on the particles (p) in the carrier liquid (wa).

1. Resonance condition: $\frac{1}{2}\lambda_y = w$
2. 1D transverse acoustophoretic force $\boldsymbol{F}_{ac,y}$
3. Stokes drag force $\boldsymbol{F}_{drag}$ balances $\boldsymbol{F}_{ac,y}$

$\Downarrow$

Theoretical microbead trajectory $y(t)$

$$y(t) = \frac{1}{k_y}\arctan\left\{\tan\left[k_y y(0)\right]\exp\left[\frac{4\Phi}{9\eta}(k_y a)^2 E_{ac}\ t\right]\right\} \quad (1)$$

Fitting parameters: E_{ac} and $\lambda_y = \dfrac{2\pi}{k_y}$

$\Phi = \dfrac{5\gamma-2}{2\gamma+1} - \dfrac{1}{\gamma\beta^2}$ acoustophoretic contrast factor

$\beta = \dfrac{c_p}{c_{wa}}$ speed of sound ratio

$\gamma = \dfrac{\rho_p}{\rho_{wa}}$ density ratio

$E_{ac} = \dfrac{p_a^2}{4\rho_{wa}c_{wa}^2}$ acoustic energy density

$\lambda_y = \dfrac{2\pi}{k_y}$ transverse wavelength

η viscosity of carrier liquid

a particle radius

Particle tracking

Focusing of polystyrene microbeads

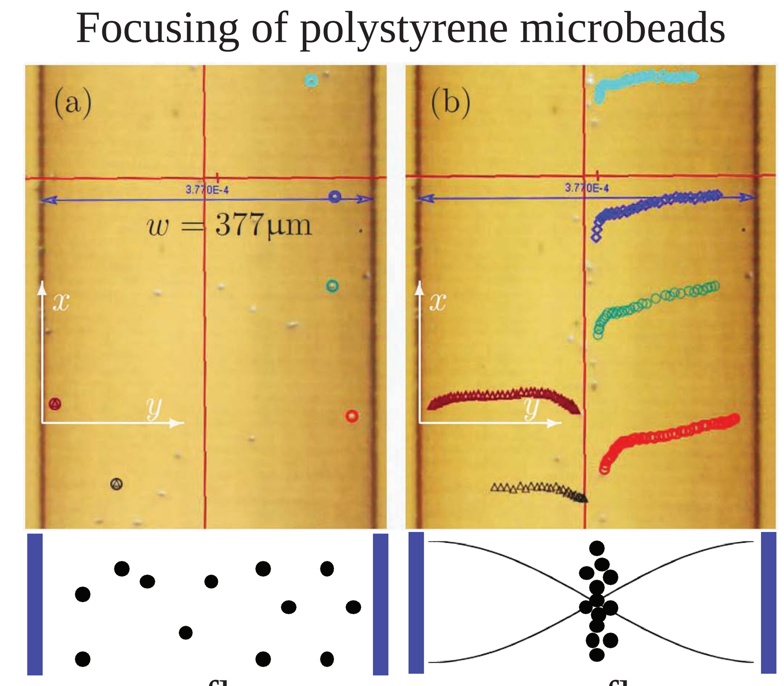

Fit microbead trajectory by Eq. (1) using resonance energy density and wavelength

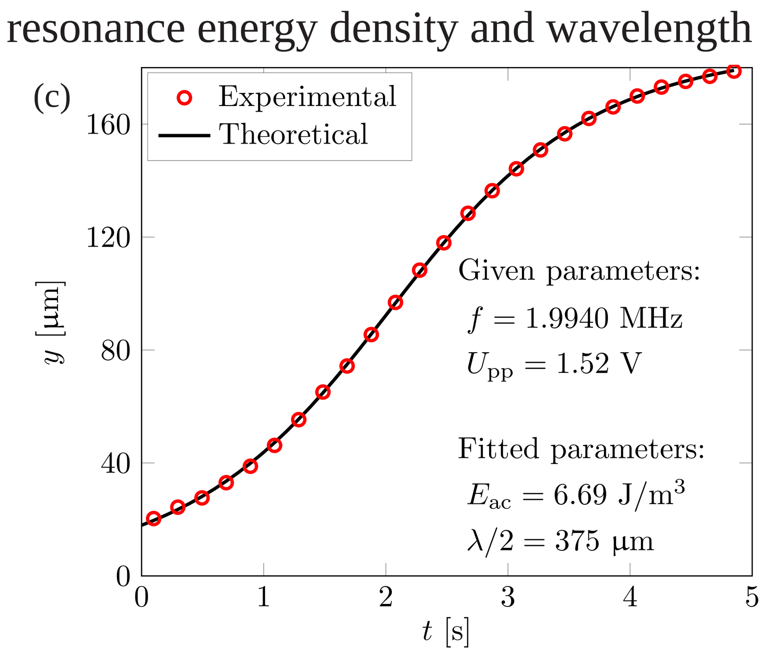

Voltage sweep

Acoustic energy density scales with the applied piezo voltage to the power 2.

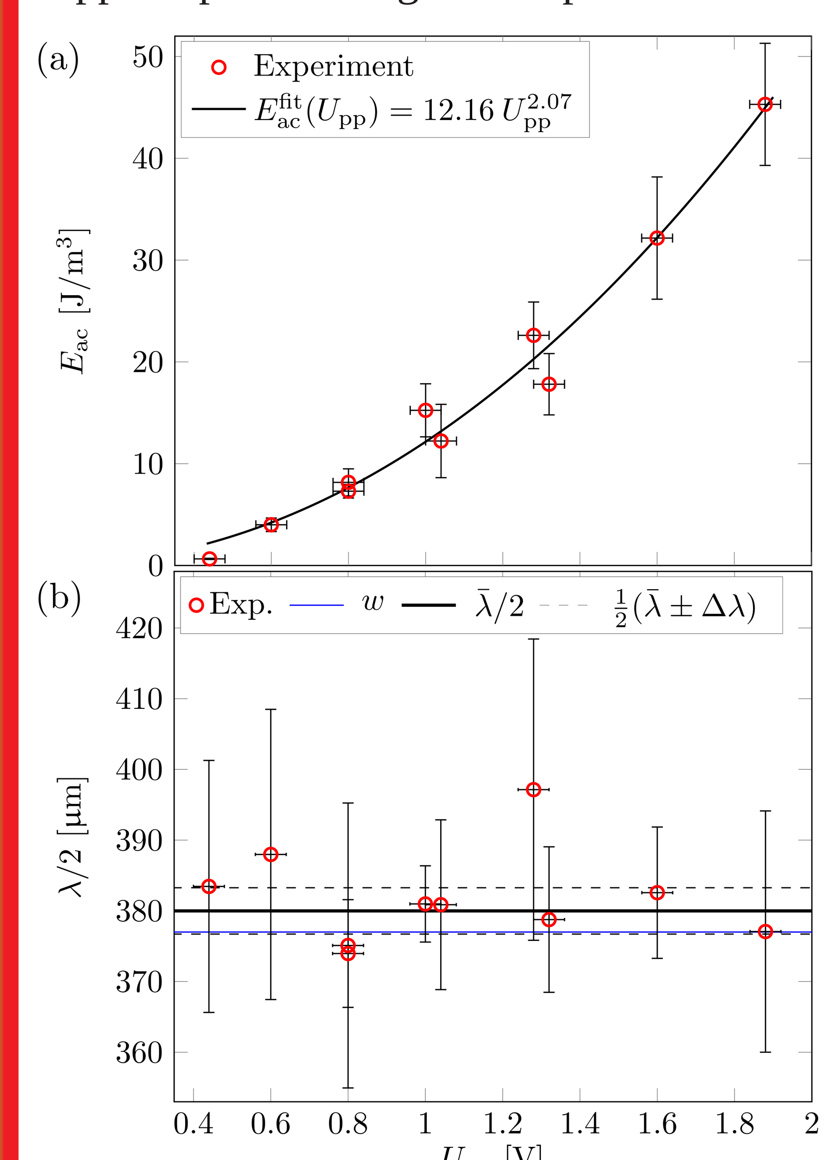

Measured half wavelength differs less than one standard deviation from the expected width of the channel.

Frequency sweep

Measured acoustic energy density spectrum is fitted to Lorentzian line-shapes to extract the resonance Q-factors.

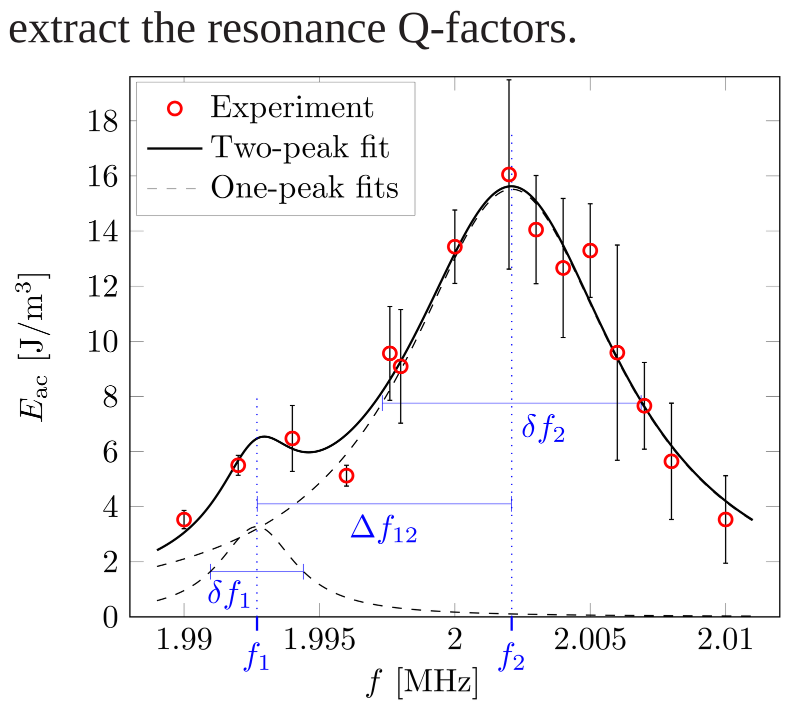

Measured peak spacing is 9.4 kHz.

2D pressure eigenmode simulation. Calculated peak spacing is 12 kHz.

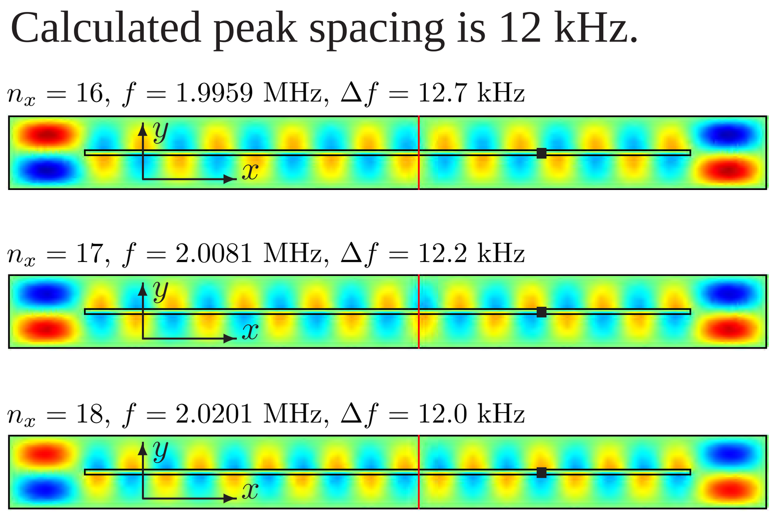

Automated PIV setup

Fully automated PIV measurement of the microbead acoustophoretic velocity field. Colors show the velocity magnitude in µm/s.

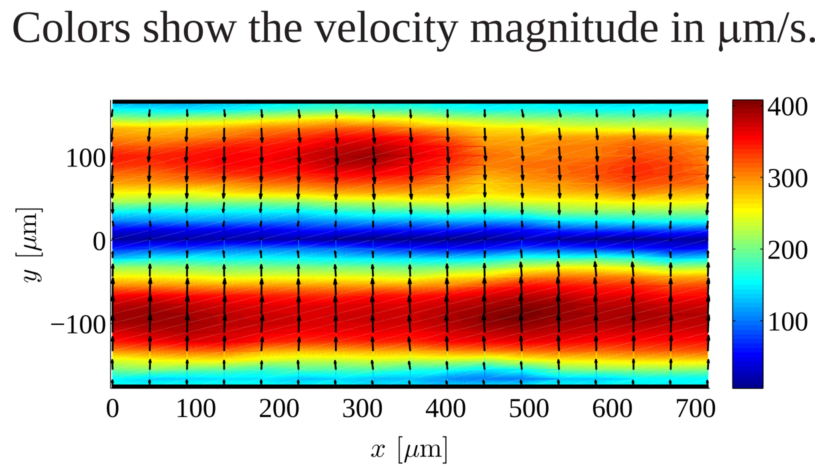

Average and standard deviation of the y-component of the velocity field along the channel showing the nearly perfect transverse period-doubled standing half wave.

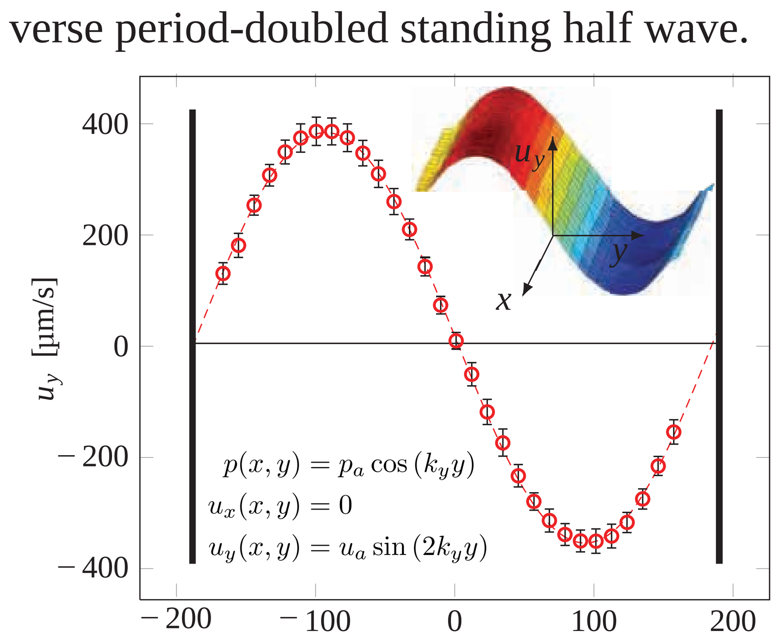

Conclusion

In situ measurements of ultrasound resonance parameters:

1. the acoustic energy density
   0.65 - 50 J/m^3
2. the local pressure amplitude
   0.08 - 0.66 MPa
3. the resonance Q-factor
   209 - 577

by tracking of individual polystyrene microbeads undergoing acoustophoresis.

Established fully automated PIV setup showing the 1D-assumption to be accurate.

Outlook

Investigation of the full 2D global resonance behaviour by use of the new PIV system having higher spatial and temporal resolution.

References

R. Barnkob, P. Augustsson, T. Laurell, and H. Bruus, *Measuring the local pressure amplitude in microchannel acoustophoresis*, Lab on a Chip **10**, 563-570 (2010)

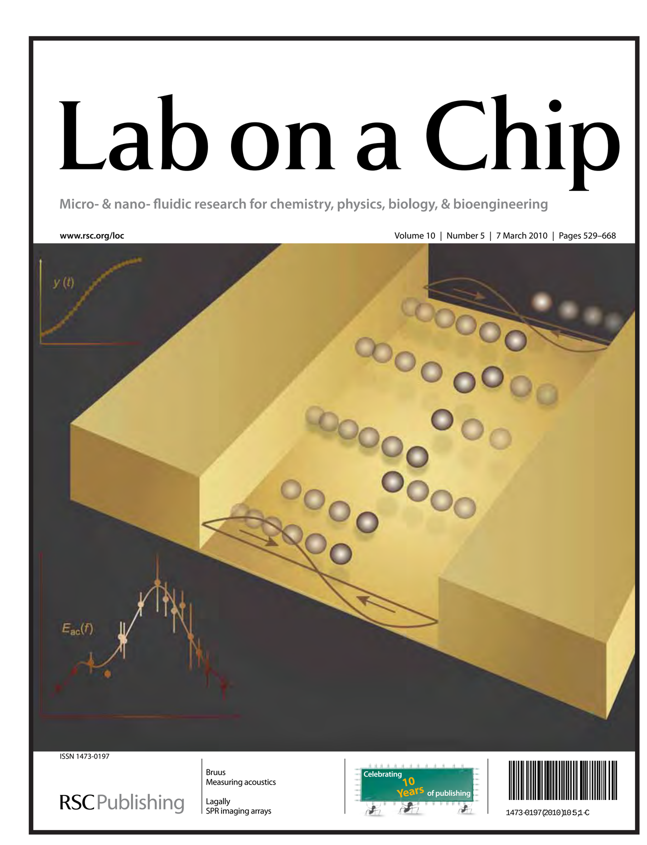

www.nanotech.dtu.dk/microfluidics

www.elmat.lth.se/forskning/nanobiotechnology_and_labonachip/

REDUCED PARTICLE SIZE DISPERSION IN FREE FLOW ACOUSTOPHORESIS USING 2D ACOUSTIC PREFOCUSING

Carl Grenvall, Per Augustsson and Thomas Laurell

Lund University, SWEDEN

Abstract

We present for the first time a 2-dimensional acoustic standing wave mode of operation in free flow acoustophoresis (FFA). A vastly improved size dispersion profile is obtained as compared to previous work by employing 2-dimensional acoustic prefocusing of the particles into a precisely confined flow stream prior to entering the FFA separation zone, Fig 1. Reduced size dispersion increases the resolving power of acoustophoresis and expands its applicability for cell fractionation based on size, density and compressibility.

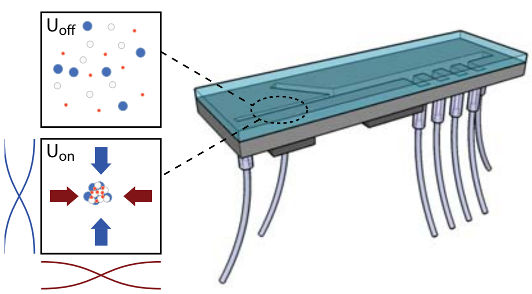

Figure 1. Schematic of the FFA-chip with the novel 2-dimensional prefocusing zone.

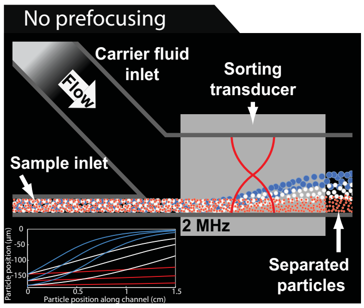

Figure 2. Basic FFA principle. Particles are laminated near the FFA channel side wall and migrates to an acoustic standing wave node in the channel center at size dependent velocities.

Operating principle

Fig 2 shows a schematic of the FFA principle. Particles exposed to a resonant acoustic pressure field migrate towards the center of a microchannel. The migration speed is determined by the size and acoustic properties of the particle and the counteracting Stoke's drag force. To further increase the separation efficiency we introduce the particles via a prefocusing segment that confines the particles laterally and vertically by means of a 2-dimensional acoustic resonance, Figs 1 and 3. As the prefocused particle stream enters the main separation channel the particles are laminated close to the side wall by a main buffer flow prior to entering the FFA zone, Fig 3.

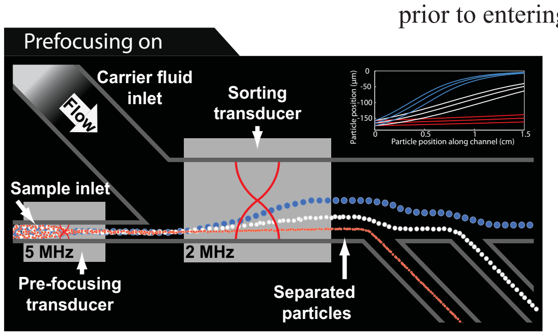

Figure 3. FFA with 2-dimensional prefocusing segment. Pre alignment of the introduced particles enables improved size discrimination in the system.

Experiments and Results

As a model system we prepared a ~1.4% by volume polystyrene particle mixture of 3 µm (0.15% by volume), 7 µm (0.65% by volume) and 10 µm (0.60% by volume). The 2-dimensional prefocusing channel was investigated by ocular inspection at different angles to confirm that particles were being focused vertically as well as horizontally. Fig 4 shows the prefocusing channel with and without the prefocusing actuator active. Multisizer (Coulter) particle analysis revealed a significantly improved sorting capability when actuating the prefocusing channel as compared to using a passive inlet channel. Inactive prefocusing recovered only ~95%, ~74% and ~84% of the 3, 7 and 10 µm particles into the intended outlet, Fig 5, whereas activation of the prefocusing channel increased the separation efficiencies to ~97%, ~93% and ~99% for the 3, 7 and 10 µm particles, respectively, Fig 6.

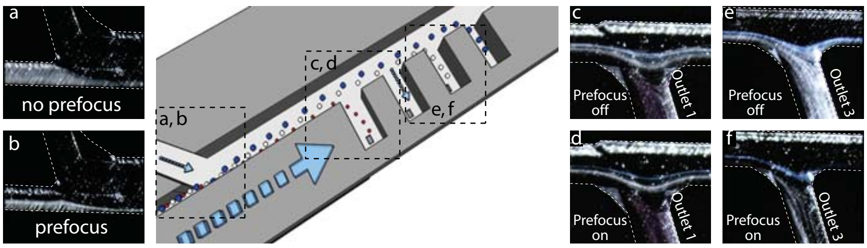

Figure 4. (a, b) Photo of particles entering the FFA channel where after being separated and (c-f) extracted. (a, c, e) Prefocusing off. (b, d, f) Prefocusing on.

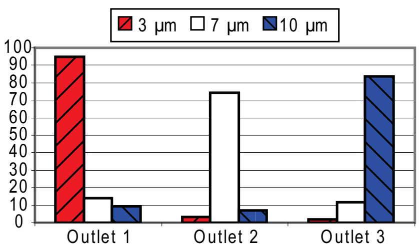

Figure 5. Relative distribution of particle sizes in each outlet. Prefocusing off.

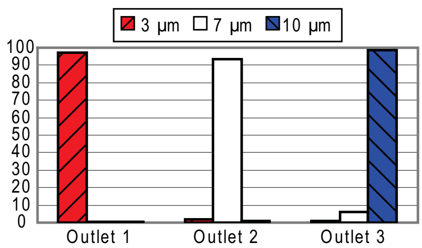

Figure 6. Relative distribution of particle sizes in each outlet. Prefocusing on.

Conclusions

The presented FFA chip constitutes a significant improvement compared to previous work. For the first time 2-dimensional acoustic prefocusing has been implemented in a particle separation system based on intrinsic acoustic properties. The reduced particle dispersion significantly increases the resolving power in FFA systems.

References

[1] F. Petersson, L. Åberg, A-M. Swärd-Nilsson and T Laurell, Anal Chem 79 (14) 5117-23, (2007)

[2] C. Grenvall, P. Augustsson, F. Petersson and T. Laurell, µTAS 2007, Paris, France (2007)

Label-Free Cell Population Studies In Disposable Acoustic Trapping Capillaries With ISET Enhanced MALDI- MS Analysis

Björn Hammarström, Thomas Laurell, Mikael Evander, Johan Nilsson and Simon Ekström

Electrical Measurements, Lund University, SWEDEN

Abstract

Technology that enables investigation of cell-cell or cell-ligand interactions on small populations of cells with high sensitivity, specificity and reproducibility has numerous high-impact applications in life science and drug discovery.

With this in mind, a system for mass spectrometric analysis (MS) of acoustically trapped small cell populations has been developed and successfully applied for analysis of red blood cells (RBC).

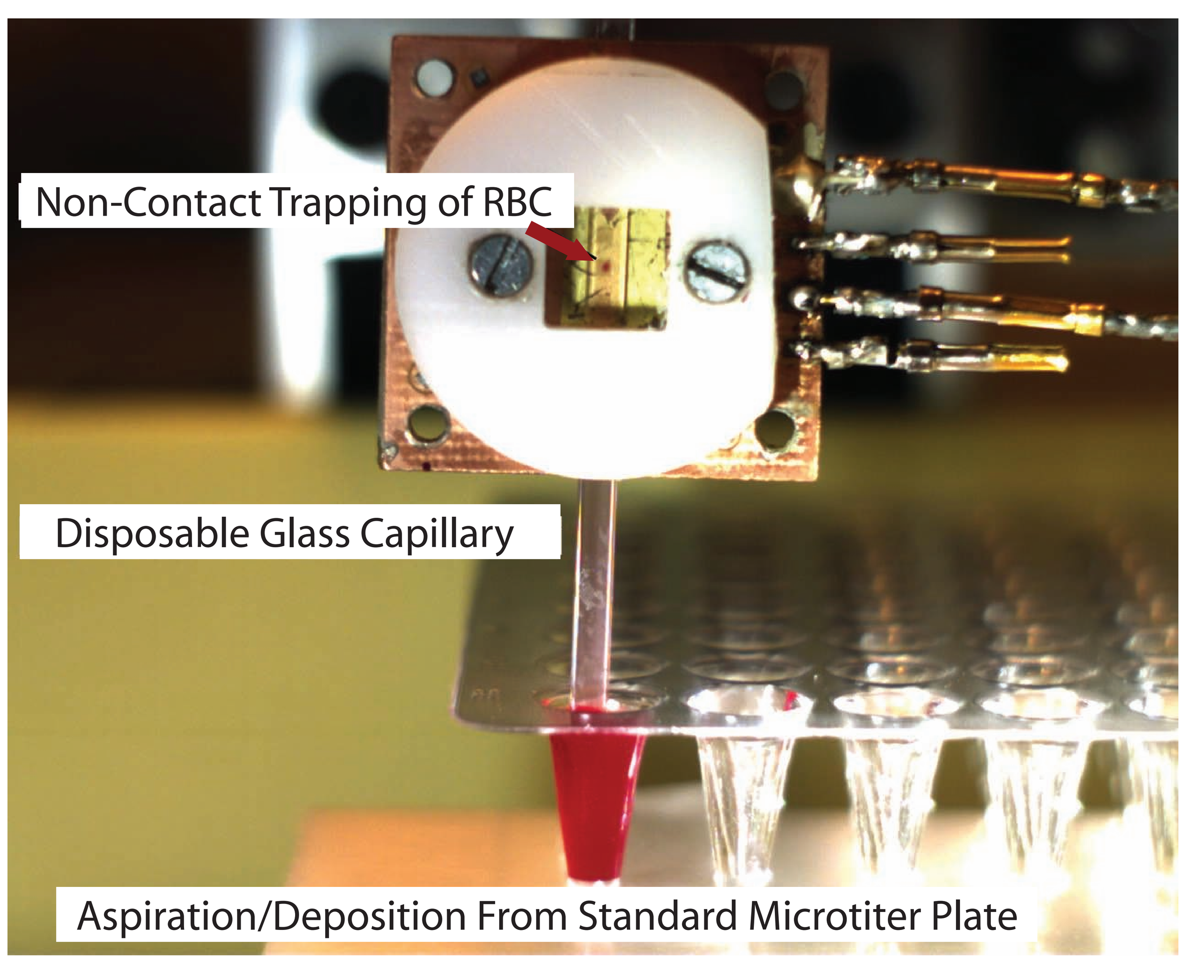

Figure 1. Acoustic trapping of red blood cells in a glas capillary mounted in a XYZ-stage allows automated cell-ligand interaction analysis of non-contact handeled cells.

Non-Contact Acoustic Trapping

The system shows for the first time acoustic trapping in disposable borosilicate capillaries. Lamination of the capillary with an ultrasonic transducer creates a three dimensionally confined acoustic standing wave caused by the sub-wavelengt thickness of the capillay walls. The localized acoustic field is capable of retaining cells or particles against a flowing liquid in a non-contact fashion.

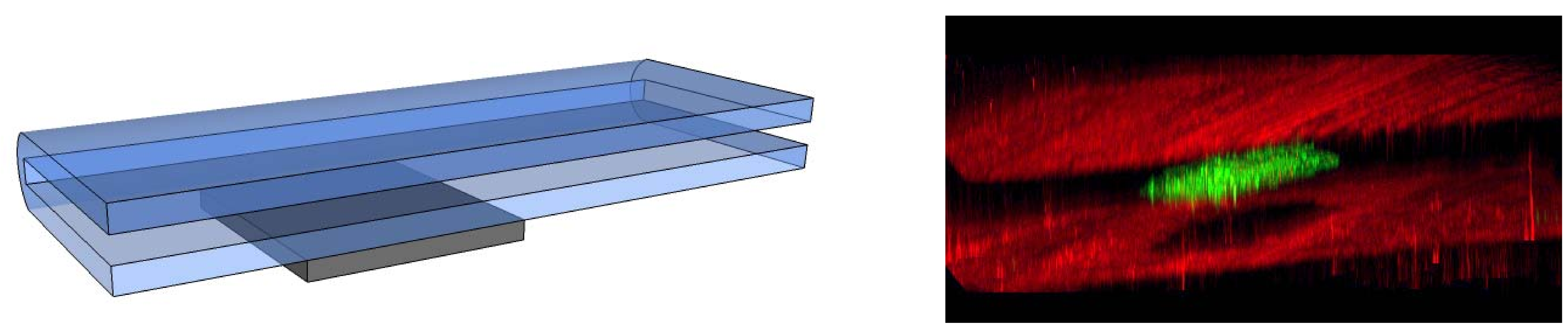

Figure 2. Non-contact trapping in an acoustic field localized to the vicinity of an ultrasonic transducer.

Automated Workflow

The trapping capillary was mounted on a programmable XYZ-stage. This allowed cells and perfusing liquids to be aspirated or deposited directly into different wells of a microtiter plate in a precise and automated manner. Subsequently the samples were robotically transfered to an ISET-plate [1] for reversed-phased solid phase extraction (SPE) prior to MALDI-MS analysis.

This automated set-up allows for analysis of sample fractions taken at different intervals to monitor any sequential treatment of the trapped bead/cell agglomerate.

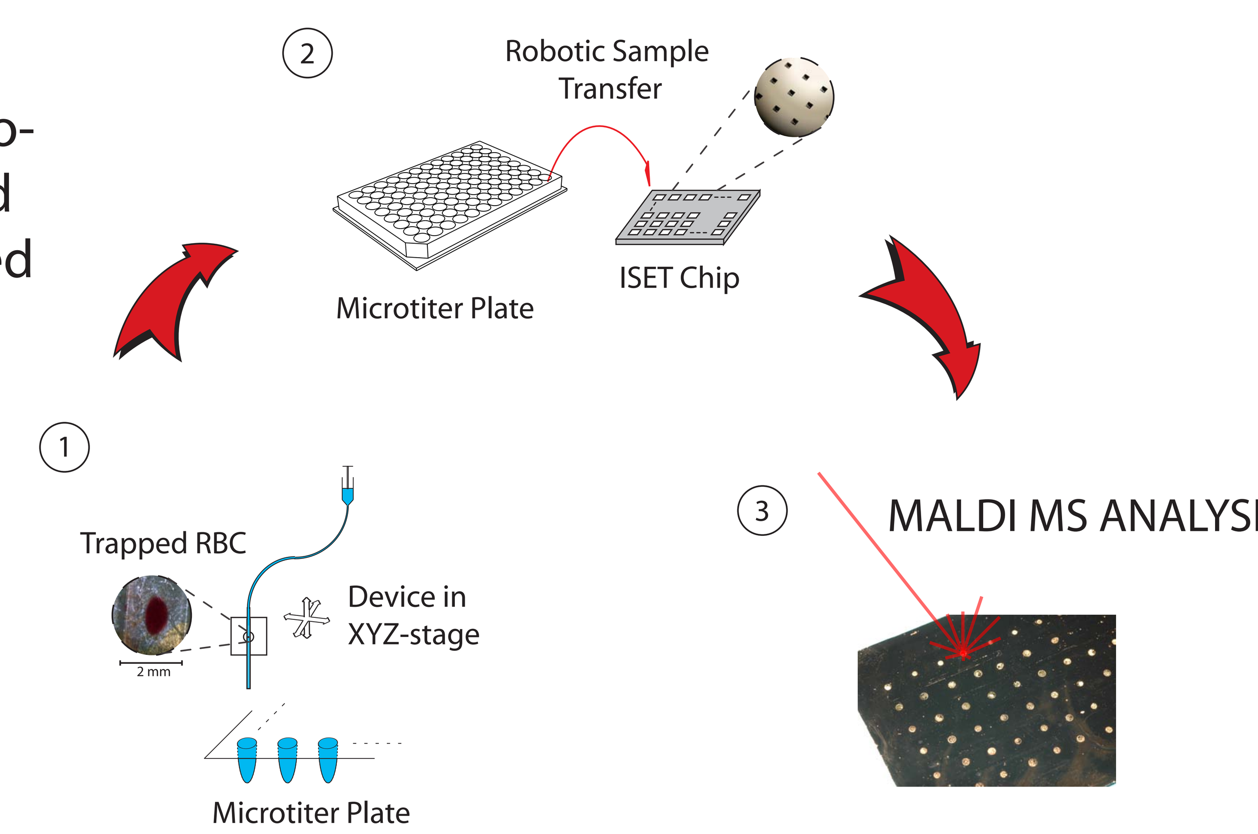

Figure 3. Sample workflow, ISET chip based SPE allow MS analysis of higly complex samples such as cell lysate.

Experiments and Results

The analytical read-out after MALDI-MS analysis of blood cells using the described system is shown below. A 50 µL blood sample was diluted to 250 µL with PBS (pH 7.4), spiked with a drug compound (40 µM) and a peptide (2 µM) followed by incubation at 37 C for 1 h. 10 µL of this sample was aspirated into the capillary, trapping a cell agglomerate consisting of approx. 500 000 RBC. The trapped cells were washed throufh perfusion with running buffer (PBS, pH 7,4), removing non-trapped cells and plasma,. Subsequently, the trapped RBC were lysed through aspiration of 25 µL RBC lysis buffer. The perfusing wash and lysis solutions were collected as fractions and MALDI analysis was performed. The data, figure 4, confirms the expected results as the spiked drug could penetrate the RBC membrane and is observed in the lysed sample (A3), but not in the preceeding wash (A2). The spiked peptide that should not be able to penetrate the RBC membrane could not be found in the lysed sample. There were also many differentially observed peaks originating from the lysed cell in the spectra, see enlargement B1-B3 in figure 4.

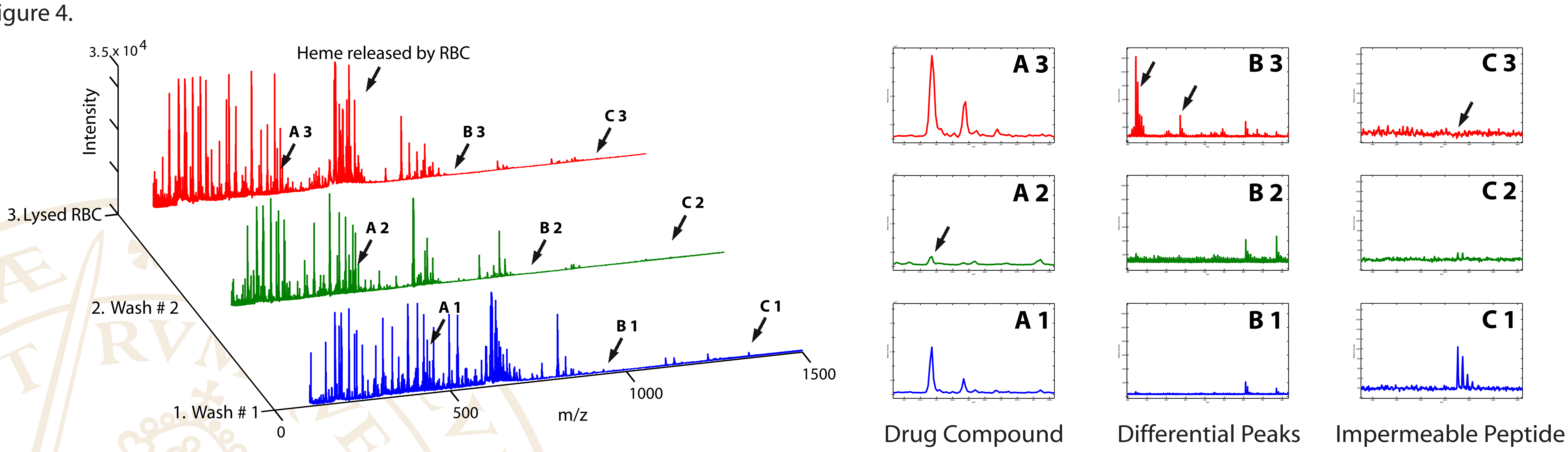

Figure 4. Analytical read-out of a single RBC cluster (~ 500 000 cells) with two wash fractions and lysis of the trapped cells. Enlargement A shows uptake of the spiked drug, B shows differential peaks originating from intracellular material released upon lysis and C shows sucessful removal of the spiked impermeable peptide.

Conclusions

A system for MS analysis of small cell populations has been implemented. This offers a controlled microenvironment, reproducible non-contact trapping, and dynamic sample handeling trough aspiration using the open capillary. This offers a versatile analysis platform with low complexity and easy integration to standard equipment.

References

[1] "Miniaturized solid-phase extraction and sample preparation for MALDI MS using a microfabricated integrated selective enrichment target," S. Ekström, L. Wallman, D. Hök, G. Marko Varga and T. Laurell, , Journal of Proteome Research, Vol. 5, pp. 1071-1081, (2006)

Ultrasonic particle manipulation for mid-infrared spectroscopy of suspensions

Markus Brandstetter[1], Bernhard Zachhuber[1], Stefan Radel[2], Johannes Schnöller[1], Martin Gröschl[2], Bernhard Lendl[1]

[1]Institute of Chemical Technologies and Analytics, Vienna University of Technology, Getreidemarkt 9, A-1060 Vienna, Austria
[2]Institute of General Physics, Vienna University of Technology, Wiedner Hauptstraße 8-10, A-1040 Vienna, Austria

Introduction

An **acoustic standing wave field,** acting on a suspension, results in the separation of the suspended particles from the host fluid. This separation effect was employed to enable **mid-infrared** absorption measurements of particles and host fluid separately using **ATR (Attenuated Total Reflection**) spectroscopy.

Different stages in the development process of this technology are presented, starting with an on-line measurement system based on a horizontal flow cell. This technology was improved by using an ATR fibre probe and the design of an attachable ultrasonic resonator.

On-line measurement

Fast suspension analysis for **reaction monitoring** was achieved by particle manipulation in a flow cell using 2 MHz ultrasound waves.

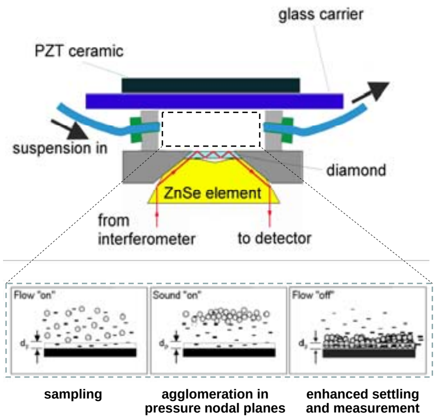

The **ultrasonic transducer**, consisting of a PZT ceramic and a glass carrier layer, generates acoustic standing waves within the flow cell.

In-line measurement

A **flexible ATR fibre probe** replaces a stationary flow cell.

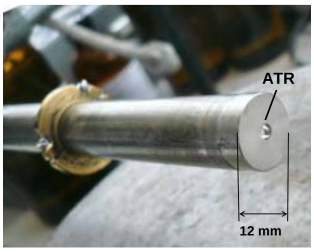

Absorption measurements are made directly in the suspension.

In-situ analysis minimises interferences and contamination.

The fibre probe head serves as acoustic reflector:

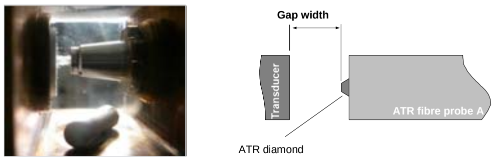

ATR probe and transducer are immersed in sample suspension.

Sample suspension: Polystyrene beads in methanol

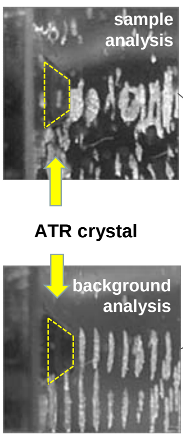

Ultrasound field is adjusted to **push suspended particles towards the ATR** crystal → Absorption spectrum of particles is acquired (*broad line*).

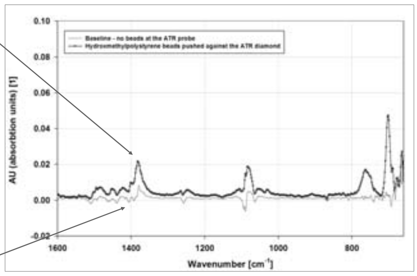

Ultrasound field is adjusted **to keep suspended particles off the ATR** crystal → Background spectrum (*narrow line*) is acquired.

Ultrasound enhanced ATR in-line fibre probe

Prototype for **semi-industrial** environment.

Mounted to bioreactor wall or plate through a standard port.

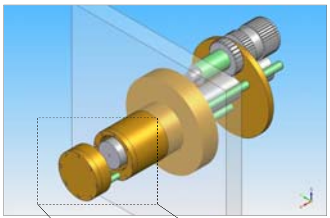

bioreactor

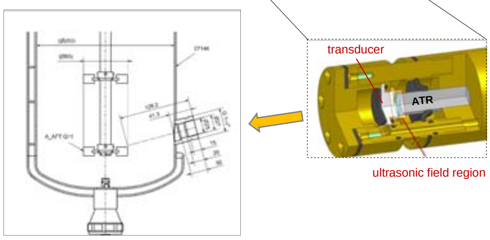

TITLE: Acoustically-bound crystals: when pulsating microbubbles self-organize

AUTHORS: Philippe Marmottant, David Rabaud, Pierre Thibault
ADDRESS: Laboratoire de Spectrométrie Physique, CNRS and Université de Grenoble, 140 Avenue de la Physique, BP87 38402 Saint Martin d’Hères, philippe.marmottant@ujf-grenoble.fr

ABSTRACT:
In this poster we present the effect of an ultrasound field on microbubbles flowing in soft PDMS channels. The manipulation of microbubbles, acting as tiny gas samples, is of interest for Lab-on-a-chip application. Because of their high compressibility bubbles pulsate and interact through acoustic Bjerknes forces. This interaction is usually attractive, resulting in bubble agglomeration, but here we show that the interaction can present a short-range repulsion leading to a finite equilibrium distance. The bubbles then spontaneously self-organize into a periodic arrangement of positions.
These "acoustically-bound crystals" move independently of the acoustic standing wave. The equilibrium distance of the crystal is tunable: around 50 times smaller than the wavelength of sound in water, it can be adjusted by changing the excitation frequency.

Best regards, Philippe

REDUCED PARTICLE SIZE DISPERSION IN FREE FLOW ACOUSTOPHORESIS USING 2D ACOUSTIC PREFOCUSING

Carl Grenvall, Per Augustsson and Thomas Laurell

Lund University, SWEDEN

Abstract

We present for the first time a 2-dimensional acoustic standing wave mode of operation in free flow acoustophoresis (FFA). A vastly improved size dispersion profile is obtained as compared to previous work by 2-dimensional acoustic prefocusing of the particles into a precisely confined flow stream prior to entering the FFA separation zone, Fig 1. Reduced size dispersion increases the resolving power of acoustophoresis and expands its applicability for cell fractionation based on size, density and compressibility.

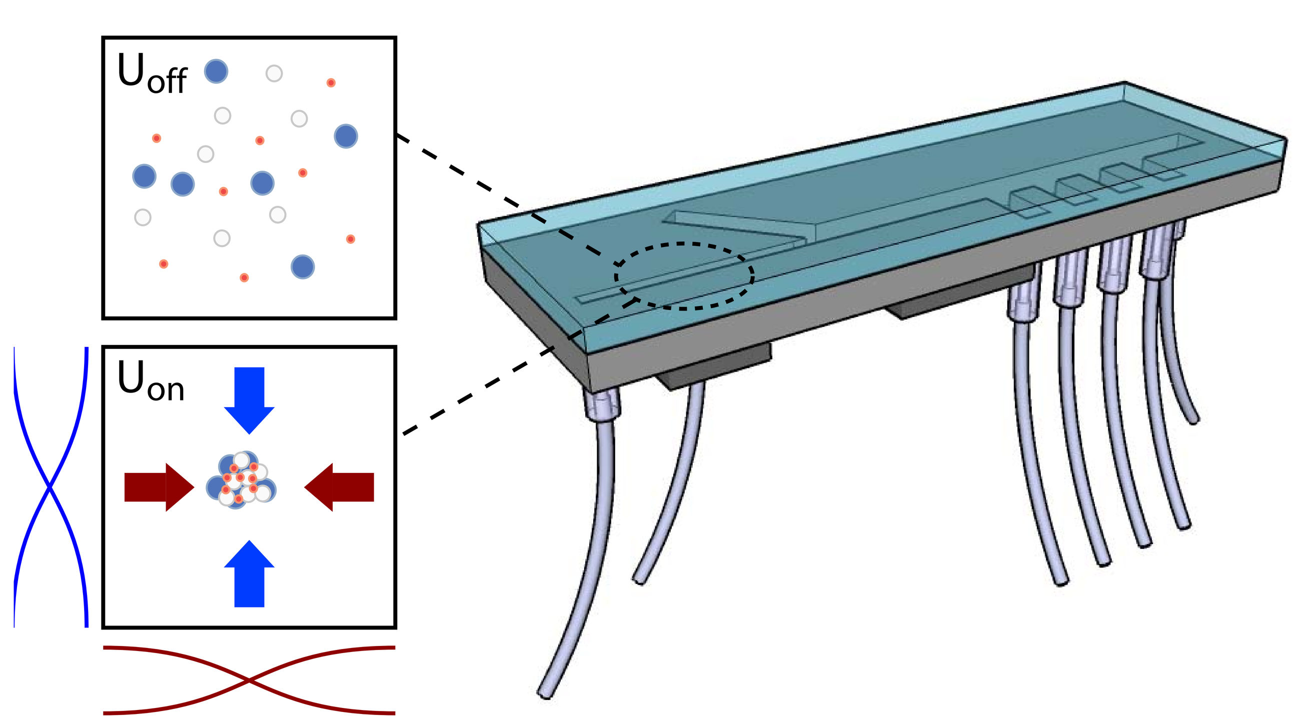

Figure 1. Schematic of the FFA-chip with the novel 2-dimensional prefocusing zone.

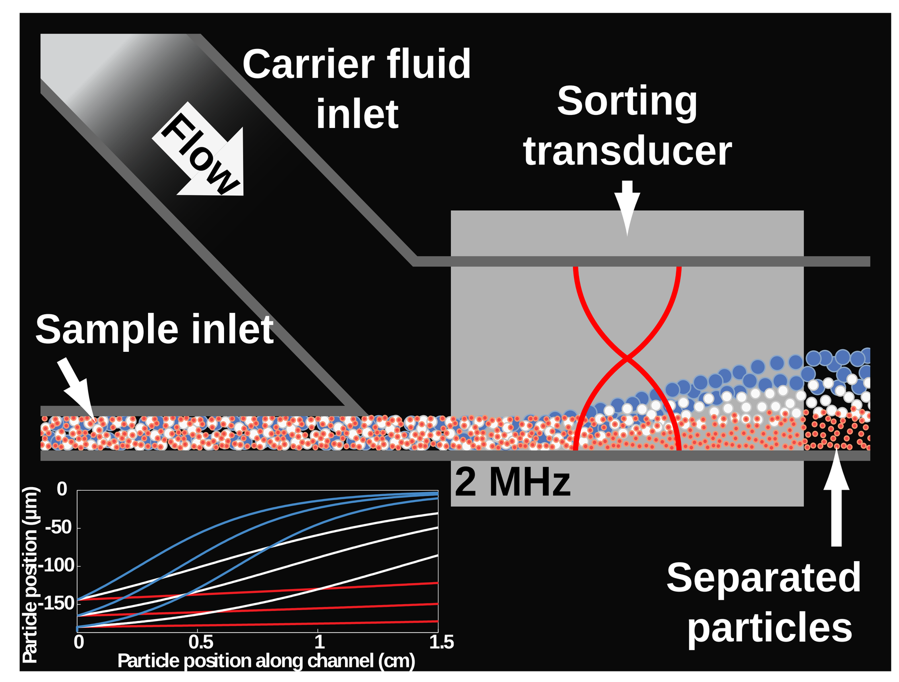

Figure 2. Basic FFA principle. Particles are laminated near the FFA channel side wall and migrates to an acoustic standing wave node in the channel center at size dependent velocities.

Operating principle

Fig 2 shows a schematic of the previos FFA principle. Particles exposed to a resonant acoustic pressure field migrates towards the center of a microchannel. The migration velocity is determined by the size and acoustic properties of the particle and the counteracting Stoke's drag force. To further increase the separation efficiency we introduce the particles via a prefocusing segment that confines the particles laterally and vertically by means of a 2-dimensional acoustic resonance, Fig 1. As the prefocused particle stream enters the main separation channel the particles are laminated close to the side wall by a main buffer flow prior to entering the FFA zone, Fig 3.

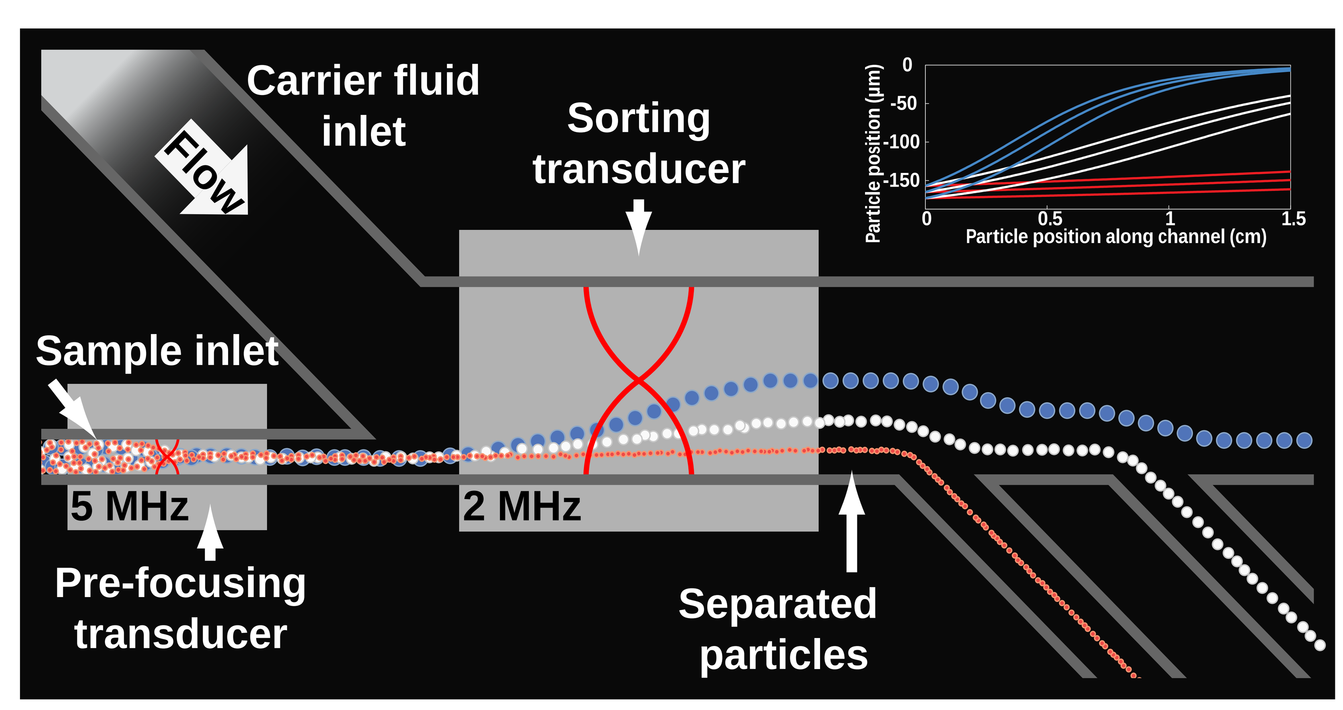

Figure 3. FFA with 2-dimensional prefocusing segment. Pre alignment of the introduced particles enables improved size discrimination in the system.

Experiments and Results

As a model system we prepared a ~1.4% by volume polystyrene particle mixture of 3 µm (0.15% by volume), 7 µm (0.65% by volume) and 10 µm (0.60% by volume). The 2-dimensional prefocusing channel was investigated by ocular inspection at different angles to confirm that particles were being focused vertically as well as horizontally. Fig 4 shows the prefocusing channel with and without the prefocusing actuator active. Coulter counter particle analysis revealed a significantly improved sorting capability when actuating the prefocusing channel as compared to using a passive inlet channel. Inactive prefocusing recovered ~95%, ~74% and ~84% of the 3, 7 and 10 µm parti-cles into the intended outlet, Fig 5. Activation of the prefocusing channel increased the separation efficiencies to ~97%, ~93% and ~99% for the 3, 7 and 10 µm particles, respectively, Fig 6.

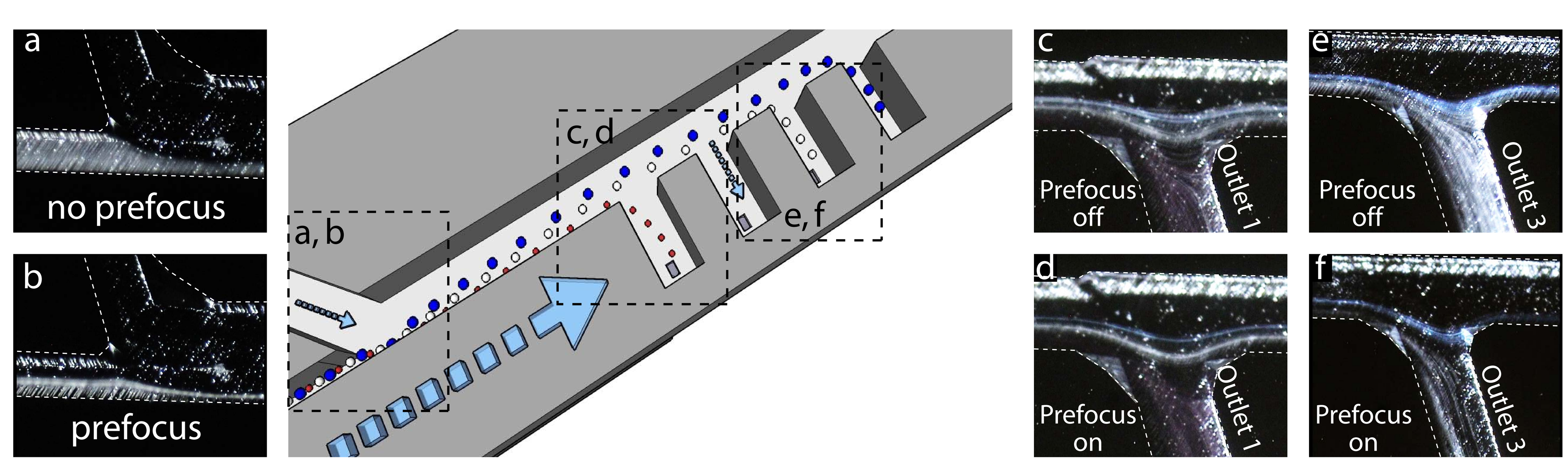

Figure 4. (a, b) Photo of particles entering the FFA channel whereafter being separated and (c-f) extracted. (a, c, e) Prefocusing off. (b, d, f) Prefocusing on.

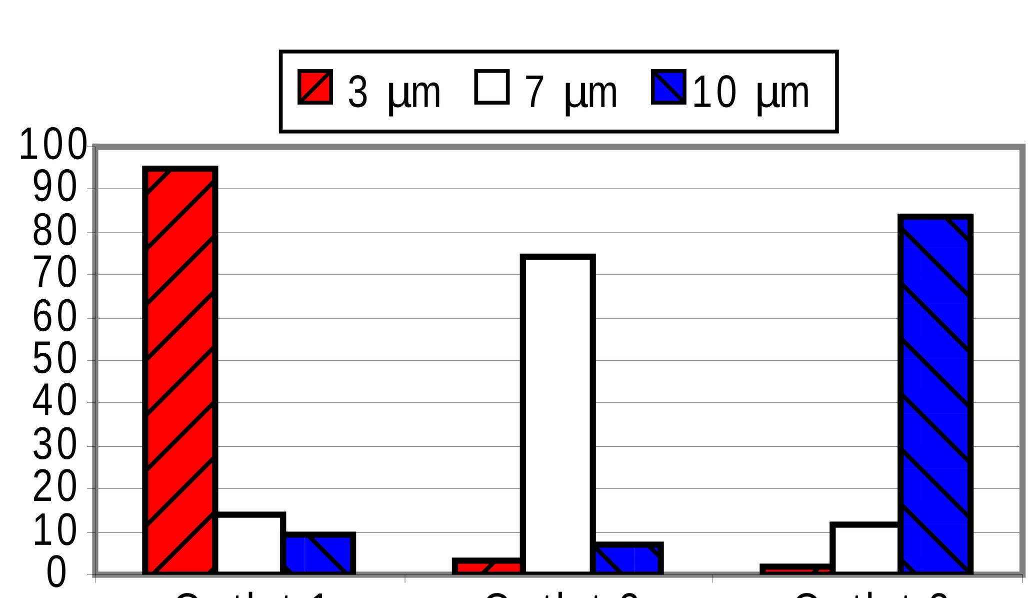

Figure 5. Relative distribution of particle sizes in each outlet. Prefocusing off.

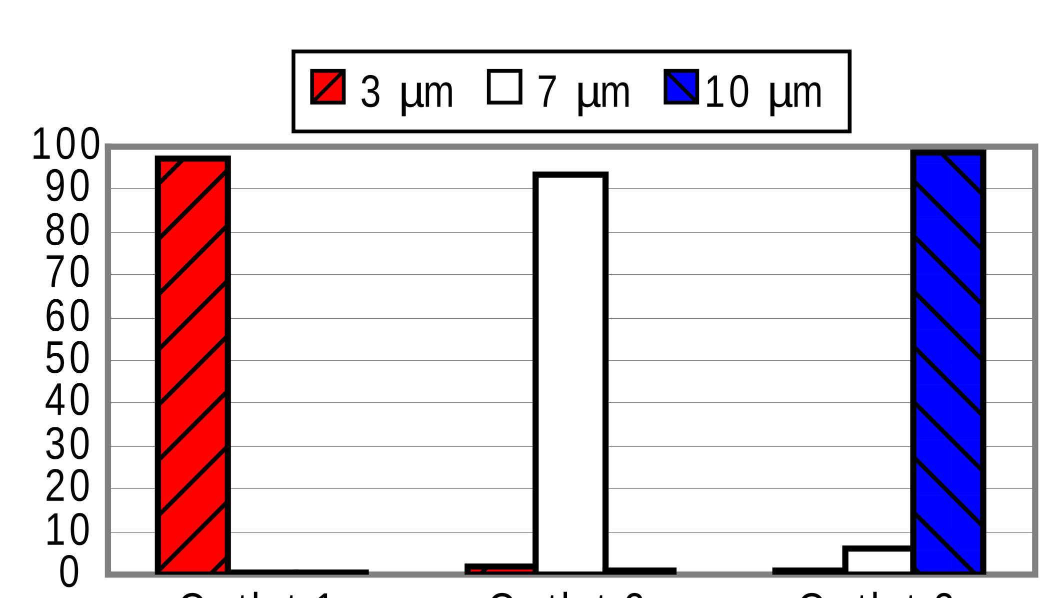

Figure 6. Relative distribution of particle sizes in each outlet. Prefocusing on.

Conclusions

The presented FFA chip constitutes a significant improvement compared to previous work. For the first time 2-dimensional acoustic prefocusing has been implemented in a particle separation system based on intrinsic acoustic properties. The reduced particle dispersion significantly increases the resolving power in FFA systems.

References

[1] F. Petersson, L. Åberg, A-M. Swärd-Nilsson and T Laurell, Anal Chem 79 (14) 5117-23, (2007)
[2] C. Grenvall, P. Augustsson, F. Petersson and T. Laurell, µTAS 2007, Paris, France (2007)

Label-Free Cell Population Studies In Disposable Acoustic Trapping Capillaries With ISET Enhanced MALDI- MS Analysis

Björn Hammarström, Thomas Laurell, Mikael Evander, Johan Nilsson and Simon Ekström

Electrical Measurements, Lund University, SWEDEN

Abstract

Technology that enables investigation of cell-cell or cell-ligand interactions on small populations of cells with high sensitivity, specificity and reproducibility has numerous high-impact applications in life science and drug discovery.

With this in mind, a system for mass spectrometric analysis (MS) of acoustically trapped small cell populations has been developed and successfully applied for analysis of red blood cells (RBC).

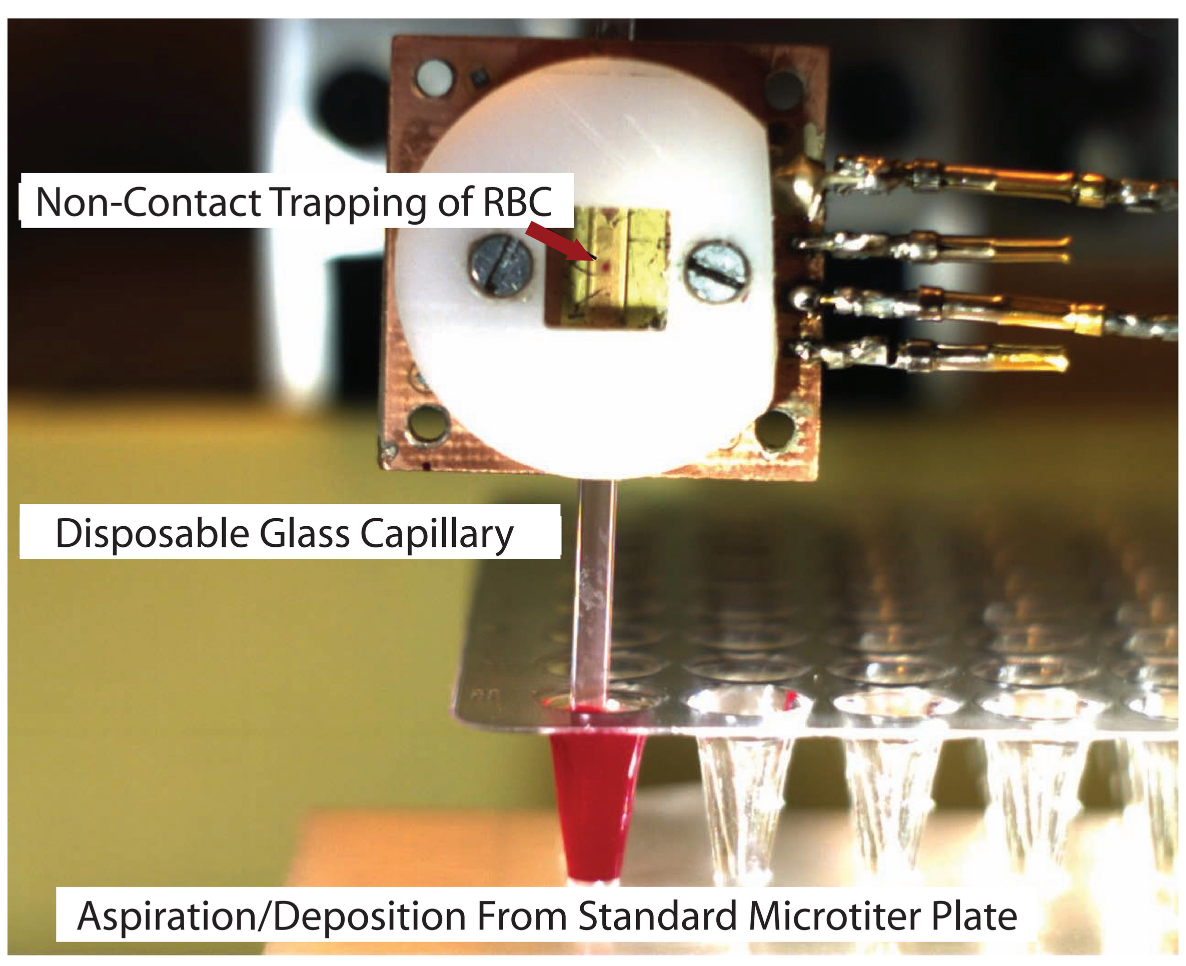

Figure 1. Acoustic trapping of red blood cells in a glas capillary mounted in a XYZ-stage allows automated cell-ligand interaction analysis of non-contact handeled cells.

Non-Contact Acoustic Trapping

The system shows for the first time acoustic trapping in disposable borosilicate capillaries. Lamination of the capillary with an ultrasonic transducer creates a three dimensionally confined acoustic standing wave caused by the sub-wavelengt thickness of the capillay walls. The localized acoustic field is capable of retaining cells or particles against a flowing liquid in a non-contact fashion.

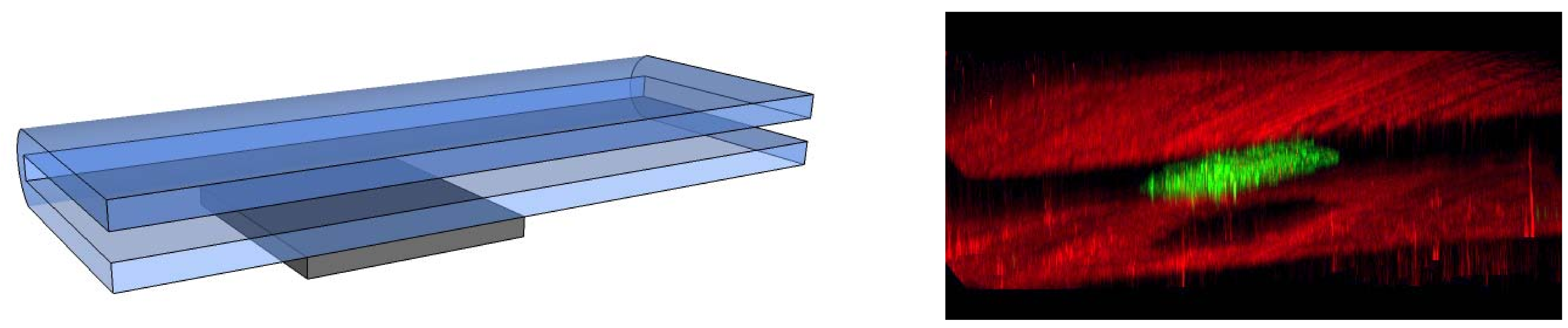

Figure 2. Non-contact trapping in an acoustic field localized to the vicinity of an ultrasonic transducer.

Automated Workflow

The trapping capillary was mounted on a programmable XYZ-stage. This allowed cells and perfusing liquids to be aspirated or deposited directly into different wells of a microtiter plate in a precise and automated manner. Subsequently the samples were robotically transfered to an ISET-plate [1] for reversed-phased solid phase extraction (SPE) prior to MALDI-MS analysis.

This automated set-up allows for analysis of sample fractions taken at different intervals to monitor any sequential treatment of the trapped bead/cell agglomerate.

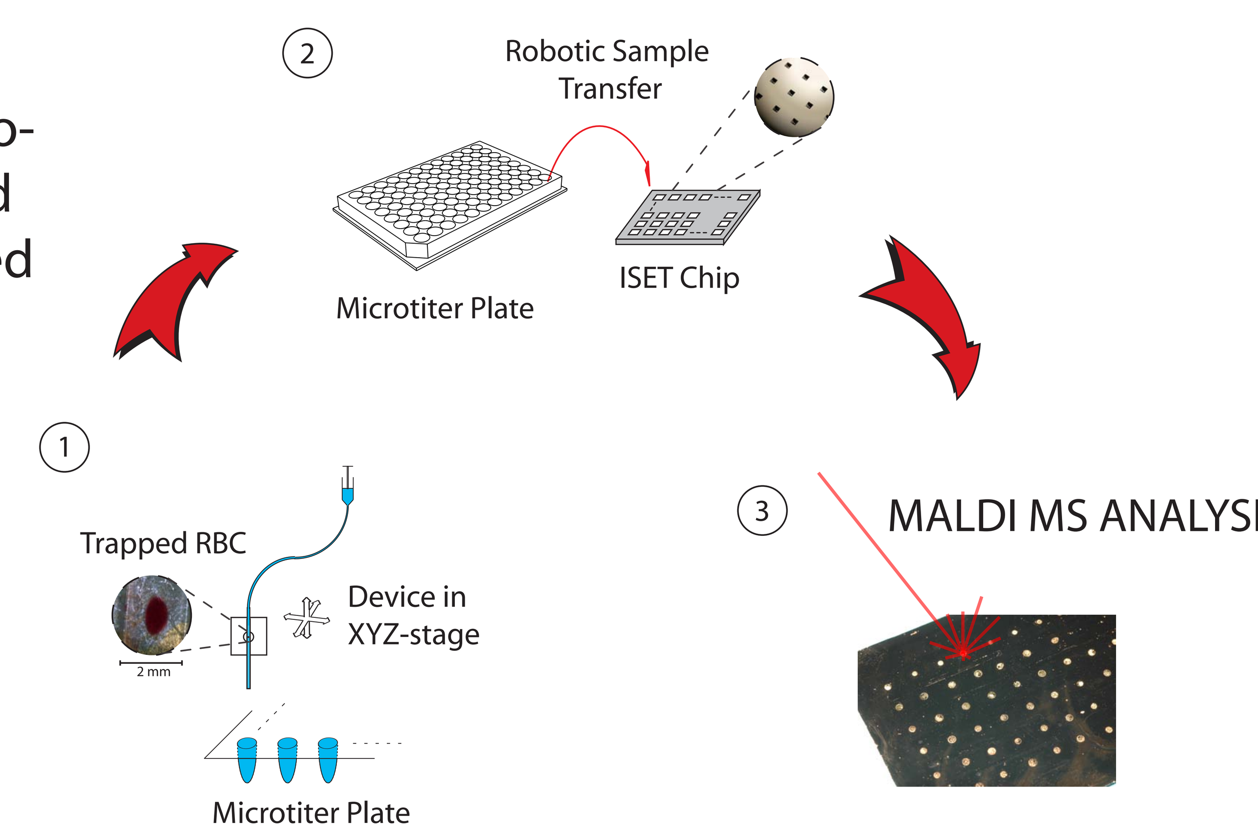

Figure 3. Sample workflow, ISET chip based SPE allow MS analysis of higly complex samples such as cell lysate.

Experiments and Results

The analytical read-out after MALDI-MS analysis of blood cells using the described system is shown below. A 50 µL blood sample was diluted to 250 µL with PBS (pH 7.4), spiked with a drug compound (40 µM) and a peptide (2 µM) followed by incubation at 37 C for 1 h. 10 µL of this sample was aspirated into the capillary, trapping a cell agglomerate consisting of approx. 500 000 RBC. The trapped cells were washed throufh perfusion with running buffer (PBS, pH 7,4), removing non-trapped cells and plasma,. Subsequently, the trapped RBC were lysed through aspiration of 25 µL RBC lysis buffer. The perfusing wash and lysis solutions were collected as fractions and MALDI analysis was performed. The data, figure 4, confirms the expected results as the spiked drug could penetrate the RBC membrane and is observed in the lysed sample (A3), but not in the preceeding wash (A2). The spiked peptide that should not be able to penetrate the RBC membrane could not be found in the lysed sample. There were also many differentially observed peaks originating from the lysed cell in the spectra, see enlargement B1-B3 in figure 4.

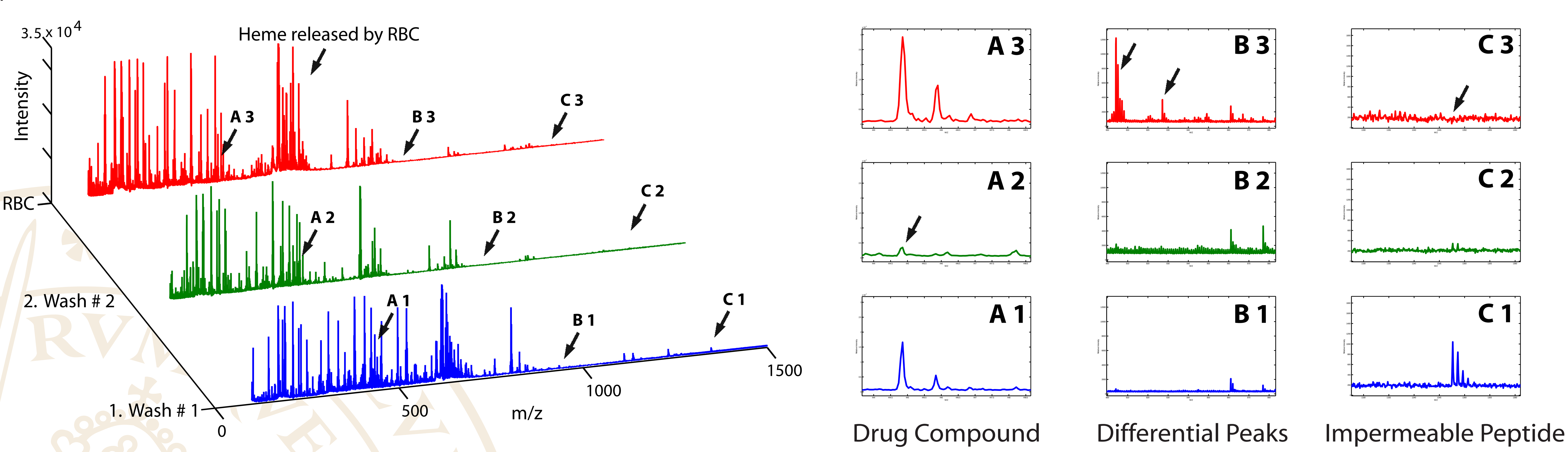

Figure 4. Analytical read-out of a single RBC cluster (~ 500 000 cells) with two wash fractions and lysis of the trapped cells. Enlargement A shows uptake of the spiked drug, B shows differential peaks originating from intracellular material released upon lysis and C shows sucessful removal of the spiked impermeable peptide.

Conclusions

A system for MS analysis of small cell populations has been implemented. This offers a controlled microenvironment, reproducible non-contact trapping, and dynamic sample handeling trough aspiration using the open capillary. This offers a versatile analysis platform with low complexity and easy integration to standard equipment.

References

[1] "Miniaturized solid-phase extraction and sample preparation for MALDI MS using using a microfabricated integrated selective enrichment target," S. Ekström, L. Wallman, D. Hök, G. Marko Varga and T. Laurell, , Journal of Proteome Research, Vol. 5, pp. 1071-1081, (2006)

Eidgenössische Technische Hochschule Zürich
Swiss Federal Institute of Technology Zurich

INSTITUT FÜR MECHANISCHE SYSTEME

Flow-free transport of particles in a macro scale chamber

Dirk Möller[1], Thomas Schwarz[1], Jurg Dual[1]

[1]Institute of Mechanical Systems, ETH Zurich, Switzerland, dirk.moeller@imes.mavt.ethz.ch

Introduction

There are needs for concentration of particles in batch mode, such as achieved with sedimentation or centrifugation. These methods are limited by either Brownian motion or lead to tightly packed agglomerates. Another solution is the use of acoustics to achieve a net mean transport of particles in a single direction[1,2,3]. Such an acoustic system can be operated in batch mode in a sealed compartment.

Method

A slow frequency sweep combined with an asymmetric excitation can be used such that an overall movement in one direction at all places within a device can be realised. The boundary which is set to vibration acts as a variable boundary. Therefore by increasing the frequency and with it the number of nodal planes, particles can be moved away from the excitation or, by decreasing the frequency continuously, particles can be moved towards the excitation boundary.

Results

Repeated frequency sweeping in a range from 1.5MHz to 2.5MHz has been used in a square (23 x 23 x 5mm) plastic (PE) chamber to collect particles along one of the sidewalls. Operating with particles with a diameter of 9µm, about 80% to 90% of the particles can be concentrated within less than 2min. Time and yield are significantly increased with 26µm particles.

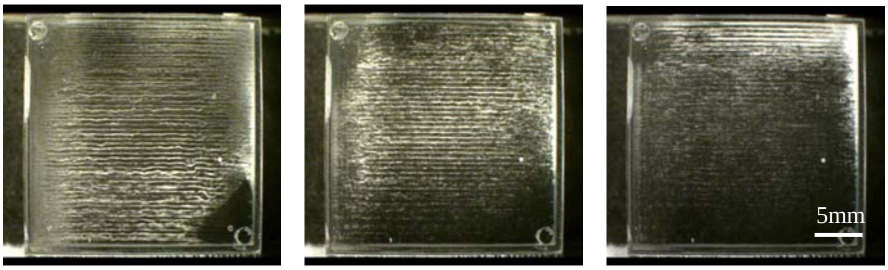

Fig. 1. Concentration of 9µm particles with a repeated frequency sweep (1.5MHz – 2.5MHz). The particle distribution is shown in initial condition on the left image, after 40s in the second image and after 120s in the third image.

A FEM simulation of such a chamber in 2D and 3D has been used to identify a significant influence of the boundaries perpendicular to the plane waves. The influence is such that for different frequencies, there is a backward movement at different spots within the chamber.

---

[1] A. Haake, Micromanipulation of Small Particles with Ultrasound, Diss. ETH No. 15681

[2] M. Saito, N. Kitamura and M. Terauchi, Jour. Of Appl. Physics, vol 92, no 12, 12 (2002), pp. 7581-7586

[3] G. Whiteworth, M.A. Grundy and W.T. Coakley, Ultrasonics, vol 29 ,12 (1991), pp. 439-444

Rotation of non spherical particles with amplitude modulation

T. Schwarz[1], G. Petit-Pierre[1], D. Möller[1], Prof. Dr. J. Dual[1]

[1]Institute of Mechanical Systems, ETH Zurich, Switzerland, schwarz@imes.mavt.ethz.ch

Introduction

The rotational manipulation of micro-particles in microfluidic devices is another step to expand the possible applications of ultrasonic manipulation. It consists in controlling the angular momentum applied to an object of very small size. The rotation speed as well as the direction of rotation are parameters which must be controlled in order to precisely manipulate the particles.

Method

Non spherical particles behave like spheres in a USW with an additional torque acting on the particle. Fibers shorter than one-fourth of the wavelength are constrained at the pressure node and are oriented perpendicular to the direction of wave propagation. It is possible to use this acoustic radiation torque for a continuous and controlled rotation of objects.
Therefore a time-varying pressure field with change of orientation of the potential well is realized with the help of the amplitude modulation of two orthogonal standing waves. By varying the amplitudes of the standing waves in x or z direction, the orientation of the force potential minima, indicated by the black arrow in figure 1, could be rotated.

Results

The 360° rotation of a glass fiber (length 200 μm) due to the amplitude modulation of two orthogonal standing waves has been shown experimentally. The device used for the experiments consists of a 3x3 mm^2 chamber etched into Silicon and covered with a glass plate. The actuation is done through a 4x4 mm^2 piezoelectric crystal fixed at the back side of the device. The actuation frequency was set to 1085 kHz with a maximum amplitude of 30 V.

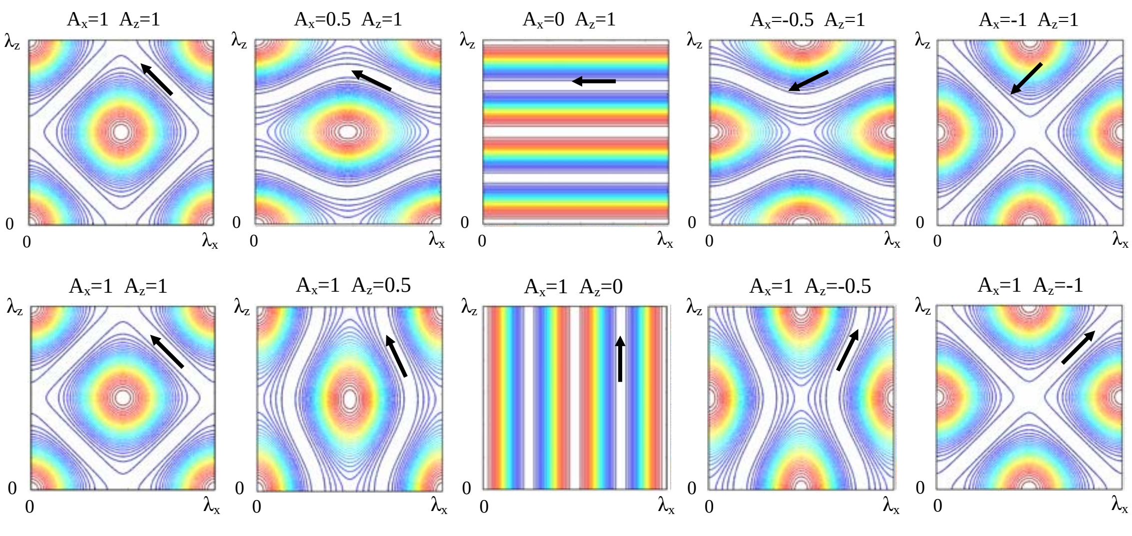

Fig. 1: Contour plot sequence of the Gor'kov force potential as result of amplitude change in x or z-direction resulting from superposition of two in phase cosine functions with identical frequency. The term A_x or A_z varies from +1 to -1. The red areas are potential maxima, the blue areas potential minima. The black arrow is representing a fiber at the force potential minima.

CFD MODELLING OF THE ACOUSTIC STREAMING INDUCED BY AN ULTRASONIC HORN REACTOR

Francisco Javier TRUJILLO[1] and Kai KNOERZER[2]
[1] CSIRO Food and Nutritional Sciences, North Ryde, New South Wales 2113, AUSTRALIA
[2] CSIRO Food and Nutritional Sciences, Werribee, Victoria 3030, AUSTRALIA

INTRODUCTION

Power ultrasonic reactors have gained a lot of interest in the food industry given the effects that can arise from sound induced cavitation. However, most of the new food processing developments have been based on empirical approaches. Thus, there is a need for mathematical models which help to understand, optimise and scale up ultrasonic reactors. In this work, a CFD model has been developed, to predict the acoustic streaming induced by an ultrasonic horn reactor.

In this work, a CFD model has been developed, to predict the acoustic streaming induced by an ultrasonic horn reactor. Acoustic streaming is a term that describes the time-average flow circulation near a vibrating surface, or the steady flow induced during the passage of an acoustic wave. The model is based on the acoustic streaming theory proposed by (Lighthill 1978), who established that at powers above 4 x10-4 W the acoustic streaming takes the form of an inertially dominated turbulent jet. The model assumes that the horn tip is an inlet where all the acoustic energy absorbed by the liquid is converted in turbulent motion, the jet. The hydrodynamic momentum rate of the incoming jet is assumed to be equal to the total acoustic momentum rate emitted by the acoustic power source. Using this assumption, the Navier-Stokes and turbulent equations were solved using COMSOL Multiphysics to determine the hydrodynamic field in the reactor; the results were compared with the experimental data obtained by (Kumar, Kumaresan et al. 2006) .CFD predictions show excellent agreement with the experimental data at all studied power densities. This model successfully describes hydrodynamic fields (streaming) generated by ultrasound fields.

MODEL DESCRIPTION

At high Reynolds numbers and sources of high acoustic power the inertia term in Naiver-Stokes equation must be included:

$$\rho\left(\vec{v}\cdot\nabla\vec{v}\right)=-\nabla p+\mu\nabla^2\vec{v}+\vec{F} \qquad (1)$$

The acoustic source releases its power as a narrow beam, where the net force (or rate of momentum) at a distance X along the sound beam is:

$$F_N=\frac{P}{c}\left(1-e^{-\beta X}\right) \qquad (2)$$

If the attenuation coefficient is very high, the streaming motion generated by the acoustic beam is a circular turbulent jet, delivering momentum at a rate .

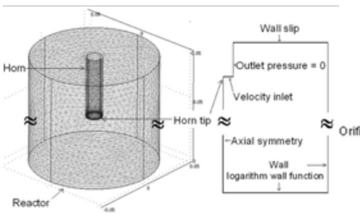

Figure 1: Schematic diagram of geometry (3D on the left) and boundary conditions (2D axial symmetric on the right).

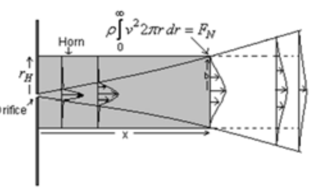

Figure 2: Schematic diagram of jet flow velocity profile superimposed in the horn.

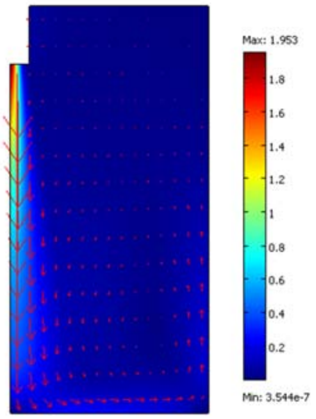

Figure 3: CFD velocity distribution predicted from approach 2 for = 35 kWm-3 and S = 0.00281.

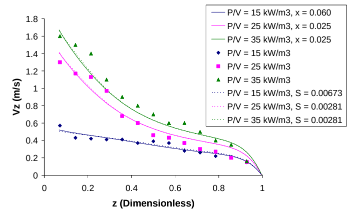

Figure 4: Axial velocity distribution below the horn tip using optimum values of x and S for approach 1 and 2 respectively.

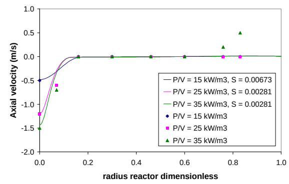

Figure 5: Radial profiles of axial velocity at different power densities for z = 0.13H. CFD prediction using approach 2 (solid lines)

(Schlichting 1979) showed that the mean flow of a turbulent jet is similar to the laminar jet solution by taking a constant eddy viscosity equal to:

$$\mu_t=0.016\left(K\right)^{1/2} \qquad (3)$$

Where $K=\rho P/c$

The ultrasonic reactor is a cylindrical as seen in figure 1. The velocity profile at the inlet is estimated following two approaches. Following approach one the velocity profile at the inlet is estimated with equations taken from (Schlichting 1979) for a turbulent jet releasing its kinematic momentum from an orifice (c.f. fig 2). Following approach two, it is assumed that the velocity profile of the acoustically generated jet flow follows a Gaussian distribution.

RESULTS

Figure 3 shows a velocity distribution inside the ultrasonic reactor. This velocity pattern is in agreement with the experimental data obtained by (Kumar, Kumaresan et al. 2006) who mapped velocities and turbulence in the reactor using Laser Doppler Anemometry (LDA). The final CFD prediction at three power densities can be seen in figure 4. Figure 5 shows the radial profiles of axial velocity at different power densities for z = 0.13H, where H is the distance between the horn tip and the bottom of the vessel. As seen in the figure CFD predictions show an excellent agreement with the experimental data following both approaches.

CONCLUSIONS

Acoustically induced ultrasound streaming at powers higher or equal than 30 W (kWm-3) can be modelled via CFD by assuming that the horn tip is an inlet where a turbulent jet flow is injected into the vessel. The hydrodynamic rate of momentum of the incoming jet can be assumed to be equal to the total acoustic momentum rate emitted by the acoustic power source. CFD predictions show excellent agreement with the experimental data at all power densities via both approaches.

CSIRO

References

LIGHTHILL, J. (1978). "Acoustic streaming." Journal fo Sound and Vibration **61**(3): 391-418.

KUMAR, A., T. KUMARESAN, et al. (2006). "Characterization of flow phenomena induced by ultrasonic horn." Chemical Engineering Science **61**: 7410-7420.

References

SCHLICHTING, H. (1979). Boundary Layer Theory, McGraw-Hill.

STUART, J. T. (1963). Unsteady Boundary Layers. Laminar Boundary Layers. L. Rosenhead. London, Oxford University Press.

Further information

contact: Francisco Javier Trujillo
phone: +61 2 94 90 84 64
email: Francisco.Trujillo@csiro.au
web: http://www.foodscience.csiro.au

www.csiro.au

Reading List

Fahy, F.1994. *Sound and Structural Vibration,* Academic Press.

Kinsler, L.E. Frey, A.R. Coppens, A.B. and Saunders, J. V. 2000. *Fundamentals of acoustics,* 4th ed, New York: Wiley.

Riley, N. 1966. On a sphere oscillating in a viscous fluid. *Q. J. Mech. Appl. Math.* 19:461–72.

Bruus, H. 2008. *Theoretical Microfluidics* Oxford University Press. Oxford.

Ristic, V. 1983.*Principles of Acoustic Devices,* Wiley.

Riley, N. 2001. Steady Streaming*, Annu. Rev. Fluid Mech.* 33:43–65.